
University of
Southampton

University of Southampton

FACULTY OF MEDICINE

Cancer Sciences

Targeting myofibroblastic cancer-associated fibroblasts to overcome T cell exclusion from tumours

by

Klaudia Piotrowska

Thesis for the degree of Doctor of Philosophy

August 2025

University of Southampton

Abstract

Faculty of Medicine

Cancer Sciences

Thesis for the degree of Doctor of Philosophy

Targeting myofibroblastic cancer-associated fibroblasts to overcome T cell exclusion from tumours

By Klaudia Piotrowska

Immune checkpoint blockade therapy (ICBT) has revolutionised cancer treatment, yet its efficacy remains limited to subset of patients. A significant barrier to successful treatment is the restricted infiltration of $CD8^+$ T cells into the tumour microenvironment (TME). Cancer-associated fibroblasts (CAFs), a key component of the TME, are highly heterogeneous and perform diverse functions, including influencing immune exclusion. Myofibroblastic CAFs (myCAFs) have been implicated in immune-excluded tumours and poor ICBT responses, highlighting the need for CAF-targeting strategies to enhance immunotherapy efficacy.

This thesis investigates the role of ataxia-telangiectasia mutated (ATM) in regulating the myCAF phenotype. We demonstrate that pharmacological inhibition of ATM in TGF-β1-differentiated fibroblasts leads to the downregulation of extracellular matrix (ECM)-associated genes and myCAF markers, while upregulating iCAF markers and altering cytokine composition. These changes correlate with enhanced $CD8^+$ T cell migration *in vitro*. Next, we explore the role of specific CAF-derived ECM proteins, CTHRC1, POSTN, and COL11A1 on myCAF phenotype and function. Using CRISPR-Cas9 knockout models, we assess whether targeting these genes influences $CD8^+$ T cell migration into tumours and enhances tumour suppressive properties in mouse models. We then investigate the activation of the cGAS-STING pathway in fibroblasts following ATM inhibition. We demonstrate that TGF-β1 suppresses the cGAS-STING pathway, whereas ATM deficiency induces a type I interferon response. Using mouse models, we show that targeting fibroblast ATM promotes intratumoural $CD8^+$ T cell infiltration and that STING expression in myCAFs is essential for suppressing tumour growth in myCAF-rich environments. Finally, we evaluate the effects of different doses of the ATM inhibitor AZD0156 on key cellular processes, including target activity inhibition, cell proliferation, cell cycle progression, DNA synthesis, and regulation of myofibroblastic markers. Our findings demonstrate that AZD0156 is effective at low doses, which may have clinical applications in minimising potential toxicities.

Our work identifies a novel pathway regulating myCAF differentiation and provides a rationale for using ATM inhibitors to overcome CAF-mediated immunotherapy resistance. By investigating ECM-targeting and ATM inhibition, we uncover new therapeutic avenues to enhance immune infiltration and improve ICBT efficacy in solid tumours.

Table of Contents

Table of Tables

Table of Figures

Table of Figures

Research Thesis: Declaration of Authorship

Print name: KLAUDIA PIOTROWSKA

Title of thesis: Targeting myofibroblastic cancer-associated fibroblasts to overcome T cell exclusion from tumours

I declare that this thesis and the work presented in it are my own and has been generated by me as the result of my own original research.

I confirm that:

1. This work was done wholly or mainly while in candidature for a research degree at this University;
2. Where any part of this thesis has previously been submitted for a degree or any other qualification at this University or any other institution, this has been clearly stated;
3. Where I have consulted the published work of others, this is always clearly attributed;
4. Where I have quoted from the work of others, the source is always given. With the exception of such quotations, this thesis is entirely my own work;
5. I have acknowledged all main sources of help;
6. Where the thesis is based on work done by myself jointly with others, I have made clear exactly what was done by others and what I have contributed myself;
7. None of this work has been published before submission

Signature: .....Date: .....

Acknowledgements

When I started my PhD over four years ago, I underestimated how challenging it would be, both scientifically and personally. I would like to take this opportunity to thank the many people who have helped me reach this stage.

Firstly, I would like to thank my supervisor, Gareth Thomas, for giving me this opportunity and for his support throughout my research journey. I am very grateful for all the advice, patience, and mentorship. I would also like to thank Chris Hanley for always finding time for me, listening, providing guidance, and sharing knowledge that has greatly contributed to my development as a scientist. My sincere thanks also go to Ian Tracy, who was there for me even when I was at my worst. Thank you for listening, understanding, and just caring.

I am grateful to BBSRC for funding this project, to SoCoBio DTP for endless development opportunities, and to Colin Robinson for making my placement in Thailand possible.

There were days when finding motivation was not easy, but I was fortunate to meet some of the best people along the way. Josie, you are the most selfless person I know, and you helped me more than you'll ever realise. I'm so glad I got to spend nearly every day, every evening, and pretty much every weekend with you over the past four years. Paige, thank you for all the laughs, the encouragement, and for making me feel human when it was most needed. You always know just what to say. I'm proud that the three of us got through this challenge together. I would also like to thank Kamila for being a great friend, thank you for sharing your knowledge and experiences. I don't think I would be where I am now without your words of wisdom. Ben, thank you for being such great company and for always being willing to help, and Mel, thank you for all the laughs and for keeping me sane.

Kasia, thank you for always being there for me and making the tough times a little easier. Lauren, thank you for helping me keep my sense of humour even during the challenges of this PhD. I couldn't ask for better friends.

I am so grateful to my partner for making this journey so much easier. Brendan, thank you for looking after me over the past couple of years. Your love, understanding, patience, and constant support have meant the world to me.

Finally, I would like to thank my family, especially my mum and dad, for believing in me and being a source of strength during the toughest times. I wouldn't be the person I am today without you. With the constant support from my parents and siblings, I know I can get through whatever life brings. I

would also like to thank my not so little sister - Lena, thank you for being my cheerleader throughout the thesis writing. I don't think I could have done this without our daily chats.

To all who have contributed to this work in one way or another, I sincerely thank you.

Definitions and Abbreviations

αSMA	Alpha smooth muscle actin
ANOVA	Analysis of variance
apCAF	Antigen presenting cancer-associated fibroblast
A-T	Ataxia-telangiectasia
ATM	Ataxia-telangiectasia mutated
ATMi	ATM inhibitor
ASPN	Asporin
ATR	Ataxia-telangiectasia and Rad3-related
AUC	Area under the curve
BAFF	B-cell activating factor
BER	Base excision repair
CAF	Cancer-associated fibroblast
CCL	Chemokine ligand
CD	Cluster of differentiation
cDNA	Complementary DNA
cGAS	Cyclic GMP-AMP synthase
Chk	Checkpoint kinase
COL	Collagen
CRC	Colorectal cancer
CRISPR	Clustered regularly interspaced short palindromic repeats
CTHRC1	Collagen triple helix repeat containing 1
CTLA-4	Cytotoxic T-lymphocyte associated protein
CXCL	C-X-C motif chemokine ligand
CXCR	C-X-C motif chemokine receptor
DC	Dendritic cell
DDR	DNA damage response
DMEM	Dulbecco’s modified eagle medium

DMSO Dimethyl sulfoxide

DNA Deoxyribonucleic acid

DNA-PKcs DNA-dependent protein kinase catalytic subunit

DSB Double-stranded break

dsDNA Double-stranded DNA

ECM Extracellular matrix

ELN Elastin

EMT Epithelial to mesenchymal transition

EndoMT Endothelial to mesenchymal transition

ERK Extracellular signal-regulated kinase

FAK Focal adhesion kinase

FAP Fibroblast activation protein

FMT Fibroblast to myofibroblast transition

FN Fibronectin

FRC Fibroblast reticular cell

gDNA Genomic DNA

H&E Haematoxylin and eosin

γH2AX H2A histone family member X phosphorylated at S139

HFFF2 Human fetal foreskin fibroblast 2

HIF-1α Hypoxia inducible factor 1 alpha

HNSCC Head and neck squamous cell carcinoma

HR Homologous repair

HSC Heat shock cognate

iCAF Inflammatory cancer-associated fibroblast

ICB Immune checkpoint blockade

ICI Immune checkpoint inhibitor

ICL Interstrand crosslinking

IFIT1 Interferon induced protein with tetratricopeptide repeats 1

IFN Interferon

IFN-I Type I interferon

IFN-γ Interferon-gamma

IHC Immunohistochemistry

IL Interleukin

iMLF Immortalised mouse lung fibroblast

IR Ionising radiation

IRF Interferon regulatory factor

ISG Interferon-stimulated gene

KO Knockout

LIF Leukaemia inhibitory factor

LOX Lysyl oxidase

MAPK Mitogen-activated protein kinase

MDSC Myeloid-derived suppressor cell

MHC Major histocompatibility complex

MLF Mouse lung fibroblast

MMP Matrix metalloprotease

MMR Mismatch repair

MOI Multiplicity of infection

mRNA Messenger ribonucleic acid

MSC Mesenchymal stromal cell

mtDNA Mitochondrial DNA

MyCAF Myofibroblastic cancer-associated fibroblast

NADPH Nicotinamide adenine dinucleotide phosphate

NER Nucleotide excision repair

NF-κB Nuclear factor-κB

NHEJ Non-homologous end joining

NK Natural killer

NOX NADPH oxidase

NSCLC Non-small cell lung cancer

P4HA3 Prolyl 4-hydroxylase subunit alpha-3

PARP Poly(ADP-ribose) polymerase

PBS Phosphate buffered saline

PCR Polymerase chain reaction

PDAC Pancreatic ductal adenocarcinoma

PDGFRα Platelet-derived growth factor receptor-alpha

PD-(L)1 Programmed cell death (ligand) 1

PDPN Podoplanin

PFA Paraformaldehyde

PI Propidium iodide

PIKK Phosphatidylinositol-3-kinase-related kinases

POSTN Periostin

RNA Ribonucleic acid

RNP Ribonucleoprotein

ROS Reactive oxygen species

RT-qPCR Reverse transcription-quantitative polymerase chain reaction

SASP Senescence-associated secretory phenotype

SD Standard deviation

SEM Standard error of the mean

sgRNA Single guide RNA

shRNA Short hairpin RNA

SSB Single-stranded break

SSBR Single-strand break repair

ssDNA Single-stranded DNA

STING Stimulator of interferon genes

TBK1 TANK-binding kinase 1

TERT Telomerase reverse transcriptase

TGF-β Transforming growth factor beta

TIL Tumour-infiltrating lymphocyte

TLS	Tertiary lymphoid structure
TMB	Tumour mutational burden
TME	Tumour microenvironment
TNBC	Triple-negative breast cancer
TNF-α	Tumour necrosis factor alpha
Treg	Regulatory T cell
UV	Ultraviolet
VCAM1	Vascular cell adhesion molecule-1
VCAN	Versican
WT	Wild-type

Chapter 1 Introduction

1.1 Tumour microenvironment

Cancer is caused by the accumulation of genetic and epigenetic changes in normal cells (Takeshima & Ushijima, 2019). Mutations arising in tumour cells can generate novel epitopes referred to as neoantigens, which are presented on the tumour cell surface by major histocompatibility complex (MHC) proteins (C. Jiang et al., 2022). Under normal circumstances, cytotoxic immune cells, such as $CD8^+$ T cells, recognise neoantigens and eliminate the more immunogenic cancer cells. During this elimination phase, cancer cell variants that are less immunogenic evade immune surveillance and continue to proliferate, leading to tumorigenesis (Gonzalez et al., 2018). Although the first oncogenic event involves generation of genetic mutations that enable cancer cells to proliferate, such mutations are generally insufficient to drive tumorigenesis on their own. Tumour formation is also a result of reciprocal interactions between cancer cells, stromal cells (including fibroblasts), infiltrating immune cells, and the non-cellular components of the tumour microenvironment (TME), such as fibrous structural proteins that constitute a dense extracellular matrix (ECM) **(Figure 1.1)** (R. Wei et al., 2020).

The concept of the tumour microenvironment dates to 1863, when Rudolph Virchow observed that leukocyte infiltration characterises solid tumours (Maman & Witz, 2018). In 1889, Stephen Paget introduced the “seed and soil” hypothesis, suggesting that some tumour cells (the “seed”) grow preferentially in the microenvironment of select organs (the “soil”). He concluded that metastases occurred only when the appropriate seed was implanted in suitable soil (Langley & Fidler, 2011; Maman & Witz, 2018). By identifying the relationship between primary tumours and their secondary sites, Paget became a pioneer in the concept of the tumour microenvironment. Following Paget’s discovery, research in this area expanded rapidly, with various studies showing that fibroblasts are a predominant stromal cellular component in most solid tumours and play a crucial role in tumour progression (Kumar et al., 2018; Olumi et al., 1999; Vaish et al., 2021; Wong et al., 2022). Fibroblasts associated with cancer have been termed cancer-associated fibroblasts (CAFs) (Kalluri, 2016).

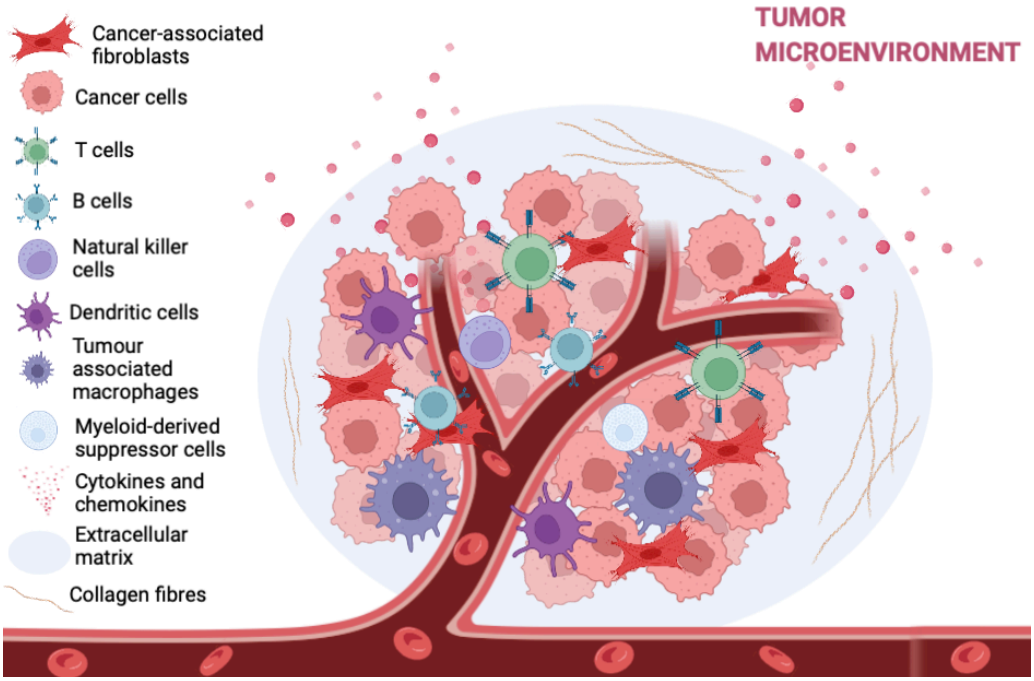

Figure 1.1: Components of the tumour microenvironment. The tumour microenvironment comprises both cellular and extracellular components. The cellular components consist of immune cells, stromal cells, and tumour cells. The extracellular components include the extracellular matrix, secreted proteins, and signalling molecules. Interactions within the tumour microenvironment play a crucial role in regulating tumorigenesis, metastasis, and cancer progression.

1.2 Fibroblasts

Fibroblasts are relatively quiescent cells that specialise in the synthesis and remodelling of the extracellular matrix, making them essential for maintaining tissue integrity (C. Li et al., 2014). Quiescence is characterised by a reversible state in which cells do not divide but retain the ability to re-enter the cell cycle and proliferate (Marescal & Cheeseman, 2020). Quiescent cells are generally associated with reduced metabolic activity, fibroblasts in this state remain metabolically active while not dividing. Fibroblasts are capable of degrading, synthesising and secreting ECM components, though the amounts secreted are tightly regulated (Lemons et al., 2010). Fibroblasts are emerging as having a diverse range of functions, including contributing to tissue homeostasis, defence against pathogens, and wound healing (Chansard et al., 2021). They can sense and respond to various tissue-damaging signals to orchestrate tissue repair. To perform this function, fibroblasts must transition from their quiescent state to a more contractile, myofibroblastic state. Transforming growth factor-β (TGF-β) is a key regulator of this phenotypic change (Plikus et al., 2021). While the transition to a myofibroblastic state is essential for tissue repair, fibroblasts at the site of a tumour, known as cancer-associated fibroblasts, differ from those in healthy tissue in that they are not removed by apoptosis when the activating stimulus is attenuated. As a result, fibroblasts continue to proliferate and differentiate into CAF subtypes,

becoming a predominant cell type within the TME (S. Wang et al., 2022). Dysregulated fibroblasts are also implicated in various range of inflammatory diseases and fibrosis (K. Wei et al., 2021).

Currently there are no molecular markers that are unique to this cell type. Vimentin and platelet-derived growth factor receptor-α (PDGFRα) are sometimes used but alongside other criteria such as morphology, location, and lack of lineage markers for epithelial cells, endothelial cells and leukocytes (Sahai et al., 2020). Fibroblasts are described as elongated spindle-shaped or stellate (star-like) cells (Movat & Fernando, 1962).

1.2.1 Role of fibroblasts in wound healing

Fibroblasts play a critical role in normal wound healing and have been extensively studied in this context. The wound healing process consists of four phases: haemostasis, inflammation, proliferation, and matrix remodelling (Schultz et al., 2011). The haemostasis phase begins with capillary damage, triggering the formation of a blood clot primarily composed of fibrin. A provisional matrix, consisting of fibrin, vitronectin, and fibronectin, fills in the lesion allowing various cells to migrate toward the site of injury (Foster et al., 2018). Subsequently, neutrophils arrive early and release cytokines, initiating the inflammatory stage. This inflammatory response is complex and transitions into the proliferative phase, during which macrophages, keratinocytes, endothelial cells, and fibroblasts become activated. These cells orchestrate wound closure, matrix deposition and angiogenesis (Wilkinson & Hardman, 2020). Resident fibroblasts and mesenchymal-derived fibroblasts respond to signalling molecules secreted by platelets, endothelial cells, and macrophages. Among these, TGF-β is a key factor that induces fibroblasts to transdifferentiate into highly contractile myofibroblasts characterised by elevated αSMA$^+$ (α-smooth muscle actin) expression (Malmstrom et al., 2004). Fibroblasts also degrade the provisional matrix and replace it with granulation tissue rich in fibronectin, collagens, and proteoglycans (Moretti et al., 2021). This granulation tissue acts as a scaffold, supporting angiogenesis and mature ECM deposition. ECM remodelling spans the entire wound healing process (Diller & Tabor, 2022). The response concludes when macrophages, endothelial cells, and fibroblasts undergo apoptosis or leave the injury site, resulting in scar formation (Foster et al., 2018; Moretti et al., 2021; Wilkinson & Hardman, 2020).

In chronic wounds, this phase fails to resolve, preventing the successful completion of the wound healing process. Interestingly, Dvorak (1986) observed that tumours display features similar to tissue regeneration, including immune response, cell proliferation, cell migration, tissue remodelling, and cell death (Dvorak, 2015; Ribatti & Tamma, 2018). Tumours often sustain an inflamed phenotype and ongoing ECM remodelling, which is why they are sometimes referred to as “wounds that do not heal”. At the same time, Dvorak suggested that “solid tumours are heterogenous in structure, and different parts of the same tumour may exhibit different stages of

healing". The desmoplastic response refers to the presence of a dense collagenous stroma within the TME. Dvorak proposed that this desmoplastic stroma surrounding tumour cells may act as a 'cacoon' shielding tumours from host's inflammatory response. Historically, desmoplasia was thought to represent the condensation of pre-existing collagen (Dvorak, 2015; Ribatti & Tamma, 2018). However, current evidence indicates that this collagen, along with other components of the ECM, is actively synthesised by myofibroblasts, as will be discussed later (Barsky et al., 1982).

1.3 Cancer-associated fibroblasts

1.3.1 Origins of cancer-associated fibroblasts

Cancer-associated fibroblasts arise from diverse cellular sources including resident fibroblasts (quiescent fibroblast), fibrocytes, myeloid cells, adipocytes, pericytes, smooth muscle cells, endothelial cells, epithelial cells, mesenchymal stromal cells, stellate cells, and mesothelial cells (De et al., 2021; Ren et al., 2025; Z.-G. Zhang et al., 2021). This multiplicity of origins contributes to the broad phenotypic and functional diversity observed in CAF subpopulations (**Figure 1.2**). In addition, studies have shown that these diverse phenotypes are able to interconvert, reflecting the complexity and plasticity of the tumour microenvironment (Biffi et al., 2018; Miyake & Kalluri, 2014).

Tissue-resident fibroblast activation is one of the major sources of CAFs. Tissue-resident fibroblasts respond to tumour-derived factors such as TGF-β (Yoon et al., 2021), hepatocyte growth factor (HGF)(X. Wu et al., 2013), sonic hedgehog (SHH)(H. Tian et al., 2009), stromal-derived factor-1 (SDF-1)(Kojima et al., 2010), platelet-derived growth factor (PDGF)(Pierce et al., 1991), and reactive oxygen species (ROS)(Arcucci et al., 2016). These modulators result in the fibroblasts undergoing a phenotypic transformation from their quiescent state to myofibroblastic state characterised by α-SMA expression and enhanced contractility (Micallef et al., 2012).

Mesenchymal stem/stromal cells (MSCs) are multipotent stem cells characterised by their ability to self-renew and differentiate into various cell types, including adipocytes, chondrocytes, osteoblasts, myocytes, and neurones (S. Ma et al., 2013). MSCs migrate to tumour sites in response to cytokines and chemokines secreted by cells within the TME. Due to the large number of these factors, they will not be described in detail here; however, further information can be found in reviews by Antoon et al., 2024; Hill et al., 2017 and Panda et al., 2024. Within the TME, MSCs transition into CAFs under the influence of TGF-β and hypoxia-inducible factors (HIFs) (I. Kim et al., 2022). Similarly, the pericyte-CAF transition is modulated by PDGF-BB-PDGFRβ (Platelet-Derived Growth-Factor-BB-Platelet-Derived Growth Factor Receptor Beta) signalling (F. Wu et al., 2021). PDGF-BB is secreted by a variety of cells in the TME and binds to the PDGFRβ on pericytes, initiating their migration and activation of intracellular signalling pathways, including

phosphoinositide 3-kinase - protein kinase B (PI3K-AKT) and mitogen-activated protein kinase (MAPK) pathways (F. Wu et al., 2021). These pathways also have roles in CAF formation (Fang et al., 2022).

Emerging evidence highlights the roles of epithelial and endothelial cells as additional sources of CAFs. Through epithelial-to-mesenchymal transition (EMT) driven by TGF-β1 and epidermal growth factor (EGF), and endothelial-to-mesenchymal transition (EndoMT) driven by TGF-β1, these cells express the mesenchymal marker fibroblast-specific protein-1 (FSP1), enabling them to acquire mesenchymal characteristics (Okada et al., 1997; Zeisberg et al., 2007).

Advances in single cell sequencing and lineage tracing techniques have proven to be valuable tools for exploring the sources of CAFs. These studies reveal that CAF populations are not only heterogenous in their origin but also in their functional roles, ranging from ECM remodelling and immune modulation to promoting angiogenesis (Monteran & Erez, 2019).

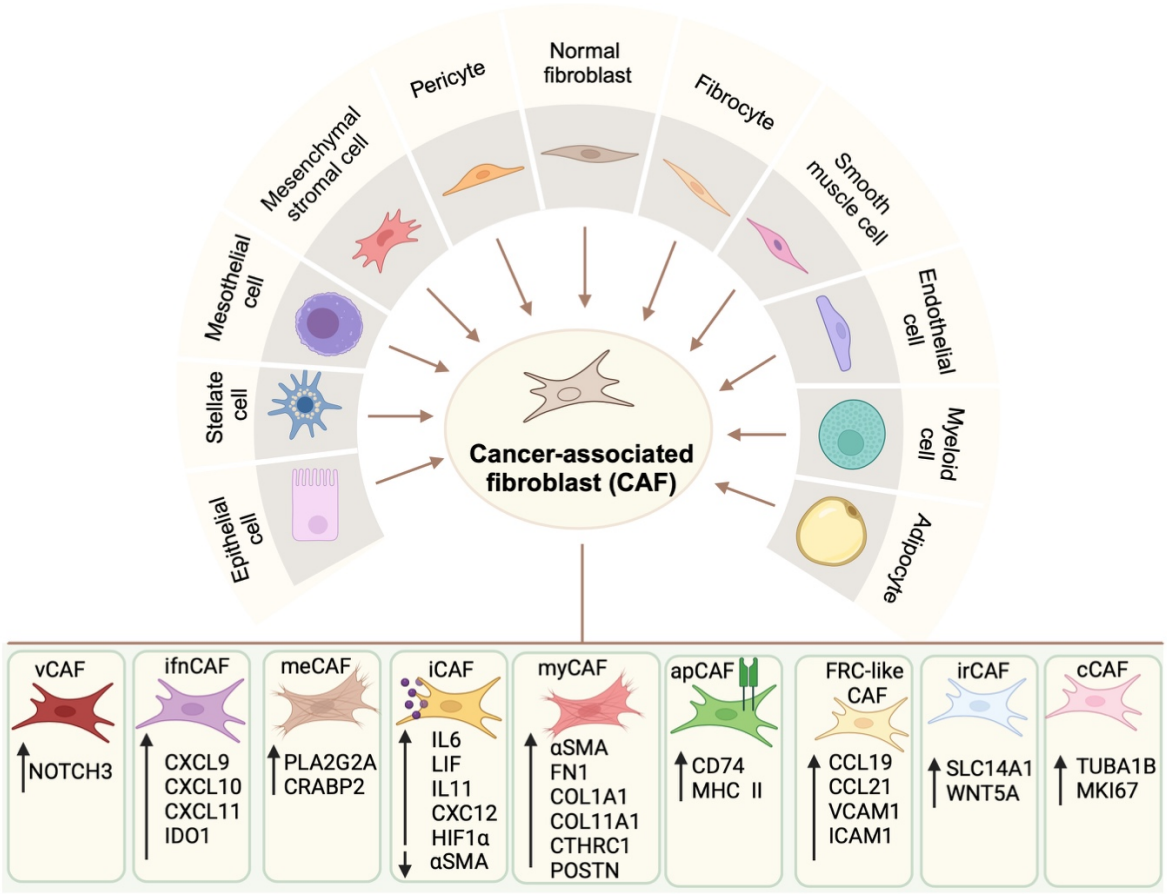

Figure 1.2: CAF origins and phenotypes. The heterogeneity of CAFs arises from the diverse origins of their precursor cells. Potential cellular sources include resident fibroblasts, fibrocytes, myeloid cells, adipocytes, pericytes, smooth muscle cells endothelial cells, epithelial cells, mesenchymal stromal cells, stellate cells, and mesothelial cells. CAFs can be classified into distinct subsets, with the main groups being myofibroblastic CAFs (myCAFs), inflammatory CAFs (iCAFs), antigen-presenting CAFs

(apCAFs), and fibroblastic reticular cell (FRC)-like CAFs. Additional subsets have been identified, including vascular CAFs (vCAFs), interferon-response CAFs (ifnCAFs), metabolically active CAFs (meCAFs), interferon-regulated CAFs (irCAFs), and cycling CAFs (cCAFs), also referred to as proliferative CAFs (pCAFs) or diving CAFs (dCAFs). Beyond their diverse origins and phenotypes, CAFs exhibit plasticity and can transition between different states.

1.3.2 The heterogeneity of cancer-associated fibroblast subpopulations

Cancer-associated fibroblasts coexist as heterogenous populations within the TME, displaying considerable variability in their molecular signatures not only across different cancer types but also within the same tumour (Kanzaki & Pietras, 2020). Despite significant advances in understanding their roles, the full spectrum of CAF subpopulations and their precise functions remain incompletely understood. To address this complexity, bioinformatics approaches, including single-cell RNA sequencing and spatial transcriptomics, have emerged as powerful tools to classify CAFs into distinct phenotypes (Cords et al., 2023). These methodologies are shedding light on the dynamic and context-dependent nature of CAF heterogeneity, offering a framework to unravel their diverse contributions to tumour progression and therapeutic resistance.

1.3.2.1 Myofibroblastic CAFs

Myofibroblastic CAFs (myCAFs/myoCAFs) are a subset of cancer-associated fibroblasts characterised by features of myofibroblasts - highly contractile cells involved in extracellular matrix deposition and remodelling within the TME. As previously described, myCAFs form a barrier around cancer cells, hindering immune cell infiltration into the TME. In pancreatic ductal adenocarcinoma (PDAC), myCAFs were initially identified as periglandular fibroblasts that express high levels of fibroblast activation protein (FAP) and α-smooth muscle actin (Öhlund et al., 2017). Öhlund et al. (2017) demonstrated that pancreatic stellate cells differentiate into myCAFs when exposed to TGF-β1. The use of recombinant TGF-β1 to induce fibroblast-to-myofibroblasts transition (FMT) *in vitro* is now a well-established method for myofibroblast differentiation. This CAF subtype is distinct in its lack of inflammatory cytokine expression and is characterised by higher expression of ECM proteins, which include collagens (e.g. COL1A1, COL1A2, COL11A, COL5A1), proteoglycans (e.g. VCAN, DCN, SDC1), and glycoproteins (e.g. FN1, CTHRC1, POSTN)(Croizer et al., 2024; E. Li et al., 2024; Salimian et al., 2024; G. Q. Zhu et al., 2023). As research expands, CAFs involved in ECM organisation and remodelling are referred to by various terms, including matrix CAFs (mCAFs), desmoplastic CAFs (dCAFs), TGF-β-

activated CAFs, ECM-remodelling CAFs, classical CAFs (cCAFs), and potentially many others (Kazakova et al., 2024). Pan-cancer survival analyses have revealed that myCAFs are associated with poor prognoses across multiple cancer types (B. Li et al., 2021).

1.3.2.2 Inflammatory CAFs

Inflammatory CAFs (iCAFs) primarily contribute to immune regulation and inflammation within the TME. Unlike myCAFs, iCAFs are less contractile and are typically located farther from cancer cells (Öhlund et al., 2017). In PDAC, iCAFs are characterised by low αSMA expression and high interleukin-6 (IL-6) expression (Öhlund et al., 2017). Additional markers identified through single-cell RNA sequencing (scRNA-seq) include LIF, IL-8, IL-11, CXCL1, CXCL2, CXCL12, CXCL14, C3, C7, CCL2, HIF1α, CFD, APOD, FBLN1, PTGDS, and GSN (Biffi et al., 2019; De La Jara Ortiz et al., n.d.; Elyada et al., 2019; Geng et al., 2021; B. H. Jenkins et al., 2025; Kazakova et al., 2024; Öhlund et al., 2017). *In vitro* induction of the iCAF phenotype is commonly achieved by treating fibroblasts with either IL-1α or IL-1β in combination with tumour necrosis factor-α (TNF-α). These cytokines, secreted by cancer cells, have been shown to upregulate iCAF markers (Biffi et al., 2019). The role of iCAFs appears to be context dependent, exhibiting both pro-tumorigenic and anti-tumorigenic effects depending on the cancer type. For example, in head and neck squamous cell carcinoma (HNSCC), bladder cancer (BCa), and low-grade glioma (LGG), a high abundance of iCAFs correlates with poor prognosis and lower response to immunotherapy (H. Chen et al., 2022; Galbo et al., 2021; Mou et al., 2023). Similarly, in rectal cancer, iCAF presence is associated with poor prognosis and reduced response to chemotherapy (Nicolas et al., 2022). Conversely, in PDAC, a higher abundance of iCAFs has been linked to improved prognosis (Hu et al., 2022).

1.3.2.3 Antigen-presenting CAFs

Antigen-presenting CAFs (apCAFs) are characterised by the expression of MHC class II molecules, which are essential for presenting peptide antigens to $CD4^+$ helper T cells (Elyada et al., 2019; Roche & Furuta, 2015). Additionally, apCAFs express CD74, a gene encoding the invariant chain that stabilises MHC class II complexes and facilitates antigen processing (Schröder, 2016). However, apCAFs lack the costimulatory molecules required to induce T cell proliferation (Elyada et al., 2019). In pancreatic cancer, mesothelial cells can transition into apCAFs by downregulating mesothelial features and acquiring fibroblastic characteristics. This transition has been confirmed *in vitro* through induction with IL-1 and TGF-β1 (H. Huang et al., 2022). Notably, in PDAC, apCAFs have been reported to lack any significant prognostic impact (B. Hu et al., 2022).

1.3.2.4 Fibroblast reticular cell-like CAFs

Reticular-like CAFs (rCAFs), also known as fibroblast reticular cell (FRC)-like CAFs, represent a subset of CAFs that share functional and molecular similarities with FRCs found in secondary lymphoid organs (S. Guo et al., 2023). In these organs, FRCs play a critical role in directing immune cell interactions and activation (De Martin et al., 2023). FRCs are characterised by specific molecular markers, including CCL19, CCL21, vascular cell adhesion molecule-1 (VCAM1), and intracellular adhesion molecule-1 (ICAM-1) (S. Guo et al., 2023). An increasing number of studies have highlighted the presence of tertiary lymphoid structures (TLSs) – immune cell aggregates found in non-lymphoid tissues, within certain tumours (Sautès-Fridman et al., 2019). The presence of TLSs is generally associated with favourable outcomes, such as improved response to immune checkpoint blockade (ICB), better prognosis and survival rates, and a reduced risk of recurrence in solid tumours (Schumacher & Thommen, 2022; Z. Zhao et al., 2021). Research has demonstrated that FRC-like CAFs within the TME exhibit tumour-suppressive functions. These include initiating and promoting TLS formation and secreting chemokines that support lymphocyte homeostasis (S. Guo et al., 2023). These findings emphasise that specific CAF subsets can exert anti-tumour functions, highlighting the diversity and complexity of CAF roles in cancer biology.

1.3.2.5 Other subtypes of CAFs

In addition to the four primary CAF subtypes, single cell sequencing studies have revealed several other subsets. Vascular CAFs (vCAFs) are characterised by high NOTCH3 expression, linking them to roles in angiogenesis and vascular remodelling (Cords et al., 2023). Interferon-regulated CAFs (irCAFs) are activated by type I interferons (IFN-1) and exhibit elevated expression of markers such as SLC14A1 and WNT5A, which are associated with promoting tumour stemness. Additionally, irCAFs express high levels of NRG1, BMP5, and STC1, which are involved in active cellular processes (Z. Ma et al., 2022; Xiao et al., 2023). Interferon-response CAFs (ifnCAFs) have been identified by the upregulation of genes responsive to interferons, including CXCL9, CXCL10, CXCL11, and IDO1. These CAFs also exhibit high differential expression of genes associated with chronic inflammation, such as IL-32 (Cords et al., 2023). Cycling CAFs (cCAFs), also known as proliferative CAFs (pCAFs) or dividing CAFs (dCAFs), are distinguished by elevated expression of genes involved in cell division, including TUBA1B and MKI67. These CAFs also show higher expression of cell cycle-related genes such as BIRC5 and TOP2A, as well as FOXM1, a key regulator of proliferation (Bartoschek et al., 2018; Cords et al., 2023; Galbo et al., 2021). Metabolically active CAFs (meCAFs) are characterised by high expression of genes such as

PLA2G2A and CRABP2, which are associated with translation, mitochondrial elongation, and glycolysis. In PDAC, a high expression of the meCAF signature has been linked to a greater risk of metastasis and poor prognosis but also a better response to immunotherapy (Y. Wang et al., 2021).

Recent advancements in research into CAFs have identified various subtypes and clusters. However, despite the identification of these subtypes using comparable markers, inconsistent nomenclature poses challenges to standardisation. For instance, the term 'dCAF' has been used to describe both desmoplastic CAFs and dividing CAFs, even though these represent distinct biological characteristics (Cords et al., 2023; K. T. Kim et al., 2024). Adding to the complexity, studies suggest that CAF subtypes exhibit plasticity rather than being fixed in terminally differentiated states (Öhlund et al., 2017). This dynamic nature complicates efforts to categorise CAFs and understand their diverse roles within the TME. Furthermore, several factors are known to drive CAF specialisation including stromal and tumour secretomes, epigenetics, miRNAs, metabolic reprogramming, oxidative stress, hypoxia, shear stress within the ECM, and the indirect effect of radiotherapy or drug therapy (De et al., 2021). These influences collectively contribute to the heterogeneity of CAFs.

1.4 Mechanisms of myofibroblast formation

1.4.1 TGF-β signalling pathways

The phenotypic transition of fibroblasts into their myofibroblastic state is predominantly controlled by TGF-β both *in vivo* and *in vitro*. TGF-β is produced as an inactive complex that must be activated to exert its functional effects. Latent TGF-β is secreted as part of a large latent complex (LLC), which consists of a latency-associated peptide (LAP) and a TGF-β-binding protein (LTBP) (Robertson et al., 2015). Activation of TGF-β requires dissociation from this complex, which can occur through various mechanisms, including the action of integrins, proteases, deglycosidases, and other proteins. Physiochemical factors such as reactive oxygen species (ROS), heat, physical shear, extreme pH, detergents, and ionizing or ultraviolet radiation can also activate TGF-β (Robertson & Rifkin, 2016). Once activated, TGF-β signals primarily through the canonical pathway involving the Smad family of transcriptional regulators (Deng et al., 2024; Massagué & Wotton, 2000). The signalling cascade begins when TGF-β binds to the TGF-β type II receptor (TGF-βRII), which subsequently phosphorylates the TGF-β type I receptor (TGF-βRI). This receptor activation phosphorylates the transcription factors Smad2 and Smad3. The phosphorylated Smad2/3 form a heterodimer with Smad4 in the cytoplasm, and this complex translocates to the nucleus, where it regulates the transcription of TGF-β target genes (Stockwell

& Schreiber, 1998). Regulation of this pathway occurs through inhibitory Smads, such as Smad6 and Smad7, which bind to activated type I receptors and block signal transduction, thereby suppressing TGF-β-mediated effects (Kamiya et al., 2010; F. Wu et al., 2021).

Canonical TGF-β signalling relies on Smad2/3 proteins as central mediators (Nakao et al., 1997; Stockwell & Schreiber, 1998). In contrast, non-canonical TGF-β signalling encompasses a variety of intracellular pathways activated independently of Smad2/3(Trojanowska, 2009). These pathways are highly complex, and a comprehensive discussion is beyond the scope of this section. However, TGF-β is known to activate several SMAD-independent pathways, including extracellular signal-regulated kinase (ERK), Rho guanosine triphosphatase (GTPase), p38 MAPK, c-Jun N-terminal kinase (JNK), nuclear factor-κB (NF-κB), phosphoinositide 3-kinase (PI3K)/AKT, and Janus kinase (JAK)/signal transducer and activator of transcription (STAT) signalling (Deng et al., 2024). Furthermore, Wu et al. (2021) provide an extensive summary of findings regarding the crosstalk between CAFs and cancer cells, highlighting the intricate interplay mediated by these signalling pathways.

1.4.2 Hypoxia

Hypoxia activates hypoxia-inducible factor-1 (HIF-1α), a transcription factor known to regulate key processes involved in tissue repair. HIF-1α induces the expression of TGF-β and vascular endothelial growth factor (VEFG), both of which are crucial for tissue healing, with VEGF playing a pivotal role in angiogenesis (Musyoka et al., 2013). The formation of new blood vessels, along with extracellular matrix deposition and remodelling, supports tissue repair. However, hypoxia is also a hallmark of solid tumours and has been correlated with poor prognosis in cancer patients (Jing et al., 2019). Under normal oxygen conditions, HIF-1α is rapidly degraded by the prolyl hydroxylases (PHDs)(Distler et al., 2004). In hypoxic conditions, reduced PHD activity prevents HIF-1α degradation, allowing it to accumulate in the cytoplasm and translocate to the nucleus (Singh et al., 2020). In the nucleus, HIF-1α dimerises with the HIF-1β subunit, forming the HIF-1 transcription factor complex. This complex binds to hypoxia-response elements (HREs) in the promoters of target genes, including TGF-β, and activates their transcription (Hung et al., 2013; Zimna & Kurpisz, 2015).

Additionally, HIF-1α has been shown to enhance epithelial-to-mesenchymal transition *in vitro*, a process thought to contribute to the origin of CAFs (Higgins et al., 2007). However, it is important to note that CAFs are a heterogenous population, and the effects of hypoxia on CAFs may vary depending on their subtype. In fact, studies have shown that the response of fibroblasts to hypoxia is tissue dependent. For example, subcutaneous, dermal, and heart fibroblasts exhibit decreased α-SMA expression under hypoxic conditions, whereas lung and liver fibroblasts show increased expression of α-SMA (Modarressi et al., 2010). Another study demonstrated that hypoxia strongly induces tumour IL-1α expression, which is required for the formation of iCAFs. These inflammatory fibroblasts were

found to be enriched in the hypoxic regions of PDAC (Mello et al., 2022). This study provides new insights into the impact of hypoxia on CAF heterogeneity. Overall, the research outlined suggests that hypoxia not only influences TGF-β signalling and promotes fibroblast-to-myofibroblast transition but also indicates that tissue-specific mechanisms contribute to heterogeneity of CAFs.

1.4.3 Mechanotransduction

Mechanotransduction refers to the process by which mechanical stimuli are converted into biochemical reactions and cellular responses (M. A. Hill & Meininger, 2012) . Forces such as compression and tension, generated by the extracellular matrix or cell-cell interactions, are key determinants of cell fate in organ development and tissue repair. The ECM, whose composition varies by tissue type, affects rigidity and elasticity. These mechanical properties create a complex 3D-network that profoundly influences biological processes. For example, ECM stiffness regulates cell growth, migration, and differentiation (Cai et al., 2021).

Myofibroblasts, characterised by their α-SMA bundles that provide contractile capabilities, play a crucial role in wound healing. They contract wounds after sufficient ECM deposition and remodelling (Kuehlmann et al., 2020). However, in pathological conditions where mechanical homeostasis is disrupted, myofibroblasts replace functional tissue, leading to a feedback loop of excessive mechanotransduction. In this cycle, a stiffer matrix enhances myofibroblast contraction and ECM deposition, which in turn further stiffens the matrix (Hinz, 2010).

A key component of this process involves TGF-β, which is activated through interactions with various integrins. These integrins bind to the latent TGF-β complex generating mechanical tension that releases TGF-β in its active form. At focal adhesions, integrin-ECM interactions generate cellular tension, which plays a pivotal role in activating TGF-β (Y. E. Zhang, 2018). The release of active TGF-β subsequently promotes fibroblast differentiation into myofibroblasts.

Solid tumours often exhibit abnormally stiff tissues due to excessive ECM accumulation and contraction (Paszek et al., 2005). Mechanotransduction pathways involving transcriptional coactivators like YAP (yes-associated protein) and TAZ (transcriptional coactivator with PDZ-binding motif) are highly active in such environments (X. Zhang et al., 2018). YAP and TAZ are downstream effectors of the Hippo pathway, which modulates cell proliferation, differentiation and survival. Dysregulation of this pathway is implicated in various diseases, including cancer (M. Fu et al., 2022). When the Hippo pathway is activated, YAP and TAZ are phosphorylated, leading to their cytoplasmic sequestration and degradation. However, mechanical cues such as ECM stiffening suppress the Hippo pathway, allowing unphosphorylated YAP and TAZ to translocate into the nucleus. There, they associate with DNA-binding transcription factors like TEAD to regulate gene expression (Jafarinia et al., 2024). In cancer, YAP and TAZ upregulate genes associated with immune suppression, cell cycle regulation, anti-apoptosis, migration/invasion,

metabolism, EMT, and stem cell properties (Yamaguchi & Taouk, 2020). For example, YAP1 expression was found to be significantly upregulated in the prostate cancer stroma, and when YAP1 expression was experimentally increased in normal fibroblasts, they transitioned into CAFs within the TME (T. Shen et al., 2020). Further *in vitro* studies provide additional evidence of mechanotransduction's role in fibroblast-to-myofibroblast differentiation. Primary cardiac fibroblasts cultured on stiff plastic differentiate into myofibroblasts, whereas culturing these cells on soft hydrogels disrupts mechanotransduction and prevents differentiation for up to nine days (Gilles et al., 2020). Another study demonstrated that fibroblasts adopt a morphology associated with stiffer substrates when grown to confluence and form cell-cell junctions on soft substrates. Researchers propose that cells may possess a binary sensor at membrane junction sites. On softer substrates, cells maintain a relaxed, rounded morphology, but on stiffer or equally stiff substrates, cells exhibit increased contractility and stress fibre formation (Yeung et al., 2005). While *in vitro* conditions differ significantly from *in vivo* environments, these findings highlight the critical role of mechanotransduction in driving fibroblast differentiation into myofibroblasts. This process, whether occurring in wound healing or pathological conditions such as cancer, underscores the interplay between mechanical cues and cellular responses.

1.4.4 Reactive oxygen species

Reactive oxygen species (ROS) are generated from both endogenous sources, such as mitochondria, NADPH oxidases, the endoplasmic reticulum, and peroxisomes, and exogenous sources, including alcohol, tobacco smoke, pollution, radiation, and certain drugs. At low to moderate levels, ROS have beneficial effects on various physiological functions, including regulating the cell cycle and programmed cell death, promoting angiogenesis, facilitating phagocytosis, and supporting antimicrobial functions and inflammatory responses (Dan Dunn et al., 2015; Patel et al., 2017; Phaniendra et al., 2015; Shekhova, 2020). However, excessive ROS levels can damage the integrity of biomolecules such as lipids, proteins, and nucleic acids, leading to increased oxidative stress, which has been implicated in numerous diseases (Phaniendra et al., 2015). In the context of carcinogenesis, ROS contribute to DNA damage, deregulate gene expression and signalling, and influence cellular functioning and stemness, thereby facilitating the development of cancer hallmarks (A. Q. Khan et al., 2021). ROS also play a key role in activating TGF-β. Specifically, ROS activate latent TGF-β either directly, through oxidation of LAP, or indirectly, by activating matrix metalloproteinases (MMP-2 and MMP-9), which cleave LAP to release active TGF-β. Furthermore, ROS can induce TGF-β via non-canonical pathways, including p38, JNK, ERK, NFκB, PI3K, and MAPK signalling cascades (C. H. Chang & Pauklin, 2021). ROS also negatively regulate PHD activity, leading to the stabilisation of HIF-1α. Reduced PHD activity prevents HIF-1α degradation, allowing it to accumulate in the cytoplasm and

translocate to the nucleus, where it activates gene expression (Liang et al., 2022). The roles of TGF-β and HIF-1α in the fibroblast-to-myofibroblast transition have been described in previous sections. Additionally, TGF-β promotes ROS production, establishing a feedback loop that sustains myofibroblast differentiation. This occurs through various mechanisms, including the upregulation of the NOX4 NADPH oxidase gene expression, the direct activation of NADPH oxidase, or by decreasing mitochondrial complex IV activity, which disrupts mitochondrial membrane potential and increases ROS production (G. Zhou et al., 2009). The nicotinamide adenine dinucleotide phosphate (NADPH) oxidase (NOX) family consists of membrane-bound enzymes whose primary function is to transfer electrons across cellular membranes to molecular oxygen, leading to the controlled generation of ROS under normal physiological conditions. This specialised role of NOX enzymes distinguishes them from other endogenous ROS sources, where ROS are typically by-products of other oxidative reactions. The NOX family includes several isoforms: NOX1-5, DUOX1 and DUOX2 (Sedeek et al., 2013; Tarafdar & Pula, 2018). Among these isoforms, NOX4 is significantly upregulated in various human cancers and is strongly associated with the accumulation of myCAFs. NOX4 has been shown to regulate fibroblast-to-myofibroblast transdifferentiation by generating intracellular ROS, independently of sustained TGF-β signalling. Ionizing radiation, used as an alternative method to upregulate NOX4, also induced myofibroblast transdifferentiation through a delayed increase in ROS levels. Furthermore, inhibition of NOX4 has been shown to revert the myCAF phenotype, characterised by α-SMA expression, back to a more fibroblast-like state. This finding suggests that the CAF phenotype is potentially reversible rather than terminally differentiated, further supporting the notion that CAFs are plastic (Hanley et al., 2018).

1.4.5 Senescence and SASP

Cellular senescence is a stable state of cell cycle arrest triggered in normal cells by various stimuli, including DNA damage, telomere dysfunction, oncogene activation, organelle stress, epigenetic changes, chromatin disorganisation, oxidative stress, and genotoxic stress (Di Micco et al., 2020; Kumari & Jat, 2021). The concept of cellular senescence was first demonstrated by Hayflick and Moorhead in 1961, who showed that normal cultured human fibroblasts have a finite capacity for cell division before entering an irreversible growth arrest (Hayflick & Moorhead, 1961). A more recent study has shown that senescent fibroblasts, induced by irradiation, H_2O_2, replicative senescence, or cisplatin treatment, acquire contractile α-SMA-positive characteristics with molecular and ultrastructural features of myofibroblasts. This process was found to depend on canonical TGF-β signalling, consistent with earlier findings that ROS activates latent TGF-β. Transcriptomic analysis of TGF-β1-treated myofibroblasts and senescent fibroblasts revealed overlapping gene expression profiles associated with contractile functions.

However, senescent fibroblasts exhibited reduced ECM deposition and organization compared to myofibroblasts. This distinction differentially promotes cancer cell invasion, suggesting heterogeneity within the α-SMA-positive CAF population (Mellone et al., 2016). Although this study highlights how a subtype of myofibroblasts can arise, it remains unclear how many distinct 'senescent phenotypes' exist. Evidence suggests that senescent cells exhibit heterogeneity depending on the cell type and the specific stimuli inducing senescence (Di Micco et al., 2020).

Despite being growth-arrested, senescent cells remain metabolically active and influence their microenvironment by secreting a variety of factors collectively termed the senescence-associated secretory phenotype (SASP) (Saito et al., 2024). The exact composition of the SASP is not fully defined, as it varies depending on the stimuli that induce senescence, the type of senescent cells involved, and the duration of senescence state. Key components of the SASP include interleukins such as IL-1α, IL-1β, IL-6, and IL-8; chemokines such as CXCR2, CCL2, CXCL1, and CXCL11; growth factors such as IGFBP7, AREG, IGFBP4, IGFBP3, MIC-1, and TGF-β1; and other factors such as PAI-1, HMBG1, STC1, MMP1, MMP3, BAFF, NAMPT, ANGPTL2, and complement factor D. Variations in the composition of the SASP can exhibit either anti-tumorigenic or pro-tumorigenic functions, depending on the cellular context and microenvironment (Dong et al., 2024). For example, in melanoma models, activation of the BRAF oncogene in primary fibroblasts induced the synthesis and secretion of IGFBP7. Through autocrine and paracrine pathways, IGFBP7 promoted senescence and apoptosis in cancer cells, thereby suppressing tumour growth (Wajapeyee et al., 2008). In addition to promoting cell cycle exit in neighbouring cells, SASP plays a crucial role in recruiting immune cells. For instance, in a murine model of liver carcinoma, a brief reactivation of endogenous p53 triggered a cellular senescence program associated with differentiation and the upregulation of inflammatory cytokines. This program activated an innate immune response that targeted tumour cells *in vivo*, contributing to tumour clearance (W. Xue et al., 2007). These findings illustrate how SASP can cooperate with the innate immune system to eliminate senescent and potentially pre-cancerous cells, providing an additional mechanism to prevent tumorigenesis.

Evidence suggests that cellular senescence has anti-tumorigenic effects early in life but may exert pro-tumorigenic effects in aged organisms. For instance, senescent human fibroblasts (WI-38 fetal lung cells) were shown to stimulate the proliferation of premalignant and malignant epithelial cells, but not normal epithelial cells, in culture. In mouse models, senescent fibroblast, much more so than presenescent fibroblasts, induced the formation of tumours by premalignant and malignant epithelial cells (Krtolica et al., 2001). Another pro-tumorigenic effect of senescent cells involves the IL-6-mediated recruitment of myeloid-derived suppressor cells (MDSCs) to the TME. These MDSCs antagonise the establishment of senescence in cancer cells by blocking IL-1α signalling. Furthermore, MDSCs contribute to immune evasion by inhibiting $CD8^+$ T cells,

through IL-6, and NK cells, through CCL2. As a result, the SASP promotes an immunosuppressive environment that facilitates tumour growth (L. Wang et al., 2022). These studies highlight the dual roles of the SASP in the TME, functioning as a tumour suppressor in some contexts and a tumour promoter in others, depending on factors such as age and immune response. There is an overlap between the SASP of senescent cells and the secretory phenotype of CAFs, including pro-inflammatory cytokines such as IL-6 and IL-8, as well as the growth factor TGF-β1. This overlap suggests a potential link between senescence pathways and the activation of fibroblasts in the TME (Sahai et al., 2020). Understanding the dual roles of senescence, SASP, and CAF subtypes in cancer, as well as the mechanisms underlying their interconnections, remains a critical area for further investigation.

1.5 DNA repair pathways

The DNA damage response (DDR) is a signalling cascade activated by DNA damage, resulting in cell cycle arrest and repair processes. DDR plays a crucial role in cellular senescence, marked by irreversible cell cycle arrest and the SASP, which includes the expression of inflammatory cytokines. Interestingly, during TGF-β1-induced differentiation, myofibroblasts upregulate several genes related to DNA repair (Mellone et al., 2016), highlighting a potential area for further investigation.

It is estimated that a cell experiences up to 10^5 spontaneous lesions per day, with approximately 10 of these being DNA double-stranded breaks, which are the most cytotoxic of DNA lesions (Aparicio et al., 2014). DNA lesions can arise from endogenous sources, including hydrolysis, oxidation, alkylation, and base mismatches, or from exogenous sources, such as ionizing radiation (IR), ultraviolet (UV) radiation, or chemical agents (Hakem, 2008). To protect against DNA damage, cells have evolved a network of mechanisms responsible for maintaining genomic stability. These mechanisms are collectively referred to as the DNA damage response, a signalling network that detects DNA damage, activates signalling pathways, and coordinates the repair of various DNA lesions. When DNA damage is too severe or irreparable, the DDR can trigger apoptosis or senescence to prevent the damaged cell from proliferating and potentially causing cancer or other diseases (Delia & Mizutani, 2017).

1.5.1 Types of DNA lesions

DNA base modifications are among the most common types of genomic damage. DNA bases can be damaged by processes such as oxidation, alkylation, deamination, and hydrolysis (Bauer et al., 2015). For example, oxidative damage to DNA can result from ROS, which are highly reactive

oxygen-containing molecules. These include the superoxide anion radical, hydrogen peroxide, singlet oxygen, and the hydroxyl radical (Hayat, 2015). Among the DNA bases, guanine is the most easily oxidised due to its lowest ionization potential. ROS can oxidise guanine by adding an oxygen atom, producing 8-oxo-7,8-dihydroguanine. This lesion is highly mutagenic because it tends to pair with adenine in a syn confirmation, leading to a guanine-to-thymine transversion mutation during DNA replication, particularly in cancer genomes (Hahm et al., 2022; Poetsch, 2020). Alkylating agents can react with nitrogen and oxygen atoms in DNA bases, forming covalent alkyl lesions. Methylation is a specific type of alkylation in which a methyl group is transferred to a DNA base. The O^6-position of guanine is a major site of methylation, producing O^6-methylguanine, which can mispair with thymine instead of cytosine during DNA replication, resulting in mutations (D. Fu et al., 2012). Deamination is a form of DNA damage that involves the removal of an amine group from a nucleotide base (Almatarneh et al., 2008). Hydrolytic deamination of cytosine to uracil generates a highly mutagenic DNA base lesion. If unrepaired, the uracil will pair with adenine instead of guanine during DNA replication, resulting in a C:G to T:A transition mutation. This mutation is a major contributor to spontaneous mutations and significantly impacts genomic instability (Prorok et al., 2013). Hydrolysis is involved not only in deamination but also in depurination, which results in the loss of purine bases (adenine and guanine) form DNA. In a depurination reaction, the N-glycosyl bond between the purine base and deoxyribose is cleaved by hydrolysis, leaving the DNA sugar-phosphate backbone intact and producing an abasic (AP) site (Freitas & De Magalhães, 2011). Abasic sites are locations in DNA where a base is missing. These sites are unstable and reactive, and they can lead to strand breaks, interstrand DNA crosslinks, and DNA-protein crosslinks (Amidon & Eichman, 2020). DNA base modifications can promote interstrand crosslinking (ICL), which involves the formation of covalent bonds between complementary bases on opposite DNA strands. ICL prevents the strand separation required for essential cellular processes such as DNA replication and transcription. Repair of ICL is particularly challenging because both strands are affected, causing severe cellular stress and toxicity. In contrast, intrastrand crosslinking occurs when covalent bonds form between adjacent bases on the same DNA strand. This type of lesion is less toxic than ICL (Y. Huang & Li, 2013). UV light and crosslinking chemotherapeutic agents, including cisplatin, mitomycin C, and nitrogen mustards (alkylating agents), are known to induce ICL formation (Deans & West, 2011; Nejedlý et al., 2001). DNA-protein crosslinks (DPCs) occur when proteins are covalently linked to DNA. If unrepaired, DPCs, like ICLs, disrupt critical DNA processes such as transcription and replication. During DNA replication, replication forks can stall at DPCs, making them vulnerable to collapse, leading to DNA breakage, genome instability and cancer (Perry & Ghosal, 2022).

DNA single-strand breaks (SSBs) are discontinuities in one strand of the DNA double helix, often accompanied by damaged or mismatched 5'- and/or 3' termini at the break sites. SSBs can arise from oxidised nucleotides or bases during oxidative stress, intermediate products of DNA repair

pathways, or the aborted activity of cellular enzymes, such as DNA topoisomerase 1(Hossain et al., 2018). SSBs are among the most common lesions in human cells, and efficient mechanisms have evolved to sense and repair these breaks, thereby minimising their pathological impact (Caldecott, 2024). If unrepaired, SSBs can interfere with DNA replication by obstructing replisomes. This interference can cause replication forks to collapse, potentially converting SSBs into DNA double-strand breaks (DSBs)(Xu et al., 2024).

DSBs are lesions that occur when both strands of the DNA duplex are broken, leaving no intact complementary strand to serve as a template for accurate repair. This lack of a template makes DSBs more challenging to repair than lesions affecting only one strand, such as SSBs or base modifications. DSBs can arise from exposure to exogenous agents, including ionizing radiation (IR), ROS, and mutagenic chemicals. The primary endogenous cause of DSBs is the collapse of DNA replication forks, which occurs when they encounter unrepaired DNA lesions (Chapman et al., 2012; Martín et al., 2012). Misrepair of DSBs can result in chromosomal rearrangements and structural variations (Zagelbaum & Gautier, 2023). DSBs are considered one of the most cytotoxic forms of DNA damage due to their potential to cause genomic instability and cell death.

1.5.2 Overview of DNA repair mechanisms

DNA repair is a crucial process for maintaining genomic stability, and several repair pathways exist to address different types of DNA damage. This section provides an overview of the major DNA repair pathways.

1.5.2.1 Specialised repair enzyme pathways

The DDR encompasses repair pathways such as base excision repair (BER), nucleotide excision repair (NER), mismatch repair (MMR), and single-strand break repair (SSBR), each specialised for specific types of DNA damage and errors, utilising specialised repair enzymes.

Base excision repair corrects small base lesions that do not significantly distort the DNA helix, typically caused by oxidation, alkylation, deamination, and hydrolysis. BER operates via two sub-pathways: short-patch BER, which replaces a single nucleotide, and long-patch BER, which replaces a stretch of 2-8 nucleotides (Krokan & Bjørås, 2013). The process begins with a DNA glycosylase excising the damaged base, generating an AP site. AP-endonuclease 1 (APE1) cleaves the DNA backbone at the AP site, creating a single-nucleotide gap with 3'-hydroxyl and 5'-deoxyribosephosphate (5'-dRP) ends. DNA polymerase β (Pol β) then removes the 5'-dRP moiety and inserts the correct nucleotide. Finally, a complex of DNA ligase III and XRCC1 seals the nick in the DNA backbone. Short-patch BER accounts for ~80% of BER events. In case where the 5'-dRP residue is oxidised or resistant to excision by Pol β, repair is initiated by Pol β, which adds the first nucleotide. A switch to replicative DNA polymerase δ or ε occurs, extending the repair

synthesis by 2-8 nucleotides and creating a 5'-DNA flap. This flap is excised by flap endonuclease-1 (FEN-1) in a proliferating cell nuclear antigen (PCNA)-dependent manner. Finally, DNA ligase I seals the nick, completing the long-patch BER pathway (Carter & Parsons, 2016).

Nucleotide excision repair is a DNA repair pathway specialised in removing bulky lesions that significantly distort the DNA double helix. These lesions are commonly caused by UV radiation, IR, and chemically active or metabolism-activated agents, including those that induce DNA-protein crosslinks (Chatterjee & Walker, 2017). NER operates through two distinct sub-pathways: global genome NER (GG-NER) and transcription-coupled NER (TC-NER) (Petruseva et al., 2014). GG-NER repairs lesions across the entire genome, including non-transcribed regions and silent chromatin, while TC-NER focuses on lesions in the transcribed strands of active genes. In GG-NER, damage recognition is initiated by the XPC protein, which detects distortions and binds to the damage site (Petruseva et al., 2014). In TC-NER, repair is triggered by the stalling of RNA polymerase II at a lesion on the transcribed strand (M. Duan et al., 2021; Naumenkoa et al., 2022). Following damage recognition in both pathways, the DNA around the lesion is unwound by XPB and XPD helicases, subunits of the TFIIH complex. The lesion-containing strand is excised on both sides of the damage by the nucleases XPF and XPG, resulting in the removal of a short DNA fragment. The resulting gap is filled by DNA polymerases, which synthesise new DNA using the undamaged strand as a template (Chitale & Richly, 2017; M. Duan et al., 2021). Finally, DNA ligase I seals the repaired strand, restoring the integrity of the DNA molecule and completing the repair process (Schärer, 2013).

Mismatch repair is a DNA repair pathway that corrects spontaneous base-base mismatches or small nucleotide insertion/deletion mispairs (G. M. Li, 2007). Repair is initiated by the binding of the MutS homodimer to the mismatched DNA. Next, a hemi-methylated dGATC site, located either 5' or 3' to the mismatch, is identified and cleaved through the coordinated action of MutS, MutL, MutH, and ATP (Hsieh & Yamane, 2008). While several models have been proposed for this stage of MMR, the strand-specific nick generated by MutH at the hemi-methylated dGATC site serves as the starting point for excision of the mispaired base. With the assistance of MutL, helicase II (UvrD) binds at the nick and unwinds the DNA duplex from the nick site toward the mismatch, generating single-stranded DNA (Hsieh & Yamane, 2008; G. M. Li, 2007). This unwound DNA is rapidly bound by single-stranded DNA-binding proteins SSB, which protect it from nuclease degradation. The exonuclease excises the nicked strand from the nick to slightly beyond the mismatch site. The resulting single-stranded gap is then filled by DNA polymerase III, using the undamaged strand as a template, and sealed by DNA ligase, completing the repair and restoring the integrity of the DNA molecule (G. M. Li, 2007).

The excision of DNA lesions through the BER, NER, and MMR pathways results in the formation of single-strand breaks (SSBs) as intermediates, which are subsequently repaired by their respective pathways (Caldecott, 2024). SSBs that are not part of these intermediates are quickly removed through the canonical single-strand break repair (SSBR) pathway. In this pathway, SSBs are first detected by the poly(ADP-ribose) polymerases, PARP1 and/or PARP2 (Abbotts & Wilson, 2016). Once activated, these PARPs modify themselves and other proteins by adding poly(ADP-ribose) chains, which then recruit the SSB scaffold protein XRCC1. XRCC1, in turn, recruits most, if not all, of the enzymes required for SSB repair (Horton et al., 2008; London, 2015). These include end-processing enzymes such as polynucleotide kinase/phosphatase (PNKP) and aprataxin (APTX), which generate the necessary 3'- hydroxyl and 5'-phosphate ends. These ends are crucial for the subsequent action of DNA Pol β and DNA ligase III, which are responsible for proper DNA synthesis and sealing nicks in the DNA backbone (Breslin et al., 2017; Caldecott, 2024).

1.5.2.2 Pathways regulated by the phosphatidylinositol-3 kinase-related kinases family

The repair of DNA double-strand breaks (DSBs) typically involves two main mechanisms: homologous recombination (HR) and non-homologous end joining (NHEJ) (Stinson & Loparo, 2021). The phosphatidylinositol-3 kinase-related kinases (PIKK) family, which includes ataxia-telangiectasia mutated (ATM), ataxia-telangiectasia and Rad3-related (ATR), and DNA-dependent protein kinase catalytic subunit (DNA-PKcs), is rapidly activated in response to DNA damage (Blackford & Jackson, 2017). ATM and DNA-PKcs primarily respond to DSBs. DNA-PKcs is a critical player in the NHEJ pathway. ATM also contributes to NHEJ by phosphorylating various components of this pathway. However, ATM's primarily role is in HR, where it is essential for the repair of DSBs through a homologous template (Shrivastav et al., 2009). In contrast, ATR is primarily activated by single-stranded DNA and stalled DNA replication forks. ATR plays a crucial role in stabilising replication forks, preventing their collapse into DSBs, and coordinating HR repair. This is achieved by promoting the recruitment of RAD51 and other factors to ssDNA regions to facilitate accurate repair (Bruhn & Foiani, 2019; Falck et al., 2005; H. Lu et al., 2023).

Non-homologous end joining is a DNA repair pathway that addresses DSBs by directly ligating the broken DNA ends without requiring a homologous template. Although efficient, NHEJ is considered error-prone because it can lead to insertion and deletion (indel) mutations at the repair site (Kelley, 2012). The NHEJ process begins with the recognition of DSBs by the Ku heterodimer, consisting of the Ku70 and Ku80 proteins. Once the Ku complex binds to the broken DNA ends, it recruits the DNA-PKcs to form the DNA-PK holoenzyme (Pannunzio et al., 2017). This complex is essential for the subsequent repair steps. The kinase activity of DNA-PKcs is activated either through autophosphorylation or by transphosphorylation by the ATM kinase, which is also activated in response to DNA damage (Menolfi & Zha, 2020). DNA-PKcs plays a critical role in

stabilising the DNA ends and protecting them from non-specific and excessive degradation. Phosphorylation of DNA-PKcs is also necessary for the recruitment of the Artemis endonuclease, which is essential for processing the broken DNA ends. Artemis, activated by DNA-PKcs, performs end processing by trimming overhangs or removing damaged nucleotides (Niewolik et al., 2006). This step is crucial because many DSBs have incompatible or damaged termini that must be processed before proper ligation can occur. In addition to Artemis, DNA polymerases (such as polymerase λ or polymerase μ) fill gaps or add nucleotides to create compatible ends for ligation. Once the DNA ends are properly processed, the DNA ligase IV-XRCC4 complex is recruited to catalyse the final ligation of the DNA ends, completing the repair process (Berdis, 2012; W. Jiang et al., 2015; Menolfi & Zha, 2020).

Homologous recombination repair (HRR) is a DNA repair pathway that corrects DSBs and ICLs. Compared to the error-prone NHEJ pathway, HR is a high-fidelity repair process that uses the undamaged sister chromatid as a template for repair, making it significantly less mutagenic (X. Li & Heyer, 2008). HR is restricted to the S and G2 phases of the cell cycle (Fugger & West, 2016). HR begins with the resection of broken DNA ends to generate single-stranded DNA with 3' overhangs, a critical substrate for the repair process (T. Liu & Huang, 2016). The initiation of HR is triggered by the activation of ATM, which responds to DSBs. ATM phosphorylates CtIP, enhancing its recruitment to the sites of damage, where it interacts with and stimulates the nuclease activity of MRE11, initiating the resection of the DSB ends to create short stretches of ssDNA (Anand et al., 2016; J. M. Oh & Myung, 2022). This resection process can be further extended by other nucleases and helicases, such as Exo 1 and BLM (F. Zhao et al., 2020) . The exposed ssDNA is quickly coated by replication protein A (RPA), a trimeric complex that prevents secondary structure formation and protects ssDNA from nucleases (Witosch et al., 2014). ATR is recruited to the RPA-coated ssDNA through its binding partner ATRIP, leading to the phosphorylation and activation of downstream factors, including Chk1 (Z. Qiu et al., 2017). This stabilises the repair machinery and activates cell-cycle checkpoints. ATR and Chk1 also facilitate the phosphorylation of RAD51 and the recruitment of repair factors such as breast cancer 2 (BRCA2) to the damage site (Z. Qiu et al., 2017). BRCA2 promotes the displacement of RPA by RAD51 recombinase. RAD51 then forms a nucleoprotein filament on the ssDNA, which searches for a homologous sequence on the undamaged sister chromatid. Upon recognition of a homologous sequence, RAD51 facilitates strand invasion, forming a displacement loop (D-loop) (J. M. Oh & Myung, 2022). This allows the damaged DNA strand to pair with its homologous counterpart, aligning the DNA for repair. DNA polymerase δ synthesises a new DNA strand using the sister chromatid as a template, restoring the sequence at the break site. In the later stages of HR, repair intermediates may form Holliday junctions, which are four-way DNA structures connecting sister chromatids (J. M. Oh & Myung, 2022; Q. Song et al., 2022). These junctions can be resolved by nucleases such as GEN1 or the SLX1-SLX4 complex, which cleave the DNA strands (Chan & West,

2015). Alternatively, the BLM helicase and topoisomerase IIIα complex can dissolve the Holliday junctions, resulting in non-crossover products without strand cleavage (Smith et al., 2010a; L. Wu et al., 2005).

The repair of double-strand breaks depends on the cellular context, the phase of the cell cycle, and the nature of the DNA damage. While NHEJ and HR are the primary DSB repair mechanisms, several alternative pathways can also contribute to repair under specific conditions. These include microhomology-mediated end joining (MMEJ), single-strand annealing (SSA), break-induced replication (BIR), and synthesis-dependent strand annealing (SDSA). These alternative pathways provide additional flexibility and serve as backup mechanisms to maintain genome integrity across a wide range of conditions (Bhargava et al., 2016; J et al., 2018; Q. W. Liu et al., 2024; Miura et al., 2012).

1.5.3 ATR and ATM activation

ATM and ATR are serine/threonine protein kinases that become activated in response to DNA damage. Once activated, they phosphorylate target proteins at specific motifs, such as Ser/Thr-Glu sequences (Maréchal & Zou, 2013). Among these phosphorylation events, some are direct, where ATM and ATR physically interact with and modify substrate proteins. Others are indirect, as ATM and ATR phosphorylate mediator proteins like Chk1 and Chk2, which further propagate the phosphorylation signal to downstream targets (Smith et al., 2010). Examples of these processes are described in the sections on the NHEJ and HR pathways. The activation of ATM and ATR checkpoint complexes initiates a cascade of cellular responses, including cell cycle arrest to prevent progression with damaged DNA, inhibition of DNA replication, stabilisation of stalled replication forks, and initiation of DNA repair mechanisms to resolve damaged DNA substrates (Maréchal & Zou, 2013; Ray et al., 2016). Further details on the activation mechanisms of ATR and ATM are provided below.

1.5.3.1 ATR activation

ATR activation is a multi-step process, as the ATR-ATRIP heterodimer cannot interact with DNA directly. Instead, it relies on nucleofilaments formed between the RPA and ssDNA for DNA binding (Awasthi et al., 2015). ATR-associated ATRIP binds to RPA-coated ssDNA, facilitating the localisation of ATR to sites of replication stress and DNA damage. The ATRIP-ATR complex then interacts with the RAD9-RAD1-HUS1 clamp (9-1-1), which is localised at ssDNA-dsDNA junctions. The 9-1-1 complex is loaded onto these junctions by the RAD17-RFC clamp loader complex, a process that is also facilitated by RPA (Day et al., 2022). Subsequently, the RAD9 subunit of 9-1-1 is phosphorylated at residue S387, enabling the recruitment of DNA

topoisomerase 2-binding protein 1 (TopBP1) to the FACT domain of ATR, leading to ATR activation (Awasthi et al., 2015). Once activated, ATR phosphorylates the mediator protein claspin, which then recruits Chk1 to the ssDNA-RPA complex. This proximity allows ATR to phosphorylate Chk1 directly at multiple sites within its C-terminal regulatory domain, most notably at serines S317 and S345 (Lindsey-Boltz & Sancar, 2011). Phosphorylation by ATR activates Chk1 kinase activity by relieving inhibition mediated by the C-terminal regulatory domain. Activated Chk1 dissociates from claspin and phosphorylates various nuclear and cytoplasmic substrates, including Cdc26A, a key regulator of the cell cycle (Smith et al., 2010). Chk1-mediated phosphorylation of Cdc25A marks it for ubiquitin/proteasome-mediated degradation, thereby preventing cyclin-dependent kinase (CDK) activation. This action halts cell cycle progression, allowing time for DNA repair (Goto et al., 2019).

1.5.3.2 ATM activation

ATM exists as a homodimer or higher order multimer in its inactive form (Bakkenist & Kastan, 2003). The MRE11-RAD50-NBS1 (MRN) complex acts as a sensor of DSBs by directly binding to broken DNA ends. This complex serves as a platform to recruit ATM to the site of damage. Specifically, ATM interacts with NBS1 via its C-terminal domain (Z. You et al., 2005). Upon recruitment to DSBs, inactive ATM dissociates into partially active monomers following autophosphorylation at residue S1981 in its FAT domain. The exact nature of the primary signal that triggers ATM autophosphorylation remains unclear. Interaction with the MRN complex, along with autophosphorylation, induce structural changes in ATM, enhancing its kinase activity and enabling efficient engagement with the MRN sensor complex. These changes facilitate ATM's ability to phosphorylate key proteins involved in the DNA damage response, including H2AX (forming γH2AX) and Chk2 (Smith et al., 2010). Phosphorylation of H2AX is essential for the recruitment and assembly of DNA repair proteins at sites containing damaged chromatin (Podhorecka et al., 2010). ATM also phosphorylates Chk2 at threonine 68 (T68), triggering Chk2 homodimerisation. Following dimerisation, Chk2 undergoes autophosphorylation at additional residues for full activation. Once activated, the Chk2 dimer dissociates into active monomers, which can then disperse throughout the nucleus to access key substrates involved in cell cycle regulation, apoptosis, and gene transcription. Chk2 phosphorylates a variety of substrates to enforce cell cycle arrest and initiate DNA damage repair. Known targets include the p53 tumour suppressor protein and its regulator MDMX, the Cdc25 family of phosphatases, the BRCA1 tumour suppressor, and transcription factors such as FOXM1 and E2F1 (Smith et al., 2010).

ATM can also be activated by ROS, such as hydrogen peroxide (H_2O_2). Unlike canonical activation, ROS-mediated ATM activation does not require the MRN complex or the presence of DNA breaks (**Figure 1.3**). In the presence of ROS, the cysteine residue at position C2991 in the ATM protein

undergoes oxidation. This oxidation leads to the formation of an intramolecular disulfide bond between ATM monomers, resulting in a conformational change that activates ATM as a dimer (Z. Guo et al., 2010). These pathways highlight the versatility of ATM, emphasising its critical roles in maintaining genetic stability and responding to oxidative stress.

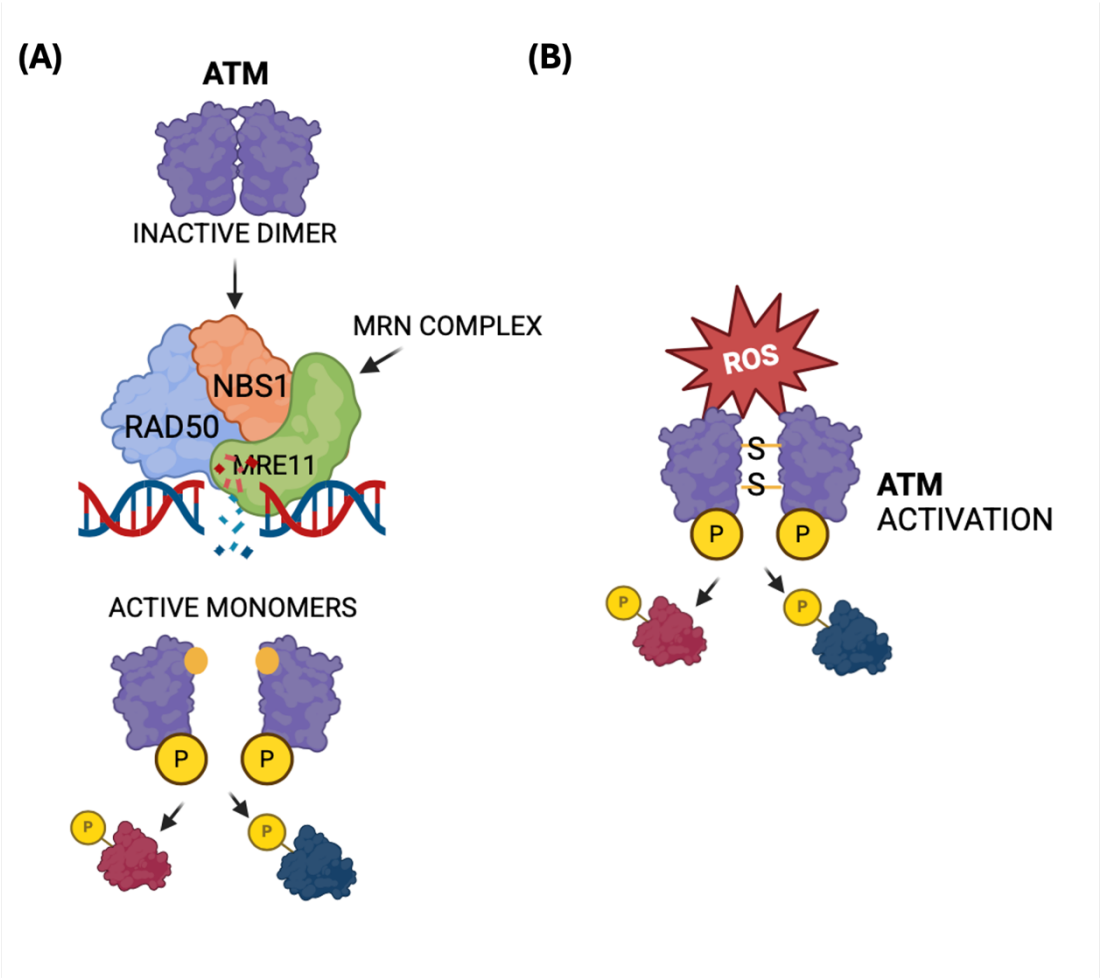

Figure 1.3: Mechanisms of ATM activation. (A) Double-stranded DNA breaks trigger ATM activation through the MRN complex (MRE11-RAD50-NBS1). The MRN complex recruits ATM to the damage site and facilitates its conversion from an inactive dimer to active monomers. Once activated, ATM phosphorylates multiple substrates, including Chk2 and H2AX, initiating DNA damage response pathways that regulate cell cycle arrest, DNA repair, and apoptosis. **(B)** In response to oxidative stress, ATM is activated independently of DNA damage and the MRN complex. Reactive oxygen species (ROS) promote the formation of disulfide bonds between ATM monomers, leading to the generation of an active covalent dimer.

1.6 DNA sensing pathways

1.6.1 Roles of ATM beyond DNA damage response

Cells are equipped with sophisticated DNA repair mechanisms to maintain genomic integrity and prevent the accumulation of mutations that could lead to tumorigenesis. Mechanisms such as non-homologous end joining and homologous recombination play critical roles in repairing double-strand breaks and other types of DNA damage. However, when DNA repair is insufficient, alternative pathways are activated to safeguard against tumour formation. One such mechanism involves the cyclic GMP-AMP synthase (cGAS) – stimulator of interferon genes (STING) pathway, which senses cytosolic DNA and triggers an innate immune response. This pathway promotes the production of proinflammatory cytokines, including type I interferons, and enhancing immune surveillance and facilitating the elimination of potentially cancerous cells (J. Zhou et al., 2023).

1.6.2 Canonical cGAS-STING activation pathway

Sources of cytosolic DNA include micronuclei and mitochondria DNA (mtDNA) (Miller et al., 2021). Micronuclei arise from various types of genomic instability. For example, they can form due to chromosome mis-segregation during mitotic errors (Zych & Hatch, 2024). Lagging chromosomes that fail to incorporate into daughter nuclei during anaphase become encapsulated in separate nuclear envelopes, forming micronuclei. Additionally, chromatin fragments can bud off the main nucleus in senescent cells, possibly representing a mechanism to eliminate defective genetic material that is either too damaged to repair or present in aberrant quantities (Miller et al., 2021). Micronuclei possess structurally weaker and less robust nuclear envelopes compared to the primary nucleus. When these envelopes rapture, the DNA within the micronucleus becomes accessible to cytosolic sensors such as cGAS (Bona & Bakhoum, 2024). Under physiological conditions, mtDNA is stored within the mitochondria. However, in response to cellular damage, oxidative stress, or apoptosis, mtDNA can be released into the cytoplasm, where it is recognised by cGAS (Pérez-Treviño et al., 2020).

cGAS is a DNA sensor localised in the cytosol, where it recognises the sugar-phosphate backbone of DNA, making its binding sequence-independent (Dvorkin et al., 2024). Upon binding to dsDNA, cGAS undergoes a conformation change that activates its enzymatic function. This activation enables cGAS to catalyse the conversion of ATP and GTP into 2',3'-cyclic GMP-AMP (cGAMP), a cyclic dinucleotide that acts as a secondary messenger (Hall et al., 2017). cGAMP binds to STING, a protein primarily located on the endoplasmic reticulum (ER), inducing a conformational change that activates STING. Activated STING recruits and activates TANK-binding kinase 1 (TBK1), which phosphorylates interferon regulatory factor 3 (IRF3), a

transcription factor (Q. Chen et al., 2016). Phosphorylated IRF3 translocates to the nucleus, where it drives the transcription of type I interferons (IFN-I) and interferon-stimulated genes (ISGs) (Lukhele et al., 2019). In parallel, STING also activates the IKK complex, leading to the translocation of NF-κB into the nucleus. NF-κB binds to the promoter regions of pro-inflammatory genes, inducing their expression (Won & Bakhoum, 2020).

1.6.3 Noncanonical cGAS-STING activation pathway in cancer

Traditionally, STING is activated by cGAS in response to cytosolic DNA. However, recent studies have revealed a cGAS-independent mechanism through which nuclear DNA damage can activate STING (Dunphy et al., 2018). In this noncanonical pathway, nuclear DSBs activate DNA damage response proteins, including ATM and PARP-1. ATM phosphorylates p53, which then interacts with IFI16, facilitating its recruitment to STING. PARP-1 amplifies the DNA damage response and may stabilise key protein interactions within this pathway. IFI16 plays a critical role in mediating the recruitment of TRAF6 to the DNA damage-induced STING complex. TRAF6 catalyses the formation of K63-linked ubiquitin chains on STING, a modification essential for downstream signalling. This leads to the activation of the IKK complex, promoting the nuclear translocation of NF-κB (Dunphy et al., 2018). Unlike the canonical cGAS-STING pathway, which primarily drives a type I interferon response, the noncanonical pathway predominantly activates NF-κB. This links nuclear damage to pro-inflammatory signalling, emphasising the connection between genomic instability and inflammation, which can significantly contribute to cancer progression.

1.6.4 Roles of cGAS-STING in cancer

The cGAS-STING pathway exhibits dual roles in cancer, acting as both a pro-tumorigenic and anti-tumorigenic factor depending on the cellular context and tumour microenvironment.

The anti-tumorigenic effects of cGAS-STING pathway activation involve the upregulation of IFN-I genes (K. Luo et al., 2022). In the TME, IFN-I stimulates antigen-dependent maturation of dendritic cells (DCs), enhances the cytotoxicity of $CD4^+$ and $CD8^+$ T cells and natural killer (NK) cells, and inhibits the activity of regulatory T cells (Tregs), myeloid-derived suppressor cells (MDSCs), and angiogenesis. Additionally, IFN-I can convert tumour-associated neutrophils into anti-tumour neutrophils. Together, these effects promote anti-tumour immunity by stimulating immune responses that target and eliminate cancer cells, thereby inhibiting tumour progression and metastasis (Zannikou et al., 2024). Support for this comes from mouse colorectal cancer models, where the loss of STING in tumour cells accelerated tumour growth in immune-competent mice (H. Zheng et al., 2023). Chronic activation of cGAS-STING can also drive cellular senescence through the production of SASP factors. The SASP can exert tumour-suppressive effects by attracting and activating immune cells (Loo et al., 2020). This was demonstrated in a mouse

model of liver carcinoma, where cellular senescence was triggered *in vivo* by inducible p53 expression. This activation initiated an innate immune response that targeted tumour cells and led to tumour regression. Inflammatory cytokines that attract macrophages, neutrophils and NK cells were upregulated shortly after p53 reactivation (W. Xue et al., 2007). Further evidence comes from another study using a mouse model of liver carcinoma, where inducible p53 expression triggered cellular senescence and caused tumour cells to secrete chemokines that recruited NK cells, ultimately leading to the elimination of senescent tumour cells (Iannello et al., 2013). In addition, cGAS-STING activation can promote apoptosis in cancer cells through the NF-κB pathway. Support for this comes from a study in human osteosarcoma, where NF-κB activation led to the expression of PUMA, a mediator of cell death. However, it is important to note that NF-κB is also known for its anti-apoptotic functions, which could complicate its role in cancer cell fate (Gao et al., 2019; W. Zheng et al., 2023).

Acute activation of the cGAS-STING signalling pathway may be beneficial in some environments, yet chronic stimulation can lead to inflammation-driven tumorigenesis (Pu et al., 2021). A study based on The Cancer Genome Atlas (TCGA) datasets, which included 18 malignant tumour types, found that cGAS-STING signalling molecules are highly expressed pan-cancer. Notably, the upregulation of cGAS-STING signalling was negatively correlated with the infiltration of certain immune cells in some tumour types. In addition, high levels of cGAS-STING signalling were predictive of poor prognosis in patients with certain cancer types (An et al., 2018). Further support comes from mouse tumour models, where high expression of STING promoted the growth and proliferation of Lewis lung cancer (LLC) cells (Lemos et al., 2016). Pro-tumorigenic effects of continuous STING activation include the recruitment of immunosuppressive cells, such as M2 macrophages, MDSCs, and Tregs, into the tumour microenvironment via chemokine activation (Y. Zhang et al., 2024). In models of liver cancer, melanoma, non-small cell lung cancer (NSCLC), and small cell lung cancer (SCLC), activation of the cGAS-STING pathway has been shown to increase the expression of programmed death-ligand 1 (PD-L1) on tumour cell surfaces, thereby attenuating cytotoxic T cell activity and dampening immune responses (Z. Tian et al., 2022). Additionally, the SASP mediated by cGAS-STING, not only promotes immunosuppression but also contributes to several processes that enhance tumour progression. These include the initiation of epithelial-to-mesenchymal transition, cancer cell stemness, angiogenesis, invasion and metastasis, fibroblast activation, and therapy resistance (Chambers et al., 2021).

Findings highlight how genomic instability and DNA damage trigger cGAS-STING activation, establishing a link between DNA damage, inflammation, cellular senescence, and cancer. In certain contexts, pathway activation enhances anti-tumour immunity and is therefore desirable. Conversely, in other contexts, activation may drive chronic inflammation, immunosuppression, or metastasis, leading to harmful outcomes. This dual role of the cGAS-STING pathway in cancer

presents significant challenges for effective therapeutic targeting, highlighting the need to further investigation. Notably, the studies outlined in this section are primarily based on cancer cell research, while the role of cGAS-STING pathways in other cell types, including CAFs, remains to be elucidated.

1.6.5 Roles of ATM in cellular senescence and inflammation

Inhibiting ATM has been extensively researched as a strategy to sensitise cancer cells to chemotherapy and radiotherapy. The rationale is that ATM inhibition disrupts the efficient repair of DSBs, leading to the accumulation of DNA damage. When DSBs are induced by chemotherapeutic agents or radiation therapy and ATM activity is blocked, cancer cells lose the ability to repair this damage effectively, resulting in cell death (Stakyte et al., 2021). However, the potential benefits of targeting ATM to activate the innate immune system remain less well studied.

Persistent DNA damage, as opposed to transient and repairable damage mediated by ATM, may lead to cell senescence and the secretion of inflammatory cytokines as part of the SASP (Rodier et al., 2009). Key SASP factors, such as IL-6 and IL-8, play central roles in driving inflammatory responses involved in tissue repair (Coppé et al., 2010). High levels of IL-6 and IL-8 have been observed in senescent cells induced by DNA damage. Studies on human colorectal adenocarcinoma (HCA2) cells and WI-38 fibroblasts revealed that ATM depletion prevented the IL-6 secretion typically observed 9-10 days after exposure to 10 Gy of X-irradiation (Rodier et al., 2009). Additionally, ATM depletion abolished IL-6 production in replicatively senescent cells. Similar effects were observed with the depletion of NBS1 and Chk2, emphasising that these factors are essential for establishing and maintaining SASP cytokine production. While ATM signalling drives only a subset of SASP factors, this subset includes the potent inflammatory cytokines IL-6 and IL-8 (Rodier et al., 2009). Notably, high expression of these cytokines in CAFs is associated with the inflammatory CAF phenotype. Persistent IL-6 signalling in the TME promotes all stages of tumorigenesis, including cell survival, angiogenesis, EMT, and metastasis (Orange et al., 2023). These findings suggest that ATM inhibition might offer therapeutic potential by suppressing cytokine production, thereby reducing tumour-promoting inflammation.

Upon activation, ATM phosphorylates various downstream targets, including NF-κB essential modifier (NEMO), a regulatory subunit of the IKK complex (Miyamoto, 2010). Following polyubiquitination, the IKK complex facilitates the translocation of NF-κB into the nucleus, where it regulates gene transcription (M. Hinz & Scheidereit, 2013). Activation of the IKK complex through the cGAS-STING pathway has been described in section 1.6.2. NF-κB activity promotes cellular senescence and regulates innate and adaptive immune responses, proliferation, and apoptosis. Pharmacological inhibition of ATM in mouse embryonic fibroblasts (MEFs) reduced

NF-κB transcriptional activity, as measured by an NF-κB luciferase assay (J. Zhao et al., 2020). This inhibition also reduced the expression of multiple senescence and SASP markers, including IL-6 and TNF-α. Furthermore, treatment of *Ercc1*$^{-/\Delta}$ mice which express only 5% of the normal level of the DNA repair endonuclease ERCC1-XPF, required for nucleotide excision, interstrand crosslink repair, and some DSB repair with an ATM inhibitor suppressed markers of senescence and SASP. These findings suggest that ATM and NF-κB are critical drivers of DNA-damage-induced senescence (J. Zhao et al., 2020).

Immune checkpoint blockade (ICB) is a class of cancer immunotherapy drugs designed to enhance anticancer effects by suppressing immune checkpoints (Q. Chen et al., 2019). The most common biomarkers routinely used to select patients for ICB include PD-L1 expression and high tumour mutational burden (TMB). High PD-L1 expression on tumour cells is associated with higher response rates to anti-PD-1/PD-L1 therapy in various cancers. Similarly, higher TMB correlates with an increased number of tumour-associated neoantigens, which can promote immune recognition and tumour cell destruction (Q. Chen et al., 2019; Dinstag et al., 2023; Negrao et al., 2019; Yi et al., 2021). Studies have shown that cancer patients with ATM mutations often exhibit high TMB and increased expression of PD-L1 and ISGs activated by the cGAS-STING pathway. In addition, in colorectal cancer (CRC) cells, ATM deficiency upregulated cGAS-STING pathway-related proteins, including CXCL10 and CCL5 (C. Li et al., 2024). These proteins are downstream effectors of the pathway. Furthermore, ATM inhibition induced MHC class I upregulation via the NF-κB/IRF1/NLRC5 pathway, independent of STING. MHC-I molecules load peptides and present them on the cell surface, signalling the immune system to detect and eliminate infected or cancerous cells (C. Li et al., 2024).

Animal experiments have demonstrated increased T cell infiltration, enhanced cytotoxic T cell function, and improved survival in mice with ATM-deficient tumours (C. Li et al., 2024; X. Wu et al., 2023). Another study found that ATM inhibition in several murine and human tumour cell lines led to downregulation of mitochondrial transcription factor A (TFAM), resulting in cytoplasmic leakage of mtDNA. This mtDNA leakage was functionally responsible for cGAS-STING activation. ATM deficiency not only induced ISG expression but also suppressed tumour growth, which depended on intratumoural lymphocyte infiltration, and sensitised tumours to PD-1 blockade (M. Hu et al., 2021). In pancreatic cancer models, ATM inhibition increased tumoral IFN-I expression through a cGAS-STING-independent mechanism. *In vivo*, ATM silencing enhanced PD-L1 expression and improved the sensitivity of pancreatic tumours to PD-L1 blocking antibody in association with increased intratumoural $CD8^+$ T cell infiltration (C. Li et al., 2024). Collectively, these studies support the use of ATM inhibitors as a therapeutic strategy to enhance sensitivity to ICB therapy. One mechanism by which the cGAS-STING pathway is triggered involves micronuclei rapture, exposing their DNA to the cytoplasm where it is detected by cGAS. The

NBS1-CtIP complex, regulated by ATM, converts DSB ends into ssDNA ends, thereby preventing cGAS from binding to micronuclei. This mechanism demonstrates how ATM indirectly suppresses cGAS-STING activation and limits excessive inflammatory responses and senescence caused by cytosolic DNA sensing (Abdisalaam et al., 2020).

ATM inhibition in cancer research has predominantly focused on cancer cells due to its therapeutic potential. However, emerging studies are beginning to explore the role of ATM in fibroblasts. Findings suggest that ATM-deficient human fibroblasts, when exposed to low levels of DNA damage, initially resist apoptosis but eventually undergo premature senescence, depending on the accumulation of DNA breaks (J. Park et al., 2013). This indicates that not only cancer cells with ATM deficiency undergo senescence, but fibroblasts as well.

1.6.5.1 ATM structure

ATM is ubiquitously expressed and spans approximately 13 kilobases, comprising 66 exons located on chromosome 11. The ATM gene encodes a protein of about 3,056 amino acids with a molecular weight of approximately 350 kDa (Taylor, 2001). As a member of the PIKK family, ATM contains a FRAP-ATM-TRRAP (FAT) domain and a FAT C-terminal (FATC) domain within its C-terminus. The FAT domain is critical for maintaining the structural integrity of ATM, facilitating substrate binding, and stabilising ATM dimers in their inactive state. This domain also contains several autophosphorylation sites, including Ser367, Ser1893, Ser1981, and Ser2996 (Ueno et al., 2022). Among these, Ser1981 is particularly associated with ATM monomerisation and activation in response to DNA damage (So et al., 2009). In addition to autophosphorylation, acetylation of Lys3016 is important for ATM activation, highlighting the complex regulation of this kinase. The FATC domain is required for full ATM activation and mediates interactions necessary for conformational changes upon DNA damage. The N-terminal region of ATM contains multiple α-helical HEAT (Huntingtin, Elongation factor 3, the A subunit of protein phosphatase 2A, and Target of rapamycin 1) repeat motifs. These HEAT motifs are essential for mediating interactions between ATM and other proteins or DNA, thereby contributing to its role in the DNA damage response (X. Jiang et al., 2006; Phan & Rezaeian, 2021; Taylor, 2001; Ueno et al., 2022).

1.6.5.2 ATM inhibitors

ATM inhibitors are a class of small molecules that suppress ATM kinase activity, disrupting the cellular response to DNA damage and impairing key DNA repair pathways such as homologous recombination (Qian et al., 2024). These inhibitors have been extensively studied to enhance the efficacy of radiotherapy and chemotherapy, as these treatments induce DNA damage that

cancer cells depend on ATM to repair. Several ATM inhibitors have progressed to clinical trials for the treatment of various cancer. These include KU60019, AZD1390, M3542, M4076, WSD0628, XRD0394, ZN-B-2262, and AZD0156, the latter being of primary interest in this project (Qian et al., 2024). These inhibitors target the ATP-binding pocket of ATM, blocking its catalytic activity and substrate phosphorylation. KU60019, a second-generation analogue of KU55933, is a potent ATM inhibitor and effective radiosensitiser (Biddlestone-Thorpe et al., 2013; Golding et al., 2009; Olivieri et al., 2022). AZD1390 is optimised for blood-brain barrier penetration, making it suitable for the treatment of central nervous system malignancies (Durant et al., 2018). Similarly, WSD0628 is brain-penetrable and targets the ATP-binding site, while XRD0394 functions as a dual ATP-competitive inhibitor of ATM and DNA-PKcs (Gilmer et al., 2024).

1.6.5.2.1 ATM inhibitor AZD0156

AZD0156 is a potent, orally active inhibitor of ATM developed by AstraZeneca, with an IC50 of 0.58 nmol/L in cell-based assays as measured by the inhibition of ATM auto-phosphorylation at serine 1981. Studies demonstrate that AZD0156 effectively radiosensitises cancer cell lines *in vitro*. In a lung xenograft model, systemic delivery of AZD0156 was shown to enhance the tumour growth-inhibitory effects of radiation treatment *in vivo* (Riches et al., 2020). Further research has indicated a clear radiosensitising effect of AZD0156 on melanoma cells, as assessed through clonogenic survival assays, demonstrating a synergistic effect. Importantly, this effect was not observed in healthy tissue fibroblasts, suggesting that AZD0156 selectively sensitises cancer cells without causing significant harm to normal cells (Scheper et al., 2023). This selective targeting is a highly desirable characteristic in cancer therapy.

AZD0156 has undergone a phase I clinical trial (NCT02588105) to evaluate its safety and preliminary efficacy at increasing doses, both as a monotherapy and in combination with other anticancer treatment in patients with advanced cancer. The results of this trial have not yet been published.

1.6.6 Other DNA sensing pathways

The cGAS-STING DNA-sensing pathway forms a part of the innate immune system, helping the body respond to infections, inflammation, and cancer (M. Jiang et al., 2020). However, it is important to note that other DNA sensing pathways exist, including AIM2 (Absent in Melanoma 2) and TLR9 (Toll-like Receptor 9). Like STING, AIM2 recognises and binds to dsDNA in the cytosol. AIM2 recognition of dsDNA leads to the assembly of a large multiprotein oligomeric complex called the inflammasome. This inflammasome assembly results in the secretion of bioactive IL-

1β and IL-18 and induces an inflammatory form of cell death known as pyroptosis (Sharma et al., 2019). TLR9 detects CpG motif-containing DNA. The binding of these motifs to TLR9 results in allosteric conformational changes and the recruitment of MyD88. Subsequently, MyD88 triggers the activation of NF-κB and interferon regulatory factor-7 (IRF7), inducing type I IFNs, which are essential for innate immunity (X. Chen et al., 2022; X. Huang & Yang, 2010). The roles of these DNA-sensing pathways in tumorigenesis can be either suppressive or promoting, depending on the context.

1.7 Major histocompatibility complex and antigen presentation pathways

Antigen presentation plays a key role in the immune response by processing antigens into smaller fragments known as immunogenic peptides (Tan et al., 2016). Two types of major histocompatibility complex (MHC) molecules mediate the presentation of these peptides: MHC class I (MHC-I) and MHC class II (MHC-II). These molecules present peptides derived from endogenous (intracellular) and exogenous (extracellular) antigens, respectively (Nuchtern et al., 1990).

1.7.1 MHC-I and the endogenous pathway

MHC-I molecules are expressed on all nucleated cells and present antigens derived from intracellular proteins (Hewitt, 2003). These include viral proteins produced during infection and abnormal proteins associated with cancer (Wargo et al., 2015).

The endogenous pathway begins with the proteasome, a protein complex that degrades intracellular proteins into short peptides through proteolysis (Blum et al., 2013). These peptides are translocated from the cytosol into the endoplasmic reticulum (ER) lumen via the transporter associated with antigen processing (TAP), which also serves as a scaffold for the final stages of MHC-I assembly, including peptide loading (Hewitt, 2003). Once loaded with peptides, MHC-I molecules are transported to the cell surface, where they present the peptides for immune surveillance. The display of foreign or abnormal peptides through this pathway is recognised by $CD8^+$ T cells, which can then eliminate the presenting cell (Desjardins, 2019).

1.7.2 MHC-II and the exogenous pathway

MHC-II molecules are expressed on professional antigen-presenting cells (APCs), including dendritic cells, macrophages, and B cells (Nonaka & Nonaka, 2016). These molecules present peptides derived from exogenous antigens, such as extracellular pathogens and cellular debris (Delamarre et al., 2003; Desjardins, 2019).

Exogenous antigens enter the endocytic pathway of APCs through processes like endocytosis, macropinocytosis, or phagocytosis. Once internalised, the antigens are delivered to late endosomes or lysosomes, where they are degraded into peptides by proteolytic enzymes activated by the compartment's acidic pH and assisted by disulphide reductases (Roche & Furuta, 2015). Meanwhile, MHC-II molecules are synthesised in the ER, where they associate with the invariant chain (Ii), also known as CD74, which blocks premature peptide binding (Blum et al., 2013; Holland et al., 2013). Ii also contains a targeting motif that directs the MHC-II-Ii complex to MHC class II compartments (MIIC), a subset of endosomal/lysosomal vesicles (Eynon et al., 1999; Rocha & Neefjes, 2007). Within the MIIC, the invariant chain is degraded, leaving a fragment called class II-associated invariant chain peptide (CLIP) in the MHC-II binding groove (Holland et al., 2013). The molecule HLA-DM catalyses the removal of CLIP and facilitates the loading of antigenic peptides onto MHC-II (Roche & Furuta, 2015). The resulting MHC-II-peptide complexes are transported to the cell surface, where they engage $CD4^+$ T cells, triggering immune responses such as cytokine production or activation of other immune cells (Desjardins, 2019; Haabeth et al., 2014; Stumptner & Benaroch, 1997).

1.7.3 Antigen cross-presentation

Antigen cross-presentation is the process by which APCs, particularly dendritic cells, present exogenous antigens on MHC-I molecules to $CD8^+$ T cells. This triggers their activation and proliferation and promotes their differentiation into cytotoxic lymphocytes capable of eliminating infected or malignant cells (Burgdorf et al., 2008; Nierkens et al., 2013). This pathway differs from the classical MHC-I route, which presents peptides derived from endogenous proteins (Hewitt, 2003).

Two major cross-presentation pathways have been described: the endosome-to-cytosol pathway and the vacuolar pathway. In the endosome-to-cytosol pathway, internalised antigens are transported from the endosomal compartment into the cytosol, where they undergo proteasomal degradation. The resulting peptides are subsequently transported by the TAP either into the ER or back into antigen-containing endosomes for loading onto MHC-I molecules (Embgenbroich & Burgdorf, 2018; Guermonprez et al., 2003). In the vacuolar pathway, both

antigen processing and MHC-I loading occur within the endo/lysosomal compartment. Following internalisation, antigens are degraded by lysosomal proteases, and the resulting peptides are loaded onto MHC-I molecules. Cathepsin S, a lysosomal protease, plays a key role in antigen degradation in this pathway (Embgenbroich & Burgdorf, 2018; L. Shen et al., 2004).

These complementary pathways ensure that antigens from a wide range of sources can be presented on MHC-I molecules, thereby maximising the immune system's capacity to detect and eliminate abnormal cells.

1.8 Immuno-oncology: the immune system's role in cancer

Genomic instability is a characteristic of most cancers. Chromosomal instability is the predominant form of genetic instability, leading to changes in both chromosome number and structure. Other forms of genomic instability have also been described, including increased frequencies of base-pair mutations and microsatellite instability, which refers to a clonal change in the number of repeated DNA nucleotide units in microsatellites (also known as short tandem repeats) (Baudrin et al., 2018; de La Chapelle & Hampel, 2010; Negrini et al., 2010). These genomic variations can lead to the production of neoantigens. The immune cells can recognise these tumour-specific antigens as foreign, thereby targeting cancer cells for destruction (Mardis, 2019). Cells of both the innate and adaptive immune systems play an essential role in cancer immunosurveillance and contribute to the modulation of tumour progression (Vesely et al., 2011). Effective immune responses can lead to the elimination of malignant cells. However, cancer cells have evolved multiple mechanisms to evade anti-cancer immune responses, such as eliminating immunogenic antigens or maintaining cancer clones without antigens, expressing immune checkpoint molecules, and recruiting immunosuppressive cell populations. The immune system offers a means of specifically destroying tumours without harming normal tissues, and immunological memory has the potential to prevent cancer recurrence (Finn, 2012). This highlights the growing importance of immunotherapy, which aims to enhance the body's immune response against cancer (Joshi & Durden, 2019).

1.8.1 The history and advances in cancer immunotherapy

Anecdotal reports, dating back to ancient Egypt and continuing through the 18th century in Europe, describe instances of tumour regression following infections accompanied by high fever. One of the earliest documented efforts to harness the immune system against cancer occurred in the 19th century. Physicians Wilhelm Busch and Friedrich Fehleisen independently observed tumour regression following accidental erysipelas infections. In 1868, Busch intentionally

infected a cancer patient with erysipelas, a bacterial skin infection, and observed tumour regression. In 1882, Fehleisen identified *Streptococcus pyogenes* as the bacterial strain responsible for erysipelas (Oelschlaeger, 2010; Oiseth & Aziz, 2017).

A breakthrough in cancer immunotherapy came from William B. Coley, who is now recognised as the 'Father of Immunotherapy' (McCarthy, 2006). William Coley injected *Streptococcus pyogenes* into a cancer patient and observed tumour regression following the resulting erysipelas infection. However, it became evident that inducing an infection was unpredictable; in some cases, it failed, in others, it triggered strong immune responses leading to tumour regression, and in some instances, it proved fatal. Due to this unpredictability, in 1891, Coley developed a method to stimulate an immune response without the risks of a live infection by injecting heat-inactivated *Streptococcus pyogenes* and *Serratia marcescens* into patients with inoperable cancers. This bacterial mixture became known as Coley's toxin, and he primarily used it to treat patients with inoperable bone and soft-tissue sarcomas. By the end of his career, Coley had treated nearly 1000 patients (Hoption Cann et al., 2003; McCarthy, 2006). Although Coley's toxin became commercially available in 1899, its mechanism of action remained unknown. In 1897, Paul Ehrlich formulated his 'side-chain theory', proposing that certain cells display side chains on their surface that play a role in specific antigen recognition (Valent et al., 2016). He also suggested that antibodies are natural proteins that bind to antigens. While Ehrlich's side-chain theory laid the foundation for understanding immune recognition, its implications for immuno-oncology were not immediately appreciated and were largely overlooked at the time (Talmage Webb Waring, 1986). In 1957, Burnet and Thomas proposed their hypothesis of 'cancer immunosurveillance'. Burnet stated: "It is by no means inconceivable that small accumulations of tumour cells may develop and because of their possession of new antigenic potentialities provoke an effective immunological reaction with regression of the tumour and no clinical hint of its existence". Burnet and Thomas speculated that lymphocytes function as sentinels, detecting and eliminating newly transformed cancer cells, a concept now known as cancer immunosurveillance. Following the introduction of the immunosurveillance hypothesis, numerous experiments were conducted to investigate its validity. However, early studies produced inconclusive results and failed to prove or disprove the concept of immunosurveillance (Dunn et al., 2002). More than three decades later, in 1998, key experimental findings provided compelling evidence supporting the role of the immune system in tumour rejection. Studies using murine fibrosarcoma cell lines demonstrated that the rejection of transplanted tumour cells was dependent on the host's endogenous production of interferon-gamma (IFN- γ) and the activation of tumour-specific T cells. Schreiber et al. showed that endogenously produced IFN-γ forms the foundation of a tumour surveillance system, controlling the development of both chemically induced and spontaneously arising tumour in mice. Their findings also suggested that certain cancers may evade immune detection by losing sensitivity to IFN-γ (Kaplan et al., 1998). Further supporting evidence emerged in 2001

when a study demonstrated that immunodeficient mice lacking either IFN-γ or RAG-2 (recombination activating gene-2) which is essential for the development of mature B and T lymphocytes, developed more spontaneous neoplasms with age and were more susceptible to methylcholanthrene (MCA)-induced sarcomas compared to wild-type mice. Additionally, 40% of MCA-induced sarcomas derived from immunodeficient *Rag2*$^{-/-}$ mice were spontaneously rejected when transplanted into naïve syngeneic wild-type mice. In contrast, all MCA-induced sarcomas originating from immunocompetent wild-type mice grew progressively when transplanted into naïve syngeneic wild-type hosts. These findings indicate that tumours developing in the presence of an intact immune system are less immunogenic than those arising in immunodeficient hosts. Consequently, it was concluded that immune pressure favours the outgrowth of tumour variants that are more capable of escaping immune detection. This led to the refinement of the cancer immunosurveillance hypothesis into the broader concept of cancer immunoediting, which described the dynamic interactions between tumours and the immune system. It is now understood that the immune system has dual functions, both protecting the host by eliminating cancer cells, and paradoxically promoting tumour evolution by selecting for immune-resistance variants (J. Chen et al., 1993; Shankaran et al., 2001; Vesely et al., 2011).

1.8.2 Cancer immunoediting theory

Schreiber and colleagues formulated the cancer immunoediting framework, which describes the dynamic interactions between the immune system and cancer through three sequential phases: elimination, equilibrium, and escape. During the 'elimination phase' (also known as immunosurveillance), cancer cells are successfully recognised and destroyed by immune cells. However, some cancer cell variants evade elimination and proceed to the 'equilibrium phase', in which immune cells control tumour growth, but selective pressure leads to the emergence of cancer cell variants that are no longer recognised by the immune system. These edited cancer cells continue to proliferate, resulting in tumour growth. Eventually, they enter the 'escape phase', where they become clinically apparent and may begin to metastasise (Vesely & Schreiber, 2013).

1.8.3 Cancer immunotherapies

The cancer immunoediting theory has been instrumental in shaping modern cancer immunotherapy, a type of treatment that enhances or modifies the body's immune system to recognise, attack, and eliminate cancer cells. Unlike chemotherapy or radiation, which directly target cancer cells, immunotherapy strengthens or redirects the immune response to fight cancer more effectively. Major types of immunotherapies include cancer vaccines, cytokine

therapy, adoptive cell transfer (ACT), and immune checkpoint inhibitors (ICI) (Y. Zhang & Zhang, 2020).

1.8.3.1 Cancer vaccines

Cancer vaccines stimulate the immune system to recognise and eliminate malignant cells. Unlike traditional prophylactic vaccines that prevent infectious diseases, cancer vaccines can be either preventive or therapeutic. Preventive vaccines target virus-induced cancers, such as Cervarix, which protects against HPV types 16 and 18, viruses commonly associated with cervical cancer. Therapeutic vaccines, on the other hand, target existing malignancies. An example of this is Sipuleucel-T (Provenge), a vaccine designed to treat prostate cancer (Petkar et al., 2023). The foundation of cancer vaccine development was laid by the discovery of tumour-associated antigens (TAAs) and tumour-specific antigens (TSAs), which help activate the patient's immune system. TAAs are proteins that are minimally expressed in normal tissues but overexpressed in cancer cells, while TSAs are unique to tumour cells and include mutations in RAS, TP53, and BRCA (Feola et al., 2020). MZ2-E, encoded by the melanoma-associated antigen (MAGE) gene family, was the first tumour-specific antigen to be identified (van der Bruggen et al., 1991). This discovery accelerated research into human cancer vaccines. The field of cancer vaccine development is rapidly expanding, utilising various preparation methods. Cancer vaccines are generally divided into four categories: cell-based vaccines, virus-based vaccines, peptide-based vaccines, and nucleic acid-based vaccines. Numerous cancer vaccines are currently in clinical trials, highlighting the ongoing advancements in the field (J. Liu et al., 2022).

1.8.3.2 Cytokine therapy

Cytokine therapy is a form of immunotherapy that utilises cytokines and signalling molecules that modulate immune system activity to treat cancer. These molecules play key roles in immune cell activation, proliferation, and differentiation, with therapeutic applications aimed at enhancing the body's natural immune response against tumours (Conlon et al., 2019). Interleukins and interferons are among the most commonly used cytokines in cancer therapy. The development of cytokine therapy began with the discovery of interleukin 2 (IL-2) in 1976 (Morgan et al., 1976). IL-2 stimulates the proliferation and activation of T cells and natural killer cells. In 1985, IL-2 administration was demonstrated to mediate tumour regression in humans for the first time. It later became one of the first curative therapies for solid tumours (Rosenberg, 2014). The FDA approved IL-2 in the 1990s for the treatment of metastatic melanoma and renal cancer, establishing it as one of the earliest FDA-approved immunotherapies (T. Jiang et al., 2016). However, the first immunotherapy agent approved by the FDA was interferon-alpha 2 in 1986 for

the treatment of hairy cell leukaemia (Eno, 2017). Currently, cytokine therapy is primarily used in specific clinical settings where immune activation is required. Despite its potential, cytokine-based treatments have limitations, including systemic toxicity, short-lived responses, and lack of tumour specificity. To overcome these challenges and improve patient outcomes, combination therapies integrating cytokines with anticancer vaccines, checkpoint inhibitors, or monoclonal antibodies are being investigated in clinical trials (Conlon et al., 2019).

1.8.3.3 Adoptive cell transfer

Adoptive cell transfer (ACT) is an immunotherapeutic approach that involves isolating immune cells, such as tumour-infiltrating lymphocytes (TILs), expanding them *ex vivo,* and subsequently reinfusing them into the patient to target and eradicate cancer cells. This approach was first demonstrated in 1988 by Rosenberg et al., who showed that TILs expanded in the presence of IL-2 could induce tumour regression in patients with metastatic melanoma (Rosenberg et al., 1988). To enhance the efficacy of ACT, researchers have developed genetically modified T cells, notably chimeric antigen receptor T cells (CAR-T), which are engineered to recognise and bind to specific antigens on cancer cells (Feins et al., 2019). Multiple CAR T cell therapies have received FDA approval (Goyco Vera et al., 2024).

1.8.3.4 Immune checkpoint inhibitors

Immune checkpoints are regulatory molecules expressed on immune cells that modulate the immune response to prevent overreaction and maintain self-tolerance (Pardoll, 2012). Key examples include CTLA-4, PD-1/PD-L1, LAG-3, and TIM-3 (Franzin et al., 2020). Under normal physiological conditions, these checkpoints ensure that immune responses are appropriately controlled. However, in the TME, cancer cells often exploit these pathways by upregulating checkpoint proteins and their ligands, thereby inhibiting immune cell activity and evading immune detection (Lim et al., 2017). Checkpoint immunotherapy works by inhibiting these receptors and/or their ligands using highly selective antibodies, which reactivate the immune system to target and eliminate cancer cells. Ipilimumab, which targets CTLA-4, was the first FDA-approved immune checkpoint inhibitor (ICI) in 2011 and has significantly improved overall survival in patients with metastatic melanoma (Knight et al., 2023). Subsequently, the FDA approved the PD-1 inhibitor nivolumab in 2014 (Gong et al., 2018). Since then, additional ICIs have been approved, either as monotherapies or in combination with other drugs, to treat various cancers (Meng et al., 2024).

1.9 CAF-related immune resistance

1.9.1 Tumour phenotypes

Tumours are often informally categorised based on their immune infiltration into three groups: immune-inflamed, immune-excluded and immune-desert (Bruni et al., 2023). Immune-inflamed tumours, commonly known as 'hot' tumours, are characterised by robust infiltration of T cells, including cytotoxic $CD8^+$ T cells, elevated interferon-γ signalling, increased PD-L1 expression, and a high tumour mutational burden. These features are generally associated with a favourable response to immune checkpoint blockade (ICB) therapies. In contrast, 'cold' tumours, which include both immune-excluded and immune-desert types, typically exhibit a low tumour mutational burden, poor antigen presentation, and minimal PD-L1 expression (B. Wu et al., 2024). Additionally, these tumours often harbour immunosuppressive cell populations, such as regulatory T cells and myeloid-derived suppressor cells (MDSCs), which further dampen antitumour immune responses (S. He et al., 2025). In immune-excluded tumours, $CD8^+$ T cells are present but remain confined to the tumour margins, whereas in immune-desert tumours, these T cells are largely absent from both the tumour and its periphery (M. M. Wang et al., 2023). Consequently, cold tumours are often less responsive to immunotherapeutic interventions due to their diminished antitumour immune activity. (Galon & Bruni, 2019; Y. T. Liu & Sun, 2021).

Non-responsiveness to immunotherapy can result from limited T cell infiltration mediated by the TME. CAFs are a key component of the TME and can significantly limit the effectiveness of cancer immunotherapy. Myofibroblastic CAFs secrete ECM proteins, leading to a dense and often disorganised ECM that acts as a physical barrier, restricting the penetration of therapeutic agents into the tumour stroma. Additionally, CAFs can non-specifically uptake administered agents, reducing the number of drug molecules that reach cancer cells. This can lead to subtherapeutic drug concentrations and contribute to drug resistance (J. Guo et al., 2020). Beyond limiting drug diffusion, the dense ECM barrier also restricts the migration of immune cells, such as cytotoxic T cells, into the tumour. Without adequate T cell infiltration into the tumour core, therapies that rely on activating these cells such as immune checkpoint inhibitors (ICIs) are less effective. Furthermore, CAFs produce immunosuppressive cytokines and chemokines that inhibit immune cell activation, promote the recruitment of immunosuppressive immune cell populations, and induce PD-L1 expression on cancer cells, further dampening the immune response to immunotherapy (Bruni et al., 2023; Pei et al., 2023). The success of cancer immunotherapy is currently limited to a fraction of cancer patients, highlighting the need to identify targetable resistance mechanisms to improve clinical outcomes. Since, myCAFs are associated with poor prognosis in most solid tumours (Han et al., 2020), addressing CAF-mediated barriers remains an active area of research aimed at enhancing responses to immunotherapies.

1.9.2 PD-L1 expression on CAFs contributes to the immunosuppressive TME

The programmed cell death-1 (PD-1) and programmed death-ligand 1 (PD-L1) pathway, which plays a crucial role in maintaining immune homeostasis, is one of the most well-studied examples of an immune escape mechanism. Under normal circumstances, checkpoint proteins such as PD-1 regulate the immune response by preventing the uncontrolled activation of T lymphocytes (X. Lin et al., 2024). However, some tumour cells evade immune surveillance by expressing inhibitory molecules like PD-L1. When PD-L1 binds to the PD-1 receptor on cytotoxic T cells, it deactivates them, thereby suppressing the antitumour immune response. (Riley, 2009) Checkpoint immunotherapy leverages this mechanism by using highly selective antibodies to inhibit receptors and/or ligands (e.g., PD-1/PD-L1), which can 'reactivate' the immune system to target and destroy cancer cells (Alsaab et al., 2017).

PD-1/PD-L1 blockade immunotherapy has been trialled across a wide range of malignancies, with some therapies showing greater efficacy than others and leading to increased long-term survival in certain patient subsets (Egen et al., 2020). Due to tumour heterogeneity, response rates vary, ranging from about 13% in head and neck carcinoma to 30-45% in melanoma (J. Y. Sun et al., 2020). Despite these variable outcomes and the potential for acquired therapy resistance leading to cancer progression or relapse, PD-1/PD-L1 blockade remains a frontline approach in cancer immunotherapy. Overall, these observations imply that additional mechanisms of immune evasion need to be elucidated to further improve therapeutic options (Yi et al., 2021). In addition to cancer cells, CAFs have been found to express PD-L1 in several cancer types, including non-small cell lung cancer (NSCLC), colon cancer, PDAC, triple-negative breast cancer (TNBC), and HNSCC (Kim et al., 2022; O'Malley et al., 2018; Takahashi et al., 2015; Teramoto et al., 2019; Yoshikawa et al., 2021). For example, in non-metastatic NSCLC and TNBC, high PD-L1 expression on CAFs has been associated with improved clinical outcomes, possibly reflecting an active antitumour response (Teramoto et al., 2019; Yoshikawa et al., 2021). This contrasts with observations in other cancers: in colon cancer, stromal PD-L1 expression correlated with enhanced tumour progression via the inhibition of $CD8^+$ T cells, and in PDAC, PD-L1 expression was associated with reduced $CD8^+$ T cells infiltration and a poorer prognosis (Nomi et al., 2007; O'Malley et al., 2018). Similarly, in HNSCC, PD-L1 expression by CAFs contributed to the creation of an immunosuppressive microenvironment (Takahashi et al., 2015). Although the canonical view is that PD-L1 engagement with PD-1 on $CD8^+$ T cells leads to their inactivation and exhaustion, these varied outcomes suggest that the role of PD-L1 may be context dependent. One plausible explanation for these differences in the heterogeneity of CAF populations, which likely exhibit diverse functional roles depending on the tumour type and microenvironment.

1.9.3 Extracellular matrix remodelling in the context of immune cell exclusion

The extracellular matrix is a complex and dynamic network of macromolecules that provides structural and biochemical support to cells (Hastings et al., 2019). It is primarily composed of structural proteins, such as collagens, which provide tensile strength, and elastin, which contributes to tissue elasticity; adhesive glycoproteins, including fibronectin, laminin, and tenascin, that mediate cell adhesion and signalling; and proteoglycans along with glycosaminoglycans, such as decorin, versican, biglycan, and hyaluronic acid, which regulate both cell behaviour and matrix properties through interactions with various growth factors, cytokines, and adhesion molecules (Kular et al., 2014; J. Wei et al., 2020). In addition, ECM-remodelling enzymes like matrix metalloproteinases (MMPs) and cross-linking proteins such as lysyl oxidases (LOXs) play crucial roles in ECM regeneration and restructuring (Afratis et al., 2018). In normal tissue, ECM remodelling is tightly regulated and essential for maintaining structural integrity and proper cellular function; however, in diseases such as cancer, the ECM is commonly dysregulated and extensively remodelled. CAFs are major contributors to ECM deposition, leading to increased tumour stiffness that not only supports tumour growth and metastasis but also creates a physical barrier that hinders the infiltration of immune cells, including cytotoxic T cells, thereby contributing to immune cell exclusion (Winkler et al., 2020). The matrisome comprises approximately 300 matrix macromolecules, and herein we focus on those most relevant to this thesis.

1.9.4 Effects of collagen on T cell infiltration

CAFs are key producers of fibrillar collagens (types I, II, III, V, XI, XXIV and XXVII), which are critical structural components of the ECM and are upregulated in various cancers at both the gene and protein levels (Nissen et al., 2019). High collagen density and collagen fibre alignment have been linked to the cold, immune-excluded phenotype. The effects of collagen density on T cell infiltration have been investigated in several studies. For example, a combination of immunostaining and real-time imaging has been used to track T cells *ex vivo* in human lung tumour slices; these studies showed that T cells accumulate in the stomal compartment and that their migration into tumour islets is impeded by networks of dense collagen fibres. Moreover, collagenase treatment reversed the obstructive effect of the tumour stroma on T cell migration (Salmon et al., 2012). A similar experimental design was implemented on fresh human ovarian and lung cancer tissue slices. The findings revealed that CD8 T cells accumulate in the stroma and exhibit slower movement, while tumour islets, although less populated, displayed zones of faster migration. The researchers further demonstrated that the orientation, spacing, and density of collagen fibres influenced the distribution and migration of CD8 T cells within the stroma. Areas with looser collagen contained a higher number of CD8 T cells with increased motility. However,

not all T cells in the less-dense collagen regions were motile, suggesting that other ECM components may also play a role in regulating T cell behaviour (Bougherara et al., 2015). Further studies have demonstrated that collagen promotes leukocyte movement by contact guidance, a process described as migration along ECM fibres and squeezing through matrix gaps along the path of least resistance. These findings indicate that collagen orientation may control T cell migration (Friedl & Weigelin, 2008). Experimental evidence supporting this comes from a study that used 3D collagen matrices to investigate different migration patterns. T cells exhibited fast motility when moving through pre-existing channels; however, when encountering regions of higher collagen density, they switched to a slower mode. It is also important to note that the diameter of the T cell nucleus acts as a rate-limiting factor, if the channels are narrower than the nucleus, T cells come to a halt until a new channel is created (Sadjadi et al., 2020). This provides evidence that the ECM serves as a scaffold for CD8 T cell migration, although its advantage is lost when dense fibre alignment is present. Moreover, T cells can reorganise their cytoskeleton, enabling them to migrate through narrow spaces. Another study investigated how collagen within the TME contributes to resistance against PD-1/PD-L1 therapies. The researchers found that increased collagen levels in lung tumours correlated with a decrease in total $CD8^+$ T cells and an increase in exhausted $CD8^+$ T cell subpopulations. This exhaustion is mediated by the leukocyte-associated immunoglobulin-like receptor 1 (LAIR1), which upon binding to collagen induces T cell exhaustion via SHP-1 signalling. Lysyl oxidase-like 2 (LOXL2) is an enzyme involved in crosslinking fibrillar collagen, this process increases collagen stability and deposition in the ECM. By suppressing LOXL2 and thereby reducing tumour collagen deposition, the study demonstrated enhanced T cell infiltration, a reduction in exhausted T cells, and an improved response to anti-PD-L1 therapy. Furthermore, blocking LAIR1-mediated immunosuppression, either by overexpressing LAIR2 or by inhibiting SHP-1 enhanced the sensitivity of resistant lung tumours to anti-PD-1 therapy. These findings suggest that targeting the collagen-LAIR1 axis could enhance the efficacy of immunotherapies (D. H. Peng et al., 2020). In another study, researchers utilised five preclinical mouse models with varying tumour microenvironments to assess the relationship between tumour stiffness, ECM architecture, and T cell migration. The specific mouse tumour models included EGI-1 for cholangiocarcinoma, MET-1 and MMTV-pyMT for breast carcinoma, and orthotopic mPDAC along with a subcutaneous KPC model for PDAC. LOX was inhibited using beta-aminopropionitrile. The results showed that all models except MET-1 displayed a reduction in mean stiffness. Collagen fibres in tumours are typically linear; however, LOX inhibition resulted in fibres that were less linear and exhibited a wavier configuration. Reversing tumour stiffness improved T cell infiltration in these models. Additionally, the efficacy of anti-PD-1 therapy as assessed in the KPC tumour model, was enhanced following LOX inhibition (Nicolas-Boluda et al., 2021). This study highlights the importance of mechanical characterisation in understanding

immunotherapy resistance and suggests that targeting ECM stiffness could enhance treatment outcomes.

Extensive desmoplastic stroma is a hallmark of PDAC, with up to 90% of the tumour volume commonly attributed to CAFs (Orth et al., 2019). Consistent with previously described models, T cell movement toward cancer cells becomes misdirected upon encountering the dense matrix of the PDAC stroma. Additionally, a dense collagen network abolished chemokine-induced T cell migration (Hartmann et al., 2014). A dual-recombinase genetic mouse model was employed to evaluate the functional consequences of type I collagen (Col1) deletion specifically in αSMA$^+$ myofibroblasts in PDAC. Deletion of Col1 resulted in an approximate 50% decrease in stromal content, which unexpectedly accelerated PDAC progression and reduced overall survival compared to control mice. Moreover, Col1 deletion was associated with enhanced immunosuppression, as evidenced by increased recruitment of myeloid-derived suppressor cells and decreased numbers of B and CD8$^+$ T lymphocytes (Y. Chen et al., 2021). These findings suggest that type I collagen in the TME plays a protective role by modulating immune responses and restraining tumour growth in PDAC. These results align with previous observations in which depletion of αSMA$^+$ myofibroblasts promoted tumour invasiveness and reduced animal survival, partly due to increased immunosuppressive Treg infiltration and a lower cytotoxic CD8$^+$/Treg ratio in PDAC (Özdemir et al., 2014). However, given that recent studies have identified heterogenous CAF populations, with interconvertible states between iCAFs and myCAFs (Biffi et al., 2019), it remains unclear whether the increased Treg presence is directly due to myofibroblast loss or a shift toward a different CAF phenotype. Additionally, since cancer cells also contribute to ECM production (C. Tian et al., 2019), their role in altering ECM properties may further influence immune cell infiltration and tumour behaviour. Overall, modulating collagen might enhance T cell penetration into tumours, which is relevant for improving immunotherapy responses.

1.9.5 Effects of other ECM components on T cell migration

Beyond collagen, several ECM components regulate T cell migration. Fibronectin (FN) is one of the most abundant ECM proteins secreted by CAFs, and its dysregulated expression is associated with tumour progression. FN interacts with other ECM proteins such as collagen, periostin, fibrillin, and tenascin-C to facilitate their assembly and organisation (Erdogan et al., 2017). Tumour matrix tracks are pathways formed by ECM remodelling, that are enriched in low-tension FN fibres, influencing immune cell infiltration. Research indicates that in early tumour development, CD8$^+$ T cells, activated macrophages (F4/80$^+$), and M2-polarized macrophages (CD206$^+$) are present within these tracks. As the tumour progresses, these tracks mature as evidenced by a reduction in their diameter in a process involving ECM changes and the role of tenascin-C. This maturation leads to a decrease in CD8$^+$ T cells and F4/80$^+$ macrophages within

the tracks, while CD206$^+$ macrophages remain unaffected. Furthermore, as CD8$^+$ T cell numbers decrease in the tracks, more CD8$^+$ T cells migrate into the tumour nests, particularly when tenascin-C is absent. These findings suggest that the structural properties of FN within the tumour matrix play a crucial role in modulating immune cell retention and distribution, thereby influencing the TME (Fonta et al., 2023).

Versican (VCAN) is an ECM proteoglycan that interacts with other ECM components including hyaluronan, type I collagen, fibrillin, FN, and selectins, influencing disease phenotypes. Transcriptomic studies have shown increased VCAN expression in multiple solid cancers, and it has been proposed to contribute to ECM remodelling and tissue stiffness. Its expression is associated with a matrisome composition linked to poor prognosis and immunotherapy resistance, suggesting that versican may contribute to an immune-excluded tumour phenotype and highlighting its potential as a therapeutic target (Hirani et al., 2021). Indeed, triple-negative breast cancer tissue staining revealed that regions with high VCAN expression had few or no CD8$^+$ T cells. Moreover, when VCAN-positive cells were present at the tumour border, fewer CD8$^+$ T cells were observed in the tumour parenchyma. This suggests that VCAN expression at the tumour border may restrict T cell migration into the stroma, preventing their access to tumour cells. However, VCAN is modified by the addition of glycosaminoglycans (GAGs), long sugar chains that influence its function. Depending on its GAG modifications, VCAN can either promote or inhibit CD8$^+$ T cell infiltration. Chondroitin sulphate, a GAG that exists in different isoforms (e.g. CS-A and CS-C), appears to modulate T cell infiltration; a high CS-A/CS-C ratio may promote T cell infiltration, whereas a low ratio, as seen in the stroma of immune-excluded tissues may impair the chemokine gradient toward the tumour. This suggests that targeting CS-C within the stroma could increase T cell migration toward tumour islands, thereby creating an environment more permissive for immunotherapy (Hirani et al., 2024). Furthermore, a study analysing tumours from colorectal cancer patients found that tumours with low levels of total VCAN and active VCAN proteolysis exhibited a tenfold increase in CD8$^+$ T cell infiltration (Hope et al., 2017). Both fibronectin and versican are examples of ECM proteins secreted by CAFs. Moreover, CAFs play a role in ECM remodelling, and proteins involved in this process have also been linked to the development of an immunosuppressive ECM.

Podoplanin (PDPN) is a transmembrane glycoprotein that is upregulated in many cancer types. Within the TME, PDPN is elevated not only in cancer and immune cells but also in the tumour stroma. Elevated PDPN expression in CAFs in several cancers including lung, breast, and pancreatic is correlated with tumour malignancy and poor prognosis. Moreover, PDPN-positive CAFs are associated with an immunosuppressive tumour environment (H. Suzuki et al., 2022). For example, research in lung adenocarcinoma demonstrated that the presence of PDPN$^+$CAFs correlates with increased infiltration of CD204$^+$ tumour associated macrophages (TAMs) and a

decreased CD8/FOXP ratio. Additionally, higher PDPN expression was associated with elevated levels of immunosuppressive cytokines and the polarization of macrophages toward the M2 phenotype (Sakai et al., 2018). Similar results were observed in lung squamous cell carcinoma (J. Suzuki et al., 2021). These findings suggest that PDPN$^+$CAFs contribute to an immunosuppressive TME, thereby facilitating tumour progression. Furthermore, platelet-derived growth factor receptor alpha (PDGFRα) which is upregulated in multiple tumours, is predominantly expressed by CAFs and is frequently used as a marker. PDGFRα-expressing CAFs contribute to ECM remodelling and participate in immunomodulation by inducing macrophage migration and M2 polarization (Han et al., 2020; Horikawa et al., 2015; T. Liu et al., 2019). Since several studies have demonstrated that TAMs suppress CD8$^+$ T cell antitumour activity (Hao et al., 2012), reducing the expression of proteins such as PDPN and PDGFRα in CAFs could indirectly improve cancer immunotherapy.

Alpha-smooth muscle actin (αSMA) is a marker of myofibroblasts, indicating that CAFs have been activated and display contractile features that contribute to ECM remodelling (Lavie et al., 2022). Using syngeneic mouse models of mammary metastatic carcinoma, researchers demonstrated that tumours enriched in αSMA$^+$CAFs exhibited reduced CD8$^+$ T cell infiltration, leading to an immune-excluded phenotype. Additionally, tumours with a high presence of αSMA$^+$CAFs displayed resistance to combination therapy targeting CTLA-4 and PD-L1. Conversely, targeting αSMA$^+$CAFs through deletion of Endo180 (a receptor predominantly expressed on myCAFs), sensitised tumours to ICB therapy, as evidenced by suppressed tumour growth, an increased number of CD8$^+$T cells, and a higher proportion of CD8$^+$ T cells in the central region of the tumour (L. Jenkins et al., 2022). These findings highlight the immunosuppressive role of the myCAF subtype in promoting immune evasion and resistance to immunotherapy.

Prolyl 4-hydroxylase subunit alpha-3 (P4HA3) is a catalytic subunit of collagen prolyl 4-hydroxylases, a group of enzymes responsible for hydroxylating proline residues in collagen. This hydroxylation is essential for stabilising the triple-helical structure of pro-collagen before it is secreted into the ECM (Y. Luo et al., 2015; Y. Wu et al., 2023). In a pan-cancer analysis, P4HA3 was found to be significantly overexpressed in most cancers and associated with poor patient prognosis. Furthermore, increased P4HA3 expression was positively correlated with the presence of CAFs. Additionally, higher P4HA3 levels were linked to alterations in immune cell populations, specifically lower levels of CD8$^+$ T cells and increased macrophage infiltration. Moreover, P4HA3 expression positively correlated with the expression of immune checkpoint genes (Y. Wu et al., 2023). More recently, The Cancer Genome Atlas (TCGA) was used to examine the role of P4HA3 as a potential biomarker for predicting immunotherapy response in patients with gastric cancer. In this study, upregulation of P4HA3 was associated with increased synthesis, deposition, and stiffening of the ECM. The results indicated that P4HA3 expression was

significantly elevated in gastric cancer and closely linked to immune checkpoint genes expression, and that the effectiveness of ICIs was limited in patients with high P4HA3 levels. It was suggested that combining P4HA3 inhibitors with traditional ICI therapy might yield more effective treatment outcomes than ICI therapy alone (Y. Yu et al., 2024). In colorectal cancer, P4HA3 expression was associated with a higher degree of malignancy and poorer prognosis. Enrichment analysis further indicated that PH4A3 may be involved in the EMT process and the development of an immunosuppressive TME (X. Guo et al., 2024). Collectively, these data suggest that P4AH3 in the TME is associated with immunosuppression.

Matrix metalloproteinases (MMPs) are a family of zinc-dependent endopeptidases that play a critical role in ECM remodelling. Under normal physiological conditions, the balance between MMPs and their inhibitors, the tissue inhibitors of metalloproteinases (TIMPs), maintains ECM homeostasis. However, in cancer, CAFs secrete various matrix-degrading proteases and activators that upregulate MMP activity. This increased activity results in significant ECM degradation, thereby facilitating cell migration and invasion, promoting tumour growth, influencing cancer cell differentiation, and enhancing angiogenesis. Overexpression of specific MMPs, such as MMP-2, MMP-9, MMP-13, and MMP14, has been directly associated with poorer prognoses in many cancers. Although CAFs are major contributors to MMPs in the TME, other cells including cancer cells also affect MMP expression through soluble factors and direct interactions (Cathcart et al., 2015; K. Peng et al., 2023; Xing et al., 2010; Y. W. Zhao et al., 2022). Emerging evidence suggests that MMPs are also involved in modulating immunity within the TME. For example, MMP-2 and MMP-9 are upregulated in many cancer types and are positively correlated with inhibitory immune checkpoints, regulatory T cells, and markers of T cell exhaustion. An *in vitro* T cell cytotoxicity assay demonstrated that inhibition of MMP-2 and MMP-9 using SB-3CT significantly increased $CD8^+$ T cell-mediated killing of melanoma cells. Additionally, in tumour mouse models of B16F10 melanoma and Lewis lung carcinoma, treatment with SB-3CT alone significantly decreased tumour growth and extended overall survival. When combined with anti-PD-1 or anti-CTLA-4 therapy, the treatment achieved even better efficacy, enhancing survival in both models. These combination treatments improved immune cell infiltration and T cell cytotoxicity while reducing the presence of immunosuppressive cells, potentially through decreased PD-L1 expression (Y. Ye et al., 2020). Similarly, a pan-cancer analysis found that the expression of MMP-13 in most cancers was significantly associated with immune checkpoints (X. Zhang et al., 2023). Likewise, a positive correlation between MMP-14 and both $CD8^+$ T cells as well as immune checkpoints, including PD-1 and CTLA-4, was observed in a study of bladder cancer. High expression of MMP-14 in muscle-invasive bladder cancer was also linked to a poorer response to ICI treatment (X. Zhang et al., 2024). MMPs are frequently overexpressed across cancers and predict poor prognosis;

consequently, they have been explored as therapeutic targets. However, clinical trials with MMP inhibitors have faced challenges, mainly due to a lack of specificity.

Overall, ECM-associated proteins regulated by CAFs play a key role in shaping the TME by contributing to immune suppression. CAFs secrete structural ECM components such as collagens, fibronectin, and versican, which increase ECM stiffness, forming a physical barrier that limits the infiltration of immune cells, particularly $CD8^+$ T cells. P4HA3, which is involved in collagen deposition and ECM restructuring, along with LOX enzymes, further remodel the ECM by crosslinking collagen fibres, thereby increasing tissue stiffness and reinforcing immune exclusion. Additionally, elevated expression of PDPN has been linked to higher levels of immunosuppressive cytokines and the polarisation of macrophages toward an M2 phenotype. Similarly, PDGFRα-expressing CAFs have been shown to promote macrophage migration and M2 polarisation. CAFs also secrete MMPs, which not only remodel the ECM but also influence immune responses by contributing to T cell exhaustion, facilitating immune cell migration, and promoting immune evasion through the upregulation of checkpoint molecules such as PD-1 or CTLA-4. The cumulative effect of these ECM-driven changes facilitates tumour progression while undermining the efficacy of immune checkpoint inhibitors. Targeting CAF-mediated ECM remodelling is emerging as a promising strategy to improve anti-tumour immunity and enhance responses to immunotherapy. In the next section, we will focus on CTHRC1, POSTN and COL11A1; ECM-secreted proteins that further influence immune cell composition within the TME.

1.9.6 Potential ECM therapeutic targets

1.9.6.1 Collagen XI alpha chain I

Collagen XI alpha chain 1 (COL11A1) expression has been found to be upregulated in various human cancers, and its expression is positively correlated with tumour progression and lymph node metastasis. High levels of this collagen are usually predictors of poor prognosis. COL11A1 is secreted into the ECM by CAFs, but cancer cells also secrete COL11A1 into the ECM to regulate their own biological behaviour as well as that of surrounding cells (Y. H. Wu & Chou, 2022). Knockdown of COL11A1 in an epithelial ovarian cancer (EOC) cell line (A2780) decreased *in vitro* cell migration and invasion, and reduced tumour progression in mice (Cheon et al., 2013). More recently, researchers have found that coculturing human ovarian fibroblasts (HOFs) with high COL11A1-expressing EOC cells or exposing them to the conditioned medium from these cells, prompted the expression of COL11A1 and induced CAF phenotypes. COL11A1 was found to promote ovarian cancer progression by activating CAFs through the NF-κB/IGFBP2/TGF-β3 axis. Additionally, the crosstalk between CAFs and cancer cells triggered IL-6 release and promoted EOC cell proliferation and invasiveness. *In vivo*, overexpression of COL11A1 in EOC cells

promoted tumour formation and CAF activation, which was inhibited by a TGF-β3 antibody, highlighting a potential treatment strategy for targeting CAFs in COL11A1-positive ovarian tumours (Y. H. Wu et al., 2021). Previous studies have shown that COL11A1 expression is associated with chemoresistance in ovarian cancer and non-small cell lung cancer (L. Shen et al., 2016; Y. H. Wu et al., 2017). More recently, COL11A1 was found to be overexpressed in oestrogen receptor-positive breast cancer and to promote tamoxifen resistance. Knockdown of COL11A1 enhanced the sensitivity of tamoxifen in tamoxifen-resistant cells both *in vitro* and *in vivo* (C. Fu et al., 2024). *In silico* studies also suggest that COL11A1 plays a role in tumour immune cell infiltration. In breast cancer, COL11A1 expression negatively correlated with B cells, $CD4^+$ T cells, and $CD8^+$ T cells, while positively correlating with macrophage infiltration (Q. Luo et al., 2022; Shi et al., 2022). Bioinformatic analyses further showed that COL11A1 expression was positively correlated with TIM3, PD-L1, CTLA4 and LAG3. Therefore, high expression of COL11A1 may result in T cell exhaustion in the TME of lung adenocarcinoma, where COL11A1 is mainly expressed by CAFs rather than by lung adenocarcinoma cells (H. Zheng et al., 2024). Despite advancements in our understanding of the biological functions of COL11A1 in cancer progression, it remains unclear whether COL11A1 secreted by cancer cells and CAFs is structurally and functionally similar, and whether it influences immune cell infiltration (Y. H. Wu & Chou, 2022). COL11A1 expression is associated with poor prognosis and may have potential value as a prognostic biomarker. However, it remains to be elucidated whether COL11A1 expression influences responses to immunotherapy, and whether other collagens can compensate for the loss to COL11A1, thereby further affecting immune cell infiltration.

1.9.6.2 Collagen triple helix repeat containing 1

Collagen triple helix repeat containing 1 (CTHRC1) is an ECM glycoprotein that is overexpressed in several solid cancers. Initially identified as a regulator of vascular remodelling, CTHRC1 has since been implicated in numerous oncogenic processes, including tumour proliferation, invasion, and accelerated metastasis (Y. Liu et al., 2024; Zhong et al., 2023). At injury sites, CTHRC1 expression was found to be associated with myofibroblasts. These sites were characterised by active TGF-β and abundant collagen synthesis (Durmus et al., 2006). CTHRC1 was identified as a metastasis-associated gene in colorectal cancer (CRC). Animal experiments have shown that CTHRC1 secreted by CRC cells promotes hepatic metastasis, this process was closely associated with macrophage infiltration, particularly M2-like (protumour) macrophages. Researchers have also demonstrated that CTHRC1 modulates macrophage polarisation toward M2 phenotypes through TGF-β signalling. One study revealed that CTHRC1 binds directly to TGF-β receptor II and TGF-β receptor III on macrophages, thereby activating TGF-β-signalling. Combined treatment with a CTHRC1 monoclonal antibody and an anti-PD-1 blocking antibody

suppressed CRC hepatic metastasis, suggesting that CTHRC1 could serve as a potential biomarker and therapeutic target (X. L. Zhang et al., 2021). High expression of CTHRC1 in pancreatic cancer and NSCLC has also been implicated in metastasis (W. He et al., 2018; E. H. Park et al., 2013). *In silico* analyses based on a HNSCC patient cohort have shown that high CTHRC1 expression positively correlates with the infiltration of M0 and M2 macrophages, while it is negatively associated with levels of M1 macrophages (typically antitumour). This suggests that CTHRC1 may mediate macrophage polarisation in a manner that leads to poor prognosis (Zhong et al., 2023). Additionally, high CTHRC1 expression in gastric cancer patients was strongly associated with M2 macrophage infiltration and poor prognosis (L. Zhao et al., 2022). Another study demonstrated that elevated levels of CTHRC1 in both tumour and stromal cells during the early stages of CRC correlate with poor patient survival. CTHRC1 was shown to upregulate CCL15 secretion by activating TGF-β and Smad signalling pathways. CCL15 can chemotactically attract macrophages and reprogram them into M2 phenotypes. Blocking CCL15 impaired macrophage infiltration in the TME, uncovering a new mechanism of CTHRC1 regulation (Y. Liu et al., 2024). In a breast cancer study, CAFs isolated from tumour tissues secreted significantly greater amounts of CTHRC1 than normal fibroblasts. Furthermore, CAFs promoted the migration, invasiveness, and EMT of breast cancer cells by secreting CTHRC1, which activates the Wnt/β-catenin signalling pathway. Neutralising antibodies against CTHRC1, as well as the specific inhibitor Dickkopf-1 (which inhibits the Wnt/β-catenin pathway), significantly alleviated the CAF-induced malignant phenotypes of breast cancer cells. This suggests that weakening the communication between CAFs and breast cancer cells through suppressing CTHRC1 expression may represent a novel therapeutic strategy (H. Li et al., 2021). Collectively, these studies demonstrate that CTHRC1 plays diverse roles in promoting metastasis and tumour-associated M2 macrophage recruitment, both of which are linked to poor patient prognosis. M2 macrophages play a crucial role in immunosuppression, thereby affecting tumour progression and resistance to chemotherapy and immunotherapy (Y. Liu et al., 2024). Therefore, exploring the relationship between CTHRC1 expression and M2 polarisation may provide a target for reducing tumour resistance and enhancing anticancer treatment efficacy, ultimately improving clinical outcomes.

1.9.6.3 Periostin

Periostin (POSTN) is an ECM protein that plays a crucial role in ECM structure and collagen assembly. POSTN is frequently overexpressed by the stromal component of solid tumours. However, periostin can be produced by both cancer cells and stromal cells in various solid cancers; for example, in prostate, lung, pancreatic, and ovarian (Cattrini et al., 2018; González-González & Alonso, 2018; Ratajczak-Wielgomas et al., 2022). In addition, POSTN is involved in key cancer hallmarks such as proliferation, invasion and metastasis, angiogenesis, and resistance to

treatment. Generally, high levels of periostin expression are associated with a more aggressive tumour phenotype, advanced tumour stages, and poorer prognosis. Periostin expression is regulated by several transcription factors as well as cytokines and growth factors, including TGF-β (González-González & Alonso, 2018). While periostin has been well studied in cancer cells, its role in CAFs remains poorly understood. In one study integrating and analysing scRNA-seq datasets from hepatocellular carcinoma (HCC) tumours, researchers identified six distinct CAF subtypes, including one marked by high POSTN expression. $POSTN^+$CAFs were primarily located in the tumour periphery, where they contributed to forming an immune barrier that hindered $CD8^+$ T cell infiltration into the TME. This CAF subtype was strongly correlated with $SPP1^+$ macrophages, which are linked to anti-inflammatory responses and tend to adopt an M2 phenotype. Consequently, patients with higher levels of both $POSTN^+$CAFs and $SPP1^+$ macrophages exhibited a significantly poorer response to anti-PD-1 therapy, highlighting the impact of an immunosuppressive microenvironment on treatment efficacy (H. Wang, Liang, et al., 2024). In pancreatic cancer where CAFs are the main contributors to POSTN levels, higher POSTN expression was associated with increased M2 macrophage infiltration, reduced $CD8^+$ T cell infiltration, and worse outcomes following ICI treatment (Y. Chen et al., 2024). Similarly, in gastric cancer, overexpression of POSTN in CAFs enhanced macrophage chemotaxis and was associated with resistance to ICB (T. You et al., 2023). Several *in vitro*, *in vivo*, and *in silico* studies have investigated the role of POSTN in glioblastoma (GBM), a highly immunosuppressive and lethal cancer driven by glioblastoma stem cells (GSCs). In GBM, POSTN was found to be expressed almost exclusively by cancer cells. Findings revealed that POSTN secreted from GSCs promotes GSC self-renewal and tumour growth via activation of the αVβ3/PI3K/AKT/β-catenin/FOSL1 pathway. Furthermore, knockdown of periostin in a murine glioma cell line reduced the number of Treg cells, increased the number of $CD8^+$ T cells and apoptotic cells, and reduced tumour growth (H. Wang, Yao, et al., 2024). An earlier study also found that periostin secreted by GSCs recruits M2 macrophages (W. Zhou et al., 2015). Given its crucial role in shaping the TME, particularly through immune cell exclusion and macrophage polarisation, targeting POSTN in CAFs presents an attractive therapeutic strategy to enhance antitumour immunity and improve responses to immune checkpoint inhibitors.

Summary

Although the role of CTHRC1, POSTN and COL11A1 in regulating immune cell infiltration has been explored using *in vitro* and *in vivo* assays with cancer cell lines, the potential benefits of targeting these genes in CAFs to enhance immune cell infiltration and improve anti-tumour responses remain unclear. Nevertheless, *in silico* findings suggest that targeting these genes may help disrupt the immunosuppressive environment and enhance the efficacy to ICB in patients with solid tumours. One limitation of these studies is their inability to precisely define how these

proteins influence prognosis and response to immunotherapy. To develop a more comprehensive understanding of their role within the TME, future research should incorporate molecular-based experiments and analyses of clinical specimens for validation. However, given the heterogeneity and plasticity of CAFs, even advanced *in vitro* and *in vivo* models may not fully recapitulate their physiological functions, highlighting the complexity of translating these findings into therapeutic strategies.

1.9.7 Cytokines associated with CAF subsets and their roles in T cell trafficking

Cytokines are small, soluble proteins that regulate inflammation and immune responses. Examples include interleukins (ILs), tumour necrosis factors (TNFs), interferons (IFNs), and transforming growth factors (TGFs). Cytokines can be categorised based on their effects on the immune system. Proinflammatory cytokines, which promote inflammation and enhance immune responses, include IL-1, IL-6, TNFα and IFN-γ. In contrast, anti-inflammatory cytokines suppress excessive immune responses to prevent tissue damage and promote healing; examples include IL-10 and TGF-β. Chemokines, a subset of cytokines, primarily function to direct the migration of immune cells (chemotaxis). They play a key role in immune surveillance and inflammation by guiding immune cells to where they are needed, such as at sites of injury and within tumours. Chemokines are categorised into four main families based on the positioning of their N-terminal cysteine residues: CXC, CC, CX3C, and XC (Chaudhry et al., 2013; Duque & Descoteaux, 2014; Turner et al., 2014; Y. Zhang et al., 2020). Cytokines released by CAFs modulate the TME, and some of these cytokines have been shown to influence $CD8^+$ T cell trafficking.

CXCL12 is a chemokine produced by CAFs in the TME that regulates immune cell trafficking. In pancreatic ductal adenocarcinoma (PDA), FAP^+ CAFs produce CXCL12, contributing to immune exclusion. Despite the presence of $CD8^+$ T cells, checkpoint inhibitors (anti-PD-L1, anti-CTLA4) were ineffective. However, depleting FAP^+CAFs or inhibiting CXCR4 (the CXCL12 receptor) enabled $CD8^+$ T cells to infiltrate cancer cell rich regions of the tumours, thereby enhancing the response to checkpoint inhibitors, leading to cancer cell reduction (Feig et al., 2013). More recently, RNA sequencing analyses of bladder cancer revealed that iCAFs are the major source of CXCL12. Patients with high CXCL12 expression tended to exhibit impaired responses to ICB therapy. Immunohistochemical analysis further demonstrated that intratumoural $CD8^+$ T cell infiltration was significantly elevated in tumour tissues negative for PDGFRα and CXCL12, which were co-expressed in iCAFs (Y. H. Du et al., 2021). Together, these findings indicate that CAF-derived CXCL12 is immunosuppressive and impacts patient responses to immunotherapy.

Additionally, a lack of response to anti-PD-L1 therapy in metastatic urothelial cancer was associated with a TGF-β signalling signature. This was especially evident in immune-excluded

patient tumours, where $CD8^+$ T cell were trapped in the stroma and prevented from entering the tumour parenchyma, thereby impairing their ability to kill cancer cells. In a mouse model that recapitulated this tumour phenotype, coadministration of a TGF-β-blocking antibody with anti-PD-L1 reduced TGF-β signalling in stromal cells, facilitated intratumoural T cell penetration, and promoted tumour regression (Mariathasan et al., 2018). Similarly, in a mouse model of metastatic colorectal cancer, TGF-β inhibition enabled a cytotoxic T cell response that prevented metastasis. In the context of liver metastases, blocking TGF-β made tumour more susceptible to anti-PD-1 therapy (Tauriello et al., 2018). In these models, TGF-β represents a promising therapeutic target due to its role in limiting the effectiveness of immunotherapy.

In addition to CXCL12, iCAFs have been characterised by enriched expression of IL-6, IL-11, CCL2, and LIF. (Elyada et al., 2019; Öhlund et al., 2017). In a study of oesophageal cancer, *in vitro* co-culture of cancer cells with fibroblasts resulted in a marked increase in IL-6 concentrations, whereas cells cultured alone produced only low levels of IL-6. Treating mouse tumours composed of both fibroblasts and cancer cells with an anti-IL-6 antibody reduced tumour growth, significantly increased $CD8^+$ T cell infiltration, and decreased Tregs, demonstrating that IL-6 in the TME contributes to immunosuppression (Kato et al., 2018). In a study of gastric cancer, IL-11 secretion was significantly elevated when CAFs were co-cultured with cancer cells, and these CAFs enhanced the migration and invasion of gastric cancer cells via IL-11 expression (X. Wang et al., 2018). Although numerous studies have focused on the role of IL-11 in invasion and metastasis, the immunomodulatory effects of CAF-derived IL-11 have not been extensively investigated. However, in a model of colitis-associated colorectal cancer induced in IL-11 knockout and wild-type mice, researchers observed increased $CD8^+$ cell infiltration in the IL-11 deficient environment (Xiong et al., 2023). In a murine liver cancer model, fibroblast activation protein (FAP) was shown to drive the formation of an iCAF subset via STAT3 activation, resulting in increased CCL2 expression. This upregulation of CCL2 promoted tumour growth by attracting MDSCs (X. Yang et al., 2016). Similarly, CAFs from lung squamous cell carcinoma (LSCC) patients were found to secrete CCL2, which attracted $CCR2^+$ monocytes and polarised them into MDSCs that suppressed $CD8^+$ T cell proliferation and IFN-γ production (Xiang et al., 2020). These findings indicate that CCL2 plays an immunosuppressive role in the TME. Leukaemia inhibitory factor (LIF) has been shown to suppress the expression of the chemokine CXCL9, reducing $CD8^+$ T cell recruitment, while simultaneously promoting increased CCL2 expression. In a study using glioblastoma patient-derived tumours with high LIF expression in combination with peripheral blood mononuclear cells (PBMCs), treatment with an anti-LIF antibody increased CXCL9 levels and reduced CCL2, leading to enhanced $CD8^+$ T cell infiltration into the tumour (Pascual-García et al., 2019). Although this study did not focus exclusively on CAF-derived LIF, its use of patient-derived tumours provides a more physiologically relevant model that captures the complexity of tumour-immune interactions observed in patients. These results suggest that targeting LIF within

the TME could be a promising strategy to enhance immune cell infiltration and improve immunotherapy responses.

CXCL9 and CXCL10 are well known for their roles in shaping antitumour immunity. These chemokines bind to CXCR3, a receptor expressed on $CD8^+$ T cells, NK cells, and T helper 1 (Th1) cells, guiding their infiltration into tumours. High intratumoural levels of CXCL9 and CXCL10 are often associated with improved responses to ICB therapies, as they enhance T cell trafficking. Although CXCL11 also binds to CXCR3, its role in the TME is more complex, as its effects vary depending on the cancer type and receptor context. CCL5 and its receptor CCR5 have also been implicated in T cell chemotaxis. Tumour-derived CCL5 was shown to enhance $CD8^+$ T cell migration, while CCL5 secreted by NK cells was crucial for recruiting cDC1s (conventional type 1 dendritic cells). These cDC1s, in turn, produced CXCL9 and CXCL10, further promoting T cell migration (Chow et al., 2019; Y. Li et al., 2022; J. Wang et al., 2024; B. Wu et al., 2024; J. Zhang et al., 2021). Tumours can evade immune detection by downregulating the expression of these chemokines, leading to immune exclusion and resistance to immunotherapy. Strategies aimed at restoring or amplifying CXCL9, CXCL10, or CCL5 signalling have the potential to improve T cell infiltration and sensitise tumours to immunotherapy. Despite the importance of these chemokines in the TME, the contributions of CAF-derived CCL5, CXCL9, and CXCL10 remain to be elucidated.

Immunotherapy benefits only a subset of patients, highlighting the need to understand the factors driving both response and resistance. Gaining insights into these determinants is crucial for improving outcomes and developing new treatment strategies. Evidence suggests that cytokine composition, which varies among different CAF subtypes, influences immune cell trafficking. Consequently, cytokine-targeted approaches may enhance the efficacy of immunotherapy.

1.9.8 Strategies for targeting CAFs

CAFs are a predominant component of the TME and play a critical role in tumour progression, metastasis, and therapy resistance. Unlike normal fibroblasts, CAFs exhibit an activated phenotype characterised by the secretion of ECM components, cytokines, and growth factors that support tumour growth. Due to these tumour-promoting functions, CAFs have emerged as promising therapeutic targets in cancer treatment. This section explores various strategies for targeting CAFs, including their depletion, reprogramming to a quiescent state, and disruption of key signalling pathways and secreted proteins.

One approach to targeting CAFs involves their selective depletion within the TME. FAP is one of the most commonly targeted markers, and therapeutic strategies aimed at FAP^+CAFs have shown

promise in alleviating immunosuppression and enhancing responses to immunotherapy. For example, in a murine colon cancer model, a DNA vaccine against FAP induced an effective $CD8^+$ T cell mediated antitumour response, suppressing primary tumour formation and inhibiting the growth of pulmonary metastases, ultimately prolonging the lifespans of vaccinated mice (Wen et al., 2010). Additionally, in mouse melanoma models, an adenoviral-vector vaccine designed to eliminate FAP^+ stromal cells reduced the number of immunosuppressive cells and alleviated $CD8^+$ T cell exhaustion (Y. Zhang & Ertl, 2016). CAR-T cells engineered to target FAP in murine models also inhibited tumour growth and demonstrated promising therapeutic outcomes (Kakarla et al., 2013; Schuberth et al., 2013; L. C. S. Wang et al., 2014). Furthermore, targeted drug delivery using anti-FAP antibody-drug conjugates (ADCs) has resulted in tumour growth inhibition and regression in preclinical models (Fabre et al., 2020; Ostermann et al., 2008). Small molecule-drug conjugates represent an alternative to ADCs, wherein the monoclonal antibody is replaced by a small organic ligand with high affinity for a tumour-associated antigen; for example, OncoFAP-Gly-Pro-MMAE demonstrated anti-cancer potency in cell-derived xenograft-bearing mice (Bocci et al., 2024). Several FAP-targeting treatments have progressed into clinical trials. A monoclonal antibody known as Siobrotuzumab, underwent a phase II clinical trial for metastatic colorectal cancer but did not demonstrate therapeutic efficacy (Hofheinz et al., 2003). Similarly, Val-boroPro (Talabostat), the first clinical inhibitor of FAP enzymatic activity, demonstrated minimal clinical efficacy (Narra et al., 2007). Although many preclinical studies have demonstrated the potential of FAP targeting, clinical trials to date have not corroborated these findings. It is also important to note that CAFs lack specific markers, and while FAP is highly expressed by CAFs, it is also present at lower levels in most tissues including skeletal muscles, bones, adipose tissue, salivary glands, and the pancreas. In mouse models, depletion of FAP-expressing cells resulted in cachexia, anaemia, and lethal bone toxicities (Contreras et al., 2021; Roberts et al., 2013; Tran et al., 2013), suggesting that FAP-targeting strategies should be approached with caution.

Rather than complete depletion, another strategy involves converting CAFs to a less active state. TGF-β signalling is central to myofibroblast differentiation and immunosuppression and has therefore gathered much interest as a potential method for targeting myCAFs. Several receptor kinase inhibitors, monoclonal antibodies, ligand traps, antisense oligonucleotides, and vaccines have been designed to target the TGF-β pathway and have been, or are currently being, evaluated clinically (B. G. Kim et al., 2021). Numerous preclinical studies have explored TGF-β inhibition alone or in combination with ICIs and achieved positive results, including limiting tumour growth, progression, and metastasis as well as increasing the antitumour response mediated by $CD8^+$ T cells in many solid tumour types. Although many therapeutic agents targeting TGF-β have been assessed as safe in clinical trials, these studies have largely failed to recapitulate the successes observed in animal models, highlighting the difficulty of translating preclinical results into clinical

benefit (B. G. Kim et al., 2021; Metropulos et al., 2022). Additionally, studies have shown that while TGF-β receptor inhibition is effective at preventing TGF-β-mediated activation, it is not capable of reverting an established myofibroblast phenotype. However, NOX4, known to act downstream of TGF-β has been identified as an important regulator of TGF-β1-mediated myCAF activation. Inhibition of NOX4 was able to both prevent and reverse myofibroblast differentiation, highlighting that CAFs are not terminally differentiated (Ford et al., 2020; Hanley et al., 2018, 2021). Setanaxib (GKT137831) is the first NOX inhibitor to progress into clinical trials (Thannickal et al., 2023). In a murine model of PDAC, calcipotriol, a vitamin D_3 analogue, has been shown to restore quiescence in stellate cells - precursors to CAFs, and enhanced chemotherapy efficacy (Sherman et al., 2014). In a subsequent study, calcipotriol was found to decrease CAF proliferation and migration while reducing the release of pro-tumorigenic factors such as prostaglandin E_2, IL-6, periostin, and LIF. However, although it diminished the tumour-supportive activity of CAFs, calcipotriol also impaired T cell effector functions, suggesting that it could potentially counteract the effects of immunotherapies by compromising patients' immunological surveillance (Gorchs et al., 2020). A phase II trial of the vitamin D analogue Seocalcitol in patients with inoperable pancreatic cancer demonstrated no antitumor activity (Evans et al., 2002), and among patients with metastatic colorectal cancer, the addition of vitamin D_3 to standard chemotherapy similarly reported no improvement (Ng et al., 2019).

CAFs contribute to an immunosuppressive TME by secreting cytokines and remodelling the ECM. Consequently, targeting immunosuppressive and tumour-promoting proteins derived from CAFs has emerged as a promising therapeutic strategy. In sections 1.9.4 – 1.9.7, several of these targets and their roles in promoting the exclusion of $CD8^+$ T cells have been described. The CXCL12-CXCR4 axis is well documented for its role in suppressing antitumour immunity and has become a key target for cancer therapy. AMD3100 (plerixafor), a CXCR4 inhibitor, was approved by the FDA for autologous transplantation in patients with non-Hodgkin's lymphoma or multiple myeloma (De Clercq, 2019). More recently, in a phase II clinical study, BL-8040 - a CXCR4 antagonist was shown to increase $CD8^+$ T cell infiltration while decreasing MDSCs and Tregs. When combined with pembrolizumab (a PD-1 inhibitor) and chemotherapy, the disease control rate reached 77% in pancreatic cancer patients, suggesting that CXCR4 blockade in conjunction with PD-1 inhibition may enhance chemotherapy efficacy (Bockorny et al., 2020). Clinical trials have also extended to targeting ECM proteins. CAFs secrete hyaluronan, which is a key ECM component that contributes to tissue stiffness and promotes tumorigenesis (K. X. Yu et al., 2024). The pegylated form of human recombinant hyaluronidase (PEGPH20) was shown in preclinical models to deplete hyaluronan in the tumour ECM. A tolerable dose of PEGPH20 in solid tumours was established in a phase I study; however, when combined with the chemotherapeutic regimen mFOLFIRINOX, it led to increased toxicity and negatively affected survival in patients with PDAC. It is hypothesised that this outcome was due either to adverse effects on the TME or an

unfavourable drug interaction (Ramanathan et al., 2019). When PEGPH20 was combined with nab-paclitaxel/gemcitabine (AG), the objective response rate increased by 11%, although there was no improvement in overall survival. Moreover, this combination was associated with increased rates of adverse events compared to placebo plus AG (Van Cutsem et al., 2020). While PEGPH20 was designed to improve chemotherapy delivery by degrading hyaluronan, its non-specific activity in normal tissues results in side effects such as musculoskeletal and extremity pain, peripheral oedema, and fatigue (Hingorani et al., 2016).

CAFs are difficult to target in cancer therapy due to their complex and dynamic roles within the TME. One major challenge is the lack of specific markers that distinguish CAFs from normal fibroblasts, which renders targeted treatments less effective and increases the risk of side effects. Additionally, CAFs exhibit considerable heterogeneity, displaying diverse functions and phenotypes that further complicate treatment efforts. Although CAF-targeting therapies have shown promise in preclinical models, they frequently fail in clinical trials. This discrepancy may be due, in part, to the fact that many experimental models do not capture the full heterogeneity of CAFs, as most research has focused predominantly on the myCAF subset. Developing more representative models that incorporate a broader range of CAF subtypes could improve the translation of these therapies into clinical success. Advances in transcriptomic studies are also aiding in the classification of CAF subpopulations, leading to more precise and context-specific treatment strategies. Continued research into CAF diversity and plasticity will be essential for creating effective and safe cancer treatments.

1.10 Project aims

Myofibroblastic CAFs are found in most solid cancer types, possess numerous tumour-promoting functions, and are resistant to immunotherapy. Although myCAFs are associated with poor outcomes, the molecular mechanisms regulating the myofibroblastic phenotype remain incompletely understood, thereby limiting therapeutic intervention strategies. Myofibroblasts were found to upregulate genes associated with DNA repair during TGF-β1-induced differentiation, and studying the role of ATM in regulating the myCAF phenotype became the primary focus. *In vivo* studies have shown that pharmacological inhibition of ATM suppressed myCAF-rich tumour growth, promoted intratumoural $CD8^+$ T cell infiltration, and potentiated the response to anti-PD-1 blockade and antitumour vaccination (Mellone et al., 2022).

Aim 1: Identify the key molecular mechanisms mediating intratumoural $CD8^+$ T cell infiltration following myofibroblast ATM inhibition, with a particular focus on its effects on extracellular matrix proteins and cytokine expression (Chapter 3).

Aim 2: Examine the role of specific CAF-derived ECM proteins, CTHRC1, POSTN, and COL11A1 on myCAF phenotype and function, and determine whether these genes individually influence $CD8^+$ T cell migration into tumours (Chapter 4).

Aim 3: Determine whether ATM inhibition activates the cGAS-STING pathway in fibroblasts and investigate its role in the type I interferon response (Chapter 5).

Aim 4: Evaluate the effects of different doses of the ATM inhibitor AZD0156 on key cellular processes, including target activity inhibition, cell proliferation, cell cycle progression, DNA synthesis, and regulation of myofibroblastic markers, to gain insight into the impact of ATM inhibition on both fibroblasts and myofibroblasts (Chapter 6).

Chapter 2 Materials and methods

2.1 Cell culture

To minimise the risk of contamination, all *in vitro* cell culture work was performed in Class II laminar flow hoods. Cells were confirmed to be mycoplasma-negative using the E-Myco Plus PCR Detection Kit (Chembio; 25237), following the manufacturer's instructions.

2.1.1 Cell lines

TC1 cells are a lung epithelial cancer cell line derived from C57BL/6 mice, expressing HPV-16 E6 and E7 oncogenes. Initially, a frozen vial of TC1 cells was kindly provided by Dr Natalia Savelyeva from the University of Southampton, Cancer Sciences Unit, Southampton General Hospital. TC1 cells were cultured in Roswell Park Memorial Institute (RPMI-1640) medium (Sigma; R0883) supplemented with 1% L-Glutamine (Sigma; G7513), 1% penicillin-streptomycin (Sigma; P4333), 1% sodium pyruvate solution (Sigma; S8636), 1% MEM Non-essential amino acid solution (Sigma; M7145), 1% HEPES solution (Sigma; H0887), 70 µM 2-Mercaptoethanol (Sigma; M3148), and 10 % (v/v) fetal bovine serum (FBS).

HEK293T cells, a human embryonic kidney cell line containing the SV40 large T antigen were used for packaging viruses. These cells were cultured in Dulbecco's Modified Eagle Medium (DMEM, Sigma; D5671) supplemented with 1% L-Glutamine (Sigma; G7513), 1% sodium pyruvate solution (Sigma; S8636), and 10 % (v/v) fetal bovine serum (FBS).

TC1 and HEK293T cell lines were grown in a humidified incubator at 37°C, 5% CO_2,

2.1.2 Primary fibroblast isolation and culture

Lung tissue from a C57BL/6 mouse was washed for 5 minutes in sterile phosphate-buffered saline (PBS) supplemented with 1% penicillin-streptomycin and 0.25 µg/ml amphotericin B. The tissue was then transferred into a sterile dish, and a scalpel was used to cut it into small pieces. These pieces were added to a 15 mL tube containing filter-sterilised 5 mL complete DMEM (10% FBS, 1% L-Glutamine, 1% penicillin-streptomycin, 1% sodium pyruvate) supplemented with 16 U/mL DNase (Sigma; D4263) and 3 U/mL Collagenase P (Roche; 11213865001). The suspension was placed in a shaker set to 150 rpm at 37°C for 60 minutes to aid tissue dissociation. Every 15 minutes, the suspension was pipetted up and down using progressively smaller pipettes. At the end of incubation, the solution was cloudy, with only small tissue fragments visible, which was critical to ensure the release of fibroblasts.

The suspension was then centrifuged at 1500 rpm for 5 minutes at room temperature. The pellet was resuspended in 2 mL red blood cell lysis buffer (RBC, BioLegend; 420301) and incubated for 10 minutes at 4°C. Following incubation, 10 mL of complete DMEM was added, and the sample was mixed thoroughly by pipetting. The sample was centrifuged again at 1500 rpm for 5 minutes at room temperature, and the pellet was resuspended in 5 mL complete DMEM. Cells were counted and seeded at 100, 000 cells/cm^2 in complete DMEM and incubated at 37°C, 3% O_2 and 5% CO_2 for 2 hours. Prolonged incubation may cause epithelial cell adherence. The culture medium was removed, and the dish was washed three times with sterile PBS.

Mouse lung fibroblasts (MLFs) were cultured in complete DMEM containing 20% FBS in a humidified, hypoxic incubator at 37°C, 3% O_2 and 5% CO_2. The medium was changed every 3 days, and cells were passaged when they reached 90% confluency.

2.1.3 CD8 T cell isolation and culture

Splenocytes were isolated using either the Lymphoprep method or the RBC method.

2.1.3.1 Lymphoprep method

A scalpel was used to mince individual spleens into small pieces and release splenocytes in 5 mL of ice-cold PBS supplemented with 0.1% FBS. The resulting suspension was passed through a 70 µm cell strainer into a sterile Falcon tube while gently pressing the remaining tissue with a syringe plunger. The volume was topped to 10 mL with ice-cold PBS supplemented with 0.1% FBS. The single-cell suspension was carefully layered on top of 15 mL of Lymphoprep (StemCell Technologies; 07851) at room temperature. The suspension was centrifuged at 800 x g for 20 minutes at 4°C with acceleration and deceleration set to 1 (no brake). The white mononuclear cell layer was carefully transferred to a fresh Falcon tube and topped up to 50 mL with ice-cold PBS. The suspension was centrifuged at 300 x g (1300 rpm) for 5 minutes at 4°C, and the supernatant was discarded. The pellet was resuspended in PBS, and cell viability was assessed using a haemocytometer and trypan blue staining. Splenocytes were counted for $CD8^+$ T cell isolation.

2.1.3.2 Red blood cell lysis method

A scalpel was used to mince individual spleens into small pieces and release splenocytes in 5 mL of ice-cold PBS supplemented with 0.1% FBS. The resulting suspension was passed through a 70 µm cell strainer into a sterile Falcon tube while gently pressing the remaining tissue with a syringe plunger. The volume was topped to 10 mL with ice-cold PBS supplemented with 0.1% FBS. The single cell suspension was centrifuged at 300 x g (1300 rpm) for 5 minutes at room temperature. The cell pellet was resuspended in 5 mL of RBC lysis buffer (BioLegend; 420301) and incubated for 5 minutes at room temperature to lyse red blood cells. The lysis was stopped by topping up

the volume to 20 mL with ice-cold PBS. The cell suspension was centrifuged at 300 x g (1300 rpm) for 5 minutes, and the pellet was resuspended in 50 mL of ice-cold PBS. Splenocytes were counted using a haemocytometer and viability was assessed using trypan blue staining.

2.1.3.3 CD8⁺ T cell isolation and activation

Isolated splenocytes were used for $CD8^+$ T cell isolation and activation using manufacturer's instructions. $CD8^+$ T cell were isolated using MACS CD8a Ly-2 Micro-beads (Miltenyi Biotec;130-117-044) and activated with Dynabeads Mouse T-Activator CD3/CD28 (Gibco; 11456D). The complete growth medium for $CD8^+$ T cells was RPMI-1640 medium (Sigma; R0883) supplemented with 1% L-Glutamine (Sigma; G7513), 1% penicillin-streptomycin (Sigma; P4333), 1% sodium pyruvate solution (Sigma; S8636), 1% MEM Non-essential amino acid solution (Sigma; M7145), 1% HEPES solution (Sigma; H0887), 70 µM 2-Mercaptoethanol (Sigma; M3148), and 10 % (v/v) FBS. $CD8^+$ T cells were incubated with activation beads in a humidified incubator at 37°C with 5% CO_2 for at least two hours before being used in downstream assays.

2.1.4 Passaging of adherent cells

Cell culture medium was typically changed every three days until cells reached approximately 90% confluency. For passaging, the medium was removed, and cells were washed with sterile PBS. Pre-warmed 0.05 % trypsin-EDTA solution (Gibco; 25300054) was added to the flask, and cells were incubated at 37°C until detachment was observed (~2 minutes for TC1 and HEK293T cells, ~5 minutes for MLFs). Complete medium was then added to neutralise the trypsin. The cell suspension was centrifuged at 300 x g (1300 rpm) for 5 minutes, and the pellet was resuspended in an appropriate volume of fresh complete medium. For routine maintenance, MLFs were normally split 1:3, TC1 cells 1:20, HEK293T cells 1:10. For experimental seeding, an aliquot of cell suspension was mixed 1:1 with trypan blue (Gibco; 15250061), and cells were counted using a haemocytometer, ensuring >95% viability before reseeding.

2.1.5 Cell freezing and thawing

Cells were trypsinised and pelleted as described above. The cell pellets were resuspended in freezing medium consisting of 90% FBS and 10% dimethyl sulfoxide (DMSO). Cells were aliquoted into cryovials and frozen at -80°C overnight in a Mr. Frosty freezing container to achieve a controlled cooling rate of -1°C per minute. The cryovials were then transferred to liquid nitrogen for long term storage.

For thawing, cryovials were removed from the liquid nitrogen storage and immediately thawed by gentle swirling in a 37°C water bath. The thawed cells were transferred to 5 mL of pre-warmed complete growth medium specific to the cell line and centrifuged at 300 x g (1300 rpm) for 5

minutes. The supernatant was carefully removed to eliminate the cryoprotectant. The cell pellet was gently resuspended in complete growth medium and transferred to a suitable culture flask, then placed in the recommended cell culture environment.

2.1.6 Cell treatments

Cells were seeded and incubated overnight to allow for attachment before treatment. The cell culture medium was refreshed with each treatment. Primary mouse lung fibroblasts were seeded at a density of 600 cells per well in 96-well plates. For 6-well plates, MLFs were seeded at a density of 50,000 cells per well for 6-day treatments or 100,000 cells per well for 3-day treatments. During the 6-day treatments, cells were treated on day 1 and day 4 with fresh media and compounds. To assess the effects of molecular compounds, fibroblasts were treated with 2 ng/mL TGF-β1 (prepared by Dr Patrick Duriez) and the test compounds simultaneously. Compound names and concentrations are provided in **Table 2.1**. All compounds were prepared according to manufacturer's instructions. The incubation times, compounds, and concentrations used are detailed in the respective figure legends.

Table 2.1: Compound names and concentrations

Target	Compound name	Concentration
ATM	AZD0156	1-500 nM
LOXL2/3	PXS-5153A	300 nM
Pan-LOX	PXS-4787	20 μM
NOX1/4	GKT137831	20 μM
TGF-β	616454	1 μM
Wee1	AZD1775	40 nM

2.2 Mouse CD8⁺ T cell migration *in vitro*

2.2.1 Migration through myofibroblast-derived ECM

The migration of CD8⁺ T cell through myofibroblast-derived ECM was assessed using 5 μm-pore transwell plates (Corning; CLS3387). To prepare the transwell plates, 600 MLFs were seeded in 100 μL of complete DMEM in the upper chamber, while the receiver wells were filled with complete DMEM. The plates were incubated overnight in a humidified, hypoxic incubator at 37°C, 3% O_2 and 5% CO_2 to allow for cell attachment. For MLF treatment, the medium in the receiver wells was replaced every other day for 7 days and supplemented with ± 2 ng/mL TGF-β1 and inhibitors as described in section 2.1.6. When collagenase D was used, the treatment was applied before the decellularisation step described below. On the final day of the assay, MLFs in the transwell upper chambers were decellularised by incubating them with PBS containing 50 mM EDTA and 0.5% (v/v) Triton X-100 for 30 minutes at 37°C. This was followed by treatment with PBS containing 20 U/mL DNase for 1 hour at room temperature. The decellularised ECM was thoroughly washed with PBS. On day 6, TC1 cells, which had reached approximately 90% confluence, were cultured in complete RPMI for 24-hours to generate conditioned medium. The conditioned medium was centrifuged at 3,500 rpm for 5 minutes to remove cellular debris, and the supernatant was supplemented with 0.1% BSA. The transwells containing the deposited ECM were then placed on top of the receiver plate containing 200 μL of TC1-conditioned medium in each well. Basic medium (RPMI supplemented with 1% L-glutamine and 0.1 % BSA) was used as a negative control. Activated CD8⁺ T cells, prepared as described in section 2.1.3, were seeded at a density of 50,000 cells per 100 μL of basic medium. This suspension was added to the upper wells of the transwell plate containing the deposited ECM. The plate was incubated in a humidified chamber at 37°C, 5% CO_2 for 2 hours. Following incubation, the transwell inserts were discarded, and the migration medium from the receiver wells was transferred to FACS tubes. Flow cytometry was used to quantify the CD8⁺ T cells that had migrated through the ECM.

2.2.2 Chemotaxis assay

T cell migration was assessed using various conditioned media and recombinant proteins (R&D systems). Specific concentrations of these compounds and the number of replicates for each condition are detailed in the figure legends. To prepare conditioned medium from MLFs, cells were seeded and treated with 2 ng/mL TGF-β1 and 0.5 μM ATMi AZD0156 twice over 6 days. The medium was refreshed with every treatment. On day 3, the composition of the medium was changed to a 1:2 ratio of complete DMEM to complete RPMI, both supplemented with FBS to

achieve a final concentration of 20% FBS. By day 6, TC1 and MLF cells reached approximately 95% confluence. At this point, their medium was replaced with basic medium (RPMI supplemented with 1% L-glutamine and 0.1% BSA) and incubated for 24 hours. The conditioned media were collected and centrifuged at 3,500 rpm for 5 minutes to remove cellular debris. The supernatant was then supplemented with 0.1% BSA. Untreated and treated MLFs were counted, and the conditioned medium was diluted with basic medium to account for cell density. Basic medium alone served as negative control. Receiver wells were filled with 200 μL of conditioned medium derived from TC1 or MLF cells or with basic medium supplemented with varying concentrations of recombinant proteins. Activated $CD8^+$ T cells were prepared as described in section 2.1.3 and seeded at a density of 50,000 cells per 100 μL in basic medium. This suspension was added to the upper wells of 5 μm-pore transwell plates (Corning; CLS3387). The plates were incubated in a humidified incubator at 37°C, 5% CO_2 for 2 hours. Following incubation, the transwell inserts were discarded, and the migration medium from the receiver wells was transferred to FACS tubes. Migrated $CD8^+$ T cells were quantified using flow cytometry.

2.3 shRNA knockdown generation in primary fibroblasts

2.3.1 Plasmids

The shRNA-expressing vector plasmids described in chapter 4 were obtained as bacterial stocks from the MISSION shRNA library (Sigma-Aldrich). These plasmids contain shRNA sequences (**Table 2.2**) inserted into the pLKO.1-puro vector and therefore are designed to work with the lentiviral plasmid system. For genes without prior validation, four shRNA clones were ordered, whereas two clones were ordered for genes with validated sequences provided on the website.

The following plasmids were ordered from MISSION shRNA library:

Table 2.2: shRNA target sequences for generation of gene knockdowns

Gene	TRC clone ID	Target Sequences (5' to 3')	Referred to as:
CTHRC1	TRCN0000090643	GCCCTTGAATGGTTCATTTAA	shCTHRC1-43
CTHRC1	TRCN0000090644	GCCCTGAGTTAAATTCAACTA	shCTHRC1-44
CTHRC1	TRCN0000090645	GCTGAATGTTCAGGACCTCTT	shCTHRC1-45
CTHRC1	TRCN0000090646	GCTACAGTTGTCCGCACCGAT	shCTHRC1-46
POSTN	TRCN0000111165	GCTAAGTCTTTGCACAGTAAA	shPOSTN-65

POSTN	TRCN0000111166	CCACATGGTTAATAAGAGAAT	shPOSTN-66
POSTN	TRCN0000111167	CGGAGTCACTAATATCCTGAA	shPOSTN-67
POSTN	TRCN0000111168	GCCATTCACATATTCCGAGAA	shPOSTN-68
COL11A1	TRCN0000091193	CGTCCATCAAAGATATAGTAA	shCOL11A1-93
COL11A1	TRCN0000091196	GCTGCCTGGTATGACGTATTA	shCOL11A1-96

Control plasmids:

Scrambled shRNA (shSCR) was used as a negative control.

MISSION pLKO.1-puro-CMV-TagRFP (Sigma-Aldrich; SHC012) was used a positive control and was kindly gifted by Dr Emre Sayan.

2.3.2 Bacterial transformations

E. coli JM109 competent cells (prepared by Dr Patrick Duriez) were thawed on ice for approximately 30 minutes. For control plasmid transformations, 20 μL of JM109 competent cells was combined with 50 ng of plasmid DNA. The DNA-cell mixture was incubated on ice for 30 minutes, followed by heat shock at 42°C for 45 seconds. The mixture was then placed back on ice for 2 minutes. 500 μL of Luria-Bertani (LB) Broth (Miller) was added to the suspension, and the cultures was incubated at 37°C with shaking at 225 rpm for 1 hour. The culture was then plated on pre-warmed LB agar plates supplemented with 100 μg/mL ampicillin and grown overnight at 37°C.

2.3.3 Streaking bacterial stocks for isolation

A sterile pipette tip was used to pick a small amount of the bacterial stock, and bacteria were streaked onto the surface of pre-warmed LB agar plates supplemented with 100 μg/mL ampicillin. The plates were incubated overnight at 37°C.

2.3.4 Plasmid preparation

Single colonies were picked from LB agar plates (see step 2.3.2 and 2.3.3) and transferred to 3 mL of LB broth supplemented with 100 μg/mL ampicillin. Starter cultures were grown at 37°C with shaking at 170 rpm for 8 hours, then transferred to 50 mL of LB broth with 100 μg/mL ampicillin. The bacterial cultures were incubated overnight at 37°C with shaking at 170 rpm. The cultures were pelleted by

centrifugation at 5000 x g for 5 minutes, and the supernatant was discarded. Plasmid DNA extraction was performed using the Macherey-Nagel NucleoBond-Xtra Midi kit (Fisher Scientific; 11932492) following the manufacturer's instructions. The procedure involves the alkaline lysis of bacterial cells, precipitation of cellular debris and chromosomal DNA, and the removal of proteins. Plasmid DNA is then bound to a silica membrane in the presence of high salt concentrations, followed by washing to remove contaminants and elution of the purified plasmid DNA. Eluted plasmid DNA was quantified using a Nanodrop spectrophotometer and stored at – 20°C.

2.3.5 Restriction digest and agarose gel analysis

To confirm sizes of the plasmids, DNA was digested with the restriction enzyme EcoRI to generate a linearised plasmid. Digestion reactions were prepared as follows:

500 ng of plasmid DNA

0.5 μL EcoRI restriction enzyme (NEB; R3101)

2 μL rCutSmart Buffer (10X)

Nuclease-free water to a final volume of 20 μL

Reactions were incubated at 37°C for 1 hour and subsequently heat-inactivated at 65°C for 15 minutes. An 0.8% (w/v) agarose gel was prepared in 1x Tris-acetate-EDTA (TAE) buffer (ThermoFisher Scientific; B49) with SYBR Safe DNA Gel Stain (Invitrogen; S33102). Both circular and linearised plasmids were mixed with 6X gel loading dye (diluted to 1X) and loaded onto the gel alongside a Quick-Load 1 kb DNA ladder (NEB; NO552S) as a size marker. The gel was electrophoresed at 100 V in TAE buffer until adequate separation was achieved, and DNA bands were visualised using UV transillumination.

2.3.6 Lentivirus generation

Day 1

Six million HEK293T cells were seeded into T75 flasks containing 15 mL of complete DMEM medium (refer to section 2.1.1) to achieve 60% confluency. After seven hours of incubation. Once the cells attached, the medium was replaced with 15 mL of fresh complete DMEM medium.

Previously aliquoted Lentiviral Packaging Mix (Sigma; SHP001) was thawed at room temperature and then placed on ice. Transfection cocktails were prepared on ice in polypropylene tubes by combining the following components in the specified order:

34 μL Lentiviral Packaging Mix (per sample)

3.4 μg transfer vector (shRNA-expressing plasmid)

237 µL serum-free DMEM medium

21 µL FuGENE 6 Transfection Reagent (Promega; E2691)

The components were mixed gently by pipetting up and down, then incubated at room temperature for 15 minutes. After incubation, the transfection cocktails were added to the corresponding T75 flasks containing HEK293T cells. Flasks were gently swirled to distribute the reagents evenly and incubated in a humidified incubator at 37°C, 5% CO_2,

Day 2

At 16 hours post-transfection, the medium from each flask was removed and replaced with 15 mL of pre-warmed complete DMEM medium. The cells were incubated for an additional 24 hours at 37°C, 5% CO_2.

Day 3

The medium containing viral particles was collected from each flask and transferred to Falcon tubes, labelled as first harvest, which were stored at 4°C. Fresh 15 mL pre-warmed complete DMEM medium was added to the flasks, and the cells were incubated for another 24 hours at 37°C, 5% CO_2,

Day 4

The second harvest of medium containing viral particles was collected and combined with the first harvest in Falcon tubes. The pooled virus-containing medium was filtered through 0.45 µM filters into fresh Falcon tubes.

2.3.7 Virus concentration by ultracentrifugation

Equal volumes of filtered medium were transferred into open-top thin-walled polypropylene ultracentrifuge tubes. The tubes were inserted into a pre-cooled rotor and centrifuged at 91 000 x g for 90 minutes at 4°C. After centrifugation, the supernatant was discarded, and the virus pellets were resuspended in 80 µL sterile PBS. The resuspended virus was aliquoted into 10 µL volumes, snap frozen and stored at -80°C.

2.3.8 Lentivirus quantification

Lentivirus particles were quantified following the manufacturer's instructions for the Lenti-X p24 Rapid Titer Kit (Takara; 631476), which detects the p24 capsid protein, a key structural component of lentiviral particles. Viral supernatants were treated with lysis buffer to release p24 protein into solution. The samples were incubated with an anti-p24 antibody, followed by a

secondary antibody conjugated to a horseradish peroxidase (HRP). The resulting colorimetric reaction was measured spectrophotometrically, with the colour intensity corresponding to the p24 levels in the samples.

2.3.9 Lentiviral transduction

2.3.9.1 Determination of optimal puromycin concentration

Puromycin was used to select for cells stably expressing the shRNA of interest. Mouse lung fibroblasts were seeded into a 12-well plate. Once cells reached approximately 90% confluence, the medium was replaced with fresh complete DMEM, and puromycin was added in 0.5 μg/mL increments (0 – 5.5 μg/mL). The minimum concentration of puromycin that resulted in complete cell death after 4 days was selected for downstream experiments. For MLFs, the optimal concentration of puromycin was determined to be 4 μg/mL.

2.3.9.2 Determination of polybrene toxicity

Polybrene was used to enhance viral transduction efficiency; however, its toxicity to cells was assessed prior to use. MLFs were seeded in duplicates into a 96-well plate. After 24 hours, the medium was replaced with fresh medium containing polybrene at 1μg/mL increments (0-8 μg/mL) for an additional 24 hours. Cell viability was then assessed using an MTS assay, following the manufacturer's instructions. Based on the results, the polybrene concentration of 6 μg/mL was selected for subsequent experiments as it maintained acceptable cell viability.

2.3.9.3 Multiplicity of infection optimisation

Multiplicity of infection (MOI) refers to the ratio of viral particles to target cell. Optimisation of MOI was performed using the SHC012 positive control plasmid, which produces RFP fluorescence in transduced cells. 30,000 MLFs were seeded into a 12-well plate and incubated in a humidified, hypoxic incubator at 37°C, 3% O_2 and 5% CO_2 for 24 hours. The medium was replaced with fresh complete DMEM containing 6 μg/mL polybrene, and lentiviral particles were added at the following MOIs: 0, 1, 2, 3, 4, 5, 6, 7, 8 10, 20, 30. Cells were incubated in a humidified incubator at 37°C, 5% CO_2 for 18 hours. After incubation, the medium containing viral particles was removed, cells were washed twice with PBS, and fresh complete DMEM was added to each well. RFP fluorescence was visible 48 hours post-transduction. The medium was replaced with complete DMEM supplemented with 4 μg/mL puromycin. When complete cell death was observed in the control well, RFP and brightfield images were captured using an EVOS microscope. The lowest MOI at which a sufficient number of MLFs survived and proliferated was selected for further experiments. For MLFs, the optimal MOI was determined to be 5.

2.3.9.4 Transduction of MLFs with target shRNAs

Mouse lung fibroblasts at passage 4 were seeded into T75 flasks with 13 mL of complete DMEM medium (refer to section 2.1.1) for each shRNA outlined in section 2.3.1. Cells were incubated in a humidified, hypoxic incubator at 37°C, 3% O_2 and 5% CO_2 for 24 hours. The medium was replaced with fresh complete DMEM containing 6 μg/mL polybrene. Lentiviral particles were added at an MOI of 5, and cells were incubated at 37°C, 5% CO_2 for 18 hours. After incubation, the medium containing viral particles was removed, cells were washed twice with PBS, and fresh complete DMEM was added. At 48 hours post-transduction, the medium was replaced with complete DMEM supplemented with 4 μg/mL puromycin (excluding non-transduced controls). Cells were grown in puromycin-supplemented medium for 1 week, with re-treatment on day 3. Once cells reached 90% confluence, they were expanded into T175 flasks. Stocks of shRNA knockdown cells were frozen once cells in T175 flasks reached approximately 90% confluence. Cells were also seeded for RT-qPCR and Western blotting (see sections 2.9 and 2.10) to evaluate the efficiency of shRNA knockdowns.

2.4 Cell immortalisation

2.4.1 Immortalisation via mTERT overexpression

Primary MLFs were immortalised through overexpression of mouse telomerase reverse transcriptase (mTERT). A lentiviral vector containing the mTERT gene, along with a hygromycin resistance marker, was provided by Dr Matthew Gillespie. Lentiviral transduction was performed as described in section 2.3.9, using MOIs of 5, 10, 20 and 30. The optimal hygromycin concentration for selection was determined to be 300 μg/mL. Under these conditions, mTERT-negative cells did not survive, while mTERT-immortalised MLFs proliferated and were subsequently expanded for future experiments. MLFs immortalised via mTERT overexpression will be referred to as mTERT MLFs.

2.4.2 Immortalisation via serial passaging

Primary MLFs were isolated and cultured as detailed in section 2.1.2. Serial passaging was performed for 22-30 passages. Morphological changes and differences in proliferation were observed as early as passage 22. Cells were further cultured to passage 30 to confirm stable immortalisation. MLFs immortalised via serial passaging will be referred to as iMLFs.

2.5 CRISPR knockout generation in fibroblasts

2.5.1 Determination of nucleofection conditions with pmaxGFP vector

To optimise nucleofection conditions for genome editing experiments, immortalised mouse lung fibroblasts were transfected with the pmaxGFP (green fluorescent protein) positive control vector. Reagents for voltage optimisation were provided in the P3 Primary Cell 4D-Nucleofector X Kit (Lonza; V4XP-3032). The manufacturer's recommended protocol for mammalian fibroblasts was followed. Passage 27 iMLFs, at approximately 80% confluency, were detached and counted using a hemacytometer. For each sample in the 4D-Nucleofector X Unit (Lonza), 100,000 cells were used in a final volume of 20 μL. Cells were pelleted by centrifugation at 90 x g for 5 minutes at room temperature, and the supernatant was completely removed. The cell pellet was resuspended in room-temperature supplemented 4D-Nucleofector solution. pmaxGFP vector (0.4 μg per well) was added, and the mixture was gently pipetted to ensure homogeneity. The prepared cell suspension was transferred into a nucleocuvette strip (20 μL per well). The nucleocuvette strip was then placed into the 4D-Nucleofector X Unit, and nucleofection was performed using fibroblast-specific programs as outlined in **Table 2.3**. After nucleofection, the nucleocuvette strip was removed, and the cells were incubated at room temperature for 10 minutes. Subsequently, 80 μL of pre-warmed complete DMEM (without penicillin-streptomycin, as used throughout CRISPR gene knockout experiments) was added to each well of the nucleocuvette strip. The cells were gently resuspended by pipetting three times and transferred to 6-well plates containing pre-warmed medium. Images of the cells were captured 48 hours post-nucleofection using a 10X objective on an EVOS microscope. At 96 hours post-nucleofection, the cells were detached, and the percentage of GFP-positive cells was quantified using flow cytometry.

Table 2.3: Nucleofector programs

	1	**2**
A	CA-137	CA-137
B	CM-138	CM-138
C	DS-150	DS-150
D	EH-100	EH-100
E	EN-150	EN-150
F	EO-114	EO-114
G	FF-113	FF-113
H	Negative control (no program)	Negative control (no program)

2.5.2 CRISPR-Cas9 ribonucleoprotein nucleofection in MLFs

The Synthego CRISPR Design Tool was used to identify three RNA sequences per gene of interest (**Table 2.4**). These sequences were purchased as chemically modified synthetic guide RNAs (sgRNAs). Synthego's synthetic sgRNAs include a scaffold sequence required for the guide RNA to complex with the *Streptococcus pyogenes* Cas9 (SpCas9).

Table 2.4: sgRNA sequences for generation of gene knockouts

Target gene	**sgRNA/PAM* (5' to 3')**
CTHRC1	CCCAGGGCTCCCATCACGACCGG
	TCACGACCGGGAACTCCTGCTGG
	TATAATGGAATGTGTCTACAAGG
POSTN	GACCATGTTTATGGCACGCTGGG
	TGACCATGTTTATGGCACGCTGG
	GTGCCATAAACATGGTCAATAGG

	GTAACTCTATAAGCAACATCTGG
COL11A1	GATTTTCACAATTCTCCAGTGGG
	AGATTTTCACAATTCTCCAGTGG

*PAM = protospacer adjacent motif

Upon receipt, the tubes containing sgRNAs were briefly centrifuged and rehydrated in 15 μL of 1X nuclease-free Tris-EDTA buffer to prepare stock solutions at 100 μM. Ribonucleoprotein (RNP) complexes were formed by incubating synthetic sgRNAs with SpCas9 protein (NEB; M0646T) at a ratio of 9:1. For each gene, three guides were used; they were first mixed (60 pmol of each, totalling 180 pmol) before the addition of Cas9 to ensure equal stoichiometry in the sgRNA:Cas9 complexes across all guides. Cas9 protein (20 pmol) was added to 180 pmol of sgRNAs, and the mixture was gently pipetted 30 times. To facilitate sgRNA:Cas9 RNP complex formation, the tubes were incubated at room temperature for 15 minutes. During this incubation, iMLF at passage 25 were detached and counted using a hemacytometer. The cells were washed with PBS and resuspended in room-temperature supplemented 4D-Nucleofector solution as previously described. After incubation, the sgRNA:Cas9 RNP complexes were mixed with the cell suspension by pipetting. The prepared cell suspension (20 μL per well) was transferred into a nucleocuvette strip. The nucleocuvette strip was placed into the 4D-Nucleofector X Unit, and nucleofection was performed using the settings outlined in **Table 2.5**. After nucleofection, the nucleocuvette strip was removed, and the cells were incubated at room temperature for 10 minutes. Subsequently, 80 μL of pre-warmed complete DMEM (without penicillin-streptomycin) was added to each well of the nucleocuvette strip. The cells were gently resuspended by pipetting three times and transferred to 6-well plates containing pre-warmed medium. Once single-nucleofected cells reached 90% confluence, 1:5 of the cells was pelleted for DNA extractions for sequencing, and the remaining cells were expanded. For double-nucleofected cells, 7:10 of the cells were used for expansion, 2:10 were pelleted for DNA extractions, and 1:10 were used for single clone expansion. Cells pelleted for DNA extractions were snap frozen and stored at – 80°C until extraction.

Table 2.5: Nucleofector settings for single and double electroporation

	1	2
A	Negative control (Cas9, no sgRNA) EN-150	Negative control (Cas9, no sgRNA) EN-150
B	POSTN KO EN-150	POSTN KO EN-150
C	CTHRC1 KO EN-150	CTHRC1 KO EN-150
D	COL11A1 KO EN-150	COL11A1 KO EN-150
E	Negative control (Cas9, no sgRNA) EN-150 + EN-150	Negative control (Cas9, no sgRNA) EN-150 + EN-150
F	POSTN KO EN-150 + EN-150	POSTN KO EN-150 + EN-150
G	CTHRC1 KO EN-150 + EN-150	CTHRC1 KO EN-150 + EN-150
H	COL11A1 KO EN-150 + EN-150	COL11A1 KO EN-150 + EN-150

2.5.2.1 Single clone expansion

For single clone expansion, cells were seeded into 96-well plates at a density of 0.5 cells per well. A total of 300 wells were seeded for each gene knockout, CRISPR control, and non-nucleofected cells. Medium was replaced every three days; and wells were regularly inspected to confirm cell growth from single cells. Cells were expanded into plates of increasing sizes. Once cells in T25 flasks reached 90% confluence, cell pellets were collected and snap frozen for DNA extractions, while the remaining cells were frozen as cell stocks.

2.5.3 Validating CRISPR knockouts

2.5.3.1 Genomic DNA extraction

Genomic DNA (gDNA) was extracted from snap-frozen cell pellets using the DNeasy Blood and Tissue Kit (Qiagen; 69506) following the manufacturer's instructions. The DNA was eluted in 30 µL of the provided elution buffer, and the concentration was measured using a Nanodrop spectrophotometer. To standardise the DNA concentration across samples, the elution buffer was used to adjust each sample to approximately 50 ng/µL The genomic DNA was stored at – 20°C until further use.

2.5.3.2 PCR amplification of the CRISPR target region

Primer pairs (~20 bp) targeting regions spanned by the sgRNAs were designed using Benchling (**Table 2.6**). For each PCR reaction, 16 μL of MegaMix Blue PCR Mastermix (Microzone; 2MMB) was combined with 1.5 μL of each forward and reverse primer (100 μM stock; Sigma-Aldrich) pre-diluted to 10 μM, and 1 μL (~50 ng) of gDNA in a 0.2 mL PCR tube (ThermoFisher Scientific; AB0620). The final reaction volume was 20 μL. PCR was carried out using a Veriti Thermal Cycler (Applied Biosystems) under the following conditions: an initial denaturation at 94°C for 2 minutes; 30 cycles of denaturation at 94°C for 30 seconds, annealing at 62°C (for CTHRC1 and POSTN primers) or 60°C (for COL11A1 primers) for 30 seconds, and extension at 72°C for 1 minute; followed by a final extension at 72°C for 15 minutes. PCR products were held at 4°C until loaded onto an agarose gel.

Table 2.6: PCR primer sequences

Gene target	Direction	Primer sequence (5' to 3')	Amplicon size
CTHRC1	Forward	ACGGACGAGGTGGGTTAGAGGG	889 bp
	Reverse	GAGCACGGCGACCAAGGACAAA	
POSTN	Forward	ATGGAGAGAGCCATGTCCATCT	968 bp
	Reverse	TGGACATGCTATCTGAAATGGCA	
COL11A1	Forward	TGCCTGCAATTGTGTACTCACCAG	1,189 bp
	Reverse	TGGGGTCAGACAGATACGGCAC	
	Reverse	GCTTTGTTGGGGCGCTGATTTG	434 bp

2.5.3.3 Preparation of agarose gels and electrophoresis of PCR products

A 3% (w/v) agarose gel was prepared in 1X TAE buffer containing SYBR Safe DNA Gel Stain. For each lane, 10 μL of PCR product was loaded alongside a 1 kb Plus DNA ladder for Safe Stains (NEB; N0559S). Electrophoresis was performed at 100 V in TAE buffer until sufficient DNA band separation was achieved. Bands were visualised using UV transillumination.

2.5.3.4 Sequencing of PCR products

To evaluate CRISPR efficiency in clones selected based on agarose gel electrophoresis results, PCR reactions were scaled up to a final volume of 100 μL. The amplified PCR products were purified using the PCR & DNA Cleanup Kit (NEB; T1030S) and submitted for Sanger sequencing (outsourced to Source BioScience). CRISPR efficiency was assessed using the Synthego Inference of CRISPR Edits (ICE) software tool.

2.6 Murine tumour models

2.6.1 Investigating the effects of the ATMi AZD0156

All experiments were conducted in compliance with UK Home Office Regulations. Procedures requiring a personal licence were performed by Dr Massimiliano Mellone. The effects of the ATM inhibitor (ATMi) AZD0156 on tumour growth and $CD8^+$ T cell infiltration were investigated using murine models. Wild-type (WT) MLF's and STING knockout (KO) MLFs were pre-treated *ex vivo* with 2 ng/mL TGF-β1 for one week prior to injection. TC1 cells were co-injected with either 4.5 x 10^5 WT or STING KO MLFs at a 1:6 ratio. The cell suspensions were prepared in PBS and injected subcutaneously into the flanks of C57BL/6 female mice. After two weeks of tumour growth, mice were weighed, and AZD0156 was administered daily via oral gavage at a dose of 20 mg/kg for an additional two weeks. Tumour dimensions were measured every 3-4 days using an electronic skin calliper, recording the longest length and width. Mice were culled when tumour size approached the humane endpoint, in accordance with the project licence and ethical guidelines. Tumour volume was calculated using the formula for the volume of a sphere, $V = (4/3)\pi r^3$, and the mean area under the curve (AUC) values were derived from tumour growth curves. Excised tumours were halved, with one portion fixed in 4% (paraformaldehyde) PFA for immunohistochemistry and the other transferred into sterile PBS for cytokine array analysis.

2.6.2 Investigating the effects of extracellular matrix gene knockouts in MLFs

Single clones containing CTHRC1, POSTN or COL11A1 gene knockouts were generated as previously described. The effects of these iMLF gene knockouts on tumour growth and $CD8^+$ T cell infiltration were investigated using murine models. Cells derived from three independent single clones for each gene (CTHRC1, POSTN, or COL11A1) and the control were counted, mixed in equal proportions, and seeded together. Knockout and control iMLFs were pre-treated *ex vivo* with 2 ng/mL TGF-β1 for one week prior to injection. TC1 cells were either injected alone or co-injected with 3 x 10^5 control or gene knockout iMLFs at a 1:6 ratio. The cell suspensions were prepared in PBS and injected subcutaneously into the flanks of C57BL/6 female mice. Injections

were performed by Ben Wigley, Deputy Manager of the Preclinical Unit. Ten days post-injection, tumour dimensions were measured every other day using an electronic skin calliper, recording the longest length and width. Mice were culled when tumour size approached the humane endpoint, in accordance with the project licence and ethical guidelines. Tumour volume was calculated using the formula for the volume of a sphere, $V = (4/3)\pi r^3$, and the mean area under the curve (AUC) values were derived from tumour growth curves. Excised tumours were fixed in 4% PFA for immunohistochemistry (IHC) and haematoxylin and eosin (H&E) analysis, which were performed by the Cellular Pathology Laboratory at University Hospital Southampton. Images were captured either by a consultant pathologist (GJT) or using an automated slide scanning system.

2.7 Tissue slice culture

Informed consent was obtained from all patients, and the study methods adhered to relevant ethical guidelines and regulations. Fresh tumour tissue samples were collected at Poole Hospital and delivered to the cancer research laboratory within 2 hours of surgical excision. Mouse tumour samples were processed following project licence requirements and ethical guidelines. Tumour samples were embedded in 4% low-melting point agarose (Sigma; A9045) prepared in PBS at 37°C. The tissue was mounted onto the vibratome's magnetic stage using a few drops of tissue glue (Fisher Scientific, 17150156) and submerged in ice-cold PBS containing 1% (v/v) penicillin-streptomycin and 5 µg/mL of amphotericin B (ThermoFisher; 15290018). Slices were prepared using a vibratome (Leica; VT100S) set to a speed of 0.2 mm/s and an amplitude of 2 mm, producing 300 µm thick sections. These slices were carefully collected with a thin brush and transferred onto 0.4 µm organotypic inserts (Millipore; PICMORG50) placed in 6-well plates containing 1.1 mL of complete medium. The medium consisted of RPMI 1640 supplemented with 10% FBS, 1% penicillin-streptomycin, 1% L-glutamine and 0.2% Normocin (InvivoGen; ant-nr-1). After 2 hours, the medium was replaced with fresh complete medium. In some experimental conditions, AZD0156 was added to the medium. Tissue slices were maintained on a plate shaker in a humidified incubator at 37°C with 5% CO_2. The medium was refreshed every 24 hours. At designated timepoints, slices were fixed in 4% paraformaldehyde. H&E staining and immunohistochemistry were performed by the Cellular Pathology Laboratory at University Hospital Southampton. Images were captured by a consultant pathologist (GJT).

2.8 Cytokine array

Tumours were excised from C57BL/6 mice and rinsed with PBS. To ensure comparability of results, each tumour was weighed and finely chopped in a sterile cell culture dish. The tissue pieces were then transferred to a well of a 12-well plate, and 2 µL of RPMI 1640 supplemented

with 1% (v/v) L-glutamine was added per 10 mg of tumour tissue. The samples were incubated overnight in a humidified incubator at 37°C and 5% CO_2. Following incubation, the contents of each well, including tumour fragments and medium, were transferred to microcentrifuge tubes. These samples were centrifuged at 0.5 x g for 5 minutes. The supernatants were collected and transferred to fresh microcentrifuge tubes, and the centrifugation step was repeated twice more to remove all visible cell debris. The clarified supernatants were stored at – 80°C until further use. The Proteome Profiler Mouse XL Cytokine Array Kit (R&D systems; ARY028) was used according to the manufacturer's instructions. This membrane-based immunoassay includes antibodies for 111 mouse cytokines, which are spotted in duplicate on a nitrocellulose membrane. Initially, target proteins present in the tumour supernatants bind to the immobilised antibodies on the membrane. These captured proteins are then detected using biotinylated detection antibodies, and the signal is visualised with chemiluminescent detection reagents. The intensity of the signal is proportional to the concentration of the analyte bound. Images of the arrays were captured using Amersham ImageQuant 800 GxP biomolecular imager. Pixel densities were quantified using GelAnalyzer software, and relative cytokine expression levels were determined by normalising the sample spot intensities to the reference spots on each membrane.

2.9 Real-time quantitative polymerase chain-reaction (RT-qPCR)

2.9.1 RNA extraction

Cells cultured for RNA extraction were washed with PBS, snap-frozen on dry ice, and stored at -80°C. RNA extractions were performed at room temperature using the ReliaPrep RNA Miniprep Systems kit (Promega; Z6012) following the manufacturer's instructions. The concentration of extracted RNA was measured using a Nanodrop spectrophotometer. RNA samples were stored at -80°C until further use.

2.9.2 cDNA synthesis

mRNA was reverse transcribed into cDNA using the RevertAid First Strand cDNA Synthesis Kit (ThermoFisher Scientific; K1622) following the manufacturer's instructions. Each reaction utilised 1 µg of RNA in a total reaction volume of 20 µL. The synthesised cDNA was diluted in nuclease-free water to the required concentration and stored at -20 °C until further use.

2.9.3 Quantitative PCR (qPCR)

Gene-specific oligonucleotide primer sequences were designed using the NCBI Primer-BLAST tool. Oligonucleotide sequences were synthesised by Sigma-Aldrich, resuspended at 100 µM in molecular-grade water, and stored at -20°C. See **Table 2.7** for primer sequences.

Table 2.7: qPCR primer sequences

Target gene	Forward primer sequence (5' to 3')	Reverse primer sequence (5' to 3')
HPRT	GTTGGGCTTACCTCACTGCT	TCATCGCTAATCACGACGCT
GAPDH	TCAAGCTCATTTCCTGGTATGACA	TAGGGCCTCTCTTGCTCAGT
PDGFRα	GCAGTTGCCTTACGACTCCAGA	GGTTTGAGCATCTTCACAGCCAC
IL6	CGGCCTTCCCTACTTCACAA	TGCCATTGCACAACTCTTTTC
PDPN	TGAAACGCAGACAACAGATAAGA	GCTCTTTAGGGCGAGAACCT
LIF	TCAACTGGCACAGCTCAATGGC	GGAAGTCTGTCATGTTAGGCGC
CD40	ACCAGCAAGGATTGCGAGGCAT	GGATGACAGACGGTATCAGTGG
CX3CL1	CAGTGGCTTTGCTCATCCGCTA	AGCCTGGTGATCCAGATGCTTC
VCAN	CCATGCACTACATCAAGCCAA	TGGGTGGTAAGGTAGGTAAGGT
P4HA3	GGCTCTTGGCTGAGAATGGT	TTGGTAGTGTGTTGGCTGGG
ASPN	CTTCCCAAATCATTAGCAGAACTC	CCGTTGTTCTCAAGAGGGTTTGC
IFIT1	TACAGCAACCATGGGAGAGAA	ACTGGACCTGCTCTGAGATT
TGF-β1	TGATACGCCTGAGTGGCTGTCT	CACAAGAGCAGTGAGCGCTGAA
CTHRC1	TGTTCAGGACCTCTTCCCATCG	GCCACATCTACCAATCCAGCAC
STING	CGGTTGATCTTACCAGGGCT	GTACAGTCTTCGGCTCCCTG
ISG15	CGCAGACTGTAGACACGCTT	GGGGCTTTAGGCCATACTCC
VCAM1	GCTATGAGGATGGAAGACTCTGG	ACTTGTGCAGCCACCTGAGATC
IRF1	TCCAAGTCCAGCCGAGACACTA	ACTGCTGTGGTCATCAGGTAGG
MMP3	CTCTGGAACCTGAGACATCACC	AGGAGTCCTGAGAGATTTGCGC
IL11	CTGACGGAGATCACAGTCTGGA	GGACATCAAGTCTACTCGAAGCC
HIF1α	TTGGCAGCGATGACACAGAA	TGGCTTTGGAGTTTCCGATGA

NOX4	TCTCAGGTGTGCATGTAGCC	CCGTCAGACCAGGAATGGTT
CXCL10	CCACGTGTTGAGATCATTGCC	TCACTCCAGTTAAGGAGCCC
IRF3	AACCCTGCACCCCAAGAAAA	ACCTCGAACTCCCATTGTTCC
IFIT1	CAAGGCAGGTTTCTGAGGAG	GACCTGGTCACCATCAGCAT
COL3A1	TCCTGGTGGTCCTGGTACTG	AGGAGAACCACTGTTGCCTG
POSTN	AGGGAGCTTCTGATTGGGGA	CGGGTTCGAATCCCTTTCCA
CCL2	CACTCACCTGCTGCTACTCA	GAGCTTGGTGACAAAAACTACAGC
COL1A1	GTGTTCCCTACTCAGCCGTC	ACTCGAACGGGAATCCATCG
COL11A1	CAGCGTGGTGAGACTGGATT	GGATGGCCACGTTCACCTAT
COL1A2	GCTGGTGTAATGGGTCCTCC	CGACCGGCATCTCCATTAGG
POSTN	TCATTTAGAGCAGCCGCCAT	GCAAAGAGCGTGAAGTGACC
ELN	AGTCTATTATCCAGGGGCTGGT	CTGCTCCAAACGTTCCCAGA
VCAN	ACATCAAGCCAAAATGGAAACCA	TGGGTGGTAAGGTAGGTAAGGT
CXCL12	TGCATCAGTGACGGTAAACCA	GCGATGTGGCTCTCGAAGAA
CCL5	ATATGGCTCGGACACCACTC	TCGAGTGACAAACACGACTGC
POSTN	AGGGAGCTTCTGATTGGGGA	TCCCTGTGTGGTCTTCAGGA
IL-7	CAGGAACTGATAGTAATTGCCCG	CTTCAACTTGCGAGCAGCACGA
ISG15	CTAGAGCTAGAGCCTGCAG	AGTTAGTCACGGACACCAG
BAFF	GCAGTTTCACAGCGATGTCC	CCGGTGTCAGGAGTTTGACT
MMP2	CAAGGATGGACTCCTGGCACAT	TACTCGCCATCAGCGTTCCCAT
MMP9	GCTGACTACGATAAGGACGGCA	TAGTGGTGCAGGCAGAGTAGGA
MMP13	GATGACCTGTCTGAGGAAGACC	GCATTTCTCGGAGCCTGTCAAC
MMP14	GGATGGACACAGAGAACTTCGTG	CGAGAGGTAGTTCTGGGTTGAG

CXCL11	CCGAGTAACGGCTGCGACAAAG	CCTGCATTATGAGGCGAGCTTG
ATM	CCAAGATGGCAGTGAACCAGAC	ATGCTGGACAGCTATGGTGGAG

Optimal primer pair concentrations were determined for each gene using 5-fold serial dilutions of cDNA. Amplification plots and melt curves were analysed to evaluate primer pair performance. For a primer pair with 100% efficiency, the slope of the standard curve should be -3.3. Primer pairs with efficiencies of - 3.3 ± 0.3 were considered optimal. For a 96-well format, each RT-qPCR reaction was conducted in a total volume of 20 µL, comprising 5 µL (10 ng) cDNA, 10 µL PowerUp SYBR Green Master Mix (Applied Biosystems; A25777), primers at their optimised concentrations and molecular-grade water to complete the volume. For 384-well plate format, reactions were carried out in a total volume of 10 µL, containing 2 µL (10 ng) cDNA, 5 µL PowerUp SYBR Green Master Mix, primers at their optimised concentrations, and molecular-grade water to complete the volume. mRNA expression levels were quantified using the delta-delta CT method, with HPRT and GAPDH serving as reference genes.

2.10 Western blotting

2.10.1 Preparation of whole-cell lysates

Cells were lysed in cell lysis buffer (Cell Signalling; 9803) composed of 20 mM Tris-HCl (pH 7.5), 150 mM NaCl, 1 mM Na_2EDTA, 1 mM EGTA, 1% Triton, 2.5 mM sodium pyrophosphate, 1 mM beta-glycerophosphate, 1 mM Na3VO4, and 1 µg/ml leupeptin. The buffer was supplemented with phosphatase and/or protease inhibitor cocktail (ThermoFisher Scientific; 78429 or 78441). After 5-minute incubation on ice, the cell lysates were centrifuged at 14,000 x g for 10 minutes at 4°C. The supernatants were transferred to fresh microcentrifuge tubes, snap-frozen, and stored at -80°C until further use.

2.10.2 Preparation of acellular protein lysates

MLFs were seeded at a density of 200,000 cells per well in a 6-well plate. Cells were treated as required and cultured in complete DMEM supplemented with 1% FBS for one week. Fibroblast lysis buffer (25 mM Tris-HCl pH 7.4, 150 mM NaCl, 0.5% Triton-X, 20 mM NH_4OH) supplemented with protease inhibitor cocktail (ThermoFisher Scientific; 78429) was added to each well (100 µL per well). The plate was incubated on a rocker at 4°C for 30 minutes to ensure complete cell lysis. Protein lysates were carefully transferred to microcentrifuge tubes without disturbing the remaining extracellular proteins. Cell lysates were centrifuged at 13,000 x g for 15 minutes at 4°C.

During this centrifugation step, 100 µL of 12.5 mM Tris-HCl (pH 6.8) supplemented with 1% SDS was added to each well to recover the acellular protein fraction. The extracellular proteins were scraped, transferred to microcentrifuge tubes, and boiled at 95°C for 5 minutes. These acellular protein fractions were snap-frozen and stored at -80°C until further use. After centrifugation, cellular protein lysates were transferred to fresh microcentrifuge tubes, snap-frozen and stored at -80°C.

2.10.3 Sample preparation for gel electrophoresis

The protein concentration of lysates was measured using the Pierce BCA Protein Assay Kit (ThermoFisher Scientific; 23225) following the manufacturer's instructions. For loading acellular proteins, the cellular fraction was quantified, and loading volumes were adjusted accordingly. Protein lysates were combined with 4X NuPAGE LDS Sample Buffer (Invitrogen; NP0007) and 10X NuPAGE Sample Reducing Agent (Invitrogen; NP0009). Molecular-grade water was added to standardise sample volumes. The prepared samples were boiled at 95°C for 5 minutes prior to gel electrophoresis.

2.10.4 Gel electrophoresis and immunoblotting

Proteins up to 260 kDa were separated on NuPAGE Bis-Tris 4-12% precast polyacrylamide gels (Invitrogen; NP0336BOX) using NuPAGE MES SDS Running Buffer (Invitrogen; NP0002). For proteins larger than 260 kDa, NuPAGE 3-8% Tris-Acetate precast polyacrylamide gels (Invitrogen; EA0378BOX) were used with NuPAGE Tris-Acetate SDS Running Buffer (Invitrogen; LA0041). NuPAGE Antioxidant (Invitrogen; NP0005) was added to the running buffer to maintain reduced protein states during the run. Gels were run at 120 V until the desired separation was achieved. PageRuler Prestained Protein Ladder (ThermoFisher Scientific; 26617) was used to estimate molecular weights. Proteins were transferred onto methanol-activated Immobilon-FL PVDF membranes (0.45 µm pore size; Millipore, IPFL00010) in transfer buffer (25 mM Tris-HCl pH 8.3, 192 mM glycine, 20% (v/v) methanol, and 0.03% (v/v) SDS). The transfer was conducted at 70 V for 1.5 – 3 hours, depending on protein size. Post-transfer, membranes were blocked for 45 minutes at room temperature in blocking buffer (5% (w/v) bovine serum albumin (BSA) in Tris-buffered saline (TBS) with 0.1 % (v/v) Tween-20 (TBST)). Membranes were incubated with primary antibodies diluted in 2.5 % (w/v) BSA blocking buffer. Incubation was carried out either overnight at 4°C or for 1-2.5 hours at room temperature (**Table 2.8**). Following primary antibody incubation, membranes were washed 5 times for 5 minutes each with 0.1 % TBST. Secondary antibody incubation was carried out for 45 minutes at room temperature in 2.5 % (w/v) BSA blocking buffer. Membranes were washed again 5 times for 5 minutes each with 0.1 % TBST. Signal detection was performed using SuperSignal West Pico PLUS Chemiluminescent Substrate (ThermoFisher

Scientific; 34579) or SuperSignal West Femto Maximum Sensitivity Substrates (ThermoFisher Scientific; 34094). Images were acquired using Amersham ImageQuant 800 GxP biomolecular imager. Pixel densities were quantified using GelAnalyzer software. Relative protein expression was determined by normalising sample band intensities to the reference protein Hsc70.

Table 2.8: Primary and secondary antibodies for Western blotting

Primary antibodies				
Target	**Host**	**Supplier**	**Catalogue #**	**Dilution**
ATM	Mouse	Santa Cruz	sc-23921	1:500
ATMpSer1981	Mouse	Invitrogen	MA1-2020	1:1000
αSMA	Mouse	Sigma-Aldrich	A2547	1:1000
cGAS	Rabbit	Cell signalling	31659	1:1000
COL1A1	Rabbit	Novus Biologicals	NBP1-30054	1:500
COL11A1	Rabbit	Invitrogen	PA5-101300	1:500
CTHRC1	Rabbit	Invitrogen	PA5-106400	1:500
CXCL10	Goat	R&D systems	AF-466	1:200
FN1	Rabbit	Invitrogen	MA5-11981	1:500
Hsc70	Mouse	Santa Cruz	sc-7298	1:1000
γH2AX	Rabbit	Sigma-Aldrich	05-636	1:500
POSTN	Rabbit	Invitrogen	PA5-34641	1:500
p53	Mouse	Santa Cruz	sc-126	1:1000
STING	Rabbit	Cell signalling	13647	1:1000
TBK1	Rabbit	Cell signalling	3504	1:1000
Secondary antibodies				

Target	Host	Supplier	Catalogue #	Dilution
Anti-Goat IgG	Rabbit	Dako	PO449	1:5000
Anti-Mouse IgG	Goat	Dako	PO447	1:5000
Anti-Rabbit IgG	Goat	Dako	PO448	1:5000

2.11 Hydroxyproline assay

Hydroxyproline is formed by the post-translational hydroxylation of proline and is predominantly found in collagen, making its measurement a useful indicator of collagen content. Mouse lung fibroblasts were seeded, treated and detached as previously described (section 2.1). Following trypsin neutralisation, cell pellets were washed with PBS and pelleted by centrifugation. The pellets were then resuspended in 1 mL of PBS. From this suspension, 100 µL was transferred to microcentrifuge tubes, and the cells were pelleted by centrifugation at 0.9 x g for 5 minutes. The supernatants were discarded, and the cell pellets were snap-frozen and stored on dry ice until further use. The remaining cell suspension was processed following the manufacturer's instructions for the Hydroxyproline Assay Kit (Sigma-Aldrich; MAK008). Cell were pelleted and resuspended in 100 µL of molecular-grade water, then transferred to pressure-tight polypropylene vials with PTFE-lined caps. To each vial, 100 µL of concentrated hydrochloric acid (HCl, ~12 M) was added, and the samples were hydrolysed at 120°C for 3 hours. During this step, proteins were extracted from the frozen cell pellets and quantified as described previously (sections 2.10.1, 2.10.3). After hydrolysis, the samples were mixed thoroughly and centrifuged at 10,000 x g for 3 minutes. In duplicates, 50 µL of the resulting supernatant was transferred to a 96-well plate, and the samples were evaporated to dryness at 60°C. Hydroxyproline standards were prepared using the standard solution provided in the kit. Once the samples were dried, 100 µL of Chloramine T/Oxidation buffer was added to each well, and the samples were incubated for 5 minutes at room temperature. Following this, 100 µL of diluted 4-(Dimethylamino) benzaldehyde (DMAB) reagent was added to each well, and the samples were incubated for 90 minutes at 60°C. Absorbance was measured at 560 nm. Protein concentrations were then used to calculate the relative hydroxyproline concentration in each sample.

2.12 Immunofluorescence

2.12.1 Cell culture and fixation

Cells were cultured in 8-well chamber slides (Sigma-Aldrich; C7182). After reaching appropriate confluence, cells were washed twice with PBS and fixed with 4% (v/v) paraformaldehyde at room temperature for 20 minutes. Post-fixation, cells were washed again with PBS and permeabilised with 0.5% (v/v) Triton X-100 (diluted in PBS) for 10 minutes. To neutralise residual aldehyde groups, cells were treated with 50 mM ammonium chloride (NH_4Cl) for 10 minutes. Cells were then washed three times with 0.1 % (v/v) Triton X-100 (diluted in PBS) to remove excess reagents.

2.12.2 Immunostaining procedure

After permeabilisation, cells were blocked using a blocking solution consisting of 2% (w/v) BSA in 0.1% (v/v) Triton X-100 for 2 hours at room temperature. Primary antibodies were diluted in blocking solution and applied to the cells. Incubation was carried out for either 1 hour at room temperature or overnight at 4°C (**Table 2.9**). Following primary antibody incubation, cells were washed three times with 0.1 % (v/v) Triton X-100 in PBS to remove unbound antibodies. Secondary antibodies, along with DAPI (Invitrogen; D1306), were diluted in blocking solution and applied to cells for 45 minutes at room temperature, protected from light (**Table 2.9**). After incubation, cells were washed three times with PBS and subsequently washed twice with double-distilled water to remove residual salts. Slides were mounted using Dako Fluorescence Mounting Medium (Agilent; S3023) and allowed to dry overnight at room temperature, protected from light.

Table 2.9: Primary and secondary antibodies for immunofluorescence

Primary antibodies				
Target	**Host**	**Supplier**	**Catalogue #**	**Dilution**
αSMA	Mouse	Abcam	Ab184675	1:500
COL1A1	Rabbit	Abcam	Ab34710	1:400
COL11A1	Rabbit	Invitrogen	PA5-101300	1:200
CTHRC1	Rabbit	Invitrogen	PA5-106400	1:200
γH2AX	Rabbit	Cell Signalling	9718	1:400
POSTN	Rabbit	Invitrogen	PA5-34641	1:200
Secondary antibodies				
Antibody	**Host**	**Supplier**	**Catalogue #**	**Dilution**
Alexa Fluor 488 anti-Rabbit IgG	Goat	Invitrogen	A-11034	1:1000
Alexa Fluor 546 anti-Rabbit IgG	Goat	Invitrogen	A-11035	1:500

2.12.3 Decellularisation of MLFs for acellular protein immunostaining

To visualise extracellular matrix proteins deposited by mouse lung fibroblasts, cells were decellularised using fibroblast lysis buffer consisting of 25 mM Tris-HCl pH 7.4, 150 mM NaCl, 0.5% Triton-X and 20 mM NH_4OH at 4°C for 30 minutes. Decellularised samples were washed thoroughly with PBS to remove cellular debris while preserving the extracellular matrix, which was fixed using 100% ice-cold methanol at -20°C for 30 minutes. Subsequent washing steps and antibody staining were performed as described in the immunostaining procedure (section 2.12.2).

2.12.4 Image acquisition and analysis

Fluorescence images were acquired from randomly selected fields of view using either an Olympus IX81 fluorescence microscope equipped with a 20X air immersion objective or an EVOS

fluorescence microscope. To ensure consistency, microscope settings ware maintained across samples. Images were processed and analysed using ImageJ software.

2.13 Click-iT EdU labelling

Cells were treated for six days as previously described. The Click-iT EdU Cell Proliferation Kit (Invitrogen; C10338) was used to detect newly synthesised DNA in different treatment groups. Half of the culture medium was replaced with fresh medium containing EdU solution at a final concentration of 10 μM. Cells were incubated for 2 hours in a humidified, hypoxic incubator at 37°C, 3% O_2 and 5% CO_2 to allow EdU incorporation. Following incubation, the medium was removed, and cells were washed twice with PBS before being fixed with 3.7% formaldehyde at room temperature for 15 minutes. After fixation, cells were washed twice with 3% BSA in PBS. Following the removal of the washing solution, cells were permeabilised with 0.5% Triton X-100 in PBS at room temperature for 20 minutes. Post-permeabilisation, cells were washed twice more with 3% BSA in PBS. The Click-iT reaction cocktail was prepared according to the manufacturer's instructions and applied to the cells for 30 minutes at room temperature, protected from light. After incubation, cells were washed once with 3% BSA in PBS, and nuclei were stained with DAPI diluted in 3% BSA in PBS for 10 minutes at room temperature. Following DAPI staining, cells were washed three times with PBS and twice with double-distilled water. Slides were mounted using Mowiol mounting medium (prepared by Dr Benjamin Sharpe) and allowed to dry overnight at room temperature, protected from light. Images were acquired and analysed as previously described (section 2.12.4).

2.14 Senescence-associated β-galactosidase staining

MLFs were seeded in a 6-well plate and treated with ± 2 ng/mL TGF-β1 twice over 6 days, with medium refreshed at each treatment. Senescence-associated β-galactosidase (SA-β-gal) staining was performed according to the manufacturer's protocol (Cell signalling; #9860). After treatment, cells were washed with PBS and fixed with the supplied fixative solution for 15 minutes at room temperature. Following fixation, cells were washed twice with PBS and incubated with β-galactosidase staining solution for 24 hours at 37°C in a dry, CO_2-free incubator. Images of 10 random fields per condition were captured using an EVOS microscope, and the percentage of β-galactosidase-positive cells was calculated.

2.15 Crystal violet staining

MLFs were seeded in a 96-well plate and treated with ± 2 ng/mL TGF-β1. Once the designated time points were reached, cells were washed twice with PBS and fixed with 4% (v/v) paraformaldehyde at room temperature for 15 minutes. After fixation, cells were washed twice with PBS and stained with crystal violet 0.5% (w/v) in water for 5 minutes at room temperature. Following staining, cells were washed several times with distilled water to remove excess dye. Finally, samples were air-dried, and images were acquired using Amersham ImageQuant 800 GxP biomolecular imager.

2.16 Flow cytometry staining

All flow cytometry experiments were performed using the BD FACSCanto II Flow Cytometer, and data were analysed using FlowJo software. Each experiment was performed in triplicates.

2.16.1 Apotracker and propidium iodide apoptosis assay

MLFs were seeded at a density of 50,000 cells per well in a 6-well plate and treated with ± 2 ng/mL TGF-β1 and/or ± 5 nM or 100 nM ATMi AZD0156 twice over 6 days, with the medium refreshed every 3 days. Cells were washed with PBS, trypsinised, and neutralised as previously described. Cells were transferred to FACS tubes and centrifuged at 1400 rpm for 5 minutes. The cell pellet was resuspended in 400 nM Apotracker Green (Biolegend; 427402) staining solution and incubated for 20 minutes at room temperature. The diluent was prepared in cell staining buffer (Biolegend; 420201). Following incubation, the cells were washed with PBS and stained with 50 μg/mL propidium iodide for 30 minutes at 37°C. Samples were analysed directly without washing using FITC and PerCP-Cy5.5 detection channels.

2.16.2 Cell viability of αSMA-positive MLFs

MLFs were seeded at a density of 50,000 cells per well in a 6-well plate and treated with ± 2 ng/mL TGF-β1 and/or ± 5 nM or 100 nM ATMi AZD0156 twice over 6 days, with the medium refreshed every 3 days. Cells were washed with PBS, detached using Accutase, and neutralised as previously described. Cells were transferred to FACS tubes and centrifuged at 1400 rpm for 5 minutes. The cell pellet was washed with PBS and stained with Zombie Violet Fixable Viability Dye (Biolegend; 423113) at a 1:100 dilution in PBS for 30 minutes at room temperature, protected from light. Cells were washed again with PBS and fixed with 4% PFA at 4°C for 20 minutes. Following fixation, cells were washed with PBS and permeabilised using 0.5% Tween-20 in PBS for 15 minutes at room temperature. Cells were washed twice with PBS and incubated with αSMA

antibody (Abcam; Ab184675) diluted 1:100 in PBS for 15 minutes at room temperature. Cells were washed twice and resuspended in FACS buffer (0.1% FBS in PBS). Events were recorded using FITC and Pacific Blue detection channels for both sample and single-stain controls.

2.16.3 Cell cycle

Cells were seeded in 6-well plates and cultured until approximately 70% confluence. To synchronise the cells, serum starvation was performed. The medium was removed, cells were washed twice with PBS, and complete DMEM medium without FBS was added to each well for 24 hours. After 24 hours of incubation, cells for the 0-hour timepoint were collected using the following procedure: cells were washed with PBS, trypsinised, and neutralised as previously described. Cells were transferred to FACS tubes and centrifuged at 1400 rpm for 5 minutes. The cell pellet was washed with PBS and centrifuged again, repeating this step twice. Cells were fixed by adding ice-cold 70% ethanol while vortexing and stored in ethanol at -20°C until all timepoint samples were collected. Cells in the remaining wells were treated with ± 2 ng/mL TGF-β1, and/or ± 5 nM or 100 nM ATMi AZD0156. Cells were collected and fixed every 4 hours following the procedure described above. Once all samples were collected, ethanol-fixed cells were washed with PBS to remove the fixative. FxCycle PI/RNase Staining Solution (Invitrogen; F10797) was used to stain DNA. Cells were incubated in the staining solution for 30 minutes at room temperature, protected from light. Samples were analysed directly without washing. Flow cytometry events were acquired, and data were analysed using FlowJo software to assess DNA content.

2.17 Cell contraction assay

To assess the contractility of mouse lung fibroblasts, one part FBS was mixed with one part 10X DMEM and rat tail collagen type I (Corning; CLS354236) to achieve a final concentration of 2.4 mg/mL (~7 parts depending on the stock concentration). Sodium hydroxide (NaOH) was used to neutralise the collagen solution to a neutral pH. Once neutralised, one part of the cell suspension containing 50,000 MLFs in complete DMEM was added to nine parts of collagen solution and mixed thoroughly. This mixture was then transferred to the wells of a 96-well plate. The cell-collagen suspension was incubated for 30 minutes in a humidified incubator at 37°C and 5% CO_2 to allow the gel to solidify. After solidification, the gels were carefully dissociated from the walls of the wells by running a sterile needle along the edges. The gels were then topped up with 10% complete DMEM and returned to the incubator for 24 hours. Following the incubation period, images of the gels were captured using the Amersham ImageQuant 800 GxP biomolecular imager. The percentage of cell contraction was calculated using ImageJ software by measuring the original and final areas of the gel. Additionally, individual gels were weighed after removing

excess medium to assess gel contraction. Each experiment was independently repeated, with three technical replicates included in each iteration.

2.18 Proliferation assay

The CellTiter 96 AQueous Non-Radioactive Cell Proliferation Assay Kit (Promega; G5421) was utilised to quantify viable cell populations. This assay relies on the reduction of MTS (3-(4,5-dimethylthiazol-2-yl)-5-(3-carboxymethoxyphenyl)-2-(4-sulfophenyl)-2H-tetrazolium) to a formazan product by dehydrogenase enzymes in metabolically active cells. Phenazine methosulfate (PMS) serves as an electron coupling reagent to facilitate this reduction. The resulting formazan product exhibits an absorbance peak at 490 nm, and the intensity of the absorbance correlates with the number of viable cells in the sample. Before conducing the assay, cells were seeded and treated according to the experimental conditions outlined in figure legends. Different media were used for different cell types as previously described. At designated time points post-seeding, the medium was replaced with 100 μL fresh medium supplemented with 20 μL of MTS solution. The plate was incubated at 37°C with 5% CO_2 for 2 hours to allow formation of the formazan product. After the incubation, the absorbance at 490 nm was measured using a microplate reader. The number of replicates for each condition is specified in the corresponding figure legends.

2.19 X-ray irradiation

MLFs were seeded in 60 mm dishes and cultured to approximately 90% confluence before being irradiated at 5, 10, 15, 20, and 50 Gy at room temperature using a 350 kV X-ray irradiation system (Faxitron). After irradiation, the medium was replaced, and cells were cultured for 1 hour prior to being snap-frozen for protein extractions. To evaluate the effectiveness of AZD0156 in MLFs, cells were treated with increasing concentrations of AZD0156, as specified in the corresponding figures, 1 hour before irradiation at 10 Gy.

2.20 Statistical analysis

All statistical analyses were performed using GraphPad Prism version 10. Data are presented as mean $\pm$ standard error of the mean (SEM) or mean $\pm$ standard deviation (SD), as indicated in the figure legends. Unpaired Student's t-test was used to compare the means between two independent groups, and statistical significance was considered when $P \leq 0.05$. One-way or two-way analysis of variance (ANOVA) was used to compare the means of three or more groups, with Bonferroni correction applied for multiple comparisons. For the analysis of tumour sizes, the area under the curve (AUC) was calculated, and statistical significance was determined by comparing

the AUC values between the control and treatment groups using a t-test. *In vivo* experiments were performed with a minimum of two biological replicates, while *in vitro* experiments included at least three independent experiments and/or technical replicates. Significant values are marked with asterisks, with the following representations: P>0.05 (ns); P≤ 0.05 (*); P≤ 0.01 (**); P≤ 0.001 (***); P≤ 0.001 (****).

Chapter 3 Studying the effects of myofibroblastic ATM inhibition

3.1 Introduction

CAFs are integral to the tumour microenvironment, and transcriptomic studies have identified heterogenous subpopulations, such as myCAFs and iCAFs (Elyada et al., 2019; Öhlund et al., 2017). MyCAFs actively deposit and remodel ECM components, creating physical barriers that prevent $CD8^+$ T cells from infiltrating solid tumours and thereby contributing to immune evasion (Hanley et al., 2021). As a result, targeting myCAFs is emerging as a promising strategy to enhance immunotherapy efficacy. Previous work from our laboratory has highlighted the role of DNA damage response pathways in myCAF differentiation, with ATM identified as a central regulator of the myCAF phenotype (Mellone et al., 2022).

ATM orchestrates the cellular response to DNA damage by coordinating repair processes and maintaining genomic integrity (Maréchal & Zou, 2013). In recent years, the clinical development of ATM inhibitors has focused on sensitising cancer cells to chemotherapy and radiotherapy, based on the rationale that ATM inhibition disrupts the efficient repair of double-strand breaks, leading to cancer cell death (Stakyte et al., 2021). However, the potential use of ATM inhibitors to target other cell types within the TME has not been fully explored. Our work demonstrates that ATM plays a critical role in maintaining the myCAF phenotype; its inhibition enhances intratumoural $CD8^+$ T cell infiltration, reduces tumour growth, and potentiates immunotherapy responses, presenting a novel strategy for immunotherapy enhancement (Mellone et al., 2022). Intriguingly, ATM inhibition has also been associated with elevated inflammatory responses (Saunders et al., 2021), suggesting that its inhibition may not only sensitise cancer cells to DNA-damaging therapies and regulate the myCAF phenotype but also reshape the TME by promoting inflammation.

This chapter aims to deepen our understanding of how ATM inhibition influences both myCAF and iCAF phenotypes by characterising alterations in ECM gene expression and inflammatory cytokines. Ultimately, this work seeks to elucidate novel mechanisms by which ATM signalling regulates the TME and to inform future therapeutic strategies that enhance $CD8^+$ T cell infiltration.

3.2 Results

3.2.1 ATM regulates the differentiation of myCAFs and can be targeted to overcome immunotherapy resistance

To provide context for the present study, this section summarises key findings from Mellone et al. (2022). This previous work conducted by Dr Massimiliano Mellone serves as the foundation for the experiments in this thesis (**Figures 3.1, 3.2**).

Gene set enrichment analysis of microdissected tumour stroma datasets showed that myoCAF/myCAF stroma of oesophageal, ovarian, colorectal, and liver cancers are enriched in genes associated with the ATM/DDR pathway (**Figure 3.1A**). Specifically, ATM but not ATR or DNA-PKcs was activated during myofibroblast differentiation (**Figures 3.1B-C**). Further experiments showed that ATM activation correlated with αSMA expression, an indicator of the myCAF phenotype. Inhibition of ATM achieved through both pharmacological agents (KU60019 and KU55933) and genetic knockdown reduced αSMA expression (**Figures 3.1D-F**) and COL1A1 deposition (**Figure 3.1G**), confirming ATM's functional role in myofibroblast differentiation. Moreover, ATM inhibition (KU55933) reduced collagen gel contraction (**Figure 3.2A**). *In vivo*, ATM targeting via shRNA knockdown and inhibition with AZD0156 both suppressed tumour growth (**Figures 3.2B, 3.3D-E**), and reduced αSMA expression (**Figures 3.2C, 3.2F**). Notably, AZD0156 had minimal effect on myCAF-low tumours, demonstrating that the efficacy of ATM inhibition is myCAF specific; it slowed tumour growth and improved overall survival only in myCAF-rich tumours (**Figure 3.2G**). Furthermore, ATM inhibition (via both shRNA knockdown and ATM inhibitor AZD0156) promoted a significant relocation of $CD8^+$ T cells from the tumour periphery to the core (**Figures 3.2H-J**). When combined with antitumour vaccination (**Figures 3.2K-M**) or anti-PD-1 blockade (**Figures 3.2N-P**), ATM inhibition enhanced intratumoural $CD8^+$ T cell infiltration and further reduced tumour growth compared to either treatment alone, suggesting that ATM inhibition can potentiate immunotherapy responses.

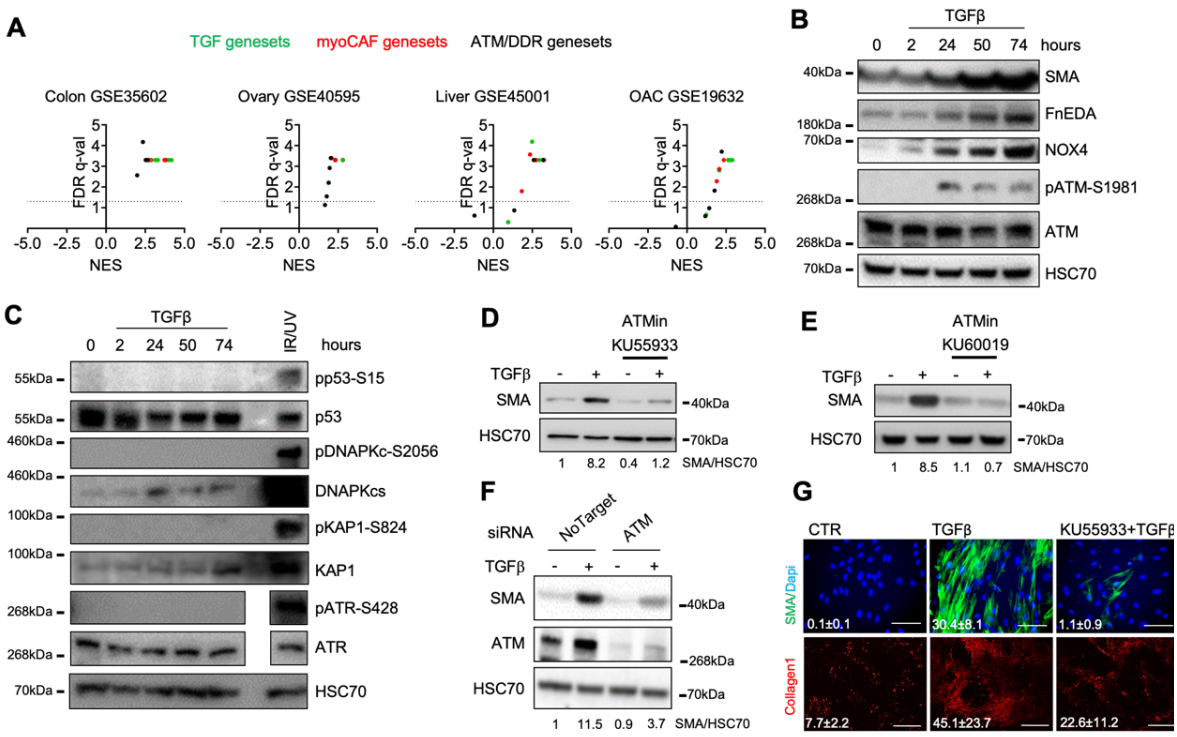

Figure 3.1: ATM as a central regulator of the myCAF phenotype. (A) Volcano plots with FDR *q* (significance) and NES (correlation) of GSEA performed on the indicated data sets from LCMD tumour versus normal stroma. The dotted line drawn at 1.3 of $-\log_{10}$ FDR *q* axis indicates FDR *q* = 0.05. **(B-C)** Western blotting of fibroblasts (HFFF2) treated with TGFβ1 over time. **(D-E)** Western blotting and its quantification of HFFF2 treated for 72 hours with TGFβ1 ± ATM inhibitors. **(F)** Western blotting of HFFF2 transfected as indicated and treated with TGFβ1 for 72 hours. **(G)** Representative immunofluorescence staining of SMA-positive stress fibers or collagen 1 deposition in HFFF2 treated with TGFβ1 ± ATM inhibitor for 3 (SMA) or 7 (collagen 1) days; relative quantification of the mean (FoV for both SMA and collagen 1 = 10). Scale bars for SMA, 100 µm and for collagen 1, 500 µm. Data from Mellone et al. (2022); experiments conducted by Massimiliano Mellone. Figure adapted from the original publication.

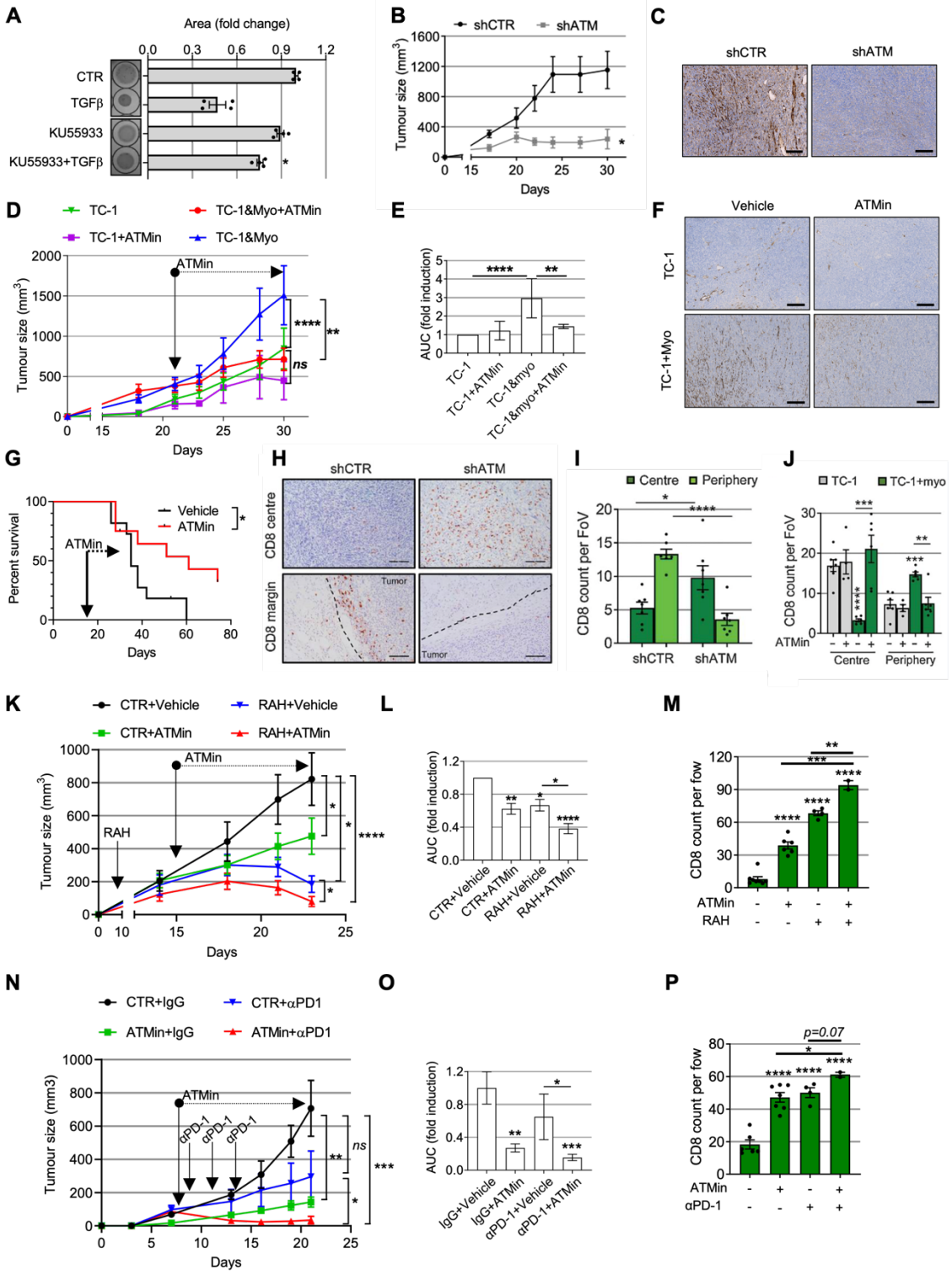

Figure 3.2: Targeting fibroblast ATM *in vivo* suppresses myCAF-rich tumour growth, promotes CD8⁺ T cell infiltration and potentiates the response to anti-PD-1 blockade and antitumour vaccination. (A) Collagen gel contraction assay and measurement of gel area. HFFF2 or normal primary oral fibroblasts were treated for 72 hours with TGFβ1 ± ATM inhibitor (13.3 μmol/L KU55933). Left, representative gel images (n_{tr} = 2). **(B)** Tumor growth curves following coinjection of tumor cells with shCTR or shATM fibroblasts (TC-1 cells + myoMLF). Data from single experiments are presented; mouse numbers = 3–8**. (C)** Representative SMA IHC from the experiments shown in **B**. **(D)** Mice injected with TC-1 ± myoMLF were treated with ATM inhibitor AZD0156 for the duration of the

experiment (mouse number = 5–8); tumor growth curves. **(E)** AUC analysis of two experiments relative to **D** (two-way ANOVA). **(F)** Representative SMA IHC from the experiments shown in **D**. **(G)** Overall survival of TC-1 + myoMLF mice treated daily with AZD0156 at days 15–28 (mouse number = 11–12; Mantel–Cox log-rank test is shown). **(H)** Representative IHC staining **(I)** and relative quantification of CD8 T cells in the core and periphery of TC-1 myo-rich tumors (described in **B**; n_{tr} = FoV = 10; dotted lines, tumor margins). **(J)** Relative quantification of CD8 T cells in the core and periphery of tumors described in **D** (n_{tr} = FoV = 10). **(K-L)** Mice were injected with TC-1 + myoMLF and treated with HPV E7 RAH vaccine±AZD0156. Control plasmid with vehicle was used as control. Tumor growth curves of a representative experiment (mouse number = 7–8); two-way ANOVA is shown and refers to AUC analysis of three experiments. **(M)** Relative quantification of CD8 T cells in the tumor core in **K** (n_{tr} = FoV = 10). **(N)** Tumor growth curves of a single experiment (mouse number = 5–8) and **(O)** relative AUC analysis. **(P)** Relative quantification of CD8 T cells in the tumor core (n_{tr} = FoV = 10). Scale bars, 200 µm. A homoscedastic Student *t* test is used throughout the figure and is relative to the control unless otherwise highlighted. ns, nonsignificant; *, $P \leq 0.05$; **, $P \leq 0.01$; ***, $P \leq 0.001$; ****, $P \leq 0.0001$. Data from Mellone et al. (2022); experiments conducted by Massimiliano Mellone. Figure adapted from the original publication.

3.2.2 ATM inhibition 'normalises' the myofibroblastic phenotype

3.2.2.1 TGF-β upregulates myofibroblastic gene expression in mouse lung fibroblasts

Mouse lung fibroblasts (MLFs) were treated with TGF-β1 to induce myofibroblast differentiation *in vitro*. This phenotype is typically characterised by elevated expression of αSMA, which is associated with increased contractile forces and upregulation of ECM-related genes involved in matrix deposition. Consistent with previous studies, TGF-β1 treatment led to the upregulation of myofibroblastic markers. Western blotting revealed a marked increase in αSMA, FN, and COL1A1 protein levels (**Figure 3.3A**). As expected, quantitative PCR demonstrated a significant upregulation of ECM-associated genes, including COL1A1, COL1A2, COL11A1, at the mRNA level compared to untreated controls (**Figure 3.3B**). These findings confirm that the myofibroblastic phenotype was successfully induced by TGF-β stimulation.

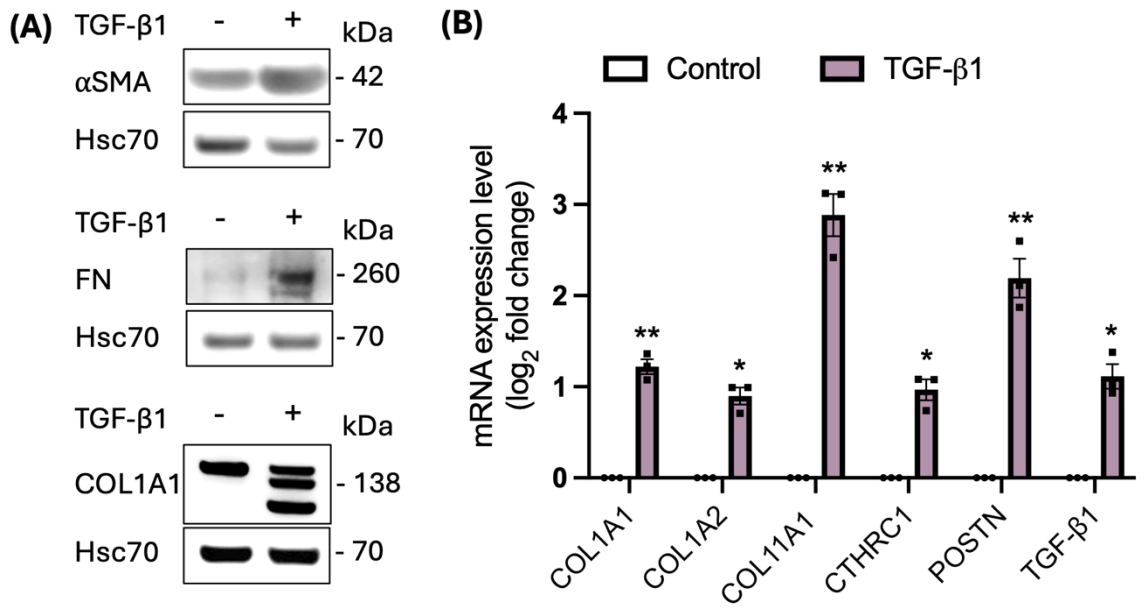

Figure 3.3: Myofibroblastic marker expression. (A) Western blotting of MLFs treated with TGF-β1 for 5 days **(B)** RT-qPCR analysis of genes associated with the myofibroblastic phenotype and ECM composition in MLFs treated with TGF-β1 for 6 days. Data are presented as mean log_2 fold change ± SEM, normalised to untreated controls (n = 3 independent experiments). Statistical analysis was conducted using a paired Student's t-test; *P≤0.05, **P≤0.01.

3.2.2.2 ATM inhibition decreases the expression levels of myofibroblastic markers

Having already established that ATM plays a role in myofibroblast/myCAF differentiation, we aimed to investigate whether inhibiting ATM *in vitro* leads to the 'normalisation' of the myCAF phenotype following TGF-β1-induced differentiation of MLFs (data previously published in Mellone et al., 2022). In this context, the term 'normalisation' refers to changes in the gene expression levels of myofibroblasts that are more characteristic of the quiescent fibroblast phenotype. To investigate the effects of ATM inhibition, primary MLFs were treated with 0.5 μM ATMi AZD0156 and 2 ng/mL TGF-β1 for 6 days. mRNA expression of myCAF-related genes, particularly those involved in ECM composition, was measured using RT-qPCR. In response to TGF-β1 treatment, myofibroblasts exhibited significantly higher expression of COL1A1, COL1A2 and COL11A1, while no significant differences were observed in COL3A1, suggesting that this collagen type may not be as strongly regulated by TGF-β1 in this context. We then evaluated the effect of AZD0156 and found that all tested collagens were significantly downregulated in both untreated and TGF-β1-treated MLFs (**Figure 3.4A**). Other ECM-related genes that were significantly upregulated upon TGF-β1 treatment included CTHRC1, POSTN, and ELN. Similarly to collagens, CTHRC1 and POSTN were significantly downregulated when treated with the ATM inhibitor in both untreated and TGF-β1-treated MLFs. However, ELN was not downregulated

under the TGF-β1 treatment condition (**Figure 3.4B**). In addition, the expression of ECM-regulating genes P4HA3, VCAN and ASPN were analysed. TGF-β1 treatment significantly downregulated P4HA3 and VCAN, while the expression of ASPN remained unaffected. Notably, ATMi did not modulate the expression of P4HA3, VCAN, or ASPN in the presence of TGF-β1. However, in the absence of TGF-β1, ATMi significantly downregulated the expression of VCAN and ASPN, while no significant changes were observed for P4HA3 (**Figure 3.2C**). These results suggest distinct regulatory patterns for these ECM-associated genes. The presence of PDPN-expressing fibroblasts has been reported as a prognostic indicator in various cancer types, though the outcomes vary depending on the cancer (Shindo et al., 2013). In our study, we found that TGF-β1 had no effect on PDPN expression in MLFs. Treatment with ATMi had no effect on fibroblasts, but in TGF-β1-treated MLFs, ATM inhibition significantly upregulated PDPN (**Figure 3.4D**). PDGFRα is a marker of fibroblasts which is typically downregulated by TGF-β1, this is consistent with our results. TGF-β1 treatment strongly suppressed PDGFRα expression, and no additional effects were observed with the ATM inhibitor. In contrast, in control fibroblasts, ATM inhibition significantly downregulated PDGFRα (**Figure 3.4E**). Both TGF-β1 and NOX4 play roles in the fibroblast-to-myofibroblast transition; therefore, we sought to investigate whether ATM inhibition affects the expression of these genes. As expected, TGF-β1 treatment resulted in the upregulation of TGF-β1 in MLFs, but there was no change in NOX4 regulation. ATM inhibition had no effect on the expression of TGF-β1 and NOX4 in control MLFs. However, upon TGF-β1 treatment, ATM inhibition significantly upregulated expression of both genes (**Figure 3.4F**). Overall, our findings show that ATM inhibition leads to the downregulation of various collagens at the mRNA level, and that some, but not all, ECM-associated genes are regulated by ATM. To confirm the gene expression observed at the mRNA level, we next examined the expression of those genes at the protein level.

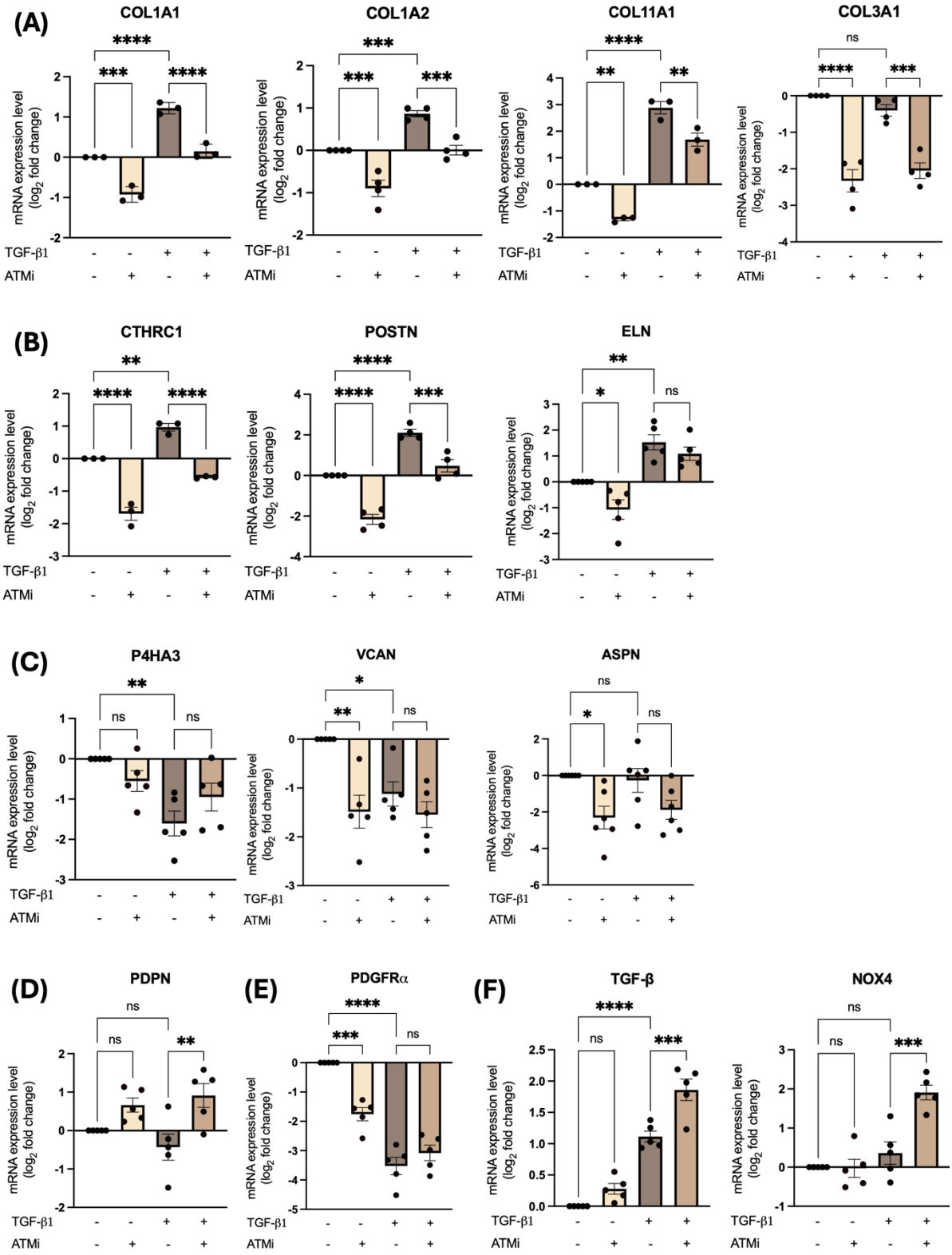

Figure 3.4: ATM regulates expression of ECM genes. (A-F) RT-qPCR analysis of genes associated with the myofibroblastic phenotype and ECM composition in MLFs treated with TGF-β1 and/or AZD0156 for 6 days. Data are presented as mean log_2 fold change ± SEM, normalised to untreated controls (each dot represents an independent experiment). Statistical analysis was conducted using one-way ANOVA with Bonferroni correction; *P≤0.05, **P≤0.01, ***P≤0.001, ****P≤0.0001, ns = not significant.

Protein production associated with the myofibroblastic gene signature was measured by Western blotting. Mouse lung fibroblasts were differentiated and treated as previously described. TGF-β1 treatment upregulated αSMA, COL11A1, FN, POSTN, and CTHRC1expression, confirming the generation of the myofibroblastic phenotype *in vitro*. In both control and TGF-β1-treated MLFs, ATM inhibition downregulated these genes (**Figures 3.5A-B**). Western blot analysis of COL1A1 expression showed varying band intensities in control MLFs and TGF-β1-treated cells; however, ATMi treatment reduced the intensity of all three bands (**Figure 3.5A**). We have demonstrated changes in the mRNA and protein expression levels of selected collagens; however, the collagen family comprises 28 members (Ricard-Blum, 2011). Given that collagen is a major structural component of the ECM, we quantified total collagen levels using the colorimetric hydroxyproline assay. Hydroxyproline is formed through the post-translational hydroxylation of proline residues in collagen. Since hydroxyproline is almost exclusively found in collagen, its levels serve as a reliable indicator for estimating total collagen content (Cissell et al., 2017; B. Qiu et al., 2014). In our study, we treated cells as previously described and quantified hydroxyproline concentration. Additionally, we measured total protein concentration to normalise the hydroxyproline levels between samples, ensuring accurate comparisons. TGF-β1-treated MLFs showed a 2.3-fold increase in hydroxyproline levels compared to untreated controls, indicating that TGF-β1 stimulates collagen synthesis. Hydroxyproline content was significantly downregulated in both control and TGF-β1-treated MLFs upon ATM inhibition (**Figure 3.5C**), suggesting that ATM inhibition suppresses collagen synthesis, even in the presence of TGF-β1 stimulation.

After confirming that ATM inhibition normalises the expression of genes associated with the myofibroblastic phenotype, we conducted a collagen gel contraction assay to evaluate whether ATM plays a functional role in modulating myofibroblast contractility. We mixed pretreated MLFs with collagen, allowing the solution to polymerise and form a 3D collagen gel. A needle was used to loosen the gel from the well plate walls to facilitate contraction. The cells then exerted mechanical forces on the gel, leading to reduction in its area (**Figure 3.5D**). Myofibroblasts exhibit enhanced contractile properties compared to fibroblasts and our data supports this observation. Gel contraction was quantified by measuring the decrease in the original gel area and the loss of gel weight over a 24-hour period. ATM inhibition did not result in significant downregulation of contractility in control MLFs or TGF-β1-treated MLFs, with the lack of significant effect in TGF-β1-treated MLFs likely due to the variations between individual experiments (**Figures 3.5E, 3.5G**). After calculating the fold changes between untreated and ATMi-treated MLFs, we confirmed that ATM inhibition had no effect on control fibroblast contractility, but it did reduce the contractility of TGF-β1-treated MLFs (**Figures 3.5F, 3.5H**). This further supports the notion that ATM inhibition normalises the myofibroblastic phenotype, returning it to a more quiescent state.

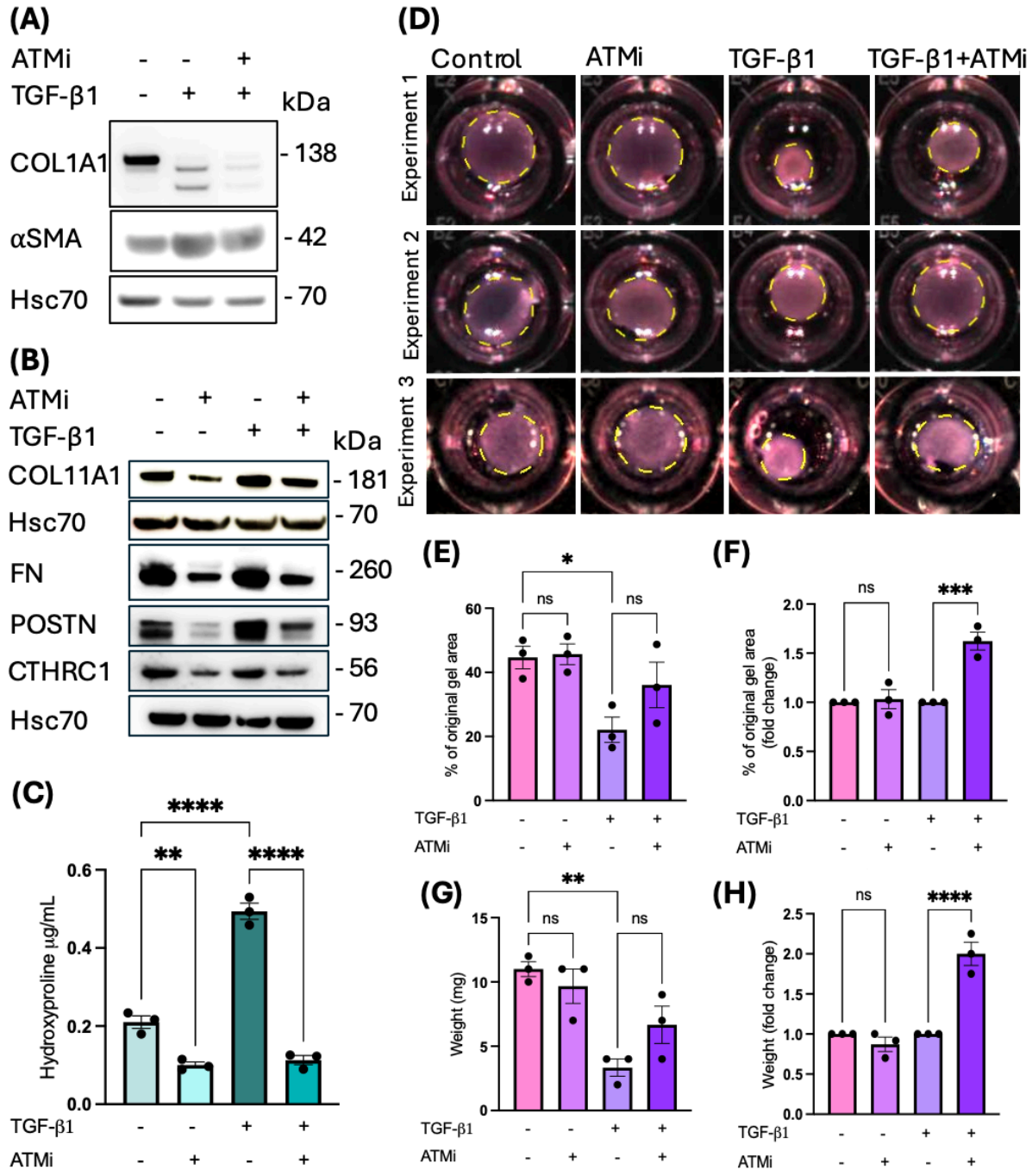

Figure 3.5: ATM regulates the expression of ECM components at the protein level. (A) Western blotting of MLFs treated with TGF-β1 and/or AZD0156 for 9 days. **(B)** Western blotting of MLFs treated with TGF-β1 and/or AZD0156 for 6 days. **(C)** Normalised hydroxyproline concentration in MLFs treated with TGF-β1 and/or AZD0156 for 6 days. **(D)** Images of gel contraction after a 24-hour period, with dotted lines indicating gel area. **(E)** Quantification of gel area as percentage and **(F)** as fold-change after 24-h contraction of MLFs treated with TGF-β1 and/or AZD0156 for 6 days prior to the assay. **(G)** Quantification of gel weight and **(H)** quantification of gel weight as fold-change after 24-h contraction of MLFs treated with TGF-β1 and/or AZD0156 for 6 days prior to this assay. Data are presented as mean ± SEM, with each dot representing an independent experiment. Statistical analysis was performed using one-way ANOVA with Bonferroni correction for all panels; *P≤0.05, **P≤0.01, ***P≤0.001, ****P≤0.0001, ns = not significant.

3.2.3 ATM inhibition enhances T cell migration through fibroblast-deposited ECM *in vitro*

Previous studies have shown that reducing collagen density leads increases T cell migration. We designed and optimised a migration assay to determine whether altering ECM composition *in vitro* affects T cell migration towards cancer cell-conditioned medium (**Appendix A Figure 1**). MLFs were seeded in transwell inserts and treated with TGF-β1 and compounds of interest for one week to allow ECM deposition. Following decellularisation, $CD8^+$ T cell migration through the deposited ECM toward a chemoattractant (TC1 cancer cell conditioned medium) was assessed (**Figure 3.6A**). First, we investigated the effects of ATM, Wee1, LOXL2, and Pan-LOX inhibition on T cell migration. We selected a Wee1 inhibitor because similar to ATM, it plays a role in the DDR (Ghelli Luserna Di Rorà et al., 2020). The primary function of the LOX family is to catalyse the covalent cross-linking of collagens and elastin in the ECM (M. Ye et al., 2020). Since collagen is known to affect T cell migration, we sought to determine whether inhibiting these enzymes will have an impact. Our results indicate that TGF-β1-treated MLFs deposited ECM, as demonstrated by an approximately 62-fold decrease in T cell migrating through the ECM compared to the non-matrix condition. We did not observe an effect on T cell migration through the ECM deposited by MLFs treated with Wee1, LOLX2, and Pan-LOX inhibitors when compared to the untreated control (**Figure 3.6B**). The lack of significant effect in Pan-LOXi-treated MLFs is likely attributable to variations between replicates. In contrast, we showed that myofibroblastic ATM inhibition significantly increased T cell migration towards the chemoattractant compared to the untreated control (**Figure 3.6B**), suggesting that the ECM deposited by these cells differs in composition, as indicated by our previous findings. Next, we demonstrated that ECM deposited by control MLFs, as well as ECM deposited by TGF-β1-treated MLFs pretreated with collagenase D, showed approximately 30-fold higher T cell migration compared to ECM deposited by TGF-β1-treated MLFs (**Figure 3.4C**). However, it is important to note that this difference was not statistically significant. In support of our previous findings, myofibroblastic ATM inhibition significantly increased T cell migration (**Figures 3.6C, 3.6D**).

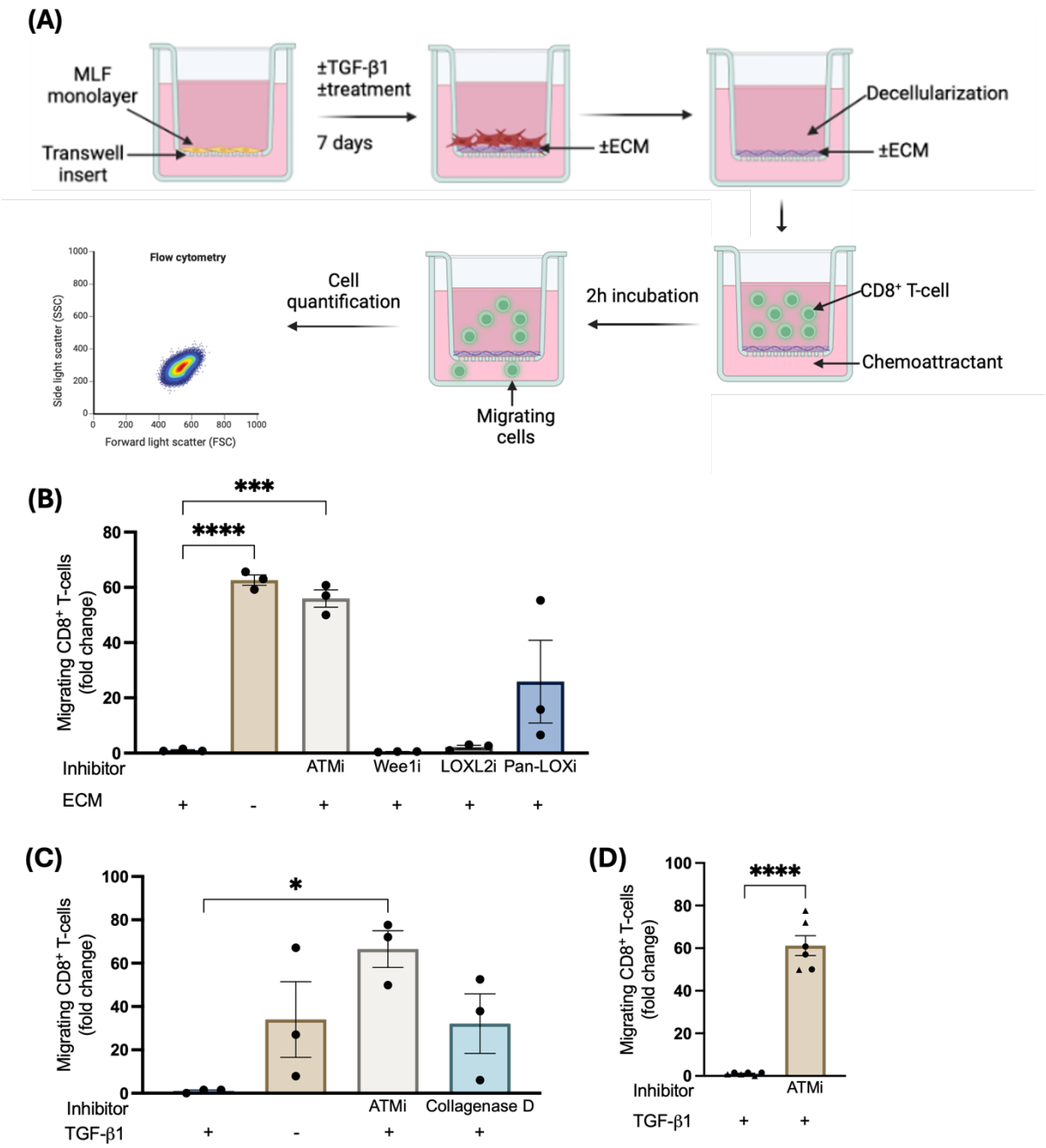

Figure 3.6: CD8⁺ T cell migration through ECM-derived matrix.(A) Schematic diagram of T cell migration assay. MLFs were cultured in transwells of a 96-well plate and treated with TGF-β1 and/or compounds of interest for one week to allow ECM deposition. Following decellularisation, 50 000 CD8⁺ T cell were seeded to assess their migration through deposited ECM toward conditioned medium collected from TC1 cancer cells. Migrated cells from the lower chamber were counted using a flow cytometer. **(B-C)** MLFs were treated with ±TGF-β1 and/or indicated inhibitors (0.5 µM ATMi, 40 nM Wee1i, 300 nm LOXL2i, 20 µM Pan-LOXi) or 0.6 mg/mL collagenase D. Numbers of migrating CD8⁺ T cells were determined. Data are presented as mean ± SEM, n_{tr} = 3. Statistical analysis was performed using one-way ANOVA and significance is indicated as follows: *P≤0.05, ***P≤0.001, ****P≤0.0001. **(D)** Numbers of migrating T cells through untreated and ATMi-treated myofibroblast-derived ECM. Data represent the mean ± SEM of two biological replicates, each with three technical replicates. Statistical analysis was performed using a homoscedastic t test; ****P≤0.0001.

3.2.4 ATM inhibition alters fibroblast cytokine secretion

Cancer-associated fibroblasts not only contribute to ECM deposition and remodelling but also release a variety of pro- and anti-inflammatory cytokines within the TME. Having demonstrated that ATM inhibition alters ECM composition, we next sought to investigate whether ATM inhibition also influences cytokine composition. Proteome profiler arrays were used to determine whether ATM inhibition affects cytokine composition *in vivo*. MLFs were pretreated *ex vivo* with 2ng/mL TGF-β1 for one week before being co-injected with TC1 cells subcutaneously into the flank of C57BL/6 female mice to initiate tumour growth. After two weeks, the mice were weighed, and the ATM inhibitor was administered daily for two weeks via oral gavage at a dose of 20 mg/kg. Mice were culled when tumour size approached the humane endpoint, in accordance with the project licence and ethical guidelines. Tumours were excised and weighed. Supernatants were generated by incubating tumour tissues in basic medium (10 mg of tumour per 2 µL of medium). Tumour-conditioned media were collected, and secretory proteins were captured on nitrocellulose membranes (**Figure 3.7A**). These proteins were detected using biotinylated antibodies and visualised with chemiluminescence reagents, following the manufacturer's protocol. Pixel density of each dot on the cytokine arrays was analysed using GelAnalyzer software for both untreated and ATM inhibitor-treated tumours (three biological replicates and two technical replicates per condition). Pixel densities were normalised to the reference dots within each array. All detected cytokines were quantified and are represented on a heatmap using a colour scale (**Appendix A Figure 2**). Cytokines upregulated in tumours treated with the ATM inhibitor AZD0156 included CCL2, CCL3, CCL5, CCL11, CCL12, CCL22, IL-1α, IL-2, IL-6, IL-17A, CD40, CXCL10, LIF, and TNF-α, with IL-2 (2.8-fold), TNF-α (2.1-fold), CXCL10 (2-fold) and IL-6 (2-fold) exhibiting the highest level of upregulation (**Figure 3.7B**). Cytokines downregulated in tumours treated with the ATM inhibitor AZD0156 included CCL6, CCL19, CCL20, CCL21, BAFF, CD160, CFD, CX3CL1, IGFBP-2, FL, PD-ECGF, and RETN, with CCL21 (3.9-fold), CCL20 (1.7-fold), BAFF (1.6-fold) and CFD (1.6-fold) exhibiting the highest level of downregulation (**Figure 3.7C**). These findings indicate that ATM inhibition affects cytokine expression within the TME. Given that myCAFs primarily contribute to ECM deposition and remodelling with limited roles in cytokine and chemokine secretion, we focused our investigation on the effects of ATM inhibition on markers associated with iCAFs, which are well-known for their paracrine signalling functions. The cytokine array results exhibit variability across biological replicates; however, a consistent trend emerges, showing elevated levels of cytokines, including CCL2, IL-6, IL-11, and LIF, in AZD0156-treated tumours (**Figure 3.8A**). Since these findings are based on tumour supernatants, and considering that in addition to CAFs, tumour cells and immune cells within the TME also

contribute to cytokine secretion, we conducted *in vitro* experiments to determine whether ATM inhibition in MLFs specifically upregulates iCAF markers.

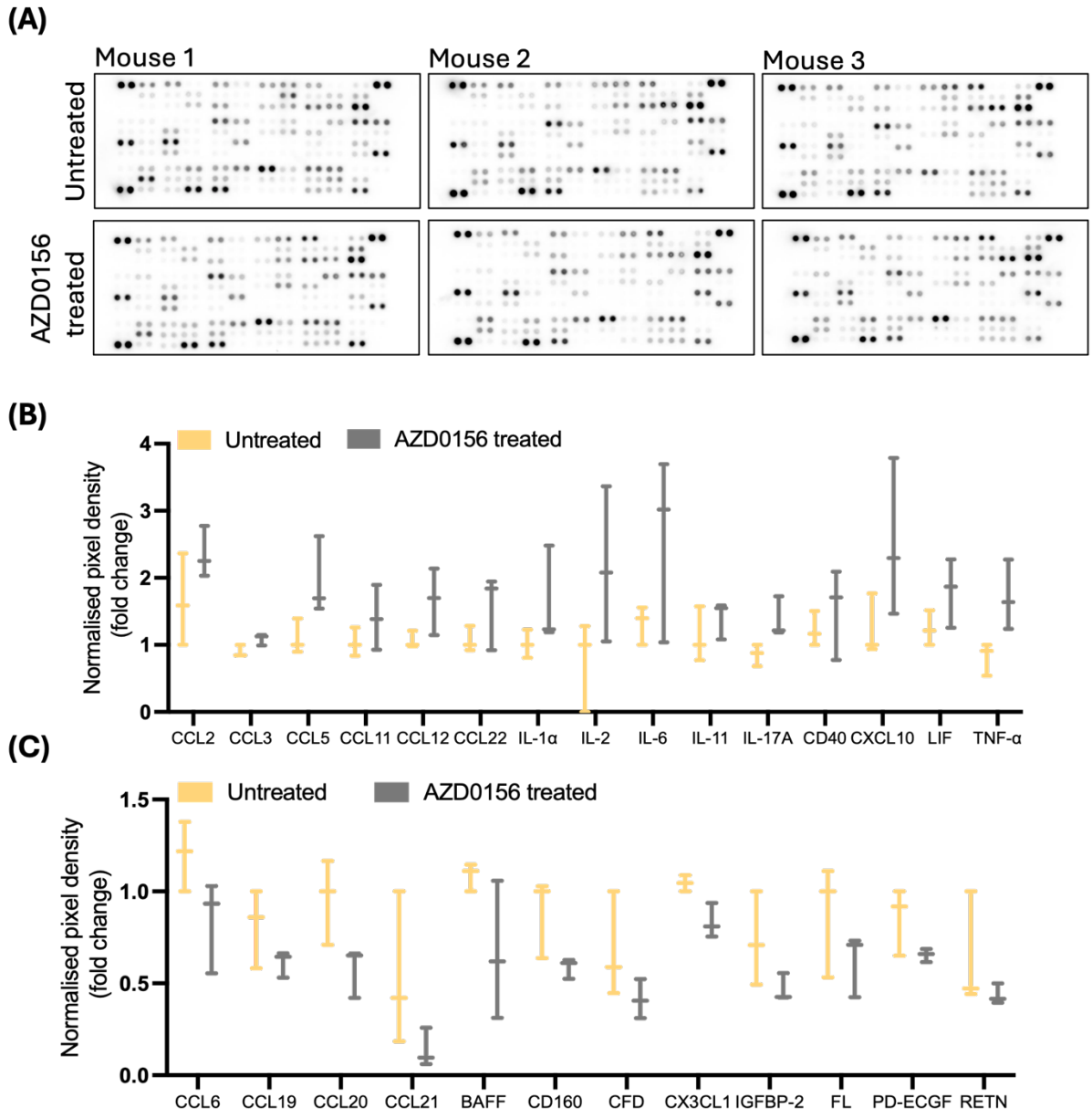

Figure 3.7: Tumour-derived cytokine expression. (A) Tumour supernatants from myofibroblast-rich tumours were analysed using proteome profiler arrays to evaluate differences in cytokine expression. Representative images of cytokine arrays for untreated and ATMi-treated tumours are shown. **(B)** Pixel density for each cytokine was quantified. Cytokines upregulated by ATM inhibition relative to untreated tumours are displayed in the graph. **(C)** Cytokines downregulated by ATM inhibition relative to untreated tumours are displayed in the graph. Data are presented as fold-change of normalised pixel density.

We observed significant downregulation of CCL2 and IL-6 following TGF-β1 treatment. In contrast, IL-11 and LIF were significantly upregulated. In line with our cytokine array findings, we demonstrate that ATM inhibition significantly increased the expression of CCL2, IL-6, IL-11, and LIF in TGF-β1 treated MLFs (**Figure 3.8B**). Other iCAF markers not included in the cytokine array, such as CXCL12 and HIF1α, were also investigated. We found that TGF-β1 treatment downregulated CXCL12, while it had no effect on HIF1α expression. Following ATM inhibition, CXCL12 was significantly downregulated in control MLFs, while no effect was observed in TGF-β1-treated MLFs. In contrast, HIF1α expression remained unaffected by ATM inhibition in both conditions (**Figure 3.8C**). Our findings suggest that ATM may play a dual role in determining fibroblast phenotype: promoting myofibroblast differentiation while inhibiting the iCAF phenotype.

Next, we investigated the role of ATM in regulating other pro-inflammatory molecules. The cytokines array results revealed variable trends; CXCL10, CD40 and CCL5 were upregulated in AZD0156 treated tumours, while CX3CL1, BAFF, and CCL19 were downregulated (**Figure 3.9A**). We then performed RT-qPCR to assess whether ATM inhibition specifically regulates the expression of selected cytokines in MLFs. CXCL10, CXCL11, and CCL5 play roles in recruiting $CD8^+$ T cell into the TME. Our results showed that both CXCL10 and CCL5 were significantly downregulated in TGF-β1-treated MLFs. However, upon ATM inhibition, CXCL10 and CCL5 expression returned to basal levels in TGF-β1-treated MLFs and was significantly upregulated in control MLFs. In contrast, CXCL11 expression was unaffected by either TGF-β1 treatment or ATM inhibition (**Figure 3.9B**). These findings align with the results from the cytokine array. Increased CX3CL1 expression in tumours is associated with enhanced anticancer immune responses, as it correlates with the accumulation of $CD4^+$ T cells, $CD8^+$ T cells, dendritic cells and NK cells (Korbecki et al., 2020). We demonstrated that TGF-β1 significantly downregulates CX3CL1 in MLFs. Additionally, ATM inhibition reduced CX3CL1 expression in control MLFs but elevated its expression in TGF-β1-treated MLFs (**Figure 3.9C**).

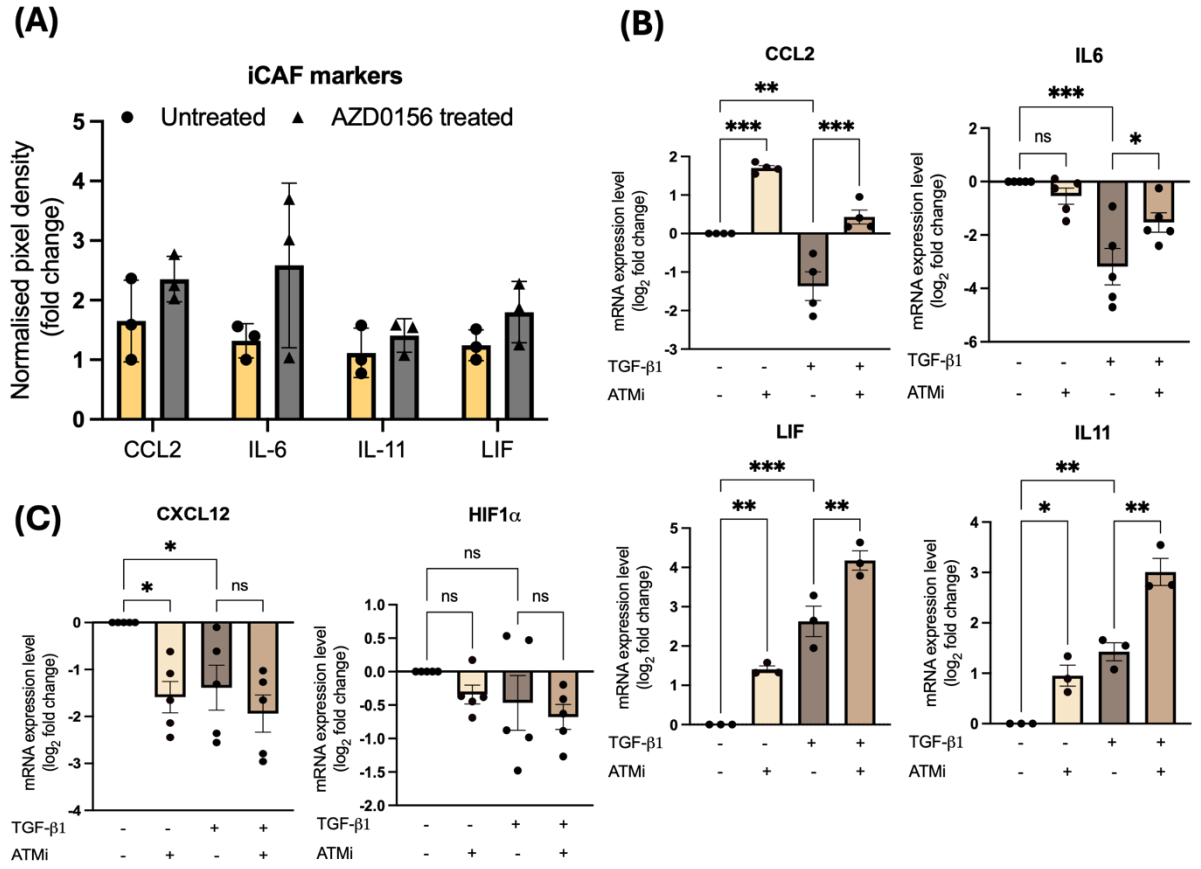

Figure 3.8: ATM inhibition enhances the expression of iCAF markers. (A) iCAF marker data derived from the cytokine array, presented as fold-change of normalised pixel density across three biological replicates. **(B-C)** RT-qPCR analysis of genes associated with the iCAF phenotype in MLFs treated with TGF-β1 and/or AZD0156 for 6 days. Data are presented as mean log_2 fold change ± SEM, normalised to untreated controls (each dot represents an independent experiment). Statistical analysis was conducted using one-way ANOVA with Bonferroni correction; *P≤0.05, **P≤0.01, ***P≤0.001, ns = not significant.

Our cytokine array results indicated that ATM inhibition leads to upregulation of CD40 expression. This finding was further validated by our RT-qPCR data, which showed significant upregulation of CD40 in both control and TGF-β1-treated MLFs following treatment with the ATM inhibitor. TGF-β1-treatment alone also significantly upregulated CD40, further suggesting that ATM inhibition plays a role in downregulating myofibroblastic genes while promoting the expression of genes associated with an inflammatory phenotype (**Figure 3.9D**). FRC-like CAF markers CCL19, VCAM1, and BAFF were downregulated following TGF-β1-treatment. Furthermore, ATM inhibition reduced the expression of CCL19 and BAFF in control MLFs but had no effect on VCAM1. In contrast, in TGF-β1-treated MLFs, ATM inhibition did not alter the expression of any of these markers (**Figure 3.9E**). These results suggest that TGF-β1 suppresses the FRC phenotype.

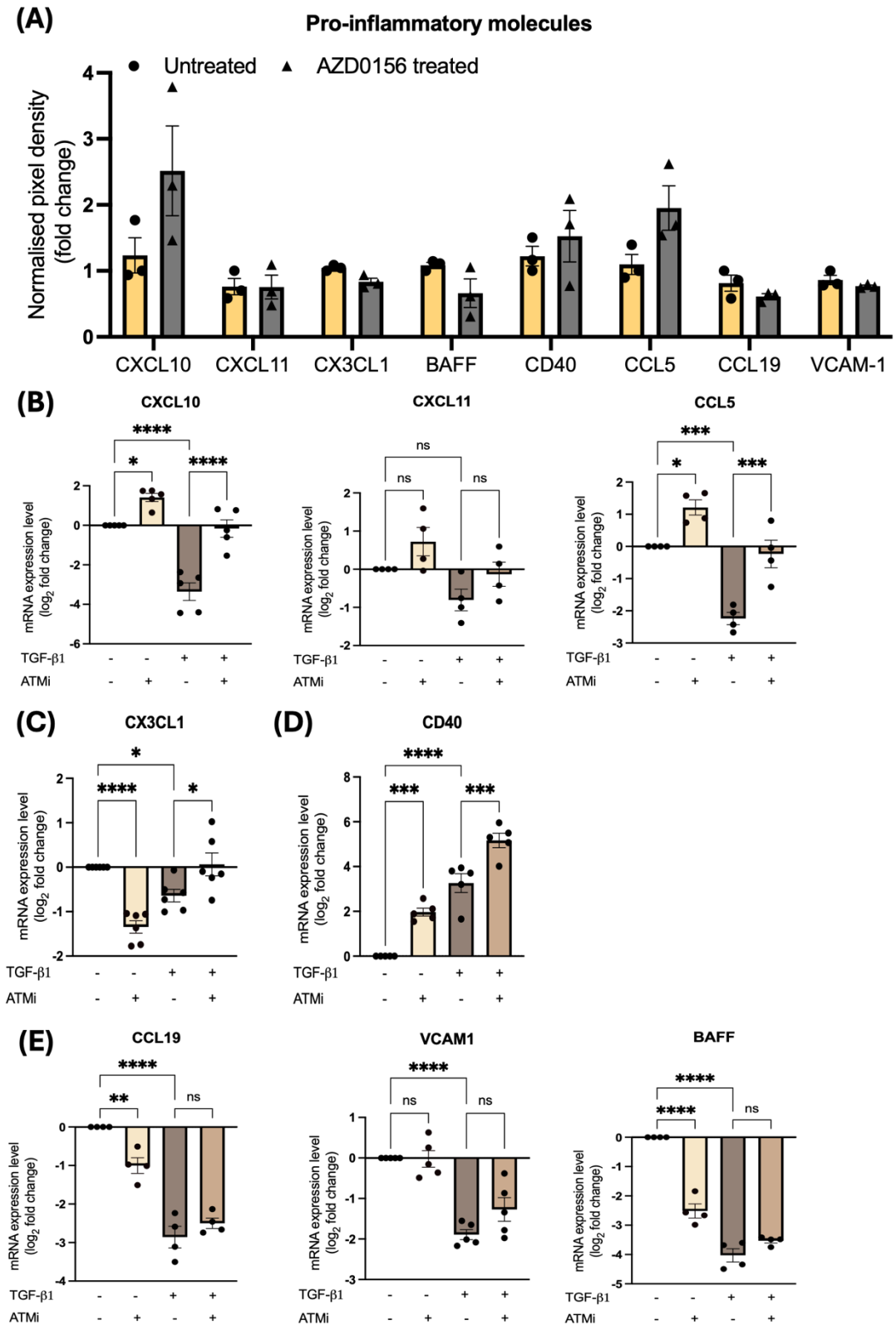

Figure 3.9: ATM inhibition regulates the expression of proinflammatory molecules. (A) Proinflammatory molecules identified in the cytokine array, presented as fold-change of normalised pixel density across three biological replicates. **(B-E)** RT-qPCR analysis of genes associated with proinflammatory molecules in MLFs treated with TGF-β1 and/or AZD0156 for 6 days. Data are presented as mean log_2 fold change ± SEM, normalised to untreated controls, with each dot representing an independent experiment. Statistical analysis was determined using one-way

ANOVA with Bonferroni correction; *P≤0.05, **P≤0.01, ***P≤0.001, ****P≤0.0001, ns = not significant.

Cancer cells, various immune cells, and CAFs produce MMPs within the TME, where they play diverse roles, including remodelling the ECM and modulating cell adhesion. Our cytokine array results indicated no differences in the expression of MMP-2, MMP-3, and MMP-9 between control and ATM inhibitor-treated tumours (**Figure 3.10A**). Our RT-qPCR data, based on *in vitro* treatments of MLFs, suggests that the expression of each MMP is differentially regulated by both TGF-β1-treatment and ATM inhibition (**Figure 3.10B**). MMP-2 expression was downregulated by both TGF-β1 treatment and ATM inhibition in control MLFs, but ATM inhibition in TGF-β1-treated MLFs had no effect on MMP-2 expression. MMP-9 was upregulated in TGF-β1-treated MLFs; however, ATM inhibition had no effect on its expression in either condition. No significant difference was observed in MMP-13 expression between control and TGF-β1-treated MLFs, but ATM inhibition increased MMP-13 expression in both conditions. MMP-14 expression showed no significant regulation with either TGF-β1 or AZD0156 treatment, and its expression varied across individual experiments.

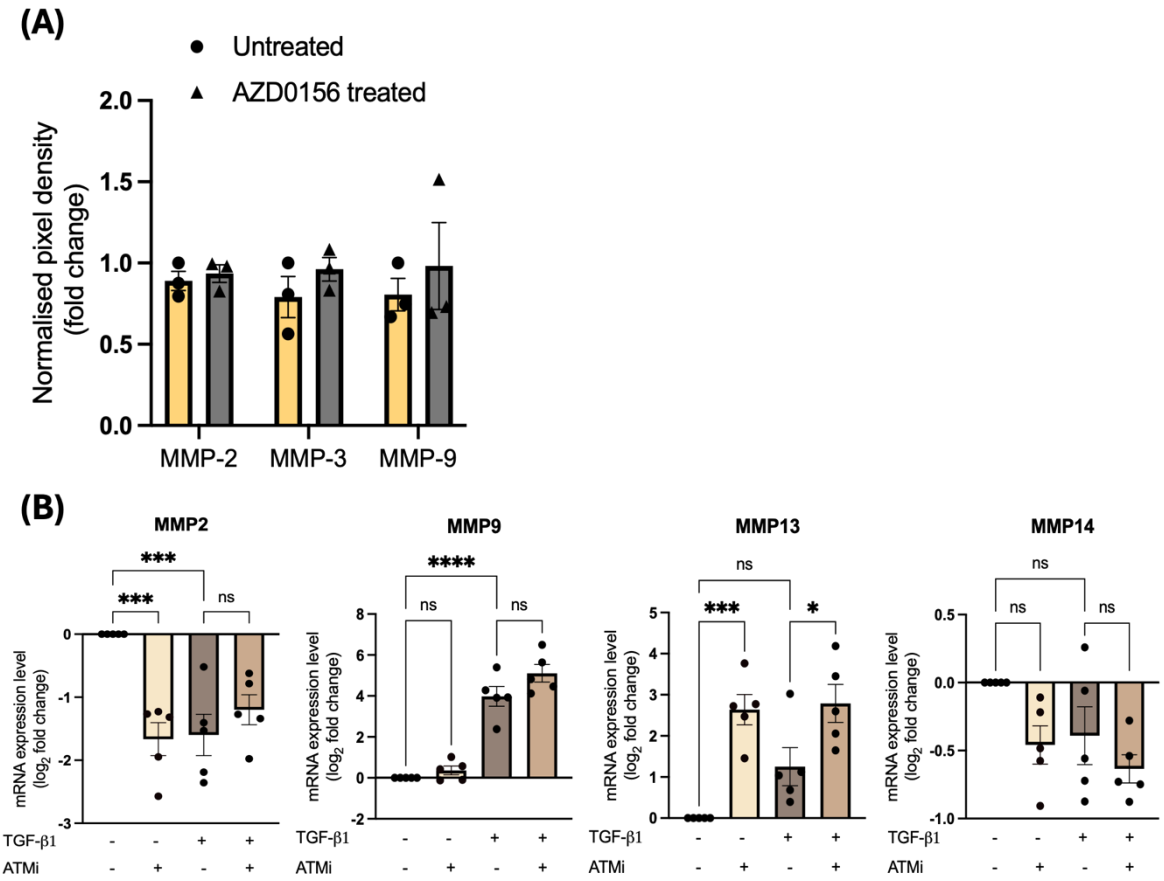

Figure 3.10: ATM inhibition has differential effects on MMP expression in MLFs. (A) MMPs identified in the cytokine array, presented as fold-change of normalised pixel density across three biological replicates. **(B)** RT-qPCR analysis of MMP expression in MLFs treated with TGF-β1 and/or AZD0156 for 6 days. Data are presented as mean log_2 fold change ± SEM, normalised to untreated controls, with each dot representing an independent experiment. Statistical significance was determined using one-way ANOVA with Bonferroni correction; *P≤0.05, ***P≤0.001, ****P≤0.0001, ns = not significant.

3.2.4.1 ATM inhibition enhances T cell migration *in vitro* by altering cytokine composition

Our results derived from analyses of tumour supernatants and *in vitro* treatments of MLFs demonstrate that ATM inhibition alters the cytokine composition. While we assessed the expression of specific cytokines and chemokines, this approach did not reveal whether whether the overall secretome of ATM-inhibited myofibroblasts contributes to antitumour effects, particularly through the recruitment of $CD8^+$ T cells into the TME. We used transwell migration assay to assess the migration of activated $CD8^+$ T cells toward various chemoattractants (**Figure 3.11A**). CXCL10 is well-established for its potency in recruiting $CD8^+$ T cell, while CCL5 has also been documented to promote $CD8^+$ T cell migration in some studies. In contrast, CCL2 predominantly attracts monocytes (L. Y. Chang et al., 2012; Gschwandtner et al., 2019; J. Liu et al., 2015). To validate the reliability of our assay, we utilised recombinant proteins of CXCL10,

CCL5, and CCL2. We observed a concentration-dependent increase in $CD8^+$ T cell migration in response to CXCL10 (**Figure 3.11B**). While CCL5 also promoted $CD8^+$ T cell migration, the number of migrating cells was lower compared to the CXCL10 condition. Notably, $CD8^+$ T cell migrated toward lower concentrations of CCL5 (10 and 40 ng/mL), but at 80 ng/mL, migration was more comparable to that observed with the basic medium alone (**Figure 3.11C**). In contrast, CCL2 did not induce significant $CD8^+$ T cell migration at any tested concentration when compared to the basic medium (**Figure 3.11D**). These findings confirmed the reliability of our experimental system and its consistency with previous reports. We next investigated whether the composition of conditioned media influences T cell migration. To generate conditioned media, TC1 cancer cells were cultured, and MLFs were treated with TGF-β1 or a combination of TGF-β1 and the ATM inhibitor AZD0156 for six days. Following treatment, complete media were removed, flasks were washed with PBS, and adherent cells were incubated in basic medium for 24 hours prior to media collection. On the day of the chemotaxis assay, MLFs from both conditions were counted to normalise for cell density, with media from flasks containing higher cell counts diluted accordingly. $CD8^+$ T cells were assessed for migration through transwells toward the different conditioned media. We found no significant difference in the number of migrating $CD8^+$ T cell toward the secretome generated by TGF-β1-treated MLFs compared to the basic medium. In contrast, the secretome from TGF-β1-treated and ATM-inhibited MLFs significantly increased $CD8^+$ T cell migration. The observed migration levels were comparable to those seen with TC1 cancer cell-conditioned media, which served as a positive control in this assay (**Figure 3.11E**).

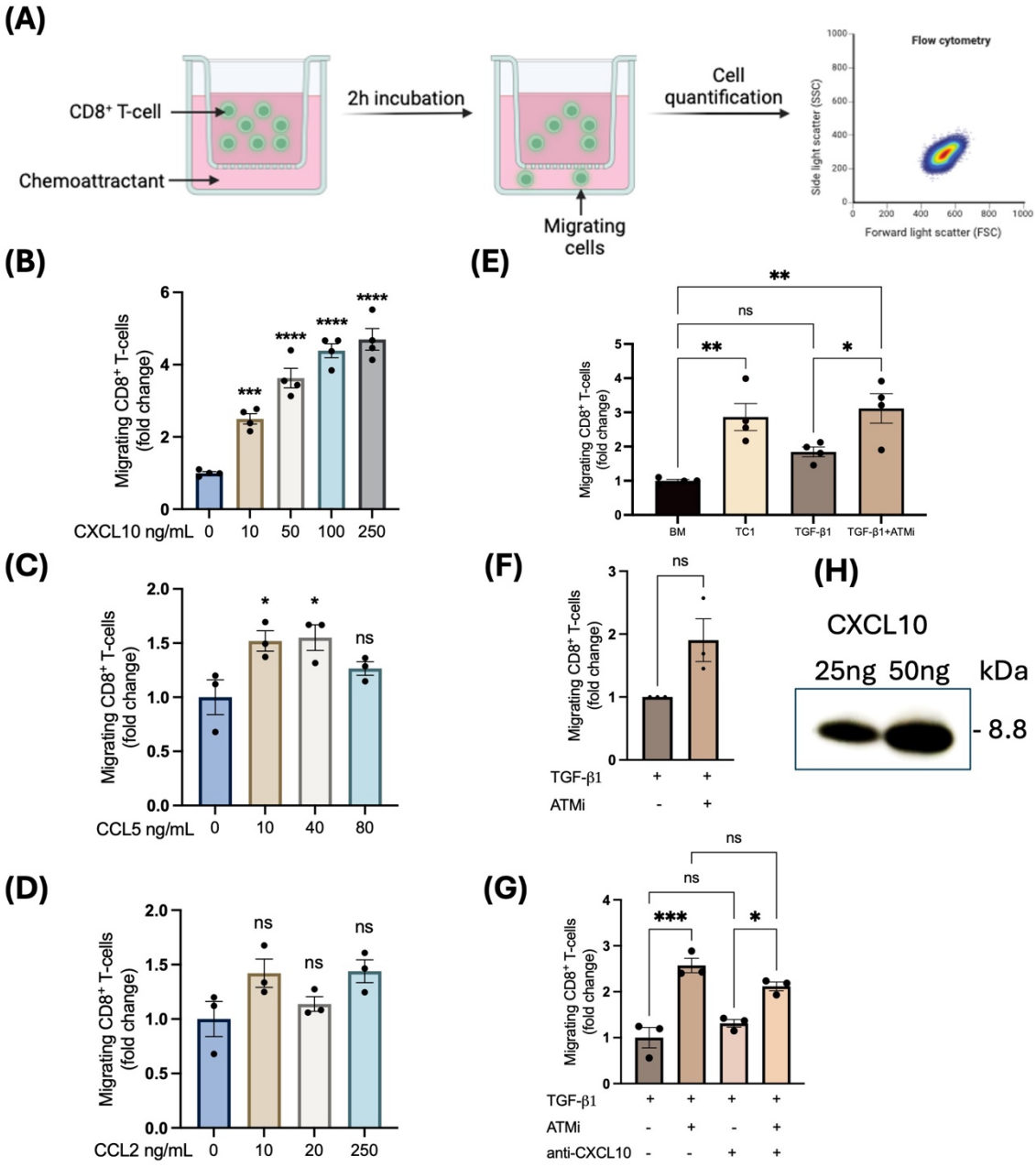

Figure 3.11: ATM inhibitor-treated myofibroblasts produce cytokines associated with increased T cell migration. (A) Schematic of the T cell migration assay. 50 000 CD8⁺ T cell were seeded to assess migration toward various chemoattractants. Migrated cells from the lower chamber were quantified by flow cytometry. **(B-D)** Migration of CD8⁺ T cells toward varying concentrations of recombinant CXCL10, CCL5, and CCL2. **(E)** Migration of CD8⁺ T cells toward conditioned media, normalised to cell density **(F)** Migration of CD8⁺ T cells toward conditioned media, normalised to cell density, with each dot representing a biological replicate. Statistical analysis was performed using a paired Student's t-test; ns = not significant. **(G)** Migration of CD8⁺ T cells toward conditioned media, normalised to cell density, in the presence or absence of anti-CXCL10. Unless otherwise stated, data for all panels are presented as mean fold change ± SEM, normalised to controls, with each dot representing a technical replicate. Statistical significance was determined using one-way ANOVA with Bonferroni correction; *P≤0.05, **P≤0.01, ***P≤0.001,

****P≤0.0001, ns = not significant. **(H)** Westen blot showing anti-CXCL10 antibody binding to recombinant CXCL10.

To validate these findings, the assay was repeated on three separate occasions using T cells isolated from the spleens of three different mice. On average, $CD8^+$ T cell migration was 1.9-fold higher toward the secretome of TGF-β1-treated and ATM-inhibited MLFs compared to TGF-β1-treated MLFs alone (**Figure 3.11F**). However, this increase did not reach statistical significance, likely due to the limited number of biological replicates and variability in the data. Given the well-established role of CXCL10 in $CD8^+$ T cell trafficking, we sought to determine whether neutralising CXCL10 with an anti-CXCL10 antibody would reduce $CD8^+$ T cell migration toward conditioned media generated from MLFs. In line with our previous findings, the secretome from TGF-β1-treated and ATM-inhibited MLFs significantly increased $CD8^+$ T cell migration, both in the presence and absence of anti-CXCL10. However, when anti-CXCL10 was added to the conditioned media from these MLFs, there was a slight reduction in $CD8^+$ T cell migration, although this difference was not statistically significant (**Figure 3.11G**). The specificity of the anti-CXCL10 antibody was confirmed by western blotting (**Figure 3.11H**). These results suggest that ATM inhibition in TGF-β1-treated MLFs leads to the upregulation of additional cytokines that promote $CD8^+$ T cell migration.

3.3 Discussion

Despite significant advancements in immunotherapy, only a small subset of patients experiences meaningful clinical benefits (Sambi et al., 2019). The effectiveness of immunotherapies is influenced by physical barriers within the tumour microenvironment that prevent activated T cells from contacting cancer cells. Dense collagen matrices characterised by high stiffness and small pore sizes have been shown to contribute to T cell exclusion (Bougherara et al., 2015; Friedl & Weigelin, 2008; Sadjadi et al., 2020; Salmon et al., 2012). Overall, previous findings suggest that modulating collagen production can favourably remodel the TME. We demonstrated that pharmacological inhibition of ATM using AZD0156 reduced the expression of fibrillar collagens, which may decrease ECM stiffness, a known barrier to T cell infiltration. This is particularly relevant because excessive collagen depletion has been linked to adverse outcomes in pancreatic cancer; deletion of type I collagen in αSMA+ myofibroblasts accelerated cancer progression, increased immunosuppression, and reduced overall survival in mice (Y. Chen et al., 2021). Our findings support the idea that modulating collagen production, rather than its total depletion, could effectively remodel the TME to promote antitumour immunity and improve treatment response while minimising protumorigenic processes. In addition, our study demonstrated that ATM inhibition significantly alters ECM composition and other myofibroblastic markers. Notably, the treatment consistently reduced the expression of POSTN, CTHRC1, FN, and αSMA; given that these are associated with an immunosuppressive TME their downregulation may be beneficial. Changes in other ECM components, including ELN, P4HA3, VCAN, ASPN, and PDGFRα, were more variable. Furthermore, our gene expression analysis of matrix metalloproteinases yielded mixed results. The lack of protein-level and activity data for MMPs is a limitation, especially since most MMPs are secreted as inactive pro-enzymes with activity regulated post-transcriptionally (Hadler-Olsen et al., 2011; Madzharova et al., 2019). While the regulation of MMPs by TGF-β is well documented, no direct research currently links ATM to MMP expression. Therefore, our data offer novel insights into the effects of ATM inhibition on MMP expression, though further investigation is warranted to fully understand these relationships. The altered ECM following ATM inhibition correlated with reduced contractility and enhanced $CD8^+$ T cell infiltration *in vitro*. These analyses of ECM components and other myofibroblastic markers provide a clearer understanding of the mechanisms underlying increased intratumoural $CD8^+$ T cell infiltration following ATM inhibition.

Interestingly, while ATM inhibition shifted myofibroblasts toward a more fibroblast-like state by reducing collagens, CTHRC1, POSTN, FN1, and αSMA, it also unexpectedly increased the expression of TGF-β1 and NOX4. Previous studies have shown that ATM deficiency leads to ROS accumulation, and that ROS can enhance TGF-β expression and activation (Barnes & Gorin, 2011; C. H. Chang & Pauklin, 2021; Lee, 2024; Lee & Paull, 2020; R. M. Liu & Desai, 2015; Reichenbach

et al., 2004). We therefore propose that ATM inhibition further increases oxidative stress in myofibroblast, upregulating both TGF-β1 and NOX4 expression. Similarly, fibroblasts from patients with ataxia telangiectasia (A-T), a disorder caused by a defective or absent ATM gene, have been found to exhibit elevated levels of NOX4 expression (Weyemia et al., 2015). These findings support the notion that ATM inhibition can drive NOX4 upregulation; however, they do not explain why this effect was observed exclusively in myofibroblasts and not in fibroblasts in our study. One possible explanation is that blocking ATM activity elevates NOX4 levels as a compensatory mechanism to enhance ATM activation, thereby attempting to maintain the myofibroblastic phenotype. Further investigation is required to identify the additional factors influencing this differential response.

Recent single-cell transcriptomic analyses reveal that CAFs comprise a range of subtypes with diverse functional properties, yet effective targeting remains elusive. This challenge partly arises from experimental models that do not capture the full spectrum of CAF heterogeneity, as most studies have predominantly focused on the myCAF phenotype. Acknowledging that preclinical successes often fail to translate clinically, we expanded our investigation to include not only myCAF-associated genes but also markers of FRC-like CAFs and iCAFs, thereby deepening our understanding of CAF plasticity *in vitro*. Our findings show that ATM inhibition did not affect FRC-like CAF markers, including CCL19 and VCAM1, while TGF-β1 treatment downregulated these markers. This confirms that these genes are not linked to the myCAF phenotype and suggest that, in this context, ATM inhibition does not exert tumour-suppressive functions via modulation of FRC-like CAF markers. iCAFs are known to regulate immune responses and inflammation in the TME (Biffi et al., 2019; Öhlund et al., 2017). We observed that TGF-β1 downregulated IL6, CCL2, and CXCL12, while elevating LIF and IL11 compared to control fibroblasts. These results suggest that TGF-β1 does not completely suppress markers associated with the iCAF phenotype by solely promoting a myofibroblastic state. Importantly, ATM inhibition in myofibroblasts upregulated pro-inflammatory cytokines; CCL2, IL6, LIF, and IL11, that are linked to immunosuppression and tumour progression (Kato et al., 2018; Pascual-García et al., 2019; Xiong et al., 2023; X. Yang et al., 2016). Our results indicate that ATM inhibition downregulates genes associate with the myofibroblastic signature while simultaneously shifting cells toward a more inflammatory profile associated with immunosuppression. Additionally, we found that the expression of chemokines involved in T cell trafficking, including CXCL10, CXCL11, CCL5 and CX3CL1, was suppressed by TGF-β1, and ATM inhibition led to the upregulation of these cytokines, although the increase for CXCL11 was not statistically significant. These cytokines are associated with improved responses to ICB, suggesting that their restoration is a positive outcome (Chow et al., 2019; Conroy & Lysaght, 2020; Korbecki et al., 2020; Y. Li et al., 2022; Siddiqui et al., 2016; J. Wang et al., 2024; B. Wu et al., 2024; J. Zhang et al., 2021). Moreover, CXCL10 and CXCL11 are marker of ifnCAFs, a phenotype associated with inflammation, IFN expression, and higher overall patient

survival (Cords et al., 2024). Migration assays confirmed that ATM inhibition in myofibroblasts modifies the secretome in a way that enhances $CD8^+$ T cell migration. Furthermore, even when anti-CXCL10 was added to the conditioned media, increased $CD8^+$ T cell migration was still observed in ATM-inhibited myofibroblasts compared to untreated cells. This suggests that while CXCL10 is important for $CD8^+$ T cell trafficking, it is not solely responsible for the increased migration; other cytokines also contribute to creating a favourable secretome.

Overall, our results demonstrate that ATM inhibition downregulates genes associated with the ECM and myCAF markers, while simultaneously inducing the expression of iCAF markers and chemokines involved in $CD8^+$ T cell trafficking. These changes in both ECM composition and secretome facilitate $CD8^+$ T cell migration *in vitro*. Additionally, ATM inhibition upregulated TGF-β1 and NOX4 in myofibroblasts, but not in fibroblasts. Since these genes are known to promote fibroblast-to-myofibroblast differentiation, their upregulation alongside the downregulation of myofibroblastic markers highlights the complexity of the response. These findings confirm that CAFs are highly plastic, and treatments may not simply revert one phenotype but rather shift cells toward another, thereby contributing to CAF heterogeneity and function.

Chapter 4 Target discovery for myofibroblastic CAF therapy

4.1 Introduction

CAFs are key architects of the TME, extensively remodelling the ECM in ways that promote cancer cell progression, metastasis, and therapy resistance (Sarkar et al., 2023). Excessive ECM deposition increases tissue stiffness and forms a physical barrier that not only shields cancer cells from immune surveillance but also hinders drug penetration (J. Guo et al., 2020). Beyond these mechanical effects, the CAF-derived ECM protein network also modulates immune cell trafficking (Monteran & Erez, 2019). Given these critical roles, targeting ECM components represents a promising strategy to overcome immune resistance and improve therapeutic outcomes.

Among the many ECM proteins implicated in tumour progression, CTHRC1, POSTN, and COL11A1 have emerged as key candidates due to their overexpression by CAFs and their association with poor prognosis across multiple cancers (Arolt et al., 2021; C. Chen et al., 2023; S. Lin et al., 2024; Y. Lu et al., 2025; C. Zhang et al., 2025; J. Zhang et al., 2023). Previous studies have examined their roles in modulating immune infiltration using *in vitro* and *in vivo* cancer cell line models (Q. Luo et al., 2022; H. Wang, Yao, et al., 2024; Z. Wang et al., 2022). Moreover, emerging *in silico* evidence suggests that targeting these genes may help disrupt the immunosuppressive TME and improve ICB responses in solid tumours (Shi et al., 2022; T. You et al., 2023b; Z. Zhang et al., 2024). However, the remaining question is whether targeting these genes specifically in myCAFs could promote $CD8^+$ T cell infiltration and enhance antitumour immunity. Experimentally addressing this in CAFs could represent a novel avenue for reducing immune evasion and improve patient outcomes.

This chapter aims to determine whether targeting CAF-derived ECM proteins - CTHRC1, POSTN, or COL11A1 can enhance T cell infiltration and affect tumour size in mouse models.

4.2 Results

4.2.1 Survival analysis of matrisome genes

A pan-cancer analysis has identified the upregulation of several matrisome proteins, including CTHRC1, POSTN, and COL11A1, with CTHRC1 emerging as the most highly upregulated matrisome protein in cancers (Harikrishnan et al., 2021). To investigate whether the upregulation of these genes is associated with survival outcomes, we used GEPIA2 to analyse Kaplan-Meier curves. In lung cancer cohorts, high POSTN expression was significantly associated with worse survival, with individuals in the high-expression group experiencing a 30% greater risk of death compared to those in the low-expression group. In contrast, no significant survival differences were observed between high- and low-expression groups for CTHRC1. For COL11A1, high expression was associated with a 20% increased risk of death; however, this trend did not reach statistical significance (p= 0.051) (**Figure 4.1A**). Pan-cancer analyses involving larger patient cohorts revealed a consistent association between high expression of these genes and worse survival outcomes. High expression of CTHRC1 and COL11A1 was each associated with a 50% increased risk of death, while high POSTN expression was linked to a 40% higher risk (**Figure 4.1B**). These findings highlight the potential prognostic significance of these matrisome proteins and their role in cancer progression across multiple cancer types.

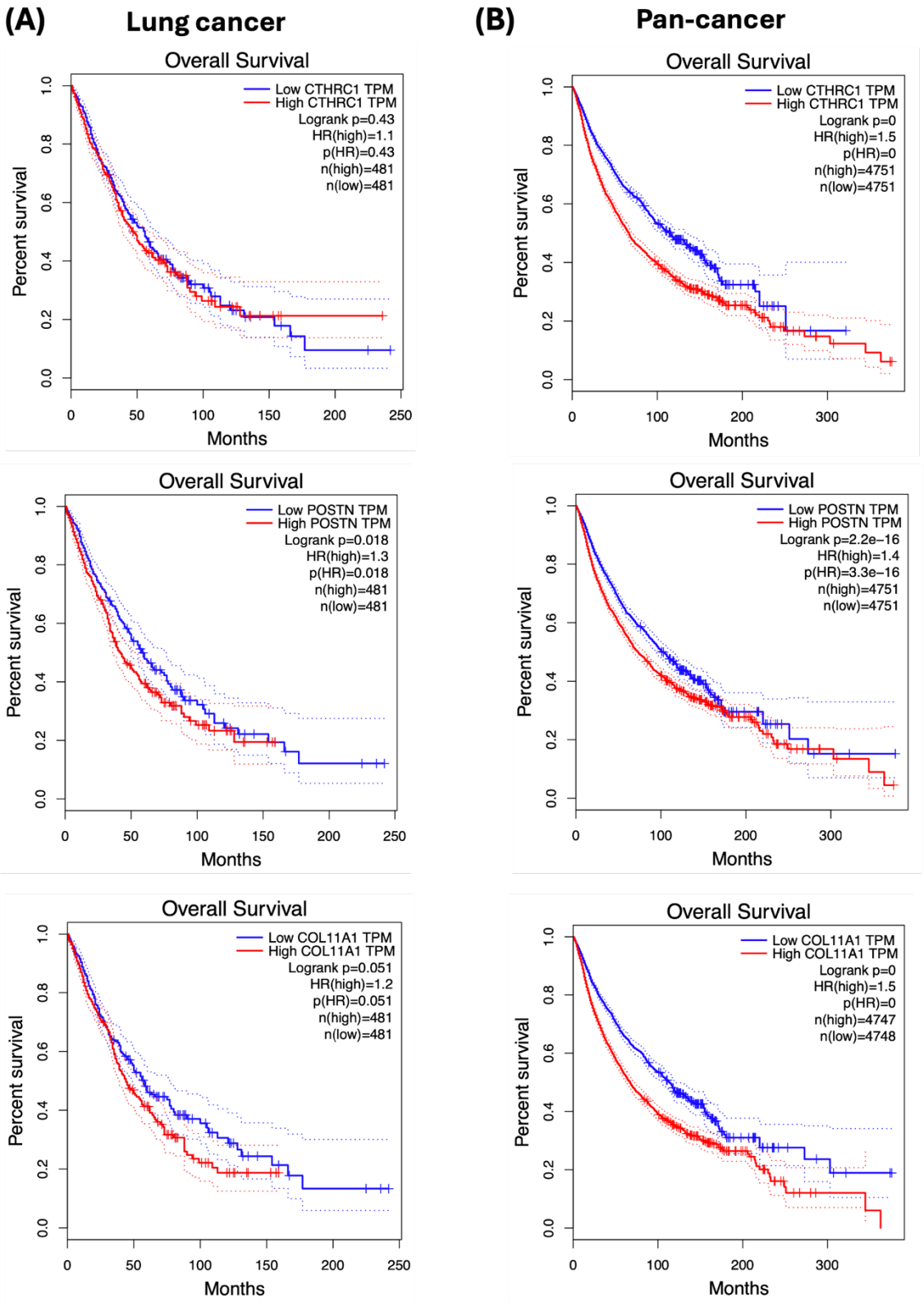

Figure 4.1: High expression of CTHRC1, POSTN, and COL11A1 is associated with worse overall survival. **(A)** Kaplan-Meier survival curves for lung cancer cohorts and **(B)** pan-cancer analysis, generated using the GEPIA2 database. The blue and red curves represent the percentage survival over time for cancers with low and high expression of the gene of interest, respectively. Hazard ratios (HR) and p-values are indicated on the graphs. An HR >1 indicates an increased risk of death for the high-expression group compared to the low-expression group, and $p \leq 0.05$ denotes statistical significance.

MyCAFs play a crucial role in ECM deposition and remodelling within the TME and have been shown to promote tumour immune evasion by excluding CD8 T cells from tumours (Ford et al., 2020). CTHRC1, POSTN, and COL11A1 are highly expressed by myCAFs and to investigate whether their downregulation in MLFs could enhance T cell infiltration and affect tumour size in mouse models, we first evaluated the growth characteristics of MLFs.

To transdifferentiate MLFs into myofibroblasts we treated the cells with TGF-β1 in either 1% or 20% FBS for three days to assess whether serum concentration influences the regulation of myofibroblastic markers. First, we performed RT-qPCR to analyse differences in the expression levels of our genes of interest. Our results demonstrate that CTHRC1, POSTN, and COL11A1 are upregulated to similar levels under both low- and high- serum conditions (**Figure 4.2A**). We then examined the expression of additional myofibroblastic markers. We observed that COL1A1, COL1A2, TGF-β1, and NOX4 were significantly upregulated under both low- and high-serum conditions, with no significant differences between serum concentrations (**Figure 4.2B**). These findings indicate that serum concentration does not interfere with TGF-β1 function during the differentiation process.

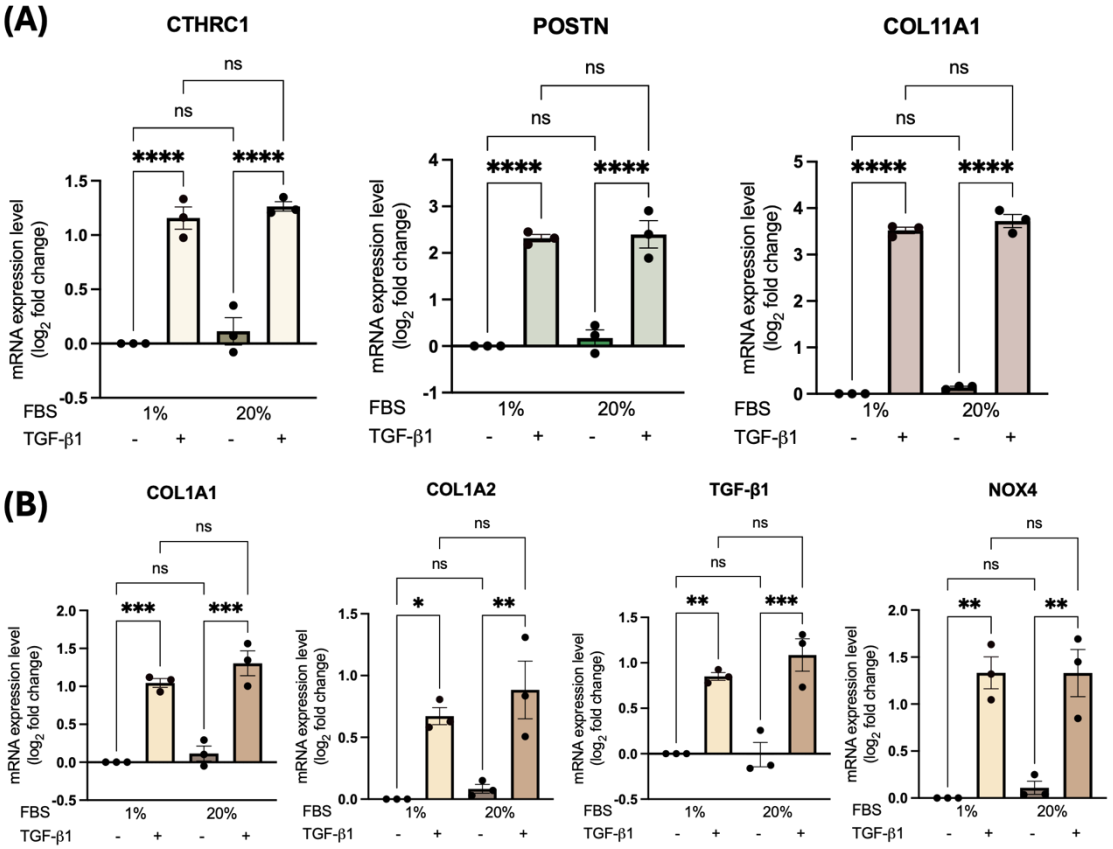

Figure 4.2: Serum concentration does not interfere with TGF-β1 function during fibroblast-to-myofibroblast differentiation.(A-B) RT-qPCR analysis of genes associated with the myofibroblastic phenotype and ECM composition in MLFs treated with TGF-β1 in either 1% or 20% serum. Data are presented as mean log_2 fold change ± SEM, normalised to control MLFs cultured in 1% serum, with each dot representing an independent experiment. Statistical analysis was performed using one-way ANOVA with Bonferroni correction; **P≤0.01, ***P≤0.001, ****P≤0.0001, ns = not significant.

4.2.2 Generating gene knockdowns

We selected lentiviral vectors for shRNA knockdown because of their ability to transduce cells independently of their division status (Dufait et al., 2012). The shRNA-expressing plasmids were obtained as bacterial stocks from the MISSION shRNA library. These plasmids contain shRNA sequences inserted into the pLKO.1-puro vector, making them compatible with the lentiviral expression system. The shRNAs were designed based on *in silico* predictions. Only the shRNA vectors targeting COL11A1 had been functionally validated; therefore, we ordered the two validated shRNA vectors for this gene, but four shRNA vectors for POSTN and CTHRC1. Lentiviral vectors were amplified, linearised, and their sizes confirmed via gel electrophoresis. Supercoiled plasmids were electrophoresed alongside their linearised counterparts. As expected, supercoiled plasmids migrated unpredictably on the agarose gel due to their compact structure. In contrast, linearised plasmids migrated consistently according to their molecular weight, with

the expected size of 7,086 bp. The SHC012 plasmid was used as a control for linearisation due to the absence of an EcoRI restriction site (**Figure 4.3A**). Following plasmid amplification, SHC012 which encodes TagRFP was used to optimise the multiplicity of infection (MOI) - the ratio of viral particles to target cells. We aimed to identify the lowest MOI at which nearly all cells were successfully infected. MLFs were seeded and allowed to adhere overnight. Viral particles were then added at various MOIs in the presence of 6 µg/mL polybrene, which is the optimised concentration for MLFs. The cells were incubated for 18 hours, washed with PBS, and fresh media was added to the wells. RFP expression was observed 48 hours post-transduction. At this point, fresh media supplemented with 4 µg/mL puromycin was added, and cells transduced at different MOIs were imaged 72 hours after puromycin selection (**Figure 4.3B**). At this timepoint, we confirmed that non-transduced control MLFs were not viable under puromycin selection. As the MOI increased, we observed a corresponding increase in cell confluence and fluorescence intensity. To achieve our goal of selecting the lowest MOI at which nearly all cells were infected, we determined that an MOI of 5 was optimal. This MOI was used for subsequent knockdown experiments. See **Appendix A Figure 3** for cell viability data.

To evaluate the effectiveness of shRNA vectors in knocking down target genes, all shRNAs were transduced into passage-four MLFs at an MOI of 5. Passage four was the earliest passage at which sufficient cell numbers could be obtained following fibroblast isolation from lungs. Once transduced cells reached confluence after puromycin selection, they were collected to assess knockdown efficiencies using RT-qPCR. Knockdown efficiency for all gene targets was calculated relative to the non-transduced control. Additionally, gene expression levels for the scrambled RNA control (shSCR) were included for comparison.

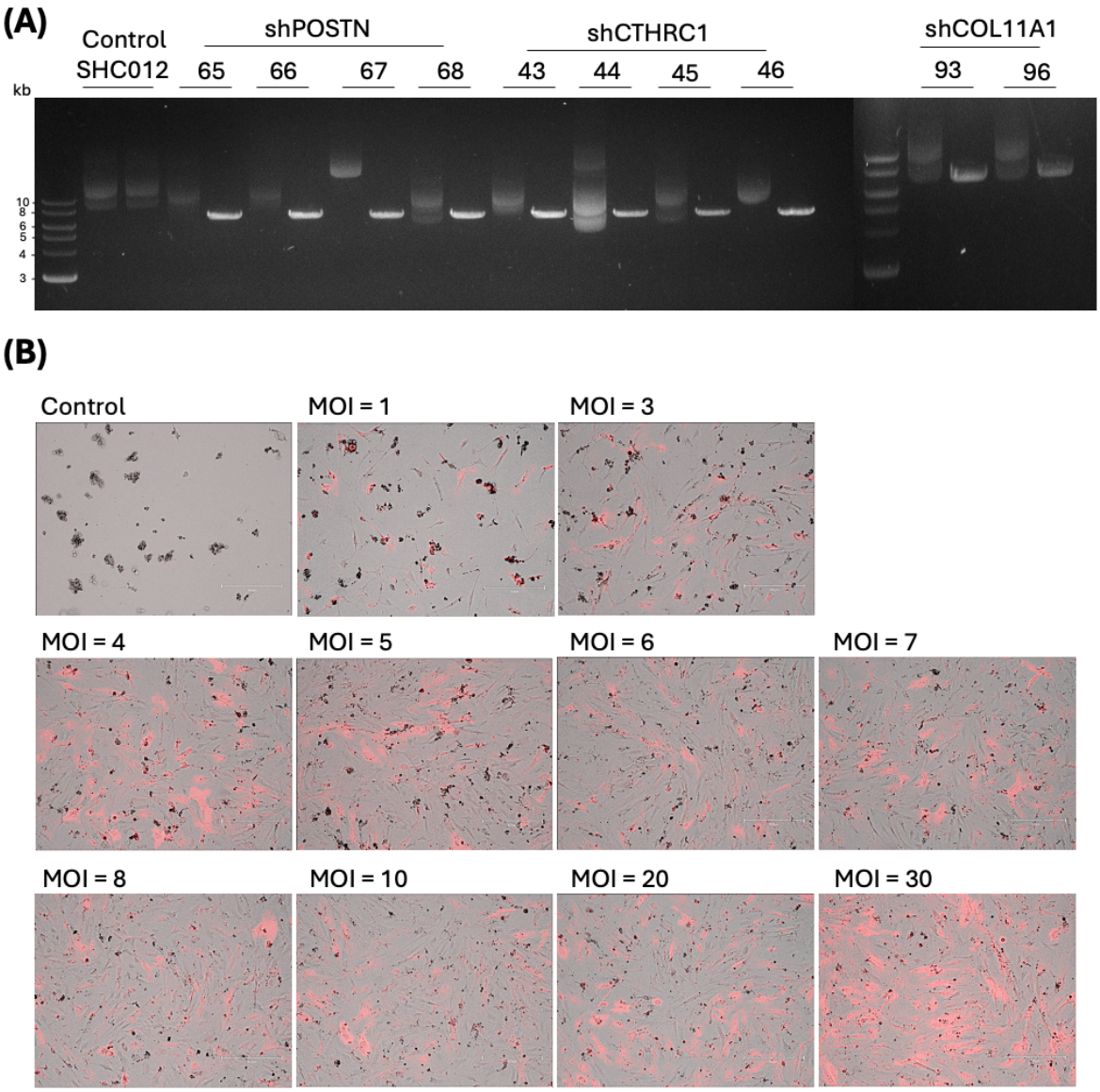

Figure 4.3: Optimisation of transduction efficiency for lentiviral vectors in MLFs. (A) Plasmid vectors for gene knockdowns were amplified, linearised using the EcoRI restriction enzyme, and electrophoresed alongside supercoiled plasmids to confirm amplification of plasmids with the expected molecular weight of 7,086 bp. **(B)** MLFs were transduced with the SHC012 lentiviral vector at the indicated MOIs in the presence of 6 µg/mL polybrene for 18 hours. RFP expression was observed 48 hours after the initiation of transduction. At this point, the media was replaced and supplemented with 4 µg/mL puromycin to select for cells that successfully incorporated the lentiviral vectors. Cells were imaged 72 hours post-selection to evaluate their viability and fluorescence intensity at the indicated MOIs. All images include a 500 µm scale bar.

Our results indicate that shRNA silencing efficacy varied among target genes. We achieved over 90% CTHRC1 knockdown in MLFs using shCTHRC1-43 and shCTHRC1-44, with downregulation persisting after TGF-β1 treatment (**Figures 4.4A, 4.4D**). While POSTN knockdown was induced, it was not sustained after TGF-β1 treatment (**Figures 4.4B, 4.4E**), and COL11A1 knockdown was unsuccessful (**Figures 4.4C, 4.4F**). To determine whether knockdown could be enhanced and sustained following TGF-β1 treatment, we increased the MOI, selecting two shRNA sequences per gene. Previously, we demonstrated that transducing MLFs with shSCR at an MOI of 5 significantly upregulated CTHRC1, this was not evident at an MOI of 10 (**Figures 4.4A, 4.5A**). Increasing the MOI from 5 to 10 had minimal effect on CTHRC1 downregulation likely because nearly all cells were transduced at an MOI of 5 (**Figure 4.5A**). Following TGF-β1 treatment, CTHRC1 downregulation remained more stable at an MOI of 5 (**Figure 4.5B**). Despite achieving over 89% CTHRC1 mRNA downregulation, Western blot analysis did not reflect this reduction at the protein level; however, control cells showed TGF-β1-induced upregulation (**Figures 4.5C-D**). For shPOSTN-65, increasing the MOI did not enhance knockdown, whereas shPOSTN-66 at a higher MOI achieved an additional 45% downregulation of POSTN (**Figure 4.6A**). However, neither knockdown was sustained after TGF-β1 treatment (**Figure 4.6B**). While both sgRNA sequences showed over 90% POSTN knockdown at the mRNA level, this was not reflected in Western blot results (**Figures 4.6C-D**), complicating the assessment of knockdown success. COL11A1 knockdown remained unsuccessful despite testing MOIs of 5, 10, 15, and 20 for shCOL11A1-93 and shCOL11A1-96. At MOIs of 5 and 15, shSCR-transduced MLFs showed COL11A1 upregulation relative to non-transduced controls (**Figure 4.7A**), but neither shRNA achieved downregulation (**Figure 4.7B**). Western blot confirmed COL11A1 upregulation following TGF-β1 treatment and the absence of successful knockdown (**Figures 4.7C-E**).

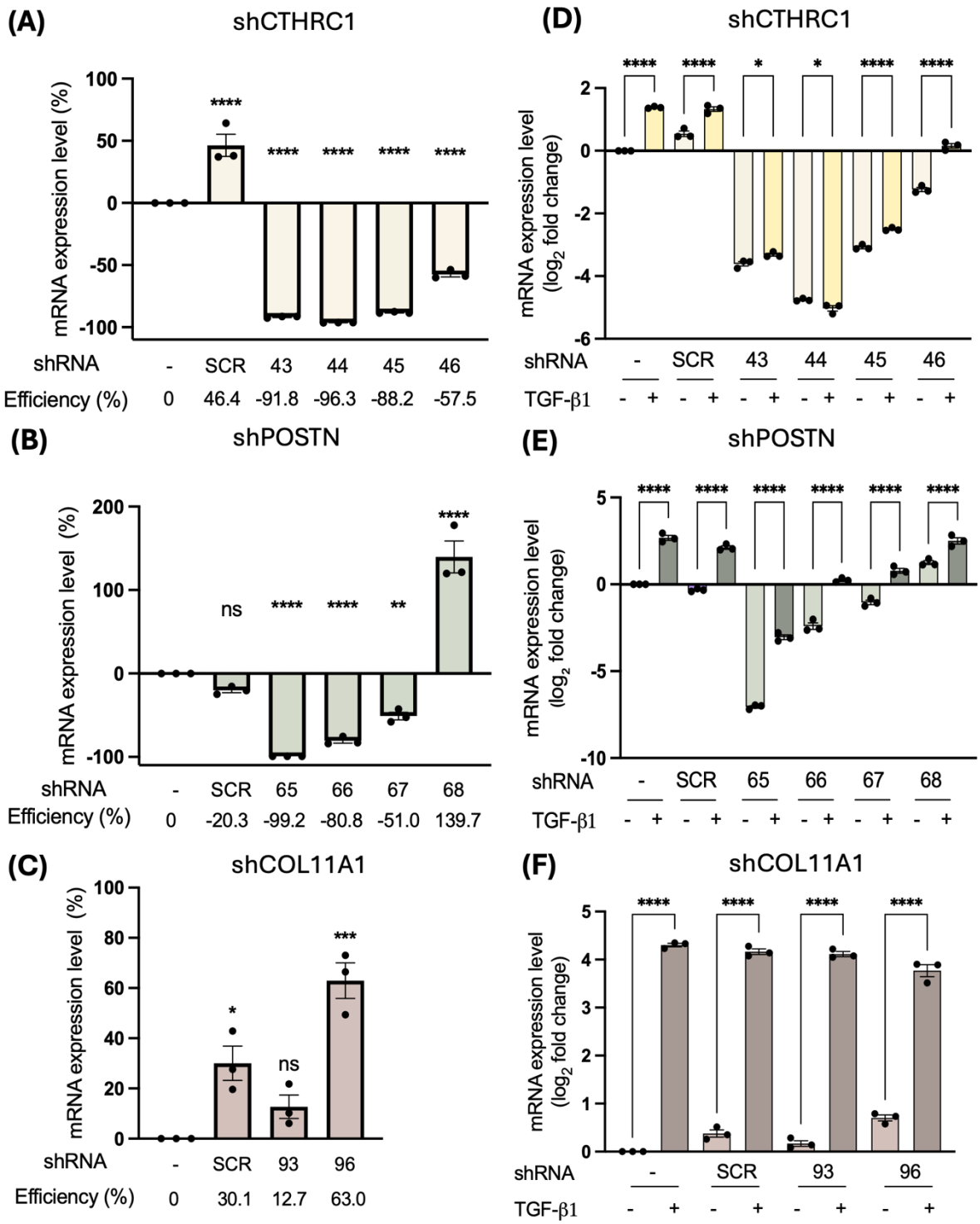

Figure 4.4: Transduction with lentiviral shRNAs alters target gene expression in MLFs. (A-C) MLFs were transduced with the indicated shRNAs at an MOI of 5. Following puromycin selection, cells were collected, and knockdown efficiencies were assessed using RT-qPCR. Data are presented as the mean percentage mRNA expression normalised to non-transduced control MLFs (n_{tr} = 3). shSCR represents a scrambled RNA control. **(D-F)** Post-knockdown, MLFs were treated with TGF-β1 for 72 hours and analysed via RT-qPCR to determine whether target genes remained downregulated after treatment. Data are presented as mean log_2 fold change ± SEM, normalised to non-transduced control MLFs (n_{tr} = 3). For all panels, statistical analysis was performed using one-way ANOVA with Bonferroni correction; *P≤0.05, **P≤0.01, ***P≤0.001, ****P≤0.0001, ns = not significant.

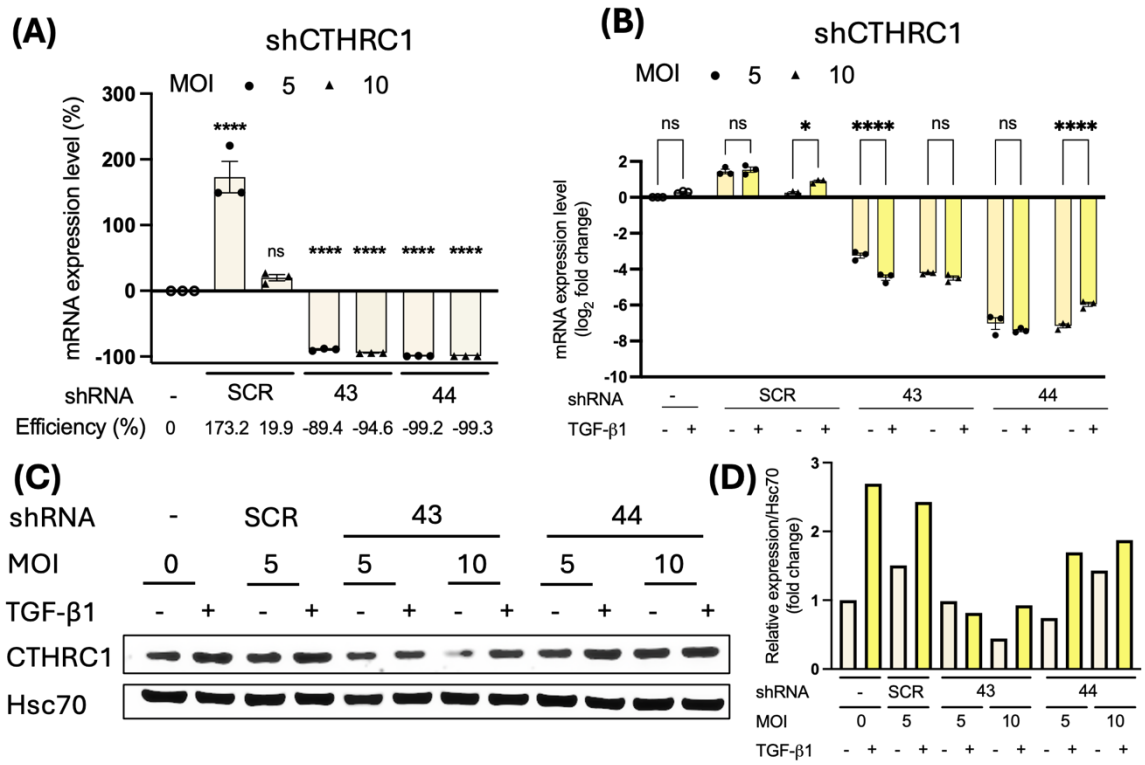

Figure 4.5: Downregulation of CTHRC1 expression in MLFs transduced with shRNAs. (A) MLFs were transduced with the indicated shRNAs at MOIs of 5 and 10. Following puromycin selection, cells were collected, and knockdown efficiencies were assessed using RT-qPCR. Data are presented as the mean percentage mRNA expression normalised to non-transduced control MLFs (n_{tr} = 3). shSCR represents a scrambled RNA control. **(B)** Post-knockdown, MLFs were treated with TGF-β1 for 72 hours and analysed via RT-qPCR to determine whether CTHRC1 expression remained downregulated after treatment. Data are presented as mean log_2 fold change ± SEM, normalised to non-transduced control MLFs (n_{tr} = 3.) Statistical analysis for panels (A) and (B) was performed using one-way ANOVA with Bonferroni correction; *P≤0.05, ****P≤0.0001, ns = not significant. **(C)** Western blot analysis of CTHRC1 expression in knockdown MLFs transduced with shCTHRC1-43 or shCTHRC1-44 at MOIs of 5 and 10, with or without TGF-β1 treatment for 72 hours. **(D)** Quantification of pixel density from Western blots, normalised to non-transduced control MLFs.

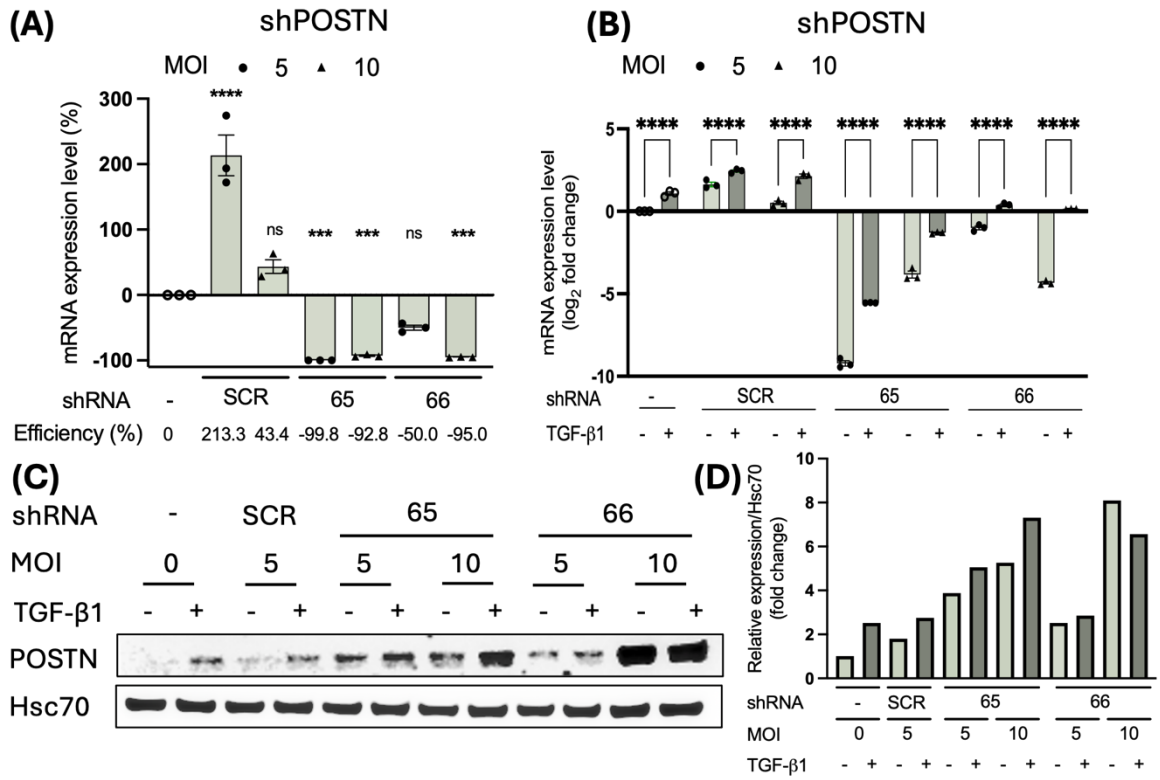

Figure 4.6: Downregulation of POSTN expression in MLFs transduced with shRNAs. (A) MLFs were transduced with the indicated shRNAs at MOIs of 5 and 10. Following puromycin selection, cells were collected, and knockdown efficiencies were assessed using RT-qPCR. Data are presented as the mean percentage mRNA expression normalised to non-transduced control MLFs (n_{tr} = 3). shSCR represents a scrambled RNA control. **(B)** Post-knockdown, MLFs were treated with TGF-β1 for 72 hours and analysed via RT-qPCR to determine whether POSTN expression remained downregulated after treatment. Data are presented as mean log_2 fold change ± SEM, normalised to non-transduced control MLFs (n_{tr} = 3.) Statistical analysis for panels (A) and (B) was performed using one-way ANOVA with Bonferroni correction; ***P≤0.001, ****P≤0.0001, ns = not significant. **(C)** Western blot analysis of POSTN expression in knockdown MLFs transduced with shPOSTN-65 or shPOSTN-66 at MOIs of 5 and 10, with or without TGF-β1 treatment for 72 hours. **(D)** Quantification of pixel density from Western blots, normalised to non-transduced control MLFs.

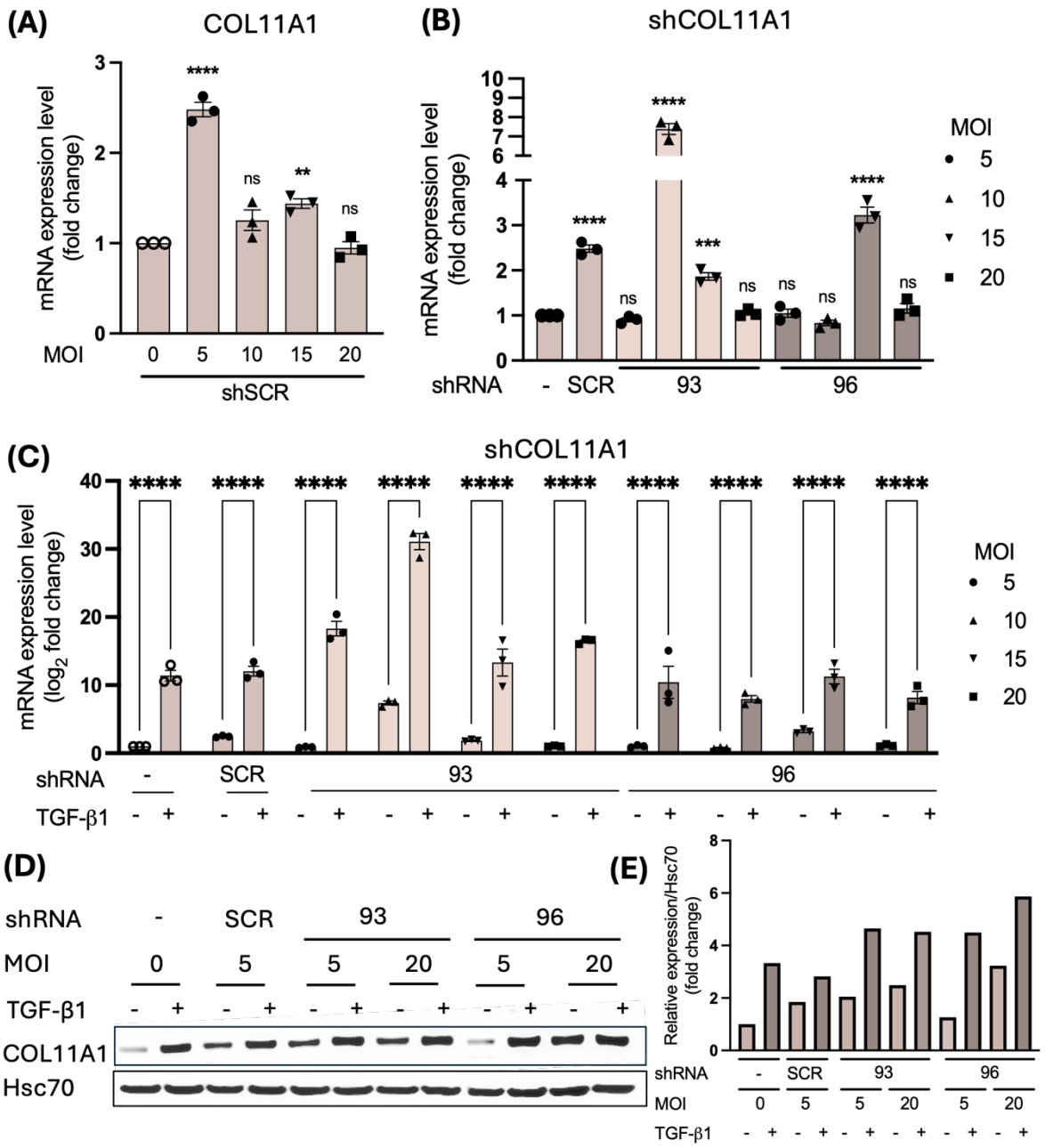

Figure 4.7: COL11A1 expression analysis in MLFs transduced with shRNAs. (A-B) MLFs were transduced with the indicated shRNAs at MOIs of 5, 10, 15 and 20. Following puromycin selection, cells were collected, and knockdown efficiencies were assessed using RT-qPCR. Data are presented as the mean percentage mRNA expression normalised to non-transduced control MLFs (n_{tr} = 3). shSCR represents a scrambled RNA control. **(C)** Post-knockdown, MLFs were treated with TGF-β1 for 72 hours and analysed via RT-qPCR to assess COL11A1 expression levels after treatment. Data are presented as mean log_2 fold change ± SEM, normalised to non-transduced control MLFs (n_{tr} = 3.) Statistical analysis for panels (A-B) and (C) was performed using one-way ANOVA with Bonferroni correction; *P≤0.05, **P≤0.01, ***P≤0.001, ****P≤0.0001, ns = not significant. **(D)** Western blot analysis of COL11A1 expression in knockdown MLFs transduced with shCOL11A1-93 or shCOL11A1-96 at MOIs of 5 and 20, with or without TGF-β1 treatment for 72 hours. **(E)** Quantification of pixel density from Western blots, normalised to non-transduced control MLFs.

Reference gene knockdowns at the protein level were validated using whole protein extracts. To explore expression disparities, we cultured knockdown MLFs with and without TGF-β1 to promote ECM deposition. Fibroblasts were lysed, and acellular proteins were collected in SDS buffer. Protein quantification of cellular extracts may explain variability in Western blot results of acellular fractions. Western blot analysis of acellular CTHRC1 fractions aligned more closely with RT-qPCR data than whole protein extracts (**Figures 4.5A-B, 4.8A**). shCTHRC1-44 was more effective in reducing CTHRC1 than shCTHRC1-43, consistent with mRNA expression. However, shCTHRC1-43 failed to downregulate CTHRC1 at the protein level, and CTHRC1 was not upregulated by TGF-β1 in this context (**Figure 4.8A**). For POSTN, Western blot analysis of acellular fractions confirmed downregulation with shPOSTN-65 but not with shPOSTN-66 (**Figure 4.8B**). Non-transduced, shSCR-, and shPOSTN-65-transduced MLFs did not exhibit POSTN upregulation after TGF-β1 treatment. This contradicts prior findings, as RT-qPCR and whole protein extracts previously indicated periostin upregulation in control cells following TGF-β1 treatment (**Figures 4.6A-B, 4.8B**).

While culturing MLFs transduced with shRNA constructs at an MOI of 5, we observed variations in cell proliferation. To quantify these differences, we performed an MTS assay, expressing proliferation rates at days 3 and 6 as fold changes relative day 1 to minimise seeding density effects (**Figures 4.8C-D**). On day 3, untreated and TGF-β1-treated MLFs transduced with shSCR, shCTHRC-43, and shPOSTN-66 exhibited lower proliferation rates than non-transduced controls. By day 6, shSCR-transduced MLFs maintained reduced proliferation compared to their respective controls. In contrast, untreated MLFs transduced with shCTHRC1-43 and shCTHRC1-44 showed no significant differences in proliferation. However, with TGF-β1 treatment, their responses diverged: shCTHRC1-43-transduced MLFs proliferated more slowly, while shCTHRC1-44-transduced MLFs proliferated more rapidly. For shPOSTN-66, proliferation remained unchanged regardless of TGF-β1 treatment. Notably, shPOSTN-65-transduced MLFs exhibited approximately twice the proliferation rate of non-transduced controls, regardless of TGF-β1 treatment (**Figures 4.8C-D**). Results are based on three technical replicates per condition, with an additional independent experiment confirming similar trends (**Appendix A Figure 4**). The lack of statistical significance is likely due to the limited number of replicates.

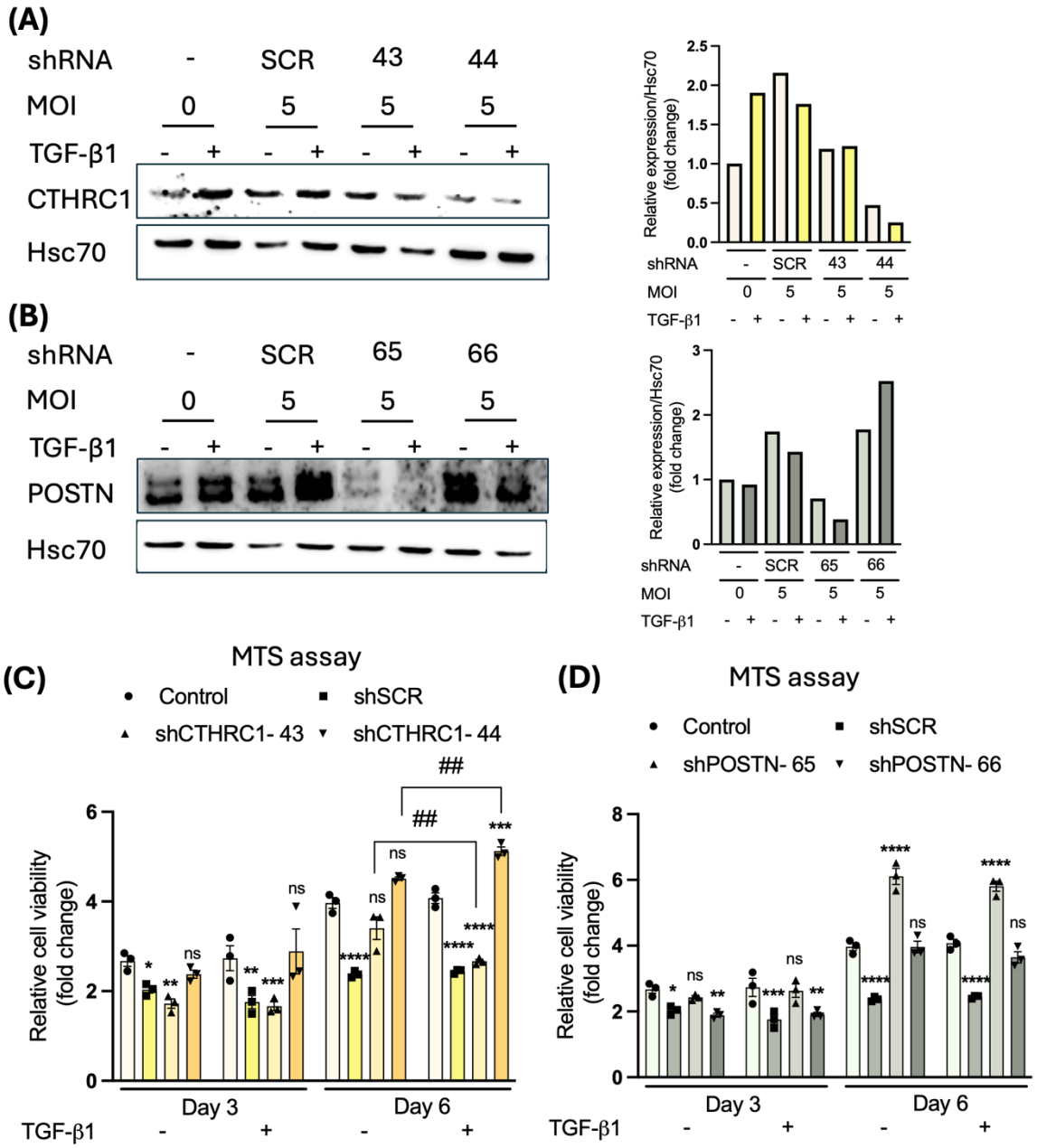

Figure 4.8: Effect of shRNA transduction and TGF-β1 treatment on ECM protein levels and proliferation in MLFs. (A-B) Western blot analysis of acellular proteins from ECM deposited by MLFs transduced with the indicated shRNAs at an MOI of 5, with or without TGF-β1 treatment for 72 hours. Graphs show pixel density quantification from Western blots, normalised to non-transduced control MLFs. **(C-D)** MTS assay measuring the proliferation rates of MLFs transduced with the indicated shRNAs at an MOI of 5, with or without TGF-β1. Data are presented as mean fold change ± SEM, normalised to MTS measurements on day 1 (n_{tr} = 3). Statistical analysis was performed using two-way ANOVA with Bonferroni correction; *P≤0.05, **P≤0.01, ***P≤0.001, ****P≤0.0001, ns = not significant.

The aim of our study was to investigate whether downregulating CTHRC1, POSTN, or COL11A1 in MLFs could enhance T cell infiltration and affect tumour size in mouse models. We initially decided to induce gene knockdowns rather than gene knockouts in MLFs, as knockdowns more closely mimic pharmacological inhibition, which typically reduces but does not entirely eliminate protein function. However, we encountered challenges in determining whether effective gene knockdowns were achieved due to discrepancies between RT-qPCR and Western blot data. Additionally, increasing MOIs for different shRNAs did not produce consistent expression patterns. Furthermore, MLFs transduced with shCTHRC1-44 and shPOSTN-65 exhibited higher proliferation rates compared to non-transduced, shSCR-transduced, and other shRNA-transduced MLFs. These increased proliferation rates represent a confounding variable that could complicate the validation of our findings when introducing MLFs transduced with two different shRNAs for each gene target into mouse models. To address these issues and eliminate variability caused by differences in gene expression and proliferation rates, we have decided to generate gene knockouts using the CRISPR-Cas9 system. Although gene knockouts are less precise in modelling the effects of pharmacological inhibition, this approach will allow us to determine whether our target genes are essential within the TME for $CD8^+$ T cell infiltration.

4.2.3 Mouse lung fibroblast immortalisation

Delivering CRISPR-Cas9 into primary fibroblasts is typically associated with low transfection efficiency and cytotoxic effects, which result in reduced cell viability (Hryhorowicz et al., 2019). Additionally, primary MLFs fail to proliferate *in vitro* when seeded sparsely, likely due to their reliance on cell-cell interactions for growth. Given the low transfection efficiency commonly observed in primary fibroblasts, it is necessary to expand cells from single clones (Bajwa et al., 2023). To address this limitation, we decided to generate immortalised MLFs (iMLFs) prior to producing gene knockouts.

We introduced mTERT into MLFs via viral transduction to restore telomerase activity, prevent telomere shortening, and enable indefinite cell division. MLFs were transduced with a lentiviral mTERT expression construct at MOIs of 5, 10, 20, and 30. The construct included a hygromycin resistance gene, allowing for the selection of transduced cells using hygromycin-containing media 48 hours post-transduction. An MOI of 5 resulted in insufficient transduction, while an MOI of 30 led to low cell viability, leaving cells too sparse to proliferate under both conditions. At an MOI of 10, transduced MLFs displayed higher viability compared to MOIs of 5 and 30; however, these cells exhibited a broad phenotype, slow proliferation, and poor survival after passaging. In contrast, MLFs transduced with mTERT at an MOI of 20 showed viability and proliferation rates comparable to those of non-transduced controls (**Figure 4.9A**). We monitored immortalised and

non-transduced control MLFs over several passages to assess their replicative lifespan. MLFs immortalised via mTERT overexpression are referred to as mTERT MLFs. At passage 20, both control and mTERT MLFs were treated with TGF-β1 for 72 hours to evaluate the expression of myofibroblastic markers. As expected, passage 5 control MLFs upregulated FN, POSTN, COL1A1, and COL11A1 in response to TGF-β1 treatment. Western blot analysis showed that non-immortalised MLFs at passage 20 expressed lower levels of POSTN, COL1A1, and COL11A1 compared to passage 5 MLFs. However, TGF-β1 treatment still induced upregulation of these proteins in passage 20 non-immortalised MLFs. In contrast, mTERT MLFs at passage 20 exhibited protein expression levels of POSTN, COL1A1 and COL11A1 similar to passage 5 control MLFs, suggesting that mTERT overexpression preserved the phenotype of lower-passage cells. While mTERT MLFs showed upregulation of FN and POSTN following TGF-β1treatment, upregulation of COL1A1 and COL11A1 was not observed, unlike in non-immortalised MLFs. Notably, FN levels increased with both TGF-β1 treatment and advancing passage number, with the highest levels observed in mTERT MLFs (**Figure 4.9B**). Although both non-immortalised and mTERT MLFs were cultured to passage 20, we observed that mTERT MLFs proliferated notably slower and exhibited a ‘broad’ morphology with increasing passage number. Additionally, mTERT MLFs could not be expanded from single clones, even at lower passages, indicating that these cells lacked the robustness required for CRISPR gene editing. Consequently, alternative methods for immortalising MLFs were necessary to achieve a more reliable phenotype.

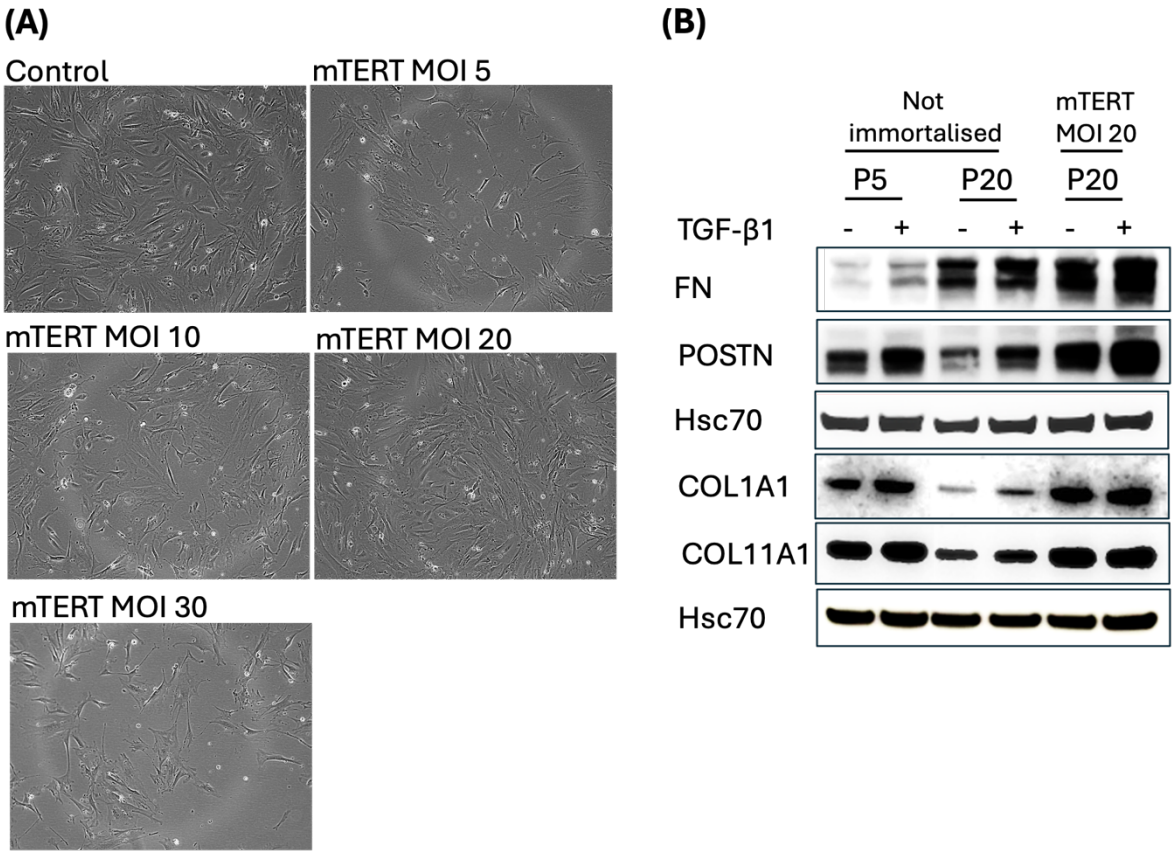

Figure 4.9: Effects of mTERT transduction on morphology and myofibroblastic marker expression in MLFs. (A) Representative cell morphology of MLFs transduced with mTERT at the indicated MOIs at passage 4, captured at 10x magnification. **(B)** Western blot analysis of MLFs treated with TGF-β1 for 72 hours, showing protein expression levels of myofibroblastic markers. Hsc70 was used as a loading control.

Primary fibroblasts typically exhibit a limited replicative lifespan; however, under certain circumstances, they can overcome this limitation. One such rare phenomenon is spontaneous immortalisation, which occurs during serial passaging. In this process, primary fibroblasts acquire the ability to divide indefinitely without undergoing senescence, even after repeated culturing *in vitro*. This approach was employed to immortalise MLFs in our study.

We observed the spontaneous immortalisation of MLFs in culture, characterised by altered cell morphology and growth properties. Immortalised MLFs (iMLFs) retained similar morphological variability compared to primary MLFs. To assess growth differences, we cultured both MLFs and iMLFs in the absence and presence of TGF-β1, monitoring their growth every 24 hours over three days. Our results showed that iMLFs (P37) proliferated more rapidly than primary MLFs (P4). Notably, at the 24-hour timepoint, iMLFs reached higher confluency despite identical seeding densities, suggesting active cell division during this period. Furthermore, both MLFs and iMLFs exhibited reduced proliferation in the presence of TGF-β1; this effect was more pronounced in iMLFs (**Figure 4.10**).

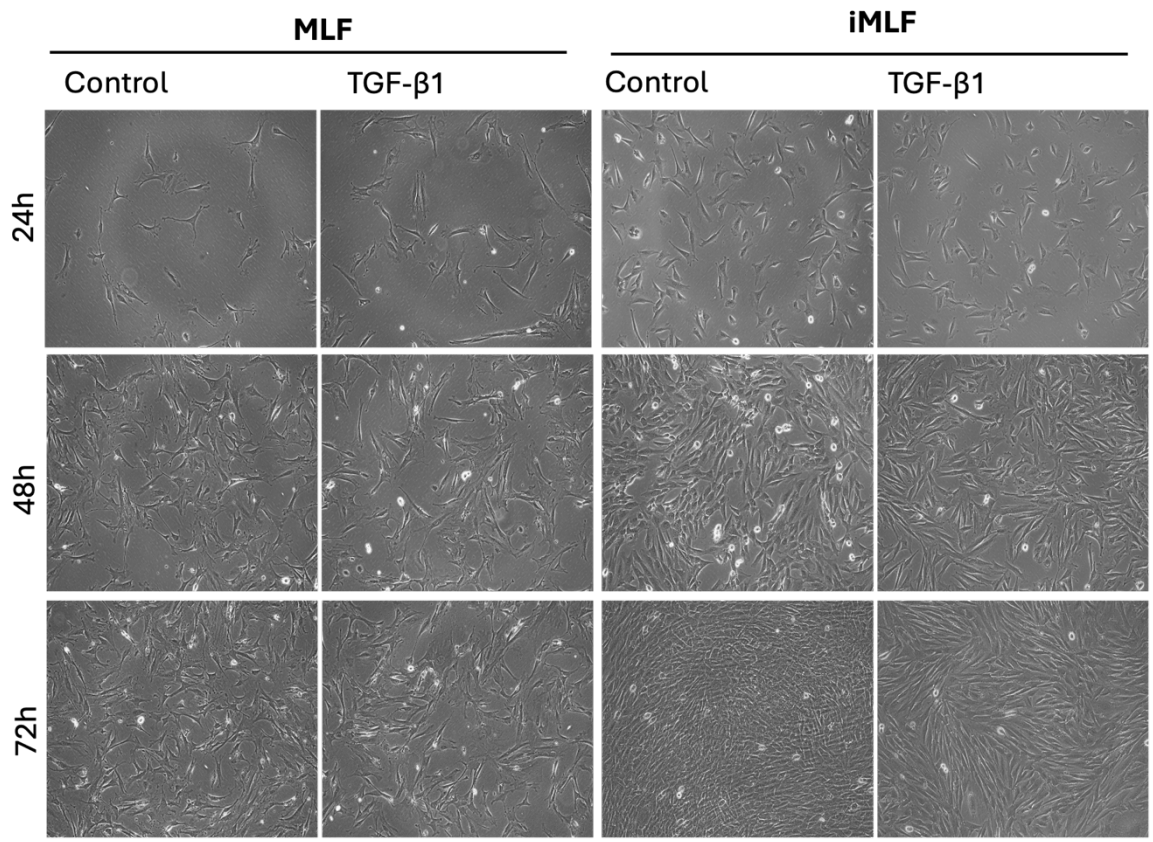

Figure 4.10: Cell morphology and growth rates of MLFs and iMLFs. Representative images of cell morphology for MLFs (P4) and iMLFs (P37). Cells were seeded at a density of 50 000 cells per well in a 6-well plate and incubated to allow attachment. At 24 hours post-seeding, cells were photographed. For control conditions, the medium was changed, while for the treatment group, the medium was changed and supplemented with TGF-β1. Additional images were captured at 48 and 72 hours to assess proliferation.

We further quantified the proliferative activity of primary MLFs and iMLFs. Crystal violet staining revealed that iMLFs reached complete confluence within 96 hours, whereas primary MLFs seeded at the same density exhibited much slower proliferation and failed to achieve confluence within this timeframe. Additionally, crystal violet staining confirmed the earlier observation that iMLFs proliferated at a reduced rate following TGF-β1 treatment comparted to untreated controls (**Figure 4.11A**). iMLFs also exhibited a higher proliferation rate compared to MLFs in the MTS assay at days 3 and 6; however, this was only observed in untreated control cells. Following TGF-β1 treatment, no significant differences in proliferation were detected between MLFs and iMLFs at the tested timepoints (**Figure 4.11B**). These findings demonstrate that immortalised MLFs can be maintained in culture and exhibit higher proliferation rates under untreated conditions. To confirm that senescence was bypassed in immortalised fibroblasts, we performed senescence-associated β-galactosidase (SA-β-gal) staining. No differences in senescence levels were

observed between control MLFs (P6) and iMLFs (P39). However, TGF-β1 treatment increased senescence levels, as indicated by higher percentages of SA-β-gal positive cells in both MLFs and iMLFs at day 3 of treatment (**Figure 4.11C**).

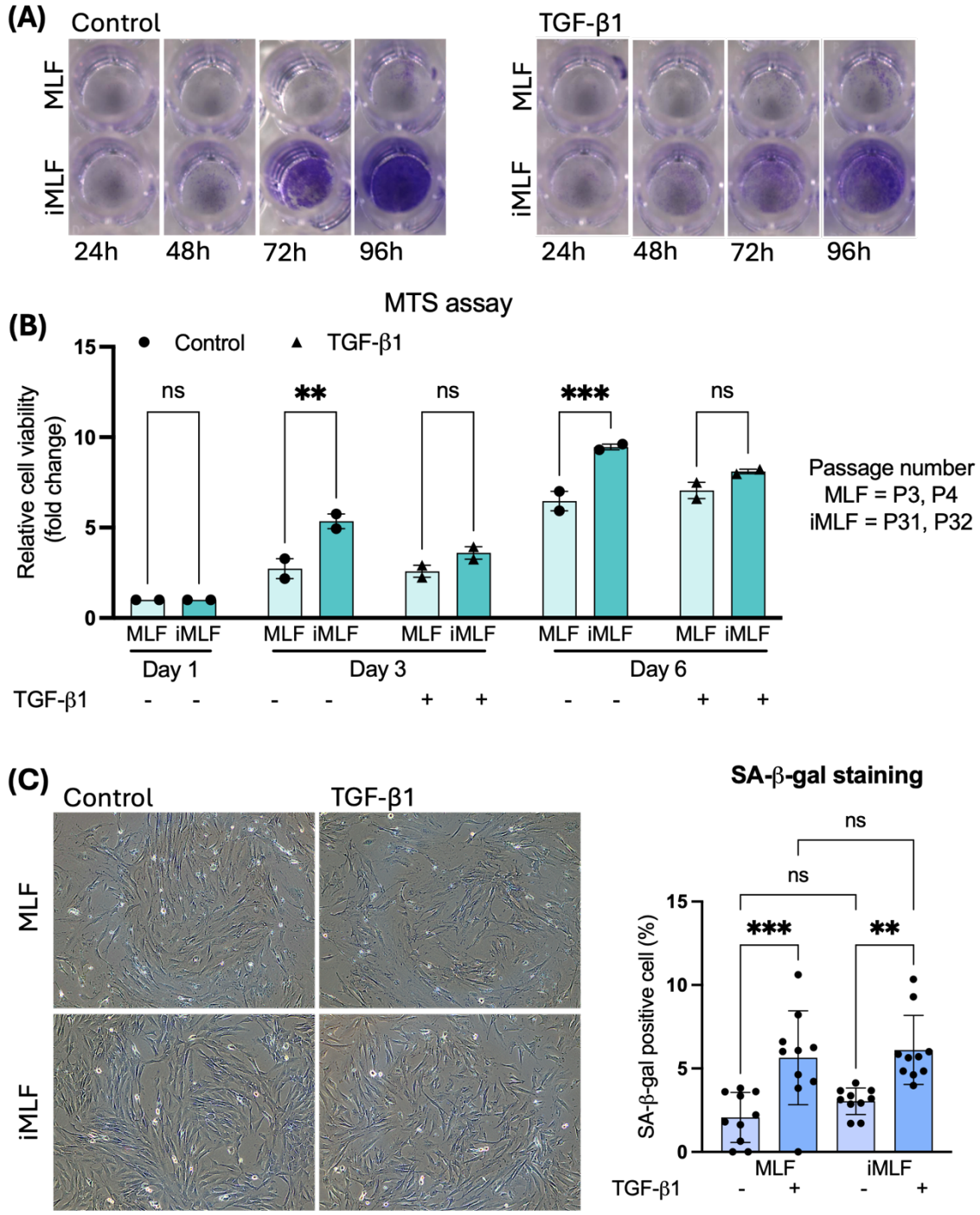

Figure 4.11: Effect of TGF-β1 on proliferation and senescence in MLFs and iMLFs. (A) MLFs and iMLFs ware seeded at a density of 600 cells per well in a 96-well plate and cultured in the absence or presence of TGF-β1. Cells were stained with crystal violet at the indicated timepoints. **(B)** Cell proliferation was assessed using the MTS assay, with 600 cells seeded per well. The assay was performed at the indicated timepoints. Data are presented as the mean fold change ± SEM, normalised to absorbance values on day 1, with each dot representing an independent experiment. Statistical analysis was performed using one-way ANOVA with Bonferroni correction; **P≤0.01, ***P≤0.001, ns = not significant. **(C)** Representative images at 10x magnification show MLFs and iMLFs with senescence-associated β-galactosidase (SA-β-gal) activity, either in the absence or following TGF-β1 treatment at the 72-hour timepoint. The percentage of SA-β-gal-positive cells was

quantified in each condition from 10 randomly selected fields of view. Data are presented as the mean percentage ± SEM. Statistical analysis was performed using one-way ANOVA with Bonferroni correction; **P≤0.01, ***P≤0.001, ns = not significant.

To investigate whether iMLFs upregulate genes associated with the myofibroblastic phenotype and ECM deposition upon TGF-β1 treatment, we performed RT-qPCR analysis. Control iMLFs exhibited lower baseline expression of COL1A1, COL11A1, POSTN and NOX4 compared to primary MLFs, while no significant differences were observed in CTHRC1 and TGF-β1 expression. These findings suggest that iMLFs may revert to a more primitive or less differentiated state or are less responsive to mechanotransduction induced by growth on stiff plastic surfaces. By contrast, primary MLFs appear to maintain slightly elevated levels of myofibroblastic markers under the same conditions. Upon TGF-β1 treatment, COL1A1, COL11A1 and TGF-β1 were upregulated to similar levels in both MLFs and iMLFs. While POSTN and NOX4 were significantly upregulated in response to TGF-β1, their expression levels in iMLFs remained lower than those observed in TGF-β1-treated MLFs. Conversely, CTHRC1 was upregulated in both cell types following TGF-β1 treatment, with a more pronounced increase in iMLFs (**Figure 4.12**). Overall, TGF-β1 treatment elevated the expression of all assessed genes compared to controls in both MLFs and iMLFs, though variability in the extent of upregulation was observed among individual markers.

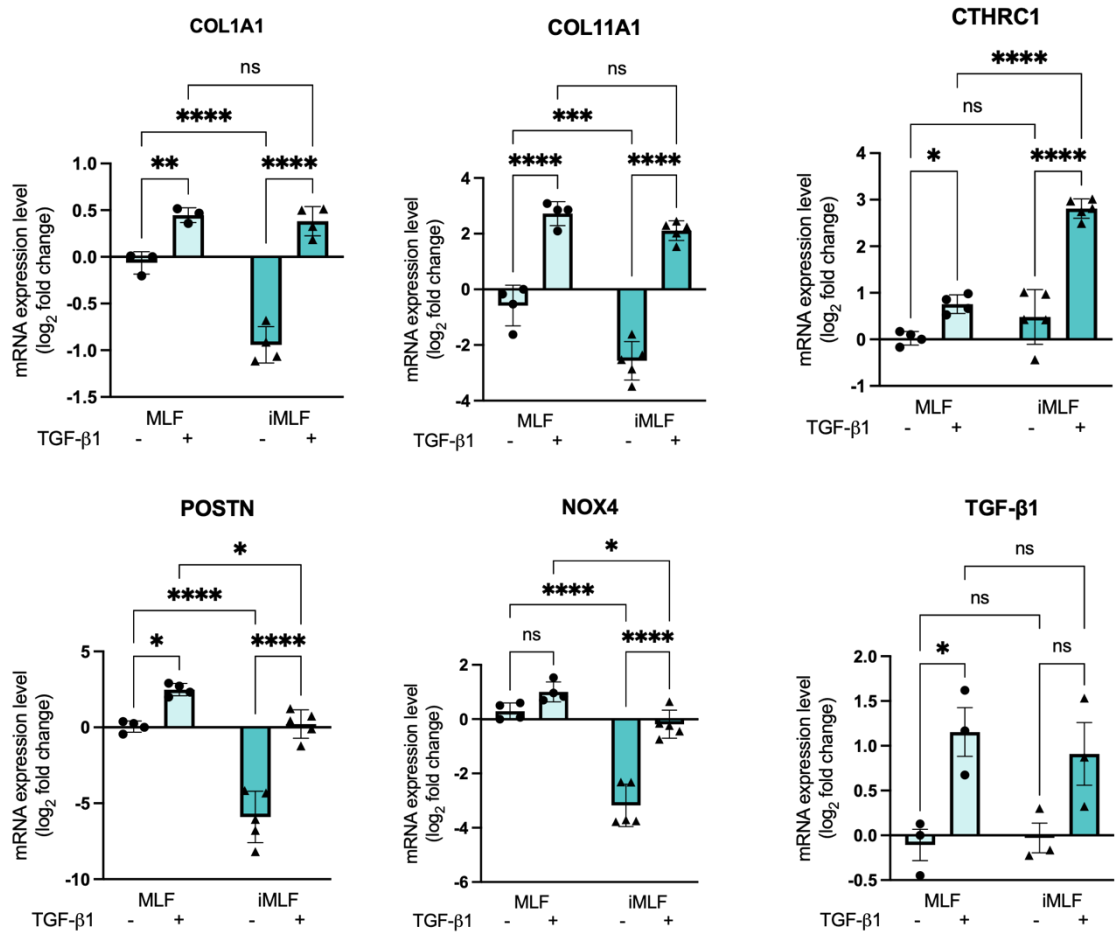

Figure 4.12: TGF-β1 induces changes in myofibroblastic and ECM-related gene expression in MLFs and iMLFs. RT-qPCR analysis of genes associated with the myofibroblastic phenotype and ECM composition in MLFs and iMLFs treated with TGF-β1 for 72 hours. Data are presented as the mean $\log_2$ fold change ± SEM, normalised to control MLFs, with each shape representing an independent experiment. Statistical analysis was performed using one-way ANOVA with Bonferroni correction; *P≤0.05, **P≤0.01, ***P≤0.001, ****P≤0.0001, ns = not significant.

We also evaluated the expression of αSMA and ECM proteins. Western blot analysis corroborated the RT-qPCR findings, demonstrating upregulation of COL11A1, POSTN, FN, and αSMA following TGF-β1 treatment. Baseline expression levels of COL11A1, POSTN, and αSMA were lower in control iMLFs compared to MLFs, whereas FN exhibited higher basal expression in control iMLFs. Notably, in MLFs, αSMA expression remained high under both control and TGF-β1 treated conditions, with no observable differences following treatment (**Figure 4.13A**). To validate these findings, we conducted flow cytometry analysis. Consistent with the Western blot results, no differences in αSMA expression were observed in primary MLFs between control and TGF-β1-treated conditions. In contrast, αSMA expression was downregulated in control iMLFs but significantly increased upon TGF-β1 treatment, reaching levels comparable to those in MLFs (**Figure 4.13B**). The tumour suppressor gene p53 is commonly inactivated in immortalised cells

(Christman et al., 2006). To investigate whether p53 downregulation contributes to the differences observed between primary and immortalised MLFs, we assessed its expression levels. Interestingly, p53 expression was more elevated in iMLFs compared to primary MLFs, normalised to Hsc70 (**Figure 4.13C**). Furthermore, p53 levels increased following TGF-β1 treatment in both primary and immortalised MLFs.

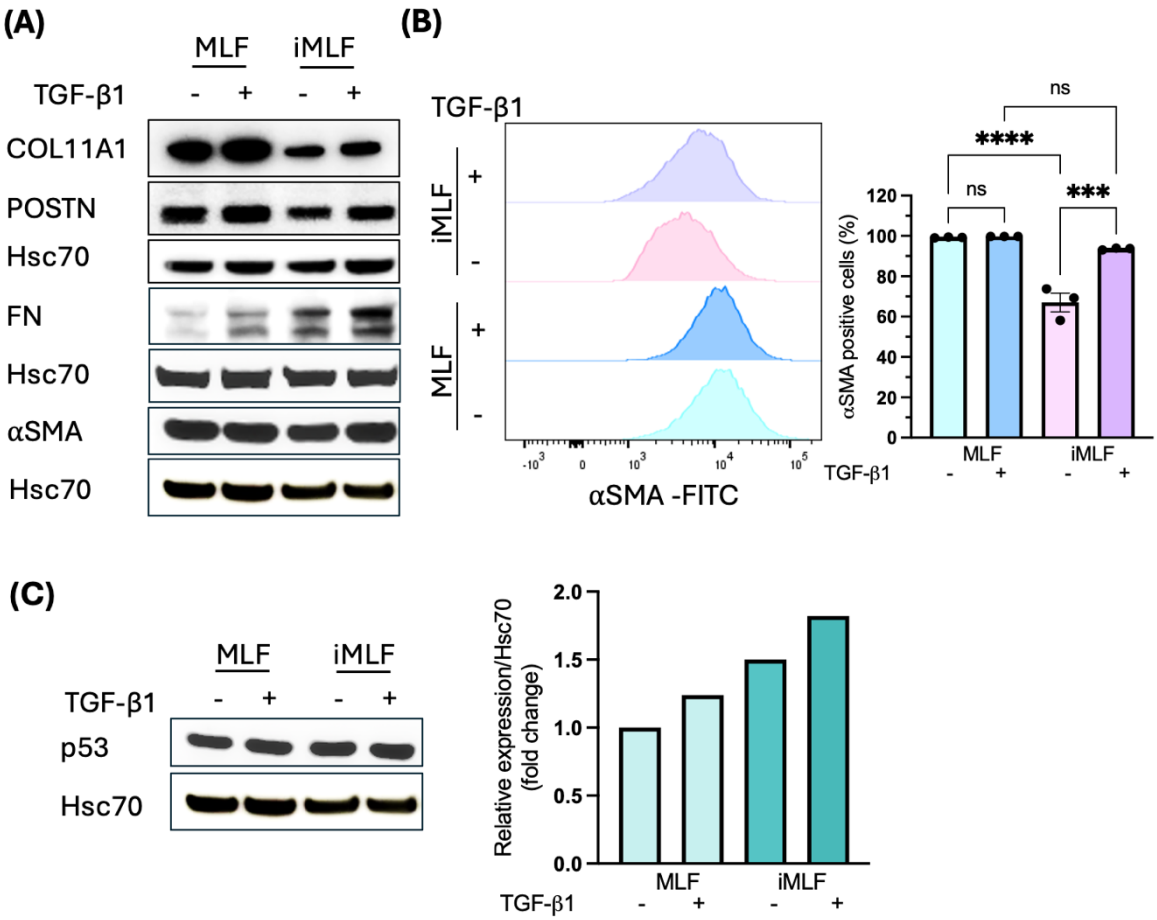

Figure 4.13: Protein expression of myofibroblastic markers and p53 in MLFs and iMLFs following TGF-β1 treatment. (A) Western blot analysis of MLFs and iMLFs treated with TGF-β1 for 72 hours, showing protein expression levels of myofibroblastic markers. Hsc70 was used as a loading control. **(B)** Expression of αSMA in untreated and TGF-β1-treated MLFs and iMLFs, assessed using flow cytometry. **(C)** Western blot analysis of MLFs and iMLFs treated with TGF-β1 for 72 hours, showing protein expression levels of p53. Hsc70 was used as a loading control.

4.2.4 Generation of gene knockouts in iMLFs

To evaluate the transfection efficiency of nucleofection in iMLFs, we introduced a plasmid encoding the GFP reporter gene using seven electroporation programs recommended by Lonza. After 48 hours, we captured images of the transfected cells (**Figure 4.14A**). Once the cells reached confluence, at 96 hours post-transfection, GFP expression levels and transfection efficiency were assessed using flow cytometry. The results indicated transfection efficiencies ranging from 17.4% to 28.5% for the pmaxGFP plasmid (**Figure 4.14B**). Among the programs tested, FF-113 demonstrated the lowest transfection efficiency, while EN-150 yielded the highest.

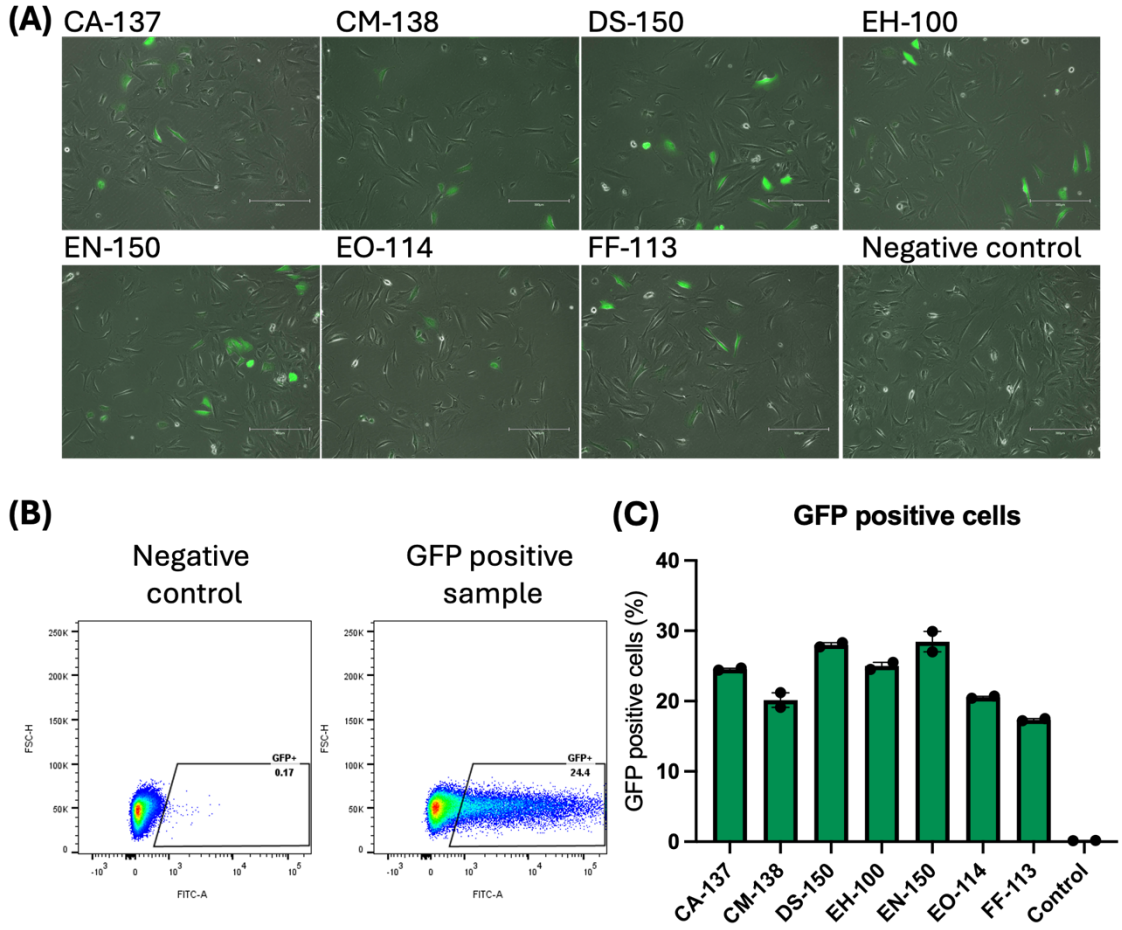

Figure 4.14: GFP fluorescence in nucleofected iMLFs. (A) Representative images of iMLFs 48 hours after nucleofection with 0.4 µg of pmaxGFP plasmid, using the electroporation programs recommended by Lonza. Images were captured at 10x magnification, with scale bars representing 300 µm. **(B)** Gating strategy used for flow cytometry analysis to identify GFP-positive cell 96 hours post-nucleofection. **(C)** Percentages of GFP-positive cells derived from flow cytometry analysis. Each dot represents a technical replicate. Control refers to non-electroporated iMLFs.

Our findings indicate that, despite immortalisation, fibroblasts remain challenging to transfect. While many *in silico* tools are available for sgRNA efficiency predictions, prior studies have shown that not all sgRNAs perform equally in generating knockouts. To enhance the likelihood of achieving a complete gene knockout, we targeted three regions within an exon. The combined action of three sgRNAs increases the probability of inducing frameshift mutations or larger deletions that result in the complete loss of gene function, which was our goal. This approach minimises the risk of generating in-frame mutations that could preserve residual gene functionality. To ensure comprehensive gene knockouts, we selected sgRNAs that target sequences present in all gene transcripts and focused on early exons (**Figure 4.15**).

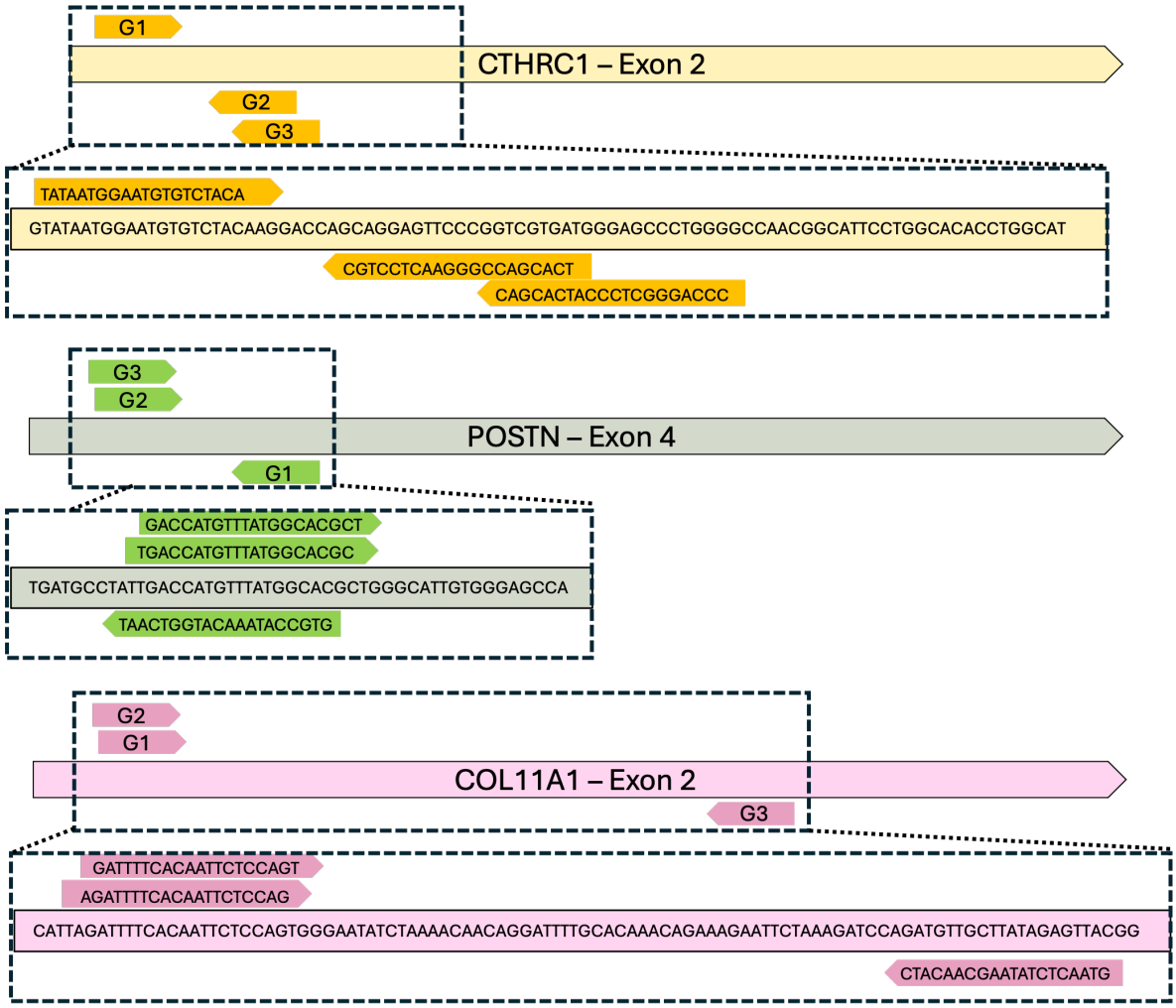

Figure 4.15: sgRNA locations for CRISPR-Cas9-mediated gene knockouts. Diagram illustrating the three sgRNA sequences and their respective target locations within the selected exons of each gene of interest.

The transfection efficiencies of iMLFs with the pmaxGFP plasmid were relatively low; however, no significant changes in cell viability were observed when the cells were seeded into wells post-nucleofection. Cells electroporated using the seven nucleofection programs, as well as control cells, reached confluence 96 hours after seeding. To enhance transfection efficiency with sgRNA:Cas9 (9:1) RNP complexes, we implemented double nucleofection programs and compared their performance to single nucleofection. In the single nucleofection approach, iMLFs were electroporated once using the EN-150 program, which yielded the highest efficiency during optimisation. Double nucleofection involved electroporating the iMLFs twice consecutively with the same program (EN-150 + EN-150). The non-nucleofected control group consisted of cells that were not subjected to electroporation. Following nucleofection, iMLFs were cultured until they reached confluence. At this point, cells were pelleted for genomic DNA isolation, while the remaining cells were either seeded for single colony expansion or expanded to prepare cell

stocks. Genomic DNA extracted from collected cell pools was amplified using primers spanning the region of interest. Gel electrophoresis was used to assess the proportions of unedited and edited cells. PCR amplifies both edited and unedited regions, resulting in a band corresponding to the wild-type sequence alongside bands representing edited alleles. For each gene of interest, we amplified regions from non-nucleofected cells to ensure that nucleofection itself did not cause any off-target effects. CRISPR control cells were electroporated with Cas9 protein without sgRNA guides. No differences in band patterns were observed between non-nucleofected and CRISPR control nucleofected iMLFs for any of the genes (**Figure 4.16A**). In single and double nucleofected samples targeting COL11A1, we observed a higher intensity band corresponding to the wild-type PCR product and a lower intensity band of smaller size, indicating a fragment deletion induced by RNP complexes. For POSTN, PCR products amplified to assess knockout efficiency showed no differences in size among non-nucleofected, CRISPR control, and gene knockout cell pools. This suggests that the indels induced may be too small to cause a noticeable size difference on the gel, making it difficult to distinguish between edited and wild-type fragments, or that only a small population of cells contained the gene knockout. In contrast, gel electrophoresis assessing gene knockout efficiency for CTHRC1 revealed that bands for both single and double nucleofected RNP complexes migrated lower than the bands for control iMLFs (**Figure 4.16A**). While gels provide a quick method to assess editing efficiency, they are mainly useful for detecting large deletions or major editing events. The limitations of this method include its inability to detect smaller indels and to quantify the proportion of edited cells accurately.

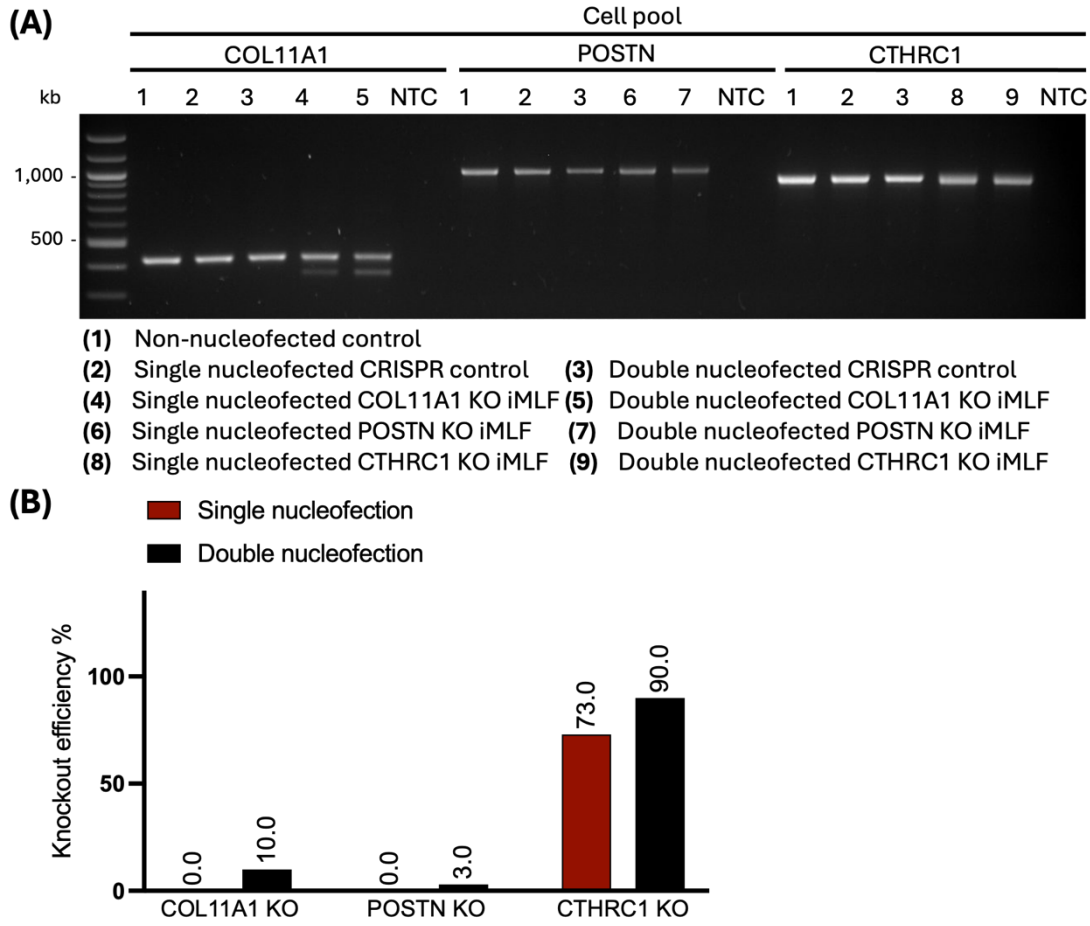

Figure 4.16: Assessment of editing efficiency in iMLF CRISPR-Cas9 gene knockouts. (A) Gel image of PCR products resolved on a 3% agarose gel. Primer pairs spanned the sgRNA targeting regions. Amplicon sizes for wild-type clones were: 889 bp for CTHRC1, 968 bp for POSTN, and 434 bp for COL11A1. Smaller PCR products represent gene-edited fragments. **(B)** CRISPR editing efficiency percentages for the indicated samples were determined using ICE software.

Sanger sequencing data from amplified PCR products of nucleofected mixed cell populations and non-nucleofected control cells were analysed using ICE software to determine editing efficiency. Single nucleofection did not induce knockouts of the COL11A1 and POSTN genes but resulted in a 73% knockout efficiency for the CTHRC1 gene. Under double nucleofection conditions, we obtained a 10% knockout efficiency for COL11A1, 3% for POSTN and 90% for CTHRC1. These findings highlight that double nucleofection was necessary for the induction of COL11A1 and POSTN gene knockouts in iMLFs. Notably, the nucleofection efficiency of RNP complexes was lower compared to the pmaxGFP plasmid. This reduced efficiency may stem from the limited stability and larger size of RNP complexes, which could impair their delivery during nucleofection. To achieve complete gene knockouts, we seeded double nucleofected cells for single-clone selection. Once sufficient numbers of cells were expanded from single clones,

genomic DNA was extracted, amplified, and analysed via gel electrophoresis. Cell populations derived from single clones were numbered and randomly selected for this analysis (**Appendix A Figure 5**). Based on these findings, we selected four single-clone-derived populations per gene for Sanger sequencing (**Figure 4.17A**). Complete gene knockouts were identified for CTHRC1 in clones 7, 10, and 35; for POSTN in clones 5, 30, and 38; and for COL11A1 in clones 22, 29, 13, and 31, when compared to non-nucleofected and double-nucleofected CRISPR controls (**Figure 4.17B**). ICE software was used to quantify all indel contributions in the sample. Sequences from controls and edited colonies were analysed, and indels contributing to editing efficiency were identified. Some cell populations exhibited only one type of genetic alteration (indel) at the target site across all cells. These included all CTHRC1 knockout clones and COL11A1 knockout clones 22,13, and 31. Conversely, other clones displayed genetic heterogeneity, with multiple indels present at the target site. The major contributors to editing efficiency are illustrated (**Figure 4.17C**).

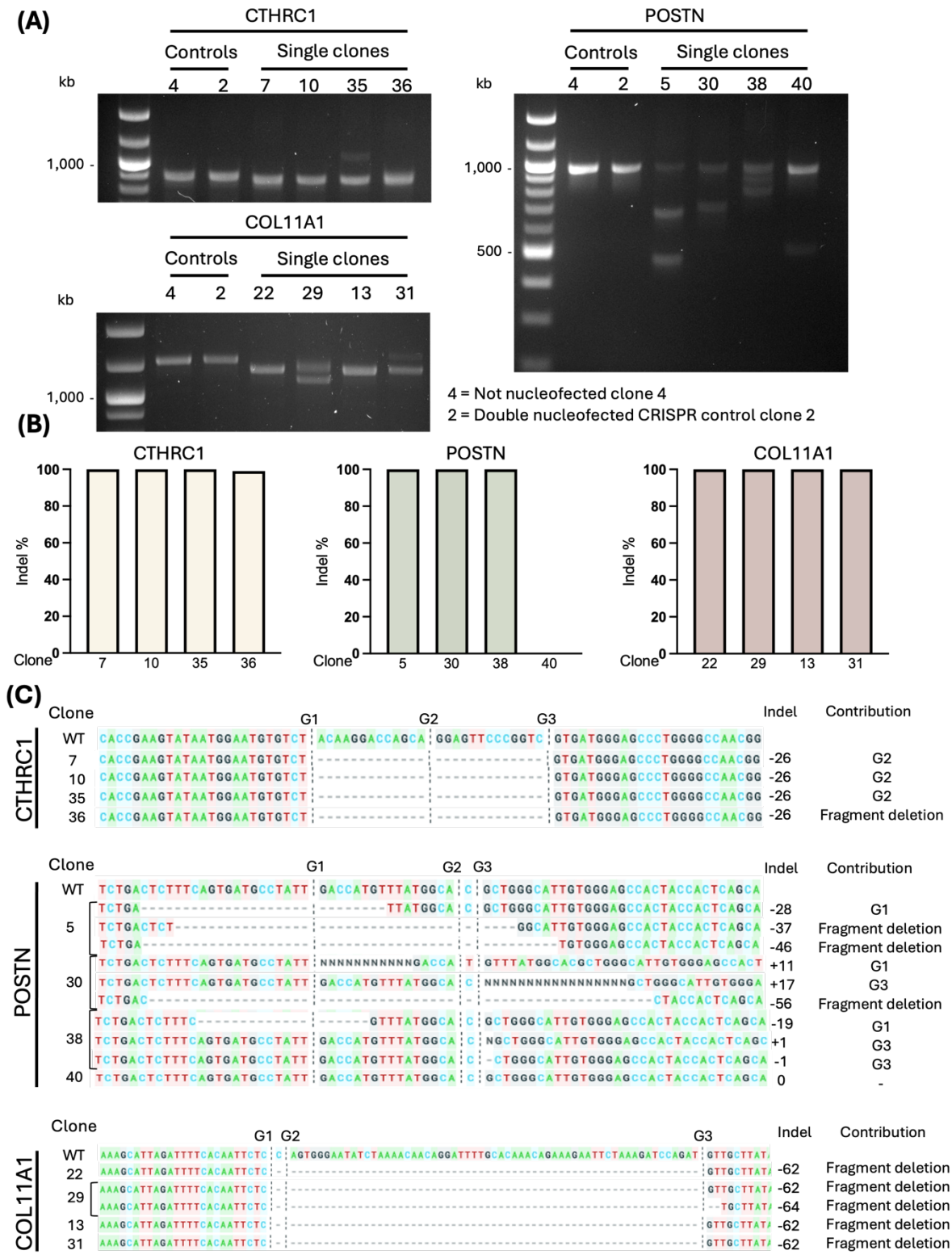

Figure 4.17: Assessment of editing efficiency in cells derived from single clones. (A) Gel images showing PCR products resolved on a 3% agarose gel. Primer pairs flanked the targeted regions of the sgRNAs. Amplicon sizes for wild-type clones were 889 bp for CTHRC1, 968 bp for POSTN, and 1189 bp for COL11A1. The presence of smaller PCR products corresponds to edited alleles resulting from gene editing. **(B)** CRISPR editing efficiency (%) determined using ICE software for the indicated samples. **(C)** Schematic representation illustrating the contributions of each sgRNA to the generation of indels, leading to gene knockouts in selected single-clone-derived cell populations.

4.2.5 Phenotypic validation of single clone-derived gene knockouts

Using single CRISPR clones in *in vivo* studies can introduce bias due to limited genetic diversity, which contrasts with the genetic heterogeneity present in natural tissues. To address this, we treated cells derived from single clones with TGF-β1 to assess their ability to upregulate genes associated with a myofibroblastic phenotype. Cells were exposed to TGF-β1 for six days in 20% serum, conditions that replicate the differentiation process planned prior to their injection into mice for tumour model generation. Three single clones per condition were selected: clones 7,10, and 35 for CTHRC1; clones 5, 30, and 38 for POSTN; and clones 13, 29, and 31 for COL11A1. Additionally, three clones each were selected for non-nucleofected controls and CRISPR controls. Overall, we observed a general trend of upregulation in COL1A1, COL1A2, COL11A1, NOX4, CTHRC1, and POSTN when expression was analysed using RT-qPCR (**Figure 4.18A**). However, some genes showed upregulation without statistical significance due to variability in gene expression across clones. For example, one CTHRC1 knockout clone demonstrated downregulation of COL1A1and COL1A2 upon TGF-β1 treatment, whereas the other two clones exhibited upregulation, consistent with our previous findings. Similarly, non-nucleofected clones and POSTN knockout clones did not show significant upregulation of COL1A2 following TGF-β1 treatment. In addition to investigating myofibroblastic differentiation following TGF-β1 treatment, we measured the expression levels of CXCL10 and CCL5, both of which play roles in trafficking T cells into the tumour microenvironment. Our prior findings have shown that TGF-β1 downregulates CXCL10 expression. Our single-clone expression data corroborates this finding; however, variations in mRNA expression levels across clones rendered the results statistically insignificant. Notably, POSTN knockout clones did not exhibit CXCL10 regulation in response to TGF-β1 treatment. In contrast, CCL5 expression was significantly downregulated in non-transduced controls, with a similar trend observed in CRISPR controls and CTHRC1 knockout clones, though these changes were not statistically significant. Comparatively, POSTN and COL11A1 knockout clones showed elevated CCL5 expression, but the increases were subtle and not significant. However, when comparing gene expression between TGF-β1-treated samples, POSTN and COL11A1 knockout clones were the only groups to show significant upregulation compared to non-transduced controls (**Figure 4.18B**).

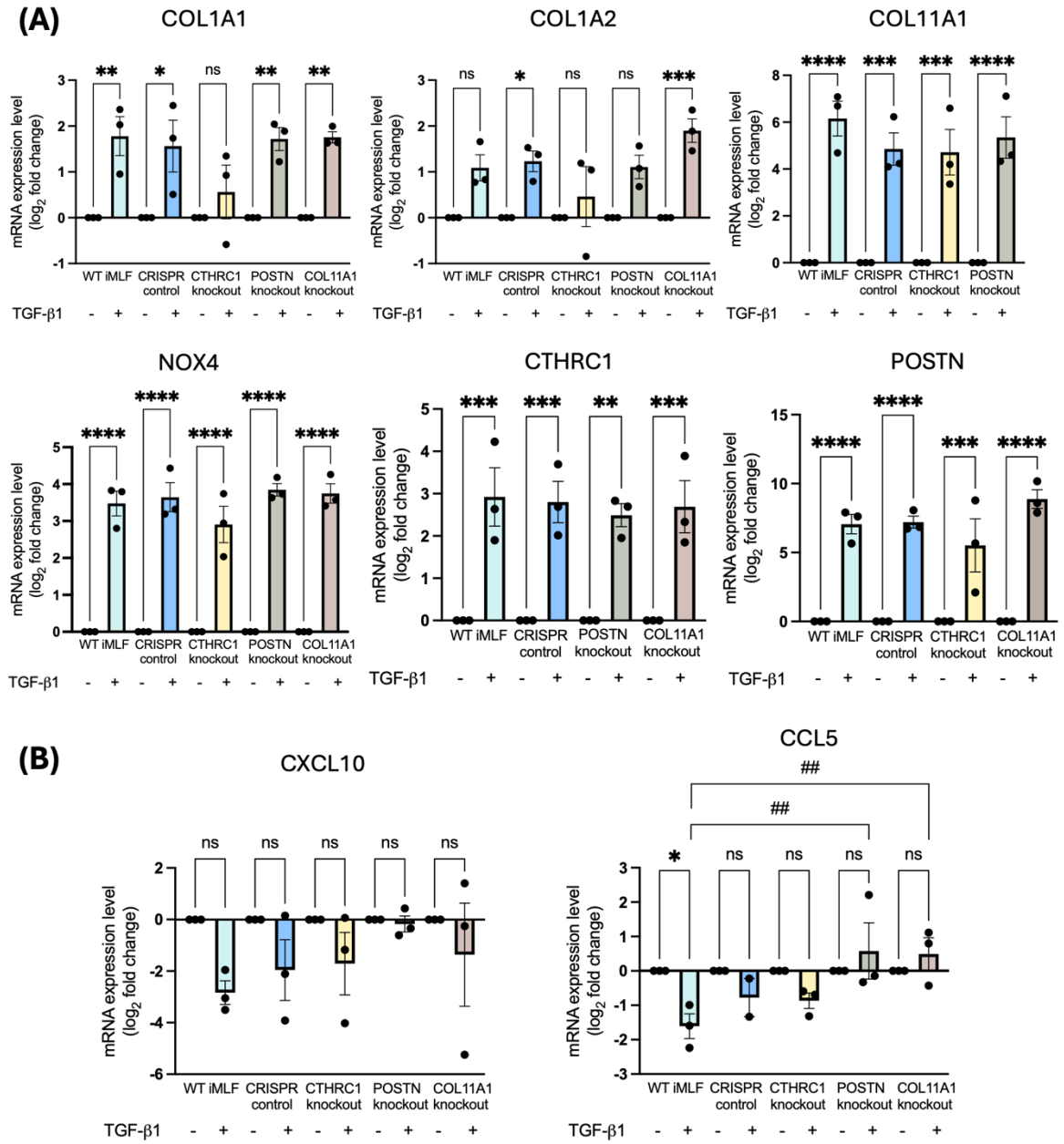

Figure 4.18: Gene expression of ECM components and cytokines in single-clone-derived cells. **(A-B)** RT-qPCR analysis of genes associated with the myofibroblastic phenotype and ECM composition in iMLFs treated with TGF-β1 for 6 days in medium supplemented with 20% serum. Data are presented as mean log_2 fold change ± SEM, normalised to untreated controls. Each data point represents a population of cells derived from a single clone. Statistical analysis was performed using one-way ANOVA with Bonferroni correction; *P≤0.05, **P≤0.01, ***P≤0.001, ****P≤0.0001, ns = not significant.

Results for gene expression of cells treated for 6 days in 5% serum are provided in **Appendix A Figure 6**. Initially we considered using a lower serum concentration due to the high proliferation rates of iMLFs. However, in previous experiments in our laboratory, fibroblasts were cultured in 20% FBS for *in vivo* studies. Therefore, we adhered to this experimental design, and findings from the 5% FBS treatments are not the primary focus of this section. Although these data are limited and based on mRNA expression levels for selected genes, the findings support the idea that cells derived from single clones represent genetic variability.

We assessed the proliferation rates of each single-clone-derived cell population using the MTS assay in untreated and TGF-β1 treated iMLFs. Proliferation rates at days 3 and 6 were expressed as fold changes relative to MTS measurements on day 1, minimising the influence of seeding density as a confounding factor. We compared the proliferation rates of knockout cells and CRISPR controls to non-nucleofected iMLFs and found no significant differences on day 3 and 6 under both conditions tested (**Figure 4.19A**). After confirming the absence of differences in cell proliferation, we mixed cells derived from three single clones at a 1:1:1 ratio for each gene and its corresponding controls to make our samples more representative. Following the mixing of single-clone-derived cells, we performed an MTS assay on day 3 and expressed the results as fold changes relative to the MTS measurement on day 1. This timepoint was chosen because, in the *in vivo* experiment, these cells would be cultured for 3 days, expanded on day 3, and subsequently treated for an additional 3 days. We observed no significant differences in cell proliferation between TGF-β1 treated MLFs across all condition. However, CTHRC1 KO control fibroblasts exhibited a slower proliferation rate (**Figure 4.19B**, **Appendix A Figure 7**). Additionally, a reduction in proliferation was evident in all conditions following TGF-β1 treatment (**Figure 4.19B**), consistent with our previous findings. These mixed-cell cultures were used in subsequent experiments.

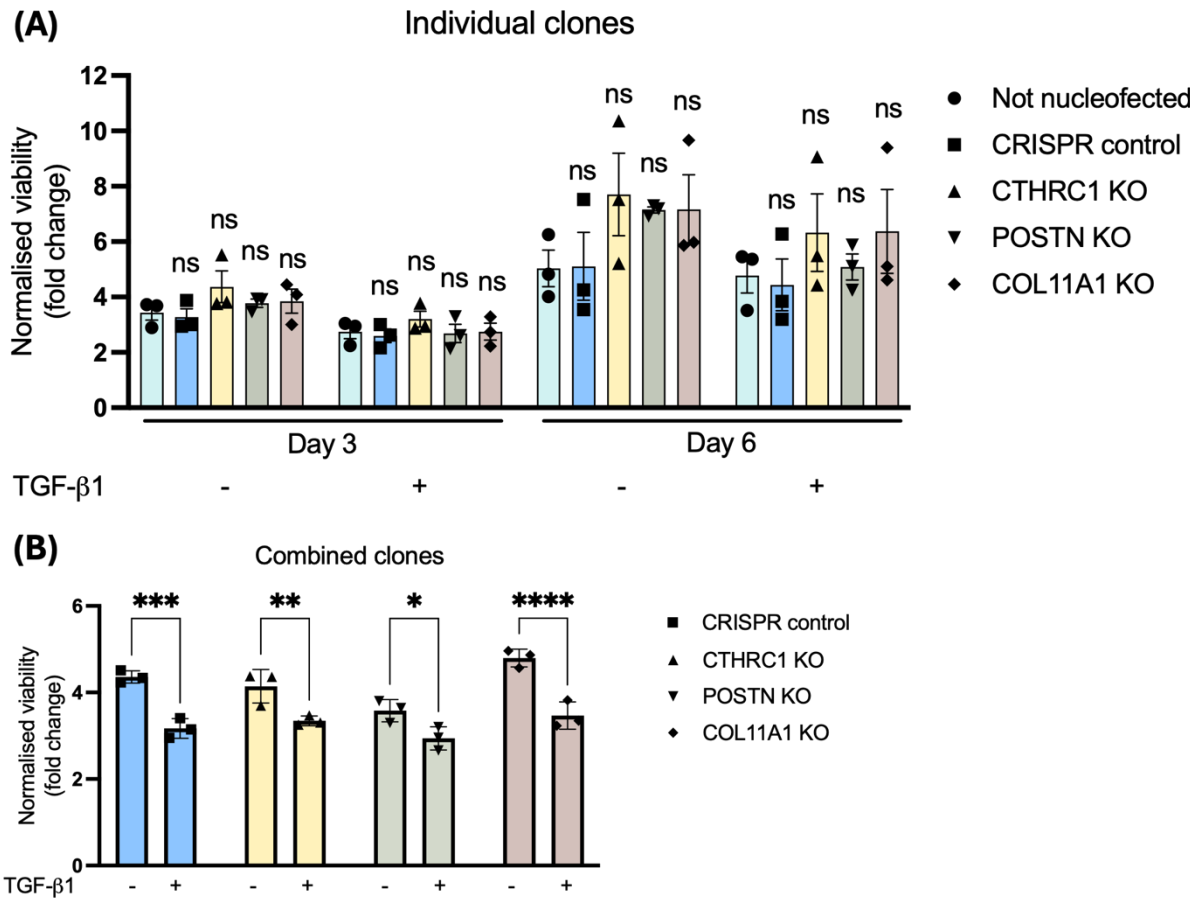

Figure 4.19: Proliferation analysis of single-clone and mixed-clone CRISPR-Cas9 KO iMLFs. (A) MTS assay measuring proliferation rates of CRISPR KO iMLFs and corresponding controls, with or without TGF-β1 treatment, at days 3 and 6. Each data point represents the mean absorbance value (n_{tr} = 3) for a population of cells derived from a single clone (n = 3). Data are presented as mean fold change ± SEM, normalised to MTS measurements on day 1. Statistical analysis was performed using two-way ANOVA with Dunnett's correction; ns = not significant. **(B)** MTS assay measuring proliferation rates of mixed CRISPR KO iMLF clones and corresponding controls, with or without TGF-β1 treatment, at 72 hours (n_{tr} = 3). Data are presented as mean fold change ± SEM, normalised to MTS measurements on day 1. Statistical analysis was performed using two-way ANOVA with Bonferroni correction; *P≤0.05, **P≤0.01, ***P≤0.001, ****P≤0.0001.

After confirming the successful differentiation of fibroblasts into myofibroblasts, we performed a collagen gel contraction assay to evaluate whether TGF-β1-treated iMLFs exhibit contractile behaviour *in vitro*, a characteristic typically observed in primary MLFs. Gel contraction was quantified by measuring the decrease in the original gel area, with the measured areas highlighted in yellow (**Figure 4.20A**). We quantified the percentages of the original gel areas and found that combined clones for CRISPR controls, POSTN KO iMLFs, and COL11A1 KO iMLFs exhibited increased contraction following TGF-β1 treatment, indicated by significantly reduced gel areas compared to their corresponding untreated iMLF clones. Interestingly, CTHRC1 KO clones showed reduced contraction under TGF-β-treated conditions compared to untreated CTHRC1 KO iMLFs, which was unexpected (**Figure 4.20B**). To validate this finding, the assay was repeated with control and CTHRC1 KO iMLFs. Consistent with the initial results, untreated CTHRC1 KO iMLFs displayed more pronounced contraction compared to their TGF-β1-treated counterparts (**Figure 4.20C**). Images of the calculated gel areas are provided in (**Appendix A Figure 8**).

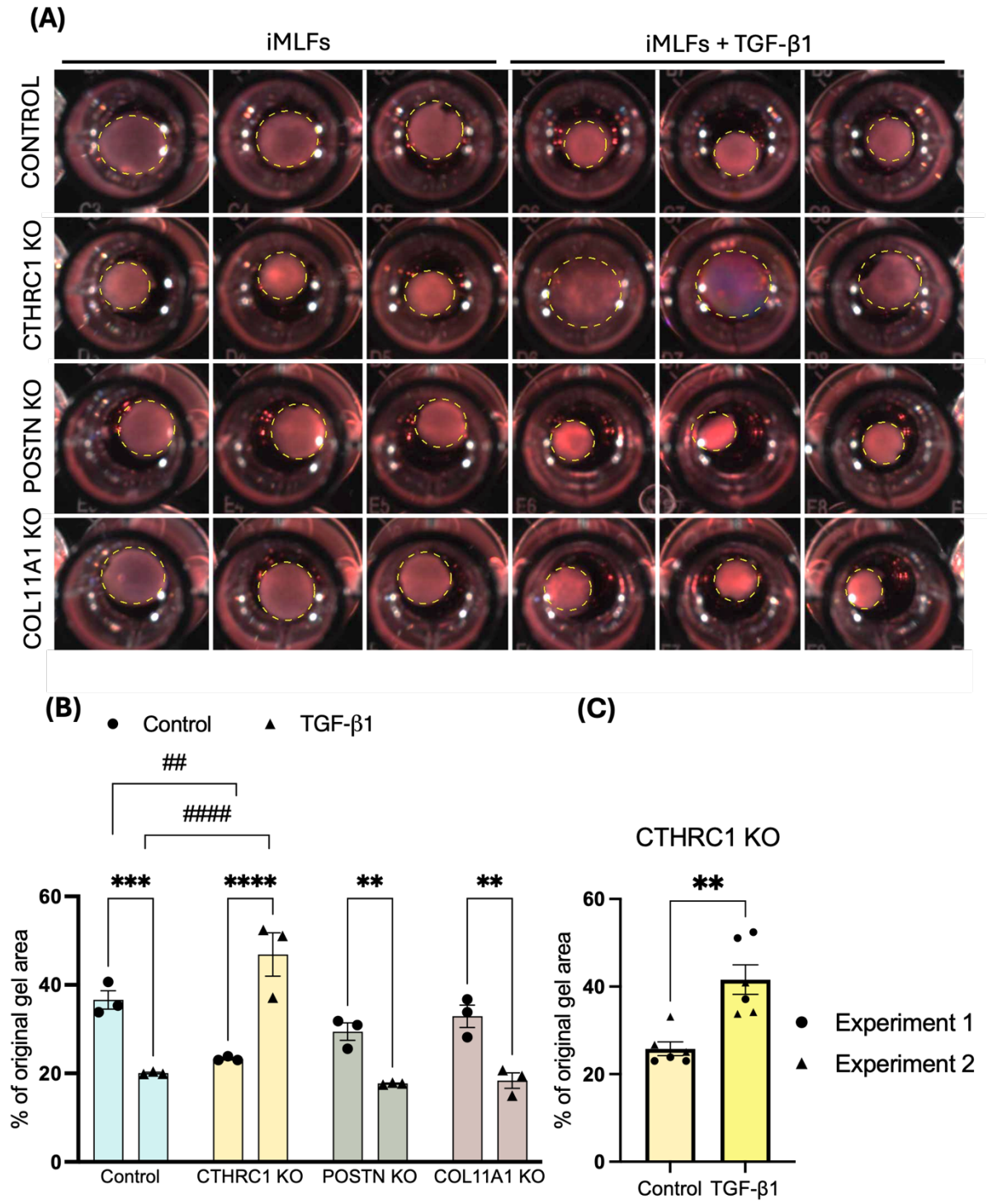

Figure 4.20: Assessment of contractile ability in CRISPR KO iMLFs *in vitro*. (A) Representative images of gel contraction after 24 hours, with dotted lines outlining the gel area. **(B)** Quantification of gel contraction, expressed as the percentage of the original gel area, for untreated iMLFs and iMLFs treated with TGF-β1 for 6 days prior to the assay. Data are presented as mean percentage ± SEM, with each dot representing a technical replicate. Statistical analysis was performed using two-way ANOVA with Bonferroni correction; **P≤0.01, ***P≤0.001, ****P≤0.0001 indicate differences between untreated and treated iMLFs, and $^{\#\#}$P≤0.01, $^{\#\#\#\#}$P≤0.0001 indicate differences between CRISPR control and knockout iMLFs. **(C)** Quantification of gel contraction in untreated and TGF-β1-

treated CTHRC1 KO iMLFs, with each shape representing an individual experiment. Statistical analysis was performed using an unpaired t test; **P≤0.01.

4.2.6 Generation of myofibroblast-rich murine tumour models to study the effects of gene knockouts

Syngeneic tumours were generated by subcutaneously injecting TC1 cancer cells alone or in combination with CRISPR control iMLFs, CTHRC1 KO iMLFs, POSTN KO iMLFs, or COL11A1 KO iMLFs (**Figure 4.21A**). All cells were tested for mycoplasma (**Appendix A Figure 9**) and treated with TGF-β1 for six days *in vitro* prior to being injected. Tumours became palpable around day 12 and were measured every 2-3 days. The experiment concluded when the tumour size in one mouse reached a humane endpoint. No differences in tumour growth were observed between the conditions tested (**Figure 4.21B**). We observed no significant difference in tumour sizes between TC1 cells alone or in combination with CRISPR control iMLFs (**Figure 4.21C**). Furthermore, no significant differences were found between TC1 and CRISPR control iMLF compared to TC1 and CTHRC1, POSTN, or COL11A1KO iMLFs (**Figure 4.21D**). However, variability in tumour growth rates between individual animals within each mouse model was observed. As the main focus of the experiment was to assess differences in $CD8^+$ T cell infiltration, only 4 mice per condition were used, so we did not expect to achieve statistical significance for tumour growth with this sample size. Tumour growth rates for individual mice in each condition are provided in **Appendix A Figure 10**.

Immunohistochemistry (IHC) for $CD8^+$ T cells was performed on tumour samples from each mouse. The stained tissue sections were scanned to analyse and quantify $CD8^+$ T cell distribution. Representative tissue scan images are shown, with $CD8^+$ T cells highlighted in the centre of the tumours and the tumour margins (**Figures 4.22A-C**). Yellow lines on the tissue scans indicate the boundaries used to calculate the number of $CD8^+$ T cells in the tumour centre and margins. Additionally, haematoxylin and eosin (H&E) staining was performed, and representative images were captured. Haematoxylin stains the nuclei, highlighting DNA and chromatin in purple, while eosin stains the cytoplasm and extracellular proteins, which appear pink (**Figure 4.22C**).

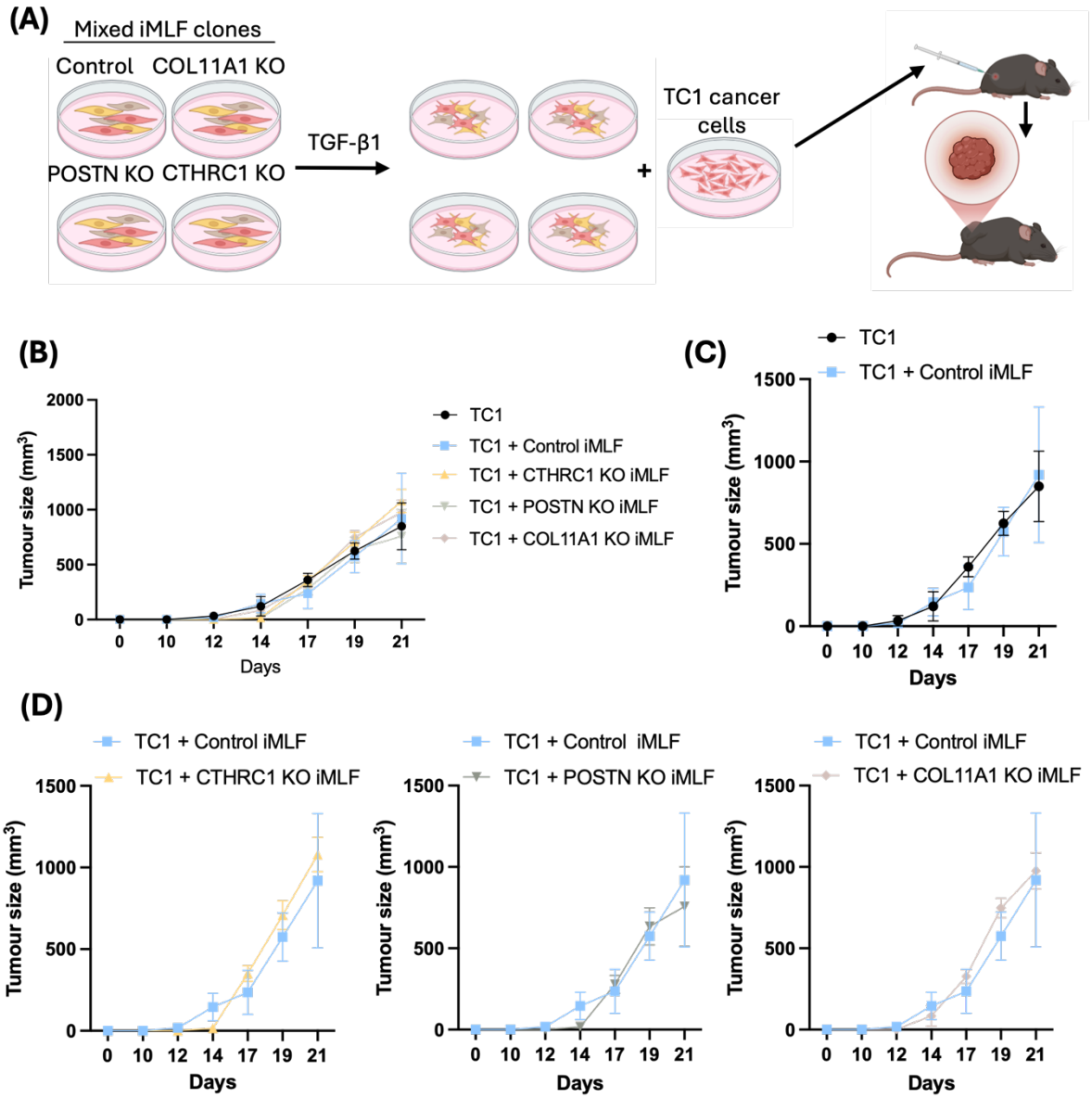

Figure 4.21: Generation and growth of myofibroblast-rich murine tumours containing gene knockouts. (A) Schematic of syngeneic tumour generation. Cells derived from three individual clones per condition were premixed and differentiated for 6 days *in vitro* though TGF-β1 treatment. Differentiated iMLFs, including CRISPR control iMLFs, CTHRC1 KO iMLFs, POSTN KO iMLFs, or COL11A1 KO iMLFs, were mixed with TC1 cells and injected subcutaneously into mice. Additionally, TC1 cells were injected alone as a control. **(B-D)** Tumour growth curves for TC1 and the indicated myCAF-rich TC1 tumours. Data are presented as the mean ± SEM, with n = 4 for each group. Area under the curve (AUC) analysis was performed, followed by a two-tailed homoscedastic t-test. No significant differences were observed between conditions.

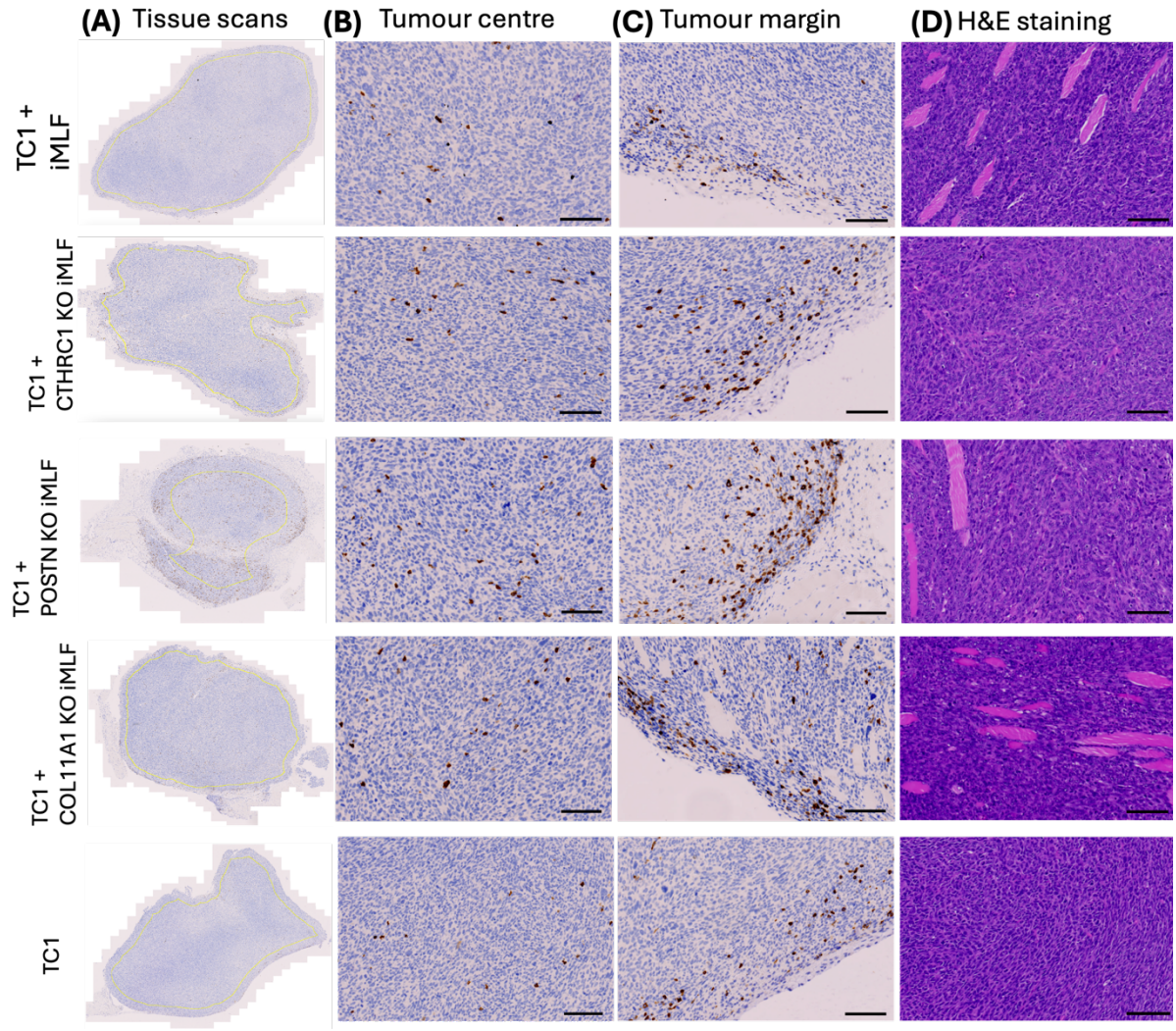

Figure 4.22: Representative images of CD8⁺ T cell infiltration and H&E staining in tumour samples. (A) Representative images of tissue scans, with yellow lines indicating the boundaries used for CD8⁺ T cell counts in the tumour margins and centre. **(B)** Representative immunohistochemistry images showing CD8⁺ T cell staining in the centre of the tumours (scale bars = 100 µm). **(C)** Representative immunohistochemistry images showing CD8⁺ T cell staining in the tumour margins (scale bars = 100 µm). **(D)** Representative images of haematoxylin and eosin (H&E) staining (scale bars = 100 µm).

We counted the number of CD8⁺ T cell per area (mm^2) and expressed the counts as percentages. Our results showed that, in all conditions, approximately 60% of CD8⁺ T cells were located at the tumour margins, while around 40% ware located beyond the indicated boundary. No significant differences were observed between iMLFs and iMLFs with gene knockouts, nor between cancer cells alone or in the presence of iMLFs (**Figure 4.23**).

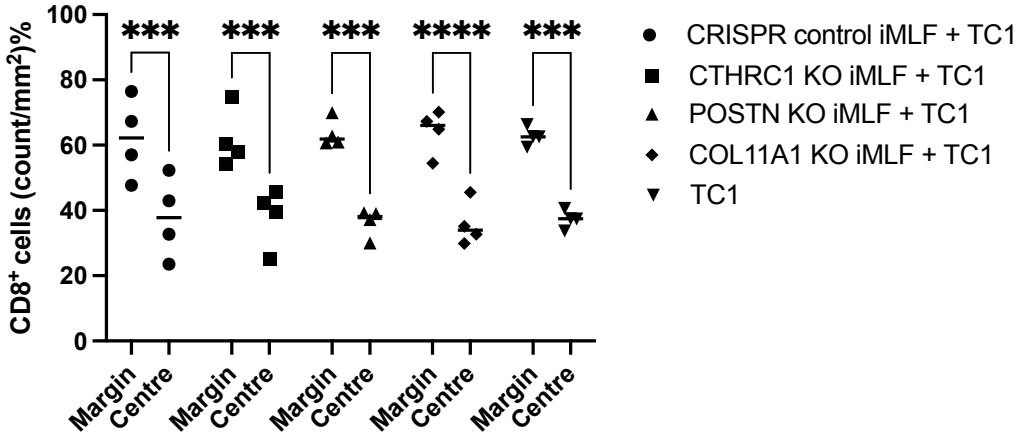

Figure 4.23: Quantification of CD8⁺ T cells in tumour sections. Graph showing the average CD8⁺ T cell count based on immunohistochemistry of tumour sections. CD8⁺ T cells were counted per area (mm^2), and the counts were expressed as percentages. Each data point represents counts for a biological replicate (n = 4). Statistical analysis was performed using two-way ANOVA with Bonferroni correction; ***P≤0.001, ****P≤0.0001.

Next, we investigated CD8⁺ T cell migration *in vitro*. Control and knockout iMLFs were seeded in transwell inserts and treated with TGF-β1 for one week to allow ECM deposition. Following decellularisation, CD8⁺ T cell migration through the deposited ECM toward a chemoattractant (TC1 cancer cell-conditioned medium) was assessed (**Figure 4.24**). Our results indicated that iMLFs retain the ability to deposit ECM. Both untreated and TGF-β1 treated iMLFs showed a significant reduction in migrating CD8⁺ T cells compared to the no matrix control. WT iMLFs (cells that have not been nucleofected), CRISPR control iMLFs, and COL11A1 KO iMLFs all exhibited significant reductions in CD8⁺ T cell migration following TGF-β1 treatment. CTHRC1 KO iMLFs showed no significant differences in CD8⁺ T cell migration before and after TGF-β1 treatment. Notably, CD8⁺ T cell migration varied between the two biological replicates (each shape represents a biological replicate, with the number of shapes corresponding to the number of technical replicates). Although a reduction in CD8⁺ T cell migration was observed in POSTN KO iMLFs following TGF-β1 treatment, these differences were not significant, likely due to data variability. Overall, we confirmed that iMLFs deposit ECM, which influences CD8⁺ T cell migration *in vitro*. As a general trend, the number of migrating CD8⁺ T cells was lower following TGF-β1 treatment.

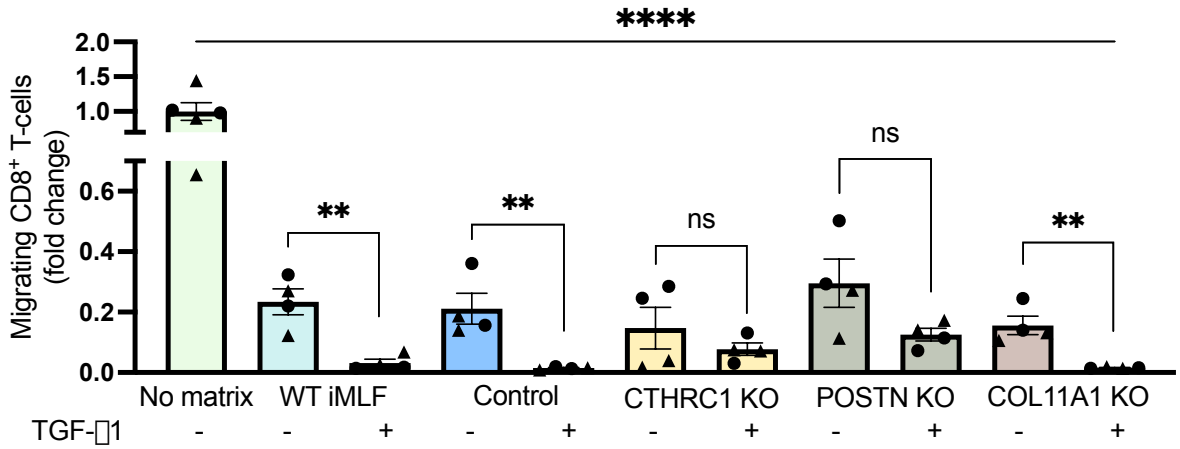

Figure 4.24: CD8⁺ T cell migration through iMLF ECM-derived matrix. Schematic diagram of the T cell migration assay. iMLFs were cultured in transwells in a 96-well plate and treated with TGF-β1 for one week to allow ECM deposition. Following decellularisation, 50 000 CD8⁺ T cells were seeded to assess their migration through deposited ECM toward conditioned medium collected from TC1 cancer cells. Migrated cells from the lower chamber were counted using a flow cytometer. Each shape represents a biological replicate, and the number of times the shape appears indicates the number of technical replicates. Data are presented as fold change ± SEM. Statistical analysis was performed using one-way ANOVA, with significance indicated as follows: **P≤0.01, ****P≤0.0001, ns = not significant.

4.3 Discussion

Excessive ECM deposition can create a physical barrier to immune cells and therapeutic agents (Yuan et al., 2023) . Thus, targeting ECM proteins is a promising therapeutic strategy. We focused on CTHRC1, POSTN and COL11A1 which are overexpressed by myCAFs. We initially decided to induce gene knockdowns rather than gene knockouts in MLFs, as knockdowns more closely mimic pharmacological inhibition, which typically reduces but does not entirely eliminate protein function. We selected lentiviral vectors to generate gene knockdowns because of their ability to transduce cells regardless of their division status (Dufait et al., 2012). Different cell lines exhibit varying levels of susceptibility to viral infections. A low MOI may result in insufficient transduction efficiency, whereas a high MOI can lead to an excessive viral load, potentially causing chromosomal instability and cell death before the desired biological effects are achieved (B. Zhang et al., 2004). We determined that an MOI of 5 was the lowest at which nearly all MLFs were successfully infected, and we used this MOI subsequently. However, we encountered challenges in determining whether effective gene knockdowns were achieved due to discrepancies between RT-qPCR and Western blot data. One explanation for these differences could be translational buffering, a regulatory mechanism whereby protein levels remain stable despite fluctuations in mRNA levels, ensuring proper protein homeostasis (Kusnadi et al., 2022). Furthermore, while shRNAs are primarily designed to downregulate gene expression, our attempt to downregulate COL11A1 expression resulted in gene upregulation. Studies have reported that this can occur due to various mechanisms, including off-target effect that disrupt endogenous miRNA pathways, as well as shRNA-induced transcriptional gene activation via epigenetic modulation (Goel & Ploski, 2022; Turunen et al., 2009). Additionally, our results indicate that scrambled shRNA controls affected the expression of our target genes at the mRNA level. In one study, researchers demonstrated that transduction with a lentiviral vector lacking an shRNA targeting the gene of interest still led to gene knockdown, highlighting the importance of using appropriate controls (Hutson et al., 2012). Moreover, shRNA-encoding vectors have been shown to induce a type I interferon response (Bridge et al., 2003; Hutson et al., 2012; Machitani et al., 2016). Type I interferons can activate NF-κB, a transcription factors that promotes cell senescence and regulates genes associated with inflammation (Chien et al., 2011; T. Liu et al., 2017; Pfeffer, 2011). Both factors may contribute to a shift in phenotype that potentially interferes with our results. Furthermore, MLFs transduced with shCTHRC1-44 and shPOSTN-65 exhibited higher proliferation rates compared to non-transduced, shSCR-transduced, and other shRNA-transduced MLFs. These increased proliferation rates represent a confounding variable that could complicate the validation of our findings when introducing MLFs transduced with two different shRNAs for each gene target into mouse models. The differences in proliferation rates

were likely attributable to off-target effects that activated or suppressed pathways involved in cell cycle regulation.

Primary fibroblasts are considered difficult to transfect. However, in recent years genetic manipulation efficiencies have improved through the use of viral-based systems and electroporation-based transfection methods (Kucharski et al., 2021). Our mRNA data show that gene knockdowns induced via lentiviral transduction can be highly efficient; however, to eliminate variability caused by differences in gene expression and proliferation rates, we have decided to generate gene knockouts using the CRISPR-Cas9 system. Delivering CRISPR-Cas9 into primary fibroblasts is typically associated with low transfection efficiency and cytotoxic effects which result in reduced cell viability (Hryhorowicz et al., 2019). Additionally, primary MLFs fail to proliferate *in vitro* when seeded sparsely, likely due to their reliance on cell-cell interactions for growth. To address this limitation, we decided to generate immortalised MLFs prior to producing gene knockouts. Given the low transfection efficiency commonly observed in primary fibroblasts, immortalisation was necessary to expand cells from single clones (Bajwa et al., 2023). Cell immortalisation is the process by which cells acquire the ability to divide indefinitely. In normal cells, division is limited by the progressive shortening of telomeres, repetitive DNA sequences located at the ends of chromosomes which shorten with each cell division (Victorelli & Passos, 2017). This gradual shortening eventually leads to replicative senescence or apoptosis (L. Sun et al., 2019). Telomerase is a ribonucleoprotein enzyme that helps to maintain telomere length by adding repetitive nucleotide sequences to the chromosome ends. The telomerase reverse transcriptase (TERT) is the catalytic subunit of telomerase responsible for this process (Steele et al., 2010). We introduced mTERT, the mouse homolog of TERT, into MLFs via lentiviral transduction to restore telomerase activity, prevent telomere shortening, and enable indefinite cell division. MLFs survived antibiotic selection, indicating successful transduction, and we confirmed this by passaging the cells. However, by passage 20 we observed that mTERT MLFs proliferated notably slower and exhibited a broader morphology compared to non-immortalised control MLFs at the same passage. Although mTERT overexpression in fibroblasts is generally associated with extended replicative capacity and delayed senescence, it is possible that our MLFs underwent senescence in response to external stressors associated with the procedure. Additionally, we were unable to expand mTERT MLFs from single clones, indicating that these cells lacked the robustness required for CRISPR-Cas9 gene editing. Consequently, we utilised MLFs immortalised spontaneously by serial passaging in our subsequent experiments.

Normal cells, including primary fibroblasts, have a finite lifespan due to telomere shortening. When telomeres become critically short, they activate a DNA damage response that leads to p53 activation, inducing cell cycle arrest via p21, which prevents further proliferation and triggers senescence (Brown et al., 1997; Westin et al., 2011). Loss of p53 or expression of a mutated p53

has been observed in the early phases of fibroblast immortalisation (Ulrich et al., 1992). To achieve unlimited cellular proliferation, p53-deficient fibroblasts must reestablish telomere maintenance to stabilise telomere length, either though TERT induction or via alternative lengthening of telomeres (ALT) (Cesare & Reddel, 2010; Chin et al., 1999; Stampfer et al., 2003). If fibroblasts do not activate telomerase or ALT, telomeres continue shortening, leading to genetic instability and ultimately cell death (Chin et al., 1999). In our study, immortalised MLFs displayed higher proliferation rates and were capable of proliferating from a single clone without the need for cell-cell contact. We observed elevated levels of p53 in immortalised MLFs compared to primary MLFs; however, we speculate that the p53 in immortalised cells is likely mutated, consistent with previous studies (H. Y. Oh et al., 2007; Ulrich et al., 1992). Although immortalised MLFs exhibited higher proliferation rates overall, we observed a reduction in proliferation following TGF-β1 treatment and no significant differences in the proliferation rates between TGF-β1-treated immortalised MLFs and primary MLFs. Furthermore, TGF-β1 treatment upregulated p53 expression in both cell types; if functional, p53 activation could explain the slower proliferation due to cell cycle arrest in response to DNA damage. Our results also show an increase in senescence, as indicated by SA-β-gal positive cells, following TGF-β1 treatment in both cell types. Although p53 is a key regulator of senescence, cells with mutated p53 can still undergo senescence via alternative pathways such as p38MAPK (Freund et al., 2011). If senescence is induced through an alternative pathway, it would also account for the reduced proliferation rates observed following TGF-β1 treatment.

Cultured myofibroblasts are characterised by stress fibres containing αSMA and by supermature focal adhesions (Hinz et al., 2003). Although αSMA stress fibres are a hallmark of the myofibroblastic phenotype, almost all fibroblasts express a basal level of αSMA (Hillsley et al., 2021). Based on the morphology of MLFs, primary fibroblasts appear to have a higher degree of stress fibre formation compared to immortalised MLFs. Additionally, our results show that immortalised MLFs have lower levels of αSMA expression; however, after TGF-β1 treatment, we did not observe differences in αSMA expression between the two cell types. Furthermore, immortalised fibroblasts exhibited lower levels of COL1A1, COL11A1, POSTN, and NOX4, while the expression of TGF-β1 and CTHRC1 remained unaltered, and FN was elevated. As expected, TGF-β1 treatment led to upregulation of these myofibroblastic markers in both cell types. Following differentiation, no differences in the expression levels of COL1A1, COL11A1, and TGF-β1 were observed, whereas POSTN and NOX4 expression remained lower and CTHRC1 expression was higher in immortalised MLFs. These findings confirm that immortalised cells respond to TGF-β1 and differentiate into a myofibroblastic phenotype. We also show that immortalised fibroblasts express lower basal levels of myofibroblastic markers and genes associated with ECM deposition. One possible explanation is that these cells are less reactive to differentiation via mechanotransduction (X. Huang et al., 2012). Given that these cells have

undergone significant mutations during immortalisation, changes in gene expression were expected. Nevertheless, since myofibroblastic markers were upregulated following TGF-β1 treatment and cells exhibited features of myofibroblasts, we proceeded to generate CRISPR-Cas9 gene knockouts using these cells.

Nucleofection is an electroporation-based method that delivers nucleic acids, ribonucleoproteins, or proteins into cells by creating temporary pores in the cell membrane, allowing for direct delivery into the nucleus (Meissner et al., 2014). An efficient delivery system is a prerequisite for successful gene editing; we used 4D-Nucleofector technology which is recognised for its high transfection efficiency in hard-to-transfect cells (Lonza). Initially, we used manufacturer-provided programs optimised for primary mammalian fibroblasts to nucleofect the pMAX-GFP control vector, which is designed to express GFP, in order to determine the most efficient program for our cells. The highest efficiency achieved was 28.5% using the EN-150 program, further confirming that fibroblasts are difficult to transfect. It has been shown that two-pulse-electroporation can increase delivery efficiency while preserving viability (Demiryurek et al., 2015). With the aim of improving transfection efficiency, we implemented both single nucleofection (one pulse) and double nucleofection (two pulses) using the EN-150 program. ICE software analysis revealed that single nucleofection resulted in 0% editing efficiency for POSTN and COL11A1 and 73% for CTHRC1, while double nucleofection increased the efficiencies to 3% for POSTN, 10% for COL11A1, and 90% for CTHRC1. Because the procedure for all three gene knockouts was performed simultaneously using the same cells and reagents, it is unlikely that the delivery system contributed to the differences in efficiencies. In fact, the high percentage obtained for the CTHRC1 knockout confirms the reliability of the system. Factors that could affect genome editing efficiency include GC content, secondary structures, chromatin state, and epigenetic modifications (Javaid & Choi, 2021; Jung et al., 2024). Although sgRNA design tools aim to optimise guide RNAs for efficient and specific gene editing by considering these factors, their predictions require experimental validation, as predicted scores do not always correlate with actual editing success due cell-type differences (Konstantakos et al., 2022). Furthermore, CRISPR-Cas9 gene editing works by inducing DNA breaks and triggering cellular DNA repair pathways that lead to targeted gene modifications (C. Xue & Greene, 2021). However, it is possible for cellular DNA repair mechanisms to counteract CRISPR-induced gene knockouts, preventing the intended knockout from occurring. Despite attempts to increase gene editing efficiency by using multiple guides, the knockout efficiencies for POSTN and COL11A1 remained low.

To determine whether gene knockouts of CTHRC1, POSTN, and COL11A1 affect $CD8^+$ T cell infiltration and tumour size, we selected single clones containing these knockouts. Our mRNA expression results confirmed that TGF-β1 treatment upregulated of COL1A1, COL1A2, COL11A1,

NOX4, CTHRC1, and POSTN; however, variability in expression was observed between clones. Additionally, the expression of CXCL10 and CCL5, chemokines involved in T cell trafficking, was highly variable, which is advantageous since cells within the TME also display heterogeneity. To mimic this environment, we mixed single clones in equal ratios. We did not observe differences in proliferation of POSTN and COL11A1 knockout fibroblasts, whereas CTHRC1 knockout fibroblasts exhibited slower proliferation rates, consistent with previous findings (Duan et al., 2022). Following TGF-β1 treatment, all cell populations exhibited reduced proliferation, and no differences were observed between gene knockout myofibroblast populations. In addition to assessing the expression of myofibroblastic markers and proliferation rates following TGF-β1 treatment, we evaluated cell contractility. As expected, TGF-β1 treatment promoted cell contractility compared to control cells; however, this increase was observed only in control, POSTN, and COL11A1 knockout fibroblasts. Interestingly, CTHRC1 knockout fibroblasts were more contractile than control fibroblasts under basal conditions yet following TGF-β1 treatment they became less contractile than both CTHRC1 knockout and control fibroblasts. CTHRC1 has been shown to activate the focal adhesion kinase (FAK) signalling pathway (X. Hu et al., 2020). Given that FAK is required for acquiring a profibrotic phenotype, with its inhibition attenuating TGF-β1-induced αSMA expression in human Tenon's fibroblasts, a disruption of FAK signalling by CTHRC1 knockout might explain the reduced contractility following TGF-β1 treatment (S. Hong et al., 2012; Lagares et al., 2012). However, this hypothesis does not clarify why CTHRC1 knockout fibroblasts are more contractile under basal conditions, leaving an avenue for further investigation. Migration assay results further validated the myofibroblastic phenotype, as immortalised MLFs treated with TGF-β1 deposited ECM that was associated with reduced $CD8^+$ T cell migration. *In vitro* findings suggest that the gene knockouts did not affect $CD8^+$ T cell migration compared to control MLFs. *In vivo*, our data confirmed these findings. We found no differences in the number of $CD8^+$ T cells in murine tumours; however, higher proportions of $CD8^+$ T cells were observed at the tumour margin compared to the tumour centre, consistent with previous reports (Ford et al., 2020; Masugi et al., 2019). Studies have shown that CAF-rich tumours restrict $CD8^+$ T cell infiltration as myCAFs deposit a stiff ECM that forms a physical barrier to immune cell penetration (Hanley & Thomas, 2020; L. Jenkins et al., 2022; Mai et al., 2024). In our study, tumour generated with cancer cells alone did not differ in $CD8^+$ T cell infiltration compared to tumours containing immortalised myofibroblasts. H&E staining of tumour sections revealed limited eosin staining corresponding to ECM deposition and cytoplasmic protein staining. ECM deposition was observed in specific areas, possibly due to localised myofibroblast activity. These results suggest that the lack of differences in $CD8^+$ T cell infiltration may be due to minimal ECM deposition. This is the first time immortalised MLFs were used in our laboratory for an *in vivo* experiment. We followed a protocol previously used for generating tumours with primary fibroblasts, where we observed ECM deposition and $CD8^+$ T cell

exclusion at the tumour boundary (results not shown). Based on our mRNA data, contraction assay results, and *in vitro* migration assays, immortalised MLFs appear to deposit ECM and exhibit contractile functions. Moreover, once treated with TGF-β1 and confluent, immortalised MLFs appeared interconnected by deposited matrix and could not be separated by trypsinisation, this was not evident in immortalised MLF controls. It is possible that the immortalised myofibroblasts lost viability *in vivo*. One explanation is that immortalised fibroblasts, due to their altered metabolism required to support higher proliferation rates, may face increased competition for nutrients with cancer cells, which can adapt well to variable oxygen and nutrient availability, thereby promoting cancer cell survival in the TME (DeBerardinis et al., 2008; Tufail et al., 2024; J. Zhu & Thompson, 2019). While immortalised MLFs are more robust in an experimental setting, they are genetically different from primary fibroblasts. Based on our results, gene editing may not necessarily yield the desirable phenotype and therefore if used in the future, translating results from immortalised fibroblasts to clinical application may not be straightforward.

Chapter 5 Establishing the differences between WT and STING KO myofibroblasts

5.1 Introduction

The TME plays a crucial role in shaping immune responses against cancer, influencing the effectiveness of immunotherapy. A key regulator of immune signalling in the TME is the cGAS-STING pathway, which detects cytosolic DNA and initiates a robust type I interferon response critical for promoting antitumour immunity and enhancing the immunotherapy efficacy (M. Jiang et al., 2020). However, tumours have evolved mechanisms to suppress STING activation, contributing to immune evasion and treatment resistance (Khoo & Chen, 2018).

ATM, a central player in the DNA damage response, is traditionally known for maintaining genomic stability by sensing and repairing double-strand breaks (Maréchal & Zou, 2013). Beyond this canonical role, ATM modulates immune signalling, including the cGAS-STING pathway. Notably, ATM inhibition leads to the accumulation of cytosolic DNA fragments, thereby activating the cGAS-STING pathway (Q. Chen et al., 2016). While studies have shown that ATM inhibition enhances immunotherapy by activating STING signalling in cancer cells (M. Hu et al., 2021; C. Li et al., 2024); this response in CAFs remains to be elucidated.

Given the growing interest in harnessing the immune system to combat cancer, there is a need to explore strategies that enhance STING-mediated immune responses to overcome immunotherapy resistance (Papaioannou et al., 2016). MyCAFs contribute to therapeutic resistance within the TME (Croizer et al., 2024). In Chapter 3, we demonstrate that ATM inhibition in myofibroblasts downregulates genes associated with the ECM and myCAF markers, while altering cytokine composition, both of which were associated with increased $CD8^+$ T cell migration *in vitro*. These findings provide insights into how ATM inhibition may potentiate immunotherapy responses in mouse models. In this chapter, we explore whether ATM inhibition activates the cGAS-STING pathway in myofibroblasts and investigate the influence of STING, TGF-β1, and ATM activity on the type I interferon response. By evaluating interferon signalling upon ATM inhibition, we aim to understand how targeting myCAFs can reshape the inflammatory environment to improve antitumour immunity.

5.2 Results

5.2.1 Effects of ATM inhibition and TGF-β1 treatment on the cGAS-STING pathway and ISG expression in WT and STING KO MLFs

To determine whether the cGAS-STING pathway is activated in MLFs following ATM inhibition and to confirm whether this activation is STING-dependent, we isolated MLFs from a STING knockout mouse and compared the expression of key proteins in the pathway via Western blotting. Cells were treated with TGF-β1 and 0.5 μM ATM inhibitor AZD0156 for six days. Our analyses show that protein levels of STING decrease following TGF-β1 treatment and are further reduced by ATM inhibition (**Figures 5.1A, 5.1B, 5.1D**). cGAS protein expression was slightly downregulated following TGF-β1 treatment, but ATM inhibition led to cGAS upregulation in both untreated and TGF-β1-treated WT and STING KO MLFs (**Figures 5.1A, 5.1C, 5.1E**). In contrast, pTBK1 expression was unaffected by either treatment in WT or STING KO MLFs (**Figures 5.1A, 5.1C, 5.1F**). We quantified protein expression from individual Western blot experiments and performed statistical analyses to assess significance. While our results show consistent trends, some data points lack statistical significance, likely due to the limited number of independent replicates (**Figures 5.1D, 5.1E, 5.1F**). Additional blots for STING KO MLFs are provided in **Appendix A Figure 11**.

We next investigated the expression of other genes linked to the cGAS-STING pathway, selecting them based on previous findings from cancer cell studies. IRF3 is activated by pTBK1; once phosphorylated, IRF3 binds to interferon-stimulated response elements, leading to the transcription of type I interferons and other interferon-stimulated genes (Chattopadhyay et al., 2016). WT and STING KO MLFs were treated with TGF-β1 and 0.5 μM ATM inhibitor AZD0156 for six days and then collected for RT-qPCR analysis. We observed no differences in mRNA expression levels of IRF3 between WT and STING KO MLFs, and our findings suggest that IRF3 is neither regulated by TGF-β1 nor by ATM inhibition (**Figure 5.2A**). IRF1 induced by interferons (IFN-γ and IFN-β), subsequently activates the expression of ISGs (Ravi Sundar Jose Geetha et al., 2024). Our data show that IRF1 mRNA expression is downregulated following TGF-β1 treatment, and its expression is not regulated by ATM inhibition (**Figure 5.2B**). This suggests that TGF-β1, in this context, may be suppressing inflammatory signalling. We next measured changes in the mRNA expression levels of several ISGs, including IFIT1, ISG15, CCL2, CCL5, and CXCL10. Similar to IRF1 expression, IFIT1 expression was also downregulated by TGF-β1 in both WT and STING KO MLFs. However, following ATM inhibition, there was a trend toward IFIT1 upregulation, which was significant only in WT fibroblasts (**Figure 5.2C**). ISG15 expression varied between WT and STING KO MLFs. We found that TGF-β1 treatment downregulated ISG15 expression in WT MLFs, while no significant difference was observed between untreated and TGF-β1-treated STING KO MLFs. Furthermore, STING KO MLFs exhibited lower ISG15 expression in untreated cells, but

higher expression in TGF-β1-treated cells compared to WT MLFs. ATM inhibition resulted in upregulation of ISG15 in both untreated and TGF-β1-treated WT MLFs, whereas in STING KO MLFs, ATM inhibition had the opposing effect, leading to downregulation of ISG15 in both conditions (**Figure 5.2D**). These results suggest that STING is necessary for ISG15 induction. STING KO MLFs appear to have higher basal levels of CCL2 expression, which were unaffected by ATM inhibition. In contrast, CCL2 expression was upregulated in ATM-inhibited WT MLFs. TGF-β1 treatment downregulated CCL2 expression in both cell types, and following ATM inhibition, its levels were upregulated in both WT and STING KO MLFs (**Figure 5.2E**). These results suggest that the regulation of CCL2 in response to ATM inhibition occurs independently of STING pathway. In contrast, STING is essential for the regulation of CCL5 expression. Our data show that basal levels of CCL5 in STING KO MLFs are lower compared to WT MLFs, and these levels remain unchanged following TGF-β1 treatment and ATM inhibition. In contrast, in WT MLFs, TGF-β1 treatment downregulated CCL5, and its levels were restored following ATM inhibition (**Figure 5.2F**). We also investigated the expression of CXCL10. We did not find differences in CXCL10 expression between control and TGF-β1-treated WT and STING KO MLFs. However, TGF-β1 treatment downregulated CXCL10 in both cell types. ATM inhibition led to upregulation of CXCL10 in TGF-β1-treated WT MLFs, but this effect was not observed in STING KO MLFs. Additionally, ATM inhibition did not induce significant changes in CXCL10 expression in untreated fibroblasts from either cell type (**Figure 5.2G**). To further validate the expression of CXCL10 in STING KO MLFs, we conducted two additional independent experiments measuring its mRNA expression. Our results confirm that CXCL10 was not upregulated following ATM inhibition (**Figure 5.2H**), suggesting that STING plays a role in the regulation of CXCL10 expression.

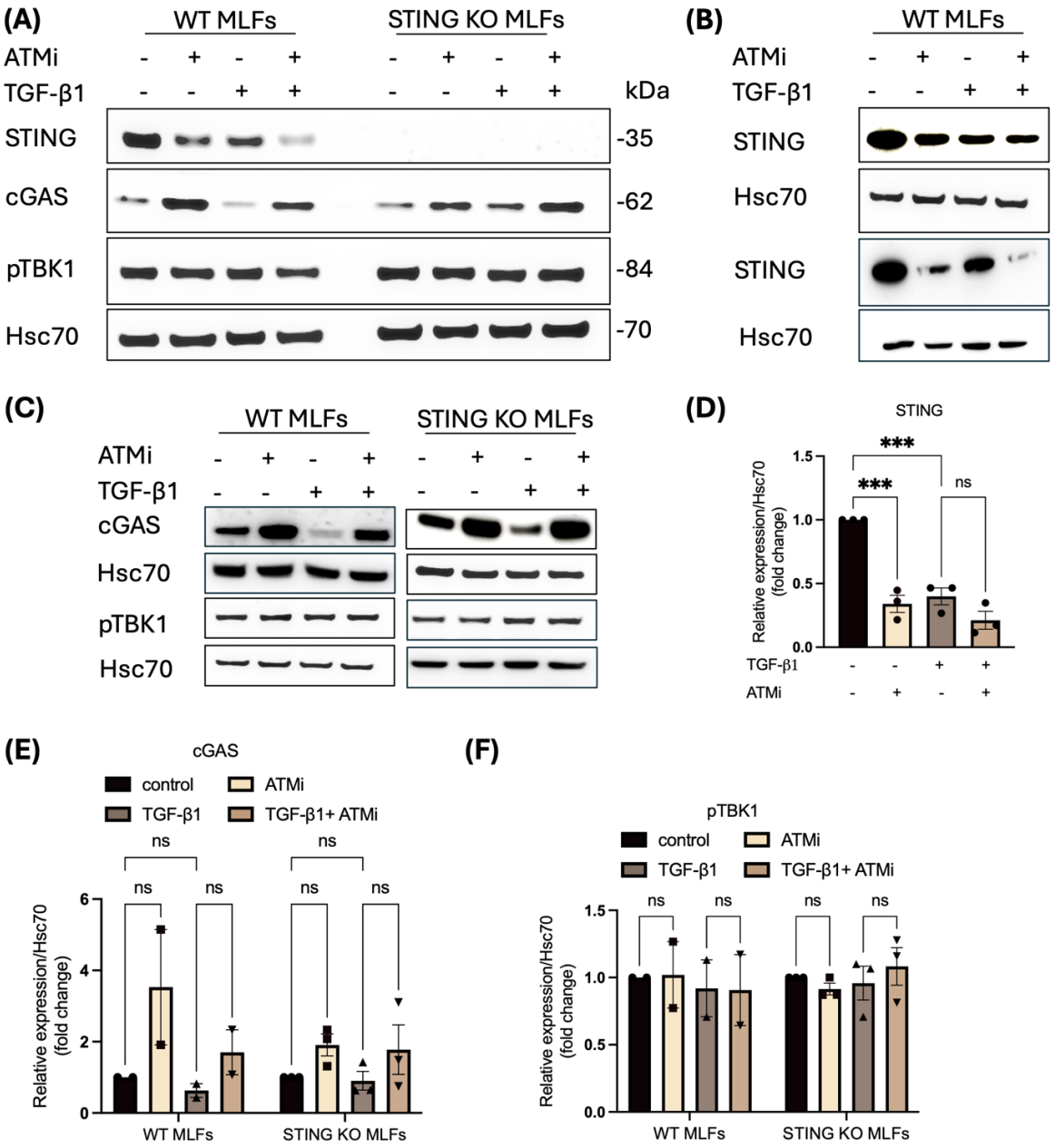

Figure 5.1: Expression levels of cGAS-STING pathway proteins. (A-C) Western blotting of WT and STING KO MLFs treated with TGF-β1 and/or 0.5 μM AZD0156 for 6 days. Each blot represents an individual experiment. **(D-F)** Quantification of pixel density from Western blots, normalised to Hsc70. Data are presented as mean fold change ± SEM, normalised to untreated controls, with each data point representing an independent experiment. Statistical significance was determined using one-way or two-way ANOVA with Bonferroni correction; ***P≤0.001, ns = not significant.

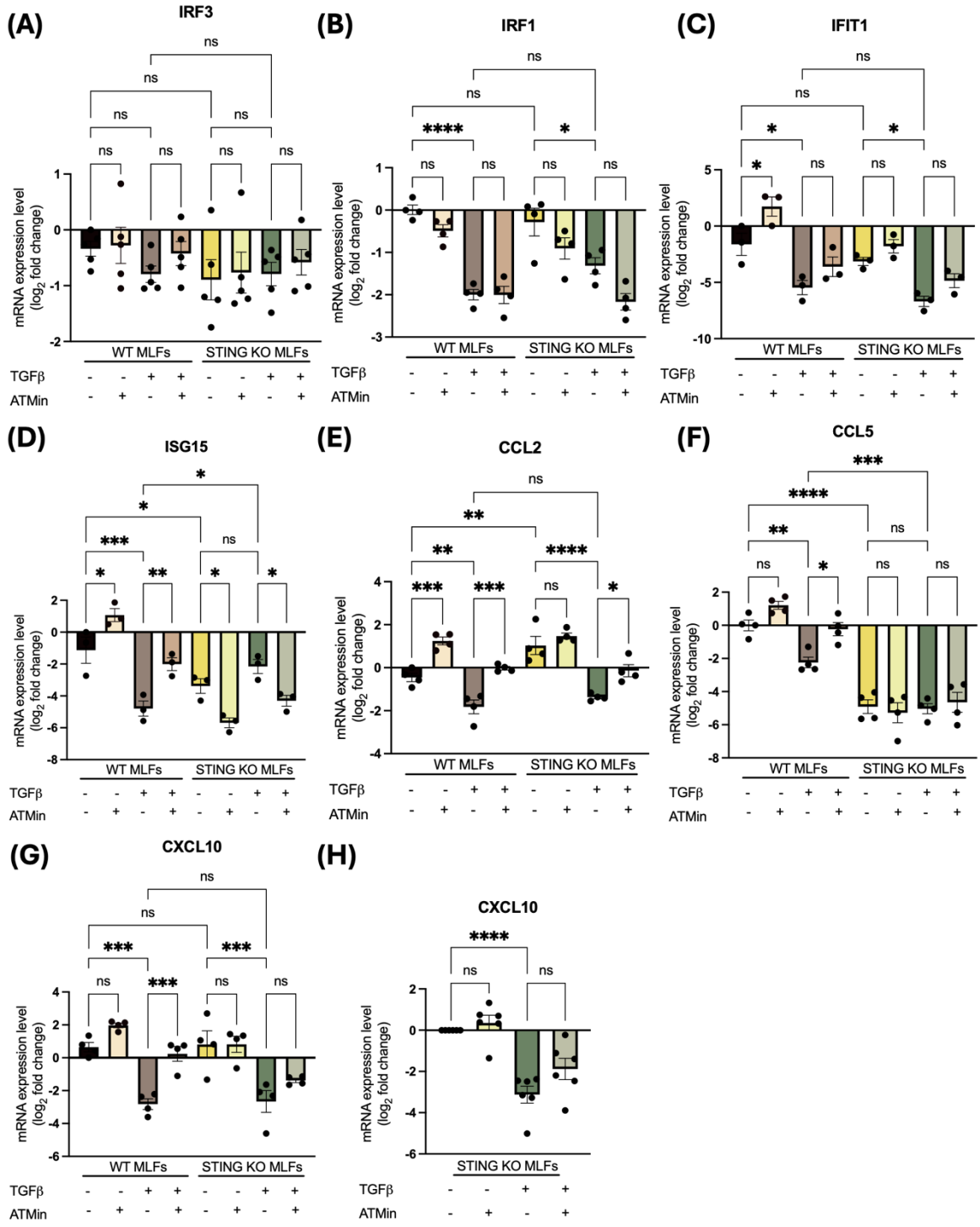

Figure 5.2: Effects of ATM inhibition and TGF-β1 treatment on the expression of genes associated with the cGAS-STING pathway. (A-G) RT-qPCR analysis of genes related to the cGAS-STING pathway and interferon-stimulated genes in WT and STING KO MLFs treated with TGF-β1 and/or AZD0156 for 6 days. Data are presented as mean $\log_2$ fold change ± SEM, normalised to WT untreated controls, with each dot representing an independent experiment. Statistical significance was determined using one-way ANOVA with Bonferroni correction; *P≤0.05, **P≤0.01, ***P≤0.001, ****P≤0.0001, ns = not significant. **(H)** RT-qPCR analysis of CXCL10 in STING KO MLFs treated with TGF-β1 and/or AZD0156 for 6 days. Data are presented as mean $\log_2$ fold change ± SEM, normalised to STING KO untreated controls, with each dot representing an independent experiment. Statistical

significance was determined using one-way ANOVA with Bonferroni correction; ****P≤0.0001, ns = not significant.

5.2.2 Effects of ATM inhibition and TGF-β1 treatment on CAF markers in WT and STING KO MLFs

Our findings from studies on WT MLFs suggest that ATM inhibition plays a dual role in shaping fibroblast phenotype by reversing the myofibroblastic phenotype and promoting the iCAF phenotype. Next, we aimed to determine whether STING expression is involved in establishing these phenotypes. Cells were differentiated and treated as previously described, and gene expression was assessed via RT-qPCR. We first measured mRNA levels of genes associated with the iCAF phenotype. No significant differences were observed in the expression of IL6, IL11 and LIF between WT and STING KO MLFs. We found that IL6 expression was downregulated in TGF-β1-treated MLFs, whereas ATM inhibition led to an upregulation of IL6 in both cell types. However, this increase was only statistically significant in TGF-β1-treated WT MLFs. TGF-β1-treatmeant resulted in the upregulation of IL11 in STING KO MLFs and LIF in both cell types. ATM inhibition further increased IL11 expression in both cell types, and although an upregulation of LIF was observed, it was not statistically significant (**Figure 5.3A**). CXCL12, another marker associated with the iCAF phenotype, was not regulated by either TGF-β1 treatment or ATM inhibition. However, our data indicated that CXCL12 was significantly downregulated in STING KO MLFs (**Figure 5.3B**), suggesting that STING is required for its regulation. STING KO MLFs exhibited lower levels of the FRC marker CCL19 compared to its basal levels in WT MLFs. This finding suggests that STING activation can enhance CCL19 expression Following TGF-β1 treatment, CCL19 expression was significantly downregulated in WT MLFs; however, this change was not significant in STING KO MLFs. ATM inhibition had no effect on CCL19 expression (**Figure 5.3C**). RT-qPCR analysis showed upregulation of CD40 in both cell types following TGF-β1 treatment and ATM inhibition (**Figure 5.3D**), suggesting that STING is not required for CD40 expression in fibroblasts.

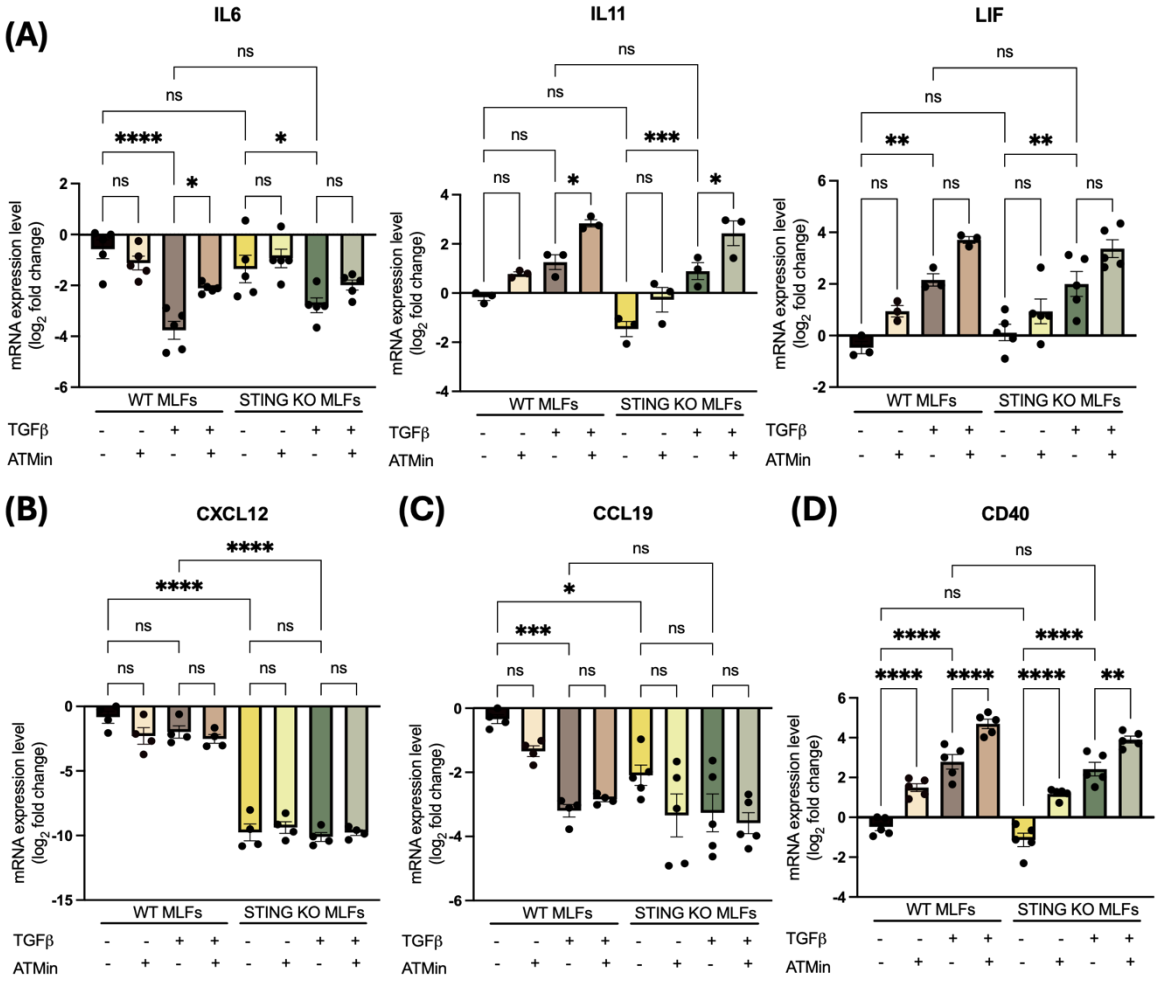

Figure 5.3: Role of STING in the expression of genes associated with the iCAF phenotype and other cytokines. (A-D) RT-qPCR analysis of genes in WT and STING KO MLFs treated with TGF-β1 and/or AZD0156 for 6 days. Data are presented as mean log_2 fold change ± SEM, normalised to WT untreated controls, with each dot representing an independent experiment. Statistical significance was determined using one-way ANOVA with Bonferroni correction; *P≤0.05, **P≤0.01, ***P≤0.001, ****P≤0.0001, ns = not significant.

We next assessed the expression of extracellular matrix genes to investigate whether the effects of TGF-β1 on fibroblast-to-myofibroblast differentiation persist in the absence of STING and whether ATM inhibition normalises the myofibroblastic phenotype in both cell types. Our findings based on mRNA levels confirmed that TGF-β1 treatment upregulated COL1A1, COL11A1, CTHRC1, and POSTN in both cell types, with no significant differences between WT and STING KO MLFs. However, basal levels of COL11A1 and POSTN appeared lower in STING KO MLFs. ATM inhibition downregulated the expression of these genes as expected, though this downregulation was not statistically significant for POSTN (**Figures 5.4A-D**). To establish significance, we included additional experimental data measuring POSTN mRNA levels. These results confirmed

that POSTN was significantly upregulated by TGF-β1 and downregulated following ATM inhibition in both cell types. However, in STING KO MLF controls, POSTN was not further downregulated by ATM inhibition (**Figure 5.4E**). This could be because basal POSTN levels in STING KO MLFs were already low and could not be reduced further.

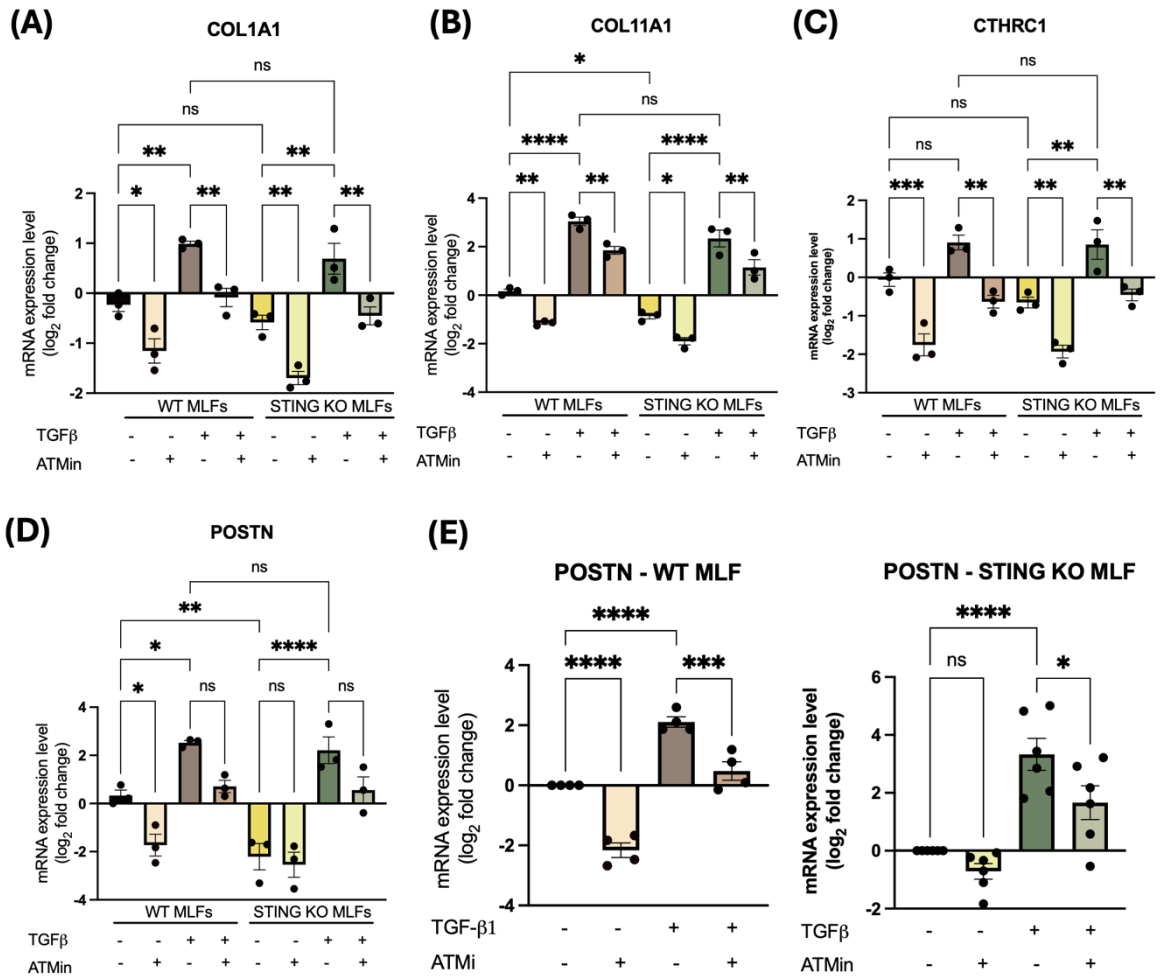

Figure 5.4: ATM inhibition downregulates ECM gene expression in WT and STING KO MLFs. (A-D) RT-qPCR analysis of extracellular matrix genes in WT and STING KO MLFs treated with TGF-β1 and/or AZD0156 for 6 days. Data are presented as mean $\log_2$ fold change ± SEM, normalised to WT untreated controls, with each dot representing an independent experiment. Statistical significance was determined using one-way ANOVA with Bonferroni correction; *P≤0.05, **P≤0.01, ***P≤0.001, ****P≤0.0001, ns = not significant. **(E)** RT-qPCR analysis of POSTN in WT and STING KO MLFs treated with TGF-β1 and/or AZD0156 for 6 days. Data are presented as mean $\log_2$ fold change ± SEM, normalised to corresponding untreated controls, with each dot representing an independent experiment. Statistical analysis was determined using one-way ANOVA with Bonferroni correction; *P≤0.05, ***P≤0.001, ****P≤0.0001, ns = not significant.

Both NOX4 and TGF-β1 are key regulators of the fibroblast-to-myofibroblast transition (Branton & Kopp, 1999; Ford et al., 2020; Hanley et al., 2018; Thannickal et al., 2003). Since ATM inhibition downregulates genes associated with the extracellular matrix and myofibroblastic phenotype, we examined the expression of these genes. WT and STING KO MLFs were treated with TGF-β1 and 0.5 μM ATM inhibitor AZD0156 for six days, followed by RT-qPCR analysis. STING KO MLFs had significantly lower basal NOX4 expression than WT MLFs (**Figure 5.5A**). Given the variability in basal NOX4 levels, statistical analysis was performed relative to untreated controls. TGF-β1 upregulated NOX4 in STING KO MLFs but not in WT MLFs, while ATM inhibition alone had no effect. However, in TGF-β1-treated cells, ATM inhibition increased NOX4 expression in both cell types (**Figures 5.5B-C**). TGF-β1 expression did not significantly differ between untreated and TGF-β1-treated WT and STING KO MLFs (**Figure 5.5D**). Due to variability in basal TGF-β1 levels, statistical analysis was applied as with NOX4. TGF-β1 treatment increased its own expression in both WT and STING KO MLFs, with ATM inhibition further enhancing this effect (**Figures 5.5E-F**). Since NOX4 was not significantly upregulated by TGF-β1 in WT MLFs, and ATM inhibition increased expression of both genes, we examined earlier timepoints. NOX4 expression increased over time even without treatment (**Figures 5.6A-D**). In WT MLFs, TGF-β1 showed a similar trend but was not significant, and this pattern was absent in STING KO MLFs (**Figures 5.6E-H**). A 24-hour TGF-β1 treatment significant upregulated NOX4 and TGF-β1 in both cell types (**Figures 5.6A-B, 5.6E-F**), with no further changes at 72 and 144 hours (**Figures 5.6C-D, 5.6G-H**). ATM inhibition significantly increased NOX4 only at 144-hours (**Figures 5.6C-D**). Though TGF-β1 expression showed an increasing trend, it was not statistically significant (**Figures 5.6E-F**). Overall, our results indicate that ATM inhibition upregulates NOX4 but not TGF-β1. TGF-β1 treatment increases both genes' expression, independent of culture duration. Additionally, NOX4 levels rise over time due to cell culture alone.

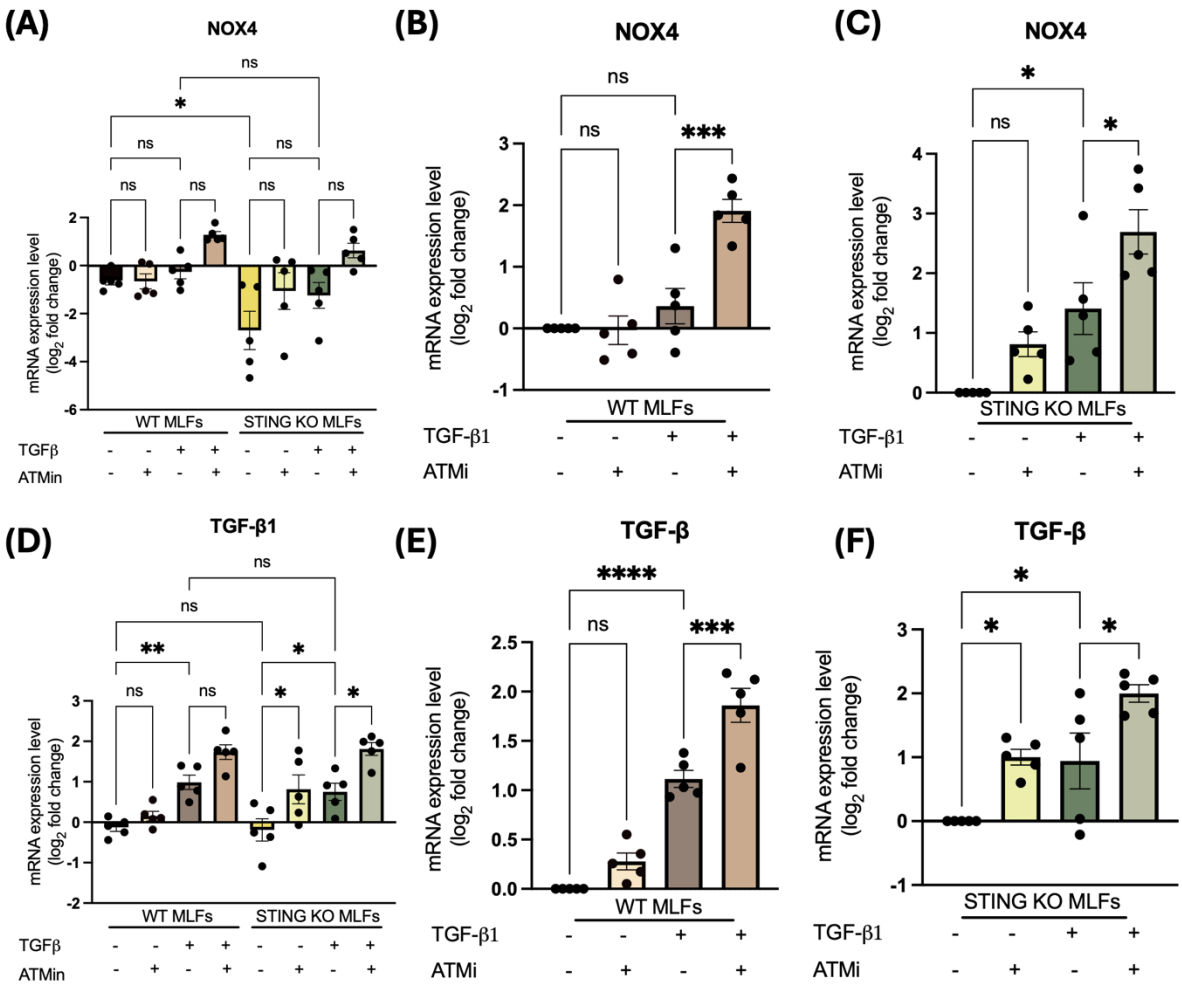

Figure 5.5: Regulation of NOX4 and TGF-β1 expression in WT and STING KO MLFs. (A,D) RT-qPCR analysis of NOX4 and TGF-β1 expression in WT and STING KO MLFs treated with TGF-β1 and/or AZD0156 for 6 days. Data are presented as mean log_2 fold change ± SEM, normalised to WT untreated controls, with each dot representing an independent experiment. Statistical analysis was performed using one-way ANOVA with Bonferroni correction; *P≤0.05, **P≤0.01, ns = not significant. **(B-C, E-F)** RT-qPCR analysis of NOX4 and TGF-β1 expression in WT and STING KO MLFs treated with TGF-β1 and/or AZD0156 for 6 days. Data are presented as mean log_2 fold change ± SEM, normalised to corresponding untreated controls, with each dot representing an independent experiment. Statistical analysis was performed using one-way ANOVA with Bonferroni correction; *P≤0.05, ***P≤0.001, ****P≤0.0001, ns = not significant.

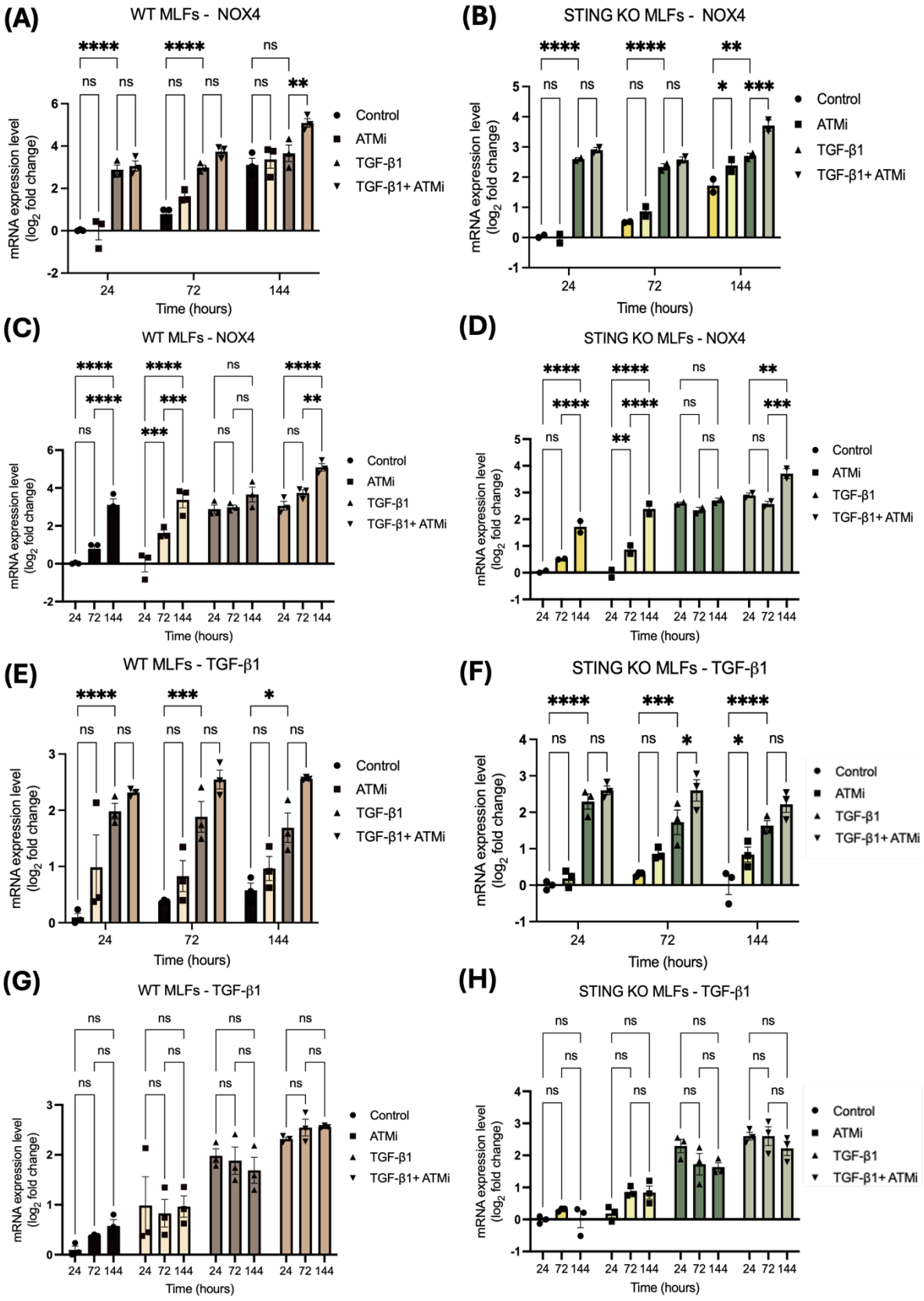

Figure 5.6: ATM inhibition upregulates NOX4 and TGF-β1 expression over time. (A-B, E-F) RT-qPCR analysis of NOX4 and TGF-β1 expression in WT and STING KO MLFs treated with TGF-β1 and/or AZD0156 for 24, 72, or 144 hours. Data are presented as mean log_2 fold change ± SEM, normalised to untreated controls at corresponding timepoints, with each data point representing an independent experiment. Statistical analysis was performed using two-way ANOVA with Bonferroni

correction; *P≤0.05, **P≤0.01, ***P≤0.001, ****P≤0.0001, ns = not significant. **(C-D, G-H)** RT-qPCR analysis of NOX4 and TGF-β1 expression in WT and STING KO MLFs treated with TGF-β1 and/or AZD0156 for 24, 72, or 144-hours. Data are presented as mean log_2 fold change ± SEM, normalised to untreated controls from the 24-hour timepoint, with each data point representing an independent experiment. Statistical analysis was performed using two-way ANOVA with Bonferroni correction; **P≤0.01, ***P≤0.001, ****P≤0.0001, ns = not significant.

Results based on mRNA level measurements showed that both WT and STING KO MLFs upregulated genes associated with extracellular matrix composition following TGF-β1 treatment. Next, we measured ECM protein and myofibroblastic marker levels via Western blotting. We found that both cell types upregulated COL1A1, COL11A1, FN and αSMA following TGF-β1 treatment, while ATM inhibition led to their downregulation (**Figure 5.7A**). We then performed a hydroxyproline assay to quantify total collagen levels. Both WT and STING KO MLFs showed increased hydroxyproline levels following TGF-β1 treatment. ATM inhibition resulted in a reduction of hydroxyproline levels. Our results showed no significant differences in hydroxyproline content between WT and STING KO MLFs. However, STING KO MLFs appeared to express slightly lower hydroxyproline levels after TGF-β1 treatment (**Figure 5.7B**). In Chapter 3, we demonstrated that WT MLFs become contractile following TGF-β1 treatment, as shown by the contraction assay. Here, we tested the contractility of STING KO MLFs using the same approach. TGF-β1 increased cell contractility, which was abolished by ATM inhibition, as indicated by the percentages of original gel area and gel weights after contraction (**Figures 5.7C-E**). Overall, our *in vitro* findings suggest that STING deficiency does not significantly alter the myofibroblastic phenotype of MLFs under the conditions tested.

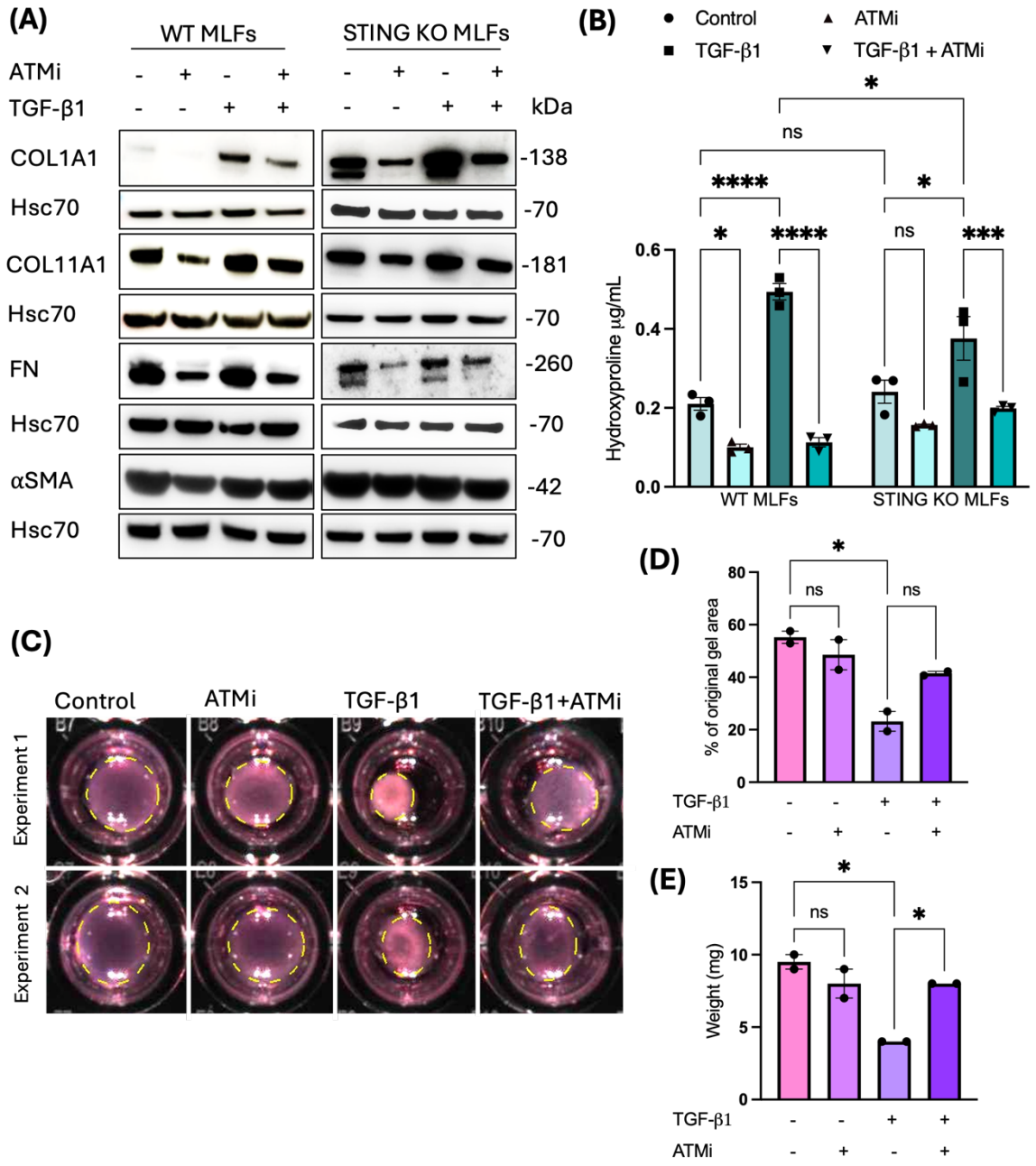

Figure 5.7: ATM regulates the expression of myofibroblastic markers and cell contractility in WT and STING KO MLFs. (A) Western blotting of WT and STING KO MLFs treated with TGF-β1 and/or AZD0156 for 6 days. **(B)** Normalised hydroxyproline concentration in WT and STING KO MLFs treated with TGF-β1 and/or AZD0156 for 6 days. Data are presented as mean ± SEM, with each dot representing an independent experiment (*P≤0.05, ***P≤0.001, ****P≤0.0001, ns = not significant; two-way ANOVA). **(C)** Representative images of gel contraction after a 24-hour period, with dotted lines outlining gel area. **(D)** Quantification of gel area as a percentage of the original size and **(E)** gel weight after 24-hour contraction. STING KO MLFs were pretreated with TGF-β1 and/or AZD0156 for 6 days prior to the contraction assay. Data are presented as mean ± SEM, with each dot representing an independent experiment. Statistical analysis was performed using one-way ANOVA with Bonferroni correction; *P≤0.05, ns = not significant.

5.2.3 Targeting ATM *in vivo* affects tumour growth and CD8$^+$ T cell infiltration

Our *in vitro* findings revealed no significant differences in the expression of myofibroblastic markers following TGF-β1 treatment and ATM inhibition. However, we observed differences in the expression of genes associated with the cGAS-STING pathway and interferon-stimulated genes. Next, we investigated whether tumour growth and CD8$^+$ T cell infiltration differed between WT and STING KO myofibroblast-rich tumours treated with the ATM inhibitor AZD0156 *in vivo*. To address this, syngeneic tumours were generated by subcutaneous injections of TC1 cancer cells combined with either WT or STING KO mouse lung fibroblasts pretreated with TGF-β1 for one week *in vitro*. Tumours were left to grow for two weeks. Once established, mice were administered vehicle or AZD0156, at a pharmacologically relevant dose of 20 mg/kg via oral gavage nearly daily. Tumour volumes were measured every 3-4 days, and tumours were resected on day 29 for further analysis (**Figure 5.8A**). In mice injected with WT myofibroblasts, we observed a significant reduction in tumour volume in those treated with the ATM inhibitor AZD0156 compared to the vehicle control. In the ATM inhibitor treatment group, the mean tumour volume was reduced by over 50% compared to control mice treated with vehicle (**Figure 5.8B**). In contrast, in mice injected with STING KO myofibroblasts, there was no significant reduction in tumour volume in the ATMi-treated group compared to the control mice. However, based on mean values, we observed an approximate 40% decrease in tumour volume in the ATMi-treated group (**Figure 5.8C**). Additionally, no significant differences were observed in the tumour volumes of vehicle-treated control groups between WT and STING KO myofibroblast-rich tumours (**Figure 5.8D**). Immunohistochemical staining was performed to determine whether ATM inhibition affects CD8$^+$ T cells in WT and STING KO myofibroblast-rich tumour samples. Representative images of CD8$^+$ T cell immunohistochemistry are shown for tumours treated with either vehicle or AZD0156 for both WT and STING KO myofibroblast-rich tumours (**Figure 5.8E**). CD8$^+$ T cells were quantified by a consultant pathologist (GJT) in ten randomly selected fields of view per tumour. The average numbers of T cells were plotted, showing that ATM inhibition in myofibroblast-rich tumours *in vivo* significantly increased CD8$^+$ T cell infiltration compared to vehicle-treated control mice. We report a 3-fold increase in CD8$^+$ T cells in WT myofibroblast-rich tumours and a 2.2-fold increase in STING KO myofibroblast-rich tumours compared to their respective vehicle controls. Additionally, no significant differences were observed in the number of infiltrating CD8$^+$ T cells between WT and STING KO myofibroblast-rich tumours (**Figure 5.8F**). These findings suggest that STING in myofibroblasts is not required for CD8$^+$ T cell trafficking.

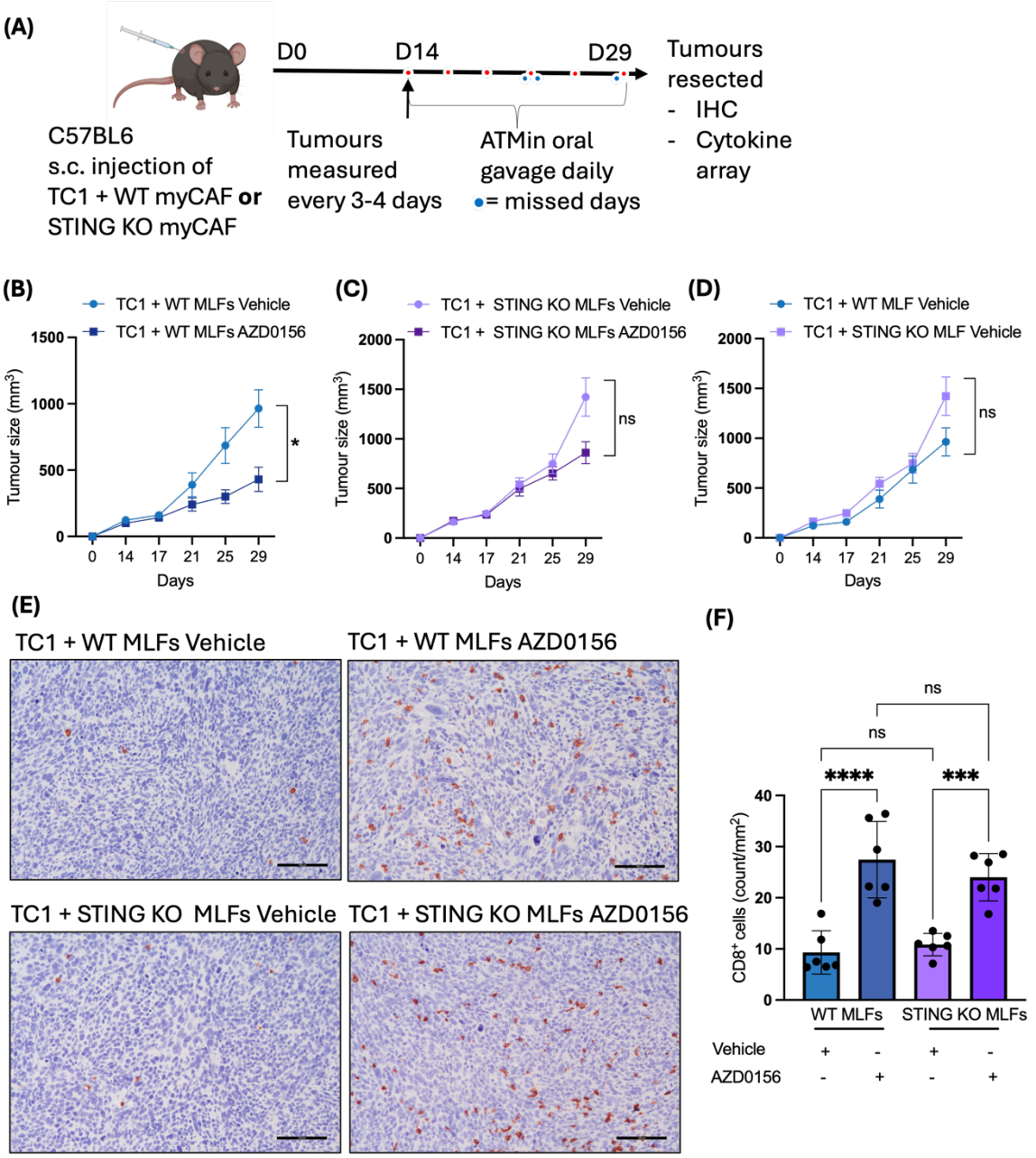

Figure 5.8: Targeting ATM with the ATMi AZD0156 reduces myCAF-rich syngeneic tumour volume and increases intratumoural CD8⁺ T cell infiltration. (A) Schematic representation of AZD0156 administration in mice with myCAF-rich MLF and TC1 syngeneic tumours. **(B-D)** Tumour growth curves illustrating the effect of 20 mg/kg ATMi AZD0156 treatment on myCAF-rich MLF-TC1 tumours. Data are presented as mean ± SEM (n = 6 for the vehicle group, n = 7 for the AZD0156 treatment group). Statistical significance was determined using AUC analysis followed by a two-tailed homoscedastic t-test (*P≤0.05). **(E)** Representative immunohistochemical (IHC) images showing the effects of ATM inhibition on CD8⁺ T cell infiltration in myCAF-rich tumours. Scale bars = 100 µm. **(F)** Quantification of average CD8⁺ T cell count based on IHC staining of tumour sections. CD8⁺ T cells were counted in ten randomly selected fields of view per mouse by a consultant pathologist (GJT). Data are presented as mean ± SD, with statistical significance determined using one-way ANOVA (***P≤0.001, ****P≤0.0001).

5.2.4 Tissue slice model culture optimisation

Cell lines are widely used as preclinical models to predict anticancer drug responses, but they have several limitations. Cell lines lack the dynamic interactions present in the TME, and those that are passaged extensively may acquire genetic and phenotypic alterations that no longer reflect the characteristics of the original patient-derived cells. Additionally, some cells lines can be difficult to culture and may not be readily available, prompting scientists to prefer more robust cell types (Sajjad et al., 2021). To address these challenges, *ex-vivo* tissue slice models are becoming increasingly popular for assessing drug response. The main advantage of using fresh tissue samples is that they preserve the tumour architecture and the spatial interactions between various cell types (Majorova et al., 2021). In slice models, the 3D structure of the tumour, including ECM interaction, is maintained. Researchers have previously used human tumour sections to study T cell motility, where collagen fibres were shown to influence T cell distribution and migration (Bougherara et al., 2015; Salmon et al., 2012). We have demonstrated that myofibroblastic ATM inhibition *in vitro* reduces the expression of ECM components. We aimed to use real-time imaging to determine whether ATM inhibitor treatment of tumour slices alters collagen composition in a manner that facilitates increased T cell migration and infiltration. To maintain the viability of our mouse and human tissue slices, we followed a general protocol provided by AstraZeneca.

The aim of this experiment was to develop optimised conditions for culturing tumour slices *ex vivo* while preserving their structure and functional integrity. Tumour tissues were embedded in low-melting point agarose to provide mechanical support, helping maintain the integrity of the tissue structure. For optimal nutrient and oxygen diffusion, the slices were placed on organotypic insets in 6-well plates containing 1.1 mL of complete medium. The samples were then placed on a rocking platform (**Figure 5.9**). Both mouse and human tumour slices were cultured at 37°C, 5% CO_2, and 95% humidity, with medium changes every 24 hours. Mouse tumours were generated from MOC1 cells and tongue fibroblasts, while human tissue slices were derived from head & neck squamous cell carcinoma (HNSCC) HPV-positive tumours. The slices were cultured for 96 hours, and samples were fixed every 24 hours for analysis. The structural integrity of the slices was assessed using H&E staining. With this method, we were able to maintain slice integrity for at least 3 days. After longer periods of *ex vivo* culture, the tissue structure became less intact (**Figure 5.10**).

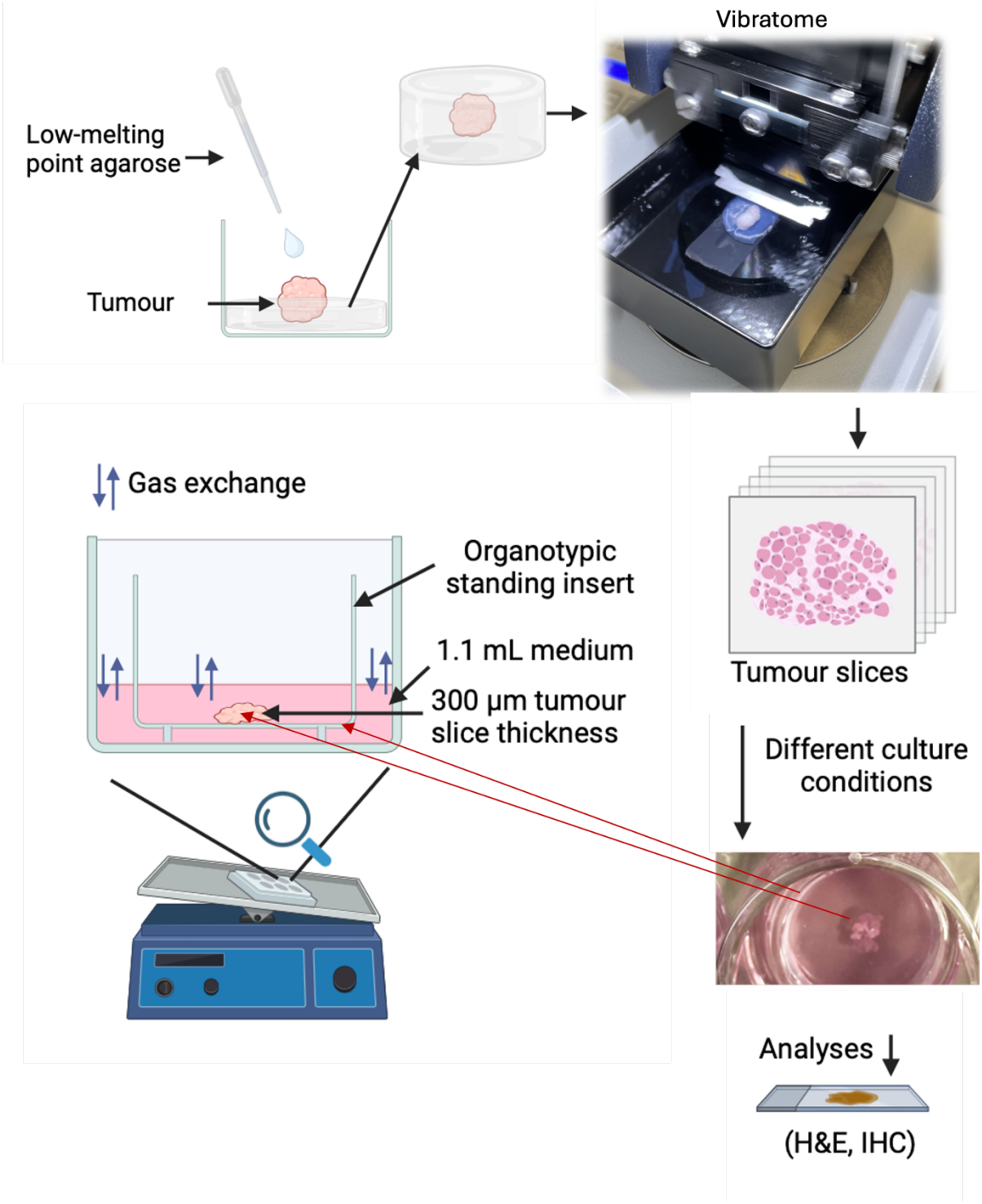

Figure 5.9: Diagram depicting the workflow of tissue slice model culture and analysis. Tumour samples were embedded in 4% low-melting point agarose. Slices were prepared using a vibratome, producing 300 µm thick sections. These slices were carefully collected with a thin brush and transferred onto 0.4 µm organotypic inserts placed in 6-well plates containing 1.1 mL of complete medium. The tissue slices were maintained on a plate shaker in a humidified incubator at 37°C with 5% CO_2. The medium was refreshed every 24 hours. At designated timepoints, slices were fixed in 4% PFA for H&E staining and IHC analysis.

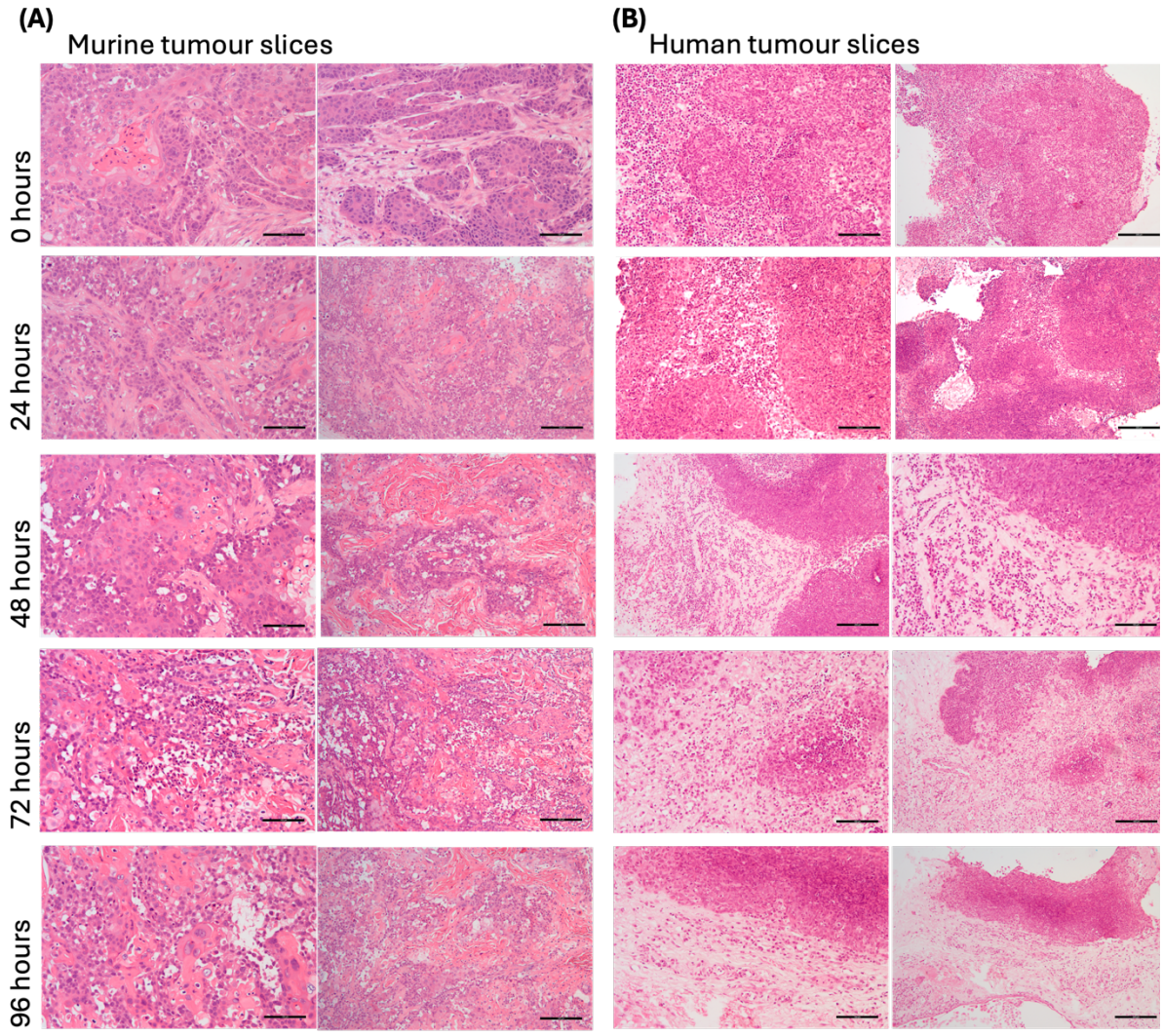

Figure 5.10: Structural integrity of mouse and human tumour slices. (A) Representative images of H&E-stained mouse tissue slices at the indicated timepoints. Mouse tumours were generated from MOC1 cells and tongue fibroblasts. **(B)** Representative images of H&E-stained human tissue slices at the indicated timepoints. Human tissue slices were derived from HPV-positive HNSCC tumours. Scale bars = 100 µm or 200 µm, as indicated.

Human tissue slices appeared structurally preserved at all five timepoints between 0 and 96 hours. Immunohistochemistry staining was performed using a selected panel of antibody markers. Pan-cytokeratin (CK) was used as an epithelial cell marker, and staining with this antibody was consistent across all timepoints, further supporting the findings from H&E staining (**Figure 5.11A**). Additional markers included FOXP3 for regulatory T cells (**Figure 5.11B**), CD68 for macrophages (**Figure 5.11C**), and CD8 for cytotoxic T cells (**Figure 5.11D**). The results indicate the presence of immune cells up to 96 hours of incubation, suggesting that immune cells are preserved under the selected culture conditions. This preservation of immune cells allows for more physiologically relevant assessment of drug effects, as it better reflects *in vivo* tumour conditions.

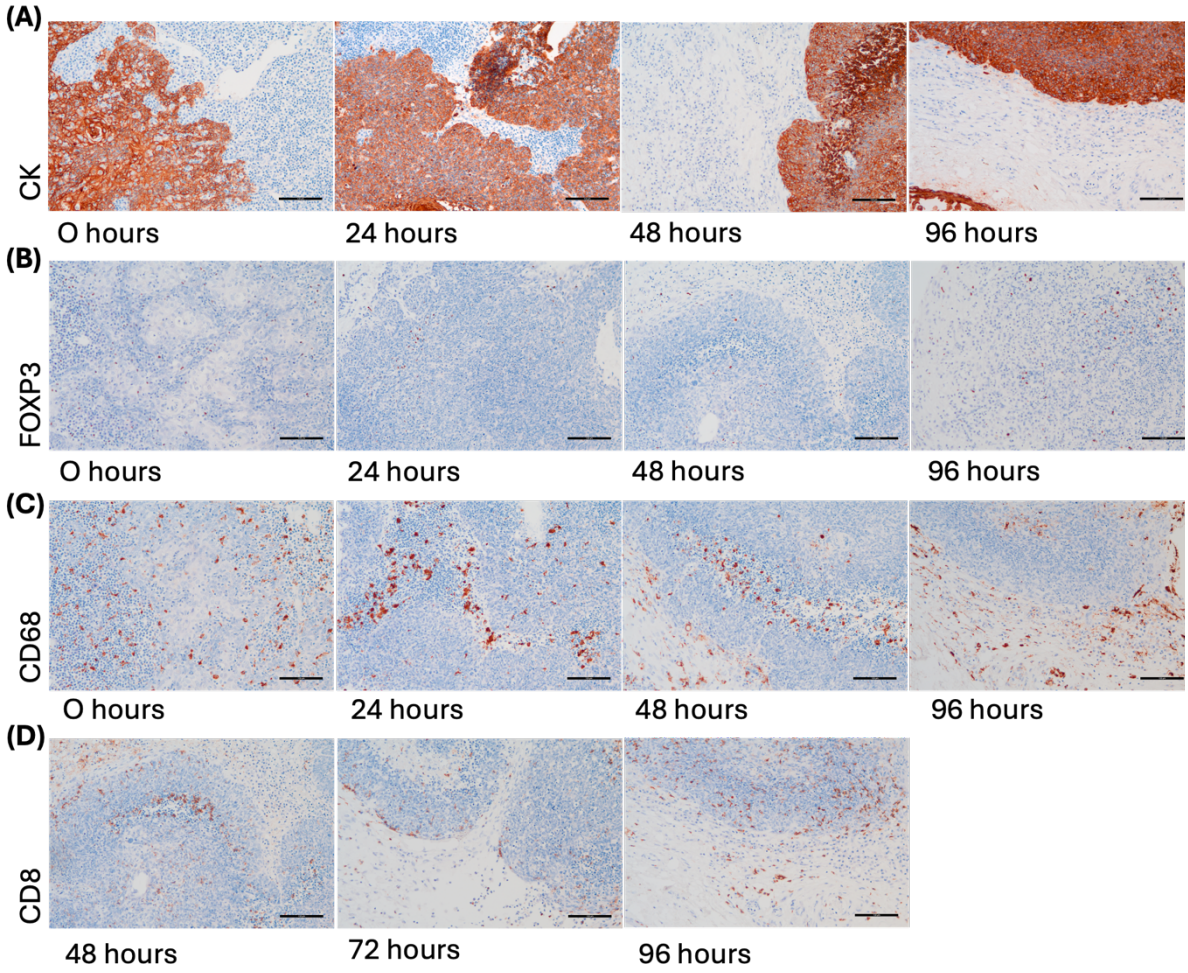

Figure 5.11: Immunohistochemistry of immune and epithelial cells in tumour slices. HNSCC HPV-positive tumour slices were cultured for up to 96 hours and fixed in 4% PFA every 24 hours. **(A)** Pan-cytokeratin (CK), an epithelial cell marker, was used to visualise tumour islands, which remained structured after 96 hours of *ex vivo* culture. **(B)** FOXP3 staining was used to visualise regulatory T cells. **(C)** Immunohistochemical staining of CD68 to identify macrophages. **(D)** Immunohistochemical staining of CD8 T cells. Scale bars = 100 µm or 200 µm, as indicated.

Furthermore, we treated HNSCC HPV-negative human tissue slices with the ATM inhibitor to assess whether there were any obvious alterations in structural integrity. Our preliminary results indicated that after a 48-hour treatment with 0.5 µM AZD0156, the tumour islands appeared more disrupted compared to the untreated controls (**Figure 5.12**). Overall, we have demonstrated that our *ex vivo* tissue slices preserve their 3D architecture and can be utilised as a platform for novel drug screening.

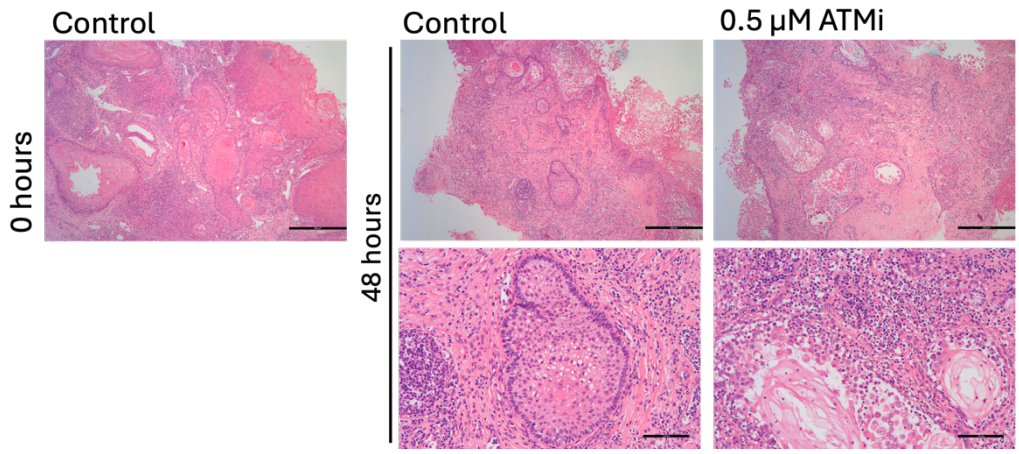

Figure 5.12: Structural integrity of human tumour slices after treatment with AZD0156. Representative images of H&E staining performed on HNSCC HPV-negative tumour slices treated with 0.5 µM AZD0156 for 48 hours prior to fixation and staining. Scale bars = 100 µm or 500 µm, as indicated.

5.3 Discussion

Recent research advancements have deepened our understanding of the potential role of the cGAS/STING pathway in anticancer therapy (Gan et al., 2022). However, the role of STING-mediated immune responses in CAFs remains poorly understood, warranting further investigation. Our data show that TGF-β1 suppressed both cGAS and STING, while ATM inhibition elevated cGAS levels but unexpectedly further reduced STING expression. The simultaneous downregulation of STING and upregulation of cGAS has not been previously reported. Although direct evidence linking TGF-β1 to STING regulation is limited, one study associated TGF-β1 derived from Tregs to decreased cGAS and STING in multiple myeloma cells, supporting our observation with TGF-β1 (D. Zhang et al., 2024). We did not anticipate the reduction in STING following ATM inhibition, as previous studies have shown that ATM deficiency leads to DNA damage and cytoplasmic DNA accumulation, events that typically activate the cGAS-STING pathway (Härtlova et al., 2015; M. Hu et al., 2021; C. Li et al., 2024; X. Song et al., 2019). Consistent with previous studies, ATM inhibition increased cGAS expression regardless of TGF-β1, suggesting that cGAS-STING regulation in CAFs is complex. As a key component of the immune system, cGAS detects cytosolic DNA and activates STING by producing the second messenger cGAMP, which then triggers the production of type I interferons and other inflammatory cytokines (Q. Chen et al., 2016; T. Li & Chen, 2018). This cascade can enhance antitumour immunity by stimulating dendritic cell maturation, promoting T cell chemotaxis, enhancing the cytotoxic functions of $CD8^+$ T cells, and facilitating the infiltration and activation of NK cells. It also supports the polarisation of macrophages toward an M1 phenotype, linking the presence of these immune cells to suppressed tumour growth (Lam et al., 2021; Marcus et al., 2018; Wheeler & Unterholzner, 2023; M. Zhu et al., 2023; Zitvogel et al., 2015). Yet, chronic activation of the cGAS-STING pathway may also support tumour progression by promoting the infiltration of immunosuppressive cells, facilitating EMT that enhances cancer cell migration and invasion, and inducing persistent inflammation through the production of a SASP (Gan et al., 2022; Z. Liu et al., 2023; Y. Zhang et al., 2024). Short-term exposure to the SASP promotes the recruitment of immune cells that eliminate pre-malignant and senescent cells, thereby preventing tumorigenesis. However, prolonged SASP exposure may lead to chronic inflammation, which in turn can drive tumorigenesis (Coppé et al., 2010; Loo et al., 2019). Our results suggest that myCAFs, in the presence of TGF-β within the TME, may help mitigate long-term chronic inflammation by downregulating STING expression which could be beneficial. Furthermore, studies have shown that cGAS-deficient mice are more susceptible to colitis-associated colon cancer compared to mice lacking STING or the type I interferon receptor. These findings indicate that cGAS suppresses colon inflammation and tumorigenesis (S. Hu et al., 2021). Given that cGAS plays a protective role, the elevated levels of cGAS observed in our study after ATM inhibition

could be associated with antitumour functions. Nevertheless, the nature of the cGAS-STING pathway in cancer appears to be context-dependent (Couillin & Riteau, 2021; J. Li & Bakhoum, 2022). Although the pathway holds promise as a target for cancer immunotherapy, its clinical application remains challenging, as STING agonists in clinical trials have shown limited efficacy (Wheeler & Unterholzner, 2023; Ying et al., 2024). Given that our results show decreased STING yet elevated cGAS levels following ATM inhibition, the net impact on TME inflammation remains uncertain.

Neither TGF-β1, ATM inhibition, nor STING affected the regulation of pTBK1 and IRF3, key effectors of the cGAS-STING pathway that drive IFN-I production. These findings suggest that alternative pathways may be compensating to sustain TBK1 activation (Lannoy et al., 2021; Ujevic et al., 2024). Because our mRNA analysis of IRF3 does not reveal its activity, we next examined type I interferons and ISGs. In cancer cells, previous studies have shown that ATM deficiency upregulates STING and induces the expression of ISGs and inflammatory cytokines. Genes induced by ATM deficiency include IFIT1, ISG15, CCL5, CCL2, CXCL10, and IL6 (Chiu et al., 2023; M. Hu et al., 2021; C. H. Huang et al., 2023). Our work expands on these findings by examining how the expression of ISGs and inflammatory cytokines is modulated in fibroblasts in the presence and absence of STING, ATM activity, and TGF-β1, providing novel insights into the complex interplay that shapes the inflammatory environment. In WT myofibroblasts, TGF-β1 suppressed IRF1, IFIT1, ISG15, CCL2, CCL5, and CXCL10. Among these, ISG15, CCL2, CCL5, and CXCL10 were upregulated by ATM inhibition. By contrast, in STING KO myofibroblasts, TGF-β1 suppressed IRF1, IFIT1, CCL2, and CXCL10, and only CCL2 was upregulated by ATM inhibition. Basal levels of ISG15 and CCL5 were lower in STING KO MLFs, while CCL2 was higher. These findings suggest that STING is necessary to sustain ISG15 expression. We hypothesise that in WT cells, STING enhances interferon signalling, which is then suppressed by TGF-β1, resulting in lower ISG15 expression. Whereas in the absence of STING, interferon signalling is already weaker, leading to lower basal levels of ISG15 and no additional effect from TGF-β1. Interestingly, in WT MLFs, ATM inhibition upregulated ISG15 both in the presence and absence of TGF-β1, consistent with findings in cancer cells. However, in STING KO MLFs, ATM inhibition resulted in downregulation of ISG15, suggesting that STING is required to sustain ISG15 expression. This observation has not been previously reported and remains to be fully understood. Regarding inflammatory cytokines, TGF-β1 suppressed CCL2 in both cell types. This is consistent with previous findings in mammary fibroblasts, where TGF-β signalling inhibited CCL2, reducing tumour-associated macrophage recruitment and metastasis (C. Y. Chen et al., 2017). Basal CCL2 levels were higher in STING KO fibroblasts, possibly due to compensatory pathway activation (C. Y. Chen et al., 2017; X. Hu et al., 2021; Nakatsumi et al., 2017). ATM inhibition increased CCL2 in both cell types, indicating that it may be promoting inflammatory properties of CAFs, in line with observations in cancer cells. Similarly, in WT myofibroblasts, CCL5 was

suppressed by TGF-β1 and increased by ATM inhibition. However, in STING KO MLFs, CCL5 was diminished and unaffected by treatments, highlighting STINGs role in its regulation (Zeng et al., 2021). Furthermore, our results show that TGF-β1 suppressed CXCL10 expression in both cell types. Notably, ATM inhibition normalised CXCL10 expression in WT myofibroblasts; although an upward trend was observed in STING KO myofibroblasts, it did not reach statistical significance. One possible explanation is that CXCL10 is predominantly induced by IFN-γ (type II interferon), with a lesser contribution from type I interferons (IFN-I) (Dufour et al., 2002; Lurie & Platanias, 2005; Makuch et al., 2022). In the absence of STING, the contribution of IFN-I may be reduced, resulting in lower CXCL10 upregulation. Collectively, these data indicate that STING influences the expression of interferon-stimulated genes and those affected by interferon signalling. In the absence of STING, lower levels of CCL5 and CXCL10, both of which are involved in $CD8^+$ T cell trafficking, suggest that STING knockout contributes to immunosuppressive environment.

Our findings from studies on WT MLFs suggest that ATM inhibition promotes the iCAF phenotype. We further investigated whether STING affects the expression of selected inflammatory genes. Our data confirm that STING does not modulate the expression of the IL-6, IL-11, and LIF iCAF markers. In line with our previous analyses, ATM inhibition tended to upregulate these iCAF markers, indicating that ATM activity normally limits inflammation. For the first time, we report that STING is required for the regulation of CXCL12 expression. CXCL12, an iCAF derived chemokine is immunosuppressive and contributes to immune exclusion (Y. H. Du et al., 2021; Feig et al., 2013). Although its expression was not modulated by either TGF-β1 or ATM inhibition, we show that STING is necessary to sustain CXCL12 levels in fibroblasts, as evidenced by the diminished expression observed in its absence. Finally, the FRC-like CAF marker CCL19 has been shown to be induced by STING in previous studies (Adachi et al., 2018; Chelvanambi et al., 2021; Falahat et al., 2023). Our data are consistent with these findings; CCL19 expression was suppressed in STING KO fibroblasts. In these cells, neither TGF-β1 nor ATM inhibition affected CCL19 regulation, whereas in WT fibroblasts, TGF-β1 downregulated CCL19. Given that CCL19 expression is associated with the formation of tertiary lymphoid structures within the TME and with better clinical outcomes (S. Guo et al., 2023), its suppression by TGF-β1 further supports the immunosuppressive role of myofibroblasts.

We also evaluated key ECM genes and confirmed that TGF-β1 upregulated myofibroblastic markers, including several collagens, CTHRC1, POSTN, FN, and αSMA, while ATM inhibition downregulated these genes in both WT and STING KO MLFs. A collagen contraction assay confirmed that STING KO MLFs are contractile when differentiated into myofibroblasts, and that ATM inhibition reduces this contractility. In Chapter 3, we demonstrated that ATM inhibition in myofibroblasts elevated levels of TGF-β1 and NOX4, both known to promote the myofibroblastic phenotype. Based on these findings, we investigated this further. The transcription factor NF-κB

regulates genes involved in inflammation, immune responses, and oxidative stress (Gao et al., 2022; T. Liu et al., 2017; McKay & Cidlowski, 1999). Studies suggest that NF-κB can upregulate NOX4 expression and that STING contributes to NF-κB activation (Q. Chen et al., 2016; J. Li et al., 2023; Manea et al., 2010; Sciarretta et al., 2013). At a 6-day timepoint, our data indicate that STING KO fibroblasts have lower basal NOX4 expression, possibly because the absence of STING reduces NF-κB signalling. No differences in TGF-β1 expression were found between the two cell types. Interestingly, TGF-β1 treatment elevated NOX4 expression in STING KO fibroblasts, an effect not evident in WT MLFs. When we examined earlier timepoints, we observed that NOX4 levels increased simply due to cell culture conditions. Consistent with the literature, culturing cells on stiff plastic surfaces upregulates myofibroblastic markers through mechanotransduction (X. Huang et al., 2012). A 24-hour TGF-β1 treatment upregulated both TGF-β1 and NOX4 expression, and the duration of culture at the selected timepoints did not further influence their levels. This confirms that TGF-β1 is a strong inducer of the myofibroblastic phenotype; once cells transition to this state, additional TGF-β1 stimulation sustains rather than further increases TGF-β1 and NOX4 expression. Furthermore, our study highlighted that TGF-β1 levels were unaffected by ATM inhibition in either WT or STING KO MLFs. However, NOX4 expression was elevated following ATM inhibition regardless of STING status, though this increase was observed only in the presence of TGF-β1 and only after 6 days of treatment. Our results indicate that ATM inhibition does not immediately lead to higher NOX4 levels; rather, it is likely that NOX4 accumulates gradually due to impaired regulatory mechanisms.

Overall, our data indicate that following ATM inhibition, myofibroblasts enter a transitional state, characterised by downregulation of myCAF markers, upregulation of iCAF markers, and simultaneous induction of certain ISGs. Given that the cGAS-STING pathway holds promise as a cancer immunotherapy target, despite the limited efficacy of STING agonists in clinical trials (Wheeler & Unterholzner, 2023; Ying et al., 2024), we further investigated the effects of STING knockout in MLFs in the context of $CD8^+$ T cell infiltration and tumour growth. Based on our mouse tumour models, we found no differences in $CD8^+$ T cell infiltration between tumours containing cancer cells and myCAFs with or without STING knockout. In both conditions, ATM inhibition increased $CD8^+$ T cell infiltration. However, while a significant reduction in tumour size was observed in WT myCAF-rich tumours following ATM inhibitor treatment, this reduction was not significant with STING KO myCAFs. A limitation of our study is that, although immunohistochemistry allowed us to identify the presence of $CD8^+$ T cells in tissue samples, it does not provide information about their functional state or exhaustion. Moreover, we did not assess the impact of STING on other immune cells, such as M1 macrophages or NK cells, that also contribute to tumour regression (Y. L. Yang et al., 2023). Elevated STING expression in cancer cells has been associated with better prognosis in several preclinical models, including liver, colorectal, and gastric cancers (Chon et al., 2019; S. Song et al., 2017; Thomsen et al., 2019). Our

findings indicate that STING expression in myCAFs exerts an antitumour effect, as evidenced by the greater reduction in tumour size in wild-type conditions. This suggests that ATM inhibition may be more effective in tumours with high STING expression in stromal cells. Further investigation is required to elucidate the effects of ATM inhibition on STING in CAFs.

Preliminary results of HNSCC tumour slices treated with the ATM inhibitor show more disrupted tumour islands compared to untreated controls. Previous research suggests that tumour islets serve as zones of faster T cell migration (Bougherara et al., 2015), therefore in the subsequent stages of the tissue slice culture experiments, we would aim to investigate the effects of ATM inhibition on collagen in tumour samples and explore how this correlates with T cell migration. Using 2-photon imaging and second harmonic generation (SHG), we would be able to assess the speed of T cell movement, their distribution within the tissue slices, and how they infiltrate the deeper layers of the tumour. However, due to time constraints, this aspect of the study has not yet been fully explored.

Chapter 6 Mechanisms associated with altering AZD0156 concentrations in MLFs

6.1 Introduction

ATM kinase plays a central role in the DNA damage response by regulating cell cycle progression and DNA repair to maintain genomic stability (Phan & Rezaeian, 2021). Inhibiting ATM improves the efficacy of radiotherapy, chemotherapy, and targeted therapy by disrupting these repair mechanisms, thereby preventing cells from recovering from treatment-induced damage. Consequently, ATM inhibitors are being explored in clinical trials (S. Du et al., 2024). However, while this strategy holds promise, it also presents significant challenges. Because ATM is essential for normal cellular homeostasis, its inhibition not only sensitises cancer cells but can also affect healthy tissues, leading to dose-limiting toxicities (Lee, 2024; Weber & Ryan, 2015). Higlighiting the importance of identifying strategies that maximise therapeutic efficacy while minimising adverse effects.

Beyond its role in DNA repair, emerging evidence suggests that ATM inhibition may have immunomodulatory effects (Lee, 2025). In earlier chapters, our work demonstrated that pharmacological targeting of ATM downregulates the expression of myCAF markers and alters the secretome composition, a transition associated with increased $CD8^+$ T cell infiltration and tumour suppression in mouse models (Mellone et al., 2022). Given that myCAFs play an immunosuppressive role in the TME, further investigation into how ATM inhibition affects this population is of importance.

One key question that remains unanswered is whether lower doses of ATM inhibitors can achieve therapeutic benefits while reducing toxicity risks. Although we have established that AZD0156 is effective at 500 nM *in vitro*, optimising the dosage of this potent inhibitor (Riches et al., 2020), could have significant clinical implications.

In this chapter, we evaluate the effects of lower doses of AZD0156 on key cellular processes and the regulation of myofibroblastic markers. If reduced doses are sufficient to promote immune cell infiltration and suppress tumour growth, this could provide a more balanced approach to ATM inhibition – enhancing antitumour responses while mitigating toxicity in patients.

6.2 Results

6.2.1 Investigating the potency of AZD0156

ATM undergoes rapid autophosphorylation in response to ionizing radiation (IR), a process triggered by DNA damage, particularly double-strand breaks. The greater the DNA damage, the higher the levels of phosphorylated-ATM (pATM) due to increased ATM activation. To validate this in primary MLFs, we exposed cells to increasing doses of IR, measured in Grays (Gy), and assessed ATM and pATM levels before and after irradiation using Western blotting. The results showed a dose-dependent increase in pATM following irradiation, while total ATM levels remained largely unchanged (**Figure 6.1A**). Next, we evaluated AZD0156 activity in MLFs by treating cells with increasing concentrations of this ATM inhibitor for 1 hour prior to irradiation at 10 Gy. Since AZD0156 inhibits ATM autophosphorylation at serine 1981, we collected protein samples 1-hour post-irradiation to assess this effect via Western blotting. Our findings confirm that AZD0156 is a potent ATM inhibitor. A dose of 1 nM was sufficient to significantly inhibit ATM autophosphorylation, and at higher concentrations, pATM was no longer detectable by Westen blot analysis (**Figure 6.1B**). Next, we assessed pATM levels in MLFs treated with TGF-β1 and/or 500 nM AZD0156 for 6 days. Untreated MLFs exhibited low basal levels of pATM, reflecting the background activity of the DNA damage surveillance machinery. TGF-β1 treatment induced pATM activation, suggesting that TGF-β1 can trigger a DNA damage response. AZD0156 reduced pATM levels in both untreated and TGF-β1 treated MLFs (**Figure 6.1C**). At the 6-day timepoint, ATM mRNA levels were also analysed. Both TGF-β1 treatment and ATM inhibition downregulated ATM expression (**Figure 6.1D**). These findings suggest that in response to TGF-β1, cells suppress ATM mRNA to limit excessive protein synthesis while enhancing existing ATM activity through phosphorylation. They also indicate that ATM inhibition triggers ATM mRNA downregulation.

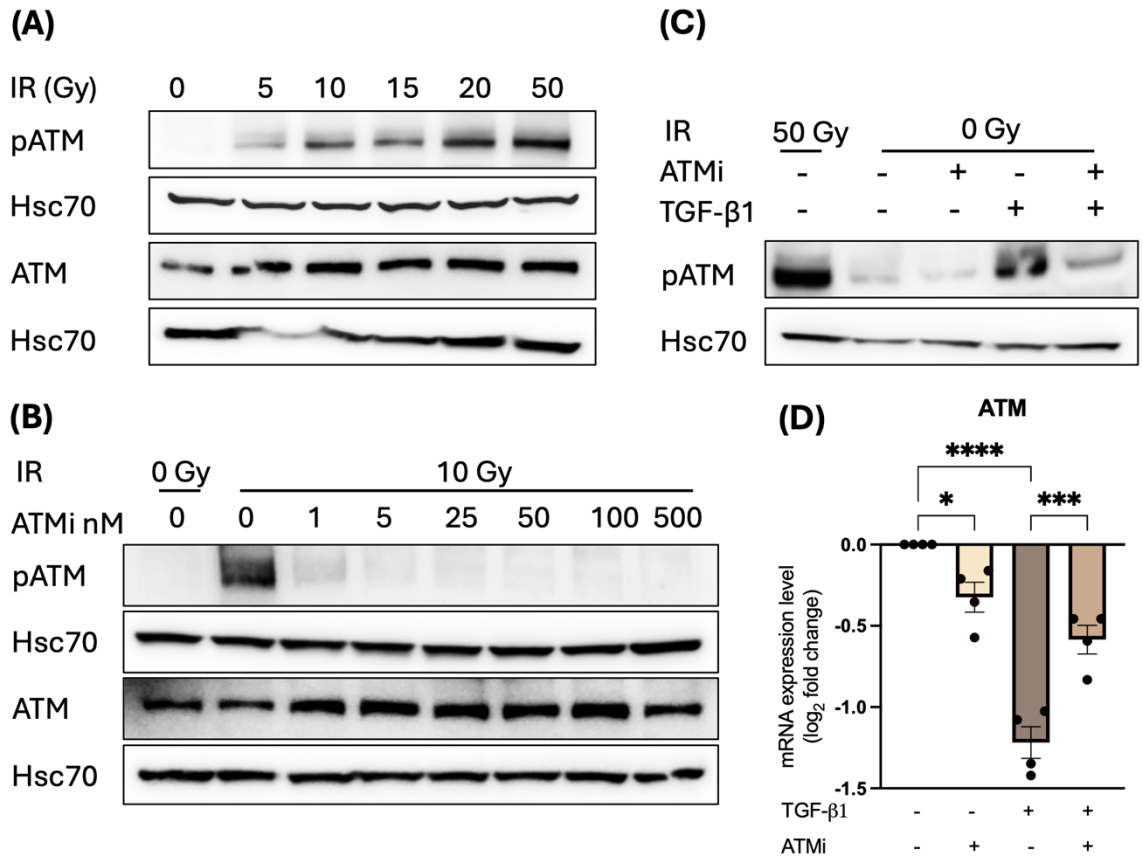

Figure 6.1: AZD0156 inhibits ATM signalling. (A) MLFs were exposed to increasing doses of ionizing radiation (Gy). After 1 hour, cell lysates were generated, and ATM phosphorylation (pATM) and total ATM levels were analysed by Western blotting. Hsc70 served as a loading control. **(B)** MLFs were treated with increasing concentrations of AZD0156 for 1 hour prior to irradiation at 10 Gy. After 1 hour, cell lysates were generated, and pATM and total ATM levels were assessed by Western blotting. **(C)** Western blotting of pATM levels in MLFs treated with TGF-β1 and/or 500 nM AZD0156 for 6 days. **(D)** RT-qPCR analysis of ATM expression in MLFs treated with TGF-β1 and/or 500 nM AZD0156 for 6 days. Data are presented as mean $\log_2$ fold change ± SEM, normalised to untreated controls, with each dot representing an independent experiment. Statistical analysis was performed using one-way ANOVA with Bonferroni correction; *P≤0.05, ***P≤0.001, ****P≤0.0001.

When DNA double-strand breaks occur, ATM activation triggers the phosphorylation of histone H2AX at serine 139, generating γH2AX (pH2AX) (Prabhu et al., 2024). Elevated γH2AX levels indicate DNA damage response activation. Western blot analysis revealed that TGF-β1 induces the DNA damage response by increasing pATM levels. To further investigate, we measured γH2AX levels using immunofluorescence (**Figure 6.2A**). Our results demonstrate that TGF-β1 enhances histone H2AX phosphorylation, indicating DNA damage. Additionally, untreated MLFs exhibited low γH2AX levels. Inhibition of ATM activity with AZD0156 prevented H2AX phosphorylation, leading to reduced γH2AX levels despite TGF-β1-induced DNA damage (**Figure 6.2B**). These findings were further validated by Western blot analysis (**Figure 6.2C**).

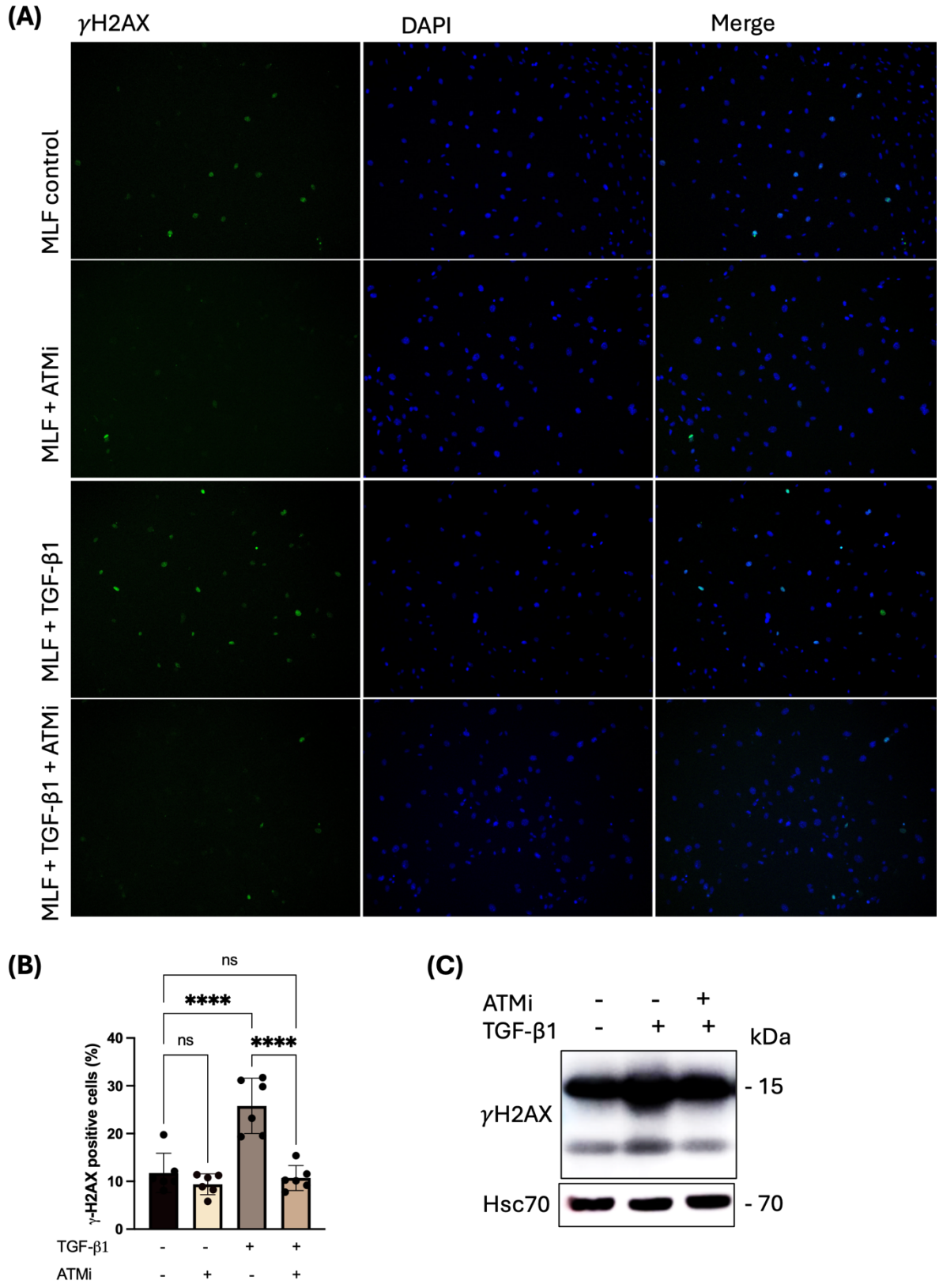

Figure 6.2: AZD0156 prevents the phosphorylation of histone H2AX. (A) Representative images of MLFs treated with TGF-β1 and/or 500 nM AZD0156 for 6 days, showing γH2AX foci (green) and nuclear staining with DAPI (blue). Images were captured using a 10X objective. **(B)** Quantification of γH2AX-positive cells in each condition from six randomly selected fields of view. Data are presented as the mean percentage ± SEM. Statistical analysis was determined using one-way ANOVA with

Bonferroni correction; ****P≤0.0001, ns = not significant. **(C)** Western blotting of γH2AX in MLFs treated with TGF-β1 and/or 500 nM AZD0156 for 9 days. Hsc70 was used as a loading control.

To assess the impact of ATM inhibition on proliferation, we treated MLFs with TGF-β1 and/or 500 nM AZD0156 for 3 and 6 days. This inhibitor concentration was chosen based on previous studies (Mellone et al., 2022) and used earlier in this thesis. Cell proliferation was measured using the MTS assay, with proliferation rates at days 3 and 6 expressed as fold changes relative to untreated controls. TGF-β1 treatment had no effect on cell proliferation at either timepoint. ATM inhibition did not significantly impact proliferation on day 3, but after 6 days, a reduction in cell number was observed (**Figure 6.3A**). This finding was confirmed by manual cell counting using trypan blue staining (**Figure 6.3B**). Western blotting results indicated that AZD0156 at a concentration as low as 5 nM reduced pATM expression to levels comparable to 500 nM. To assess the impact on cell proliferation, we treated MLFs with TGF-β1 and/or a range of AZD0156 concentrations for 3 and 6 days and performed MTS assay. No differences in cell proliferation were observed between untreated, DMSO-treated, and TGF-β1-treated MLFs at either timepoint. On day 3, MTS results showed a reduction in cell proliferation in control MLFs treated with AZD0156 at 25, 50, 100 and 500 nM, as well as in TGF-β1-treated MLFs at 50, 100, and 500 nM concentrations. On day 6, a further reduction in cell proliferation was observed, with significant differences in both untreated and TGF-β1-treated MLFs at ATM inhibitor concentrations as low as 5 nM, increasing up to 500 nM (**Figure 6.3C**). These findings were confirmed by manual cell counting using trypan blue staining (**Figure 6.3D**). However, a lower range of AZD0156 concentrations was tested in this experiment. These findings demonstrate that a concentration as low as 5 nM is sufficient to diminish ATM activation and reduce cell growth; this could possibly be explained by a decrease in cell proliferation, an increase in cell death, or both. We therefore investigated the effects of lower concentrations of AZD0156 on MLFs.

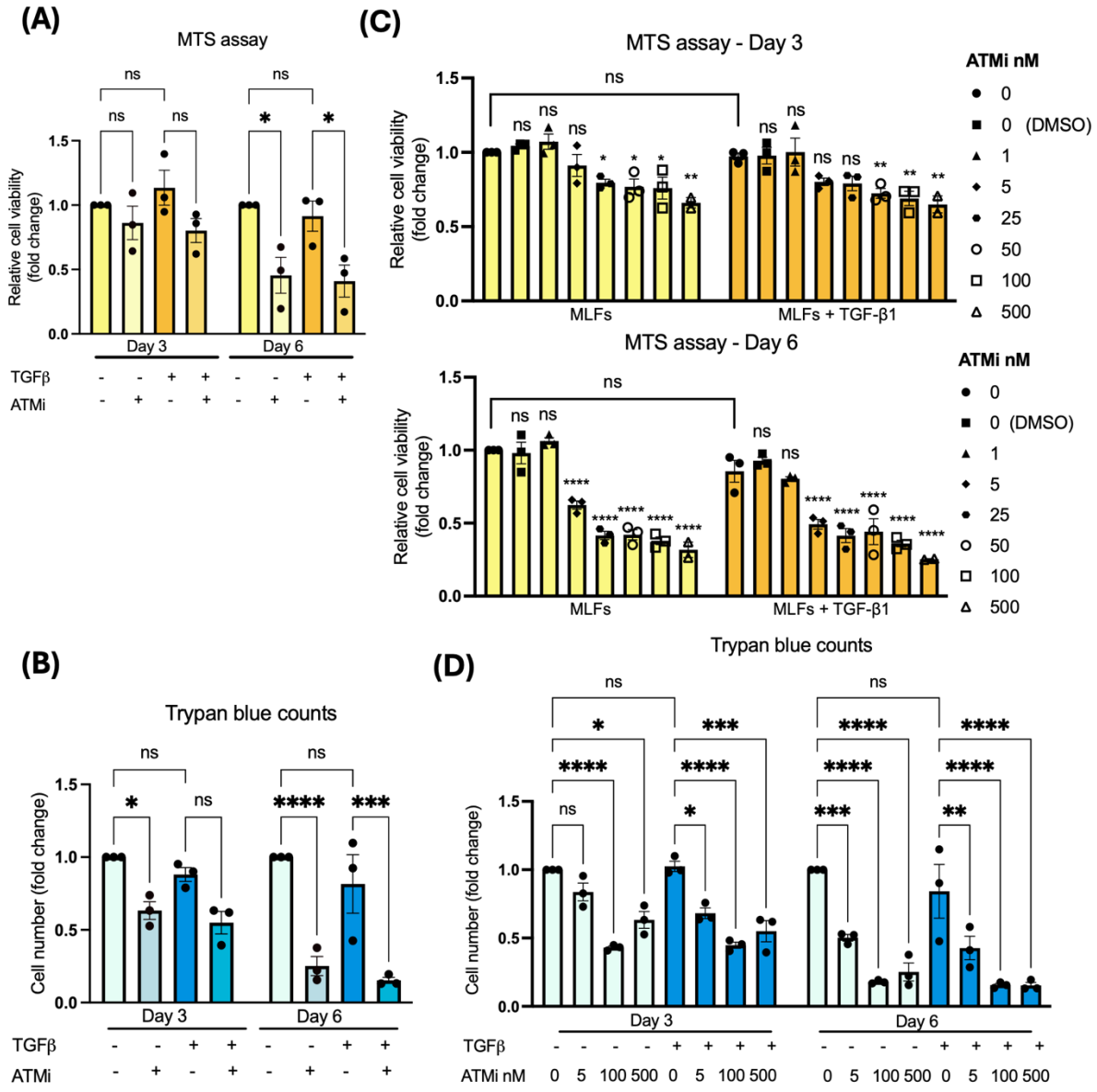

Figure 6.3: Effects of different ATMi concentrations on MLF proliferation. (A,C) MTS assay measuring MLF proliferation rates following treatment with various concentrations of AZD0156, with or without TGF-β1 on days 3 and 6. **(B,D)** Trypan blue counts of live MLFs treated with various concentrations of AZD0156, with or without TGF-β1 on days 3 and 6. For all panels, data are presented as mean fold change ± SEM, normalised to untreated controls, with each data point representing an individual experiment. Statistical analysis was performed using two-way ANOVA with Bonferroni correction; *P≤0.05, **P≤0.01, ***P≤0.001, ****P≤0.0001, ns = not significant.

First, we used flow cytometry to quantify the effect of ATM inhibition on MLF cell death and myofibroblast differentiation. MLFs were treated with TGF-β1 and/or 5 nM or 100 nM AZD0156 for 6 days before staining. Zombie dye was used as a viability marker in flow cytometry to distinguish live from dead cells. Our results show no differences in cell viability between untreated and TGF-β1-treated MLFs. Additionally, 5 nM AZD0156 did not induce statistically significant cell death in either control or TGF-β1-treated MLFs. However, treatment with 100 nM AZD0156 resulted in approximately 20% higher cell death in both control and TGF-β1-treated MLFs, though statistical significance was only observed in control MLFs. Despite the lack of statistical significance in some conditions, a trend toward increased cell death was evident in AZD0156-treated cells (**Figures 6.4A-B**). Next, we investigated whether cell death preferentially occurred within the myofibroblast population, as indicated by αSMA expression. MLFs exhibited high αSMA expression regardless of TGF-β1 treatment; however, ATM inhibition led to αSMA downregulation, consistent with our previous findings. This effect was more pronounced in TGF-β1-treated cells (**Figures 6.4C-D**). Notably, over 98% of live MLFs were αSMA-positive. While 100 nM AZD0156 treatment significantly reduced αSMA expression in live MLFs, the decrease was only approximately 1% (**Figure 6.4E**). Therefore, these findings indicate that ATM inhibition does not selectively induce cell death in αSMA-positive MLFs.

A limitation of Zombie dye staining is that it only distinguishes between live and dead cells. To further characterise cell viability, apoptosis, and necrosis, we used propidium iodide (PI) in conjunction with Apotracker. This approach assesses differences in plasma membrane integrity and permeability. Cells in early apoptosis externalise phosphatidylserine (PS) residues, to which the Apotracker probe binds, while their membranes remain intact, preventing PI from entering. In contrast, late apoptotic and necrotic cells have compromised membranes, allowing both Apotracker to bind to externalised PS residues and PI to pass through the membrane, intercalate into nucleic acids, and emit red fluorescence (Rieger et al., 2011).

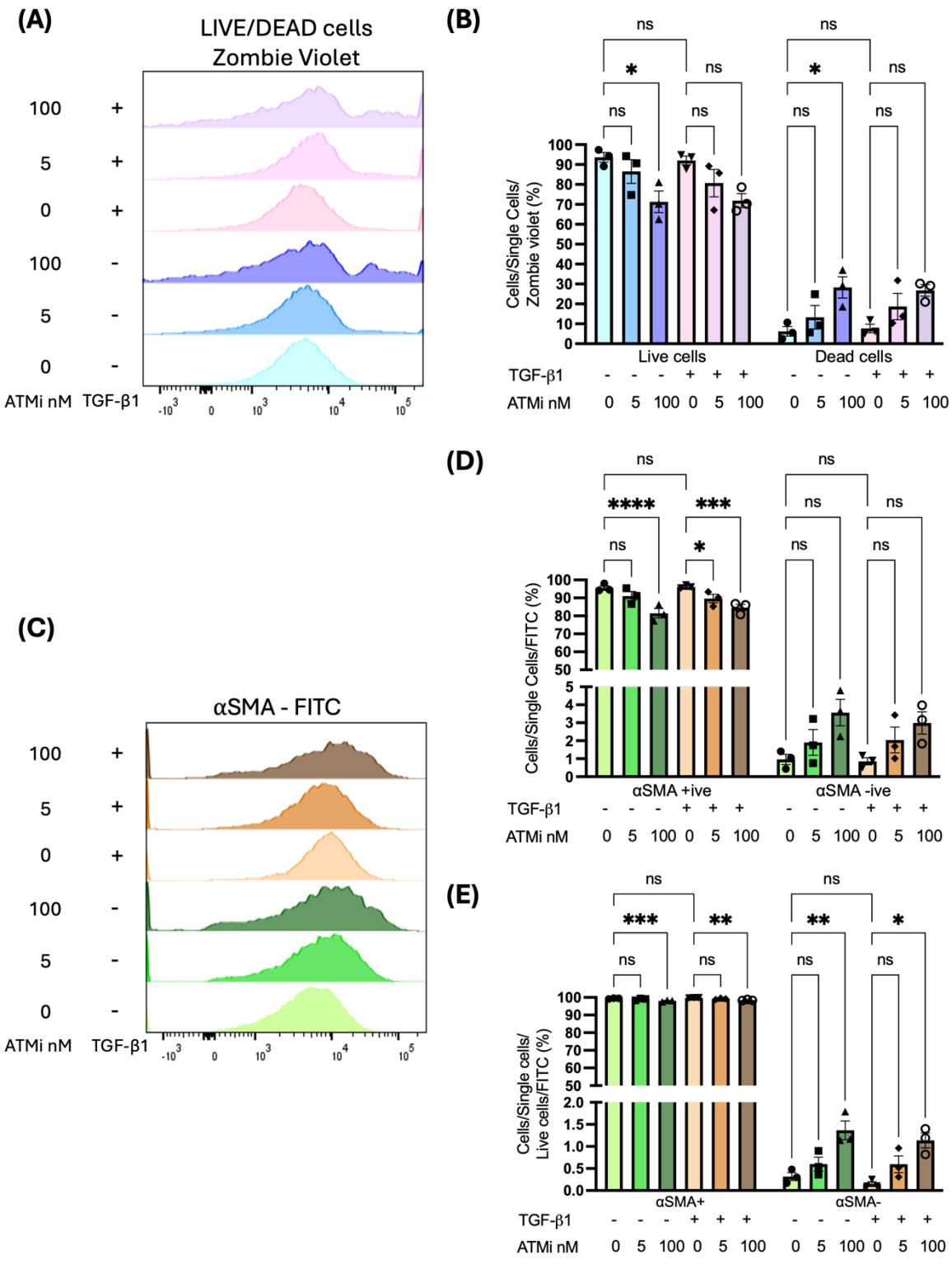

Figure 6.4: Effects of different ATMi concentrations on αSMA-positive MLF viability. MLFs were treated with TGF-β1 and/or 5 nM or 100 nM AZD0156 for 6 days before staining. **(A)** Flow cytometric analysis of live and dead cells using Zombie violet dye. **(B)** Quantification of live and dead cells within single cell populations. **(C)** Flow cytometric analysis of αSMA (FITC) expression under specified conditions. **(D)** Quantification of αSMA expression in single cells based on flow cytometry data. **(E)** Quantification of αSMA expression in live single cells based on flow cytometry data. All data are presented as the percentage of indicated cell populations, with each data point representing an

independent experiment. Statistical analysis was performed using two-way ANOVA with Tukey's correction; *P≤0.05, **P≤0.01, ***P≤0.001, ****P≤0.0001, ns = not significant.

Cells that are PI-positive and Apotracker-negative are fully ruptured, with only the nucleus remaining. This is often observed in highly necrotic samples or mechanically damaged cells. MLFs were treated with TGF-β1 and/or 5 nM or 100 nM AZD0156 for 6 days before staining (**Figure 6.5A**). No statistically significant differences were observed between control and treatment conditions in the proportions of live and necrotic/late apoptotic cells. However, trends show fewer live cells in the TGF-β1-treated condition and an increase in necrotic/late apoptotic cells (**Figures 6.5B-C**). In control MLFs, 5 nM AZD0156 had no effect on the percentages of early apoptotic cell populations, while 100 nM led to an increase; however, this was not statistically significant. In TGF-β1-treated cells, both 5 nM and 100 nM AZD0156 showed a trend for an increase in early apoptotic cells, but statistical significance was observed only at the higher concentration (**Figure 6.5D**).

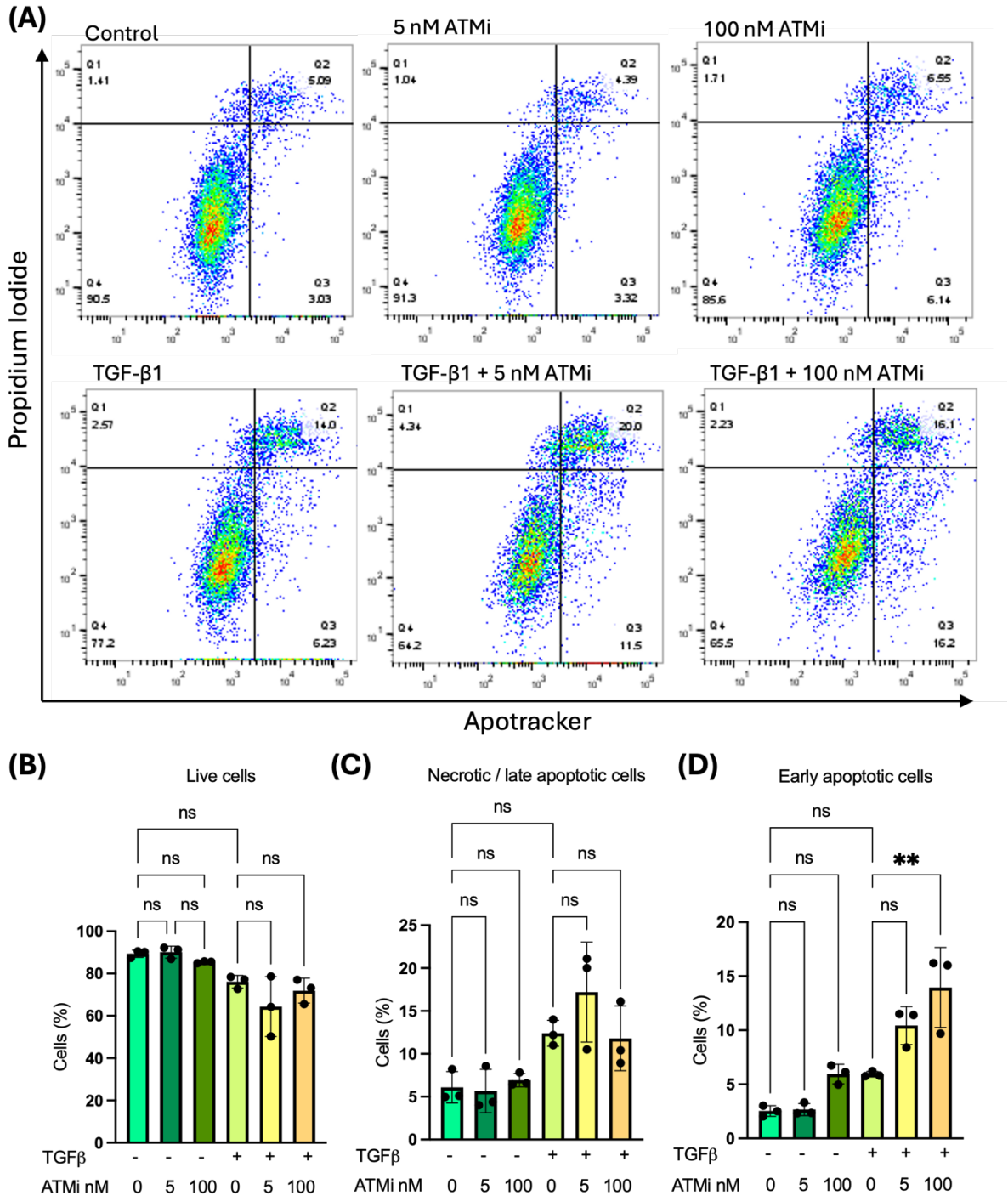

Figure 6.5: Flow cytometry analysis of apoptosis and necrosis in ATM-inhibited MLFs. MLFs were treated with TGF-β1 and/or 5 nM or 100 nM AZD0156 for 6 days prior to cell staining. **(A)** Representative gating strategy for the indicated samples. Q1 corresponds to naked nuclei, Q2 represents necrotic and late apoptotic cells, Q3 corresponds to early apoptotic cells, and Q4 represents the live cell population. **(B)** Quantification of live cells within the single-cell population. **(C)** Quantification of necrotic and late apoptotic cells within the single-cell population. **(D)** Quantification of early apoptotic cells within the single-cell population. All data are presented as the percentage of the indicated cell populations, with each data point representing an independent experiment. Statistical analysis was performed using one-way ANOVA with Tukey's correction; **P≤0.01, ns = not significant.

6.2.2 Effects of ATM inhibition on cell cycle progression

The MTS assay measures metabolic activity, which is often correlated with cell proliferation but is not a direct measure of cell number. One possible explanation for a lower MTS signal is cell death, as supported by our flow cytometry data analysis. However, alternative explanations exist for the reduced metabolic activity observed in AZD0156-treated samples, including slower cell cycle progression. If cells progress more slowly through the cell cycle, they will divide less frequently, leading to reduced overall metabolic activity over the assay period. To investigate this, we first conducted an optimisation experiment to determine whether we could detect changes in cell cycle length and establish the typical cycling duration for primary MLFs. We assessed the effects of a 36-hour treatment with TGF-β1 and/or AZD0156 at 5nM and 100 nM concentrations (**Figure 6.6A**). The cell cycle of MLFs was synchronised by serum starvation, temporarily arresting approximately 90% of cells in the G0/G1 phase. We determined that 48 hours after starvation, 4% more cells were in the G0/G1 phase compared to the 24-hour timepoint (**Figure 6.6B**). However, we selected the shorter starvation period for subsequent experiments, as prolonged starvation in sensitive cells is associated with increased stress or apoptosis. After 24 hours of starvation, serum was reintroduced to allow cells to re-enter the cell cycle, and treatments were administered simultaneously. Cells were collected every four hours, and DNA content at each cell cycle stage was analysed using a PI flow cytometric assay. Our data indicate that cells transition to the S phase between 16 and 20 hours, and by the 24-hour timepoint, they begin transitioning to the G2 phase. At this timepoint, approximately 10% of cells treated with 100 nM AZD0156 appear to remain in the G1 phase, whereas untreated cells and those treated with 5 nM AZD0156 progress through the cell cycle. Between 28 and 32 hours, we observe that untreated cells complete the cell cycle, as indicated by an increasing percentage of cells in the G1 phase and decreasing percentage in the G2 phase. However, cell cycle progression appears slower in MLFs treated with 5 nM ATM AZD0156. The differences in cell cycle progression become more pronounced in MLFs treated with 100 nM AZD0156. At 32 and 36 hours, there are no observed differences in the percentage of cells in the S phase between conditions, nor between untreated and 5 nM inhibitor treated cells. However, cells treated with 100 nM AZD0156 remain in the G2 phase and exhibit lower percentage of cells in the G1 phase. Notably, this effect is less evident in TGF-β1-treated cells (**Figure 6.6C**).

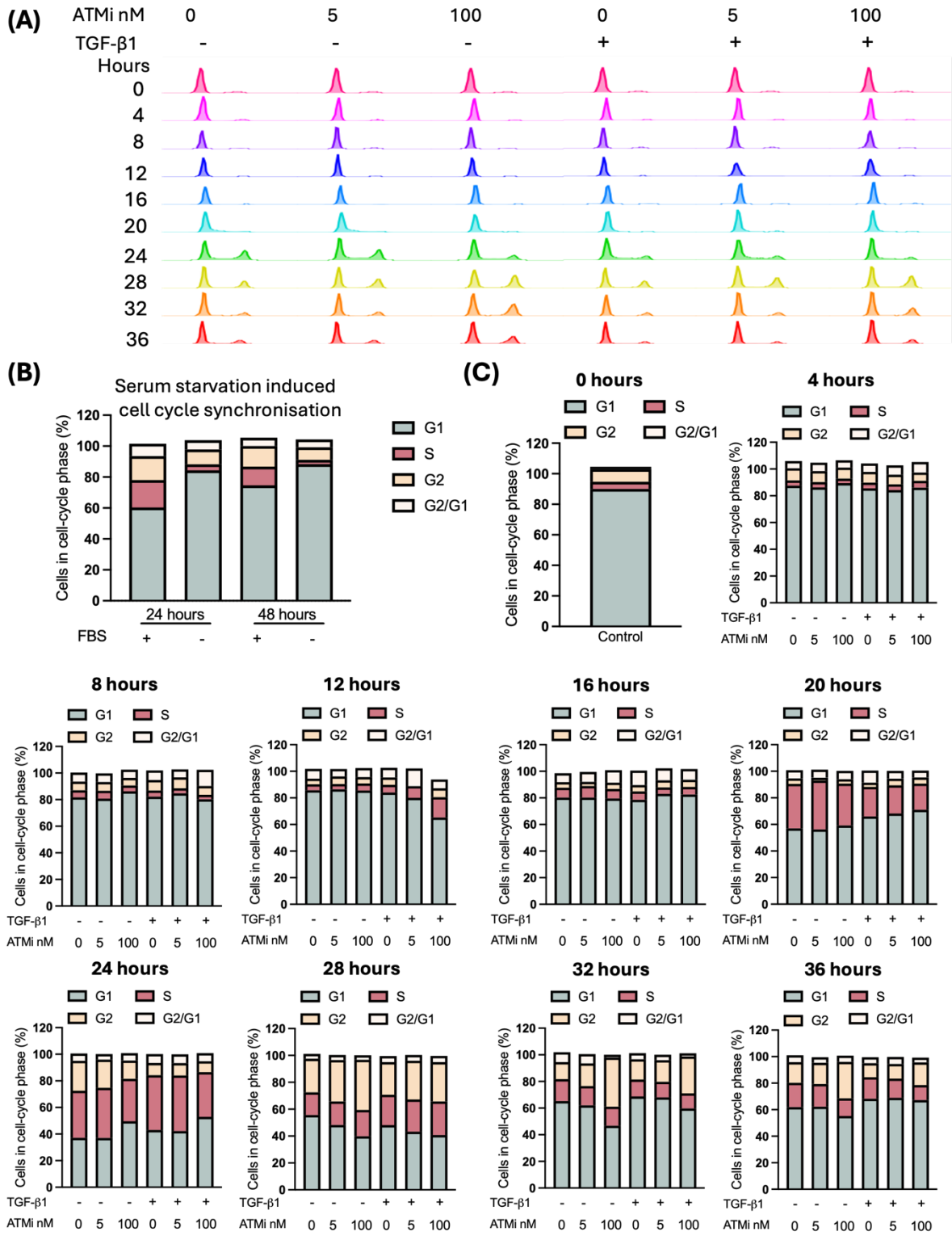

Figure 6.6: Determining the effects of TGF-β1 and AZD0156 on cell cycle duration. (A) Cell cycle histograms showing the effects of a 36-hour treatment with TGF-β1 and/or AZD0156 at 5 nM and 100 nM concentrations following a 24-hour cell synchronisation. **(B)** Quantification of cells in each cell cycle phase after 24-hour and 48-hour serum starvation, along with corresponding controls. **(C)** MLFs were serum-starved for 24 hours, after which serum was reintroduced to allow cells to re-enter the cell cycle. TGF-β1 and/or AZD0156 at 5 nM and 100 nM were administered simultaneously. Cells were collected every 4 hours, and DNA content at each cell cycle stage was analysed using a PI flow cytometric assay. Graphs represent the percentage of cells in each cell cycle phase.

This pilot study demonstrated that ATM inhibition may influence cell cycle progression. To further investigate, we expanded our study by conducting three additional individual experiments. Since we established that MLFs begin entering the S phase between 16 and 20 hours, we collected cells between 12 and 44 hours in this extended study. Our findings up to 32 hours are consistent with those from the pilot study, with cells treated with 100 nM AZD0156 exhibiting a higher percentage in the G2 phase and a lower percentage in the G1 phase. Between 36 and 44 hours, the differences in the G1 phase population of 100 nM AZD0156 treated cells were 1.6% lower at 36 hours, 3.7% at 40 hours, and 6.6% lower at 44 hours compared to the untreated control in the absence of TGF-β1. Similar to our pilot study, the differences in the G1phase population were smaller in TGF-β1-treated cells, with 3% fewer cells in the G1 phase at 36 hours, 0.55% fewer at 40 hours, and 0.63% fewer at 44 hours in the 100 nM AZD0156-treated condition. Between 32 and 44 hours, approximately 10% more control MLFs treated with 100 nM AZD0156 remained in the G2 phase compared to untreated control. However, in TGF-β1-treated cells, the difference in the ATM-inhibited population was approximately 5% compared to TGF-β1-treated controls. Additionally, we did not observe any differences in cell cycle progression between control and TGF-β1-treated MLFs (**Figure 6.7**). Overall, although we observed changes in cell cycle progression, these trends were not statistically significant (**Appendix A Figure 12**). These cell cycle experiments were conducted over 44 hours; however, the MTS assay and trypan blue counts were performed at 3 and 6 days. Based on our analysis, MLFs take approximately 24 to 28 hours to complete a full cycle; therefore, at longer timepoints, multiple divisions would have occurred. Since our standard treatment duration with 500 nM AZD0156 was 6 days, we next assessed the cell cycle at this timepoint. For this experiment, cells were not synchronised, as they had undergone multiple cycles over the 6-day period. We conduced three independent experiments and quantified the cell populations in each cell cycle phase (**Figures 6.8A-B**). Our findings indicate that, in the absence of TGF-β1, ATM inhibition prolongs the G2 phase, with approximately three times more cells in this phase compared to untreated cells. This is also reflected in a significantly lower proportion of cells in the G1 phase, suggesting that MLFs cycle more slowly and enter G1 at a reduced rate. No differences were observed in the percentage of cells in the S phase. Similarly, in TGF-β1 treated MLFs, ATM inhibition prolonged the G2 phase, with approximately twice as many cells in this phase compared to TGF-β1 treated controls. Although fewer cells were found in the G1 phase following ATM inhibition, these differences were not statistically significant. Additionally, no significant differences were observed in the S phase (**Figures 6.8C**). Overall, our results suggest that ATM inhibition in MLFs leads to increased apoptosis and slower cell cycle progression, both of which may explain the metabolic rate changes detected in the MTS assay.

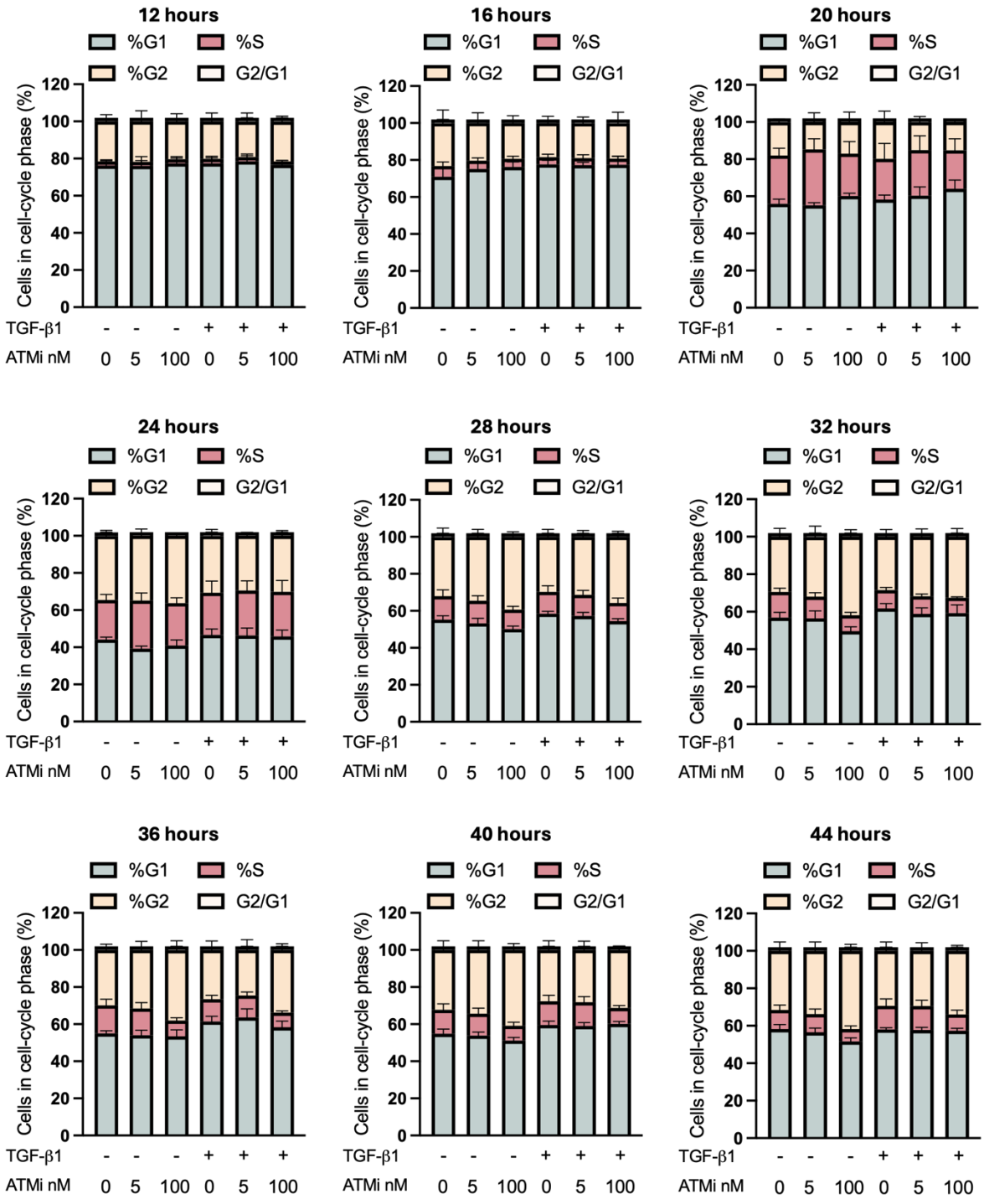

Figure 6.7: ATM inhibition affects cell cycle progression. MLFs were synchronised through a 24-hour serum starvation, after which serum was reintroduced to allow cells to re-enter the cell cycle. TGF-β1 and/or AZD0156 at 5nM and 100 nM were administered simultaneously. Cells were collected every 4 hours, and DNA content at each cell cycle stage was analysed using PI flow cytometric assay. Graphs represent the percentage of cells in each cell cycle phase based on three independent experiments. Statistical analysis was performed using two-way ANOVA with Tukey's correction; significance levels are not indicated, as all observed changes were not statistically significant.

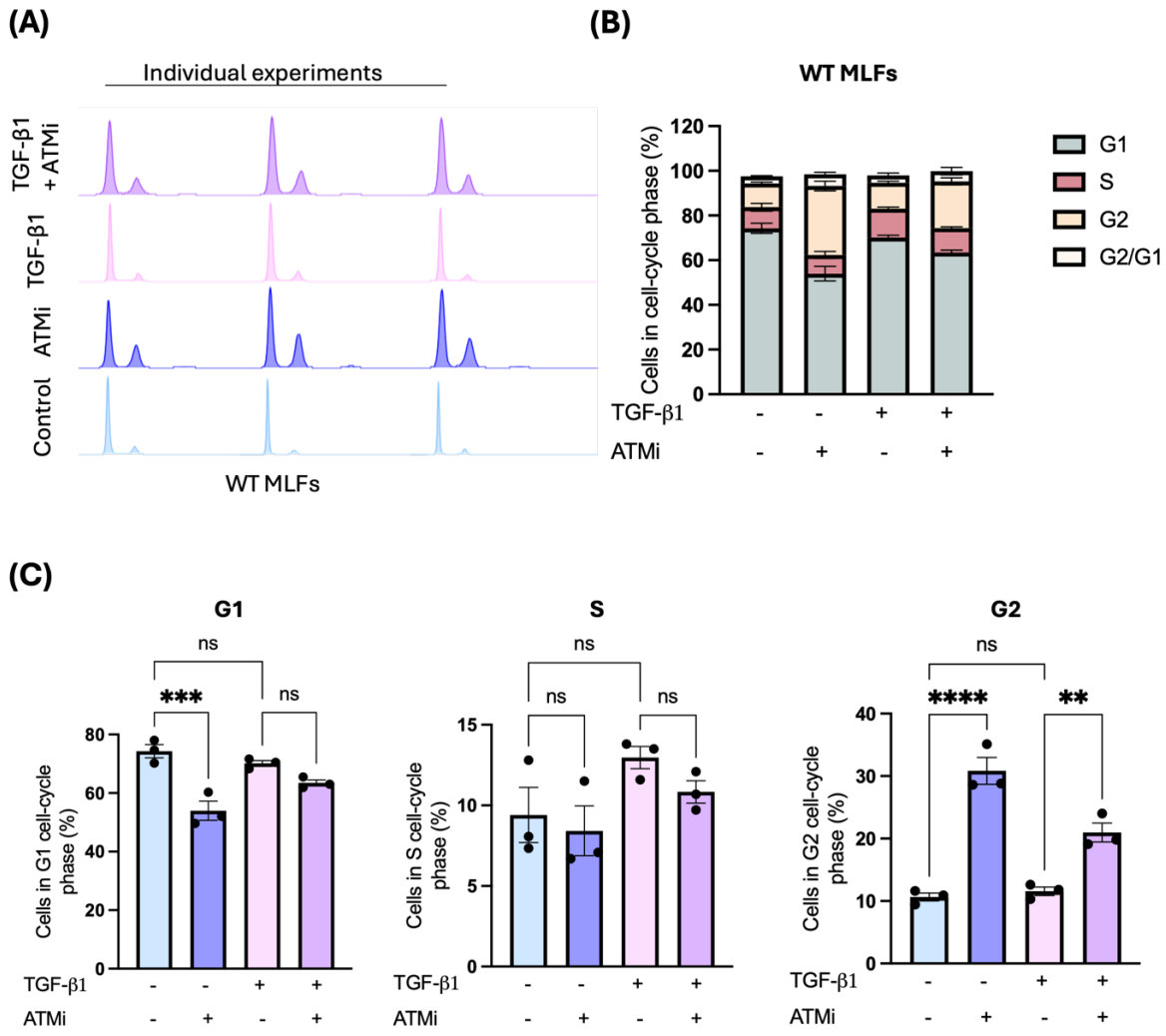

Figure 6.8: ATM inhibition leads to G2 phase accumulation. (A) Cell cycle histograms of MLFs treated with TGF-β1 and/or 500 nM AZD0156 for 6 days, stained with propidium iodide. **(B)** Graph showing the percentage of cells in each cell cycle phase. **(C)** Quantification of cells in each cell cycle phase, with each data point representing an individual experiment. Statistical analysis was performed using one-way ANOVA with Bonferroni's correction; **P≤0.01, ***P≤0.001, ****P≤0.0001, ns = not significant.

EdU (5-ethynyl-2'-deoxyuridine) staining is used to assess DNA synthesis and cell proliferation by labelling newly synthesised DNA during the S phase of the cell cycle. We treated cells with 500 nM AZD0156 for 6 days and performed immunofluorescence to detect EdU-positive cells (**Figure 6.9A**). Our findings demonstrated that TGF-β1 significantly increased the percentage of EdU-positive fibroblasts from 6.3% to 13.7% compared to the untreated cells. However, ATM inhibition blocked this TGF-β1-induced increase in DNA synthesis, reducing EdU incorporation to 3.4%. Additionally, no differences were observed between untreated and ATM-inhibited control fibroblasts (**Figure 6.9B**). Overall, our results indicate that TGF-β1 increases both DNA synthesis

(EdU incorporation) and DNA damage (γH2AX) but does not alter the overall S-phase population in cell cycle analysis. ATM inhibition prevents both TGF-β1-induced γH2AX expression and EdU incorporation.

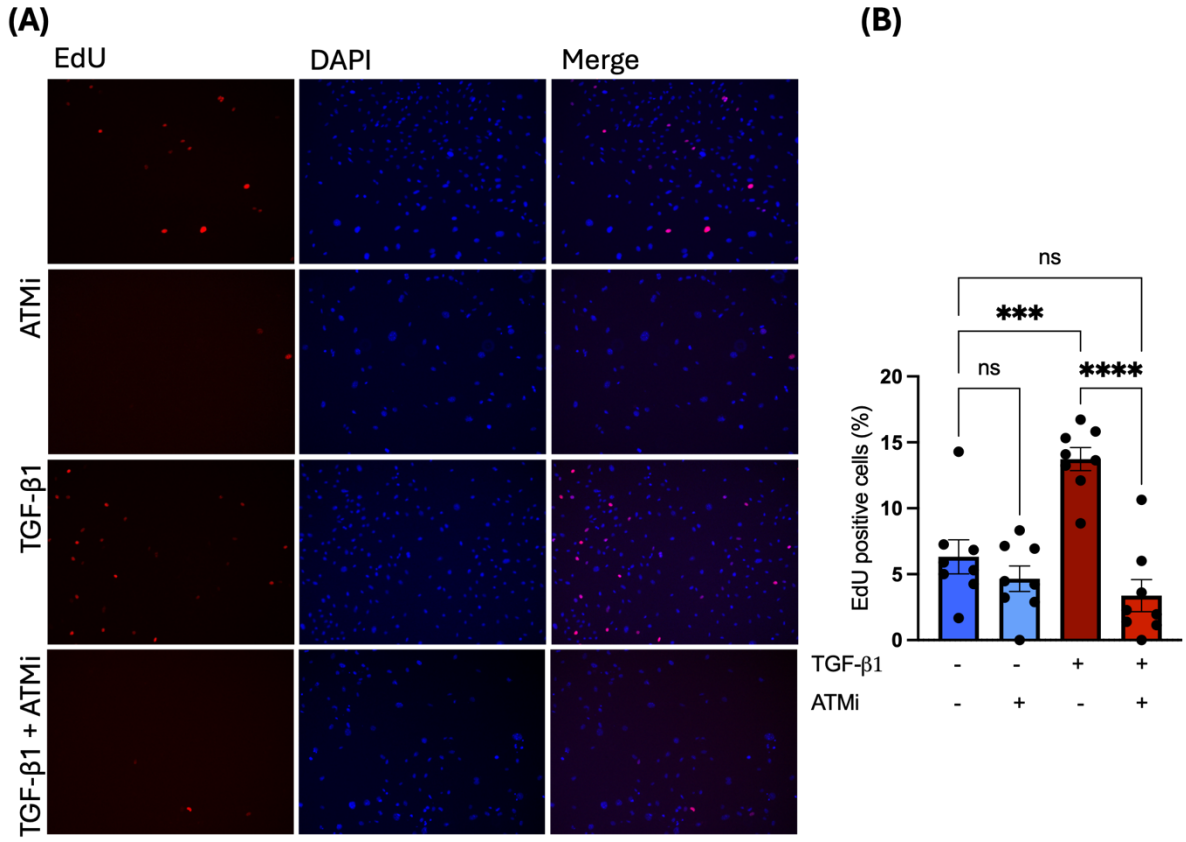

Figure 6.9: TGF-β1 treatment enhances DNA synthesis in MLFs. (A) Representative EdU staining images of MLFs treated with TGF-β1 and/or 500 nM AZD0156 for 6 days (EdU: red, nuclei: blue). **(B)** Quantification of EdU-positive cells in eight random fields of view. Data are presented as mean percentages ± SEM. Statistical analysis was performed using one-way ANOVA with Bonferroni correction; ***P≤0.001, ****P≤0.0001, ns = not significant.

6.2.3 Downregulation of myofibroblastic markers by lower AZD0156 concentrations

Throughout our studies, we have used an AZD0156 concentration of 500 nM. However, based on our recent findings, we sought to investigate whether lower inhibitor concentrations could also lead to the downregulation of myofibroblastic gene expression. To test this, we treated MLFs with various concentrations of AZD0156 in the presence or absence of TGF-β1 for 3 and 6 days and measured mRNA expression levels via RT-qPCR analysis. Consistent with previous findings, TGF-β1 treatment significantly induced the expression of COL1A1, COL11A1, and POSTN on day 3. At this timepoint, ATM inhibition did not result in significant gene downregulation, except for 50 nM AZD0156, which led to a statistically significant reduction in COL1A1 expression (**Figure 6.10A**). On day 6, COL11A1 and POSTN remained significantly upregulated following TGF-β1 treatment, whereas COL1A1 did not show a significant increase. However, based on our previous results, this is likely due to basal levels of COL1A1 increasing in control fibroblasts over time. Our results demonstrate that as little as 5 nM AZD0156 was sufficient to significantly downregulate COL1A1 and COL11A1 expression. While POSTN expression also showed a downward trend, this change was not statistically significant, likely due to the inclusion of fewer data points. Additionally, we observed a dose-dependent effect, where increasing AZD0156 concentrations (1, 5, 50, 100 nM) led to a more pronounced downregulation of COL1A1, COL11A1, and POSTN, although these changes were relatively subtle (**Figure 6.10B**). These findings are consistent with our Western blot results which showed that 5 nM AZD0156 was sufficient to inhibit pATM, whereas at 1 nM, ATM remained active but at a reduced level compared to the untreated control.

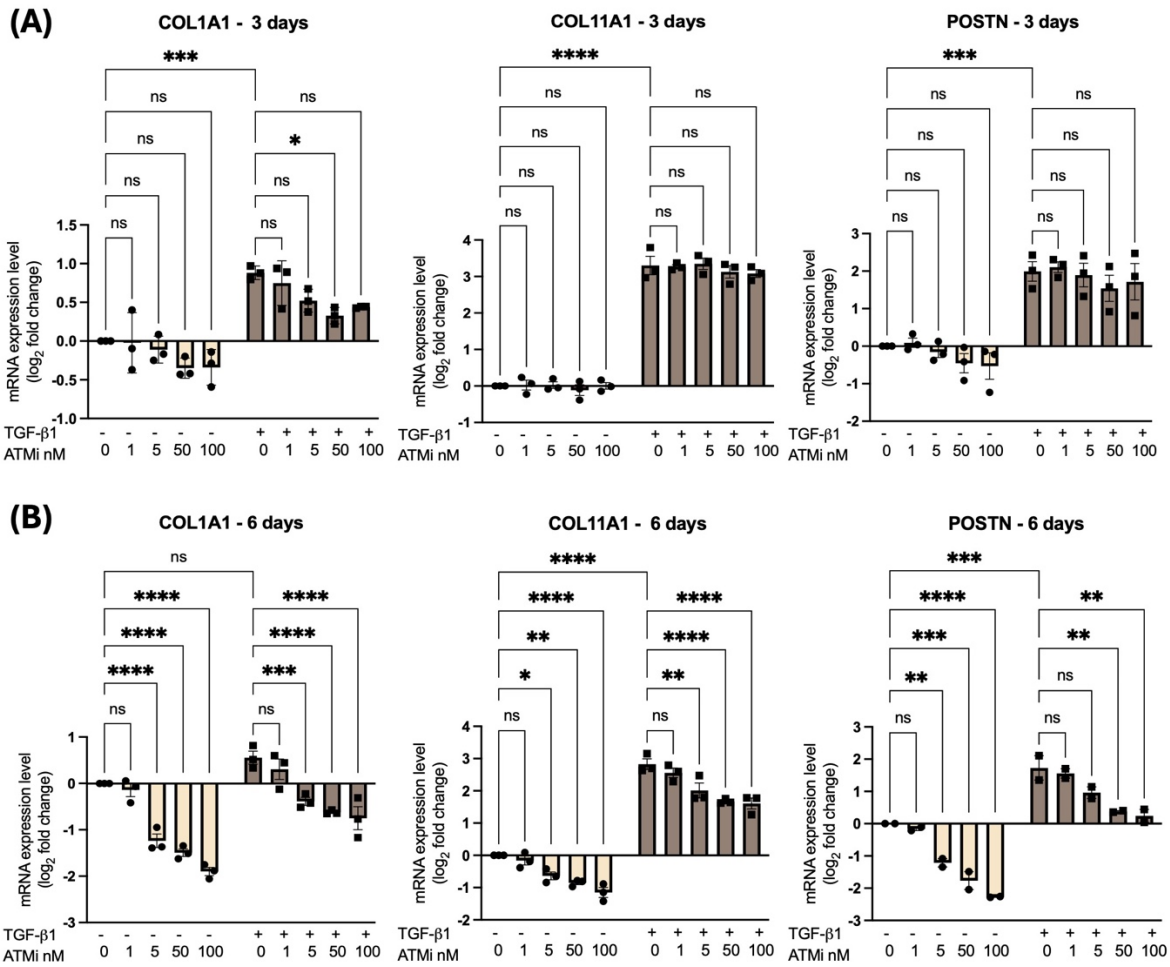

Figure 6.10: AZD0156 regulates the expression of ECM components at low concentrations. (A-B) RT-qPCR analysis of genes associated with the myofibroblastic phenotype and ECM composition in MLFs treated with TGF-β1 and/or the indicated concentrations of AZD0156 for 3 or 6 days. Data are presented as mean log_2 fold change ± SEM, normalised to untreated controls, with each data point representing an independent experiment. Statistical analysis was conducted using two-way ANOVA with Bonferroni correction; *P≤0.05, **P≤0.01, ***P≤0.001, ****P≤0.0001, ns = not significant.

6.3 Discussion

The potency of AZD0156 in fibroblasts was demonstrated in our study, where we showed that a 1 nM dose was sufficient to inhibit ATM autophosphorylation, and at 5 nM pATM was no longer detectable by Western blot analysis. Additionally, we observed that MLFs exhibit low baseline levels of pATM, reflecting the intrinsic activity of the DNA damage surveillance machinery (Alberts et al., 2002; Chatterjee & Walker, 2017). Upon TGF-β1 treatment, DNA damage increased, as evidenced by higher pATM levels and elevated γH2AX. These findings align with previous reports that TGF-β1-induced differentiation in myofibroblasts is associated with the upregulation of multiple genes involved in DNA repair (Hanley et al., 2018). In untreated MLFs, low levels of pATM, γH2AX, and EdU-positive cells suggest minimal DNA damage under basal conditions. In Chapter 5, we demonstrated that cell culture alone elevates NOX4 levels. Given that ROS can activate ATM, this may explain the observed baseline levels of pATM. Additionally, the fibroblast-to-myofibroblast transition, driven by mechanotransduction (Gilles et al., 2020), may contribute to the low baseline DNA damage observed in untreated fibroblasts. Although ATM inhibition reduced pATM levels in fibroblasts, it did not decrease γH2AX. This suggests that baseline DNA damage may be repaired by alternative kinases, as H2AX phosphorylation can also be mediated by ATR or DNA-PKcs (Paull et al., 2000). Such compensation may also explain why ATM inhibition did not alter the percentage of EdU-positive cells. However, this potential compensatory mechanism was not tested experimentally, which is a limitation of this study. Under TGF-β1 stimulation, DNA damage increased. Notably, pATM, γH2AX, and EdU-positive cells were all reduced following ATM inhibition. The reduction in pATM confirms that AZD0156 effectively inhibits ATM activity. However, the decrease in γH2AX does not necessarily indicate that DNA damage is resolved; rather, the damage may persist but remain undetected due to the loss of ATM-dependent signalling. This suggests that in myofibroblasts, ATM is the primary kinase responsible for H2AX phosphorylation. Furthermore, ATM inhibition in myofibroblasts led to a reduction in the percentage of cells in S-phase, as indicated by the decrease in EdU-positive cells. This reduction in S-phase entry could contribute to the lower γH2AX levels, since fewer replicating cells would generate fewer replication-associated DNA breaks. Our cell cycle analysis supports this hypothesis; untreated fibroblasts and myofibroblasts complete the cell cycle more quickly, resulting in a higher proportion of cells in S-phase at any given time. In contrast, a higher concentration of ATM inhibitor (100 nM) reduced the proportion of cells in S-phase between 32 and 44 hours, although this difference was not statistically significant. After 144 hours of ATM inhibition, a significant reduction in the S-phase population was not observed, though a downregulation trend was evident. Interestingly, ATM inhibition led to increased proportions of cells in G2 phase. The G2 checkpoint delays entry into mitosis when DNA damage is detected, allowing time for repair or triggering apoptosis if the damage is irreparable (M. G. M. Khan & Wang,

2022; Stark & Taylor, 2004). This checkpoint is regulated by multiple signalling pathways, including those involving ATR and ATM (Reinhardt & Yaffe, 2009). One explanation for the prolonged G2 arrest in the presence of ATM inhibitor could be compensatory DNA repair by ATR when normal ATM-mediated repair is impaired (Mladenov et al., 2019). Prolonged G2/M accumulation was also observed in cells from patients with ataxia-telangiectasia, which further supports our findings (J. H. Hong et al., 1994). Additionally, since ATM contributes to G1 checkpoint control by slowing cell cycle progression in response to DNA damage (F. Li et al., 2022), the reduction in the proportion of cells in G1 phase observed after 6 days of ATM inhibition, significant in fibroblasts but not myofibroblasts, might be due to a failure to properly arrest in this phase. Without ATM, damaged cells may enter S-phase more readily, thereby reducing the number of cells in G1.

ATM and ATR are kinases that activate the checkpoint kinases Chk2 and Chk1, respectively, in response to DNA damage (Smith et al., 2010). Once phosphorylated, these checkpoint kinases trigger cell-cycle arrest, allowing time for DNA repair. However, if the DNA damage is too extensive, cells may instead undergo senescence or cell death (De Zio et al., 2013). Our cell cycle analyses showed that ATM inhibition increased the proportion of cells in G2 phase, suggesting that cells arrested in G2 may eventually undergo apoptosis rather than completing mitosis. We assessed cell viability using Zombie staining and propidium iodide (PI) staining, but our results appeared somewhat contradictory. With Zombie staining, we observed no differences in viability between fibroblasts and myofibroblasts. There was a trend toward decreased viability with increasing ATM inhibitor concentration, both in absence and presence of TGF-β1; however, this decrease was statistically significant only when comparing untreated fibroblasts to those treated with 100 nM AZD0156. In contrast, when assessing necrosis and apoptosis using PI and Apotracker dye, we did not detect significant differences in the proportions of live, necrotic, or late apoptotic cells. These discrepancies may be attributed to the different staining mechanisms. PI is a DNA-binding dye that only enters cells with compromised membranes, marking late apoptosis and necrosis, whereas Zombie dyes primary bind to amine groups on proteins (Crowley et al., 2016). According to the manufacturer (Biolegend), Zombie dyes bind low levels of surface amines on live cells but more intensely in dead or dying cells as the dye gains access to intracellular amines through compromised membranes. If mid-to-late apoptotic cells in our experimental setup took up increasing amounts of the Zombie dye, this could lead to the detection of a higher number of dying cells. However, this remains speculative and would benefit from further validation using additional cell populations. Furthermore, the combined PI/Apotracker staining provided additional insights; treatment with 100 nM AZD0156 significantly increased the early apoptotic cell population in myofibroblast, whereas the effect was not statistically significant in fibroblasts or at lower ATM inhibitor concentrations. This suggests that ATM activity normally promotes cell survival by preventing DNA damage-induced apoptosis. In

the absence of ATM, cells begin the apoptotic process but based on our limited investigation at the 6-day timepoint, they have not yet progressed to late-stage apoptosis or necrosis. It remains unclear whether these cells will eventually undergo late apoptosis or necrosis. A more reliable method for confirming apoptosis would be the measurement of caspase activation. Since caspases are key executioner enzymes in apoptosis, an increase in their activity would provide a clear indicator of apoptotic cell death and help distinguish it from necrosis or other forms of cell death (Nakajima & Kuranaga, 2017).

Fibroblasts from A-T patients typically exhibit lower proliferation rates compared to normal fibroblasts (Campbell et al., 2015; T. Zhou et al., 2007). We observed a similar trend in fibroblasts and myofibroblasts treated with the ATM inhibitor, with this effect becoming more pronounced after six days of treatment compared to three days. This is likely due to control cells undergoing more cell divisions over the extended timeframe. Our Westen blot results showed that 5 nM AZD0156 was sufficient to diminish ATM phosphorylation and in our proliferation assay, we observed significant differences in cell proliferation across ATM inhibitor concentrations ranging from 5 nM to 500 nM. However, 1 nM AZD0156 did not significantly reduce proliferation, which aligns with our Westen blot data indicating that this concentration was insufficient to fully inhibit ATM activity, allowing some pATM to persist in the cells. Lower MTS readings in cells treated with various concentrations of AZD0156 can likely be attributed to reduced proliferation, as indicated by our cell cycle analysis, which shows delayed cell cycle progression and G2-phase arrest. If DNA damage is too extensive, cells may enter senescence or undergo cell death. While we investigated cell death and found significant differences only in myofibroblasts treated with 100 nM AZD0156 (as assessed by Zombie staining), these differences were not observed using PI and Apotracker staining. A limitation of our study is that we did not assess whether senescence contributes to the observed reduction in proliferation rates. Primary fibroblasts from A-T patients exhibit premature senescence when cultured in ambient oxygen concentrations, but reducing oxygen levels to 3% has been shown to extend their proliferative lifespan (Haj et al., 2023). Since MLFs in our study were cultured in 3% oxygen, oxygen availability was unlikely to be a contributing factor to senescence. Additionally, our pilot study on the effects of lower AZD0156 concentrations on ECM gene expression corroborated our Western blot findings. At a 6-day timepoint, 1 nM AZD0156 did not significantly downregulate ECM genes, whereas 5, 50, and 100 nM AZD0156 led to significant, concentration dependent downregulation of COL1A1, COL11A1, and POSTN in fibroblasts, as well as COL1A1 and COL11A1 in myofibroblasts. However, a limitation of this investigation is that we only assessed three genes. Given more time, we would expand our analysis to include additional myofibroblastic markers, ECM genes, and inflammatory genes to gain a more comprehensive understanding of the effects of ATM inhibition on the fibroblast phenotype.

Overall, our results confirm that AZD0156 is a potent inhibitor. Although Zombie staining of myofibroblasts indicated an increase in cell death, the lack of a significant rise in necrotic cells suggests that ATM inhibition does not induce overwhelming toxicity. These findings support the potential use of AZD0156 as an immunotherapy adjuvant.

Chapter 7 Discussion

Immune checkpoint blockade has revolutionised cancer therapy, yet its benefits are limited to a subset of patients (Morad et al., 2021). A significant barrier to ICB efficacy is the presence of myCAFs which remodel the extracellular matrix and alter secretory profiles, thereby creating a barrier that excludes T cells from tumours (M. Chen et al., 2024). Overcoming this T cell exclusion by targeting myCAFs is therefore critical to enhancing ICB responses. However, targeting CAFs is challenging due to their complex, heterogenous, and dynamic roles within the TME (Biffi et al., 2018; Cords et al., 2023; Elyada et al., 2019; Öhlund et al., 2017; D. Yang et al., 2023). Although single-cell RNA sequencing has revealed distinct CAF subtypes, their precise functions remain unclear, which may explain why promising preclinical strategies have yet to translate into clinical success (Monteran & Erez, 2019). While most research has focused on myCAFs, our studies incorporate a boarder range of genetic markers to develop a more comprehensive understanding of CAF plasticity *in vitro*.

ATM was identified as a key regulator of the myCAF phenotype. *In vivo*, targeting ATM suppressed tumour growth in myCAF-rich models, promoted intratumoural $CD8^+$ T cell infiltration, and potentiated responses to anti-PD-1 blockade and antitumour vaccination (Mellone et al., 2022). Chapter 3 details the molecular mechanisms involved in mediating $CD8^+$ T cell infiltration, with a particular focus on ECM proteins and cytokine composition. We found that ATM inhibition downregulates genes associated with the myCAF phenotype while simultaneously inducing the expression of iCAF markers and chemokines involved in $CD8^+$ T cell trafficking, including CXCL10 and CXCL11 which are markers of ifnCAFs. These changes in both ECM composition and secretome following ATM inhibition in myofibroblasts facilitate $CD8^+$ T cell migration *in vitro*. Collectively, these findings confirm that CAFs are highly plastic; therapeutic interventions may not simply revert one phenotype but rather shift cells toward another, thereby contributing to CAF heterogeneity and function. This highlights the importance of understanding how potential immunotherapy adjuvants affect CAF heterogeneity, with the ultimate goal of developing therapies that shift CAFs toward an antitumour phenotype.

In cancer cell studies, ATM deficiency has been shown to activate the cGAS-STING pathway, suggesting that it may induce a pro-inflammatory response (Chiu et al., 2023; M. Hu et al., 2021; C. H. Huang et al., 2023). Chapter 5 explores the complex interplay between STING expression, ATM activity, and TGF-β1 in fibroblasts. Our data reveal that TGF-β1 suppresses both cGAS and STING, while ATM inhibition elevates cGAS levels but unexpectedly further reduces STING expression. The simultaneous downregulation of STING and upregulation of cGAS has not been previously reported. In cancer cell studies, ATM deficiency typically induces genes such as

STING, IFIT1, ISG15, CCL5, CCL2, CXCL10, and IL6 (Chiu et al., 2023; M. Hu et al., 2021; C. H. Huang et al., 2023). For the first time, we show that in wild-type myofibroblasts, these interferon stimulated genes and inflammatory cytokines are suppressed by TGF-β1, yet ATM inhibition leads to significant upregulation of ISG15, CCL5, CCL2, CXCL10, and IL6, despite the downregulation of STING. This discrepancy opens an avenue for further investigation, including whether similar dynamics occur in primary fibroblasts from other organs. In contrast, in STING knockout myofibroblasts, only CCL2 was significantly upregulated following ATM inhibition, suggesting that the presence of STING is necessary for the regulation of these ISGs. Moreover, our data indicate that STING is essential for the induction of CCL5 in fibroblasts, as compensatory pathways in its absence were insufficient to maintain CCL5 expression (Zeng et al., 2021). To our knowledge, this is the first report that STING is required for regulating CXCL12, as evidenced by its diminished expression in the absence of STING. Given that CXCL12 is known to contribute to immune cell exclusion and impaired responses to ICB, its induction via STING may reinforce immunosuppressive functions (Y. H. Du et al., 2021; Feig et al., 2013). Based on our mouse tumour models, we observed no differences in $CD8^+$ T cell infiltration between tumours containing cancer cells and myCAFs with or without STING knockout. ATM inhibition increased $CD8^+$ T cell infiltration in both conditions; however, a significant reduction in tumour size was observed only in wild-type myCAF-rich tumours following ATM inhibitor treatment, while this effect was not significant in tumours with STING knockout myCAFs. These findings suggest that ATM inhibition may be more effective in tumours with high STING expression in stromal cells.

In Chapter 6, we confirmed that AZD0156 is a potent inhibitor, with 5 nM sufficient to diminish ATM activity. We demonstrated that fibroblasts and myofibroblasts treated with the ATM inhibitor exhibit lower proliferation rates, which may be attributed to slower cell cycle progression and G2-phase arrest, as evidenced by our findings, and we observe no significant signs of toxicity. Additionally, our pilot study indicates that a concentration 100-fold lower than that initially reported in the literature was capable of downregulating selected ECM genes. In future work, it will be valuable to determine whether 5 nM AZD0156 is sufficient to revert the myofibroblastic phenotype to a more fibroblast-like state, and whether reducing the dose *in vivo* would similarly affect tumour size and $CD8^+$ T cell infiltration. Furthermore, if the dose required to stimulate immune infiltration is lower than that necessary to sensitise cancer cells to DNA-damaging therapies, associated side effects may be minimised. These findings provide a rationale for using ATM inhibitors to overcome CAF-mediated immunotherapy resistance. Given that AZD0156 has already been evaluated in clinical trials for other indications, we believe it could soon serve as an immunotherapy adjuvant to improve outcomes in patients with solid tumours.

Excessive ECM deposition can create a physical barrier to immune cells and therapeutic agents (Cho et al., 2020). Consequently, targeting CAF-derived ECM proteins has emerged as a promising therapeutic strategy. Our aim was to target CTHRC1, POSTN, and COL11A1 to elucidate their roles in regulating $CD8^+$ T cell infiltration and tumour growth. In Chapter 4, we discuss the challenges associated with the selected gene editing methods, which revealed that even *in vitro*, fibroblasts are plastic and do not always yield a desired phenotype. Nevertheless, we confirmed that lentiviral transduction can achieve high gene editing efficiency in primary fibroblasts. However, our shRNA control also altered gene expression, in line with previous reports, highlighting the importance of appropriate controls (Hutson et al., 2012). We further demonstrated that nucleofection is an effective transfection method in fibroblasts and that double nucleofection, characterised by dual-pulse electroporation, can increase CRISPR-Cas9 editing efficiency. A key limitation of our study is the use of immortalised fibroblasts, which while more robust experimentally, are genetically different from primary fibroblasts. In mouse models immortalised myofibroblasts failed to recapitulate the properties of primary myofibroblasts, such as $CD8^+$ T cell exclusion that we have observed previously. Therefore, translating results from immortalised fibroblast to clinical application may be challenging. Continued research into CAF diversity and plasticity *in vitro* will be essential for developing effective and safe cancer treatments, as our studies highlight the plasticity induced by the experimental procedures themselves.

Targeting single molecules in CAFs has yielded limited therapeutic success, likely due to the complex and plastic nature of these cells. A more effective strategy may involve simultaneously modulating ECM composition and cytokine signalling to address the broader functional network that sustains the tumour-promoting properties of CAFs. In this regard, ATM inhibition is a promising approach, as it reprograms CAFs by altering both ECM composition and cytokine secretion, thereby enhancing intratumoural $CD8^+$ T cell infiltration. Importantly, we did not detect toxic effects with this treatment, suggesting that ATM inhibition may serve as a viable immunotherapy adjuvant. Although our attempts to target individual ECM components overexpressed by CAFs, including CTHRC1, POSTN, and COL11A1 were limited by our experimental approach, it is also plausible that targeting a single ECM protein would not induce sufficient structural remodelling to enhance immune infiltration. This reinforces the notion that broader, multi-target interventions may be necessary to overcome the immunosuppressive properties of CAFs.

Appendix A Supplementary data

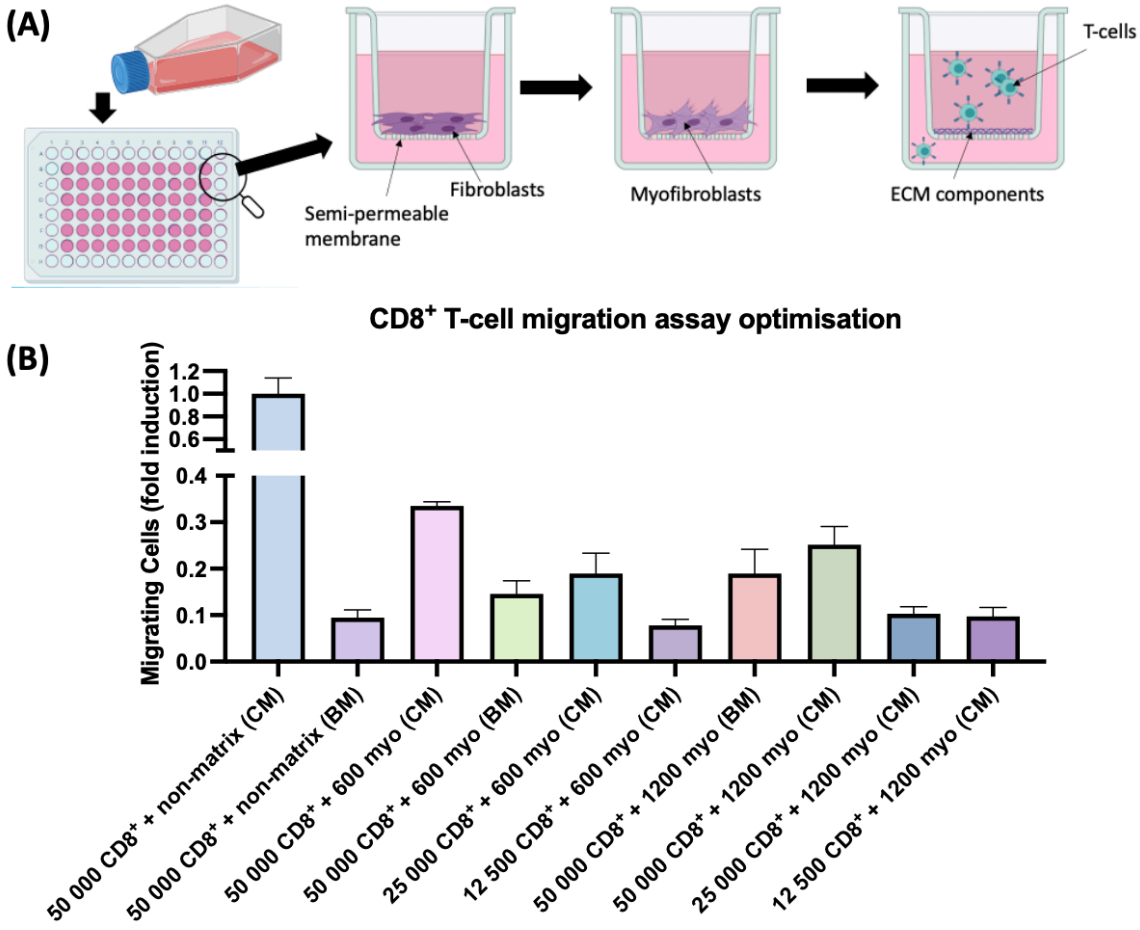

Appendix A Figure 1: Migration assay optimisation. (A) Schematic diagram illustrating T cell migration. MLFs were seeded at 600 and 1200 cells per transwell in a 96-well plate and treated with TGF-β1 (myo) for one week to allow ECM deposition. Following decellularisation, varying numbers of $CD8^+$ T cells were seeded to assess their migration through the deposited ECM toward conditioned medium (CM) or basic medium (BM). **(B)** Migrated cells from the lower chamber were counted using a flow cytometer and expressed as fold change (n_{tr} = 4). Based on these results, the condition with 600 MLFs and 50 000 $CD8^+$ T cells was selected for subsequent experiments.

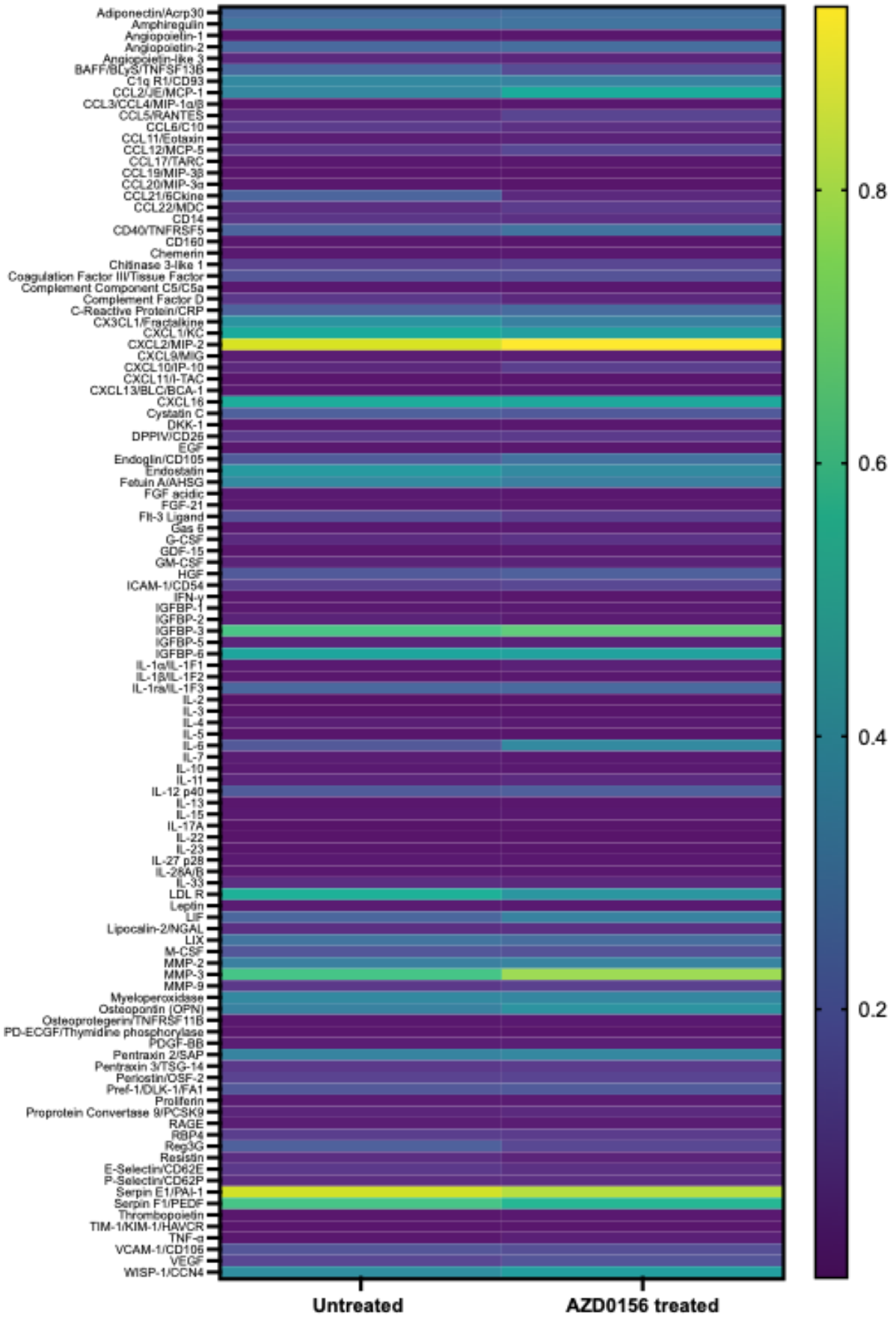

Appendix A Figure 2: Heat map of tumour-derived cytokine expression. Tumour supernatants from myCAF-rich tumours, both untreated and treated with the ATM inhibitor AZD0156 were analysed using proteome profiler arrays to assess differences in cytokine expression (n = 3 mice per

condition). Pixel densities were normalised to the reference dots within each array. All detected cytokines were quantified and are represented on a heatmap using a colour scale.

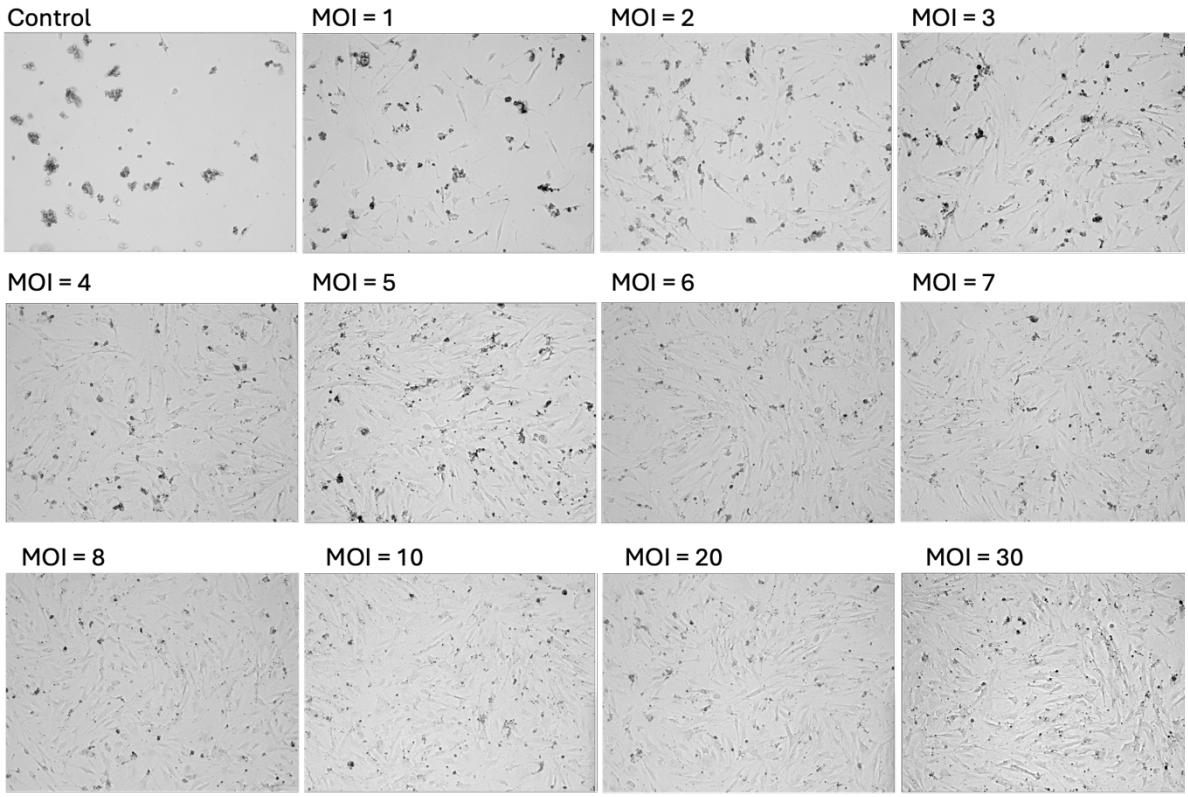

Appendix A Figure 3: Optimisation of transduction efficiency for lentiviral vectors in MLFs. MLFs were transduced with the SHC012 lentiviral vector at the indicated MOIs in the presence of 6 µg/mL polybrene for 18 hours. RFP expression was observed 48 hours after the initiation of transduction. At this point, the media was replaced and supplemented with 4 µg/mL puromycin to select for cells that successfully incorporated the lentiviral vectors. Cells were imaged 72 hours post-selection to evaluate their viability and confluence at the indicated MOIs.

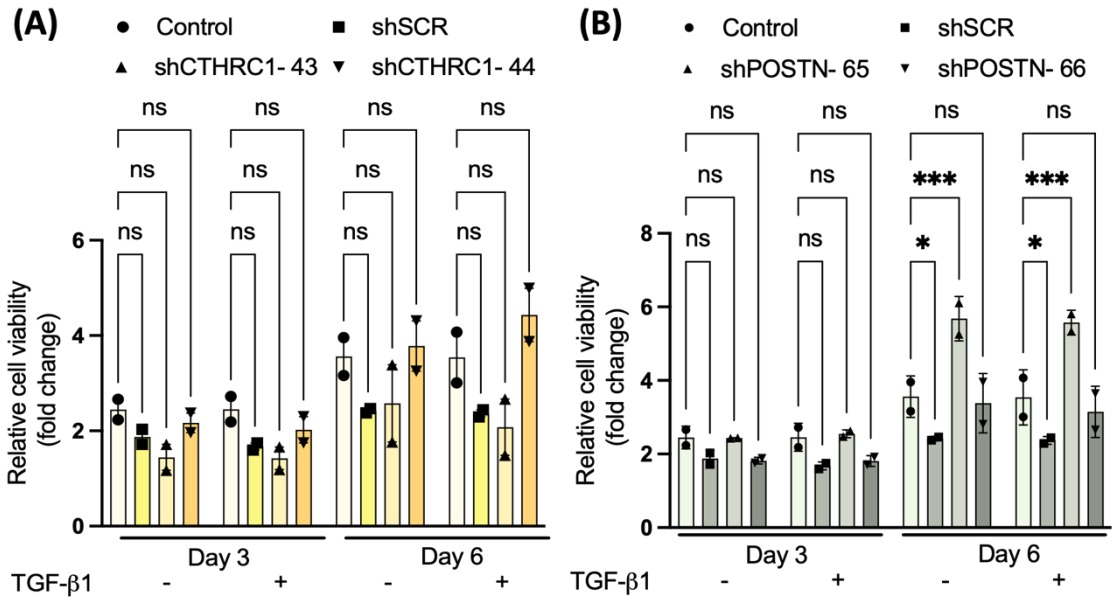

Appendix A Figure 4: Effect of shRNA transduction and TGF-β1 treatment on proliferation in MLFs. (A-B) MTS assay measuring the proliferation rates of MLFs transduced with the indicated shRNAs at an MOI of 5, with or without TGF-β1. Data are presented as mean fold change ± SEM, normalised to MTS measurements on day 1. Each data point represents an individual experiment. Statistical analysis was performed using two-way ANOVA with Bonferroni correction; *P≤0.05, ***P≤0.001, ns = not significant.

4 = Not nucleofected clone 4
2 = Double nucleofected CRISPR control clone 2

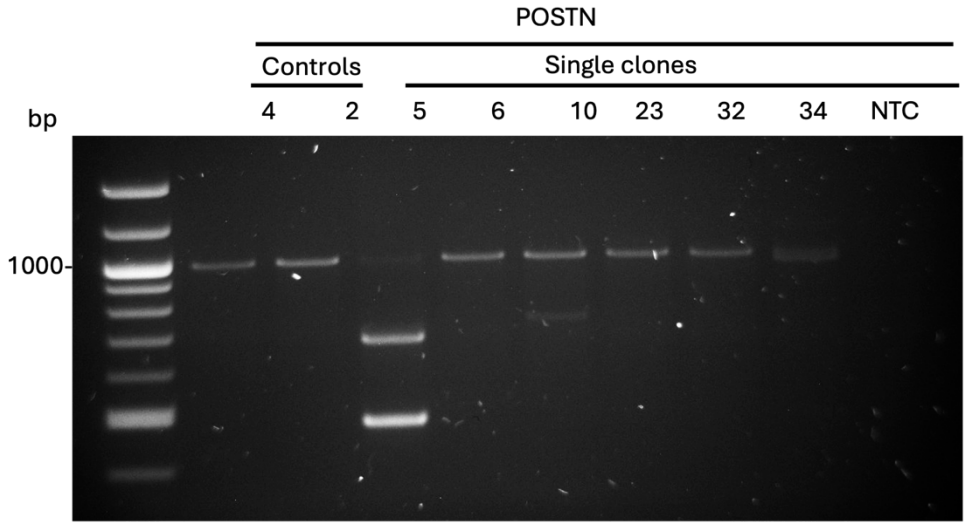

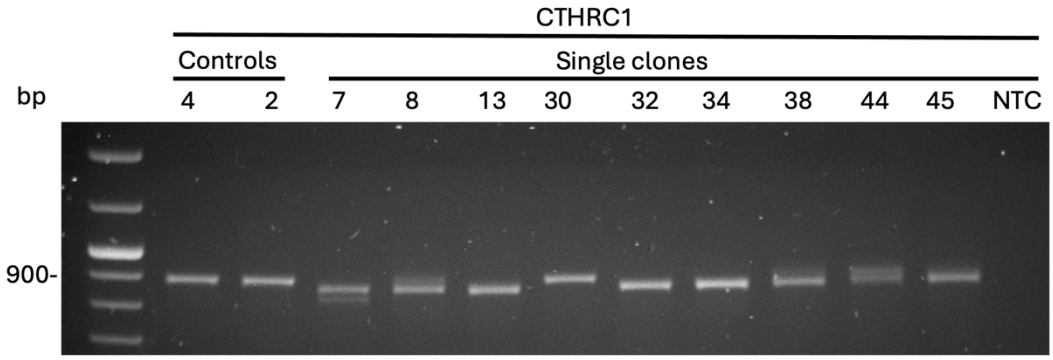

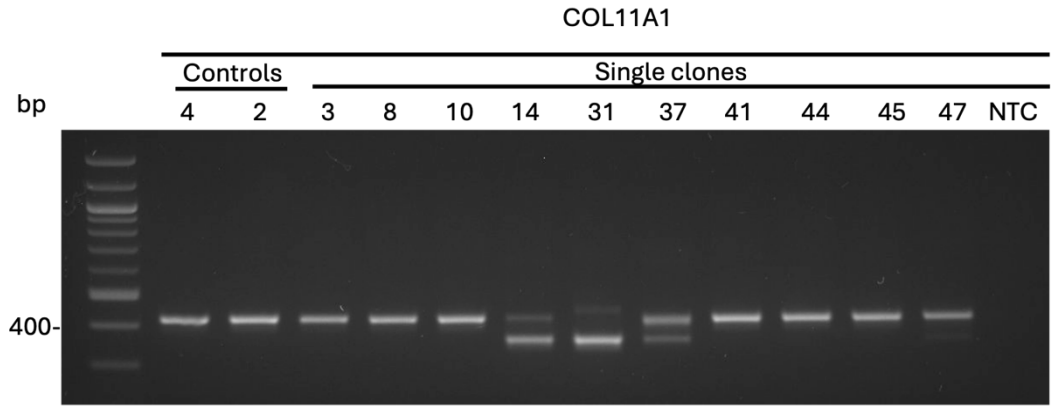

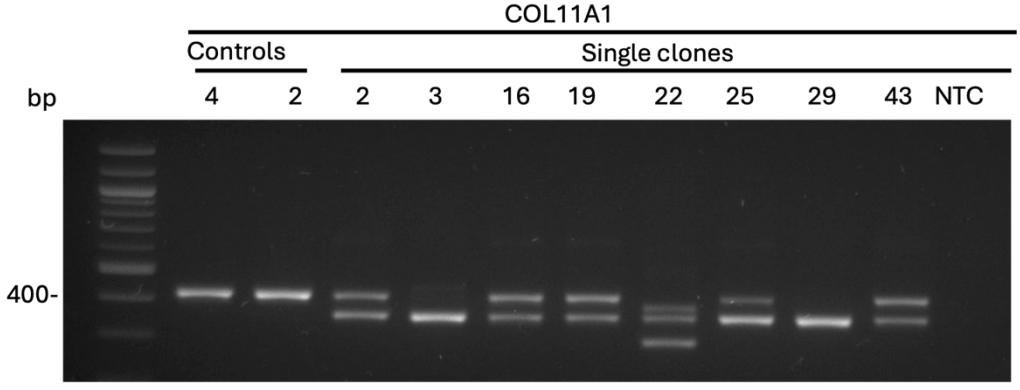

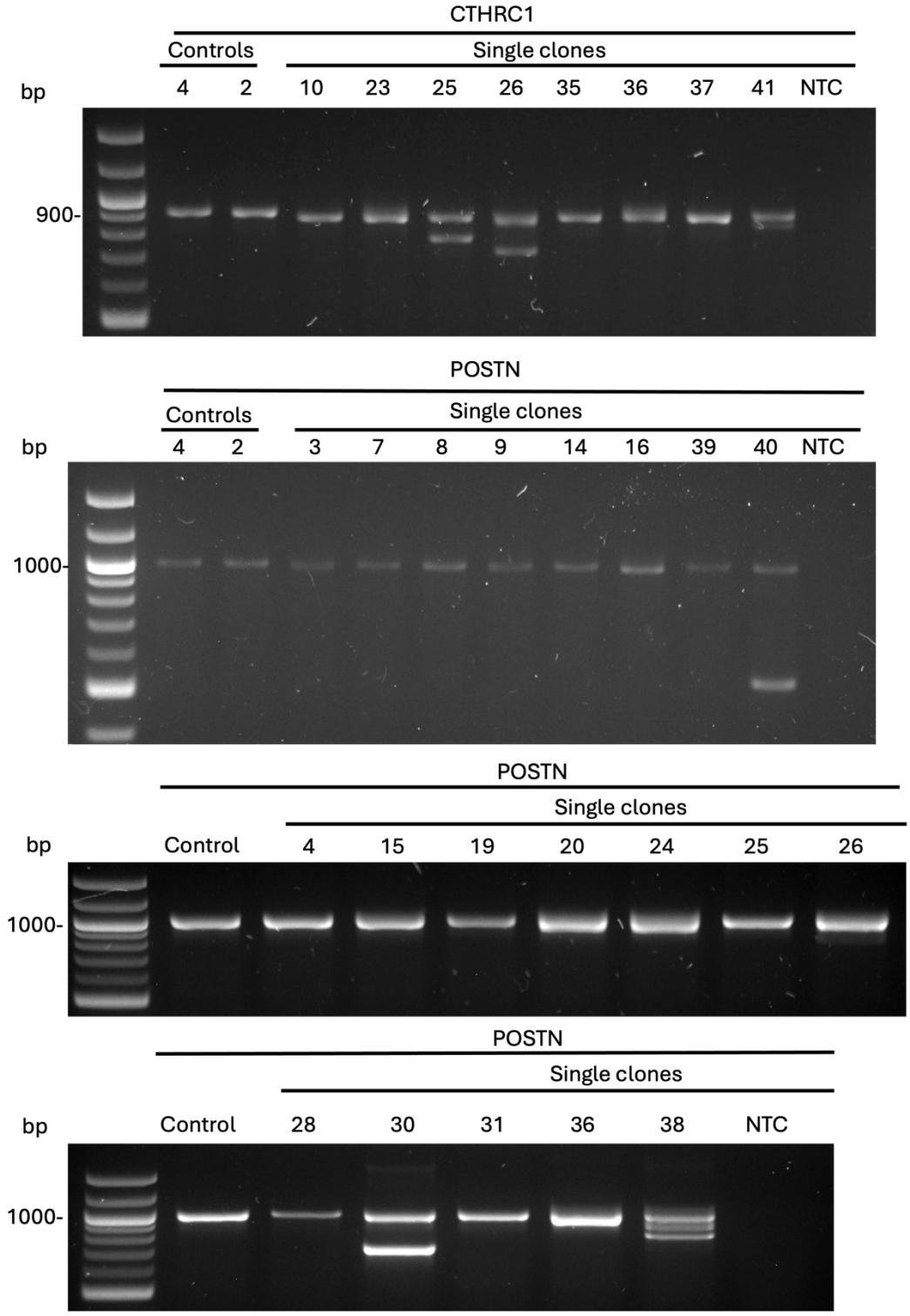

Appendix A Figure 5: Detection of gene editing in single-clone-derived cells via PCR analysis. Gel images showing PCR products resolved on a 3% agarose gel. Primer pairs flanked the targeted regions of the sgRNAs. Amplicon sizes for wild-type clones were 889 bp for CTHRC1, 968 bp for POSTN, and 434 bp for COL11A1. The presence of smaller PCR products corresponds to edited alleles resulting from gene editing.

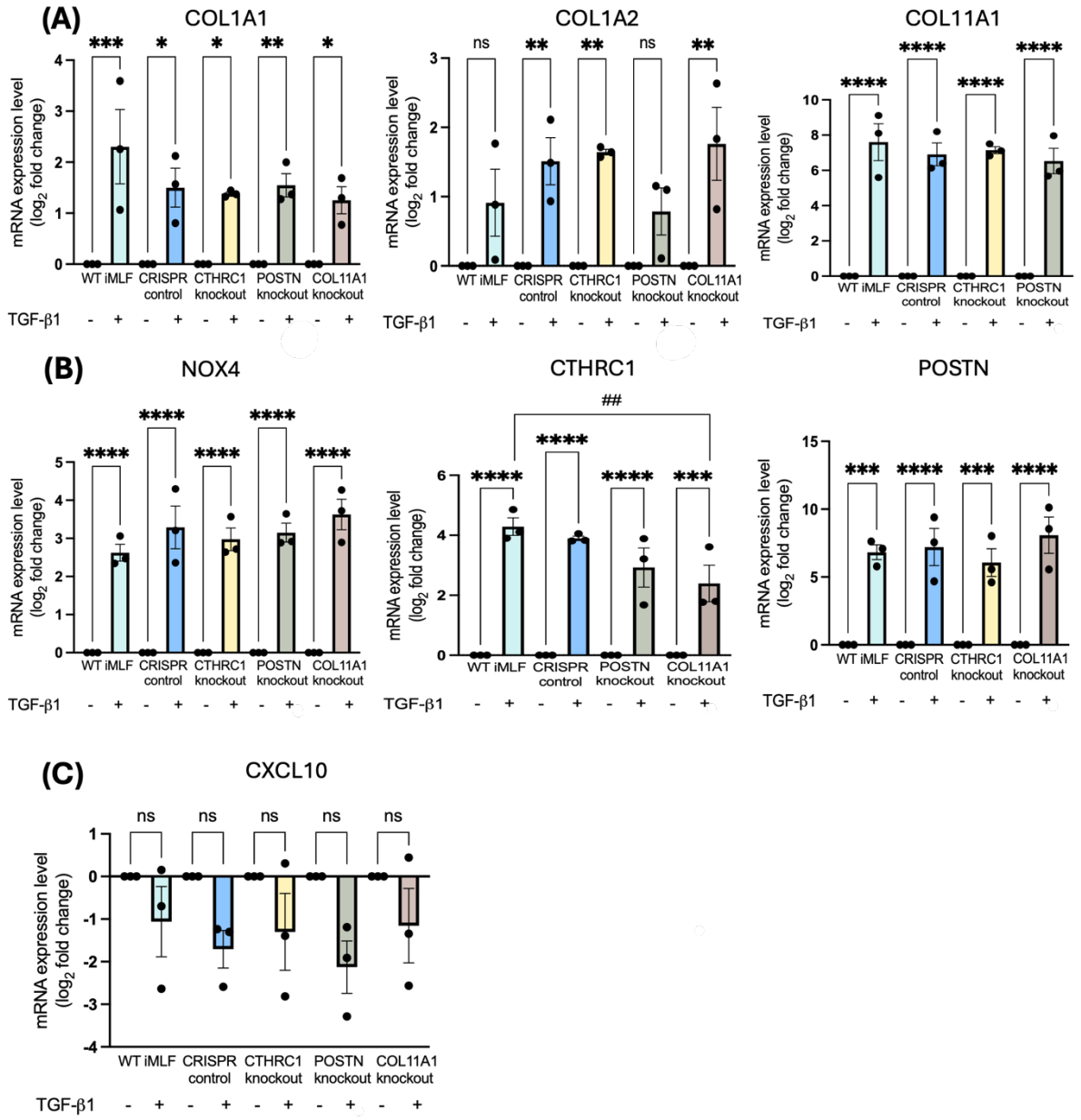

Appendix A Figure 6: Gene expression of ECM components and CXCL10 in single-clone-derived cells. (A-C) RT-qPCR analysis of genes associated with the myofibroblastic phenotype and ECM composition in iMLFs treated with TGF-β1 for 6 days in medium supplemented with 5% serum. Data are presented as mean log_2 fold change ± SEM, normalised to untreated controls. Each data point represents a population of cells derived from a single clone. Statistical analysis was performed using one-way ANOVA with Bonferroni correction; *P≤0.05, **P≤0.01, ***P≤0.001, ****P≤0.0001, ns = not significant.

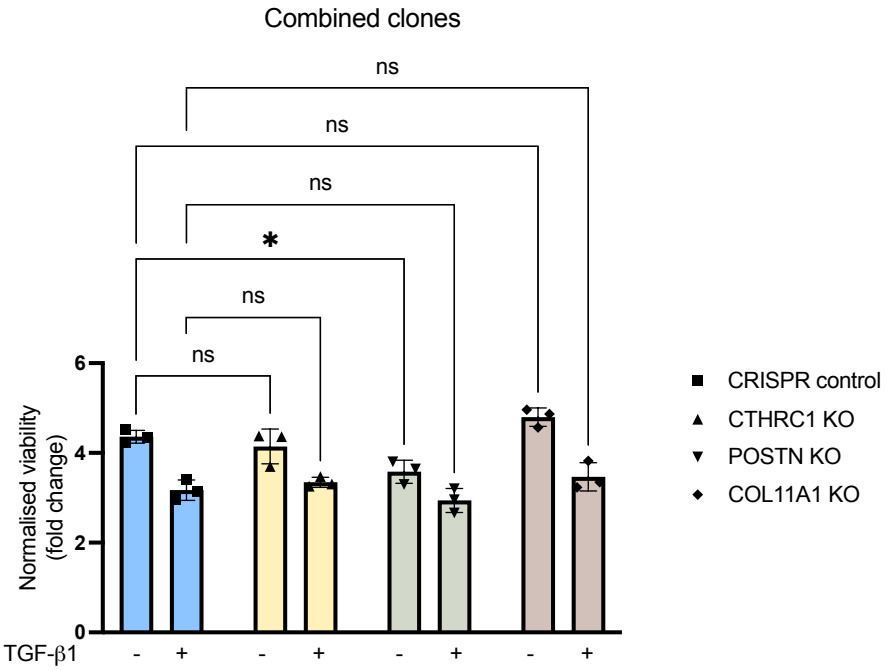

Appendix A Figure 7: Proliferation analysis of mixed clone CRISPR KO iMLFs. MTS assay measuring proliferation rates of mixed CRISPR KO iMLF clones and corresponding controls, with or without TGF-β1 treatment, at 72 hours (n_{tr} = 3). Data are presented as mean fold change ± SEM, normalised to MTS measurements on day 1. Statistical analysis was performed using two-way ANOVA with Bonferroni correction; *P≤0.05, ns = not significant.

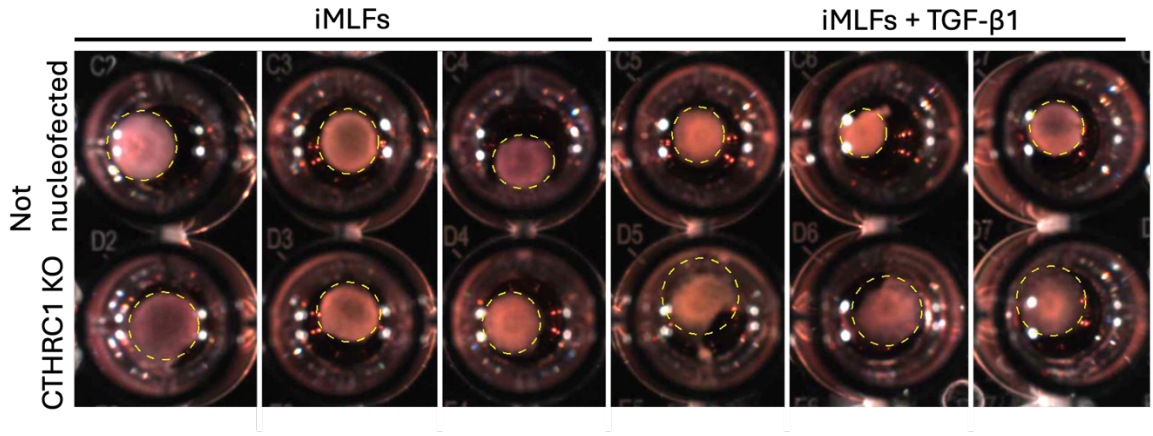

Appendix A Figure 8: Evaluation of contractile ability in CTHRC1 KO iMLFs *in vitro*. Representative images of gel contraction after 24 hours, with dotted lines outlining the gel areas used for quantification.

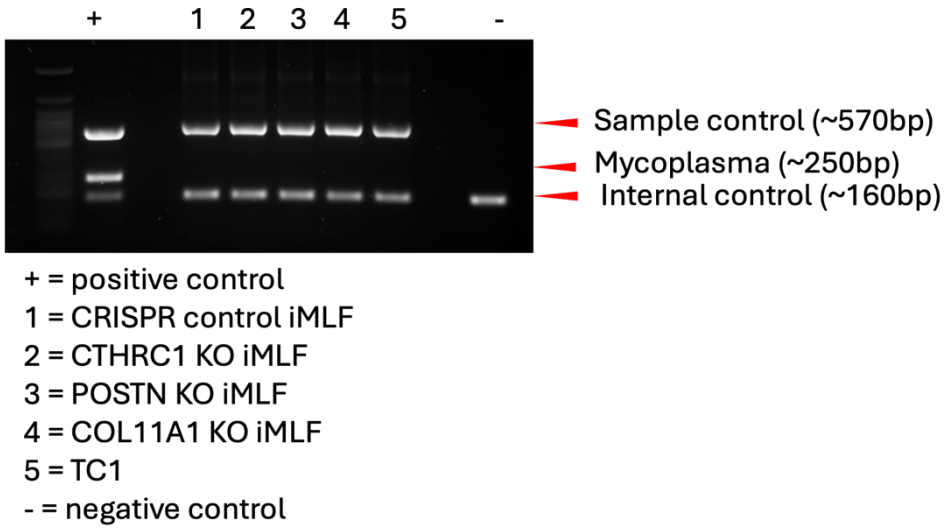

Appendix A Figure 9: Detection of mycoplasma contamination. Representative gel image showing PCR products resolved on a 1.5% agarose gel. The sample control verifies the quality of the template DNA, ensuring its suitability for PCR. The internal control is a PCR amplification product distinct from the target mycoplasma, which confirms that the PCR reaction has proceeded correctly.

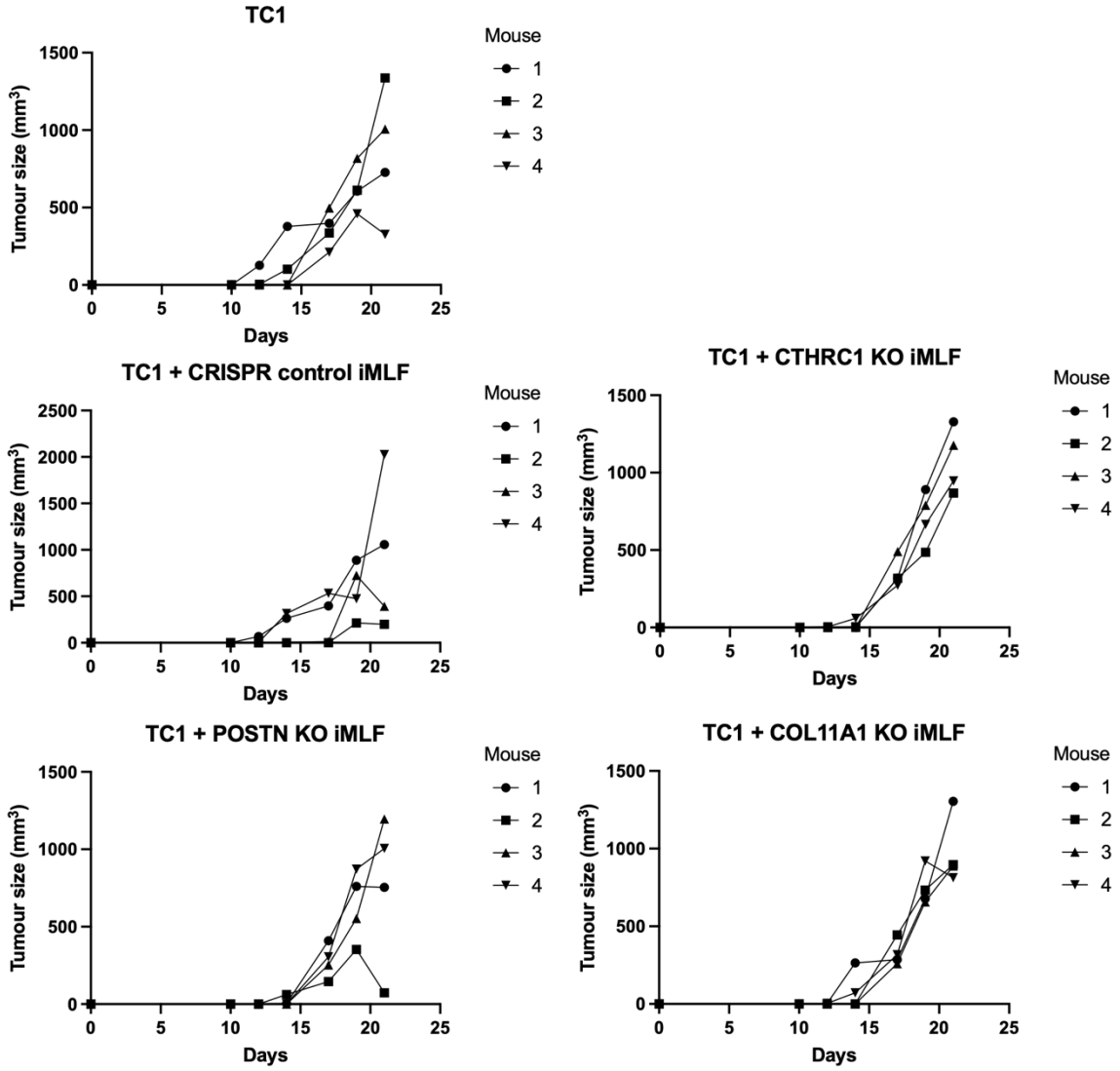

Appendix A Figure 10: Growth of myofibroblast-rich murine tumours containing gene knockouts. Tumour growth curves for TC1 and the indicated iMLFs in individual mice (n=4 per condition).

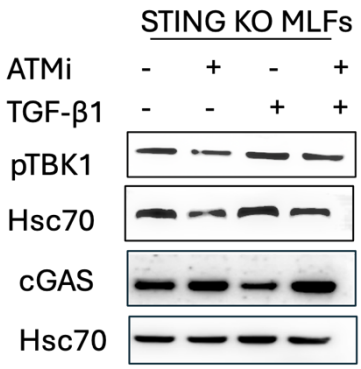

Appendix A Figure 11: Protein expression levels of pTBK1 and cGAS in STING KO MLFs. Western blotting of STING KO MLFs treated with TGF-β1 and/or 0.5 μM AZD0156 for 6 days.

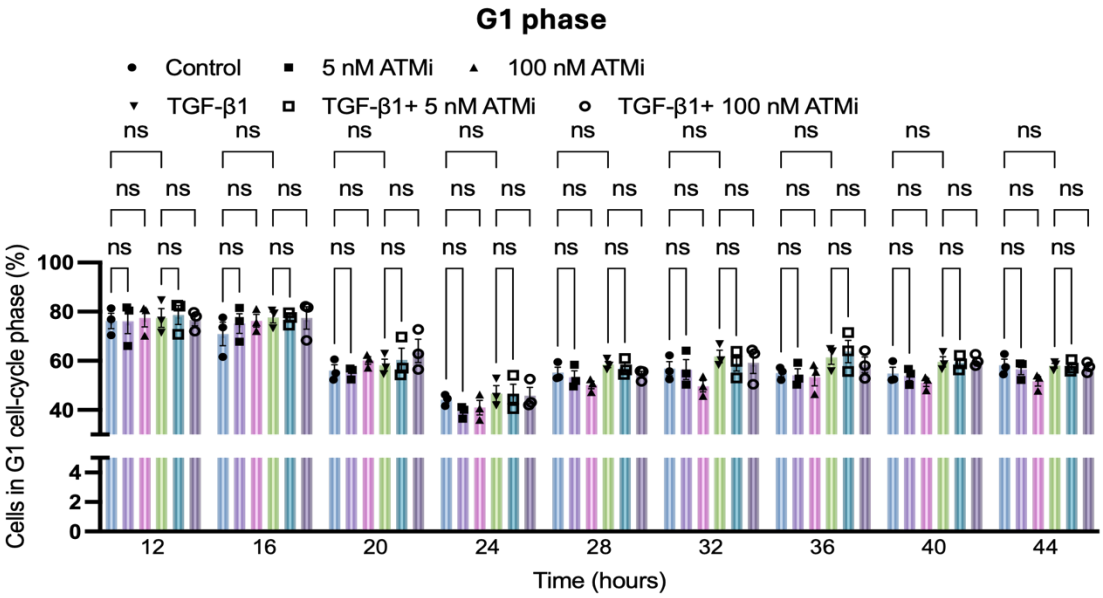
G1 phase
Control
5 nM ATMi
100 nM ATMi
TGF-β1
TGF-β1+ 5 nM ATMi
TGF-β1+ 100 nM ATMi
Cells in G1 cell-cycle phase (%)
Time (hours)

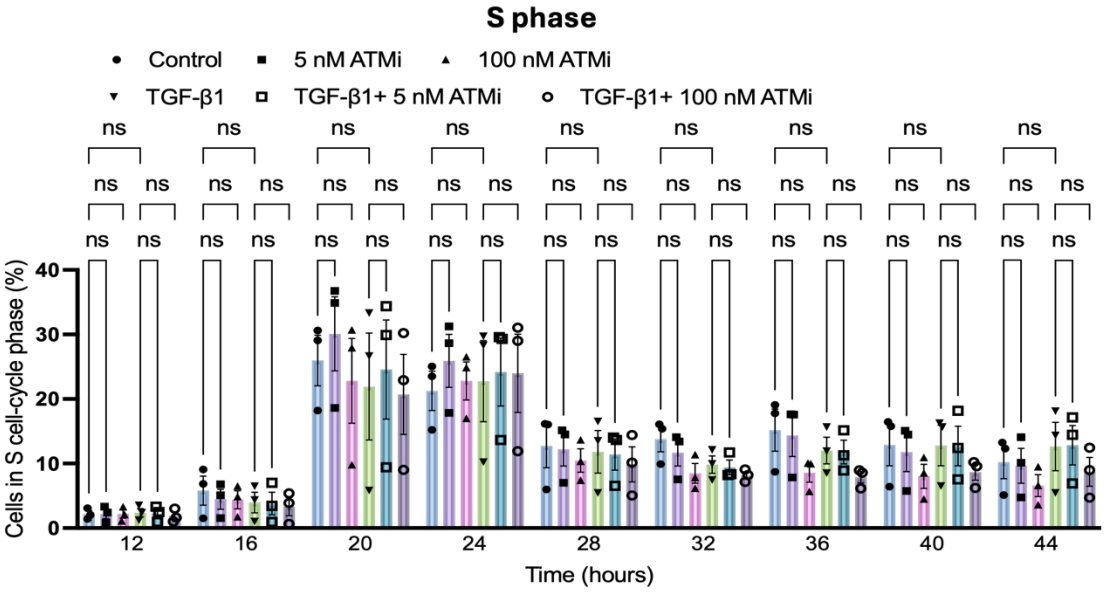
S phase
Control
5 nM ATMi
100 nM ATMi
TGF-β1
TGF-β1+ 5 nM ATMi
TGF-β1+ 100 nM ATMi
Cells in S cell-cycle phase (%)
Time (hours)

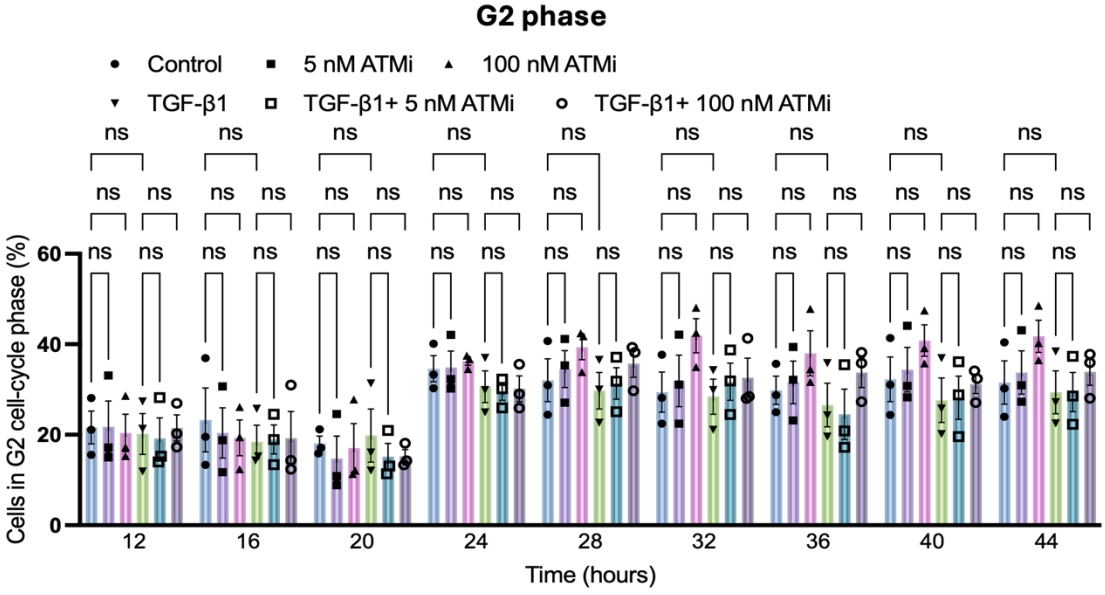
G2 phase
Control
5 nM ATMi
100 nM ATMi
TGF-β1
TGF-β1+ 5 nM ATMi
TGF-β1+ 100 nM ATMi
Cells in G2 cell-cycle phase (%)
Time (hours)

Appendix A Figure 12: Quantification of cells in each cell cycle phase following TGF-β1 treatment and ATM inhibition. MLFs were synchronised through a 24-hour serum starvation, after which serum was reintroduced to allow cells to re-enter the cell cycle. TGF-β1 and/or AZD0156 at 5nM and 100 nM were administered simultaneously. Cells were collected every 4 hours, and DNA content at each cell cycle phase was analysed using a propidium iodide flow cytometric assay. Graphs represent the percentage of cells in each cell cycle phase based on three independent experiments. Statistical analysis was performed using two-way ANOVA with Tukey's correction; ns = not significant.

List of References

Abbotts, R., & Wilson, D. M. (2016). Coordination of DNA Single Strand Break Repair. *Free Radical Biology & Medicine*, *107*, 228. https://doi.org/10.1016/J.FREERADBIOMED.2016.11.039

Abdisalaam, S., Mukherjee, S., Bhattacharya, S., Sinha, D., Kumari, S., Sadek, H. A., Ortega, J., Li, G.-M., & Asaithamby, A. (2020). *NBS1-CtIP–Mediated DNA End Resection Regulates cGAS Binding to Micronuclei*. https://doi.org/10.1101/2020.07.27.222380

Adachi, K., Kano, Y., Nagai, T., Okuyama, N., Sakoda, Y., & Tamada, K. (2018). IL-7 and CCL19 expression in CAR-T cells improves immune cell infiltration and CAR-T cell survival in the tumor. *Nature Biotechnology 2018 36:4*, *36*(4), 346–351. https://doi.org/10.1038/nbt.4086

Afratis, N. A., Klepfish, M., Karamanos, N. K., & Sagi, I. (2018). The apparent competitive action of ECM proteases and cross-linking enzymes during fibrosis: Applications to drug discovery. *Advanced Drug Delivery Reviews*, *129*, 4–15. https://doi.org/10.1016/J.ADDR.2018.03.004

Alberts, B., Johnson, A., Lewis, J., Raff, M., Roberts, K., & Walter, P. (2002). *Intracellular Control of Cell-Cycle Events*. https://www.ncbi.nlm.nih.gov/books/NBK26856/

Almatarneh, M. H., Flinn, C. G., & Poirier, R. A. (2008). Mechanisms for the deamination reaction of cytosine with H 2O/OH- and 2H2O/OH-: A computational study. *Journal of Chemical Information and Modeling*, *48*(4), 831–843. https://doi.org/10.1021/CI7003219/SUPPL_FILE/CI7003219-FILE006.PDF

Alsaab, H. O., Sau, S., Alzhrani, R., Tatiparti, K., Bhise, K., Kashaw, S. K., & Iyer, A. K. (2017). PD-1 and PD-L1 Checkpoint Signaling Inhibition for Cancer Immunotherapy: Mechanism, Combinations, and Clinical Outcome. *Frontiers in Pharmacology*, *8*(AUG), 561. https://doi.org/10.3389/FPHAR.2017.00561

Amidon, K. M., & Eichman, B. F. (2020). Structural biology of DNA abasic site protection by SRAP proteins. *DNA Repair*, *94*, 102903. https://doi.org/10.1016/J.DNAREP.2020.102903

An, X., Zhu, Y., Zheng, T., Wang, G., Zhang, M., Li, J., Ji, H., Li, S., Yang, S., Xu, D., Li, Z., Wang, T., He, Y., Zhang, L., Yang, W., Zhao, R., Hao, D., & Li, X. (2018). An Analysis of the Expression and Association with Immune Cell Infiltration of the cGAS/STING Pathway in Pan-Cancer. *Molecular Therapy. Nucleic Acids*, *14*, 80. https://doi.org/10.1016/J.OMTN.2018.11.003

Anand, R., Ranjha, L., Cannavo, E., & Cejka, P. (2016). Phosphorylated CtIP Functions as a Co-factor of the MRE11-RAD50-NBS1 Endonuclease in DNA End Resection. *Molecular Cell*, *64*(5), 940–950. https://doi.org/10.1016/J.MOLCEL.2016.10.017

Antoon, R., Overdevest, N., Saleh, A. H., & Keating, A. (2024). Mesenchymal stromal cells as cancer promoters. *Oncogene 2024 43:49*, *43*(49), 3545–3555. https://doi.org/10.1038/s41388-024-03183-1

Aparicio, T., Baer, R., & Gautier, J. (2014). DNA double-strand break repair pathway choice and cancer. *DNA Repair*, *19*, 169. https://doi.org/10.1016/J.DNAREP.2014.03.014

Arcucci, A., Ruocco, M. R., Granato, G., Sacco, A. M., & Montagnani, S. (2016). Cancer: An Oxidative Crosstalk between Solid Tumor Cells and Cancer Associated Fibroblasts. *BioMed Research International*, *2016*. https://doi.org/10.1155/2016/4502846

Arolt, C., Hoffmann, F., Nachtsheim, L., Wolber, P., Guntinas-Lichius, O., Buettner, R., von Eggeling, F., Quaas, A., & Klußmann, J. P. (2021). Mutually Exclusive Expression of COL11A1 by CAFs and Tumour Cells in a Large panCancer and a Salivary Gland Carcinoma Cohort. *Head and Neck Pathology*, *16*(2), 394. https://doi.org/10.1007/S12105-021-01370-0

Awasthi, P., Foiani, M., & Kumar, A. (2015). ATM and ATR signaling at a glance. *Journal of Cell Science*, *128*(23), 4255–4262. https://doi.org/10.1242/JCS.169730/260510/AM/ATM-AND-ATR-SIGNALING-AT-A-GLANCE

Bajwa, K. K., Punetha, M., Kumar, D., Yadav, P. S., Long, C. R., & Selokar, N. L. (2023). Electroporation-based CRISPR gene editing in adult buffalo fibroblast cells. *Animal Biotechnology*, *34*(9), 5055–5066. https://doi.org/10.1080/10495398.2023.2271030

Bakkenist, C. J., & Kastan, M. B. (2003). DNA damage activates ATM through intermolecular autophosphorylation and dimer dissociation. *Nature 2003 421:6922*, *421*(6922), 499–506. https://doi.org/10.1038/nature01368

Barnes, J. L., & Gorin, Y. (2011). Myofibroblast differentiation during fibrosis: role of NAD(P)H oxidases. *Kidney International*, *79*(9), 944–956. https://doi.org/10.1038/KI.2010.516

Barsky, S. H., Rao, C. N., Grotendorst, G. R., & Liotta, L. A. (1982). Increased content of Type V Collagen in desmoplasia of human breast carcinoma. *The American Journal of Pathology*, *108*(3), 276. /pmc/articles/PMC1916045/?report=abstract

Bartoschek, M., Oskolkov, N., Bocci, M., Lövrot, J., Larsson, C., Sommarin, M., Madsen, C. D., Lindgren, D., Pekar, G., Karlsson, G., Ringnér, M., Bergh, J., Björklund, Å., & Pietras, K. (2018). Spatially and functionally distinct subclasses of breast cancer-associated fibroblasts revealed by single cell RNA sequencing. *Nature Communications 2018 9:1*, *9*(1), 1–13. https://doi.org/10.1038/s41467-018-07582-3

Baudrin, L. G., Deleuze, J. F., & How-Kit, A. (2018). Molecular and computational methods for the detection of microsatellite instability in cancer. *Frontiers in Oncology*, *8*(DEC), 621. https://doi.org/10.3389/FONC.2018.00621/BIBTEX

Bauer, N. C., Corbett, A. H., & Doetsch, P. W. (2015). The current state of eukaryotic DNA base damage and repair. *Nucleic Acids Research*, *43*(21), 10083. https://doi.org/10.1093/NAR/GKV1136

Berdis, A. J. (2012). Chemotherapeutic Intervention by Inhibiting DNA Polymerases. *DNA Repair in Cancer Therapy: Molecular Targets and Clinical Applications*, 75–107. https://doi.org/10.1016/B978-0-12-384999-1.10005-8

Bhargava, R., Onyango, D. O., & Stark, J. M. (2016). Regulation of Single Strand Annealing and its role in genome maintenance. *Trends in Genetics : TIG*, *32*(9), 566. https://doi.org/10.1016/J.TIG.2016.06.007

Biddlestone-Thorpe, L., Sajjad, M., Rosenberg, E., Beckta, J. M., Valerie, N. C. K., Tokarz, M., Adams, B. R., Wagner, A. F., Khalil, A., Gilfor, D., Golding, S. E., Deb, S., Temesi, D. G., Lau, A., O'Connor, M. J., Choe, K. S., Parada, L. F., Lim, S. K., Mukhopadhyay, N. D., & Valerie, K. (2013). ATM kinase inhibition preferentially sensitizes p53-mutant glioma to ionizing radiation. *Clinical Cancer Research*, *19*(12), 3189–3200. https://doi.org/10.1158/1078-0432.CCR-12-3408/85691/AM/ATM-KINASE-INHIBITION-PREFERENTIALLY-SENSITIZES

Biffi, G., Oni, T. E., Spielman, B., Hao, Y., Elyada, E., Park, Y., Preall, J., & Tuveson, D. A. (2018). IL-1-induced JAK/STAT signaling is antagonized by TGF-β to shape CAF heterogeneity in pancreatic ductal adenocarcinoma. *Cancer Discovery*, *9*(2), 282. https://doi.org/10.1158/2159-8290.CD-18-0710

Biffi, G., Oni, T. E., Spielman, B., Hao, Y., Elyada, E., Park, Y., Preall, J., & Tuveson, D. A. (2019). IL1-Induced JAK/STAT Signaling Is Antagonized by TGFβ to Shape CAF Heterogeneity in Pancreatic Ductal Adenocarcinoma. *Cancer Discovery*, *9*(2), 282–301. https://doi.org/10.1158/2159-8290.CD-18-0710

Blackford, A. N., & Jackson, S. P. (2017). ATM, ATR, and DNA-PK: The Trinity at the Heart of the DNA Damage Response. *Molecular Cell*, *66*(6), 801–817. https://doi.org/10.1016/J.MOLCEL.2017.05.015/ASSET/E5CA219F-E236-4342-895F-1346AE0ACA72/MAIN.ASSETS/GR3.JPG

Blum, J. S., Wearsch, P. A., & Cresswell, P. (2013). Pathways of Antigen Processing. *Annual Review of Immunology*, *31*, 443. https://doi.org/10.1146/ANNUREV-IMMUNOL-032712-095910

Bocci, M., Zana, A., Principi, L., Lucaroni, L., Prati, L., Gilardoni, E., Neri, D., Cazzamalli, S., & Galbiati, A. (2024). In vivo activation of FAP-cleavable small molecule-drug conjugates for the targeted delivery of camptothecins and tubulin poisons to the tumor microenvironment. *Journal of Controlled Release*, *367*, 779–790. https://doi.org/10.1016/J.JCONREL.2024.02.014

Bockorny, B., Semenisty, V., Macarulla, T., Borazanci, E., Wolpin, B. M., Stemmer, S. M., Golan, T., Geva, R., Borad, M. J., Pedersen, K. S., Park, J. O., Ramirez, R. A., Abad, D. G., Feliu, J., Muñoz, A., Ponz-Sarvise, M., Peled, A., Lustig, T. M., Bohana-Kashtan, O., … Hidalgo, M. (2020). BL-8040, a CXCR4 antagonist, in combination with pembrolizumab and chemotherapy for pancreatic cancer: the COMBAT trial. *Nature Medicine 2020 26:6*, *26*(6), 878–885. https://doi.org/10.1038/s41591-020-0880-x

Bona, M. Di, & Bakhoum, S. F. (2024). Micronuclei and Cancer. *Cancer Discovery*, *14*(2), 214. https://doi.org/10.1158/2159-8290.CD-23-1073

Bougherara, H., Mansuet-Lupo, A., Alifano, M., Ngô, C., Damotte, D., Le Frère-Belda, M. A., Donnadieu, E., & Peranzoni, E. (2015). Real-Time Imaging of Resident T Cells in Human Lung and Ovarian Carcinomas Reveals How Different Tumor Microenvironments Control T Lymphocyte Migration. *Frontiers in Immunology*, *6*(OCT). https://doi.org/10.3389/FIMMU.2015.00500

Branton, M. H., & Kopp, J. B. (1999). TGF-β and fibrosis. *Microbes and Infection*, *1*(15), 1349–1365. https://doi.org/10.1016/S1286-4579(99)00250-6

Breslin, C., Mani, R. S., Fanta, M., Hoch, N., Weinfeld, M., & Caldecott, K. W. (2017). The Rev1 interacting region (RIR) motif in the scaffold protein XRCC1 mediates a low-affinity interaction with polynucleotide kinase/phosphatase (PNKP) during DNA single-strand break repair. *Journal of Biological Chemistry*, *292*(39), 16024–16031. https://doi.org/10.1074/JBC.M117.806638

Bridge, A. J., Pebernard, S., Ducraux, A., Nicoulaz, A. L., & Iggo, R. (2003). Induction of an interferon response by RNAi vectors in mammalian cells. *Nature Genetics 2003 34:3*, *34*(3), 263–264. https://doi.org/10.1038/ng1173

Brown, J. P., Wei, W., & Sedivy, J. M. (1997). Bypass of senescence after disruption of p21CIP1/WAF1 gene in normal diploid human fibroblasts. *Science (New York, N.Y.)*, *277*(5327), 831–834. https://doi.org/10.1126/SCIENCE.277.5327.831

Bruhn, C., & Foiani, M. (2019). A model of DNA damage response activation at stalled replication forks by SPRTN. *Nature Communications 2019 10:1*, *10*(1), 1–3. https://doi.org/10.1038/s41467-019-13610-7

Bruni, S., Mercogliano, M. F., Mauro, F. L., Cordo Russo, R. I., & Schillaci, R. (2023). Cancer immune exclusion: breaking the barricade for a successful immunotherapy. *Frontiers in Oncology*, *13*, 1135456. https://doi.org/10.3389/FONC.2023.1135456/BIBTEX

Burgdorf, S., Schölz, C., Kautz, A., Tampé, R., & Kurts, C. (2008). Spatial and mechanistic separation of cross-presentation and endogenous antigen presentation. *Nature Immunology 2008 9:5*, *9*(5), 558–566. https://doi.org/10.1038/ni.1601

Cai, X., Wang, K. C., & Meng, Z. (2021). Mechanoregulation of YAP and TAZ in Cellular Homeostasis and Disease Progression. *Frontiers in Cell and Developmental Biology*, *9*, 1333. https://doi.org/10.3389/FCELL.2021.673599/BIBTEX

Caldecott, K. W. (2024). Causes and consequences of DNA single-strand breaks. *Trends in Biochemical Sciences*, *49*(1), 68–78. https://doi.org/10.1016/J.TIBS.2023.11.001/ASSET/171C885D-41FB-4451-AF4F-81A8CD722940/MAIN.ASSETS/GR4.JPG

Campbell, A., Krupp, B., Bushman, J., Noble, M., Pröschel, C., & Mayer-Pröschel, M. (2015). A novel mouse model for ataxia-telangiectasia with a N-terminal mutation displays a behavioral defect and a low incidence of lymphoma but no increased oxidative burden. *Human Molecular Genetics*, *24*(22), 6331–6349. https://doi.org/10.1093/HMG/DDV342

Carter, R. J., & Parsons, J. L. (2016). Base Excision Repair, a Pathway Regulated by Posttranslational Modifications. *Molecular and Cellular Biology*, *36*(10), 1426. https://doi.org/10.1128/MCB.00030-16

Cathcart, J., Pulkoski-Gross, A., & Cao, J. (2015). Targeting matrix metalloproteinases in cancer: Bringing new life to old ideas. *Genes & Diseases*, *2*(1), 26–34. https://doi.org/10.1016/J.GENDIS.2014.12.002

Cesare, A. J., & Reddel, R. R. (2010). Alternative lengthening of telomeres: models, mechanisms and implications. *Nature Reviews Genetics 2010 11:5*, *11*(5), 319–330. https://doi.org/10.1038/nrg2763

Chambers, C. R., Ritchie, S., Pereira, B. A., & Timpson, P. (2021). Overcoming the senescence-associated secretory phenotype (SASP): a complex mechanism of resistance in the treatment of cancer. *Molecular Oncology*, *15*(12), 3242. https://doi.org/10.1002/1878-0261.13042

Chan, Y. W., & West, S. (2015). GEN1 promotes Holliday junction resolution by a coordinated nick and counter-nick mechanism. *Nucleic Acids Research*, *43*(22), 10882. https://doi.org/10.1093/NAR/GKV1207

Chang, C. H., & Pauklin, S. (2021). ROS and TGFβ: from pancreatic tumour growth to metastasis. *Journal of Experimental and Clinical Cancer Research*, *40*(1), 1–11. https://doi.org/10.1186/S13046-021-01960-4/FIGURES/3

Chang, L. Y., Lin, Y. C., Mahalingam, J., Huang, C. T., Chen, T. W., Kang, C. W., Peng, H. M., Chu, Y. Y., Chiang, J. M., Dutta, A., Day, Y. J., Chen, T. C., Yeh, C. T., & Lin, C. Y. (2012). Tumor-derived chemokine CCL5 enhances TGF-β-mediated killing of CD8 + T cells in colon cancer by T-regulatory cells. *Cancer Research*, *72*(5), 1092–1102. https://doi.org/10.1158/0008-5472.CAN-11-2493/650132/AM/TUMOR-DERIVED-CHEMOKINE-CCL5-ENHANCES-TGF-MEDIATED

Chansard, A., Dubrulle, N., Poujol de Molliens, M., Falanga, P. B., Stephen, T., Hasan, M., van Zandbergen, G., Aulner, N., Shorte, S. L., & David-Watine, B. (2021). Unveiling Interindividual Variability of Human Fibroblast Innate Immune Response Using Robust Cell-Based Protocols. *Frontiers in Immunology*, *11*, 3341. https://doi.org/10.3389/FIMMU.2020.569331/BIBTEX

Chapman, J. R., Taylor, M. R. G., & Boulton, S. J. (2012). Playing the End Game: DNA Double-Strand Break Repair Pathway Choice. *Molecular Cell*, *47*(4), 497–510. https://doi.org/10.1016/J.MOLCEL.2012.07.029

Chatterjee, N., & Walker, G. C. (2017). Mechanisms of DNA damage, repair and mutagenesis. *Environmental and Molecular Mutagenesis*, *58*(5), 235. https://doi.org/10.1002/EM.22087

Chattopadhyay, S., Kuzmanovic, T., Zhang, Y., Wetzel, J. L., & Sen, G. C. (2016). Ubiquitination of the Transcription Factor IRF-3 Activates RIPA, the Apoptotic Pathway that Protects Mice from Viral Pathogenesis. *Immunity*, *44*(5), 1151–1161. https://doi.org/10.1016/J.IMMUNI.2016.04.009

Chaudhry, H., Zhou, J., Zhong, Y., Ali, M. M., Mcguire, F., Nagarkatti, P. S., & Nagarkatti, M. (2013). Role of Cytokines as a Double-edged Sword in Sepsis. *In Vivo (Athens, Greece)*, *27*(6), 669. https://pmc.ncbi.nlm.nih.gov/articles/PMC4378830/

Chelvanambi, M., Fecek, R. J., Taylor, J. L., & Storkus, W. J. (2021). STING agonist-based treatment promotes vascular normalization and tertiary lymphoid structure formation in the therapeutic melanoma microenvironment. *Journal for Immunotherapy of Cancer*, *9*(2). https://doi.org/10.1136/JITC-2020-001906

Chen, C., Guo, Q., Liu, Y., Hou, Q., Liao, M., Guo, Y., Zang, Y., Wang, F., Liu, H., Luan, X., Liang, Y., Guan, Z., Li, Y., Liu, H., Dong, X., Zhang, X., Liu, J., & Xu, Q. (2023). Single-cell and spatial transcriptomics reveal POSTN + cancer-associated fibroblasts correlated with immune suppression and tumour progression in non-small cell lung cancer. *Clinical and Translational Medicine*, *13*(12), e1515. https://doi.org/10.1002/CTM2.1515

Chen, C. Y., Fuh, L. J., Huang, C. C., Hsu, C. J., Su, C. M., Liu, S. C., Lin, Y. M., & Tang, C. H. (2017). Enhancement of CCL2 expression and monocyte migration by CCN1 in osteoblasts through inhibiting miR-518a-5p: Implication of rheumatoid arthritis therapy. *Scientific Reports*, *7*(1). https://doi.org/10.1038/S41598-017-00513-0

Chen, H., Yang, W., Xue, X., Li, Y., Jin, Z., & Ji, Z. (2022). Integrated Analysis Revealed an Inflammatory Cancer-Associated Fibroblast-Based Subtypes with Promising Implications in Predicting the Prognosis and Immunotherapeutic Response of Bladder Cancer Patients. *International Journal of Molecular Sciences*, *23*(24), 15970. https://doi.org/10.3390/IJMS232415970/S1

Chen, J., Lansford, R., Stewart, V., Young, F., & Alt, F. W. (1993). RAG-2-deficient blastocyst complementation: an assay of gene function in lymphocyte development. *Proceedings of the National Academy of Sciences of the United States of America*, *90*(10), 4528–4532. https://doi.org/10.1073/PNAS.90.10.4528

Chen, M., Chen, F., Gao, Z., Li, X., Hu, L., Yang, S., Zhao, S., & Song, Z. (2024). CAFs and T cells interplay: The emergence of a new arena in cancer combat. *Biomedicine & Pharmacotherapy*, *177*, 117045. https://doi.org/10.1016/J.BIOPHA.2024.117045

Chen, Q., Sun, L., & Chen, Z. J. (2016). Regulation and function of the cGAS–STING pathway of cytosolic DNA sensing. *Nature Immunology 2016 17:10*, *17*(10), 1142–1149. https://doi.org/10.1038/ni.3558

Chen, X., Zhang, Y., & Fu, Y. (2022). The critical role of Toll-like receptor-mediated signaling in cancer immunotherapy. *Medicine in Drug Discovery*, *14*, 100122. https://doi.org/10.1016/J.MEDIDD.2022.100122

Chen, Y., Kim, J., Yang, S., Wang, H., Wu, C. J., Sugimoto, H., LeBleu, V. S., & Kalluri, R. (2021). Type I collagen deletion in αSMA+ myofibroblasts enhances immune suppression and accelerates progression of pancreatic cancer. *Cancer Cell*, *39*(4), 548. https://doi.org/10.1016/J.CCELL.2021.02.007

Chen, Y., Zhang, F., Zhang, B., Trojanowicz, B., Hämmerle, M., Kleeff, J., & Sunami, Y. (2024). Periostin is associated with prognosis and immune cell infiltration in pancreatic adenocarcinoma based on integrated bioinformatics analysis. *Cancer Reports*, *7*(2), e1990. https://doi.org/10.1002/CNR2.1990

Cheon, D. J., Tong, Y., Sim, M. S., Dering, J., Berel, D., Cui, X., Lester, J., Beach, J. A., Tighiouart, M., Walts, A. E., Karlan, B. Y., & Orsulic, S. (2013). A collagen-remodeling gene signature regulated by TGFβ signaling is associated with metastasis and poor survival in serous ovarian cancer. *Clinical Cancer Research : An Official Journal of the American Association for Cancer Research*, *20*(3), 711. https://doi.org/10.1158/1078-0432.CCR-13-1256

Chien, Y., Scuoppo, C., Wang, X., Fang, X., Balgley, B., Bolden, J. E., Premsrirut, P., Luo, W., Chicas, A., Lee, C. S., Kogan, S. C., & Lowe, S. W. (2011). Control of the senescence-associated secretory phenotype by NF-κB promotes senescence and enhances chemosensitivity. *Genes & Development*, *25*(20), 2125. https://doi.org/10.1101/GAD.17276711

Chin, L., Artandi, S. E., Shen, Q., Tam, A., Lee, S. L., Gottlieb, G. J., Greider, C. W., & DePinho, R. A. (1999). p53 Deficiency Rescues the Adverse Effects of Telomere Loss and Cooperates with Telomere Dysfunction to Accelerate Carcinogenesis. *Cell*, *97*(4), 527–538. https://doi.org/10.1016/S0092-8674(00)80762-X

Chitale, S., & Richly, H. (2017). Timing of DNA lesion recognition: Ubiquitin signaling in the NER pathway. *Cell Cycle*, *16*(2), 163–171. https://doi.org/10.1080/15384101.2016.1261227

Chiu, L. Y., Sun, Q., Zenke, F. T., Blaukat, A., & Vassilev, L. T. (2023). Selective ATM inhibition augments radiation-induced inflammatory signaling and cancer cell death. *Aging (Albany NY)*, *15*(2), 492. https://doi.org/10.18632/AGING.204487

Cho, W., Elizabeth Hospital, Q., Kong, H., Xiao, H., Kornek, M., Chandra Tripathi, S., Henke, E., Nandigama, R., & Ergün, S. (2020). Extracellular Matrix in the Tumor Microenvironment and Its Impact on Cancer Therapy. *Frontiers in Molecular Biosciences*, *6*, 160. https://doi.org/10.3389/FMOLB.2019.00160

Chon, H. J., Kim, H., Noh, J. H., Yang, H., Lee, W. S., Kong, S. J., Lee, S. J., Lee, Y. S., Kim, W. R., Kim, J. H., Kim, G., & Kim, C. (2019). STING signaling is a potential immunotherapeutic target in colorectal cancer. *Journal of Cancer*, *10*(20), 4932–4938. https://doi.org/10.7150/JCA.32806

Chow, M. T., Ozga, A. J., Servis, R. L., Frederick, D. T., Lo, J. A., Fisher, D. E., Freeman, G. J., Boland, G. M., & Luster, A. D. (2019). Intratumoral Activity of the CXCR3 Chemokine System Is Required for the Efficacy of Anti-PD-1 Therapy. *Immunity*, *50*(6), 1498-1512.e5. https://doi.org/10.1016/J.IMMUNI.2019.04.010/ATTACHMENT/3B8E0434-E4A3-404F-A67E-38E06472D704/MMC2.PDF

Christman, S. A., Kong, B. W., Landry, M. M., Kim, H., & Foster, D. N. (2006). Contributions of differential p53 expression in the spontaneous immortalization of a chicken embryo fibroblast cell line. *BMC Cell Biology*, *7*(1), 1–12. https://doi.org/10.1186/1471-2121-7-27/FIGURES/5

Cissell, D. D., Link, J. M., Hu, J. C., & Athanasiou, K. A. (2017). A Modified Hydroxyproline Assay Based on Hydrochloric Acid in Ehrlich's Solution Accurately Measures Tissue Collagen Content. *Tissue Engineering. Part C, Methods*, *23*(4), 243. https://doi.org/10.1089/TEN.TEC.2017.0018

Conlon, K. C., Miljkovic, M. D., & Waldmann, T. A. (2019). Cytokines in the Treatment of Cancer. *Journal of Interferon & Cytokine Research*, *39*(1), 6. https://doi.org/10.1089/JIR.2018.0019

Conroy, M. J., & Lysaght, J. (2020). CX3CL1 Signaling in the Tumor Microenvironment. *Advances in Experimental Medicine and Biology*, *1231*, 1–12. https://doi.org/10.1007/978-3-030-36667-4_1

Contreras, O., Rossi, F. M. V., & Theret, M. (2021). Origins, potency, and heterogeneity of skeletal muscle fibro-adipogenic progenitors—time for new definitions. *Skeletal Muscle 2021 11:1*, *11*(1), 1–25. https://doi.org/10.1186/S13395-021-00265-6

Coppé, J. P., Desprez, P. Y., Krtolica, A., & Campisi, J. (2010). The Senescence-Associated Secretory Phenotype: The Dark Side of Tumor Suppression. *Annual Review of Pathology*, *5*, 99. https://doi.org/10.1146/ANNUREV-PATHOL-121808-102144

Cords, L., Engler, S., Haberecker, M., Rüschoff, J. H., Moch, H., de Souza, N., & Bodenmiller, B. (2024). Cancer-associated fibroblast phenotypes are associated with patient outcome in non-small cell lung cancer. *Cancer Cell*, *42*(3), 396-412.e5. https://doi.org/10.1016/J.CCELL.2023.12.021/ATTACHMENT/AEC94956-0E47-40FD-BF8D-66B7897BD0F4/MMC2.PDF

Cords, L., Tietscher, S., Anzeneder, T., Langwieder, C., Rees, M., de Souza, N., & Bodenmiller, B. (2023). Cancer-associated fibroblast classification in single-cell and spatial proteomics data. *Nature Communications 2023 14:1*, *14*(1), 1–13. https://doi.org/10.1038/s41467-023-39762-1

Couillin, I., & Riteau, N. (2021). STING Signaling and Sterile Inflammation. *Frontiers in Immunology*, *12*, 753789. https://doi.org/10.3389/FIMMU.2021.753789/PDF

Croizer, H., Mhaidly, R., Kieffer, Y., Gentric, G., Djerroudi, L., Leclere, R., Pelon, F., Robley, C., Bohec, M., Meng, A., Meseure, D., Romano, E., Baulande, S., Peltier, A., Vincent-Salomon, A., & Mechta-Grigoriou, F. (2024). Deciphering the spatial landscape and plasticity of immunosuppressive fibroblasts in breast cancer. *Nature Communications 2024 15:1*, *15*(1), 1–28. https://doi.org/10.1038/s41467-024-47068-z

Crowley, L. C., Scott, A. P., Marfell, B. J., Boughaba, J. A., Chojnowski, G., & Waterhouse, N. J. (2016). Measuring Cell Death by Propidium Iodide Uptake and Flow Cytometry. *Cold Spring Harbor Protocols*, *2016*(7), 647–651. https://doi.org/10.1101/PDB.PROT087163

Dan Dunn, J., Alvarez, L. A. J., Zhang, X., & Soldati, T. (2015). Reactive oxygen species and mitochondria: A nexus of cellular homeostasis. *Redox Biology*, *6*, 472–485. https://doi.org/10.1016/J.REDOX.2015.09.005

Day, M., Oliver, A. W., & Pearl, L. H. (2022). Structure of the human RAD17–RFC clamp loader and 9–1–1 checkpoint clamp bound to a dsDNA–ssDNA junction. *Nucleic Acids Research*, *50*(14), 8279. https://doi.org/10.1093/NAR/GKAC588

De Clercq, E. (2019). Mozobil® (Plerixafor, AMD3100), 10 years after its approval by the US Food and Drug Administration. *Antiviral Chemistry & Chemotherapy*, *27*, 2040206619829382. https://doi.org/10.1177/2040206619829382

de La Chapelle, A., & Hampel, H. (2010). Clinical Relevance of Microsatellite Instability in Colorectal Cancer. *Journal of Clinical Oncology*, *28*(20), 3380. https://doi.org/10.1200/JCO.2009.27.0652

De La Jara Ortiz, F., Cimmino, C., Grech, K., Huynen, M. A., Janssen, E., Wagenaar, V., Van Zwam, M. C., Van Den Dries, K., Ventre, M., & Cambi, A. (n.d.). *In vitro-generated inflammatory fibroblasts secrete extracellular matrix with biochemical and biophysical properties similar to tissue-remodelling fibroblasts*. https://doi.org/10.1101/2024.09.26.614950

De Martin, A., Stanossek, Y., Lütge, M., Cadosch, N., Onder, L., Cheng, H. W., Brandstadter, J. D., Maillard, I., Stoeckli, S. J., Pikor, N. B., & Ludewig, B. (2023). PI16+ reticular cells in human palatine tonsils govern T cell activity in distinct subepithelial niches. *Nature Immunology 2023 24:7*, *24*(7), 1138–1148. https://doi.org/10.1038/s41590-023-01502-4

De, P., Aske, J., Dey, N., Hojjat-Farsangi, M., & Namdar, A. (2021). Cancer-Associated Fibroblast Functions as a Road-Block in Cancer Therapy. *Cancers 2021, Vol. 13, Page 5246*, *13*(20), 5246. https://doi.org/10.3390/CANCERS13205246

De Zio, D., Cianfanelli, V., & Cecconi, F. (2013). New Insights into the Link Between DNA Damage and Apoptosis. *Antioxidants & Redox Signaling*, *19*(6), 559. https://doi.org/10.1089/ARS.2012.4938

Deans, A. J., & West, S. C. (2011). DNA interstrand crosslink repair and cancer. *Nature Reviews. Cancer*, *11*(7), 467. https://doi.org/10.1038/NRC3088

DeBerardinis, R. J., Lum, J. J., Hatzivassiliou, G., & Thompson, C. B. (2008). The Biology of Cancer: Metabolic Reprogramming Fuels Cell Growth and Proliferation. *Cell Metabolism*, *7*(1), 11–20. https://doi.org/10.1016/J.CMET.2007.10.002

Delamarre, L., Holcombe, H., & Mellman, I. (2003). Presentation of Exogenous Antigens on Major Histocompatibility Complex (MHC) Class I and MHC Class II Molecules Is Differentially Regulated during Dendritic Cell Maturation. *The Journal of Experimental Medicine*, *198*(1), 111. https://doi.org/10.1084/JEM.20021542

Delia, D., & Mizutani, S. (2017). The DNA damage response pathway in normal hematopoiesis and malignancies. *International Journal of Hematology*, *106*(3), 328–334. https://doi.org/10.1007/S12185-017-2300-7/FIGURES/1

Demiryurek, Y., Nickaeen, M., Zheng, M., Yu, M., Zahn, J. D., Shreiber, D. I., Lin, H., & Shan, J. W. (2015). Transport, resealing, and re-poration dynamics of two-pulse electroporation-mediated molecular delivery. *Biochimica et Biophysica Acta (BBA) - Biomembranes*, *1848*(8), 1706–1714. https://doi.org/10.1016/J.BBAMEM.2015.04.007

Deng, Z., Fan, T., Xiao, C., Tian, H., Zheng, Y., Li, C., & He, J. (2024). TGF-β signaling in health, disease and therapeutics. *Signal Transduction and Targeted Therapy 2024 9:1*, *9*(1), 1–40. https://doi.org/10.1038/s41392-024-01764-w

Desjardins, M. (2019). Antigen cross-presentation: proteasome location, location, location. *The EMBO Journal*, *38*(16), e102799. https://doi.org/10.15252/EMBJ.2019102799

Di Micco, R., Krizhanovsky, V., Baker, D., & d'Adda di Fagagna, F. (2020). Cellular senescence in ageing: from mechanisms to therapeutic opportunities. *Nature Reviews Molecular Cell Biology 2020 22:2*, *22*(2), 75–95. https://doi.org/10.1038/s41580-020-00314-w

Diller, R. B., & Tabor, A. J. (2022). The Role of the Extracellular Matrix (ECM) in Wound Healing: A Review. *Biomimetics*, *7*(3), 87. https://doi.org/10.3390/BIOMIMETICS7030087

Dinstag, G., Elis, E., Ben-Zvi, D. S., Aldape, K., Ruppin, E., Beker, T., Berger, R., & Aharonov, R. (2023). 157 A transcriptomics-based response predictor identifies potential responders among patients with negative standard markers for response to immune checkpoint blockers. *Journal for ImmunoTherapy of Cancer*, *11*(Suppl 1), A177–A177. https://doi.org/10.1136/JITC-2023-SITC2023.0157

Distler, J. H. W., Wenger, R. H., Gassmann, M., Kurowska, M., Hirth, A., Gay, S., & Distler, O. (2004). Physiologic Responses to Hypoxia and Implications for Hypoxia-Inducible Factors in the Pathogenesis of Rheumatoid Arthritis. *Arthritis and Rheumatism*, *50*(1), 10–23. https://doi.org/10.1002/ART.11425

Dong, Z., Luo, Y., Yuan, Z., Tian, Y., Jin, T., & Xu, F. (2024). Cellular senescence and SASP in tumor progression and therapeutic opportunities. *Molecular Cancer 2024 23:1*, *23*(1), 1–19. https://doi.org/10.1186/S12943-024-02096-7

Du, S., Liang, Q., & Shi, J. (2024). Progress of ATM inhibitors: Opportunities and challenges. *European Journal of Medicinal Chemistry*, *277*, 116781. https://doi.org/10.1016/J.EJMECH.2024.116781

Du, Y. H., Cao, J., Jiang, X., Cai, X. W., Wang, B., Wang, Y., Wang, X. Z., & Xue, B. X. (2021). Comprehensive analysis of CXCL12 expression reveals the significance of inflammatory

fibroblasts in bladder cancer carcinogenesis and progression. *Cancer Cell International*, *21*(1), 1–15. https://doi.org/10.1186/S12935-021-02314-Y/FIGURES/8

Duan, M., Speer, R. M., Ulibarri, J., Liu, K. J., & Mao, P. (2021). Transcription-coupled Nucleotide Excision Repair: New Insights Revealed by Genomic Approaches. *DNA Repair, 103*, 103126. https://doi.org/10.1016/J.DNAREP.2021.103126

Duan, X., Yuan, X., Yao, B., Song, W., Li, Z., Enhejirigala, Kong, Y., Wang, Y., Fu, X., & Huang, S. (2022). The role of CTHRC1 in promotion of cutaneous wound healing. *Signal Transduction and Targeted Therapy 2022 7:1*, *7*(1), 1–4. https://doi.org/10.1038/s41392-022-01008-9

Dufait, I., Liechtenstein, T., Lanna, A., Bricogne, C., Laranga, R., Padella, A., Breckpot, K., & Escors, D. (2012). Retroviral and Lentiviral Vectors for the Induction of Immunological Tolerance. *Scientifica*, *2012*, 694137. https://doi.org/10.6064/2012/694137

Dufour, J. H., Dziejman, M., Liu, M. T., Leung, J. H., Lane, T. E., & Luster, A. D. (2002). IFN-γ-Inducible Protein 10 (IP-10; CXCL10)-Deficient Mice Reveal a Role for IP-10 in Effector T Cell Generation and Trafficking. *The Journal of Immunology*, *168*(7), 3195–3204. https://doi.org/10.4049/JIMMUNOL.168.7.3195

Dunn, G. P., Bruce, A. T., Ikeda, H., Old, L. J., & Schreiber, R. D. (2002). Cancer immunoediting: from immunosurveillance to tumor escape. *Nature Immunology 2002 3:11*, *3*(11), 991–998. https://doi.org/10.1038/ni1102-991

Dunphy, G., Flannery, S. M., Almine, J. F., Connolly, D. J., Paulus, C., Jønsson, K. L., Jakobsen, M. R., Nevels, M. M., Bowie, A. G., & Unterholzner, L. (2018). Non-canonical Activation of the DNA Sensing Adaptor STING by ATM and IFI16 Mediates NF-κB Signaling after Nuclear DNA Damage. *Molecular Cell*, *71*(5), 745-760.e5. https://doi.org/10.1016/J.MOLCEL.2018.07.034/ATTACHMENT/2CCC98F8-9833-4860-8DCA-01DBF5120CFA/MMC2.PDF

Duque, G. A., & Descoteaux, A. (2014). Macrophage cytokines: Involvement in immunity and infectious diseases. *Frontiers in Immunology*, *5*(OCT), 117833. https://doi.org/10.3389/FIMMU.2014.00491/PDF

Durant, S. T., Zheng, L., Wang, Y., Chen, K., Zhang, L., Zhang, T., Yang, Z., Riches, L., Trinidad, A. G., Fok, J. H. L., Hunt, T., Pike, K. G., Wilson, J., Smith, A., Colclough, N., Reddy, V. P., Sykes, A., Janefeldt, A., Johnström, P., … Pass, M. (2018). The brain-penetrant clinical ATM inhibitor AZD1390 radiosensitizes and improves survival of preclinical brain tumor models. *Science Advances*, *4*(6), eaat1719. https://doi.org/10.1126/SCIADV.AAT1719

Durmus, T., LeClair, R. J., Park, K. S., Terzic, A., Yoon, J. K., & Lindner, V. (2006). Expression analysis of the novel gene collagen triple helix repeat containing-1 (Cthrc1). *Gene Expression Patterns*, *6*(8), 935–940. https://doi.org/10.1016/J.MODGEP.2006.03.008

Dvorak, H. F. (2015). Tumors: Wounds that do not heal--Redux. *Cancer Immunology Research*, *3*(1), 1. https://doi.org/10.1158/2326-6066.CIR-14-0209

Dvorkin, S., Cambier, S., Volkman, H. E., & Stetson, D. B. (2024). New frontiers in the cGAS-STING intracellular DNA-sensing pathway. *Immunity*, *57*(4), 718–730. https://doi.org/10.1016/J.IMMUNI.2024.02.019

Egen, J. G., Ouyang, W., & Wu, L. C. (2020). Human Anti-tumor Immunity: Insights from Immunotherapy Clinical Trials. *Immunity*, *52*(1), 36–54. https://doi.org/10.1016/J.IMMUNI.2019.12.010

Elyada, E., Bolisetty, M., Laise, P., Flynn, W. F., Courtois, E. T., Burkhart, R. A., Teinor, J. A., Belleau, P., Biffi, G., Lucito, M. S., Sivajothi, S., Armstrong, T. D., Engle, D. D., Yu, K. H., Hao, Y., Wolfgang, C. L., Park, Y., Preall, J., Jaffee, E. M., … Tuveson, D. A. (2019). Cross-species single-cell analysis of pancreatic ductal adenocarcinoma reveals antigen-presenting cancer-associated fibroblasts. *Cancer Discovery*, *9*(8), 1102. https://doi.org/10.1158/2159-8290.CD-19-0094

Embgenbroich, M., & Burgdorf, S. (2018). Current Concepts of Antigen Cross-Presentation. *Frontiers in Immunology*, *9*(JUL), 1643. https://doi.org/10.3389/FIMMU.2018.01643

Eno, MS, PA-C, J. (2017). Immunotherapy Through the Years. *Journal of the Advanced Practitioner in Oncology*, *8*(7), 747. https://doi.org/10.6004/jadpro.2017.8.7.8

Erdogan, B., Ao, M., White, L. M., Means, A. L., Brewer, B. M., Yang, L., Washington, M. K., Shi, C., Franco, O. E., Weaver, A. M., Hayward, S. W., Li, D., & Webb, D. J. (2017). Cancer-associated fibroblasts promote directional cancer cell migration by aligning fibronectin. *The Journal of Cell Biology*, *216*(11), 3799. https://doi.org/10.1083/JCB.201704053

Evans, T. R. J., Colston, K. W., Lofts, F. J., Cunningham, D., Anthoney, D. A., Gogas, H., De Bono, J. S., Hamberg, K. J., Skov, T., & Mansi, J. L. (2002). A phase II trial of the vitamin D analogue Seocalcitol (EB1089) in patients with inoperable pancreatic cancer. *British Journal of Cancer*, *86*(5), 680–685. https://doi.org/10.1038/SJ.BJC.6600162

Eynon, E. E., Schlax, C., & Pieters, J. (1999). A Secreted Form of the Major Histocompatibility Complex Class II-associated Invariant Chain Inhibiting T Cell Activation. *Journal of Biological Chemistry*, *274*(37), 26266–26271. https://doi.org/10.1074/JBC.274.37.26266

Fabre, M., Ferrer, C., Domínguez-Hormaetxe, S., Bockorny, B., Murias, L., Seifert, O., Eisler, S. A., Kontermann, R. E., Pfizenmaier, K., Lee, S. Y., Vivanco, M. D. M., López-Casas, P. P., Perea,

S., Abbas, M., Richter, W., Simon, L., & Hidalgo, M. (2020). OMTX705, a novel FAP-targeting ADC demonstrates activity in chemotherapy and pembrolizumab-resistant solid tumor models. *Clinical Cancer Research*, *26*(13), 3420–3430. https://doi.org/10.1158/1078-0432.CCR-19-2238/75825/AM/OMTX705-A-NOVEL-FAP-TARGETING-ADC-DEMONSTRATES

Falahat, R., Berglund, A., Perez-Villarroel, P., & Mulé, J. (2023). 1509-B STING signaling-intact tumors display a 12-chemokine gene signature associated with tertiary lymphoid structures and favorable prognosis. *Journal for ImmunoTherapy of Cancer*, *11*(Suppl 2), A1855–A1855. https://doi.org/10.1136/JITC-2023-SITC2023.1509-B

Falck, J., Coates, J., & Jackson, S. P. (2005). Conserved modes of recruitment of ATM, ATR and DNA-PKcs to sites of DNA damage. *Nature 2005 434:7033*, *434*(7033), 605–611. https://doi.org/10.1038/nature03442

Fang, Z., Meng, Q., Xu, J., Wang, W., Zhang, B., Liu, J., Liang, C., Hua, J., Zhao, Y., Yu, X., & Shi, S. (2022). Signaling pathways in cancer-associated fibroblasts: recent advances and future perspectives. *Cancer Communications*, *43*(1), 3. https://doi.org/10.1002/CAC2.12392

Feig, C., Jones, J. O., Kraman, M., Wells, R. J. B., Deonarine, A., Chan, D. S., Connell, C. M., Roberts, E. W., Zhao, Q., Caballero, O. L., Teichmann, S. A., Janowitz, T., Jodrell, D. I., Tuveson, D. A., & Fearon, D. T. (2013). Targeting CXCL12 from FAP-expressing carcinoma-associated fibroblasts synergizes with anti-PD-L1 immunotherapy in pancreatic cancer. *Proceedings of the National Academy of Sciences of the United States of America*, *110*(50), 20212–20217. https://doi.org/10.1073/PNAS.1320318110

Feins, S., Kong, W., Williams, E. F., Milone, M. C., & Fraietta, J. A. (2019). An introduction to chimeric antigen receptor (CAR) T-cell immunotherapy for human cancer. *American Journal of Hematology*, *94*(S1), S3–S9. https://doi.org/10.1002/AJH.25418

Feola, S., Chiaro, J., Martins, B., & Cerullo, V. (2020). Uncovering the Tumor Antigen Landscape: What to Know about the Discovery Process. *Cancers*, *12*(6), 1660. https://doi.org/10.3390/CANCERS12061660

Finn, O. J. (2012). Immuno-oncology: understanding the function and dysfunction of the immune system in cancer. *Annals of Oncology*, *23*(Suppl 8), viii6. https://doi.org/10.1093/ANNONC/MDS256

Fonta, C. M., Loustau, T., Li, C., Poilil Surendran, S., Hansen, U., Murdamoothoo, D., Benn, M. C., Velazquez-Quesada, I., Carapito, R., Orend, G., & Vogel, V. (2023). Infiltrating CD8+ T cells and M2 macrophages are retained in tumor matrix tracks enriched in low tension fibronectin fibers. *Matrix Biology*, *116*, 1–27. https://doi.org/10.1016/J.MATBIO.2023.01.002

Ford, K., Hanley, C. J., Mellone, M., Szyndralewiez, C., Heitz, F., Wiesel, P., Wood, O., Machado, M., Lopez, M. A., Ganesan, A. P., Wang, C., Chakravarthy, A., Fenton, T. R., King, E. V., Vijayanand, P., Ottensmeier, C. H., Al-Shamkhani, A., Savelyeva, N., & Thomas, G. J. (2020). NOX4 Inhibition Potentiates Immunotherapy by Overcoming Cancer-Associated Fibroblast-Mediated CD8 T-cell Exclusion from Tumors. *Cancer Research*, *80*(9), 1846–1860. https://doi.org/10.1158/0008-5472.CAN-19-3158

Foster, D. S., Jones, R. E., Ransom, R. C., Longaker, M. T., & Norton, J. A. (2018). The evolving relationship of wound healing and tumor stroma. *JCI Insight*, *3*(18). https://doi.org/10.1172/JCI.INSIGHT.99911

Franzin, R., Netti, G. S., Spadaccino, F., Porta, C., Gesualdo, L., Stallone, G., Castellano, G., & Ranieri, E. (2020). The Use of Immune Checkpoint Inhibitors in Oncology and the Occurrence of AKI: Where Do We Stand? *Frontiers in Immunology*, *11*, 2619. https://doi.org/10.3389/FIMMU.2020.574271/BIBTEX

Freitas, A. A., & De Magalhães, J. P. (2011). A review and appraisal of the DNA damage theory of ageing. *Mutation Research/Reviews in Mutation Research*, *728*(1–2), 12–22. https://doi.org/10.1016/J.MRREV.2011.05.001

Freund, A., Patil, C. K., & Campisi, J. (2011). p38MAPK is a novel DNA damage response-independent regulator of the senescence-associated secretory phenotype. *The EMBO Journal*, *30*(8), 1536. https://doi.org/10.1038/EMBOJ.2011.69

Friedl, P., & Weigelin, B. (2008). Interstitial leukocyte migration and immune function. *Nature Immunology*, *9*(9), 960–969. https://doi.org/10.1038/NI.F.212

Fu, C., Duan, S., Zhou, X., Meng, Y., & Chen, X. (2024). Overexpression of COL11A1 confers tamoxifen resistance in breast cancer. *Npj Breast Cancer 2024 10:1*, *10*(1), 1–10. https://doi.org/10.1038/s41523-024-00645-3

Fu, D., Calvo, J. A., & Samson, L. D. (2012). SERIES: Genomic instability in cancer Balancing repair and tolerance of DNA damage caused by alkylating agents. *Nature Reviews. Cancer*, *12*(2), 104. https://doi.org/10.1038/NRC3185

Fu, M., Hu, Y., Lan, T., Guan, K. L., Luo, T., & Luo, M. (2022). The Hippo signalling pathway and its implications in human health and diseases. *Signal Transduction and Targeted Therapy 2022 7:1*, *7*(1), 1–20. https://doi.org/10.1038/s41392-022-01191-9

Fugger, K., & West, S. C. (2016). Keeping homologous recombination in check. *Cell Research*, *26*(4), 397. https://doi.org/10.1038/CR.2016.25

Galbo, P. M., Zang, X., & Zheng, D. (2021). Implication of cancer associated fibroblast subtypes on cancer pathogenesis, prognosis, and immunotherapy resistance. *Clinical Cancer*

Research : An Official Journal of the American Association for Cancer Research, *27*(9), 2636. https://doi.org/10.1158/1078-0432.CCR-20-4226

Galbo, P. M., Zang, X., & Zheng, D. (2021). Molecular features of cancer-associated fibroblast subtypes and their implication on cancer pathogenesis, prognosis, and immunotherapy resistance. *Clinical Cancer Research*, *27*(9), 2636–2647. https://doi.org/10.1158/1078-0432.CCR-20-4226/79067/AM/IMPLICATION-OF-CANCER-ASSOCIATED-FIBROBLAST

Galon, J., & Bruni, D. (2019). Approaches to treat immune hot, altered and cold tumours with combination immunotherapies. *Nature Reviews Drug Discovery 2018 18:3*, *18*(3), 197–218. https://doi.org/10.1038/s41573-018-0007-y

Gan, Y., Li, X., Han, S., Liang, Q., Ma, X., Rong, P., Wang, W., & Li, W. (2022). The cGAS/STING Pathway: A Novel Target for Cancer Therapy. *Frontiers in Immunology*, *12*, 795401. https://doi.org/10.3389/FIMMU.2021.795401

Gao, W., Gao, J., Chen, L., Ren, Y., & Ma, J. (2019). Targeting XIST induced apoptosis of human osteosarcoma cells by activation of NF-kB/PUMA signal. *Bioengineered*, *10*(1), 261. https://doi.org/10.1080/21655979.2019.1631104

Gao, W., Guo, L., Yang, Y., Wang, Y., Xia, S., Gong, H., Zhang, B. K., & Yan, M. (2022). Dissecting the Crosstalk Between Nrf2 and NF-κB Response Pathways in Drug-Induced Toxicity. *Frontiers in Cell and Developmental Biology*, *9*, 809952. https://doi.org/10.3389/FCELL.2021.809952/PDF

Geng, X., Chen, H., Zhao, L., Hu, J., Yang, W., Li, G., Cheng, C., Zhao, Z., Zhang, T., Li, L., & Sun, B. (2021). Cancer-Associated Fibroblast (CAF) Heterogeneity and Targeting Therapy of CAFs in Pancreatic Cancer. *Frontiers in Cell and Developmental Biology*, *9*, 655152. https://doi.org/10.3389/FCELL.2021.655152/BIBTEX

Ghelli Luserna Di Rorà, A., Cerchione, C., Martinelli, G., & Simonetti, G. (2020). A WEE1 family business: regulation of mitosis, cancer progression, and therapeutic target. *Journal of Hematology & Oncology 2020 13:1*, *13*(1), 1–17. https://doi.org/10.1186/S13045-020-00959-2

Gilles, G., McCulloch, A. D., Brakebusch, C. H., & Herum, K. M. (2020). Maintaining resting cardiac fibroblasts in vitro by disrupting mechanotransduction. *PLoS ONE*, *15*(10 October). https://doi.org/10.1371/JOURNAL.PONE.0241390

Gilmer, T. M., Lai, C. H., Guo, K., Deland, K., Ashcraft, K. A., Stewart, A. E., Wang, Y., Fu, J., Wood, K. C., Kirsch, D. G., & Kastan, M. B. (2024). A Novel Dual ATM/DNA-PK Inhibitor, XRD-0394, Potently Radiosensitizes and Potentiates PARP and Topoisomerase I Inhibitors. *Molecular*

Cancer Therapeutics, *23*(6), 751–765. https://doi.org/10.1158/1535-7163.MCT-23-0890/742919/AM/A-NOVEL-DUAL-ATM-DNA-PK-INHIBITOR-XRD-0394

Goel, K., & Ploski, J. E. (2022). RISC-y Business: Limitations of Short Hairpin RNA-Mediated Gene Silencing in the Brain and a Discussion of CRISPR/Cas-Based Alternatives. *Frontiers in Molecular Neuroscience*, *15*, 914430. https://doi.org/10.3389/FNMOL.2022.914430/XML/NLM

Golding, S. E., Rosenberg, E., Valerie, N., Hussaini, I., Frigerio, M., Cockcroft, X. F., Wei, Y. C., Hummersone, M., Rigoreau, L., Menear, K. A., O'Connor, M. J., Povirk, L. F., Van Meter, T., & Valerie, K. (2009). Improved ATM kinase inhibitor KU-60019 radiosensitizes glioma cells, compromises insulin, AKT and ERK prosurvival signaling, and inhibits migration and invasion. *Molecular Cancer Therapeutics*, *8*(10), 2894. https://doi.org/10.1158/1535-7163.MCT-09-0519

Gong, J., Chehrazi-Raffle, A., Reddi, S., & Salgia, R. (2018). Development of PD-1 and PD-L1 inhibitors as a form of cancer immunotherapy: a comprehensive review of registration trials and future considerations. *Journal for Immunotherapy of Cancer*, *6*(1), 8. https://doi.org/10.1186/S40425-018-0316-Z

Gonzalez, H., Hagerling, C., & Werb, Z. (2018). Roles of the immune system in cancer: from tumor initiation to metastatic progression. *Genes & Development*, *32*(19–20), 1267. https://doi.org/10.1101/GAD.314617.118

González-González, L., & Alonso, J. (2018). Periostin: A Matricellular Protein With Multiple Functions in Cancer Development and Progression. *Frontiers in Oncology*, *8*(JUN). https://doi.org/10.3389/FONC.2018.00225

Gorchs, L., Ahmed, S., Mayer, C., Knauf, A., Fernández Moro, C., Svensson, M., Heuchel, R., Rangelova, E., Bergman, P., & Kaipe, H. (2020). The vitamin D analogue calcipotriol promotes an anti-tumorigenic phenotype of human pancreatic CAFs but reduces T cell mediated immunity. *Scientific Reports*, *10*(1). https://doi.org/10.1038/S41598-020-74368-3

Goto, H., Natsume, T., Kanemaki, M. T., Kaito, A., Wang, S., Gabazza, E. C., Inagaki, M., & Mizoguchi, A. (2019). Chk1-mediated Cdc25A degradation as a critical mechanism for normal cell cycle progression. *Journal of Cell Science*, *132*(2). https://doi.org/10.1242/JCS.223123/265877/AM/CHK1-MEDIATED-CDC25A-DEGRADATION-AS-A-CRITICAL

Goyco Vera, D., Waghela, H., Nuh, M., Pan, J., & Lulla, P. (2024). Approved CAR-T therapies have reproducible efficacy and safety in clinical practice. *Human Vaccines & Immunotherapeutics*, *20*(1), 2378543. https://doi.org/10.1080/21645515.2024.2378543

Gschwandtner, M., Derler, R., & Midwood, K. S. (2019). More Than Just Attractive: How CCL2 Influences Myeloid Cell Behavior Beyond Chemotaxis. *Frontiers in Immunology*, *10*, 491100. https://doi.org/10.3389/FIMMU.2019.02759/BIBTEX

Guermonprez, P., Saveanu, L., Kleijmeer, M., Davoust, J., Van Endert, P., & Amigorena, S. (2003). ER–phagosome fusion defines an MHC class I cross-presentation compartment in dendritic cells. *Nature 2003 425:6956*, *425*(6956), 397–402. https://doi.org/10.1038/nature01911

Guo, J., Zeng, H., & Chen, Y. (2020). Emerging Nano Drug Delivery Systems Targeting Cancer-Associated Fibroblasts for Improved Antitumor Effect and Tumor Drug Penetration. *Molecular Pharmaceutics*, *17*(4), 1028–1048. https://doi.org/10.1021/ACS.MOLPHARMACEUT.0C00014/ASSET/IMAGES/LARGE/MP0C00014_0009.JPEG

Guo, S., Yuan, J., Meng, X., Feng, X., Ma, D., Han, Y., & Li, K. (2023). Cancer-associated fibroblasts: Just on the opposite side of antitumour immunity? *International Immunopharmacology*, *122*, 110601. https://doi.org/10.1016/J.INTIMP.2023.110601

Guo, X., Zhang, Y., Peng, L., Wang, Y., He, C. W., Li, K., Hao, K., Li, K., Wang, Z., Huang, H., & Miao, X. (2024). Collagen synthase P4HA3 as a novel biomarker for colorectal cancer correlates with prognosis and immune infiltration. *Heliyon*, *10*(11), e31695. https://doi.org/10.1016/J.HELIYON.2024.E31695

Guo, Z., Kozlov, S., Lavin, M. F., Person, M. D., & Paull, T. T. (2010). ATM activation by oxidative stress. *Science*, *330*(6003), 517–521. https://doi.org/10.1126/SCIENCE.1192912/SUPPL_FILE/GUO.SOM.PDF

Haabeth, O. A. W., Tveita, A. A., Fauskanger, M., Schjesvold, F., Lorvik, K. B., Hofgaard, P. O., Omholt, H., Munthe, L. A., Dembic, Z., Corthay, A., & Bogen, B. (2014). How do CD4+ T cells detect and eliminate tumor cells that either lack or express MHC class II molecules? *Frontiers in Immunology*, *5*(APR), 86845. https://doi.org/10.3389/FIMMU.2014.00174/BIBTEX

Hadler-Olsen, E., Fadnes, B., Sylte, I., Uhlin-Hansen, L., & Winberg, J. O. (2011). Regulation of matrix metalloproteinase activity in health and disease. *The FEBS Journal*, *278*(1), 28–45. https://doi.org/10.1111/J.1742-4658.2010.07920.X

Hahm, J. Y., Park, J., Jang, E. S., & Chi, S. W. (2022). 8-Oxoguanine: from oxidative damage to epigenetic and epitranscriptional modification. *Experimental & Molecular Medicine 2022 54:10*, *54*(10), 1626–1642. https://doi.org/10.1038/s12276-022-00822-z

Haj, M., Levon, A., Frey, Y., Hourvitz, N., Campisi, J., Tzfati, Y., Elkon, R., Ziv, Y., & Shiloh, Y. (2023). Accelerated replicative senescence of ataxia-telangiectasia skin fibroblasts is retained at

physiologic oxygen levels, with unique and common transcriptional patterns. *Aging Cell*, *22*(8), e13869. https://doi.org/10.1111/ACEL.13869

Hakem, R. (2008). DNA-damage repair; the good, the bad, and the ugly. *The EMBO Journal*, *27*(4), 589. https://doi.org/10.1038/EMBOJ.2008.15

Hall, J., Ralph, E. C., Shanker, S., Wang, H., Byrnes, L. J., Horst, R., Wong, J., Brault, A., Dumlao, D., Smith, J. F., Dakin, L. A., Schmitt, D. C., Trujillo, J., Vincent, F., Griffor, M., & Aulabaugh, A. E. (2017). The catalytic mechanism of cyclic GMP-AMP synthase (cGAS) and implications for innate immunity and inhibition. *Protein Science : A Publication of the Protein Society*, *26*(12), 2367. https://doi.org/10.1002/PRO.3304

Han, C., Liu, T., & Yin, R. (2020). Biomarkers for cancer-associated fibroblasts. *Biomarker Research*, *8*(1), 1–8. https://doi.org/10.1186/S40364-020-00245-W/TABLES/2

Hanley, C. J., Mellone, M., Ford, K., Thirdborough, S. M., Mellows, T., Frampton, S. J., Smith, D. M., Harden, E., Szyndralewiez, C., Bullock, M., Noble, F., Moutasim, K. A., King, E. V., Vijayanand, P., Mirnezami, A. H., Underwood, T. J., Ottensmeier, C. H., & Thomas, G. J. (2018). Targeting the Myofibroblastic Cancer-Associated Fibroblast Phenotype Through Inhibition of NOX4. *JNCI Journal of the National Cancer Institute*, *110*(1), 109. https://doi.org/10.1093/JNCI/DJX121

Hanley, C. J., & Thomas, G. J. (2020). T-cell tumour exclusion and immunotherapy resistance: a role for CAF targeting. *British Journal of Cancer*, *123*(9), 1353. https://doi.org/10.1038/S41416-020-1020-6

Hanley, C. J., Thomas, G. J., Hanley, C. J., & Thomas, G. J. (2021). Targeting cancer associated fibroblasts to enhance immunotherapy: emerging strategies and future perspectives. *Oncotarget*, *12*(14), 1427–1433. https://doi.org/10.18632/ONCOTARGET.27936

Hao, N. B., Lü, M. H., Fan, Y. H., Cao, Y. L., Zhang, Z. R., & Yang, S. M. (2012). Macrophages in Tumor Microenvironments and the Progression of Tumors. *Clinical and Developmental Immunology*, *2012*, 948098. https://doi.org/10.1155/2012/948098

Harikrishnan, K., Prabhu, S. S., & Balasubramanian, N. (2021). A pan-cancer analysis of matrisome proteins reveals CTHRC1and LOXL2 as major ECM regulators across cancers. *BioRxiv*, 2021.04.27.441627. https://doi.org/10.1101/2021.04.27.441627

Härtlova, A., Erttmann, S. F., Raffi, F. A. M., Schmalz, A. M., Resch, U., Anugula, S., Lienenklaus, S., Nilsson, L. M., Kröger, A., Nilsson, J. A., Ek, T., Weiss, S., & Gekara, N. O. (2015). DNA Damage Primes the Type I Interferon System via the Cytosolic DNA Sensor STING to Promote Anti-Microbial Innate Immunity. *Immunity*, *42*(2), 332–343. https://doi.org/10.1016/J.IMMUNI.2015.01.012

Hartmann, N., Giese, N. A., Giese, T., Poschke, I., Offringa, R., Werner, J., & Ryschich, E. (2014). Prevailing role of contact guidance in intrastromal T-cell trapping in human pancreatic cancer. *Clinical Cancer Research : An Official Journal of the American Association for Cancer Research*, *20*(13), 3422–3433. https://doi.org/10.1158/1078-0432.CCR-13-2972

Hastings, J. F., Skhinas, J. N., Fey, D., Croucher, D. R., & Cox, T. R. (2019). The extracellular matrix as a key regulator of intracellular signalling networks. *British Journal of Pharmacology*, *176*(1), 82–92. https://doi.org/10.1111/BPH.14195

Hayat, M. A. (2015). Introduction to Autophagy: Cancer, Other Pathologies, Inflammation, Immunity, Infection, and Aging, Volume 7. *Autophagy: Cancer, Other Pathologies, Inflammation, Immunity, Infection, and Aging*, *7*, 1–53. https://doi.org/10.1016/B978-0-12-801043-3.00001-7

Hayflick, L., & Moorhead, P. S. (1961). The serial cultivation of human diploid cell strains. *Experimental Cell Research*, *25*(3), 585–621. https://doi.org/10.1016/0014-4827(61)90192-6

He, S., Zheng, L., & Qi, C. (2025). Myeloid-derived suppressor cells (MDSCs) in the tumor microenvironment and their targeting in cancer therapy. *Molecular Cancer 2025 24:1*, *24*(1), 1–24. https://doi.org/10.1186/S12943-024-02208-3

He, W., Zhang, H., Wang, Y., Zhou, Y., Luo, Y., Cui, Y., Jiang, N., Jiang, W., Wang, H., Xu, D., Li, S., Wang, Z., Chen, Y., Sun, Y., Zhang, Y., Tseng, H. R., Zou, X., Wang, L., & Ke, Z. (2018). CTHRC1 induces non-small cell lung cancer (NSCLC) invasion through upregulating MMP-7/MMP-9. *BMC Cancer*, *18*(1), 400. https://doi.org/10.1186/S12885-018-4317-6

Hewitt, E. W. (2003). The MHC class I antigen presentation pathway: strategies for viral immune evasion. *Immunology*, *110*(2), 163. https://doi.org/10.1046/J.1365-2567.2003.01738.X

Higgins, D. F., Kimura, K., Bernhardt, W. M., Shrimanker, N., Akai, Y., Hohenstein, B., Saito, Y., Johnson, R. S., Kretzler, M., Cohen, C. D., Eckardt, K. U., Iwano, M., & Haase, V. H. (2007). Hypoxia promotes fibrogenesis in vivo via HIF-1 stimulation of epithelial-to-mesenchymal transition. *The Journal of Clinical Investigation*, *117*(12), 3810. https://doi.org/10.1172/JCI30487

Hill, B. S., Pelagalli, A., Passaro, N., Zannetti, A., Hill, B. S., Pelagalli, A., Passaro, N., & Zannetti, A. (2017). Tumor-educated mesenchymal stem cells promote pro-metastatic phenotype. *Oncotarget*, *8*(42), 73296–73311. https://doi.org/10.18632/ONCOTARGET.20265

Hill, M. A., & Meininger, G. A. (2012). Myogenic Tone and Mechanotransduction. *Muscle*, *2*, 1243–1257. https://doi.org/10.1016/B978-0-12-381510-1.00093-4

Hillsley, A., Santos, J. E., & Rosales, A. M. (2021). A deep learning approach to identify and segment alpha-smooth muscle actin stress fiber positive cells. *Scientific Reports 2021 11:1*, *11*(1), 1–11. https://doi.org/10.1038/s41598-021-01304-4

Hingorani, S. R., Harris, W. P., Beck, J. T., Berdov, B. A., Wagner, S. A., Pshevlotsky, E. M., Tjulandin, S. A., Gladkov, O. A., Holcombe, R. F., Korn, R., Raghunand, N., Dychter, S., Jiang, P., Shepard, H. M., & Devoe, C. E. (2016). Phase Ib study of PEGylated recombinant human hyaluronidase and gemcitabine in patients with advanced pancreatic cancer. *Clinical Cancer Research*, *22*(12), 2848–2854. https://doi.org/10.1158/1078-0432.CCR-15-2010/128627/AM/PHASE-1B-STUDY-OF-PEGYLATED-RECOMBINANT-HUMAN

Hinz, B. (2010). The myofibroblast: Paradigm for a mechanically active cell. *Journal of Biomechanics*, *43*(1), 146–155. https://doi.org/10.1016/J.JBIOMECH.2009.09.020

Hinz, B., Dugina, V., Ballestrem, C., Wehrle-Haller, B., & Chaponnier, C. (2003). α-Smooth Muscle Actin Is Crucial for Focal Adhesion Maturation in Myofibroblasts. *Molecular Biology of the Cell*, *14*(6), 2508. https://doi.org/10.1091/MBC.E02-11-0729

Hinz, M., & Scheidereit, C. (2013). The IκB kinase complex in NF-κB regulation and beyond. *EMBO Reports*, *15*(1), 46. https://doi.org/10.1002/EMBR.201337983

Hirani, P., Gauthier, V., Allen, C. E., Wight, T. N., & Pearce, O. M. T. (2021). Targeting Versican as a Potential Immunotherapeutic Strategy in the Treatment of Cancer. *Frontiers in Oncology*, *11*, 3410. https://doi.org/10.3389/FONC.2021.712807/BIBTEX

Hirani, P., McDermott, J., Rajeeve, V., Cutillas, P. R., Jones, J. L., Pennington, D. J., Wight, T. N., Santamaria, S., Alonge, K. M., & Pearce, O. M. T. (2024). Versican Associates with Tumor Immune Phenotype and Limits T-cell Trafficking via Chondroitin Sulfate. *Cancer Research Communications*, *4*(4), 970. https://doi.org/10.1158/2767-9764.CRC-23-0548

Hofheinz, R. D., Al-Batran, S. E., Hartmann, F., Hartung, G., Jäger, D., Renner, C., Tanswell, P., Kunz, U., Amelsberg, A., Kuthan, H., & Stehle, G. (2003). Stromal Antigen Targeting by a Humanised Monoclonal Antibody: An Early Phase II Trial of Sibrotuzumab in Patients with Metastatic Colorectal Cancer. *Onkologie*, *26*(1), 44–48. https://doi.org/10.1159/000069863

Holland, C. J., Cole, D. K., & Godkin, A. (2013). Re-directing CD4+ T cell responses with the flanking residues of MHC class II-bound peptides: The core is not enough. *Frontiers in Immunology*, *4*(JUL), 54167. https://doi.org/10.3389/FIMMU.2013.00172/BIBTEX

Hong, J. H., Gatti, R. A., Huo, Y. K., Chiang, C. S., & McBride, W. H. (1994). G2/M-phase arrest and release in ataxia telangiectasia and normal cells after exposure to ionizing radiation. *Radiation Research*, *140*(1), 17–23. https://doi.org/10.2307/3578563

Hong, S., Lee, J. B., Iizuka, Y., Song, Y. K., Seong, G. J., & Han, S. H. (2012). The Role of Focal Adhesion Kinase in the TGF-β-Induced Myofibroblast Transdifferentiation of Human Tenon's Fibroblasts. *Korean Journal of Ophthalmology : KJO*, *26*(1), 45. https://doi.org/10.3341/KJO.2012.26.1.45

Hope, C., Emmerich, P. B., Papadas, A., Pagenkopf, A., Matkowskyj, K. A., Hey, D. R. Van De, Payne, S. N., Clipson, L., Callander, N. S., Hematti, P., Miyamoto, S., Johnson, M. G., Deming, D. A., & Asimakopoulos, F. (2017). Versican-derived matrikines regulate Batf3-dendritic cell differentiation and promote T-cell infiltration in colorectal cancer. *Journal of Immunology (Baltimore, Md. : 1950)*, *199*(5), 1933. https://doi.org/10.4049/JIMMUNOL.1700529

Hoption Cann, S. A., van Netten, J. P., & van Netten, C. (2003). Dr William Coley and tumour regression: a place in history or in the future. *Postgraduate Medical Journal*, *79*(938), 672. /pmc/articles/PMC1742910/?report=abstract

Horikawa, S., Ishii, Y., Hamashima, T., Yamamoto, S., Mori, H., Fujimori, T., Shen, J., Inoue, R., Nishizono, H., Itoh, H., Majima, M., Abraham, D., Miyawaki, T., & Sasahara, M. (2015). PDGFRα plays a crucial role in connective tissue remodeling. *Scientific Reports*, *5*, 17948. https://doi.org/10.1038/SREP17948

Horton, J. K., Watson, M., Stefanick, D. F., Shaughnessy, D. T., Taylor, J. A., & Wilson, S. H. (2008). XRCC1 and DNA polymerase β in cellular protection against cytotoxic DNA single-strand breaks. *Cell Research 2008 18:1*, *18*(1), 48–63. https://doi.org/10.1038/cr.2008.7

Hossain, M. A., Lin, Y., & Yan, S. (2018). Single-Strand Break End Resection in Genome Integrity: Mechanism and Regulation by APE2. *International Journal of Molecular Sciences*, *19*(8), 2389. https://doi.org/10.3390/IJMS19082389

Hryhorowicz, M., Grześkowiak, B., Mazurkiewicz, N., Śledziński, P., Lipiński, D., & Słomski, R. (2019). Improved Delivery of CRISPR/Cas9 System Using Magnetic Nanoparticles into Porcine Fibroblast. *Molecular Biotechnology*, *61*(3), 173–180. https://doi.org/10.1007/S12033-018-0145-9/FIGURES/6

Hsieh, P., & Yamane, K. (2008). DNA mismatch repair: Molecular mechanism, cancer, and ageing. *Mechanisms of Ageing and Development*, *129*(7–8), 391–407. https://doi.org/10.1016/J.MAD.2008.02.012

Hu, B., Wu, C., Mao, H., Gu, H., Dong, H., Yan, J., Qi, Z., Yuan, L., Dong, Q., & Long, J. (2022). Subpopulations of cancer-associated fibroblasts link the prognosis and metabolic features of pancreatic ductal adenocarcinoma. *Annals of Translational Medicine*, *10*(5), 262. https://doi.org/10.21037/ATM-22-407

Hu, M., Zhou, M., Bao, X., Pan, D., Jiao, M., Liu, X., Li, F., & Li, C. Y. (2021). ATM inhibition enhances cancer immunotherapy by promoting mtDNA leakage and cGAS/STING activation. *The Journal of Clinical Investigation*, *131*(3). https://doi.org/10.1172/JCI139333

Hu, S., Fang, Y., Chen, X., Cheng, T., Zhao, M., Du, M., Li, T., Li, M., Zeng, Z., Wei, Y., Gu, Z., Zhang, C., Sun, L., & Chen, Z. J. (2021). cGAS restricts colon cancer development by protecting intestinal barrier integrity. *Proceedings of the National Academy of Sciences of the United States of America*, *118*(23), e2105747118. https://doi.org/10.1073/PNAS.2105747118/SUPPL_FILE/PNAS.2105747118.SAPP.PDF

Hu, X., Bian, Y., Wen, X., Wang, M., Li, Y., & Wan, X. (2020). Collagen triple helix repeat containing 1 promotes endometrial cancer cell migration by activating the focal adhesion kinase signaling pathway. *Experimental and Therapeutic Medicine*, *20*(2), 1405–1414. https://doi.org/10.3892/ETM.2020.8833

Hu, X., li, J., Fu, M., Zhao, X., & Wang, W. (2021). The JAK/STAT signaling pathway: from bench to clinic. *Signal Transduction and Targeted Therapy 2021 6:1*, *6*(1), 1–33. https://doi.org/10.1038/s41392-021-00791-1

Huang, C. H., Huang, Y. C., Xu, J. K., Chen, S. Y., Tseng, L. C., Huang, J. L., & Lin, C. S. (2023). ATM Inhibition-Induced ISG15/IFI27/OASL Is Correlated with Immunotherapy Response and Inflamed Immunophenotype. *Cells*, *12*(9), 1288. https://doi.org/10.3390/CELLS12091288/S1

Huang, H., Wang, Z., Zhang, Y., Pradhan, R. N., Ganguly, D., Chandra, R., Murimwa, G., Wright, S., Gu, X., Maddipati, R., Müller, S., Turley, S. J., & Brekken, R. A. (2022). Mesothelial cell-derived antigen-presenting cancer-associated fibroblasts induce expansion of regulatory T cells in pancreatic cancer. *Cancer Cell*, *40*(6), 656. https://doi.org/10.1016/J.CCELL.2022.04.011

Huang, X., Yang, N., Fiore, V. F., Barker, T. H., Sun, Y., Morris, S. W., Ding, Q., Thannickal, V. J., & Zhou, Y. (2012). Matrix Stiffness–Induced Myofibroblast Differentiation Is Mediated by Intrinsic Mechanotransduction. *Https://Doi.Org/10.1165/Rcmb.2012-0050OC*, *47*(3), 340–348. https://doi.org/10.1165/RCMB.2012-0050OC

Huang, X., & Yang, Y. (2010). Targeting the TLR9-MyD88 pathway in the regulation of adaptive immune responses. *Expert Opinion on Therapeutic Targets*, *14*(8), 787. https://doi.org/10.1517/14728222.2010.501333

Huang, Y., & Li, L. (2013). DNA crosslinking damage and cancer - a tale of friend and foe. *Translational Cancer Research*, *2*(3), 144. https://doi.org/10.3978/J.ISSN.2218-676X.2013.03.01

Hung, S. P., Yang, M. H., Tseng, K. F., & Lee, O. K. (2013). Hypoxia-induced secretion of TGF-β1 in mesenchymal stem cell promotes breast cancer cell progression. *Cell Transplantation*, *22*(10), 1869–1882. https://doi.org/10.3727/096368912X657954

Hutson, T. H., Foster, E., Dawes, J. M., Hindges, R., Yáñez-Muñoz, R. J., & Moon, L. D. F. (2012). Lentiviral vectors encoding shRNAs efficiently transduce and knockdown LINGO-1 but induce an interferon response and cytotoxicity in CNS neurons. *The Journal of Gene Medicine*, *14*(5), 299. https://doi.org/10.1002/JGM.2626

Iannello, A., Thompson, T. W., Ardolino, M., Lowe, S. W., & Raulet, D. H. (2013). p53-dependent chemokine production by senescent tumor cells supports NKG2D-dependent tumor elimination by natural killer cells. *The Journal of Experimental Medicine*, *210*(10), 2057. https://doi.org/10.1084/JEM.20130783

J, K., B, O., & A, M. (2018). Break Induced Replication: the where, the why, and the how. *Trends in Genetics : TIG*, *34*(7), 518. https://doi.org/10.1016/J.TIG.2018.04.002

Jafarinia, H., Khalilimeybodi, A., Barrasa-Fano, J., Fraley, S. I., Rangamani, P., & Carlier, A. (2024). Insights gained from computational modeling of YAP/TAZ signaling for cellular mechanotransduction. *Npj Systems Biology and Applications 2024 10:1*, *10*(1), 1–14. https://doi.org/10.1038/s41540-024-00414-9

Javaid, N., & Choi, S. (2021). CRISPR/Cas System and Factors Affecting Its Precision and Efficiency. *Frontiers in Cell and Developmental Biology*, *9*, 761709. https://doi.org/10.3389/FCELL.2021.761709/FULL

Jenkins, B. H., Tracy, I., Rodrigues, M. F. S. D., Smith, M. J. L., Martinez, B. R., Edmond, M., Mahadevan, S., Rao, A., Zong, H., Liu, K., Aggarwal, A., Li, L., Diehl, L., King, E. V., Bates, J. G., Hanley, C. J., & Thomas, G. J. (2025). Single cell and spatial analysis of immune-hot and immune-cold tumours identifies fibroblast subtypes associated with distinct immunological niches and positive immunotherapy response. *Molecular Cancer*, *24*(1), 1–21. https://doi.org/10.1186/S12943-024-02191-9/FIGURES/7

Jenkins, L., Jungwirth, U., Avgustinova, A., Iravani, M., Mills, A., Haider, S., Harper, J., & Isacke, C. M. (2022). Cancer-Associated Fibroblasts Suppress CD8+ T-cell Infiltration and Confer Resistance to Immune-Checkpoint Blockade. *Cancer Research*, *82*(16), 2904–2917. https://doi.org/10.1158/0008-5472.CAN-21-4141/705119/AM/CANCER-ASSOCIATED-FIBROBLASTS-SUPPRESS-CD8-T-CELL

Jiang, C., Schaafsma, E., Hong, W., Zhao, Y., Zhu, K., Chao, C. C., & Cheng, C. (2022). Influence of T Cell-Mediated Immune Surveillance on Somatic Mutation Occurrences in Melanoma. *Frontiers in Immunology*, *12*, 5780. https://doi.org/10.3389/FIMMU.2021.703821/BIBTEX

Jiang, M., Jiang, M., Chen, P., Chen, P., Wang, L., Li, W., Chen, B., Liu, Y., Liu, Y., Wang, H., Wang, H., Zhao, S., Ye, L., He, Y., & Zhou, C. (2020). CGAS-STING, an important pathway in cancer immunotherapy. *Journal of Hematology and Oncology*, *13*(1), 1–11. https://doi.org/10.1186/S13045-020-00916-Z/FIGURES/4

Jiang, T., Zhou, C., & Ren, S. (2016). Role of IL-2 in cancer immunotherapy. *Oncoimmunology*, *5*(6), e1163462. https://doi.org/10.1080/2162402X.2016.1163462

Jiang, W., Crowe, J. L., Liu, X., Nakajima, S., Wang, Y., Li, C., Lee, B. J., Dubois, R. L., Liu, C., Yu, X., Lan, L., & Zha, S. (2015). Differential phosphorylation of DNA-PKcs regulates the interplay between end-processing and end-ligation during nonhomologous end-joining. *Molecular Cell*, *58*(1), 172–185. https://doi.org/10.1016/j.molcel.2015.02.024

Jiang, X., Sun, Y., Chen, S., Roy, K., & Price, B. D. (2006). The FATC Domains of PIKK Proteins Are Functionally Equivalent and Participate in the Tip60-dependent Activation of DNA-PKcs and ATM. *Journal of Biological Chemistry*, *281*(23), 15741–15746. https://doi.org/10.1074/JBC.M513172200

Jing, X., Yang, F., Shao, C., Wei, K., Xie, M., Shen, H., & Shu, Y. (2019). Role of hypoxia in cancer therapy by regulating the tumor microenvironment. *Molecular Cancer 2019 18:1*, *18*(1), 1–15. https://doi.org/10.1186/S12943-019-1089-9

Joshi, S., & Durden, D. L. (2019). Combinatorial Approach to Improve Cancer Immunotherapy: Rational Drug Design Strategy to Simultaneously Hit Multiple Targets to Kill Tumor Cells and to Activate the Immune System. *Journal of Oncology*, *2019*. https://doi.org/10.1155/2019/5245034

Jung, W. J., Park, S. J., Cha, S., & Kim, K. (2024). Factors affecting the cleavage efficiency of the CRISPR-Cas9 system. *Animal Cells and Systems*, *28*(1), 75. https://doi.org/10.1080/19768354.2024.2322054

Kakarla, S., Chow, K. K. H., Mata, M., Shaffer, D. R., Song, X. T., Wu, M. F., Liu, H., Wang, L. L., Rowley, D. R., Pfizenmaier, K., & Gottschalk, S. (2013). Antitumor Effects of Chimeric Receptor Engineered Human T Cells Directed to Tumor Stroma. *Molecular Therapy*, *21*(8), 1611. https://doi.org/10.1038/MT.2013.110

Kalluri, R. (2016). The biology and function of fibroblasts in cancer. *Nature Reviews Cancer 2016 16:9*, *16*(9), 582–598. https://doi.org/10.1038/nrc.2016.73

Kamiya, Y., Miyazono, K., & Miyazawa, K. (2010). Smad7 Inhibits Transforming Growth Factor-β Family Type I Receptors through Two Distinct Modes of Interaction. *Journal of Biological Chemistry*, *285*(40), 30804–30813. https://doi.org/10.1074/JBC.M110.166140

Kanzaki, R., & Pietras, K. (2020). Heterogeneity of cancer-associated fibroblasts: Opportunities for precision medicine. *Cancer Science*, *111*(8), 2708. https://doi.org/10.1111/CAS.14537

Kaplan, D. H., Shankaran, V., Dighe, A. S., Stockert, E., Aguet, M., Old, L. J., & Schreiber, R. D. (1998). Demonstration of an interferon γ-dependent tumor surveillance system in immunocompetent mice. *Proceedings of the National Academy of Sciences of the United States of America*, *95*(13), 7556–7561. https://doi.org/10.1073/PNAS.95.13.7556/ASSET/EDE174A5-CF98-408C-9AFD-91E390C365AE/ASSETS/GRAPHIC/PQ1281384004.JPEG

Kato, T., Noma, K., Ohara, T., Kashima, H., Katsura, Y., Sato, H., Komoto, S., Katsube, R., Ninomiya, T., Tazawa, H., Shirakawa, Y., & Fujiwara, T. (2018). Cancer-Associated Fibroblasts Affect Intratumoral CD8+ and FoxP3+ T Cells Via IL6 in the Tumor Microenvironment. *Clinical Cancer Research : An Official Journal of the American Association for Cancer Research*, *24*(19), 4820–4833. https://doi.org/10.1158/1078-0432.CCR-18-0205

Kazakova, A. N., Lukina, M. M., Anufrieva, K. S., Bekbaeva, I. V., Ivanova, O. M., Shnaider, P. V., Slonov, A., Arapidi, G. P., & Shender, V. O. (2024). Exploring the diversity of cancer-associated fibroblasts: insights into mechanisms of drug resistance. *Frontiers in Cell and Developmental Biology*, *12*, 1403122. https://doi.org/10.3389/FCELL.2024.1403122/BIBTEX

Kelley, M. R. (2012). Introduction and Overview of DNA Repair Targets: From Bench to Clinic. *DNA Repair in Cancer Therapy: Molecular Targets and Clinical Applications*, 1–16. https://doi.org/10.1016/B978-0-12-384999-1.10001-0

Khan, A. Q., Rashid, K., AlAmodi, A. A., Agha, M. V., Akhtar, S., Hakeem, I., Raza, S. S., & Uddin, S. (2021). Reactive oxygen species (ROS) in cancer pathogenesis and therapy: An update on the role of ROS in anticancer action of benzophenanthridine alkaloids. *Biomedicine & Pharmacotherapy*, *143*, 112142. https://doi.org/10.1016/J.BIOPHA.2021.112142

Khan, M. G. M., & Wang, Y. (2022). Advances in the Current Understanding of How Low-Dose Radiation Affects the Cell Cycle. *Cells 2022, Vol. 11, Page 356*, *11*(3), 356. https://doi.org/10.3390/CELLS11030356

Khoo, L. T., & Chen, L.-Y. (2018). Role of the cGAS–STING pathway in cancer development and oncotherapeutic approaches. *EMBO Reports*, *19*(12), e46935. https://doi.org/10.15252/EMBR.201846935

Kim, B. G., Malek, E., Choi, S. H., Ignatz-Hoover, J. J., & Driscoll, J. J. (2021). Novel therapies emerging in oncology to target the TGF-β pathway. *Journal of Hematology & Oncology 2021 14:1*, *14*(1), 1–20. https://doi.org/10.1186/S13045-021-01053-X

Kim, D. K., Jeong, J., Lee, D. S., Hyeon, D. Y., Park, G. W., Jeon, S., Lee, K. B., Jang, J. Y., Hwang, D., Kim, H. M., & Jung, K. (2022). PD-L1-directed PlGF/VEGF blockade synergizes with chemotherapy by targeting CD141+ cancer-associated fibroblasts in pancreatic cancer. *Nature Communications 2022 13:1*, *13*(1), 1–19. https://doi.org/10.1038/s41467-022-33991-6

Kim, I., Choi, S., Yoo, S., Lee, M., & Kim, I. S. (2022). Cancer-Associated Fibroblasts in the Hypoxic Tumor Microenvironment. *Cancers*, *14*(14), 3321. https://doi.org/10.3390/CANCERS14143321

Kim, K. T., Lee, M. H., Shin, S. J., Cho, I., Kuk, J. C., Yun, J., & Choi, Y. Y. (2024). Decorin as a key marker of desmoplastic cancer-associated fibroblasts mediating first-line immune checkpoint blockade resistance in metastatic gastric cancer. *Gastric Cancer : Official Journal of the International Gastric Cancer Association and the Japanese Gastric Cancer Association*. https://doi.org/10.1007/S10120-024-01567-6

Knight, A., Karapetyan, L., & Kirkwood, J. M. (2023). Immunotherapy in Melanoma: Recent Advances and Future Directions. *Cancers*, *15*(4), 1106. https://doi.org/10.3390/CANCERS15041106

Kojima, Y., Acar, A., Eaton, E. N., Mellody, K. T., Scheel, C., Ben-Porath, I., Onder, T. T., Wang, Z. C., Richardson, A. L., Weinberg, R. A., & Orimo, A. (2010). Autocrine TGF-β and stromal cell-derived factor-1 (SDF-1) signaling drives the evolution of tumor-promoting mammary stromal myofibroblasts. *Proceedings of the National Academy of Sciences of the United States of America*, *107*(46), 20009–20014. https://doi.org/10.1073/PNAS.1013805107/-/DCSUPPLEMENTAL

Konstantakos, V., Nentidis, A., Krithara, A., & Paliouras, G. (2022). CRISPR–Cas9 gRNA efficiency prediction: an overview of predictive tools and the role of deep learning. *Nucleic Acids Research*, *50*(7), 3616. https://doi.org/10.1093/NAR/GKAC192

Korbecki, J., Simińska, D., Kojder, K., Grochans, S., Gutowska, I., Chlubek, D., & Baranowska-Bosiacka, I. (2020). Fractalkine/CX3CL1 in Neoplastic Processes. *International Journal of Molecular Sciences*, *21*(10), 3723. https://doi.org/10.3390/IJMS21103723

Krokan, H. E., & Bjørås, M. (2013). Base Excision Repair. *Cold Spring Harbor Perspectives in Biology*, *5*(4), a012583. https://doi.org/10.1101/CSHPERSPECT.A012583

Krtolica, A., Parrinello, S., Lockett, S., Desprez, P. Y., & Campisi, J. (2001). Senescent fibroblasts promote epithelial cell growth and tumorigenesis: A link between cancer and aging. *Proceedings of the National Academy of Sciences of the United States of America*, *98*(21), 12072. https://doi.org/10.1073/PNAS.211053698

Kucharski, M., Mrowiec, P., & Ocłoń, E. (2021). Current standards and pitfalls associated with the transfection of primary fibroblast cells. *Biotechnology Progress*, *37*(4). https://doi.org/10.1002/BTPR.3152

Kuehlmann, B., Bonham, C. A., Zucal, I., Prantl, L., & Gurtner, G. C. (2020). Mechanotransduction in Wound Healing and Fibrosis. *Journal of Clinical Medicine*, *9*(5). https://doi.org/10.3390/JCM9051423

Kular, J. K., Basu, S., & Sharma, R. I. (2014). The extracellular matrix: Structure, composition, age-related differences, tools for analysis and applications for tissue engineering. *Journal of Tissue Engineering*, *5*, 2041731414557112. https://doi.org/10.1177/2041731414557112

Kumar, D., New, J., Vishwakarma, V., Joshi, R., Enders, J., Lin, F., Dasari, S., Gutierrez, W. R., Leef, G., Ponnurangam, S., Chavan, H., Ganaden, L., Thornton, M. M., Dai, H., Tawfik, O., Straub, J., Shnayder, Y., Kakarala, K., Tsue, T. T., … Thomas, S. M. (2018). Cancer-associated fibroblasts drive glycolysis in a targetable signaling loop implicated in head and neck squamous cell carcinoma progression. *Cancer Research*, *78*(14), 3769–3782. https://doi.org/10.1158/0008-5472.CAN-17-1076/652969/AM/CANCER-ASSOCIATED-FIBROBLASTS-DRIVE-GLYCOLYSIS-IN

Kumari, R., & Jat, P. (2021). Mechanisms of Cellular Senescence: Cell Cycle Arrest and Senescence Associated Secretory Phenotype. *Frontiers in Cell and Developmental Biology*, *9*, 645593. https://doi.org/10.3389/FCELL.2021.645593/BIBTEX

Kusnadi, E. P., Timpone, C., Topisirovic, I., Larsson, O., & Furic, L. (2022). Regulation of gene expression via translational buffering. *Biochimica et Biophysica Acta (BBA) - Molecular Cell Research*, *1869*(1), 119140. https://doi.org/10.1016/J.BBAMCR.2021.119140

Lagares, D., Busnadiego, O., García-Fernández, R. A., Kapoor, M., Liu, S., Carter, D. E., Abraham, D., Shi-Wen, X., Carreira, P., Fontaine, B. A., Shea, B. S., Tager, A. M., Leask, A., Lamas, S., & Rodríguez-Pascual, F. (2012). Inhibition of focal adhesion kinase prevents experimental lung fibrosis and myofibroblast formation. *Arthritis and Rheumatism*, *64*(5), 1653. https://doi.org/10.1002/ART.33482

Lam, K. C., Araya, R. E., Huang, A., Chen, Q., Di Modica, M., Rodrigues, R. R., Lopès, A., Johnson, S. B., Schwarz, B., Bohrnsen, E., Cogdill, A. P., Bosio, C. M., Wargo, J. A., Lee, M. P., & Goldszmid, R. S. (2021). Microbiota triggers STING-type I IFN-dependent monocyte reprogramming of the tumor microenvironment. *Cell*, *184*(21), 5338-5356.e21. https://doi.org/10.1016/J.CELL.2021.09.019

Langley, R. R., & Fidler, I. J. (2011). The seed and soil hypothesis revisited - the role of tumor-stroma interactions in metastasis to different organs. *International Journal of Cancer. Journal International Du Cancer*, *128*(11), 2527. https://doi.org/10.1002/IJC.26031

Lannoy, V., Côté-Biron, A., Asselin, C., & Rivard, N. (2021). Phosphatases in toll-like receptors signaling: the unfairly-forgotten. *Cell Communication and Signaling 2021 19:1*, *19*(1), 1–15. https://doi.org/10.1186/S12964-020-00693-9

Lavie, D., Ben-Shmuel, A., Erez, N., & Scherz-Shouval, R. (2022). Cancer-associated fibroblasts in the single-cell era. *Nature Cancer*, *3*(7), 793. https://doi.org/10.1038/S43018-022-00411-Z

Lee, J. H. (2024). Oxidative stress and the multifaceted roles of ATM in maintaining cellular redox homeostasis. *Redox Biology*, *75*, 103269. https://doi.org/10.1016/J.REDOX.2024.103269

Lee, J. H. (2024). Targeting the ATM pathway in cancer: Opportunities, challenges and personalized therapeutic strategies. *Cancer Treatment Reviews*, *129*, 102808. https://doi.org/10.1016/J.CTRV.2024.102808

Lee, J. H. (2025). ATM in immunobiology: From lymphocyte development to cancer immunotherapy. *Translational Oncology*, *52*, 102268. https://doi.org/10.1016/J.TRANON.2024.102268

Lee, J. H., & Paull, T. T. (2020). Mitochondria at the crossroads of ATM-mediated stress signaling and regulation of reactive oxygen species. *Redox Biology*, *32*, 101511. https://doi.org/10.1016/J.REDOX.2020.101511

Lemons, J. M. S., Coller, H. A., Feng, X. J., Bennett, B. D., Legesse-Miller, A., Johnson, E. L., Raitman, I., Pollina, E. A., Rabitz, H. A., & Rabinowitz, J. D. (2010). Quiescent Fibroblasts Exhibit High Metabolic Activity. *PLOS Biology*, *8*(10), e1000514. https://doi.org/10.1371/JOURNAL.PBIO.1000514

Lemos, H., Mohamed, E., Huang, L., Ou, R., Pacholczyk, G., Arbab, A. S., Munn, D., & Mellor, A. L. (2016). STING promotes the growth of tumors characterized by low antigenicity via IDO activation. *Cancer Research*, *76*(8), 2076. https://doi.org/10.1158/0008-5472.CAN-15-1456

Li, B., Pei, G., Yao, J., Ding, Q., Jia, P., & Zhao, Z. (2021). Cell-type deconvolution analysis identifies cancer-associated myofibroblast component as a poor prognostic factor in multiple cancer types. *Oncogene 2021 40:28*, *40*(28), 4686–4694. https://doi.org/10.1038/s41388-021-01870-x

Li, C. /, Guo, /, Multipotential, :, Guo, Z., Chang, Y., & Li, H. (2014). Mesenchymal Stem Cell-Like Properties in Fibroblasts. *Cellular Physiology and Biochemistry*, *34*(3), 703–714. https://doi.org/10.1159/000363035

Li, C., Wang, B., Tu, J., Liu, C., Wang, Y., Chen, J., Huang, Y., Liu, B., & Yuan, X. (2024). ATM inhibition enhance immunotherapy by activating STING signaling and augmenting MHC

Class I. *Cell Death & Disease 2024 15:7*, *15*(7), 1–14. https://doi.org/10.1038/s41419-024-06911-3

Li, E., Cheung, H. C., & Ma, S. (2024). CTHRC1+ fibroblasts and SPP1+ macrophages synergistically contribute to pro-tumorigenic tumor microenvironment in pancreatic ductal adenocarcinoma. *Scientific Reports 2024 14:1*, *14*(1), 1–15. https://doi.org/10.1038/s41598-024-68109-z

Li, F., Mladenov, E., Dueva, R., Stuschke, M., Timmermann, B., & Iliakis, G. (2022). Shift in g1-checkpoint from atm-alone to a cooperative atm plus atr regulation with increasing dose of radiation. *Cells*, *11*(1), 63. https://doi.org/10.3390/CELLS11010063/S1

Li, G. M. (2007). Mechanisms and functions of DNA mismatch repair. *Cell Research 2008 18:1*, *18*(1), 85–98. https://doi.org/10.1038/cr.2007.115

Li, H., Liu, W., Zhang, X., & Wang, Y. F. (2021). Cancer-associated fibroblast-secreted collagen triple helix repeat containing-1 promotes breast cancer cell migration, invasiveness and epithelial-mesenchymal transition by activating the Wnt/β-catenin pathway. *Oncology Letters*, *22*(6), 814. https://doi.org/10.3892/OL.2021.13075

Li, J., & Bakhoum, S. F. (2022). The pleiotropic roles of cGAS–STING signaling in the tumor microenvironment. *Journal of Molecular Cell Biology*, *14*(4), 19. https://doi.org/10.1093/JMCB/MJAC019

Li, J., Wang, L., Wang, B., Zhang, Z., Jiang, L., Qin, Z., Zhao, Y., & Su, B. (2023). *NOX4 is a potential therapeutic target in septic acute kidney injury by inhibiting mitochondrial dysfunction and inflammation*. *13*(9), 2863–2878. https://doi.org/10.7150/thno.81240

Li, T., & Chen, Z. J. (2018). The cGAS–cGAMP–STING pathway connects DNA damage to inflammation, senescence, and cancer. *The Journal of Experimental Medicine*, *215*(5), 1287. https://doi.org/10.1084/JEM.20180139

Li, X., & Heyer, W. D. (2008). Homologous recombination in DNA repair and DNA damage tolerance. *Cell Research*, *18*(1), 99. https://doi.org/10.1038/CR.2008.1

Li, Y., Han, S., Wu, B., Zhong, C., Shi, Y., Lv, C., Fu, L., Zhang, Y., Lang, Q., Liang, Z., Yu, Y., & Tian, Y. (2022). CXCL11 Correlates with Immune Infiltration and Impacts Patient Immunotherapy Efficacy: A Pan-Cancer Analysis. *Frontiers in Immunology*, *13*, 951247. https://doi.org/10.3389/FIMMU.2022.951247

Liang, S., Dong, S., Liu, W., Wang, M., Tian, S., Ai, Y., & Wang, H. (2022). Accumulated ROS Activates HIF-1α-Induced Glycolysis and Exerts a Protective Effect on Sensory Hair Cells Against Noise-Induced Damage. *Frontiers in Molecular Biosciences*, *8*, 806650. https://doi.org/10.3389/FMOLB.2021.806650/BIBTEX

Lim, S., Phillips, J. B., Da Silva, L. M., Zhou, M., Fodstad, O., Owen, L. B., & Tan, M. (2017). Interplay Between Immune Checkpoint Proteins and Cellular Metabolism. *Cancer Research*, *77*(6), 1245. https://doi.org/10.1158/0008-5472.CAN-16-1647

Lin, S., Zhou, M., Cheng, L., Shuai, Z., Zhao, M., Jie, R., Wan, Q., Peng, F., & Ding, S. (2024). Exploring the association of POSTN+ cancer-associated fibroblasts with triple-negative breast cancer. *International Journal of Biological Macromolecules*, *268*, 131560. https://doi.org/10.1016/J.IJBIOMAC.2024.131560

Lin, X., Kang, K., Chen, P., Zeng, Z., Li, G., Xiong, W., Yi, M., & Xiang, B. (2024). Regulatory mechanisms of PD-1/PD-L1 in cancers. *Molecular Cancer 2024 23:1*, *23*(1), 1–50. https://doi.org/10.1186/S12943-024-02023-W

Lindsey-Boltz, L. A., & Sancar, A. (2011). Tethering DNA Damage Checkpoint Mediator Proteins Topoisomerase IIβ-binding Protein 1 (TopBP1) and Claspin to DNA Activates Ataxia-Telangiectasia Mutated and RAD3-related (ATR) Phosphorylation of Checkpoint Kinase 1 (Chk1). *Journal of Biological Chemistry*, *286*(22), 19229–19236. https://doi.org/10.1074/JBC.M111.237958

Liu, J., Fu, M., Wang, M., Wan, D., Wei, Y., & Wei, X. (2022). Cancer vaccines as promising immuno-therapeutics: platforms and current progress. *Journal of Hematology & Oncology 2022 15:1*, *15*(1), 1–26. https://doi.org/10.1186/S13045-022-01247-X

Liu, J., Li, F., Ping, Y., Wang, L., Chen, X., Wang, D., Cao, L., Zhao, S., Li, B., Kalinski, P., Thorne, S. H., Zhang, B., Zhang, Y., Liu, J., Li, F., Ping, Y., Wang, L., Chen, X., Wang, D., … Zhang, Y. (2015). Local production of the chemokines CCL5 and CXCL10 attracts CD8 + T lymphocytes into esophageal squamous cell carcinoma. *Oncotarget*, *6*(28), 24978–24989. https://doi.org/10.18632/ONCOTARGET.4617

Liu, Q. W., Yang, Z. W., Tang, Q. H., Wang, W. E., Chu, D. S., Ji, J. F., Fan, Q. Y., Jiang, H., Yang, Q. X., Zhang, H., Liu, X. Y., Xu, X. S., Wang, X. F., Liu, J. Bin, Fu, D., Tao, K., & Yu, H. (2024). The power and the promise of synthetic lethality for clinical application in cancer treatment. *Biomedicine & Pharmacotherapy*, *172*, 116288. https://doi.org/10.1016/J.BIOPHA.2024.116288

Liu, R. M., & Desai, L. P. (2015). Reciprocal regulation of TGF-β and reactive oxygen species: A perverse cycle for fibrosis. *Redox Biology*, *6*, 565. https://doi.org/10.1016/J.REDOX.2015.09.009

Liu, T., Han, C., Wang, S., Fang, P., Ma, Z., Xu, L., & Yin, R. (2019). Cancer-associated fibroblasts: An emerging target of anti-cancer immunotherapy. *Journal of Hematology and Oncology*, *12*(1), 1–15. https://doi.org/10.1186/S13045-019-0770-1/TABLES/2

Liu, T., & Huang, J. (2016). DNA End Resection: Facts and Mechanisms. *Genomics, Proteomics & Bioinformatics*, *14*(3), 126. https://doi.org/10.1016/J.GPB.2016.05.002

Liu, T., Zhang, L., Joo, D., & Sun, S. C. (2017). NF-κB signaling in inflammation. *Signal Transduction and Targeted Therapy 2017 2:1*, *2*(1), 1–9. https://doi.org/10.1038/sigtrans.2017.23

Liu, Y., Chen, X., Xu, Y., Yang, T., Wang, H., Wang, Z., Hu, Z., Chen, L., Zhang, Z., & Wu, Y. (2024). CTHRC1 promotes colorectal cancer progression by recruiting tumor-associated macrophages via up-regulation of CCL15. *Journal of Molecular Medicine*, *102*(1), 81–94. https://doi.org/10.1007/S00109-023-02399-0/FIGURES/6

Liu, Y. T., & Sun, Z. J. (2021). Turning cold tumors into hot tumors by improving T-cell infiltration. *Theranostics*, *11*(11), 5365. https://doi.org/10.7150/THNO.58390

Liu, Z., Wang, D., Zhang, J., Xiang, P., Zeng, Z., Xiong, W., & Shi, L. (2023). cGAS-STING signaling in the tumor microenvironment. *Cancer Letters*, *577*, 216409. https://doi.org/10.1016/J.CANLET.2023.216409

London, R. E. (2015). The structural basis of XRCC1-mediated DNA repair. *DNA Repair*, *30*, 90. https://doi.org/10.1016/J.DNAREP.2015.02.005

Loo, T. M., Miyata, K., Tanaka, Y., & Takahashi, A. (2019). Cellular senescence and senescence-associated secretory phenotype via the cGAS-STING signaling pathway in cancer. *Cancer Science*, *111*(2), 304. https://doi.org/10.1111/CAS.14266

Loo, T. M., Miyata, K., Tanaka, Y., & Takahashi, A. (2020). Cellular senescence and senescence-associated secretory phenotype via the cGAS-STING signaling pathway in cancer. *Cancer Science*, *111*(2), 304–311. https://doi.org/10.1111/CAS.14266

Lu, H., Zhang, Q., Laverty, D. J., Puncheon, A. C., Augustine, M. M., Williams, G. J., Nagel, Z. D., Chen, B. P. C., & Davis, A. J. (2023). ATM phosphorylates the FATC domain of DNA-PKcs at threonine 4102 to promote non-homologous end joining. *Nucleic Acids Research*, *51*(13), 6770–6783. https://doi.org/10.1093/NAR/GKAD505

Lu, Y., Chen, Y., Wang, Z., Shen, H., Xu, L., Huang, C., Tong, Y., Shao, Y., Zhang, H., & Fu, Z. (2025). Single-cell and spatial transcriptome profiling reveal CTHRC1+ fibroblasts promote EMT through WNT5A signaling in colorectal cancer. *Journal of Translational Medicine*, *23*(1), 282. https://doi.org/10.1186/S12967-025-06236-5

Lukhele, S., Boukhaled, G. M., & Brooks, D. G. (2019). Type I interferon signaling, regulation and gene stimulation in chronic virus infection. *Seminars in Immunology*, *43*, 101277. https://doi.org/10.1016/J.SMIM.2019.05.001

Luo, K., Li, N., Ye, W., Gao, H., Luo, X., & Cheng, B. (2022). Activation of Stimulation of Interferon Genes (STING) Signal and Cancer Immunotherapy. *Molecules*, *27*(14), 4638. https://doi.org/10.3390/MOLECULES27144638

Luo, Q., Li, J., Su, X., Tan, Q., Zhou, F., & Xie, S. (2022). COL11A1 serves as a biomarker for poor prognosis and correlates with immune infiltration in breast cancer. *Frontiers in Genetics*, *13*, 935860. https://doi.org/10.3389/FGENE.2022.935860/FULL

Luo, Y., Xu, W., Chen, H., Warburton, D., Dong, R., Qian, B., Selman, M., Gauldie, J., Kolb, M., & Shi, W. (2015). A novel profibrotic mechanism mediated by TGF-β-stimulated collagen prolyl hydroxylase expression in fibrotic lung mesenchymal cells. *The Journal of Pathology*, *236*(3), 384. https://doi.org/10.1002/PATH.4530

Lurie, R. H., & Platanias, L. C. (2005). Mechanisms of type-I- and type-II-interferon-mediated signalling. *Nature Reviews Immunology 2005 5:5*, *5*(5), 375–386. https://doi.org/10.1038/nri1604

Ma, S., Xie, N., Li, W., Yuan, B., Shi, Y., & Wang, Y. (2013). Immunobiology of mesenchymal stem cells. *Cell Death & Differentiation 2014 21:2*, *21*(2), 216–225. https://doi.org/10.1038/cdd.2013.158

Ma, Z., Li, X., Mao, Y., Wei, C., Huang, Z., Li, G., Yin, J., Liang, X., & Liu, Z. (2022). Interferon-dependent SLC14A1+ cancer-associated fibroblasts promote cancer stemness via WNT5A in bladder cancer. *Cancer Cell*, *40*(12), 1550-1565.e7. https://doi.org/10.1016/j.ccell.2022.11.005

Machitani, M., Sakurai, F., Wakabayashi, K., Takayama, K., Tachibana, M., & Mizuguchi, H. (2016). Type I Interferons Impede Short Hairpin RNA-Mediated RNAi via Inhibition of Dicer-Mediated Processing to Small Interfering RNA. *Molecular Therapy. Nucleic Acids*, *6*, 173. https://doi.org/10.1016/J.OMTN.2016.12.007

Madzharova, E., Kastl, P., Sabino, F., & auf dem Keller, U. (2019). Post-Translational Modification-Dependent Activity of Matrix Metalloproteinases. *International Journal of Molecular Sciences*, *20*(12), 3077. https://doi.org/10.3390/IJMS20123077

Mai, Z., Lin, Y., Lin, P., Zhao, X., & Cui, L. (2024). Modulating extracellular matrix stiffness: a strategic approach to boost cancer immunotherapy. *Cell Death & Disease 2024 15:5*, *15*(5), 1–16. https://doi.org/10.1038/s41419-024-06697-4

Majorova, D., Atkins, E., Martineau, H., Vokral, I., Oosterhuis, D., Olinga, P., Wren, B., Cuccui, J., & Werling, D. (2021). Use of Precision-Cut Tissue Slices as a Translational Model to Study Host-Pathogen Interaction. *Frontiers in Veterinary Science*, *8*, 612. https://doi.org/10.3389/FVETS.2021.686088/BIBTEX

Makuch, E., Jasyk, I., Kula, A., Lipiński, T., & Siednienko, J. (2022). IFNβ-Induced CXCL10 Chemokine Expression Is Regulated by Pellino3 Ligase in Monocytes and Macrophages. *International Journal of Molecular Sciences*, *23*(23), 14915. https://doi.org/10.3390/IJMS232314915

Malmstrom, J., Linberg, H., Lindberg, C., Bratt, C., Wieslander, E., Delander, E. L., Särnstrand, B., Burns, J. S., Mose-Larsen, P., Fey, S., & Marko-Varga, G. (2004). Transforming growth factor-beta 1 specifically induce proteins involved in the myofibroblast contractile apparatus. *Molecular & Cellular Proteomics : MCP*, *3*(5), 466–477. https://doi.org/10.1074/MCP.M300108-MCP200

Maman, S., & Witz, I. P. (2018). A history of exploring cancer in context. *Nature Reviews. Cancer*, *18*(6), 359–376. https://doi.org/10.1038/S41568-018-0006-7

Manea, A., Tanase, L. I., Raicu, M., & Simionescu, M. (2010). Transcriptional regulation of NADPH oxidase isoforms, Nox1 and Nox4, by nuclear factor-κB in human aortic smooth muscle cells. *Biochemical and Biophysical Research Communications*, *396*(4), 901–907. https://doi.org/10.1016/J.BBRC.2010.05.019

Marcus, A., Mao, A. J., Lensink-Vasan, M., Wang, L. A., Vance, R. E., & Raulet, D. H. (2018). Tumor-Derived cGAMP Triggers a STING-Mediated Interferon Response in Non-tumor Cells to Activate the NK Cell Response. *Immunity*, *49*(4), 754-763.e4. https://doi.org/10.1016/J.IMMUNI.2018.09.016

Mardis, E. R. (2019). Neoantigens and genome instability: Impact on immunogenomic phenotypes and immunotherapy response. *Genome Medicine*, *11*(1), 1–12. https://doi.org/10.1186/S13073-019-0684-0/TABLES/2

Maréchal, A., & Zou, L. (2013). DNA Damage Sensing by the ATM and ATR Kinases. *Cold Spring Harbor Perspectives in Biology*, *5*(9), a012716. https://doi.org/10.1101/CSHPERSPECT.A012716

Marescal, O., & Cheeseman, I. M. (2020). Cellular Mechanisms and Regulation of Quiescence. *Developmental Cell*, *55*(3), 259. https://doi.org/10.1016/J.DEVCEL.2020.09.029

Mariathasan, S., Turley, S. J., Nickles, D., Castiglioni, A., Yuen, K., Wang, Y., Kadel, E. E., Koeppen, H., Astarita, J. L., Cubas, R., Jhunjhunwala, S., Banchereau, R., Yang, Y., Guan, Y., Chalouni, C., Ziai, J., Şenbabaoğlu, Y., Santoro, S., Sheinson, D., … Powles, T. (2018). TGFβ attenuates tumour response to PD-L1 blockade by contributing to exclusion of T cells. *Nature 2018 554:7693*, *554*(7693), 544–548. https://doi.org/10.1038/nature25501

Martín, M., Terradas, M., Tusell, L., & Genescà, A. (2012). ATM and DNA-PKcs make a complementary couple in DNA double strand break repair. *Mutation Research/Reviews in Mutation Research*, *751*(1), 29–35. https://doi.org/10.1016/J.MRREV.2011.12.006

Massagué, J., & Wotton, D. (2000). NEW EMBO MEMBER'S REVIEW: Transcriptional control by the TGF-β/Smad signaling system. *The EMBO Journal*, *19*(8), 1745. https://doi.org/10.1093/EMBOJ/19.8.1745

Masugi, Y., Abe, T., Ueno, A., Fujii-Nishimura, Y., Ojima, H., Endo, Y., Fujita, Y., Kitago, M., Shinoda, M., Kitagawa, Y., & Sakamoto, M. (2019). Characterization of spatial distribution of tumor-infiltrating CD8+ T cells refines their prognostic utility for pancreatic cancer survival. *Modern Pathology : An Official Journal of the United States and Canadian Academy of Pathology, Inc*, *32*(10), 1495–1507. https://doi.org/10.1038/S41379-019-0291-Z

McCarthy, E. F. (2006). The Toxins of William B. Coley and the Treatment of Bone and Soft-Tissue Sarcomas. *The Iowa Orthopaedic Journal*, *26*, 154. /pmc/articles/PMC1888599/

McKay, L. I., & Cidlowski, J. A. (1999). Molecular Control of Immune/Inflammatory Responses: Interactions Between Nuclear Factor-κB and Steroid Receptor-Signaling Pathways. *Endocrine Reviews*, *20*(4), 435–459. https://doi.org/10.1210/EDRV.20.4.0375

Meissner, T. B., Mandal, P. K., Ferreira, L. M. R., Rossi, D. J., & Cowan, C. A. (2014). Genome Editing for Human Gene Therapy. *Methods in Enzymology*, *546*(C), 273–295. https://doi.org/10.1016/B978-0-12-801185-0.00013-1

Mello, A. M., Ngodup, T., Lee, Y., Donahue, K. L., Li, J., Rao, A., Carpenter, E. S., Crawford, H. C., Pasca di Magliano, M., & Lee, K. E. (2022). Hypoxia promotes an inflammatory phenotype of fibroblasts in pancreatic cancer. *Oncogenesis 2022 11:1*, *11*(1), 1–9. https://doi.org/10.1038/s41389-022-00434-2

Mellone, M., Hanley, C. J., Thirdborough, S., Mellows, T., Garcia, E., Woo, J., Tod, J., Frampton, S., Jenei, V., Moutasim, K. A., Kabir, T. D., Brennan, P. A., Venturi, G., Ford, K., Herranz, N., Lim, K. P., Clarke, J., Lambert, D. W., Prime, S. S., … Thomas, G. J. (2016). Induction of fibroblast senescence generates a non-fibrogenic myofibroblast phenotype that differentially impacts on cancer prognosis. *Aging (Albany NY)*, *9*(1), 114. https://doi.org/10.18632/AGING.101127

Mellone, M., Piotrowska, K., Venturi, G., James, L., Bzura, A., Lopez, M. A., James, S., Wang, C., Ellis, M. J., Hanley, C. J., Buckingham, J. F., Cox, K. L., Hughes, G., Valge-Archer, V., King, E. V., Beers, S. A., Jaquet, V., Jones, G. D. D., Savelyeva, N., … Thomas, G. J. (2022). ATM Regulates Differentiation of Myofibroblastic Cancer-Associated Fibroblasts and Can Be Targeted to Overcome Immunotherapy Resistance. *Cancer Research*, *82*(24), 4571–4585. https://doi.org/10.1158/0008-5472.CAN-22-0435/710507/P/ATM-REGULATES-DIFFERENTIATION-OF-MYOFIBROBLASTIC

Meng, L., Wu, H., Wu, J., Ding, P., He, J., Sang, M., & Liu, L. (2024). Mechanisms of immune checkpoint inhibitors: insights into the regulation of circular RNAS involved in cancer hallmarks. *Cell Death & Disease 2024 15:1*, *15*(1), 1–26. https://doi.org/10.1038/s41419-023-06389-5

Menolfi, D., & Zha, S. (2020). ATM, ATR and DNA-PKcs kinases—the lessons from the mouse models: inhibition ≠ deletion. *Cell & Bioscience 2020 10:1*, *10*(1), 1–15. https://doi.org/10.1186/S13578-020-0376-X

Metropulos, A. E., Munshi, H. G., & Principe, D. R. (2022). The difficulty in translating the preclinical success of combined TGFβ and immune checkpoint inhibition to clinical trial. *EBioMedicine*, *86*, 104380. https://doi.org/10.1016/J.EBIOM.2022.104380

Micallef, L., Vedrenne, N., Billet, F., Coulomb, B., Darby, I. A., & Desmoulière, A. (2012). The myofibroblast, multiple origins for major roles in normal and pathological tissue repair. *Fibrogenesis and Tissue Repair*, *5*(SUPPL.1), 1–5. https://doi.org/10.1186/1755-1536-5-S1-S5/FIGURES/2

Miller, K. N., Victorelli, S. G., Salmonowicz, H., Dasgupta, N., Liu, T., Passos, J. F., & Adams, P. D. (2021). Cytoplasmic DNA: sources, sensing, and role in aging and disease. *Cell*, *184*(22), 5506. https://doi.org/10.1016/J.CELL.2021.09.034

Miura, T., Yamana, Y., Usui, T., Ogawa, H. I., Yamamoto, M. T., & Kusano, K. (2012). Homologous Recombination via Synthesis-Dependent Strand Annealing in Yeast Requires the Irc20 and Srs2 DNA Helicases. *Genetics*, *191*(1), 65. https://doi.org/10.1534/GENETICS.112.139105

Miyake, T., & Kalluri, R. (2014). Cell plasticity helps hearts to repair. *Nature 2014 514:7524*, *514*(7524), 575–576. https://doi.org/10.1038/nature13928

Miyamoto, S. (2010). Nuclear initiated NF-κB signaling: NEMO and ATM take center stage. *Cell Research 2011 21:1*, *21*(1), 116–130. https://doi.org/10.1038/cr.2010.179

Mladenov, E., Fan, X., Paul-Konietzko, K., Soni, A., & Iliakis, G. (2019). DNA-PKcs and ATM epistatically suppress DNA end resection and hyperactivation of ATR-dependent G2-checkpoint in S-phase irradiated cells. *Scientific Reports 2019 9:1*, *9*(1), 1–16. https://doi.org/10.1038/s41598-019-51071-6

Modarressi, A., Pietramaggiori, G., Godbout, C., Vigato, E., Pittet, B., & Hinz, B. (2010). Hypoxia impairs skin myofibroblast differentiation and function. *Journal of Investigative Dermatology*, *130*(12), 2818–2827. https://doi.org/10.1038/jid.2010.224

Monteran, L., & Erez, N. (2019). The dark side of fibroblasts: Cancer-associated fibroblasts as mediators of immunosuppression in the tumor microenvironment. *Frontiers in Immunology*, *10*(AUG), 1835. https://doi.org/10.3389/FIMMU.2019.01835/BIBTEX

Morad, G., Helmink, B. A., Sharma, P., & Wargo, J. A. (2021). Hallmarks of response, resistance, and toxicity to immune checkpoint blockade. *Cell*, *184*(21), 5309–5337. https://doi.org/10.1016/J.CELL.2021.09.020

Moretti, L., Stalfort, J., Barker, T. H., & Abebayehu, D. (2021). The interplay of fibroblasts, the extracellular matrix, and inflammation in scar formation. *The Journal of Biological Chemistry*, *298*(2), 101530. https://doi.org/10.1016/J.JBC.2021.101530

Morgan, D. A., Ruscetti, F. W., & Gallo, R. (1976). Selective in vitro growth of T lymphocytes from normal human bone marrows. *Science (New York, N.Y.)*, *193*(4257), 1007–1008. https://doi.org/10.1126/SCIENCE.181845

Mou, T., Zhu, H., Jiang, Y., Xu, X., Cai, L., Zhong, Y., Luo, J., & Zhang, Z. (2023). Heterogeneity of cancer-associated fibroblasts in head and neck squamous cell carcinoma. *Translational Oncology*, *35*, 101717. https://doi.org/10.1016/J.TRANON.2023.101717

Movat, H. Z., & Fernando, N. V. P. (1962). The fine structure of connective tissue: I. The fibroblast. *Experimental and Molecular Pathology*, *1*(6), 509–534. https://doi.org/10.1016/0014-4800(62)90040-0

Musyoka, J. N., Liu, M. C. P., Pouniotis, D. S., Wong, C. S. F., Bowtell, D. D., Little, P. J., Getachew, R., Möller, A., & Darby, I. A. (2013). Siah2-deficient mice show impaired skin wound repair. *Wound Repair and Regeneration*, *21*(3), 437–447. https://doi.org/10.1111/WRR.12045

Nakajima, Y. I., & Kuranaga, E. (2017). Caspase-dependent non-apoptotic processes in development. *Cell Death & Differentiation 2017 24:8*, *24*(8), 1422–1430. https://doi.org/10.1038/cdd.2017.36

Nakao, A., Imamura, T., Souchelnytskyi, S., Kawabata, M., Ishisaki, A., Oeda, E., Tamaki, K., Hanai, J. I., Heldin, C. H., Miyazono, K., & Ten Dijke, P. (1997). TGF-beta receptor-mediated signalling through Smad2, Smad3 and Smad4. *The EMBO Journal*, *16*(17), 5353. https://doi.org/10.1093/EMBOJ/16.17.5353

Nakatsumi, H., Matsumoto, M., & Nakayama, K. I. (2017). Noncanonical Pathway for Regulation of CCL2 Expression by an mTORC1-FOXK1 Axis Promotes Recruitment of Tumor-Associated Macrophages. *Cell Reports*, *21*(9), 2471–2486. https://doi.org/10.1016/J.CELREP.2017.11.014

Narra, K., Mullins, S. R., Lee, H. O., Strzemkowski-Brun, B., Magalong, K., Christiansen, V. J., McKee, P. A., Egleston, B., Cohen, S. J., Weiner, L. M., Meropol, N. J., & Cheng, J. D. (2007). Phase II trial of single agent Val-boroPro (talabostat) inhibiting fibroblast activation protein in patients with metastatic colorectal cancer. *Cancer Biology & Therapy*, *6*(11), 1691–1699. https://doi.org/10.4161/CBT.6.11.4874

Naumenkoa, N. V., Petrusevaa, I. O., & Lavrik, O. I. (2022). Bulky Adducts in Clustered DNA Lesions: Causes of Resistance to the NER System. *Acta Naturae*, *14*(4), 38. https://doi.org/10.32607/ACTANATURAE.11741

Negrao, M. V., Lam, V. K., Reuben, A., Rubin, M. L., Landry, L. L., Roarty, E. B., Rinsurongkawong, W., Lewis, J., Roth, J. A., Swisher, S. G., Gibbons, D. L., Wistuba, I. I., Papadimitrakopoulou, V., Glisson, B. S., Blumenschein, G. R., Lee, J. J., Heymach, J. V., & Zhang, J. (2019). PD-L1 Expression, Tumor Mutational Burden, and Cancer Gene Mutations Are Stronger Predictors of Benefit from Immune Checkpoint Blockade than HLA Class I Genotype in Non–Small Cell Lung Cancer. *Journal of Thoracic Oncology*, *14*(6), 1021–1031. https://doi.org/10.1016/J.JTHO.2019.02.008

Negrini, S., Gorgoulis, V. G., & Halazonetis, T. D. (2010). Genomic instability--an evolving hallmark of cancer. *Nature Reviews. Molecular Cell Biology*, *11*(3), 220–228. https://doi.org/10.1038/NRM2858

Nejedlý, K., Kittner, R., Pospíšilová, Š., & Kypr, J. (2001). Crosslinking of the complementary strands of DNA by UV light: dependence on the oligonucleotide composition of the UV irradiated DNA. *Biochimica et Biophysica Acta (BBA) - Gene Structure and Expression*, *1517*(3), 365–375. https://doi.org/10.1016/S0167-4781(00)00299-2

Ng, K., Nimeiri, H. S., McCleary, N. J., Abrams, T. A., Yurgelun, M. B., Cleary, J. M., Rubinson, D. A., Schrag, D., Miksad, R., Bullock, A. J., Allen, J., Zuckerman, D., Chan, E., Chan, J. A., Wolpin, B. M., Constantine, M., Weckstein, D. J., Faggen, M. A., Thomas, C. A., … Fuchs, C. S. (2019). Effect of High-Dose vs Standard-Dose Vitamin D3 Supplementation on Progression-Free Survival Among Patients With Advanced or Metastatic Colorectal Cancer: The SUNSHINE Randomized Clinical Trial. *JAMA*, *321*(14), 1370–1379. https://doi.org/10.1001/JAMA.2019.2402

Nicolas, A. M., Pesic, M., Engel, E., Ziegler, P. K., Diefenhardt, M., Kennel, K. B., Buettner, F., Conche, C., Petrocelli, V., Elwakeel, E., Weigert, A., Zinoveva, A., Fleischmann, M., Häupl, B., Karakütük, C., Bohnenberger, H., Mosa, M. H., Kaderali, L., Gaedcke, J., … Greten, F. R. (2022). Inflammatory fibroblasts mediate resistance to neoadjuvant therapy in rectal cancer. *Cancer Cell*, *40*(2), 168-184.e13. https://doi.org/10.1016/J.CCELL.2022.01.004

Nicolas-Boluda, A., Vaquero, J., Vimeux, L., Guilbert, T., Barrin, S., Kantari-Mimoun, C., Ponzo, M., Renault, G., Deptula, P., Pogoda, K., Bucki, R., Cascone, I., Courty, J., Fouassier, L., Gazeau, F., & Donnadieu, E. (2021). Tumor stiffening reversion through collagen crosslinking inhibition improves t cell migration and anti-pd-1 treatment. *ELife*, *10*. https://doi.org/10.7554/ELIFE.58688

Nierkens, S., Tel, J., Janssen, E., & Adema, G. J. (2013). Antigen cross-presentation by dendritic cell subsets: one general or all sergeants? *Trends in Immunology*, *34*(8), 361. https://doi.org/10.1016/J.IT.2013.02.007

Niewolik, D., Pannicke, U., Lu, H., Ma, Y., Wang, L. C. V., Kulesza, P., Zandi, E., Lieber, M. R., & Schwarz, K. (2006). DNA-PKcs Dependence of Artemis Endonucleolytic Activity, Differences between Hairpins and 5' or 3' Overhangs. *Journal of Biological Chemistry*, *281*(45), 33900–33909. https://doi.org/10.1074/JBC.M606023200

Nissen, N. I., Karsdal, M., & Willumsen, N. (2019). Collagens and Cancer associated fibroblasts in the reactive stroma and its relation to Cancer biology. *Journal of Experimental and Clinical Cancer Research*, *38*(1), 1–12. https://doi.org/10.1186/S13046-019-1110-6/TABLES/1

Nomi, T., Sho, M., Akahori, T., Hamada, K., Kubo, A., Kanehiro, H., Nakamura, S., Enomoto, K., Yagita, H., Azuma, M., & Nakajima, Y. (2007). Clinical significance and therapeutic potential of the programmed death-1 ligand/programmed death-1 pathway in human pancreatic cancer. *Clinical Cancer Research : An Official Journal of the American Association for Cancer Research*, *13*(7), 2151–2157. https://doi.org/10.1158/1078-0432.CCR-06-2746

Nonaka, M., & Nonaka, M. I. (2016). The Evolution of Major Histocompatibility Complex in Teleosts. *The Evolution of the Immune System: Conservation and Diversification*, 331–349. https://doi.org/10.1016/B978-0-12-801975-7.00014-1

Nuchtern, J. G., Biddison, W. E., & Klausner, R. D. (1990). Class II MHC molecules can use the endogenous pathway of antigen presentation. *Nature 1990 343:6253*, *343*(6253), 74–76. https://doi.org/10.1038/343074a0

Oelschlaeger, T. A. (2010). Bacteria as tumor therapeutics? *Bioengineered Bugs*, *1*(2), 146. https://doi.org/10.4161/BBUG.1.2.11248

Oh, H. Y., Jin, X., Kim, J. G., Oh, M. J., Pian, X., Kim, J. M., Yoon, M. S., Son, C. I., Lee, Y. S., Hong, K. C., Kim, H., Choi, Y. J., & Whang, K. Y. (2007). Characteristics of primary and immortalized fibroblast cells derived from the miniature and domestic pigs. *BMC Cell Biology*, *8*, 20. https://doi.org/10.1186/1471-2121-8-20

Oh, J. M., & Myung, K. (2022). Crosstalk between different DNA repair pathways for DNA double strand break repairs. *Mutation Research/Genetic Toxicology and Environmental Mutagenesis*, *873*, 503438. https://doi.org/10.1016/J.MRGENTOX.2021.503438

Öhlund, D., Handly-Santana, A., Biffi, G., Elyada, E., Almeida, A. S., Ponz-Sarvise, M., Corbo, V., Oni, T. E., Hearn, S. A., Lee, E. J., Chio, I. I. C., Hwang, C. Il, Tiriac, H., Baker, L. A., Engle, D. D., Feig, C., Kultti, A., Egeblad, M., Fearon, D. T., … Tuveson, D. A. (2017). Distinct

populations of inflammatory fibroblasts and myofibroblasts in pancreatic cancer. *The Journal of Experimental Medicine*, *214*(3), 579–596. https://doi.org/10.1084/JEM.20162024

Oiseth, S. J., & Aziz, M. S. (2017). Cancer immunotherapy: a brief review of the history, possibilities, and challenges ahead. *Journal of Cancer Metastasis and Treatment*, *3*(10), 250–261. https://doi.org/10.20517/2394-4722.2017.41

Okada, H., Danoff, T. M., Kalluri, R., & Neilson, E. G. (1997). Early role of Fsp1 in epithelial-mesenchymal transformation. *American Journal of Physiology - Renal Physiology*, *273*(4 42-4). https://doi.org/10.1152/AJPRENAL.1997.273.4.F563/ASSET/IMAGES/LARGE/AFLU2101009.JPEG

Olivieri, C., Li, G. C., Wang, Y., Manu, V. S., Walker, C., Kim, J., Camilloni, C., De Simone, A., Vendruscolo, M., Bernlohr, D. A., Taylor, S. S., & Veglia, G. (2022). ATP-competitive inhibitors modulate the substrate binding cooperativity of a kinase by altering its conformational entropy. *Science Advances*, *8*(30), eabo0696. https://doi.org/10.1126/SCIADV.ABO0696

Olumi, A., Grossfeld, G., Hayward, S., Carroll, P., Cunha, G., Hein, P., & Tlsty, T. (1999). Carcinoma-associated fibroblasts direct tumor progression of initiated human prostatic epithelium. *Cancer Research*, *59*(19). https://doi.org/10.1186/BCR138

O'Malley, G., Treacy, O., Lynch, K., Naicker, S. D., Leonard, N. A., Lohan, P., Dunne, P. D., Ritter, T., Egan, L. J., & Ryan, A. E. (2018). Stromal Cell PD-L1 Inhibits CD8+ T-cell Antitumor Immune Responses and Promotes Colon Cancer. *Cancer Immunology Research*, *6*(11), 1426–1441. https://doi.org/10.1158/2326-6066.CIR-17-0443

Orange, S. T., Leslie, J., Ross, M., Mann, D. A., & Wackerhage, H. (2023). The exercise IL-6 enigma in cancer. *Trends in Endocrinology & Metabolism*, *34*(11), 749–763. https://doi.org/10.1016/J.TEM.2023.08.001

Orth, M., Metzger, P., Gerum, S., Mayerle, J., Schneider, G., Belka, C., Schnurr, M., & Lauber, K. (2019). Pancreatic ductal adenocarcinoma: biological hallmarks, current status, and future perspectives of combined modality treatment approaches. *Radiation Oncology 2019 14:1*, *14*(1), 1–20. https://doi.org/10.1186/S13014-019-1345-6

Ostermann, E., Garin-Chesa, P., Heider, K. H., Kalat, M., Lamche, H., Puri, C., Kerjaschki, D., Rettig, W. J., & Adolf, G. R. (2008). Effective Immunoconjugate Therapy in Cancer Models Targeting a Serine Protease of Tumor Fibroblasts. *Clinical Cancer Research*, *14*(14), 4584–4592. https://doi.org/10.1158/1078-0432.CCR-07-5211

Özdemir, B. C., Pentcheva-Hoang, T., Carstens, J. L., Zheng, X., Wu, C. C., Simpson, T. R., Laklai, H., Sugimoto, H., Kahlert, C., Novitskiy, S. v., DeJesus-Acosta, A., Sharma, P., Heidari, P.,

Mahmood, U., Chin, L., Moses, H. L., Weaver, V. M., Maitra, A., Allison, J. P., … Kalluri, R. (2014). Depletion of carcinoma-associated fibroblasts and fibrosis induces immunosuppression and accelerates pancreas cancer with reduced survival. *Cancer Cell*, *25*(6), 719–734. https://doi.org/10.1016/j.ccr.2014.04.005

Panda, S. K., Robinson, N., & Desiderio, V. (2024). Decoding secret role of mesenchymal stem cells in regulating cancer stem cells and drug resistance. *Biochimica et Biophysica Acta (BBA) - Reviews on Cancer*, *1879*(6), 189205. https://doi.org/10.1016/J.BBCAN.2024.189205

Pannunzio, N. R., Watanabe, G., & Lieber, M. R. (2017). Nonhomologous DNA end-joining for repair of DNA double-strand breaks. *The Journal of Biological Chemistry*, *293*(27), 10512. https://doi.org/10.1074/JBC.TM117.000374

Papaioannou, N. E., Beniata, O. V., Vitsos, P., Tsitsilonis, O., & Samara, P. (2016). Harnessing the immune system to improve cancer therapy. *Annals of Translational Medicine*, *4*(14). https://doi.org/10.21037/ATM.2016.04.01

Pardoll, D. M. (2012). The blockade of immune checkpoints in cancer immunotherapy. *Nature Reviews. Cancer*, *12*(4), 252. https://doi.org/10.1038/NRC3239

Park, E. H., Kim, S., Jo, J. Y., Kim, S. J., Hwang, Y., Kim, J. M., Song, S. Y., Lee, D. K., & Koh, S. S. (2013). Collagen triple helix repeat containing-1 promotes pancreatic cancer progression by regulating migration and adhesion of tumor cells. *Carcinogenesis*, *34*(3), 694–702. https://doi.org/10.1093/CARCIN/BGS378

Park, J., Jo, Y. H., Cho, C. H., Choe, W., Kang, I., Baik, H. H., & Yoon, K. S. (2013). ATM-deficient human fibroblast cells are resistant to low levels of DNA double-strand break induced apoptosis and subsequently undergo drug-induced premature senescence. *Biochemical and Biophysical Research Communications*, *430*(1), 429–435. https://doi.org/10.1016/J.BBRC.2012.11.040

Pascual-García, M., Bonfill-Teixidor, E., Planas-Rigol, E., Rubio-Perez, C., Iurlaro, R., Arias, A., Cuartas, I., Sala-Hojman, A., Escudero, L., Martínez-Ricarte, F., Huber-Ruano, I., Nuciforo, P., Pedrosa, L., Marques, C., Braña, I., Garralda, E., Vieito, M., Squatrito, M., Pineda, E., … Seoane, J. (2019). LIF regulates CXCL9 in tumor-associated macrophages and prevents CD8+ T cell tumor-infiltration impairing anti-PD1 therapy. *Nature Communications 2019 10:1*, *10*(1), 1–11. https://doi.org/10.1038/s41467-019-10369-9

Paszek, M. J., Zahir, N., Johnson, K. R., Lakins, J. N., Rozenberg, G. I., Gefen, A., Reinhart-King, C. A., Margulies, S. S., Dembo, M., Boettiger, D., Hammer, D. A., & Weaver, V. M. (2005). Tensional homeostasis and the malignant phenotype. *Cancer Cell*, *8*(3), 241–254. https://doi.org/10.1016/j.ccr.2005.08.010

Patel, R., Rinker, L., Peng, J., & Chilian, W. M. (2017). Reactive Oxygen Species: The Good and the Bad. *Reactive Oxygen Species (ROS) in Living Cells*. https://doi.org/10.5772/INTECHOPEN.71547

Paull, T. T., Rogakou, E. P., Yamazaki, V., Kirchgessner, C. U., Gellert, M., & Bonner, W. M. (2000). A critical role for histone H2AX in recruitment of repair factors to nuclear foci after DNA damage. *Current Biology*, *10*(15), 886–895. https://doi.org/10.1016/S0960-9822(00)00610-2

Pei, L., Liu, Y., Liu, L., Gao, S., Gao, X., Feng, Y., Sun, Z., Zhang, Y., & Wang, C. (2023). Roles of cancer-associated fibroblasts (CAFs) in anti- PD-1/PD-L1 immunotherapy for solid cancers. *Molecular Cancer 2023 22:1*, *22*(1), 1–18. https://doi.org/10.1186/S12943-023-01731-Z

Peng, D. H., Rodriguez, B. L., Diao, L., Chen, L., Wang, J., Byers, L. A., Wei, Y., Chapman, H. A., Yamauchi, M., Behrens, C., Raso, G., Soto, L. M. S., Cuentes, E. R. P., Wistuba, I. I., Kurie, J. M., & Gibbons, D. L. (2020). Collagen promotes anti-PD-1/PD-L1 resistance in cancer through LAIR1-dependent CD8+ T cell exhaustion. *Nature Communications 2020 11:1*, *11*(1), 1–18. https://doi.org/10.1038/s41467-020-18298-8

Peng, K., Zhang, Y., Liu, D., & Chen, J. (2023). MMP2 is a immunotherapy related biomarker and correlated with cancer-associated fibroblasts infiltrate in melanoma. *Cancer Cell International*, *23*(1), 1–11. https://doi.org/10.1186/S12935-023-02862-5/FIGURES/5

Pérez-Treviño, P., Velásquez, M., & García, N. (2020). Mechanisms of mitochondrial DNA escape and its relationship with different metabolic diseases. *Biochimica et Biophysica Acta (BBA) - Molecular Basis of Disease*, *1866*(6), 165761. https://doi.org/10.1016/J.BBADIS.2020.165761

Perry, M., & Ghosal, G. (2022). Mechanisms and Regulation of DNA-Protein Crosslink Repair During DNA Replication by SPRTN Protease. *Frontiers in Molecular Biosciences*, *9*, 916697. https://doi.org/10.3389/FMOLB.2022.916697

Petkar, P. B., Mendhe, H. G., & Choudhari, S. G. (2023). Vaccines for cancer prevention and cure. *Journal of Family Medicine and Primary Care*, *12*(8), 1749. https://doi.org/10.4103/JFMPC.JFMPC_758_23

Petruseva, I. O., Evdokimov, A. N., & Lavrik, O. I. (2014). Molecular Mechanism of Global Genome Nucleotide Excision Repair. *Acta Naturae*, *6*(1), 23. https://doi.org/10.32607/20758251-2014-6-1-23-34

Pfeffer, L. M. (2011). The Role of Nuclear Factor κB in the Interferon Response. *Journal of Interferon & Cytokine Research*, *31*(7), 553. https://doi.org/10.1089/JIR.2011.0028

Phan, L. M., & Rezaeian, A. H. (2021). ATM: Main Features, Signaling Pathways, and Its Diverse Roles in DNA Damage Response, Tumor Suppression, and Cancer Development. *Genes*, *12*(6), 845. https://doi.org/10.3390/GENES12060845

Phaniendra, A., Jestadi, D. B., & Periyasamy, L. (2015). Free Radicals: Properties, Sources, Targets, and Their Implication in Various Diseases. *Indian Journal of Clinical Biochemistry*, *30*(1), 11. https://doi.org/10.1007/S12291-014-0446-0

Pierce, G. F., Mustoe, T. A., Altrock, B. W., Deuel, T. F., & Thomason, A. (1991). Role of platelet-derived growth factor in wound healing. *Journal of Cellular Biochemistry*, *45*(4), 319–326. https://doi.org/10.1002/JCB.240450403

Plikus, M. v., Wang, X., Sinha, S., Forte, E., Thompson, S. M., Herzog, E. L., Driskell, R. R., Rosenthal, N., Biernaskie, J., & Horsley, V. (2021). Fibroblasts: origins, definitions, and functions in health and disease. *Cell*, *184*(15), 3852. https://doi.org/10.1016/J.CELL.2021.06.024

Podhorecka, M., Skladanowski, A., & Bozko, P. (2010). H2AX Phosphorylation: Its Role in DNA Damage Response and Cancer Therapy. *Journal of Nucleic Acids*, *2010*, 920161. https://doi.org/10.4061/2010/920161

Poetsch, A. R. (2020). The genomics of oxidative DNA damage, repair, and resulting mutagenesis. *Computational and Structural Biotechnology Journal*, *18*, 207–219. https://doi.org/10.1016/J.CSBJ.2019.12.013

Prabhu, K. S., Kuttikrishnan, S., Ahamad, N., Habeeba, U., Mariyam, Z., Suleman, M., Bhat, A. A., & Uddin, S. (2024). H2AX: A key player in DNA damage response and a promising target for cancer therapy. *Biomedicine & Pharmacotherapy*, *175*, 116663. https://doi.org/10.1016/J.BIOPHA.2024.116663

Prorok, P., Alili, D., Saint-Pierre, C., Gasparutto, D., Zharkov, D. O., Ishchenko, A. A., Tudek, B., & Saparbaev, M. K. (2013). Uracil in duplex DNA is a substrate for the nucleotide incision repair pathway in human cells. *Proceedings of the National Academy of Sciences of the United States of America*, *110*(39), E3695–E3703. https://doi.org/10.1073/PNAS.1305624110/SUPPL_FILE/PNAS.201305624SI.PDF

Pu, F., Chen, F., Liu, J., Zhang, Z., & Shao, Z. (2021). Immune Regulation of the cGAS-STING Signaling Pathway in the Tumor Microenvironment and Its Clinical Application. *OncoTargets and Therapy*, *14*, 1501. https://doi.org/10.2147/OTT.S298958

Qian, C., Li, X., Zhang, J., & Wang, Y. (2024). Small Molecular Inhibitors That Target ATM for Drug Discovery: Current Research and Potential Prospective. *Journal of Medicinal Chemistry*, *67*(17), 14742–14767.

https://doi.org/10.1021/ACS.JMEDCHEM.4C01064/ASSET/IMAGES/LARGE/JM4C01064_0011.JPEG

Qiu, B., Wei, F., Sun, X., Wang, X., Duan, B., Shi, C., Zhang, J., Zhang, J., Qiu, W., & Mu, W. (2014). Measurement of hydroxyproline in collagen with three different methods. *Molecular Medicine Reports*, *10*(2), 1157–1163. https://doi.org/10.3892/MMR.2014.2267/HTML

Qiu, Z., Oleinick, N. L., & Zhang, J. (2017). ATR/CHK1 inhibitors and cancer therapy. *Radiotherapy and Oncology : Journal of the European Society for Therapeutic Radiology and Oncology*, *126*(3), 450. https://doi.org/10.1016/J.RADONC.2017.09.043

Ramanathan, R. K., McDonough, S. L., Philip, P. A., Hingorani, S. R., Lacy, J., Kortmansky, J. S., Thumar, J., Chiorean, E. G., Shields, A. F., Behl, D., Mehan, P. T., Gaur, R., Seery, T., Guthrie, K. A., & Hochster, H. S. (2019). Phase IB/II Randomized Study of FOLFIRINOX Plus Pegylated Recombinant Human Hyaluronidase Versus FOLFIRINOX Alone in Patients With Metastatic Pancreatic Adenocarcinoma: SWOG S1313. *Journal of Clinical Oncology*, *37*(13), 1062. https://doi.org/10.1200/JCO.18.01295

Ravi Sundar Jose Geetha, A., Fischer, K., Babadei, O., Smesnik, G., Vogt, A., Platanitis, E., Müller, M., Farlik, M., & Decker, T. (2024). Dynamic control of gene expression by ISGF3 and IRF1 during IFNβ and IFNγ signaling. *EMBO Journal*, *43*(11), 2233–2263. https://doi.org/10.1038/S44318-024-00092-7/SUPPL_FILE/44318_2024_92_MOESM9_ESM.PDF

Ray, A., Blevins, C., Wani, G., & Wani, A. A. (2016). ATR- and ATM-Mediated DNA Damage Response Is Dependent on Excision Repair Assembly during G1 but Not in S Phase of Cell Cycle. *PLOS ONE*, *11*(7), e0159344. https://doi.org/10.1371/JOURNAL.PONE.0159344

Reichenbach, J., Schubert, R., Schindler, D., Müller, K., Böhles, H., & Zielen, S. (2004). Elevated Oxidative Stress in Patients with Ataxia Telangiectasia. *Https://Home.Liebertpub.Com/Ars*, *4*(3), 465–469. https://doi.org/10.1089/15230860260196254

Reinhardt, H. C., & Yaffe, M. B. (2009). Kinases that Control the Cell Cycle in Response to DNA Damage: Chk1, Chk2, and MK2. *Current Opinion in Cell Biology*, *21*(2), 245. https://doi.org/10.1016/J.CEB.2009.01.018

Ren, F., Meng, L., Zheng, S., Cui, J., Song, S., Li, X., Wang, D., Liu, Q., Bu, W., & Sun, H. (2025). Myeloid cell-derived apCAFs promote HNSCC progression by regulating proportion of CD4+ and CD8+ T cells. *Journal of Experimental and Clinical Cancer Research*, *44*(1), 1–24. https://doi.org/10.1186/S13046-025-03290-1/FIGURES/9

Ribatti, D., & Tamma, R. (2018). A revisited concept. Tumors: Wounds that do not heal. *Critical Reviews in Oncology/Hematology*, *128*, 65–69. https://doi.org/10.1016/J.CRITREVONC.2018.05.016

Ricard-Blum, S. (2011). The Collagen Family. *Cold Spring Harbor Perspectives in Biology*, *3*(1), 1–19. https://doi.org/10.1101/CSHPERSPECT.A004978

Riches, L. C., Trinidad, A. G., Hughes, G., Jones, G. N., Hughes, A. M., Thomason, A. G., Gavine, P., Cui, A., Ling, S., Stott, J., Clark, R., Peel, S., Gill, P., Goodwin, L. M., Smith, A., Pike, K. G., Barlaam, B., Pass, M., O'Connor, M. J., … Cadogan, E. B. (2020a). Pharmacology of the ATM inhibitor AZD0156: Potentiation of irradiation and olaparib responses preclinically. *Molecular Cancer Therapeutics*, *19*(1), 13–25. https://doi.org/10.1158/1535-7163.MCT-18-1394/88396/AM/PHARMACOLOGY-OF-THE-ATM-INHIBITOR-AZD0156

Riches, L. C., Trinidad, A. G., Hughes, G., Jones, G. N., Hughes, A. M., Thomason, A. G., Gavine, P., Cui, A., Ling, S., Stott, J., Clark, R., Peel, S., Gill, P., Goodwin, L. M., Smith, A., Pike, K. G., Barlaam, B., Pass, M., O'Connor, M. J., … Cadogan, E. B. (2020b). Pharmacology of the ATM Inhibitor AZD0156: Potentiation of Irradiation and Olaparib Responses Preclinically. *Molecular Cancer Therapeutics*, *19*(1), 13–25. https://doi.org/10.1158/1535-7163.MCT-18-1394

Rieger, A. M., Nelson, K. L., Konowalchuk, J. D., & Barreda, D. R. (2011). Modified Annexin V/Propidium Iodide Apoptosis Assay For Accurate Assessment of Cell Death. *Journal of Visualized Experiments : JoVE*, *50*, 2597. https://doi.org/10.3791/2597

Riley, J. L. (2009). PD-1 signaling in primary T cells. *Immunological Reviews*, *229*(1), 114. https://doi.org/10.1111/J.1600-065X.2009.00767.X

Roberts, E. W., Deonarine, A., Jones, J. O., Denton, A. E., Feig, C., Lyons, S. K., Espeli, M., Kraman, M., McKenna, B., Wells, R. J. B., Zhao, Q., Caballero, O. L., Larder, R., Coll, A. P., O'Rahilly, S., Brindle, K. M., Teichmann, S. A., Tuveson, D. A., & Fearon, D. T. (2013). Depletion of stromal cells expressing fibroblast activation protein-α from skeletal muscle and bone marrow results in cachexia and anemia. *The Journal of Experimental Medicine*, *210*(6), 1137. https://doi.org/10.1084/JEM.20122344

Robertson, I. B., Horiguchi, M., Zilberberg, L., Dabovic, B., Hadjiolova, K., & Rifkin, D. B. (2015). Latent TGF-β-binding proteins. *Matrix Biology : Journal of the International Society for Matrix Biology*, *47*, 44. https://doi.org/10.1016/J.MATBIO.2015.05.005

Robertson, I. B., & Rifkin, D. B. (2016). Regulation of the Bioavailability of TGF-β and TGF-β-Related Proteins. *Cold Spring Harbor Perspectives in Biology*, *8*(6), a021907. https://doi.org/10.1101/CSHPERSPECT.A021907

Rocha, N., & Neefjes, J. (2007). MHC class II molecules on the move for successful antigen presentation. *The EMBO Journal*, *27*(1), 1. https://doi.org/10.1038/SJ.EMBOJ.7601945

Roche, P. A., & Furuta, K. (2015). The ins and outs of MHC class II-mediated antigen processing and presentation. *Nature Reviews. Immunology*, *15*(4), 203. https://doi.org/10.1038/NRI3818

Rodier, F., Coppé, J. P., Patil, C. K., Hoeijmakers, W. A. M., Muñoz, D. P., Raza, S. R., Freund, A., Campeau, E., Davalos, A. R., & Campisi, J. (2009). Persistent DNA damage signalling triggers senescence-associated inflammatory cytokine secretion. *Nature Cell Biology 2009 11:8*, *11*(8), 973–979. https://doi.org/10.1038/ncb1909

Rosenberg, S. A. (2014). IL-2: The First Effective Immunotherapy for Human Cancer. *The Journal of Immunology*, *192*(12), 5451–5458. https://doi.org/10.4049/JIMMUNOL.1490019

Rosenberg, S. A., Packard, B. S., Aebersold, P. M., Solomon, D., Topalian, S. L., Toy, S. T., Simon, P., Lotze, M. T., Yang, J. C., Seipp, C. A., Simpson, C., Carter, C., Bock, S., Schwartzentruber, D., Wei, J. P., & White, D. E. (1988). Use of tumor-infiltrating lymphocytes and interleukin-2 in the immunotherapy of patients with metastatic melanoma. A preliminary report. *The New England Journal of Medicine*, *319*(25), 1676–1680. https://doi.org/10.1056/NEJM198812223192527

Sadjadi, Z., Zhao, R., Hoth, M., Qu, B., & Rieger, H. (2020). Migration of Cytotoxic T Lymphocytes in 3D Collagen Matrices. *Biophysical Journal*, *119*(11), 2141. https://doi.org/10.1016/J.BPJ.2020.10.020

Sahai, E., Astsaturov, I., Cukierman, E., DeNardo, D. G., Egeblad, M., Evans, R. M., Fearon, D., Greten, F. R., Hingorani, S. R., Hunter, T., Hynes, R. O., Jain, R. K., Janowitz, T., Jorgensen, C., Kimmelman, A. C., Kolonin, M. G., Maki, R. G., Powers, R. S., Puré, E., … Werb, Z. (2020). A framework for advancing our understanding of cancer-associated fibroblasts. *Nature Reviews Cancer 2020 20:3*, *20*(3), 174–186. https://doi.org/10.1038/s41568-019-0238-1

Saito, Y., Yamamoto, S., & Chikenji, T. S. (2024). Role of cellular senescence in inflammation and regeneration. *Inflammation and Regeneration 2024 44:1*, *44*(1), 1–12. https://doi.org/10.1186/S41232-024-00342-5

Sajjad, H., Imtiaz, S., Noor, T., Siddiqui, Y. H., Sajjad, A., & Zia, M. (2021). Cancer models in preclinical research: A chronicle review of advancement in effective cancer research. *Animal Models and Experimental Medicine*, *4*(2), 87–103. https://doi.org/10.1002/AME2.12165

Sakai, T., Aokage, K., Neri, S., Nakamura, H., Nomura, S., Tane, K., Miyoshi, T., Sugano, M., Kojima, M., Fujii, S., Kuwata, T., Ochiai, A., Iyoda, A., Tsuboi, M., & Ishii, G. (2018). Link

between tumor-promoting fibrous microenvironment and an immunosuppressive microenvironment in stage I lung adenocarcinoma. *Lung Cancer*, *126*, 64–71. https://doi.org/10.1016/J.LUNGCAN.2018.10.021

Salimian, N., Peymani, M., Ghaedi, K., Hashemi, M., & Rahimi, E. (2024). Collagen 1A1 (COL1A1) and Collagen11A1(COL11A1) as diagnostic biomarkers in Breast, colorectal and gastric cancers. *Gene*, *892*. https://doi.org/10.1016/J.GENE.2023.147867

Salmon, H., Franciszkiewicz, K., Damotte, D., Dieu-Nosjean, M. C., Validire, P., Trautmann, A., Mami-Chouaib, F., & Donnadieu, E. (2012). Matrix architecture defines the preferential localization and migration of T cells into the stroma of human lung tumors. *The Journal of Clinical Investigation*, *122*(3), 899–910. https://doi.org/10.1172/JCI45817

Sambi, M., Bagheri, L., & Szewczuk, M. R. (2019). Current Challenges in Cancer Immunotherapy: Multimodal Approaches to Improve Efficacy and Patient Response Rates. *Journal of Oncology*, *2019*, 4508794. https://doi.org/10.1155/2019/4508794

Sarkar, M., Nguyen, T., Gundre, E., Ogunlusi, O., El-Sobky, M., Giri, B., & Sarkar, T. R. (2023). Cancer-associated fibroblasts: The chief architect in the tumor microenvironment. *Frontiers in Cell and Developmental Biology*, *11*, 1089068. https://doi.org/10.3389/FCELL.2023.1089068

Saunders, R. A., Michniacki, T. F., Hames, C., Moale, H. A., Wilke, C., Kuo, M. E., Nguyen, J., Hartlerode, A. J., Moore, B. B., & Sekiguchi, J. A. M. (2021). Elevated inflammatory responses and targeted therapeutic intervention in a preclinical mouse model of ataxia-telangiectasia lung disease. *Scientific Reports 2021 11:1*, *11*(1), 1–15. https://doi.org/10.1038/s41598-021-83531-3

Sautès-Fridman, C., Petitprez, F., Calderaro, J., & Fridman, W. H. (2019). Tertiary lymphoid structures in the era of cancer immunotherapy. *Nature Reviews Cancer 2019 19:6*, *19*(6), 307–325. https://doi.org/10.1038/s41568-019-0144-6

Schärer, O. D. (2013). Nucleotide Excision Repair in Eukaryotes. *Cold Spring Harbor Perspectives in Biology*, *5*(10), a012609. https://doi.org/10.1101/CSHPERSPECT.A012609

Scheper, J., Hildebrand, L. S., Faulhaber, E. M., Deloch, L., Gaipl, U. S., Symank, J., Fietkau, R., Distel, L. V., Hecht, M., & Jost, T. (2023). Tumor-specific radiosensitizing effect of the ATM inhibitor AZD0156 in melanoma cells with low toxicity to healthy fibroblasts. *Strahlentherapie Und Onkologie*, *199*(12), 1128–1139. https://doi.org/10.1007/S00066-022-02009-X/FIGURES/4

Schröder, B. (2016). The multifaceted roles of the invariant chain CD74 — More than just a chaperone. *Biochimica et Biophysica Acta (BBA) - Molecular Cell Research*, *1863*(6), 1269–1281. https://doi.org/10.1016/J.BBAMCR.2016.03.026

Schuberth, P. C., Hagedorn, C., Jensen, S. M., Gulati, P., van den Broek, M., Mischo, A., Soltermann, A., Jüngel, A., Marroquin Belaunzaran, O., Stahel, R., Renner, C., & Petrausch, U. (2013). Treatment of malignant pleural mesothelioma by fibroblast activation protein-specific re-directed T cells. *Journal of Translational Medicine*, *11*(1), 1–11. https://doi.org/10.1186/1479-5876-11-187

Schultz, G. S., Chin, G. A., Moldawer, L., & Diegelmann, R. F. (2011). Principles of Wound Healing. *Diabetic Foot Problems*, 395–402. https://doi.org/10.1142/9789812791535_0028

Schumacher, T. N., & Thommen, D. S. (2022). Tertiary lymphoid structures in cancer. *Science*, *375*(6576). https://doi.org/10.1126/SCIENCE.ABF9419/ASSET/06447C15-9D52-4218-B18A-3AE8DB83A22F/ASSETS/IMAGES/LARGE/SCIENCE.ABF9419-FA.JPG

Sciarretta, S., Zhai, P., Shao, D., Zablocki, D., Nagarajan, N., Terada, L. S., Volpe, M., & Sadoshima, J. (2013). Activation of NADPH oxidase 4 in the endoplasmic reticulum promotes cardiomyocyte autophagy and survival during energy stress through the protein kinase RNA-activated-like endoplasmic reticulum kinase/eukaryotic initiation factor 2α/activating transcription factor 4 pathway. *Circulation Research*, *113*(11), 1253–1264. https://doi.org/10.1161/CIRCRESAHA.113.301787/-/DC1

Sedeek, M., Nasrallah, R., Touyz, R. M., & Hébert, R. L. (2013). NADPH Oxidases, Reactive Oxygen Species, and the Kidney: Friend and Foe. *Journal of the American Society of Nephrology*, *24*(10), 1512–1518. https://doi.org/10.1681/ASN.2012111112

Shankaran, V., Ikeda, H., Bruce, A. T., White, J. M., Swanson, P. E., Old, L. J., & Schreiber, R. D. (2001). IFNγ and lymphocytes prevent primary tumour development and shape tumour immunogenicity. *Nature 2001 410:6832*, *410*(6832), 1107–1111. https://doi.org/10.1038/35074122

Sharma, B. R., Karki, R., & Kanneganti, T. D. (2019). Role of AIM2 inflammasome in inflammatory diseases, cancer and infection. *European Journal of Immunology*, *49*(11), 1998–2011. https://doi.org/10.1002/EJI.201848070

Shekhova, E. (2020). Mitochondrial reactive oxygen species as major effectors of antimicrobial immunity. *PLOS Pathogens*, *16*(5), e1008470. https://doi.org/10.1371/JOURNAL.PPAT.1008470

Shen, L., Sigal, L. J., Boes, M., & Rock, K. L. (2004). Important role of cathepsin S in generating peptides for TAP-independent MHC class I crosspresentation in vivo. *Immunity*, *21*(2), 155–165. https://doi.org/10.1016/J.IMMUNI.2004.07.004

Shen, L., Yang, M., Lin, Q., Zhang, Z., Zhu, B., & Miao, C. (2016). COL11A1 is overexpressed in recurrent non-small cell lung cancer and promotes cell proliferation, migration, invasion and drug resistance. *Oncology Reports*, *36*(2), 877–885. https://doi.org/10.3892/OR.2016.4869/HTML

Shen, T., Li, Y., Zhu, S., Yu, J., Zhang, B., Chen, X., Zhang, Z., Ma, Y., Niu, Y., & Shang, Z. (2020). YAP1 plays a key role of the conversion of normal fibroblasts into cancer-associated fibroblasts that contribute to prostate cancer progression. *Journal of Experimental and Clinical Cancer Research*, *39*(1), 1–16. https://doi.org/10.1186/S13046-020-1542-Z/FIGURES/5

Sherman, M. H., Yu, R. T., Engle, D. D., Ding, N., Atkins, A. R., Tiriac, H., Collisson, E. A., Connor, F., Van Dyke, T., Kozlov, S., Martin, P., Tseng, T. W., Dawson, D. W., Donahue, T. R., Masamune, A., Shimosegawa, T., Apte, M. V., Wilson, J. S., Ng, B., … Evans, R. M. (2014). Vitamin D receptor-mediated stromal reprogramming suppresses pancreatitis and enhances pancreatic cancer therapy. *Cell*, *159*(1), 80–93. https://doi.org/10.1016/J.CELL.2014.08.007/ATTACHMENT/0FE5F809-5779-4960-AAF6-88548D5E19E5/MMC4.PDF

Shi, W., Chen, Z., Liu, H., Miao, C., Feng, R., Wang, G., Chen, G., Chen, Z., Fan, P., Pang, W., & Li, C. (2022). COL11A1 as an novel biomarker for breast cancer with machine learning and immunohistochemistry validation. *Frontiers in Immunology*, *13*, 937125. https://doi.org/10.3389/FIMMU.2022.937125/FULL

Shindo, K., Aishima, S., Ohuchida, K., Fujiwara, K., Fujino, M., Mizuuchi, Y., Hattori, M., Mizumoto, K., Tanaka, M., & Oda, Y. (2013). Podoplanin expression in cancer-associated fibroblasts enhances tumor progression of invasive ductal carcinoma of the pancreas. *Molecular Cancer*, *12*(1), 168. https://doi.org/10.1186/1476-4598-12-168

Shrivastav, M., Miller, C. A., De Haro, L. P., Durant, S. T., Chen, B. P. C., Chen, D. J., & Nickoloff, J. A. (2009). DNA-PKcs and ATM Co-Regulate DNA Double-Strand Break Repair. *DNA Repair*, *8*(8), 920. https://doi.org/10.1016/J.DNAREP.2009.05.006

Siddiqui, I., Erreni, M., Van Brakel, M., Debets, R., & Allavena, P. (2016). Enhanced recruitment of genetically modified CX3CR1-positive human T cells into Fractalkine/CX3CL1 expressing tumors: importance of the chemokine gradient. *Journal for ImmunoTherapy of Cancer*, *4*(1), 21. https://doi.org/10.1186/S40425-016-0125-1

Singh, A., Schofield, C. J., & Chen, R. (2020). Hypoxia-inducible factor (HIF) prolyl hydroxylase inhibitors induce autophagy and have a protective effect in an in-vitro ischaemia model. *Scientific Reports 2020 10:1*, *10*(1), 1–19. https://doi.org/10.1038/s41598-020-58482-w

Smith, J., Mun Tho, L., Xu, N., & A. Gillespie, D. (2010). The ATM–Chk2 and ATR–Chk1 Pathways in DNA Damage Signaling and Cancer. *Advances in Cancer Research*, *108*(C), 73–112. https://doi.org/10.1016/B978-0-12-380888-2.00003-0

So, S., Davis, A. J., & Chen, D. J. (2009). Autophosphorylation at serine 1981 stabilizes ATM at DNA damage sites. *The Journal of Cell Biology*, *187*(7), 977. https://doi.org/10.1083/JCB.200906064

Song, Q., Hu, Y., Yin, A., Wang, H., & Yin, Q. (2022). DNA Holliday Junction: History, Regulation and Bioactivity. *International Journal of Molecular Sciences*, *23*(17), 9730. https://doi.org/10.3390/IJMS23179730

Song, S., Peng, P., Tang, Z., Zhao, J., Wu, W., Li, H., Shao, M., Li, L., Yang, C., Duan, F., Zhang, M., Zhang, J., Wu, H., Li, C., Wang, X., Wang, H., Ruan, Y., & Gu, J. (2017). Decreased expression of STING predicts poor prognosis in patients with gastric cancer. *Scientific Reports*, *7*. https://doi.org/10.1038/SREP39858

Song, X., Ma, F., & Herrup, K. (2019). Accumulation of Cytoplasmic DNA Due to ATM Deficiency Activates the Microglial Viral Response System with Neurotoxic Consequences. *The Journal of Neuroscience*, *39*(32), 6378. https://doi.org/10.1523/JNEUROSCI.0774-19.2019

Stakyte, K., Rotheneder, M., Lammens, K., Bartho, J. D., Grädler, U., Fuchß, T., Pehl, U., Alt, A., van de Logt, E., & Hopfner, K. P. (2021). Molecular basis of human ATM kinase inhibition. *Nature Structural & Molecular Biology 2021 28:10*, *28*(10), 789–798. https://doi.org/10.1038/s41594-021-00654-x

Stampfer, M. R., Garbe, J., Nijjar, T., Wigington, D., Swisshelm, K., & Yaswen, P. (2003). Loss of p53 function accelerates acquisition of telomerase activity in indefinite lifespan human mammary epithelial cell lines. *Oncogene 2003 22:34*, *22*(34), 5238–5251. https://doi.org/10.1038/sj.onc.1206667

Stark, G. R., & Taylor, W. R. (2004). Analyzing the G2/M checkpoint. *Methods in Molecular Biology (Clifton, N.J.)*, *280*, 51–82. https://doi.org/10.1385/1-59259-788-2:051

Steele, S. L., Wu, Y., Kolb, R. J., Gooz, M., Haycraft, C. J., Keyser, K. T., Guay-Woodford, L., Yao, H., & Bell, P. D. (2010). Telomerase immortalization of principal cells from mouse collecting duct. *American Journal of Physiology - Renal Physiology*, *299*(6), F1507. https://doi.org/10.1152/AJPRENAL.00183.2010

Stinson, B. M., & Loparo, J. J. (2021). Repair of DNA Double-Strand Breaks by the Non-homologous End Joining Pathway. *Annual Review of Biochemistry*, *90*, 137. https://doi.org/10.1146/ANNUREV-BIOCHEM-080320-110356

Stockwell, B. R., & Schreiber, S. L. (1998). Probing the role of homomeric and heteromeric receptor interactions in TGF-β signaling using small molecule dimerizers. *Current Biology*, *8*(13), 761–773. https://doi.org/10.1016/S0960-9822(98)70299-4

Stumptner, P., & Benaroch, P. (1997). Interaction of MHC class II molecules with the invariant chain: Role of the invariant chain (81-90) region. *EMBO Journal*, *16*(19), 5807–5818. https://doi.org/10.1038/SJ.EMBOJ.7590555/ASSET/80B5B9E1-0A4E-4A16-B7FD-76C62C5BA164/ASSETS/GRAPHIC/EMBJ7590555-FIG-0009-M.JPG

Sun, J. Y., Zhang, D., Wu, S., Xu, M., Zhou, X., Lu, X. J., & Ji, J. (2020). Resistance to PD-1/PD-L1 blockade cancer immunotherapy: mechanisms, predictive factors, and future perspectives. *Biomarker Research*, *8*(1). https://doi.org/10.1186/S40364-020-00212-5

Sun, L., Chiang, J. Y., Choi, J. Y., Xiong, Z. M., Mao, X., Collins, F. S., Hodes, R. J., & Cao, K. (2019). Transient induction of telomerase expression mediates senescence and reduces tumorigenesis in primary fibroblasts. *Proceedings of the National Academy of Sciences of the United States of America*, *116*(38), 18983–18993. https://doi.org/10.1073/PNAS.1907199116/-/DCSUPPLEMENTAL

Suzuki, H., Kaneko, M. K., & Kato, Y. (2022). Roles of Podoplanin in Malignant Progression of Tumor. *Cells*, *11*(3), 575. https://doi.org/10.3390/CELLS11030575

Suzuki, J., Aokage, K., Neri, S., Sakai, T., Hashimoto, H., Su, Y., Yamazaki, S., Nakamura, H., Tane, K., Miyoshi, T., Sugano, M., Kojima, M., Fujii, S., Kuwata, T., Ochiai, A., Tsuboi, M., & Ishii, G. (2021). Relationship between podoplanin-expressing cancer-associated fibroblasts and the immune microenvironment of early lung squamous cell carcinoma. *Lung Cancer*, *153*, 1–10. https://doi.org/10.1016/J.LUNGCAN.2020.12.020

Takahashi, H., Sakakura, K., Kawabata-Iwakawa, R., Rokudai, S., Toyoda, M., Nishiyama, M., & Chikamatsu, K. (2015). Immunosuppressive activity of cancer-associated fibroblasts in head and neck squamous cell carcinoma. *Cancer Immunology, Immunotherapy : CII*, *64*(11), 1407. https://doi.org/10.1007/S00262-015-1742-0

Takeshima, H., & Ushijima, T. (2019). Accumulation of genetic and epigenetic alterations in normal cells and cancer risk. *Npj Precision Oncology 2019 3:1*, *3*(1), 1–8. https://doi.org/10.1038/s41698-019-0079-0

Talmage Webb Waring, D. W. (1986). The Acceptance and Rejection of Immunological Concepts. *Https://Doi.Org/10.1146/Annurev.Iy.04.040186.000245*, *4*(1), 1–12. https://doi.org/10.1146/ANNUREV.IY.04.040186.000245

Tan, Q., Ma, S., Hu, J., Chen, X., Yu, Y., Zang, G., & Tang, Z. (2016). Role of tripeptidyl peptidase II in MHC class I antigen presentation: Biological characteristics, cellular crosstalk and signaling. *Biomedicine & Pharmacotherapy*, *84*, 1954–1958. https://doi.org/10.1016/J.BIOPHA.2016.11.004

Tarafdar, A., & Pula, G. (2018). The Role of NADPH Oxidases and Oxidative Stress in Neurodegenerative Disorders. *International Journal of Molecular Sciences*, *19*(12), 3824. https://doi.org/10.3390/IJMS19123824

Tauriello, D. V. F., Palomo-Ponce, S., Stork, D., Berenguer-Llergo, A., Badia-Ramentol, J., Iglesias, M., Sevillano, M., Ibiza, S., Cañellas, A., Hernando-Momblona, X., Byrom, D., Matarin, J. A., Calon, A., Rivas, E. I., Nebreda, A. R., Riera, A., Attolini, C. S. O., & Batlle, E. (2018). TGFβ drives immune evasion in genetically reconstituted colon cancer metastasis. *Nature 2018 554:7693*, *554*(7693), 538–543. https://doi.org/10.1038/nature25492

Taylor, A. M. R. (2001). Ataxia Telangiectasia. *Encyclopedia of Genetics*, 113–115. https://doi.org/10.1006/RWGN.2001.1546

Teramoto, K., Igarashi, T., Kataoka, Y., Ishida, M., Hanaoka, J., Sumimoto, H., & Daigo, Y. (2019). Clinical significance of PD-L1-positive cancer-associated fibroblasts in pN0M0 non-small cell lung cancer. *Lung Cancer (Amsterdam, Netherlands)*, *137*, 56–63. https://doi.org/10.1016/J.LUNGCAN.2019.09.013

Thannickal, V. J., Jandeleit-Dahm, K., Szyndralewiez, C., & Török, N. J. (2023). Pre-clinical evidence of a dual NADPH oxidase 1/4 inhibitor (setanaxib) in liver, kidney and lung fibrosis. *Journal of Cellular and Molecular Medicine*, *27*(4), 471. https://doi.org/10.1111/JCMM.17649

Thannickal, V. J., Lee, D. Y., White, E. S., Cui, Z., Larios, J. M., Chacon, R., Horowitz, J. C., Day, R. M., & Thomas, P. E. (2003). Myofibroblast differentiation by transforming growth factor-β1 is dependent on cell adhesion and integrin signaling via focal adhesion kinase. *Journal of Biological Chemistry*, *278*(14), 12384–12389. https://doi.org/10.1074/jbc.M208544200

Thomsen, M. K., Skouboe, M. K., Boularan, C., Vernejoul, F., Lioux, T., Leknes, S. L., Berthelsen, M. F., Riedel, M., Cai, H., Joseph, J. V., Perouzel, E., Tiraby, M., Vendelbo, M. H., & Paludan, S. R. (2019). The cGAS-STING pathway is a therapeutic target in a preclinical model of hepatocellular carcinoma. *Oncogene 2019 39:8*, *39*(8), 1652–1664. https://doi.org/10.1038/s41388-019-1108-8

Tian, C., Clauser, K. R., Öhlund, D., Rickelt, S., Huang, Y., Gupta, M., Mani, D. R., Carr, S. A., Tuveson, D. A., & Hynes, R. O. (2019). Proteomic analyses of ECM during pancreatic ductal adenocarcinoma progression reveal different contributions by tumor and stromal cells. *Proceedings of the National Academy of Sciences of the United States of America*, *116*(39), 19609–19618. https://doi.org/10.1073/PNAS.1908626116/SUPPL_FILE/PNAS.1908626116.SD04.XLSX

Tian, H., Callahan, C. A., Dupree, K. J., Darbonne, W. C., Ahn, C. P., Scales, S. J., & De Sauvage, F. J. (2009). Hedgehog signaling is restricted to the stromal compartment during pancreatic carcinogenesis. *Proceedings of the National Academy of Sciences of the United States of America*, *106*(11), 4254. https://doi.org/10.1073/PNAS.0813203106

Tian, Z., Zeng, Y., Peng, Y., Liu, J., & Wu, F. (2022). Cancer immunotherapy strategies that target the cGAS-STING pathway. *Frontiers in Immunology*, *13*, 996663. https://doi.org/10.3389/FIMMU.2022.996663/BIBTEX

Tran, E., Chinnasamy, D., Yu, Z., Morgan, R. A., Lee, C. C. R., Restifo, N. P., & Rosenberg, S. A. (2013). Immune targeting of fibroblast activation protein triggers recognition of multipotent bone marrow stromal cells and cachexia. *The Journal of Experimental Medicine*, *210*(6), 1125. https://doi.org/10.1084/JEM.20130110

Trojanowska, M. (2009). Noncanonical transforming growth factor β signaling in scleroderma fibrosis. *Current Opinion in Rheumatology*, *21*(6), 623. https://doi.org/10.1097/BOR.0B013E32833038CE

Tufail, M., Jiang, C.-H., & Li, N. (2024). Altered metabolism in cancer: insights into energy pathways and therapeutic targets. *Molecular Cancer 2024 23:1*, *23*(1), 1–40. https://doi.org/10.1186/S12943-024-02119-3

Turner, M. D., Nedjai, B., Hurst, T., & Pennington, D. J. (2014). Cytokines and chemokines: At the crossroads of cell signalling and inflammatory disease. *Biochimica et Biophysica Acta (BBA) - Molecular Cell Research*, *1843*(11), 2563–2582. https://doi.org/10.1016/J.BBAMCR.2014.05.014

Turunen, M. P., Lehtola, T., Heinonen, S. E., Assefa, G. S., Korpisalo, P., Girnary, R., Glass, C. K., Väisänen, S., & Ylä-Herttuala, S. (2009). Efficient regulation of VEGF expression by promoter-targeted lentiviral shRNAs based on epigenetic mechanism a novel example of epigenetherapy. *Circulation Research*, *105*(6), 604–609. https://doi.org/10.1161/CIRCRESAHA.109.200774/SUPPL_FILE/200774-R2_ONLINE.PDF

Ueno, S., Sudo, T., & Hirasawa, A. (2022). ATM: Functions of ATM Kinase and Its Relevance to Hereditary Tumors. *International Journal of Molecular Sciences*, *23*(1), 523. https://doi.org/10.3390/IJMS23010523

Ujevic, A., Knizkova, D., Synackova, A., Pribikova, M., Trivic, T., Dalinskaya, A., Drobek, A., Niederlova, V., Paprckova, D., De Guia, R., Kasparek, P., Prochazka, J., Labaj, J., Fedosieieva, O., Roeck, B. F., Mihola, O., Trachtulec, Z., Sedlacek, R., Stepanek, O., & Draber, P. (2024). TBK1-associated adapters TANK and AZI2 protect mice against TNF-induced cell death and severe autoinflammatory diseases. *Nature Communications 2024 15:1*, *15*(1), 1–18. https://doi.org/10.1038/s41467-024-54399-4

Ulrich, E., Boehmelt, G., Bird, A., & Beug, H. (1992). Immortalization of conditionally transformed chicken cells: loss of normal p53 expression is an early step that is independent of cell transformation. *Genes & Development*, *6*(5), 876–887. https://doi.org/10.1101/GAD.6.5.876

Vaish, U., Jain, T., Are, A. C., & Dudeja, V. (2021). Cancer-Associated Fibroblasts in Pancreatic Ductal Adenocarcinoma: An Update on Heterogeneity and Therapeutic Targeting. *International Journal of Molecular Sciences*, *22*(24). https://doi.org/10.3390/IJMS222413408

Valent, P., Groner, B., Schumacher, U., Superti-Furga, G., Busslinger, M., Kralovics, R., Zielinski, C., Penninger, J. M., Kerjaschki, D., Stingl, G., Smolen, J. S., Valenta, R., Lassmann, H., Kovar, H., Jäger, U., Kornek, G., Müller, M., & Sörgel, F. (2016). Paul Ehrlich (1854-1915) and His Contributions to the Foundation and Birth of Translational Medicine. *Journal of Innate Immunity*, *8*(2), 111–120. https://doi.org/10.1159/000443526

Van Cutsem, E., Tempero, M. A., Sigal, D., Oh, D. Y., Fazio, N., MacArulla, T., Hitre, E., Hammel, P., Hendifar, A. E., Bates, S. E., Li, C. P., Hingorani, S. R., De La Fouchardiere, C., Kasi, A., Heinemann, V., Maraveyas, A., Bahary, N., Layos, L., Sahai, V., … Bullock, A. J. (2020). Randomized phase III trial of pegvorhyaluronidase alfa with nab-paclitaxel plus gemcitabine for patients with hyaluronan-high metastatic pancreatic adenocarcinoma. *Journal of Clinical Oncology*, *38*(27), 3185–3194. https://doi.org/10.1200/JCO.20.00590/SUPPL_FILE/PROTOCOL_JCO.20.00590.PDF

van der Bruggen, P., Traversari, C., Chomez, P., Lurquin, C., de Plaen, E., van den Eynde, B., Knuth, A., & Boon, T. (1991). A gene encoding an antigen recognized by cytolytic T lymphocytes on a human melanoma. *Science*, *254*(5038), 1643–1647. https://doi.org/10.1126/SCIENCE.1840703

Vesely, M. D., Kershaw, M. H., Schreiber, R. D., & Smyth, M. J. (2011). Natural Innate and Adaptive Immunity to Cancer. *Https://Doi.Org/10.1146/Annurev-Immunol-031210-101324*, *29*, 235–271. https://doi.org/10.1146/ANNUREV-IMMUNOL-031210-101324

Vesely, M. D., & Schreiber, R. D. (2013). Cancer Immunoediting: antigens, mechanisms and implications to cancer immunotherapy. *Annals of the New York Academy of Sciences*, *1284*(1), 1. https://doi.org/10.1111/NYAS.12105

Victorelli, S., & Passos, J. F. (2017). Telomeres and Cell Senescence - Size Matters Not. *EBioMedicine*, *21*, 14–20. https://doi.org/10.1016/J.EBIOM.2017.03.027

Wajapeyee, N., Serra, R. W., Zhu, X., Mahalingam, M., & Green, M. R. (2008). Oncogenic BRAF Induces Senescence and Apoptosis through Pathways Mediated by the Secreted Protein IGFBP7. *Cell*, *132*(3), 363. https://doi.org/10.1016/J.CELL.2007.12.032

Wang, H., Liang, Y., Liu, Z., Zhang, R., Chao, J., Wang, M., Liu, M., Qiao, L., Xuan, Z., Zhao, H., & Lu, L. (2024). POSTN+ cancer-associated fibroblasts determine the efficacy of immunotherapy in hepatocellular carcinoma. *Journal for Immunotherapy of Cancer*, *12*(7), e008721. https://doi.org/10.1136/JITC-2023-008721

Wang, H., Yao, L., Chen, J., Li, Y., Su, Z., Liu, Y., Li, W., Xiong, Y., Gao, H., Zhang, X., & Zhou, Y. (2024). The dual role of POSTN in maintaining glioblastoma stem cells and the immunosuppressive phenotype of microglia in glioblastoma. *Journal of Experimental and Clinical Cancer Research*, *43*(1), 1–22. https://doi.org/10.1186/S13046-024-03175-9/FIGURES/8

Wang, J., Ouyang, X., Zhu, W., Yi, Q., & Zhong, J. (2024). The Role of CXCL11 and its Receptors in Cancer: Prospective but Challenging Clinical Targets. *Cancer Control*, *31*. https://doi.org/10.1177/10732748241241162/ASSET/IMAGES/LARGE/10.1177_10732748241241162-FIG2.JPEG

Wang, L. C. S., Lo, A., Scholler, J., Sun, J., Majumdar, R. S., Kapoor, V., Antzis, M., Cotner, C. E., Johnson, L. A., Durham, A. C., Solomides, C. C., June, C. H., Puré, E., & Albelda, S. M. (2014). Targeting fibroblast activation protein in tumor stroma with chimeric antigen receptor T cells can inhibit tumor growth and augment host immunity without severe toxicity. *Cancer Immunology Research*, *2*(2), 154–166. https://doi.org/10.1158/2326-6066.CIR-13-0027

Wang, L., Lankhorst, L., & Bernards, R. (2022). Exploiting senescence for the treatment of cancer. *Nature Reviews Cancer 2022 22:6*, *22*(6), 340–355. https://doi.org/10.1038/s41568-022-00450-9

Wang, M. M., Coupland, S. E., Aittokallio, T., & Figueiredo, C. R. (2023). Resistance to immune checkpoint therapies by tumour-induced T-cell desertification and exclusion: key mechanisms, prognostication and new therapeutic opportunities. *British Journal of Cancer 2023 129:8*, *129*(8), 1212–1224. https://doi.org/10.1038/s41416-023-02361-4

Wang, S., Liang, Y., & Dai, C. (2022). Metabolic Regulation of Fibroblast Activation and Proliferation during Organ Fibrosis. *Kidney Diseases*, *8*(2), 115. https://doi.org/10.1159/000522417

Wang, X., Che, X., Liu, C., Fan, Y., Bai, M., Hou, K., Shi, X., Zhang, X., Liu, B., Zheng, C., Liu, Y., & Qu, X. (2018). Cancer-associated fibroblasts-stimulated interleukin-11 promotes metastasis of gastric cancer cells mediated by upregulation of MUC1. *Experimental Cell Research*, *368*(2), 184–193. https://doi.org/10.1016/J.YEXCR.2018.04.028

Wang, Y., Liang, Y., Xu, H., Zhang, X., Mao, T., Cui, J., Yao, J., Wang, Y., Jiao, F., Xiao, X., Hu, J., Xia, Q., Zhang, X., Wang, X., Sun, Y., Fu, D., Shen, L., Xu, X., Xue, J., & Wang, L. (2021). Single-cell analysis of pancreatic ductal adenocarcinoma identifies a novel fibroblast subtype associated with poor prognosis but better immunotherapy response. *Cell Discovery 2021 7:1*, *7*(1), 1–17. https://doi.org/10.1038/s41421-021-00271-4

Wang, Z., Zhang, S., Zheng, C., Xia, K., Sun, L., Tang, X., Zhou, F., Ouyang, Y., & Tang, F. (2022). CTHRC1 is a Potential Prognostic Biomarker and Correlated with Macrophage Infiltration in Breast Cancer. *International Journal of General Medicine*, *15*, 5701. https://doi.org/10.2147/IJGM.S366272

Wargo, J. A., Reuben, A., Cooper, Z. A., Oh, K. S., & Sullivan, R. J. (2015). Immune Effects of Chemotherapy, Radiation, and Targeted Therapy and Opportunities for Combination With Immunotherapy. *Seminars in Oncology*, *42*(4), 601–616. https://doi.org/10.1053/J.SEMINONCOL.2015.05.007

Weber, A. M., & Ryan, A. J. (2015). ATM and ATR as therapeutic targets in cancer. *Pharmacology & Therapeutics*, *149*, 124–138. https://doi.org/10.1016/J.PHARMTHERA.2014.12.001

Wei, J., Hu, M., Huang, K., Lin, S., & Du, H. (2020). Roles of Proteoglycans and Glycosaminoglycans in Cancer Development and Progression. *International Journal of Molecular Sciences*, *21*(17), 5983. https://doi.org/10.3390/IJMS21175983

Wei, K., Nguyen, H. N., & Brenner, M. B. (2021). Fibroblast pathology in inflammatory diseases. *The Journal of Clinical Investigation*, *131*(20). https://doi.org/10.1172/JCI149538

Wei, R., Liu, S., Zhang, S., Min, L., & Zhu, S. (2020). Cellular and Extracellular Components in Tumor Microenvironment and Their Application in Early Diagnosis of Cancers. *Analytical Cellular Pathology (Amsterdam)*, *2020*. https://doi.org/10.1155/2020/6283796

Wen, Y., Wang, C. T., Ma, T. T., Li, Z. Y., Zhou, L. N., Mu, B., Leng, F., Shi, H. S., Li, Y. O., & Wei, Y. Q. (2010). Immunotherapy targeting fibroblast activation protein inhibits tumor growth and increases survival in a murine colon cancer model. *Cancer Science*, *101*(11), 2325. https://doi.org/10.1111/J.1349-7006.2010.01695.X

Westin, E. R., Aykin-Burns, N., Buckingham, E. M., Spitz, D. R., Goldman, F. D., & Klingelhutz, A. J. (2011). The p53/p21WAF/CIP Pathway Mediates Oxidative Stress and Senescence in

Dyskeratosis Congenita Cells with Telomerase Insufficiency. *Antioxidants & Redox Signaling*, *14*(6), 985. https://doi.org/10.1089/ARS.2010.3444

Weyemia, U., Redon, C. E., Aziz, T., Choudhuri, R., Maeda, D., Parekh, P. R., Bonner, M. Y., Arbiser, J. L., & Bonner, W. M. (2015). NADPH oxidase 4 is a critical mediator in Ataxia telangiectasia disease. *Proceedings of the National Academy of Sciences of the United States of America*, *112*(7), 2121–2126. https://doi.org/10.1073/PNAS.1418139112/-/DCSUPPLEMENTAL

Wheeler, O. P. G., & Unterholzner, L. (2023). DNA sensing in cancer: Pro-tumour and anti-tumour functions of cGAS–STING signalling. *Essays in Biochemistry*, *67*(6), 905. https://doi.org/10.1042/EBC20220241

Wilkinson, H. N., & Hardman, M. J. (2020). Wound healing: cellular mechanisms and pathological outcomes. *Open Biology*, *10*(9). https://doi.org/10.1098/RSOB.200223

Winkler, J., Abisoye-Ogunniyan, A., Metcalf, K. J., & Werb, Z. (2020). Concepts of extracellular matrix remodelling in tumour progression and metastasis. *Nature Communications 2020 11:1*, *11*(1), 1–19. https://doi.org/10.1038/s41467-020-18794-x

Witosch, J., Wolf, E., & Mizuno, N. (2014). Architecture and ssDNA interaction of the Timeless-Tipin-RPA complex. *Nucleic Acids Research*, *42*(20), 12912–12927. https://doi.org/10.1093/NAR/GKU960

Won, J. K., & Bakhoum, S. F. (2020). The cytosolic DNA-sensing cGAS–sting pathway in cancer. *Cancer Discovery*, *10*(1), 26–39. https://doi.org/10.1158/2159-8290.CD-19-0761/43910/P/THE-CYTOSOLIC-DNA-SENSING-CGAS-STING-PATHWAY-IN

Wong, K. Y., Cheung, A. H. K., Chen, B., Chan, W. N., Yu, J., Lo, K. W., Kang, W., & To, K. F. (2022). Cancer-associated fibroblasts in nonsmall cell lung cancer: From molecular mechanisms to clinical implications. *International Journal of Cancer*, *151*(8), 1195–1215. https://doi.org/10.1002/IJC.34127

Wu, B., Zhang, B., Li, B., Wu, H., & Jiang, M. (2024). Cold and hot tumors: from molecular mechanisms to targeted therapy. *Signal Transduction and Targeted Therapy 2024 9:1*, *9*(1), 1–65. https://doi.org/10.1038/s41392-024-01979-x

Wu, F., Yang, J., Liu, J., Wang, Y., Mu, J., Zeng, Q., Deng, S., & Zhou, H. (2021). Signaling pathways in cancer-associated fibroblasts and targeted therapy for cancer. *Signal Transduction and Targeted Therapy 2021 6:1*, *6*(1), 1–35. https://doi.org/10.1038/s41392-021-00641-0

Wu, L., Chan, K. L., Ralf, C., Bernstein, D. A., Garcia, P. L., Bohr, V. A., Vindigni, A., Janscak, P., Keck, J. L., & Hickson, I. D. (2005). The HRDC domain of BLM is required for the dissolution of double Holliday junctions. *The EMBO Journal*, *24*(14), 2679. https://doi.org/10.1038/SJ.EMBOJ.7600740

Wu, X., Chen, X., Zhou, Q., Li, P., Yu, B., Li, J., Qu, Y., Yan, J., Yu, Y., Yan, M., Zhu, Z., Liu, B., & Su, L. (2013). Hepatocyte growth factor activates tumor stromal fibroblasts to promote tumorigenesis in gastric cancer. *Cancer Letters*, *335*(1), 128–135. https://doi.org/10.1016/J.CANLET.2013.02.002

Wu, X., Li, T., Jiang, R., Yang, X., Guo, H., & Yang, R. (2023). Targeting MHC-I molecules for cancer: function, mechanism, and therapeutic prospects. *Molecular Cancer 2023 22:1*, *22*(1), 1–17. https://doi.org/10.1186/S12943-023-01899-4

Wu, Y. H., & Chou, C. Y. (2022). Collagen XI Alpha 1 Chain, a Novel Therapeutic Target for Cancer Treatment. *Frontiers in Oncology*, *12*, 925165. https://doi.org/10.3389/FONC.2022.925165

Wu, Y. H., Huang, Y. F., Chang, T. H., Chen, C. C., Wu, P. Y., Huang, S. C., & Chou, C. Y. (2021). COL11A1 activates cancer-associated fibroblasts by modulating TGF-β3 through the NF-κB/IGFBP2 axis in ovarian cancer cells. *Oncogene 2021 40:26*, *40*(26), 4503–4519. https://doi.org/10.1038/s41388-021-01865-8

Wu, Y. H., Huang, Y. F., Chang, T. H., & Chou, C. Y. (2017). Activation of TWIST1 by COL11A1 promotes chemoresistance and inhibits apoptosis in ovarian cancer cells by modulating NF-κB-mediated IKKβ expression. *International Journal of Cancer*, *141*(11), 2305–2317. https://doi.org/10.1002/IJC.30932

Wu, Y., Zhang, B., Nong, J., Rodrìguez, R. A., Guo, W., Liu, Y., Zhao, S., & Wei, R. (2023). Systematic pan-cancer analysis of the potential tumor diagnosis and prognosis biomarker P4HA3. *Frontiers in Genetics*, *14*, 1045061. https://doi.org/10.3389/FGENE.2023.1045061/FULL

Xiang, H., Ramil, C. P., Hai, J., Zhang, C., Wang, H., Watkins, A. A., Afshar, R., Georgiev, P., Sze, M. A., Song, X. S., Curran, P. J., Cheng, M., Miller, J. R., Sun, D., Loboda, A., Jia, Y., Moy, L. Y., Chi, A., & Brandish, P. E. (2020). Cancer-associated fibroblasts promote immunosuppression by inducing ROS-generating monocytic MDSCs in lung squamous cell carcinoma. *Cancer Immunology Research*, *8*(4), 436–450. https://doi.org/10.1158/2326-6066.CIR-19-0507/470826/AM/CANCER-ASSOCIATED-FIBROBLASTS-PROMOTE

Xiao, C., Li, C., & He, J. (2023). Novel contributor to chemotherapy resistance: an interferon-dependent subtype of cancer-associated fibroblast. *Molecular Biomedicine*, *4*(1), 12. https://doi.org/10.1186/S43556-023-00123-5

Xing, F., Saidou, J., & Watabe, K. (2010). Cancer associated fibroblasts (CAFs) in tumor microenvironment. *Frontiers in Bioscience : A Journal and Virtual Library*, *15*(1), 166. https://doi.org/10.2741/3613

Xiong, W., Chen, Y., Zhang, C., Li, J., Huang, H., Zhu, Y., Deng, G., Cheng, J., Lin, Y., Shi, Z., & Mou, T. (2023). Pharmacologic inhibition of IL11/STAT3 signaling increases MHC-I expression and

T cell infiltration. *Journal of Translational Medicine*, *21*(1), 416. https://doi.org/10.1186/S12967-023-04079-6

Xu, S., Wei, J., Sun, S., Zhang, J., Chan, T. F., & Li, Y. (2024). SSBlazer: a genome-wide nucleotide-resolution model for predicting single-strand break sites. *Genome Biology*, *25*(1), 1–20. https://doi.org/10.1186/S13059-024-03179-W/TABLES/2

Xue, C., & Greene, E. C. (2021). DNA repair pathway choices in CRISPR-Cas9 mediated genome editing. *Trends in Genetics : TIG*, *37*(7), 639. https://doi.org/10.1016/J.TIG.2021.02.008

Xue, W., Zender, L., Miething, C., Dickins, R. A., Hernando, E., Krizhanovsky, V., Cordon-Cardo, C., & Lowe, S. W. (2007a). Senescence and tumour clearance is triggered by p53 restoration in murine liver carcinomas. *Nature*, *445*(7128), 656. https://doi.org/10.1038/NATURE05529

Xue, W., Zender, L., Miething, C., Dickins, R. A., Hernando, E., Krizhanovsky, V., Cordon-Cardo, C., & Lowe, S. W. (2007b). Senescence and tumour clearance is triggered by p53 restoration in murine liver carcinomas. *Nature*, *445*(7128), 656. https://doi.org/10.1038/NATURE05529

Yamaguchi, H., & Taouk, G. M. (2020). A Potential Role of YAP/TAZ in the Interplay Between Metastasis and Metabolic Alterations. *Frontiers in Oncology*, *10*, 928. https://doi.org/10.3389/FONC.2020.00928/BIBTEX

Yang, D., Liu, J., Qian, H., & Zhuang, Q. (2023). Cancer-associated fibroblasts: from basic science to anticancer therapy. *Experimental & Molecular Medicine 2023 55:7*, *55*(7), 1322–1332. https://doi.org/10.1038/s12276-023-01013-0

Yang, X., Lin, Y., Shi, Y., Li, B., Liu, W., Yin, W., Dang, Y., Chu, Y., Fan, J., & He, R. (2016). FAP Promotes immunosuppression by cancer-associated fibroblasts in the tumor microenvironment via STAT3-CCL2 Signaling. *Cancer Research*, *76*(14), 4124–4135. https://doi.org/10.1158/0008-5472.CAN-15-2973/652272/AM/FAP-PROMOTES-IMMUNOSUPPRESSION-BY-CANCER

Yang, Y. L., Yang, F., Huang, Z. Q., Li, Y. Y., Shi, H. Y., Sun, Q., Ma, Y., Wang, Y., Zhang, Y., Yang, S., Zhao, G. R., & Xu, F. H. (2023). T cells, NK cells, and tumor-associated macrophages in cancer immunotherapy and the current state of the art of drug delivery systems. *Frontiers in Immunology*, *14*, 1199173. https://doi.org/10.3389/FIMMU.2023.1199173

Ye, M., Song, Y., Pan, S., Chu, M., Wang, Z. W., & Zhu, X. (2020). Evolving roles of lysyl oxidase family in tumorigenesis and cancer therapy. *Pharmacology & Therapeutics*, *215*, 107633. https://doi.org/10.1016/J.PHARMTHERA.2020.107633

Ye, Y., Kuang, X., Xie, Z., Liang, L., Zhang, Z., Zhang, Y., Ma, F., Gao, Q., Chang, R., Lee, H. H., Zhao, S., Su, J., Li, H., Peng, J., Chen, H., Yin, M., Peng, C., Yang, N., Wang, J., … Chen, X. (2020). Small-molecule MMP2/MMP9 inhibitor SB-3CT modulates tumor immune surveillance by

regulating PD-L1. *Genome Medicine*, *12*(1), 1–19. https://doi.org/10.1186/S13073-020-00780-Z/FIGURES/7

Yeung, T., Georges, P. C., Flanagan, L. A., Marg, B., Ortiz, M., Funaki, M., Zahir, N., Ming, W., Weaver, V., & Janmey, P. A. (2005). Effects of substrate stiffness on cell morphology, cytoskeletal structure, and adhesion. *Cell Motility and the Cytoskeleton*, *60*(1), 24–34. https://doi.org/10.1002/CM.20041

Yi, M., Niu, M., Xu, L., Luo, S., & Wu, K. (2021). Regulation of PD-L1 expression in the tumor microenvironment. *Journal of Hematology & Oncology 2021 14:1*, *14*(1), 1–13. https://doi.org/10.1186/S13045-020-01027-5

Ying, X., Chen, Q., Yang, Y., Wu, Z., Zeng, W., Miao, C., Huang, Q., & Ai, K. (2024). Nanomedicines harnessing cGAS-STING pathway: sparking immune revitalization to transform 'cold' tumors into 'hot' tumors. *Molecular Cancer 2024 23:1*, *23*(1), 1–43. https://doi.org/10.1186/S12943-024-02186-6

Yoon, H., Tang, C. M., Banerjee, S., Delgado, A. L., Yebra, M., Davis, J., & Sicklick, J. K. (2021). TGF-β1-mediated transition of resident fibroblasts to cancer-associated fibroblasts promotes cancer metastasis in gastrointestinal stromal tumor. *Oncogenesis 2021 10:2*, *10*(2), 1–12. https://doi.org/10.1038/s41389-021-00302-5

Yoshikawa, K., Ishida, M., Yanai, H., Tsuta, K., Sekimoto, M., & Sugie, T. (2021). Immunohistochemical comparison of three programmed death-ligand 1 (PD-L1) assays in triple-negative breast cancer. *PloS One*, *16*(9). https://doi.org/10.1371/JOURNAL.PONE.0257860

Yoshikawa, K., Ishida, M., Yanai, H., Tsuta, K., Sekimoto, M., & Sugie, T. (2021). Prognostic significance of PD-L1-positive cancer-associated fibroblasts in patients with triple-negative breast cancer. *BMC Cancer*, *21*(1), 1–10. https://doi.org/10.1186/S12885-021-07970-X/TABLES/5

You, T., Tang, H., Wu, W., Gao, J., Li, X., Li, N., Xu, X., Xing, J., Ge, H., Xiao, Y., Guo, J., Wu, B., Li, X., Zhou, L., Zhao, L., Bai, C., Han, Q., Sun, Z., & Zhao, R. C. (2023). POSTN Secretion by Extracellular Matrix Cancer-Associated Fibroblasts (eCAFs) Correlates with Poor ICB Response via Macrophage Chemotaxis Activation of Akt Signaling Pathway in Gastric Cancer. *Aging and Disease*, *14*(6), 2177. https://doi.org/10.14336/AD.2023.0503

You, Z., Chahwan, † Charly, Bailis, J., Hunter, T., & Russell, P. (2005). ATM Activation and Its Recruitment to Damaged DNA Require Binding to the C Terminus of Nbs1. *Molecular and Cellular Biology*, *25*(13), 5363. https://doi.org/10.1128/MCB.25.13.5363-5379.2005

Yu, K. X., Yuan, W. J., Wang, H. Z., & Li, Y. X. (2024). Extracellular matrix stiffness and tumor-associated macrophage polarization: new fields affecting immune exclusion. *Cancer Immunology, Immunotherapy : CII*, *73*(6), 115. https://doi.org/10.1007/S00262-024-03675-9

Yu, Y., Luo, K., Liu, M., Chen, L., Gao, X., Zhang, L., Li, X., & Zhang, H. (2024). Comprehensive analysis reveals that P4HA3 is a prognostic and diagnostic gastric cancer biomarker that can predict immunotherapy efficacy. *Scientific Reports 2024 14:1*, *14*(1), 1–15. https://doi.org/10.1038/s41598-024-73784-z

Yuan, S., Mu, W., Liu, S., Liu, M., Xia, Z., Liang, S., Gao, T., Fu, S., Liu, J., Huang, X., Liu, Y., & Zhang, N. (2023). Transforming Cancer-Associated Fibroblast Barrier into Drug Depots to Boost Chemo-Immunotherapy in "Shooting Fish in a Barrel" Pattern. *ACS Nano*, *17*(14), 13611–13626. https://doi.org/10.1021/ACSNANO.3C02272/SUPPL_FILE/NN3C02272_SI_001.PDF

Zagelbaum, J., & Gautier, J. (2023). Double-strand break repair and mis-repair in 3D. *DNA Repair*, *121*, 103430. https://doi.org/10.1016/J.DNAREP.2022.103430

Zannikou, M., Fish, E. N., & Platanias, L. C. (2024). Signaling by Type I Interferons in Immune Cells: Disease Consequences. *Cancers*, *16*(8), 1600. https://doi.org/10.3390/CANCERS16081600

Zeisberg, E. M., Potenta, S., Xie, L., Zeisberg, M., & Kalluri, R. (2007). Discovery of Endothelial to Mesenchymal Transition as a Source for Carcinoma-Associated Fibroblasts. *Cancer Research*, *67*(21), 10123–10128. https://doi.org/10.1158/0008-5472.CAN-07-3127

Zeng, Z., Lan, T., Wei, Y., & Wei, X. (2021). CCL5/CCR5 axis in human diseases and related treatments. *Genes & Diseases*, *9*(1), 12. https://doi.org/10.1016/J.GENDIS.2021.08.004

Zhang, B., Metharom, P., Jullie, H., Ellem, K. A. O., Cleghorn, G., West, M. J., & Wei, M. Q. (2004). The significance of controlled conditions in lentiviral vector titration and in the use of multiplicity of infection (MOI) for predicting gene transfer events. *Genetic Vaccines and Therapy*, *2*, 6. https://doi.org/10.1186/1479-0556-2-6

Zhang, C., Zhou, W., Xu, H., Xu, J., Li, J., Liu, X., Lu, X., Dai, J., Jiang, Y., Wang, W., Zhang, E., & Guo, R. (2025). Cancer-associated fibroblasts promote EGFR-TKI resistance via the CTHRC1/glycolysis/H3K18la positive feedback loop. *Oncogene 2025*, 1–15. https://doi.org/10.1038/s41388-025-03318-y

Zhang, D., Zhan, D., Zhang, R., Sun, Y., Duan, C., Yang, J., Wei, J., Li, X., Lu, Y., & Lai, X. (2024). Treg-derived TGF-β1 dampens cGAS-STING signaling to downregulate the expression of class I MHC complex in multiple myeloma. *Scientific Reports 2024 14:1*, *14*(1), 1–11. https://doi.org/10.1038/s41598-024-62298-3

Zhang, J., Lu, S., Lu, T., Han, D., Zhang, K., Gan, L., Wu, X., Li, Y., Zhao, X., Li, Z., Shen, Y., Hu, S., Yang, F., Wen, W., & Qin, W. (2023). Single-cell analysis reveals the COL11A1+ fibroblasts are cancer-specific fibroblasts that promote tumor progression. *Frontiers in Pharmacology*, *14*, 1121586. https://doi.org/10.3389/FPHAR.2023.1121586/FULL

Zhang, J., Tao, J., Gao, R. N., Wei, Z. Y., He, Y. S., Ren, C. Y., Li, Q. C., Liu, Y. S., Wang, K. W., Yang, G., Qian, C., & Chen, J. H. (2021). Cytotoxic T-Cell Trafficking Chemokine Profiles Correlate With Defined Mucosal Microbial Communities in Colorectal Cancer. *Frontiers in Immunology*, *12*, 715559. https://doi.org/10.3389/FIMMU.2021.715559/FULL

Zhang, X., Deng, Q., Wan, X., Zhao, J., Zheng, X., Wang, H., Wang, H. Q., & Yang, W. (2023). Pan-cancer analysis reveals the associations between MMP13 high expression and carcinogenesis and its value as a serum diagnostic marker. *Aging (Albany NY)*, *15*(6), 2115. https://doi.org/10.18632/AGING.204599

Zhang, X., Hong, B., Li, H., Zhao, J., Li, M., Wei, D., Wang, Y., & Zhang, N. (2024). Basement membrane-related MMP14 predicts poor prognosis and response to immunotherapy in bladder cancer. *BMC Cancer*, *24*(1), 1–13. https://doi.org/10.1186/S12885-024-12489-Y/FIGURES/6

Zhang, X. L., Hu, L. P., Yang, Q., Qin, W. T., Wang, X., Xu, C. J., Tian, G. A., Yang, X. M., Yao, L. L., Zhu, L., Nie, H. Z., Li, Q., Xu, Q., Zhang, Z. G., Zhang, Y. L., Li, J., Wang, Y. H., & Jiang, S. H. (2021). CTHRC1 promotes liver metastasis by reshaping infiltrated macrophages through physical interactions with TGF-β receptors in colorectal cancer. *Oncogene 2021 40:23*, *40*(23), 3959–3973. https://doi.org/10.1038/s41388-021-01827-0

Zhang, X., Zhao, H., Li, Y., Xia, D., Yang, L., Ma, Y., & Li, H. (2018). The role of YAP/TAZ activity in cancer metabolic reprogramming. *Molecular Cancer*, *17*(1), 1–10. https://doi.org/10.1186/S12943-018-0882-1/FIGURES/5

Zhang, Y. E. (2018). Mechanistic insight into contextual TGF-β signaling. *Current Opinion in Cell Biology*, *51*, 1. https://doi.org/10.1016/J.CEB.2017.10.001

Zhang, Y., & Ertl, H. C. J. (2016). Depletion of FAP+ cells reduces immunosuppressive cells and improves metabolism and functions CD8+T cells within tumors. *Oncotarget*, *7*(17), 23282. https://doi.org/10.18632/ONCOTARGET.7818

Zhang, Y., Guan, X. Y., & Jiang, P. (2020). Cytokine and Chemokine Signals of T-Cell Exclusion in Tumors. *Frontiers in Immunology*, *11*, 3093. https://doi.org/10.3389/FIMMU.2020.594609/BIBTEX

Zhang, Y., Wang, Y., Mu, P., Zhu, X., & Dong, Y. (2024). Bidirectional regulation of the cGAS-STING pathway in the immunosuppressive tumor microenvironment and its association with

immunotherapy. *Frontiers in Immunology*, *15*, 1470468. https://doi.org/10.3389/FIMMU.2024.1470468/BIBTEX

Zhang, Y., & Zhang, Z. (2020). The history and advances in cancer immunotherapy: understanding the characteristics of tumor-infiltrating immune cells and their therapeutic implications. *Cellular & Molecular Immunology 2020 17:8*, *17*(8), 807–821. https://doi.org/10.1038/s41423-020-0488-6

Zhang, Z., Ren, X., Wang, Y., Liu, P., Lin, P., Jin, S., & Xu, C. (2024). CTHRC1 is a prognostic biomarker correlated with immune infiltration in head and neck squamous cell carcinoma. *BMC Oral Health*, *24*(1), 742. https://doi.org/10.1186/S12903-024-04525-X

Zhang, Z.-G., Ouyang, G., Manoukian, P., Nl, M., Bijlsma, M., & Van Laarhoven, H. (2021). The Cellular Origins of Cancer-Associated Fibroblasts and Their Opposing Contributions to Pancreatic Cancer Growth. *Frontiers in Cell and Developmental Biology*, *9*, 743907. https://doi.org/10.3389/FCELL.2021.743907

Zhao, F., Kim, W., Kloeber, J. A., & Lou, Z. (2020). DNA end resection and its role in DNA replication and DSB repair choice in mammalian cells. *Experimental & Molecular Medicine 2020 52:10*, *52*(10), 1705–1714. https://doi.org/10.1038/s12276-020-00519-1

Zhao, J., Zhang, L., Lu, A., Han, Y., Colangelo, D., Bukata, C., Scibetta, A., Yousefzadeh, M. J., Li, X., Gurkar, A. U., McGowan, S. J., Angelini, L., O'Kelly, R., Li, H., Corbo, L., Sano, T., Nick, H., Pola, E., Pilla, S. P. S., … Robbins, P. D. (2020). ATM is a key driver of NF-κB-dependent DNA-damage-induced senescence, stem cell dysfunction and aging. *Aging*, *12*(6), 4688–4710. https://doi.org/10.18632/AGING.102863

Zhao, L., Wang, W., Niu, P., Luan, X., Zhao, D., & Chen, Y. (2022). The molecular mechanisms of CTHRC1 in gastric cancer by integrating TCGA, GEO and GSA datasets. *Frontiers in Genetics*, *13*, 900124. https://doi.org/10.3389/FGENE.2022.900124/BIBTEX

Zhao, Y. W., Ma, W., Jiang, F., Xie, Y., & Tang, L. (2022). Upregulation of matrix metalloproteinase 14 (MMP14) is associated with poor prognosis in renal clear cell carcinoma-a bioinformatics analysis. *Translational Andrology and Urology*, *11*(11), 1523–1534. https://doi.org/10.21037/TAU-22-619/COIF

Zhao, Z., Ding, H., Lin, Z. Bin, Qiu, S. H., Zhang, Y. R., Guo, Y. G., Chu, X. D., Sam, L. I., Pan, J. H., & Pan, Y. L. (2021). Relationship between Tertiary Lymphoid Structure and the Prognosis and Clinicopathologic Characteristics in Solid Tumors. *International Journal of Medical Sciences*, *18*(11), 2327. https://doi.org/10.7150/IJMS.56347

Zheng, H., Tan, J., Qin, F., Zheng, Y., Yang, X., Qin, X., & Liao, H. (2024). Analysis of cancer-associated fibroblasts related genes identifies COL11A1 associated with lung

adenocarcinoma prognosis. *BMC Medical Genomics*, *17*(1), 1–16. https://doi.org/10.1186/S12920-024-01863-1/FIGURES/10

Zheng, H., Wu, L., Xiao, Q., Meng, X., Hafiz, A., Yan, Q., Lu, R., & Cao, J. (2023). Epigenetically suppressed tumor cell intrinsic STING promotes tumor immune escape. *Biomedicine & Pharmacotherapy*, *157*, 114033. https://doi.org/10.1016/J.BIOPHA.2022.114033

Zheng, W., Liu, A., Xia, N., Chen, N., Meurens, F., & Zhu, J. (2023). How the Innate Immune DNA Sensing cGAS-STING Pathway Is Involved in Apoptosis. *International Journal of Molecular Sciences*, *24*(3), 3029. https://doi.org/10.3390/IJMS24033029

Zhong, R., Yang, M., Zhu, R., Zhang, J., & Wang, L. (2023). CTHRC1 is associated with immune cell infiltration and functions as an adverse marker for prognosis in head and neck squamous cell carcinoma. *Oncology Letters*, *25*(4), 133. https://doi.org/10.3892/OL.2023.13719

Zhou, G., Dada, L. A., Wu, M., Kelly, A., Trejo, H., Zhou, Q., Varga, J., & Sznajder, J. I. (2009). Hypoxia-induced alveolar epithelial-mesenchymal transition requires mitochondrial ROS and hypoxia-inducible factor 1. *American Journal of Physiology - Lung Cellular and Molecular Physiology*, *297*(6), L1120. https://doi.org/10.1152/AJPLUNG.00007.2009

Zhou, J., Zhuang, Z., Li, J., & Feng, Z. (2023). Significance of the cGAS-STING Pathway in Health and Disease. *International Journal of Molecular Sciences*, *24*(17), 13316. https://doi.org/10.3390/IJMS241713316

Zhou, T., Chou, J., Zhou, Y., Simpson, D. A., Cao, F., Bushel, P. R., Paules, R. S., & Kaufmann, W. K. (2007). ATM-dependent DNA damage checkpoint functions regulate gene expression in human fibroblasts. *Molecular Cancer Research : MCR*, *5*(8), 813. https://doi.org/10.1158/1541-7786.MCR-07-0104

Zhou, W., Ke, S. Q., Huang, Z., Flavahan, W., Fang, X., Paul, J., Wu, L., Sloan, A. E., McLendon, R. E., Li, X., Rich, J. N., & Bao, S. (2015). Periostin secreted by glioblastoma stem cells recruits M2 tumour-associated macrophages and promotes malignant growth. *Nature Cell Biology 2014 17:2*, *17*(2), 170–182. https://doi.org/10.1038/ncb3090

Zhu, G. Q., Tang, Z., Huang, R., Qu, W. F., Fang, Y., Yang, R., Tao, C. Y., Gao, J., Wu, X. L., Sun, H. X., Zhou, Y. F., Song, S. S., Ding, Z. Bin, Dai, Z., Zhou, J., Ye, D., Wu, D. J., Liu, W. R., Fan, J., & Shi, Y. H. (2023). CD36+ cancer-associated fibroblasts provide immunosuppressive microenvironment for hepatocellular carcinoma via secretion of macrophage migration inhibitory factor. *Cell Discovery 2023 9:1*, *9*(1), 1–22. https://doi.org/10.1038/s41421-023-00529-z

Zhu, J., & Thompson, C. B. (2019). Metabolic regulation of cell growth and proliferation. *Nature Reviews. Molecular Cell Biology*, *20*(7), 436. https://doi.org/10.1038/S41580-019-0123-5

Zhu, M., Tang, X., Zhu, Z., Gong, Z., Tang, W., Hu, Y., Cheng, C., Wang, H., Sarwar, A., Chen, Y., Liu, F., Huo, J., Wang, X., & Zhang, Y. (2023). STING activation in macrophages by vanillic acid exhibits antineoplastic potential. *Biochemical Pharmacology*, *213*, 115618. https://doi.org/10.1016/J.BCP.2023.115618

Zimna, A., & Kurpisz, M. (2015). Hypoxia-Inducible Factor-1 in Physiological and Pathophysiological Angiogenesis: Applications and Therapies. *BioMed Research International*, *2015*, 549412. https://doi.org/10.1155/2015/549412

Zitvogel, L., Galluzzi, L., Kepp, O., Smyth, M. J., & Kroemer, G. (2015). Type I interferons in anticancer immunity. *Nature Reviews Immunology 2015 15:7*, *15*(7), 405–414. https://doi.org/10.1038/nri3845

Zych, M. G., & Hatch, E. M. (2024). Small spaces, big problems: The abnormal nucleoplasm of micronuclei and its consequences. *Current Opinion in Structural Biology*, *87*, 102839. https://doi.org/10.1016/J.SBI.2024.102839